Metal isotopic fingerprinting of rock weathering and nutrient cycling along a climate and vegetation gradient

Dissertation

zur Erlangung des Grades eines
Doktors der Naturwissenschaften (doctor rerum naturalium)

am Fachbereich Geowissenschaften

der Freien Universität Berlin

vorgelegt von:
Ralf Andreas Oeser
Berlin 2020

Erstgutachter:	Friedhelm von Blanckenburg
Zweitgutachter:	Michaela Dippold
Tag der Disputation:	14.09.2020

Eidesstattliche Erklärung

Hiermit erkläre ich, dass ich diese Dissertation mit dem Titel *„Metal isotopic fingerprinting of rock weathering and nutrient cycling along a climate and vegetation gradient“* selbstständig und ohne unzulässige Hilfe verfasst habe. Bei der Verfassung dieser Dissertation wurden keine anderen, als die im Text und Literaturverzeichnis aufgeführten, Hilfsmittel und Quellen verwendet. Beiträge von Koautoren zu publizierten oder zur Publikation vorbereiteten Manuskripten sind im Vorwort (“Preface”) dieser Arbeit offen gelegt. Ich versichere, dass die vorgelegte elektronische mit der schriftlichen Version der Dissertation übereinstimmt. Ein Promotionsverfahren zu einem früheren Zeitpunkt an einer anderen Hochschule oder einem anderen Fachbereich wurde nicht beantragt.

Dresden, 25. Juni 2020

_____

Ralf Oeser

Danksagung

Diese Dissertation hat mir viel Spaß, Freude und schlaflose Nächte beschert. Ich möchte mich daher bei allen bedanken, die mich in dieser Zeit begleitet und einen noch so geringen Beitrag zu dieser Arbeit geleistet haben. Besonderer Dank gilt meinem Doktorvater Prof. Dr. Friedhelm von Blanckenburg. Vielen Dank für das Vertrauen und die Freiheit, meinen Forschungsschwerpunkt eigenständig zu entwickeln und die gleichzeitige wissenschaftliche Führung. Seine fachliche Betreuung, inspirierenden Diskussionen, und seine stetige Unterstützung waren eine große Hilfe in der Anfertigung dieser Arbeit. Ich danke ihm auch für den Antrag des DFG-Projektes "Biogenic weathering: opening the black box with new isotope systems and *in situ* mineral decomposition experiments (EarthShape – BioSoils)", der Deutschen Forschungsgemeinschaft (DFG) für die Förderung des Projektes (DFG-SPP 1803) sowie den WissenschaftlerInnen im "EarthShape" SPP für ihre Unterstützung.

Ich danke all meinen Kollegen der Sektion 3.3 "Geochemie der Erdoberfläche" des GFZ Potsdam für Seminare, Diksussionen und Bier (Daniel!). Besonders habe ich von den bestens in Schuss gehaltenen HELGES Laboren während meiner Zeit am GFZ profitiert. In diesem Sinne möchte ich Jutta Schlegel und Cathrin Schulz für ihre unermüdliche Arbeit in den Reinraumlaboren danken, ohne deren Hilfe so manche Arbeit schlicht nicht möglich gewesen wäre. Dr. Jan Schüssler, Dr. Daniel Frick und Josi Buhk danke ich für ihren exzellenten Support an der Neptune. Dank gebührt auch den unermüdlichen Korrekturlesern meiner Texte, Dr. Patrick J. Frings, Dr. Michael Henehan, Emma Lodes und Dr. Nicole Stroncik, für schnelles und unwiderrufliches löschen von "respectively" aus diesen Texten und anderen Verbesserungsvorschlägen. Und nicht zu vergessen, die gute Seele in unserer Sektion: Connie Dettlaff, die uns so manche lästige Arbeit abnimmt und immer für gute Laune im Sekretariat sorgt. Vielen Dank.

Abschließender Dank gebührt meiner Familie: Meinen Eltern und meinem Bruder Maik, die zwar nie verstanden haben, was ich "da" so mache, mich aber stets voll und ganz unterstützt haben. Meiner Lali, einst EarthShape Leidensgenossin während der Feldarbeit, dann Freundin, spätere Co-Autorin des ersten echten EarthShape Resultats - unserer Tochter Charlie - und jetzt Ehefrau dafür, dass sie mich immer geduldig unterstützt und mir stets den Rücken freigehalten hat. Nicht genug kann ich meinen beiden Frauen dafür danken, dass sie immer mehr oder weniger viel Verständnis dafür gezeigt haben, dass Papa Ral mal wieder keine Zeit zum kuscheln oder spielen hatte und mir immer wieder ein breites Lächeln ins Gesicht zaubern. Ohne Euch wäre diese Arbeit nicht möglich gewesen. Danke.

Summary

The Earth's Critical Zone ranges from deep, unweathered rock to the canopy of the highest trees and is the zone, where rock meets life. Physical, chemical, and biological processes shape this zone. Over timescales that can range from minutes to millennia, they form habitats for myriads of organisms. Weathering converts pristine rock into regolith (comprised of weathered rock, saprolite and soil) by means of inorganic and biogenic disintegration. These processes include physical and chemical alteration of rock and provide nutrients which are necessary to fulfill plants' physiological needs. Terrestrial plants act as a gigantic geochemical pump that continuously passes water and mineral-derived nutrients from the rooting zone towards the soil and the top of the canopy. In doing so, they directly and indirectly modulate the shape and architecture of the Critical Zone.

One widely accepted paradigm is that plants enhance weathering to constantly liberate nutrients by (1) mechanically weakening rock and regolith, (2) directing photosynthetic energy to soil microbiota, (3) increasing the solubility of minerals through acidification, and by (4) regulating surface runoff and water residence times at depth. Regardless of whether the resulting weathering serves to fulfill plant-physiological needs or is merely a side effect of the presence of plants, the question arises whether we can identify the geochemical imprints of plant nutrition. This is the central topic of this thesis. I focus on the below-ground geochemical characterization of four different ecosystems and of the associated above ground vegetation. I further use radiogenic and stable Sr isotopes as a proxy for mineral nutrient sources and geochemical mass balances to quantify the fluxes and sources from rock weathering into plants.

How the architecture and chemistry of the Critical Zone varies along a gradient of mean annual precipitation (MAP; 10 – 1100 mm yr^{-1}) and net primary productivity (NPP; 30 – 500 g_C m^{-2} yr^{-1}) was explored in the four "EarthShape: Earth Surface Shaping by Biota" (DFG-SPP 1803) study sites. These are situated along the Chilean Coastal Cordillera in arid (Pan de Azúcar), semi-arid (Santa Gracia), mediterranean (La Campana), and humid-temperate (Nahuelbuta) climate conditions. These sites were chosen to isolate the effect mean annual precipitation (MAP) and net primary productivity (NPP) and to minimize variability in confounding variables on weathering. Accordingly, all sites are underlain by granitoid rock and with roughly uniform rock uplift rates. In contrast, mantling soils range from poorly developed Regosol in the arid site to mature umbric Podzol in the humid-temperate site. Vegetation cover increases along this gradient from 5% to 100% ground cover and the prevailing plant species change from desert shrubs to deciduous and evergreen species. At all sites, I quantified the rate and the degree of chemical weathering, and hence the release and availability of mineral-derived nutrients to terrestrial ecosystems. Weathering rates are lowest in the arid and sparsely vegetated site and highest in the mediterranean site with almost complete vegetation cover. In the semi-arid and humid-temperate site however,

weathering rates are similar despite massive differences in MAP, NPP, and vegetation cover. A trend similar to that observed for weathering rate applies to the relative degree of chemical weathering among the four sites: It is lowest in the arid site and highest in the mediterranean site. Due to differences in mineralogy, however, the degree of chemical weathering in the semi-arid site is higher than in the humid-temperate site. Yet, at none of the sites the regolith is entirely depleted in its stock of primary minerals, such that mineral nutrients remain available for plant nutrition. The absence of statistically significant differences in the degree and rate of chemical weathering between the sites (excluding the arid Pan de Azúcar) does not allow for distinguishing the abiotic (purely climate-related) from the biotic (climate- and bio-related) drivers of weathering.

After quantifying the nutrient availability in these sites, I quantified their accessibility to plants and the fluxes into and out of the different ecosystems. These fluxes characterize the geogenic nutrient pathway (i.e. long-term nutrient supply through weathering) and the organic nutrient cycle (i.e. nutrient uptake by plants and subsequent recycling of leaf litter). Key to this characterization is knowledge of the weathering release fluxes, the size of the nutrient-reservoir available to plants, and a representative chemical composition of the ecosystem dominant plant taxa. The latter information is nearly impossible to acquire purely by means of sampling and chemical analysis of plants. Thus, I applied an allometric model which allocates relative growth rates between stems/ twigs and leaves to estimate bulk plants′ representative chemical composition. Bio-availability of most elements in soil, bar a few exceptions, increase from the arid to mediterranean site. However, despite featuring the thickest soils, element bio-availability is lowest in the humid-temperate site. The pattern of elemental release is rather uniform across the different climate regimes and levels of NPP, and so does not correlate with the size of the bio-available pool. In contrast, plants′ nutrient uptake rates increase in spite of the rather uniform weathering release rates from the semi-arid to the humid-temperate site. Hence, recycling rates (Rec^X) increase along this gradient and the ecosystems with high NPP maintain their nutrient supply by increasing recycling rather than increasing weathering. The organic nutrient pathway thus intensifies, whereas the geogenic nutrient pathway stays steady despite increasing MAP and NPP.

Weathering and ecosystem nutrition are intimately linked through the supply of fresh mineral nutrients from regolith and bedrock (i.e. the "geogenic nutrient pathway") that must replace any nutrient leakage. This link is muted if re-utilization of nutrients from plant litter during re-mineralization is efficient (i.e. the "organic nutrient cycle"). The shifting balance between these two cycles along the EarthShape climate and vegetation gradient was quantified by applying Sr isotope geochemistry in combination with mass balance calculations. Radiogenic and stable Sr isotope ratios as well as molar Ca/Sr ratios in the different compartments of the Critical Zone (bedrock, bulk regolith, the bio-available fraction being representative for regolith fluid, and vegetation) were measured to define the Sr sources and to quantify

its fluxes. Sr is released through weathering over the entire depth of the regolith profiles. This release is isotopically congruent and no shift in isotope ratios of the released Sr occurs during secondary mineral formation and its initial transfer into the bio-available pool. However, Sr contained in the bio-available fraction is isotopically heavier than in rock and regolith. The cause of this offset was found in the plants ability to fractionate Sr. Although $^{88}Sr/^{86}Sr$ in organs of plants at all four study sites systematically increases from roots towards their leaves, bulk plants preferentially take up Sr with low $^{88}Sr/^{86}Sr$. The shift in $^{88}Sr/^{86}Sr$ in the bio-available pool occurs after preferential uptake of isotopically light Sr into plants and its subsequent export in the form of fractionated organic solids (i.e. leaf litter) from the ecosystems. This export effectively diminishes the litter pool that is available for nutrient re-utilization and decreases the "net" nutrient recycling factor (Rec^X). Accordingly, Rec^X is essentially unaltered in the arid and semi-arid site where Sr export fluxes are low but shifts from 1 to almost zero recycling in the mediterranean site, and roughly halves recycling from 5 to 2 – 3 in the humid-temperate site.

The major outcomes of this thesis are that (1) Ecosystems exert a substantial control over weathering by both directly and indirectly modulating processes which either enhance or reduce weathering fluxes. The silicate-weathering fluxes become effectively decoupled from the ultimate nutrient demands of biota by intensifying the organic nutrient cycle; and (2) Organic solids proving a significant export path of elements released during weathering. This export potentially impairs the ability for direct nutrient (re-) acquisition from leaf litter and thus reduces the recycling factor.

Zusammenfassung

Die „Critical Zone“ (deutsch: Kritische Zone) der Erde reicht vom tiefen unverwitterten Gestein bis hin zum Blätterdach der höchsten Bäume und ist der Bereich der Erde, wo Gestein auf Leben trifft. Physikalische, chemische und biologische Prozesse formen die Critical Zone. Über Jahrtausende hinweg bilden diese Prozesse Lebensräume für unzählige Organismen. Frisches, unverwittertes Gestein wird durch anorganische und biogene Verwitterungsprozesse in Regolith (bestehend aus verwittertem Gestein, Saprolith und Boden) umgewandelt. Diese Prozesse umfassen die physikalische und chemische Veränderung des Gesteins und liefern die mineralischen Nährstoffe, die zur Erfüllung der physiologischen Bedürfnisse der Pflanzen erforderlich sind. An Land fungieren Pflanzen als gigantische geochemische Pumpen. Sie transportieren kontinuierlich Wasser und die aus Mineralen gewonnene Nährstoffe von der Wurzelzone in Richtung Boden und letztendlich auch in das Blätterdach. Dabei modulieren sie direkt und indirekt die Form und den Aufbau der Critical Zone.

Eine weit verbreitete Sichtweise besteht darin, dass Pflanzen die Verwitterung beschleunigen, um konstant Nährstoffe freizusetzen. Dies geschieht (1) durch die mechanische Schwächung von Gestein und Regolith; (2) indem gewonnene Energie aus der Photosynthese an Mikrobiota im Boden weitergegeben wird; (3) durch eine Erhöhung der Minerallöslichkeit aufgrund der durch Pflanzen hervorgerufenen Versauerung des Bodens; und (4) durch eine Erhöhung des Oberflächenabfluss und der Wasserverweilzeiten in der Tiefe. Unabhängig davon, ob die resultierende Verwitterung zur Erfüllung pflanzenphysiologischer Bedürfnisse dient oder lediglich eine Nebenwirkung des Vorhandenseins von Pflanzen ist, stellt sich die Frage, ob wir die geochemischen Fingerabdrücke der biogenen Verwitterung identifizieren können. Das ist das zentrale Thema dieser Arbeit, in der ich mich auf die geochemische Charakterisierung von vier verschiedenen Ökosystemen im Untergrund und der zugehörigen Vegetation darüber konzentriere. Zusätzlich verwende ich radiogene und stabile Sr-Isotope als Proxy für mineralische Nährstoffquellen und geochemische Massenbilanzen, um die Nährstoffflüsse und -Quellen ausgehend von der Verwitterung des Gesteins hin in die Pflanzen zu quantifizieren.

Die Veränderung des Aufbaus und der Chemie der Critical Zone entlang eines Gradienten mittleren Jahresniederschlags (MAP; $10-1100\,\mathrm{mm\,yr^{-1}}$) und netto Primärproduktion (NPP; $30-500\,\mathrm{g_C\,m^{-2}\,yr^{-1}}$) wurde in den vier „EarthShape: Earth Surface Shaping by Biota“ (DFG-SPP 1803) Standorten untersucht. Diese liegen entlang der chilenischen Küstenkordillere in aridem (Pan de Azúcar), semi-aridem (Santa Gracia), mediterranem (La Campana) und feucht-gemäßigtem (Nahuelbuta) Klima. Die Standorte wurden so gewählt, dass der Effekt von MAP und NPP auf Verwitterung isoliert betrachtet werden kann und der Einfluss von (geologischen) Störgrößen minimiert wird. Alle Standorte liegen in Gebieten mit ähnlichem Gestein (Granitoide) im Untergrund und in etwa gleichen Hebungsraten. Im Gegensatz dazu

reichen die darüber liegenden Böden von schlecht entwickeltem Regosol am ariden Standort bis hin zu reifem umbrischem Podzol am feucht-gemäßigten Standort. Die Vegetationsbedeckung nimmt entlang dieses Gradienten von 5% auf 100% zu, und die vorherrschenden Pflanzenarten wechseln von Wüstensträuchern zu laubwerfenden und immergrünen Arten. Die Raten und der Grad der chemischen Verwitterung und der damit verbundenen Freisetzung und Verfügbarkeit von mineralischen Nährstoffen für terrestrische Ökosysteme wurden an allen Standorten quantifiziert. Die Verwitterungsraten sind am ariden und dünn bewachsenen Untersuchungsgebiet am niedrigsten und am mediterranen Standort mit fast vollständiger Vegetationsbedeckung am höchsten. In den semiariden und feucht-gemäßigten Gebieten sind die Verwitterungsraten trotz massiver Unterschiede in MAP, NPP und der Vegetationsbedeckung ähnlich hoch. Ein ähnlicher Trend zeigt sich im Grad der chemischen Verwitterung zwischen den vier Standorten: Er ist am ariden Standort am niedrigsten und am mediterranen Standort am höchsten. Aufgrund von Unterschieden in der Mineralogie ist der Grad der chemischen Verwitterung im semiariden Untersuchungsgebiet allerdings höher als am feucht-gemäßigten Standort. An keinem der vier Standorte ist der Regolith vollständig in seinem Vorrat an unverwitterten Primärmineralien erschöpft. Das heißt, dass mineralische Nährstoffe aus Primärmineralen für die Pflanzenernährung verfügbar bleiben. Da keine statistisch signifikanten Unterschiede im Grad und den Raten der chemischen Verwitterung zwischen den verschiedenen Standorten (mit Ausnahme des ariden Pan de Azúcar) existieren, kann nicht zwischen abiotischen (rein klimabezogenen) und biotischen (klima- und biobezogenen) Treibern der Verwitterung unterschieden werden.

Nachdem ich die Nährstoffverfügbarkeit an diesen Standorten quantifiziert habe, bestimmte ich ihre Zugänglichkeit für Pflanzen und die Nährstoffflüsse in und aus den verschiedenen Ökosystemen. Diese Flüsse charakterisieren den „geogenen Nährstoffweg“ (d.h. die langfristige Nährstoffversorgung durch Verwitterung) und den „organischen Nährstoffkreislauf“ (d.h. Nährstoffaufnahme durch Pflanzen und anschließendes Recycling von Laub und anderer Pflanzenstreu). Der Schlüssel zu dieser Charakterisierung ist die Kenntnis der Verwitterungsfreisetzungsflüsse, der Größe des pflanzenverfügbaren Nährstoffreservoirs, und einer repräsentativen chemischen Zusammensetzung der Pflanzentaxa der jeweiligen Ökosysteme. Die letztgenannte Information lässt sich allerdings kaum allein durch Probenahme und die anschließende chemische Analyse von Pflanzen gewinnen. Daher habe ich ein allometrisches Modell angewendet, das die relativen Wachstumsraten zwischen Stämmen bzw. Zweigen und Blättern zuordnet. Somit konnte eine repräsentative chemische Zusammensetzung von Pflanzen abgeschätzt werden. Die Bioverfügbarkeit der meisten Elemente im Boden nimmt, bis auf wenige Ausnahmen, vom ariden zum mediterranen Standort zu. Trotz der mächtigsten Böden ist die Bioverfügbarkeit von Elementen am feucht-gemäßigten Standort am geringsten. Über die verschiedenen Klimaregime und Größenordnungen an Primärproduktion hinweg sind die Elementfreisetzungsmuster weitestgehend einheitlich. Sie korrelieren daher nicht mit der Größe des bioverfügbaren Nährstoffpools. Im Gegensatz

dazu nehmen die Raten, mit denen die Pflanzen ihre Nährstoffe aufnehmen trotz der relativ gleichmäßigen Verwitterungsraten vom semiariden bis zum feucht-gemäßigten Standort zu. Als Resultat steigen die Recyclingraten (Rec^X) entlang dieses Gradienten. Die Ökosysteme mit hoher Primärproduktion halten also ihre Nährstoffversorgung aufrecht, indem sie das Recycling und nicht die Verwitterung erhöhen. Somit intensiviert sich der organische Nährstoffkreislauf, während der geogene Nährstoffweg trotz steigendem Niederschlag und steigender Primärproduktion stabil bleibt.

Verwitterung und Ökosystemernährung sind eng miteinander verbunden. Um den steten Verlust mineralischer Nährstoffe auszugleichen, werden frische Nährstoffe durch Verwitterung von Gestein und Regolith zugeführt. Das ist der geogene Nährstoffweg. Dieser direkte Zusammenhang wird allerdings gekappt, wenn das Recycling von Nährstoffen aus Pflanzenstreu während der Remineralisierung effizient ist (der organische Nährstoffkreislauf). Mittels einer Kombination aus geochemischen Massenbilanzen und Sr-Isotopengeochemie wurde die Verschiebung des Gleichgewichts zwischen dem geogenen Nährstoffweg und dem organischen Nährstoffkreislauf entlang des EarthShape Klima- und Vegetationsgradienten detektiert und quantifiziert. Die Verhältnisse von radiogenem und stabilem Sr sowie molare Ca/Sr-Verhältnisse wurden in den verschiedenen Kompartimenten der Critical Zone (bestehend aus Gestein, Regolith, Bodenlösung und Vegetation) bestimmt und so die Sr-Quellen und seine Flüsse zwischen den einzelnen Kompartimenten detektiert und quantifiziert. Sr wird über die gesamte Tiefe der Regolithprofile durch Verwitterung freigesetzt. Diese Freisetzung ist isotopenkongruent. Das heißt, dass keine Verschiebung des Sr-Isotopenverhältnisses während der Bildung von Sekundärmineralen und dem initialen Übergang in die bioverfügbare Fraktion stattfindet. Trotzdem ist das in der bioverfügbaren Fraktion enthaltene Sr isotopisch schwerer als in Gestein und Regolith. Die Ursache für diesen Unterschied liegt in der Fähigkeit der Pflanzen Sr während der Aufnahme aus dem Boden zu fraktionieren. Obwohl $^{88}Sr/^{86}Sr$ in den Pflanzenorganen an allen vier Untersuchungsorten systematisch von den Wurzeln zu ihren Blättern zunimmt, wird von der Gesamtpflanze bevorzugt Sr mit einem niedrigen $^{88}Sr/^{86}Sr$ Verhältnis aufgenommen. Die Verschiebung von $^{88}Sr/^{86}Sr$ im bioverfügbaren Pool erfolgt nach bevorzugter Aufnahme von isotopisch leichtem Sr in die Pflanzen und dessen anschließendem Export in Form von fraktionierten organischen Feststoffen (zum Beispiel als Laubstreu) aus den Ökosystemen. Dieser Export verringert den zum Nährstoffrecycling zur Verfügung stehenden Pool und dem-entsprechend auch den Recyclingfaktor (Rec^X). An den ariden und semiariden Standorten, an denen der Sr-Export gering ist, bleibt Rec^{Sr} folglich nahezu unverändert. Im mediterranen Standort verringert sich Rec^{Sr} allerdings von 1 auf nahezu null und halbiert sich am feucht gemäßigten Standort von 5 auf in etwa 2 – 3.

Die wichtigsten Ergebnisse dieser Arbeit sind, dass (1) Ökosysteme eine wesentliche Kontrolle auf die Verwitterung ausüben, indem sie sowohl durch direkte als auch indirekte Prozesse, die

die Verwitterungsflüsse entweder anheben oder verringern. Die Verwitterung von Silikatmineralen wird letztendlich durch eine Intensivierung des organischen Nährstoffkreislaufes vom Nährstoffbedarf der Pflanzen entkoppelt. (2) Organische Feststoffe stellen einen wichtigen Exportweg von Elementen dar. Dieser Export beeinträchtigt möglicherweise die Fähigkeit zur direkten (Wieder-) Gewinnung von Nährstoffen aus Pflanzenstreu und verringert somit den Recyclingfaktor.

Preface

In this cumulative PhD thesis I present my research work in form of an introductory chapter and three further chapters. These are prepared as journal manuscripts and are either published or submitted to a scientific journal. Each individual chapter is thus prepared in a way that they can be read and understood separately. Therefore, some introductory information and methods' description is repeated in the individual chapters. Here, I briefly summarize the individual chapters and indicate the contribution of the co-authors.

- **Chapter 1** presents a general introduction on the architecture of the weathering zone, and on how and why plants enhance weathering. It includes a brief introduction into the EarthShape research framework and the four study sites. It provides an overview of the total and elemental mass fluxes into, from, and within ecosystems, and introduces the basic principles behind the radiogenic and stable Sr isotope system along with its application in Earth sciences.

- **Chapter 2** represents the first EarthShape baseline publication and focuses on the weathering zone. It aims to provide a detailed characterization of the Critical Zone geochemistry and the effect of climate and vegetation on weathering and microbial abundances in the Chilean Coastal Cordillera. This manuscript is published in *Catena Vol. 170*, pages 183-203 ("Chemistry and microbiology of the Critical Zone along a steep climate and vegetation gradient in the Chilean Coastal Cordillera" by **Ralf A. Oeser**, Nicole Stroncik, Lisa-Marie Moskwa, Nadine Bernhard, Mirjam Schaller, Rafaella Canessa, Liesbeth van den Brink, Moritz Köster, Emanuel Brucker, Svenja Stock, Juan Pablo Fuentes, Roberto Godoy, Francisco Javier Matus, Rómulo Oses Pedraza, Pablo Osses McIntyre, Leandro Paulino, Oscar Seguel, Maaike Y. Bader, Jens Boy, Michaela A. Dippold, Todd A. Ehlers, Peter Kühn, Yakov Kuzyakov, Peter Leinweber, Thomas Scholten, Sandra Spielvogel, Marie Spohn, Kirstin Übernickel, Katja Tielbörger, Dirk Wagner, and Friedhelm von Blanckenburg; doi.org/10.1016/j.catena.2018.06.002)

  This chapter provides a first interpretation of a comprehensive geochemical data set and addresses how climate and vegetation cover influence weathering, microbial abundance, and mineral nutrient supply to the different ecosystems along the Chilean Coastal Cordillera. It was shown that an increase in denudation rates from north to

south coincides with increasing mean annual precipitation (MAP) and vegetation cover. Denudation rates are highest in the mediterranean site of La Campana, where hillslopes are steepest. Further south in Nahuelbuta, where MAP and vegetation cover are highest, these rates are lower than in La Campana. Chemical depletion and microbial abundances are low in the arid and sparsely vegetated site Pan de Azúcar. In the three sites located further south, no significant difference exists in terms of chemical depletion and microbial abundance. Thus, no clear trend of chemical depletion and microbial abundance with increasing MAP and vegetation cover was discovered. It was further shown that although a difference in soil thickness between the north- and the south-facing slopes exists, the expected differences in the degree of chemical weathering between the two adjacent slopes could not be chemically resolved.

This chapter was conducted within the framework of the DFG-SPP 1803 "EarthShape - Earth surface shaping by biota". Friedhelm von Blanckenburg and Todd Ehlers designed the study and chose the study sites. Fieldwork was conducted by Lisa-Marie Moskwa, Nadine Bernhard, and me. Preparation and analysis of most samples were done by Nicole Stroncik and me. Mirjam Schaller provided soil denudation rates. Microbial abundances and pedogenic oxides were determined by Lisa-Marie Moskwa and Moritz Köster, respectively. Friedhelm von Blanckenburg and I interpreted data and wrote the manuscript with input from all co-authors. This manuscript was reviewed by two anonymous reviewers.

- **Chapter 3** reports on the nutrient fluxes from rock and regolith which are made available for plant uptake through weathering. It presents the links between rock weathering and nutrient supply to plants along a gradient of precipitation and NPP on the Chilean Coastal Cordillera. This chapter has been submitted to *Biogeosciences Discussions* ("Do degree and rate of silicate weathering depend on plant productivity?" by **Ralf A. Oeser** and Friedhelm von Blanckenburg; doi.org/10.5194/bg-2020-69) and undergoes a process of open discussion and review since early March 2020.

  This chapter builds on the previous chapter in so much as the focus of this research was set to be the determination of the element fluxes in the so called "geogenic nutrient pathway" and the "organic nutrient cycle". The geochemical data set obtained in Chapter 2 (Oeser et al. 2018a) was complemented with bulk chemical analysis of plants and the determination of the bio-available fraction in saprolite and soil. Regarding the four EarthShape sites it was shown that despite a steep north-south gradient in MAP and NPP no such a gradient exists in weathering rates and -intensity. It was thus concluded that the ecosystems with high NPP maintain their nutrient supply by increasing recycling rather than increasing biogenic weathering. In other words, the "organic nutrient cycle" intensifies from north to south, whereas the "geogenic nutrient pathway" stays steady despite increasing MAP and NPP.

This chapter was conducted within the framework of the DFG-SPP 1803 "EarthShape - Earth surface shaping by biota". Friedhelm von Blanckenburg is the sole co-author. He designed the study and selected the study sites. Further, he interpreted data and wrote text. I conducted field sampling, analyzed samples, interpreted data and wrote text.

- **Chapter 4** reports on the release of Sr from rock and regolith through weathering, uptake by plants, and its subsequent loss from the ecosystem using radiogenic and stable Sr isotopes. This chapter has been submitted to *Chemical Geology* ("Element release and cycling in the Critical Zone along a climate and vegetation gradient from Sr radiogenic and stable isotope ratios"). Co-author is Friedhelm von Blanckenburg.

  This chapter completes the geochemical data set of the four EarthShape study sites and the focus of this research was the application of Sr isotopes in combination with mass balance calculations to quantify how the balance between the "geogenic nutrient pathway" and the "organic nutrient cycle" shifts along the EarthShape climate and primary production gradient in the coastal mountains of Chile. Radiogenic and stable Sr isotopes as well as molar Ca/Sr ratios in the different compartments of the Critical Zone (bedrock, bulk regolith, the bio-available fraction being representative for regolith fluid, and vegetation) were determined to detect the Sr sources and quantify its fluxes. Sr release through weathering was found to be isotopically congruent and the isotope ratios of the released Sr do not shift during secondary mineral formation and Sr transfer into the exchangeable pool, respectively. However, Sr contained in the bio-available fraction is higher than its $^{88}Sr/^{86}Sr$ ratio in rock and regolith. The cause of this offset was found in plants: While $^{88}Sr/^{86}Sr$ in the plant organs at the four sites systematically increases from roots towards their leaves, bulk plants preferentially take up Sr with a low $^{88}Sr/^{86}Sr$. An estimate of whole-plant Sr isotope composition revealed that the shift in the bio-available Sr must occur after preferential uptake of isotopically light Sr into plants and its subsequent export as fractionated organic solids from the ecosystems. This export provides further evidence for organic solids proving a significant export path of elements released during weathering. Thus, this export potentially impairs the ability for direct Sr acquisition from leaf litter and thus, reduces the recycling factor of Sr and possibly of other mineral nutrients.

  This chapter was conducted within the framework of the DFG-SPP 1803 "EarthShape - Earth surface shaping by biota". Friedhelm von Blanckenburg is the sole co-author. He designed the study and selected the study sites. He further interpreted data and wrote text. I conducted field sampling, analyzed samples, interpreted data and wrote text.

List of Figures

1.1 Vertical structure of the weathering zone in a sloping landscape and weathering end-member settings. . . . 2
1.2 Isotope ratios as source tracer . . . 12
1.3 Stable isotope fractionation . . . 14
1.4 Vegetation formations in Chile . . . 16
1.5 The EarthShape climate and vegetation gradient . . . 17

2.1 Intrusion age and spatial extension of the granitoid rocks in the EarthShape study sites . . . 23
2.2 Mean annual temperature and precipitation. . . . 24
2.3 Photographs of the S-facing mid slope regolith profile in Pan de Azúcar . . . 25
2.4 Photographs of the S-facing mid slope regolith profile in Santa Gracia . . . 27
2.5 Photographs of the S-facing mid slope regolith profile in La Campana . . . 29
2.6 Photographs of the S-facing mid slope regolith profile in Nahuelbuta . . . 30
2.7 Classification diagrams for siliceous igneous and volcanic rocks. . . . 37
2.8 Depth-dependent major element composition . . . 38
2.9 Weathering trends in the ternary space of A–CN–K and A–CNK–FM . . . 39
2.10 Ti and Zr concentration measured in soil, saprolite, and bedrock. . . . 40
2.11 Chemical Depletion Fraction (CDF). . . . 41
2.12 Elemental mass transfer coefficient (τ). . . . 42
2.13 Volumetric strain (ε). . . . 43
2.14 Al and Fe concentrations of the pedogenic oxide fraction relative to total sample concentration. . . . 45
2.15 Concentration of extracted DNA, averaged over the entire sampled saprolite depth. . . . 46
2.16 Abundance of bacterial and archaeal 16S rRNA gene copy numbers per gram of regolith . . . 47
2.17 Mixing model between average Na and Mg concentrations of Nahuelbuta saprolites and andesitic ash. . . . 50

3.1 Variations in D, NPP, plant cover, MAP, and W along the EarthShape transect. . 75

3.2 Conceptual framework of the CZ. 80
3.3 Chemical depletion fraction (CDF) 81
3.4 Chemical weathering flux vs. ecosystem uptake fluxes 83
3.5 Radiogenic Sr ratios 87
3.6 P-normalized element composition in bulk plants and the bio-available fraction. 90
A3.1 Tau values 107
A3.2 Bio-available fraction 108
A3.3 Bio-available fraction of total 109
A3.4 Chemical weathering flux, ecosystem nutrient-uptake fluxes, and nutrient recycling factors corrected for atmospheric deposition 110

4.1 Radiogenic and stable Sr isotope composition, Pan de Azúcar 144
4.2 Radiogenic and stable Sr isotope composition, Santa Gracia 145
4.3 Radiogenic and stable Sr isotope composition, La Campana 146
4.4 Radiogenic and stable Sr isotope composition, Nahuelbuta 147
4.5 Sr isotope fractionation during uptake by plants 158
4.6 Sr isotope box model in the weathering zone 161
4.7 Sr loss fraction 162
4.8 Dependency of e_{org}^{Sr} 165

List of Tables

S2.1 Catena properties. 57
S2.2 Major and Trace elemental composition bedrock samples. 58
S2.3 Modal bedrock composition. 59
S2.4 Regolith chemistry 60
S2.4 ...continuation 61
S2.4 ...continuation 62
S2.4 ...continuation 63
S2.5 Weathering indizes CDF, CIA, τ, and ε. 64
S2.6 Chemical weathering and physical erosion rates. 65
S2.7 Relative microbial abundances in the four study areas. 65

3.1 Study-site characteristics 73
3.2 Glossary of metrics 82
3.3 Elemental fluxes fluxes. 84
3.4 Inventories. 85
3.5 Ecosystem chemistry. 86
3.6 $^{87}Sr/^{86}Sr$ isotope ratios 88
3.7 Nutrient recycling factor. 91
3.8 Turnover times. 93
A3.1 Pearson's correlation coefficients entire study area 104
A3.2 Pearson's correlation coefficients w/o La Campana 105
A3.3 ANOVA 106
S3.1 Bedrock composition. 113
S3.2 Weathering indizes & radiogenic $^{87}Sr/^{86}Sr$ ratio. 114
S3.2 ...continuation 115
S3.2 ...continuation 116
S3.2 ...continuation 117
S3.3 Bio-available fraction. 118
S3.3 ...continuation 119
S3.3 ...continuation 120
S3.3 ...continuation 121

S3.4 Sequential extractions. 122
S3.4 ...continuation 123
S3.4 ...continuation 124
S3.4 ...continuation 125
S3.5 Plant chemical composition. 126
S3.5 ...continuation 127

4.1 Chemical characterization and Sr isotopic data. 139
4.1 ...continuation 140
4.1 ...continuation 141
4.1 ...continuation 142
4.2 Plant chemical composition. 148
4.2 ...continuation 149
4.2 ...continuation 150
4.2 ...continuation 151
4.3 Sr isotopic composition & Ca/Sr ratio 155
4.4 D, NPP, inventories, and & residence times. 164
A4.1 Elemental fluxes. 169

Contents

List of Figures xi

List of Tables xiii

1 Introduction 1
1.1 Four reasons why plants accelerate weathering . . . 3
1.2 How are the biological and geological fluxes linked? . . . 5
1.3 Research question and main objectives . . . 6
1.4 Geochemical background and methods . . . 7
1.4.1 Total mass loss fluxes in the Critical Zone, the degree of weathering . . 7
1.4.2 Elemental mass fluxes in the Critical Zone . . . 8
1.4.3 Representative chemical mineral nutrient contents of plants . . . 8
1.4.4 Sequential extractions . . . 9
1.4.5 Strontium and its isotopes . . . 10
1.5 Introduction to the "EarthShape" study area . . . 15

2 Chemistry and microbiology of the Critical Zone along a steep climate and vegetation gradient in the Chilean Coastal Cordillera 18
2.1 Introduction . . . 20
2.2 Study area . . . 22
2.2.1 Geological and climatic conditions . . . 22
2.2.2 Critical Zone description . . . 24
2.3 Material and analytical methods . . . 31
2.3.1 Sampling . . . 31
2.3.2 Bedrock and regolith geochemistry . . . 32
2.3.3 Cosmogenic ^{10}Be in Quartz . . . 33
2.3.4 DNA extraction and quantification of 16S rRNA gene copies . . . 33
2.3.5 Calculation of weathering indicators and denudation rates . . . 34
2.4 Results . . . 36
2.4.1 Chemical and mineralogical bedrock composition and classification . . 36
2.4.2 Regolith chemistry and weathering patterns . . . 37

2.5 Discussion . . . 47
2.5.1 The continental trend . . . 48
2.5.2 The local trend: N-facing versus S-facing hillslopes . . . 51
2.5.3 The in-situ trend: vertical structure of the weathering zone . . . 52
2.5.4 Is the biogenic weathering engine discernable? . . . 53
2.6 Conclusions . . . 54
2.7 Supplementary material . . . 56

3 Do degree and rate of silicate weathering depend on plant productivity? 66
3.1 Introduction . . . 68
3.2 Conceptual perspectives . . . 70
3.3 Study area and previous results . . . 72
3.4 Methods . . . 76
3.4.1 Sampling . . . 76
3.4.2 Analytical methods . . . 77
3.4.3 Parameterizing geogenic and biogenic element fluxes in a terrestrial ecosystem . . . 79
3.5 Results . . . 79
3.5.1 Element fluxes contributing to the geogenic nutrient pathway . . . 80
3.5.2 Availability of mineral nutrients to plants . . . 83
3.5.3 Plant element composition and nutrient-uptake fluxes . . . 84
3.5.4 $^{87}Sr/^{86}Sr$ isotope ratios . . . 87
3.6 Discussion . . . 89
3.6.1 The source of mineral nutrients . . . 89
3.6.2 An increase in nutrient recycling with NPP . . . 90
3.6.3 Processes that set the size of the bio-available pool . . . 91
3.6.4 Concepts for biotas role in setting fluxes in the geogenic and the organic nutrient cycle . . . 93
3.6.5 Is weathering modulated by biota? A statistical analysis . . . 95
3.6.6 Do negative feedbacks decouple biomass growth from weathering rate and degree? . . . 97
3.7 Conclusions . . . 99
3.8 Appendices . . . 100
3.9 Supplementary material . . . 112

4 Element release and cycling in the Critical Zone along a climate and vegetation gradient from Sr radiogenic and stable isotope ratios 128
4.1 Introduction . . . 130
4.2 Study area and previous results . . . 132
4.3 Methods . . . 134

4.3.1 Sampling 134
4.3.2 Analytical methods 135
4.4 Results 137
4.4.1 Element concentrations 137
4.4.2 Sr isotope ratios 138
4.5 Discussion 152
4.5.1 Strontium isotopes in the weathering zone 152
4.5.2 Strontium isotope and Ca/Sr fractionation by plants during uptake and translocation 156
4.5.3 A lost Sr flux 159
4.6 Conclusion 166
4.7 Appendices 167

References **171**

CHAPTER 1

Introduction

Imagine a zone that ranges from the top of the vegetation canopy down to unweathered bedrock (Fig. 1.1a). This cross section of the Earth's outermost rim features a complex mixture of air, water, biota, and geologic materials, encompassing soils and terrestrial ecosystems. This zone has become to be known as the "Critical Zone" (e.g. Amundson et al. 2007; Brantley et al. 2006; 2007; Lin 2010a), the essential playground for a multitude of ecosystem processes.

Physical, chemical, and biological processes shape the Critical Zone and form, over timescales which can range from minutes to millennia, a habitat for myriads of organisms. Weathering converts pristine rock into "regolith" (comprised of weathered rock, saprolite and soil; Scott and Pain 2008) by means of inorganic and biogenic disintegration. These processes include physical and chemical alteration of rock. The physical processes increase the rocks' specific surface and thereby their susceptibility to chemical weathering. The processes of chemical alteration involve the dissolution of primary minerals and the partitioning of their constituents into solutes and secondary solids such as clay minerals and (amorphous) oxyhydroxides. The rate at which chemical weathering occurs is primarily set by the kinetic and thermodynamic properties of primary mineral dissolution, precipitation of secondary materials, and their chemical equilibrium which depends on the flow of undersaturated water (Maher 2010; Maher and Chamberlain 2014; White and Brantley 2003; Winnick and Maher 2018). It is secondarily set by the rate of supply of unweathered primary minerals into the "weathering reactor" by the combination of uplift, deposition, and erosion.

Minerals contain nutrients, which are necessary to fulfill the plants' physiological needs. The relevance of these elements can be divided into two main groups: plant-essential and plant beneficial elements (Marschner 1993). The former set of nutrients comprise elements that are necessary for plants to complete their life cycle, are directly involved in plant metabolism, and cannot be functionally replaced by any other element. This set of nutrients is further partitioned into micro-nutrients and macro-nutrients. Micro-nutrients (e.g. B, Cu, Fe, Zn) are predominantly cofactors of enzymes and are hence only needed in low abundance.

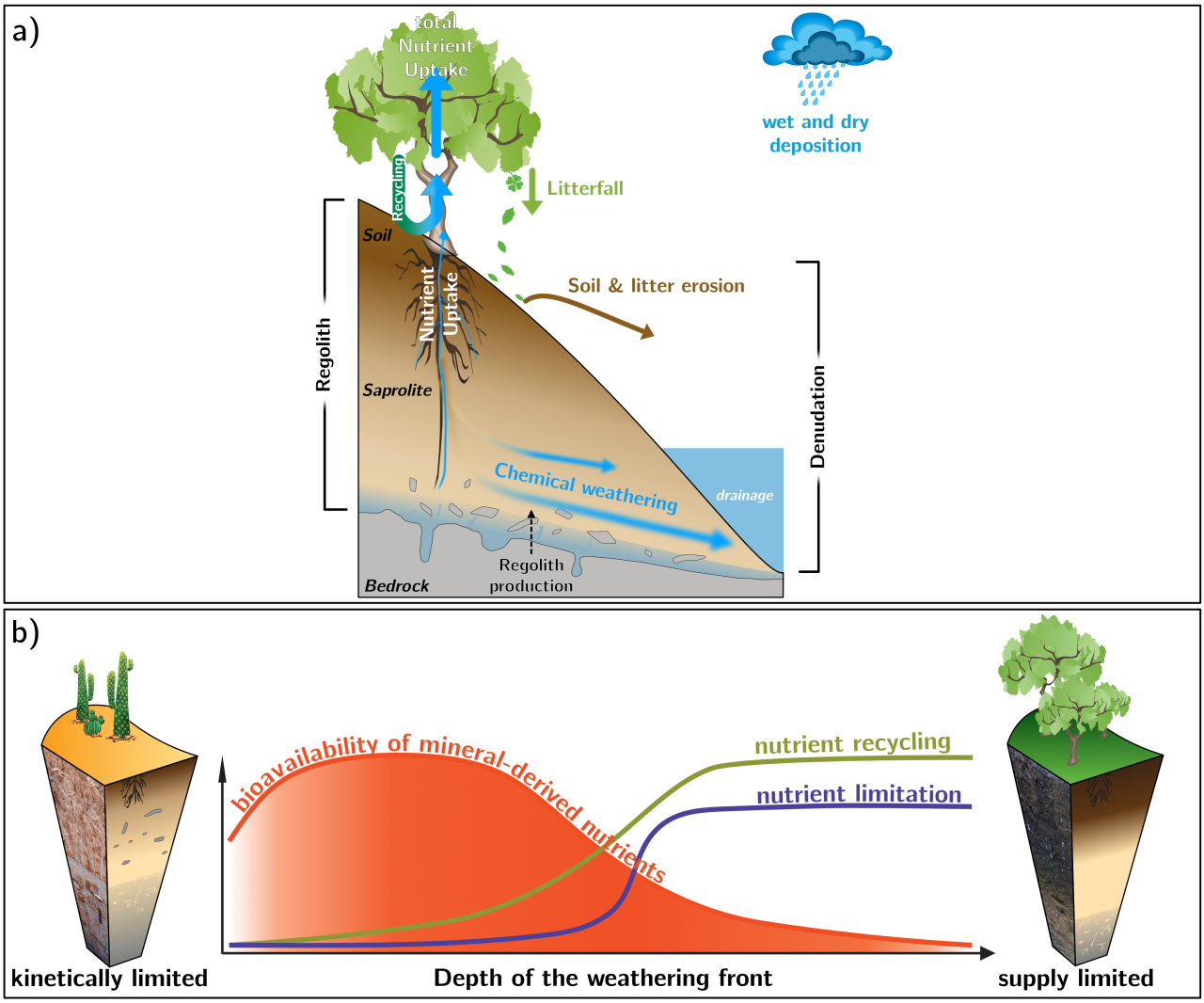

Figure 1.1: a) Sketch of the vertical structure of the weathering zone in a sloping landscape. Bedrock is transformed in regolith (comprised of saprolite and soil) through abiotic (purely chemical) and biogenic weathering. Plants acquire their essential nutrients through uptake from weathering-solutes, recycling, as well as wet and dry deposition. In steady state the rate at which regolith is produced from below equals its denudation in the form of solids and solutes. **b)** Weathering end-member settings. In the kinetically limited weathering regime (left) erosion is sufficiently high such that weatherable minerals exist throughout and the weathering rate is limited by mineral-dissolution kinetics. Ecosystems acquire their nutrients primarily from weathering. In the supply limited weathering regime (right) all weatherable minerals that cross the weathering front are dissolved and the depth of the weathering front is high. Ecosystems fulfill their nutrient demand through recycling.

In contrast, macro-nutrients (e.g. Ca, K, N, Mg, P, S) are contained in organic compounds (e.g. proteins and nucleic acids) and are thus needed in higher abundance. Plant-beneficial elements are those that compensate for the toxic effects of other elements or substitute for elements and cover some of their less-specific functions (e.g. maintaining osmotic pressure; Al, Na, Si). However, whether an element is essential or beneficial to plants is

species dependent (Marschner 1993). Throughout this thesis, I refer to the elements Al, Fe, Na, and Si as plant-beneficial, and to Ca, K, Mg, Mn, and P as plant-essential elements. Although Sr is not a plant-essential element itself, I will include it in this latter group due to its similar (bio-) chemical behavior to Ca (e.g. Blum et al. 2012; Faure and Powell 1972; Faure and Mensing 2005; Poszwa et al. 2002). These mineral nutrients are either liberated from local (weathering of bedrock and regolith) or external sources (atmospheric wet and dry deposition) prior their uptake by plants.

1.1 Four reasons why plants accelerate weathering

Terrestrial plants act as a gigantic geochemical pump that continuously passes water and mineral-derived nutrients from the rooting zone towards the soil and the top of their canopy (e.g. Jasechko et al. 2013; Jobbágy and Jackson 2004; Sterner and Elser 2003). In doing so, they directly and indirectly modulate the shape and architecture of the Critical Zone (Balogh-Brunstad et al. 2008a; Pawlik et al. 2016; Roering et al. 2010; van Breemen et al. 2000). One widely accepted paradigm is that they enhance weathering to constantly liberate essential and beneficial elements. For many elements these fluxes are much larger than those contained in river runoff and plants can thus be seen as the largest geochemical agents on Earth (Amundson et al. 2007). Several main reasons exist how and why plants accelerate weathering:

(1) Roots increase regolith thickness. Plant roots penetrate regolith along preexisting pathways and potentially extend fractures as well as detach and disaggregate rock. Roots provide mechanical support, serve as energy storage, and transport solutes contained in water. Further, fine roots absorb water along with plant-essential and plant-beneficial elements from soil solution (e.g. Adams et al. 2013; Eissenstat et al. 2015; Pawlik et al. 2016), ultimately facilitating nutrient uplift and their accumulation in the soil horizons (e.g. Jobbágy and Jackson 2004). In supply-limited weathering regimes, plants have developed deep-rooting systems which can acquire nutrients from depth at the weathering front. They do so by e.g. exuding organic acids from growing cluster roots (see next paragraphs, and e.g. Lambers et al. 2008; 2019) and through fine roots that penetrate bedrock by several meters along joints and fracture planes (Hasenmueller et al. 2017). In the kinetically-limited weathering regime, roots increase chemical weathering rates by enhancing moisture fluxes along roots and within root channels, and they further increase the rocks′ specific surface area as a result of mechanical weakening (Pawlik 2013; Pawlik et al. 2016; Roering et al. 2010). As a result, the bare physical existence of roots triggers a large array of physico-chemical processes which have a profound effect on weathering and regolith deepening.

(2) Soil microbiota direct photosynthetic energy from plants to minerals and organic matter to enhance nutrient liberation. Soil microbiota (i.e. bacteria and mycorrhizal fungi) play an essential role in releasing nutrients from primary minerals and their cycling between soil and plants (e.g. Andrino et al. 2019; Bonneville et al. 2009; Calvaruso et al. 2006; Landeweert et al. 2001; Quirk et al. 2012; Uroz et al. 2009; 2011) and it has been suggested that plants and their associated microbiota accelerate silicate weathering by a factor of 1.5 to < 10 (Berner et al. 2003). Although direct evidence of bacterial induced mineral weathering has been shown recently (Frey et al. 2010), the role of arbuscular mycorrhizal (AM) and ectomycorrhizal mycorrhizal (EM) fungi in intensifying mineral weathering has been known for a longer time (e.g. Jongmans et al. 1997; van Breemen 1998). Mycorrhizal fungi associate with roots, where they trade photosynthetically produced carbohydrates from trees for water and nutrients. The fungal hyphae attach directly to the mineral surfaces (e.g. Bonneville et al. 2011; Landeweert et al. 2001) and alter the crystal structure, reduce ferric (Fe^{3+}) iron to ferrous iron (Fe^{2+}), and lower the pH at the interface of hyphae and minerals (Bonneville et al. 2011). At the hyphal tips, low-molecular weight organic anions (Jongmans et al. 1997) and organic chelates (e.g. oxalate; van Scholl et al. 2006a) are exuded, aiding to penetrate minerals and generate microsites ("mineral tunnelling") which are else inaccessible to plant roots. Nutrients dissolved by the mycorrhizal fungi potentially bypass the bio-available fraction and are directly transported to the fungal host plant (van Breemen et al. 2000). In doing so, mycorrhizal fungi increase silicate weathering and prevent nutrients from being eroded as solutes. The rapid formation of such tunnels has been shown by e.g. Boy et al. (2014) studying biotite and muscovite grains after two years of exposure to the roots and mycorrhizal fungi of a *Nothofagus antarctica*. This fungal mineral tunneling can increase weathering by a factor of 3 and more (van Scholl et al. 2006b) and contribute up to 50% of total mineral weathering in podzols (van Breemen et al. 2000).

(3) Plants increase the solubility of primary minerals through acidification of the rhizosphere. Plants directly modify the pH in the rhizosphere by excreting protons (H^+), hydroxyl ions (OH^-), or through the respiratory release of CO_2. In doing so, they can lower the pH by more than 2.5 pH units (Lucas 2001). Mineral dissolution rates at the rhizosphere are thus greatly enhanced through ionic exchange (release of H^+ for e.g. Ca^{2+}, K^+, Mg^{2+}) and additional excretion of organic chelates which form soluble complexes with Al, Fe and other metals (Berner et al. 2003). Of particular importance in plant-induced mineral weathering is the excretion of CO_2 into soil. Biologically derived CO_2 in soil exceeds atmospheric pCO_2 by several orders of magnitude (Brantley et al. 2011b) and forms carbonic acid (H_2CO_3). In turn, the equilibrium elemental solubility is increased which results in higher dissolution rates of primary carbonate and silicate minerals (e.g. Amundson et al. 2007; Berner et al. 2003; Winnick and Maher 2018).

(4) Terrestrial plants regulate surface runoff and water residence times at depth. Plants exert a major control on the regional and local scale hydrological cycle by modifying evapo-transpiration (ET) and total runoff (e.g. Drever and Zobrist 1992; Kelly et al. 1998; Ibarra et al. 2019). The uptake of water by plants has two main effects on the local hydrological cycle, the reduction of surface runoff and an increase in water residence times at depth (Lucas 2001). Whereas the former effect would result in decreased surface erosion rates (E), the latter effect allows for an increase in the degree of mineral weathering (Maher and Chamberlain 2014). Roots might have a larger effect on mineral weathering if they provide preferential flow-paths deep into the regolith down to the weathering front. In settings where water is a limited resource, plants develop functional roots at greater depth (Fan et al. 2017), thus maintaining extraction of water and nutrients over most of the growing season (Brantley et al. 2017). This constant removal of solutes in turn allows for a continuous flow of undersaturated water at the weathering front. Further, deep-rooting plants provide means of plant access to groundwater, which would otherwise be shielded from evapotranspiration (Boyce and Lee 2017; Lee and Boyce 2010), thus enabling an increase in water flow and hence total weathering fluxes (Ibarra et al. 2019).

1.2 How are the biological and geological fluxes linked?

Conceptual models describe the relationship between weathering and ecosystem functioning. They either emphasize the role of erosion and hence nutrient supply by landscape rejuvenation for ecosystem nutrition (Buendía et al. 2010; Porder et al. 2007), or account for a coupled weathering – uptake – recycling system which links the biological nutrient cycle with the largely geological and hydrological driven cycle fostering mineral nutrient inputs to and outputs from terrestrial ecosystems (Powers et al. 2015; Vitousek et al. 1998). The latter models have recently been adapted for geochemistry (Uhlig and von Blanckenburg 2019). In these, the so-called "organic nutrient cycle" comprises a set of strategies for efficient nutrient re-utilization through microbial mineralization from plant litter and organic matter and requires rapid nutrient turnover. However, these nutrients are permanently lost via plant litter erosion (Heartsill Scalley et al. 2012; Scatena and Lugo 1995) or are exported as solutes after litter and root decomposition (Baskaran et al. 2017; Chaudhuri et al. 2007; Moore et al. 2005; Silver and Miya 2001). Despite this constant mass removal, soils cover approximately 95% on Earth's terrestrial surface. Hence, over geologic timescales a delicate balance between regolith production and erosion exists during which the weathering zone is constantly rejuvenated by supply of fresh minerals. The rate and degree of rock weathering controls the release, distribution, and cycling of mineral nutrients at the Earth's surface. This cycling controls how ecosystems develop and how they are sustained (acquiring vs. recycling ecosystems; Lang et al. 2016; Wilcke et al. 2002).

In eroding landscapes, two distinct weathering end member settings can be defined (Fig. 1.1b), namely the kinetically limited (e.g. Dixon and von Blanckenburg 2012; Schoonejans et al.

2016; West et al. 2005) and the supply limited weathering regime (e.g. Arens and Kleidon 2011; Dixon et al. 2009a; Hewawasam et al. 2013; Riebe et al. 2004; Schuessler et al. 2018; West et al. 2005). Kinetically limited weathering regimes are encountered in mountainous landscapes in which uplift and erosion rates are at a sufficiently fast, such that unweathered primary minerals exist throughout the regolith. In these settings, the weathering flux W is thus limited by the kinetics of mineral dissolution. In such settings the concentration of elements low in solubility like Si are likely in equilibrium with respect to primary mineral dissolution and secondary mineral formation (Maher and Chamberlain 2014). In this regime plants can take up mineral nutrients predominantly from soil solutions and are per se not required to actively foster the advance of the weathering front at depth to obtain sufficient mineral nutrients. They might still however increase weathering rates. Supply limited weathering regimes are typically found in moderately sloping or flat landscapes under both humid temperate and humid tropical climate regimes. They are located in tectonically relatively quiescent landscapes, where uplift and erosion rates are either low or absent. Thus, weatherable primary minerals that eventually pass through the weathering front face sufficiently long soil residence times, such that chemical weathering results in complete dissolution. In order to maintain their physiological needs, plants thus efficiently recycle nutrients (e.g. Schuessler et al. 2018; Turner et al. 2018; Uhlig and von Blanckenburg 2019). Some of these nutrients, however, are constantly lost via erosion of organic material or by its dissolution through chemical weathering and subsequent drainage. Hence, plants need to replace these nutrients by dissolving fresh primary minerals at or close to the weathering front nevertheless; unless they rely on external (e.g. atmospheric) inputs.

1.3 Research question and main objectives

Above I have presented four mechanisms on how plants might accelerate, or at least facilitate weathering. Regardless of whether the resulting weathering serves to fulfill plant-physiological needs or is merely a side effect of the presence of plants, the question arises whether we can identify the geochemical imprints of plant nutrition. My thesis is focused on the below-ground geochemical characterization of four different ecosystems situated in arid, semi-arid, mediterranean, and humid-temperate climate conditions. My first research question is whether a profound contrast in the chemistry and architecture of the Critical Zone in these four ecosystems exists that is linked to the prevailing differences in mean annual precipitation (MAP), mean annual air temperature (MAT), solar radiation, and as a result vegetation cover. The second question is whether plants exert an additional control to liberate plant-essential and plant-beneficial elements from rock to sustain their physiological needs, and if the increase in net primary productivity (NPP) from the arid to the humid-temperate site is accommodated by additional nutrient supply from weathering or an intensified organic nutrient cycle. My final question is what the plants' nutrient sources are and through which pathway they are lost after plant uptake.

To answer these questions, I make use of a comprehensive geochemical toolbox. It is comprised of: (1) Methods to determine the elemental composition of bulk rock and regolith samples and a novel approach to determine the representative elemental composition (i.e. stoichiometry) in plants from analysis of stem, twig and leaf samples. Hence, it enables the determination of weathering pattern and element fluxes in the Critical Zone; (2) Sequential extractions on bulk regolith samples to assess the accessibility of nutrients to plants; and (3) Radiogenic and stable Sr isotopes to determine the source of Sr as a proxy for mineral nutrients and to identify how Sr is lost once taken up by plants.

1.4 Geochemical background and methods

1.4.1 Total mass loss fluxes in the Critical Zone, the degree of weathering

The vertical structure of a weathering profile is illustrated in Fig. 1.1a. Such a profile is typically comprised of unweathered parent bedrock at its base, which is overlain by regolith. At steady state, the rate at which bedrock is transformed into regolith, i.e. the regolith production rate (RP), is coupled to the weathering profile's total mass loss (i.e. denudation, D; e.g. Heimsath et al. 1997; Lebedeva et al. 2010), such that a constant regolith thickness is maintained over time. Total denudation involves the mass losses as particulate matter (physical erosion, E) and in dissolved form (chemical weathering, W):

$$D = E + W \tag{1.1}$$

To derive average "landscape lowering rates" of entire ecosystems, catchment-average concentrations of cosmogenic nuclides such as *in-situ* ^{10}Be produced in quartz (see e.g. von Blanckenburg and Willenbring 2014, for the underlying physical principles) are measured in bedload sediment sampled at the outlet of a watershed (e.g. Granger and Riebe 2014; Norton et al. 2011; Riebe et al. 2004; van Dongen et al. 2019; von Blanckenburg 2005; Wittmann et al. 2011; 2020). Typically, these rates are reported in either length per time (e.g. mm kyr^{-1}) or mass per area per time (t km^{-2} yr^{-1}) and integrate over timescales of about 10^3 to 10^5 years. Mass losses in dissolved form and as solids can be disentangled from total denudation fluxes by quantifying the degree of chemical depletion in regolith. To calculate the relative mass losses in regolith caused by chemical weathering the chemical depletion fraction (CDF; Riebe et al. 2003) is used:

$$\mathrm{CDF} = 1 - \frac{[X_i]_{\mathrm{parent}}}{[X_i]_{\mathrm{weathered}}}. \tag{1.2}$$

It relates the concentration of a refractory element during weathering reactions (e.g. Zr, Nb, Ti; Chadwick et al. 1990; White et al. 1998) in unweathered parent material to its concentration in weathered regolith. These elements are hosted in inert minerals (e.g. rutile,

zircon) and are thus, enriched in regolith whereas more soluble elements are dissolved and exported as solutes (Brimhall and Dietrich 1987). Total chemical weathering fluxes (W) are calculated from the denudation rate (D) using the chemical depletion fraction (CDF) by

$$W = D \times CDF. \tag{1.3}$$

The subsequent calculation of the erosion flux E is straightforward from Eq. 1.1.

1.4.2 Elemental mass fluxes in the Critical Zone

Total mass fluxes can be converted into elemental mass fluxes. The magnitude of these fluxes differs from element to element and are thus of particular interest in the case of nutrients. By assuming steady state (meaning that regolith thickness is constant over the method integration timescale), the rate at which element X is released from rock by weathering (RP^X) at the weathering front is identical to its loss over the entire regolith profile ($RP \equiv D$) such that

$$RP^X = D \times [X], \tag{1.4}$$

where [X] denotes the concentration of the element of interest in unweathered rock. Like the calculation of total chemical weathering fluxes (Eq. 1.3, elemental chemical weathering fluxes ($W^X_{regolith}$) are calculated by multiplying the elemental regolith production rate RP^X with the negative of the elements' fractional loss from regolith:

$$W^X_{regolith} = D \times [X]_{parent} \times \left(-\tau^X_{X_i}\right). \tag{1.5}$$

To estimate this relative loss, the elemental mass transfer coefficient (τ; Anderson et al. 2002; Brimhall and Dietrich 1987) is used:

$$\tau^X = \frac{[X]_{weathered}}{[X]_{parent}} \times \frac{[X_i]_{parent}}{[X_i]_{weathered}} - 1. \tag{1.6}$$

As the τ-value accounts for the formation of secondary weathering products as well, $W^X_{regolith}$ represents the net flux of dissolved elements in the weathering zone.

1.4.3 Representative chemical mineral nutrient contents of plants

To accurately determine the plants' representative chemical composition, I applied a general allometric model that predicts the relationships among annual leaf, stem, and root biomass production. This approach was necessary because entire plants, including roots and the full canopy could normally not be sampled in the field nor chemically digested in its entirety. In this model, the scaling exponents for annual growth rates of leaves, stem, and roots (GL, GS, and GR, respectively) are analytically determined (see Niklas and Enquist 2002; Poorter et al. 2012, for a detailed review on allometric theory) and result in dimensionless organ growth quotients GL/GS (leaf growth relative to stem growth) and GL/GR (leaf growth relative to

root growth). These quotients equal the respective allometric constants and are used to empirically calculate the relative percentage of leaf, stem, and root growth on a plant's total annual growth.

The sampling and analysis of roots was excluded because of the difficulties that arise in associating the roots to a specific plant. During elemental analysis this difficulty is further compounded by the need to remove any remaining soil particles or attached precipitates that might bias measured concentrations. However, several prerequisites allow for the estimation of the plants' chemical composition: (1) Roots' biomass growth attribute only little to total plant growth, namely 9% in angiosperms and 17% in gymnosperms (Niklas and Enquist 2002). Thus, roots and stems/ twigs were treated as one plant compartment. The pooled relative growth of root, stem, and twig amounts to 68% and 52% in angiosperms and gymnosperms, respectively. (2) Differences in biomass allocation and relative growth are only relevant between angiosperms and gymnosperms ant not between single plant species of a given class. (3) The pattern of relative growth and standing biomass allocation holds true across a minimum of eight orders of magnitude of species size (Niklas and Enquist 2002).

Finally, the single species' average chemical or isotopic composition was weighted in accordance with their relative abundance to derive the average plant composition per ecosystem.

1.4.4 Sequential extractions

Sequential extraction methods are commonly applied on sediment and regolith samples to determine the degree of anthropogenic heavy metal contamination (e.g. As, Co, Pb, Mo, U, Zn; Bacon et al. 2006; Hall et al. 1997; Rauret et al. 1999; Stone and Droppo 1996). Similarly, these methods are used in environmental studies to assess the mobile fraction of nutritive elements that are available for ecosystem nutrition (e.g. in the bio-available fraction; Uhlig and von Blanckenburg 2019). In this thesis I applied a modified sequential extraction procedure following the methods described in Arunachalam et al. (1996), He et al. (1995), and Tessier et al. (1979) to determine the depth distribution of plant-beneficial (Al, Fe, Na, Si) and plant-essential (Ca, K, Mg, Mn, P; Marschner 1983) elements together with Sr in the readily bio-available fraction. Generally, this procedure comprises a set of five extraction steps with each step releases elements that are progressively bound more strongly to bulk regolith: (1) the water soluble fraction, (2) the exchangeable fraction, (3) the acid soluble fraction, (4) the reducible fraction, and (5) the oxidizable fraction. These steps thus reflect the increasing effort a plant must exert to access any given nutrient from bulk regolith.

Steps (1) and (2) comprise the readily bio-available fraction: The water-soluble fraction constitutes the most labile compartment in regolith and is most accessible to plants (He et al., 1995). It contains water-soluble species which are made up of free ions and ions which are complexed with soluble organic matter. The amount of nutrients being released with demonized water (in this thesis I used 18 MΩ Milli-Q H_2O), however is limited (review by

Filgueiras et al. 2002, and references therein) and re-adsorption of very insoluble elements is likely (Rauret et al. 1999). The exchangeable fraction comprises elements forming weak electrostatic bonds between the hydrated surfaces of phyllosilicates (e.g. clays and micas), oxyhydroxide minerals (e.g. boehmite, diaspore, goethite, lepidocrocite, ferrihydrite), and organic matter, respectively. Thus, these elements are either extracted by salt solutions of replaceable cations (e.g. $CaCl_2$, $MgCl_2$, $NaNO_3$) or by changing the ionic strength of the sample solution with ammonium salts (e.g. NH_4OAc), chloride salts (e.g. $MgCl_2$), or nitrate salts (e.g. $NaNO_3$; Arunachalam et al. 1996; Filgueiras et al. 2002; Krishnamurti et al. 1995; Stone and Droppo 1996). In this thesis I used 1 M NH_4OAc to extract the exchangeable fractions for two reasons. First, NH_4OAc prevents re-adsorption or precipitation of the extraction ions (Filgueiras et al. 2002). Second, although 0.01 M NH_4OAc is most frequently used to extract this fraction, the use of 1 M NH_4OAc facilitates an extraction efficiency that is four times higher (Arunachalam et al. 1996).

1.4.5 Strontium and its isotopes

Strontium is an alkaline earth element of group IIA in the periodic table of elements and is in the same group with Be, Mg, Ca, Ba, and Ra. With approximately 350 µg g^{-1}, Sr belongs to the most abundant trace elements in the upper continental crust (Taylor and McLennan 1995) and is partitioned as trace element in many (bio-) geochemical processes affecting minerals, water, and vegetation (e.g. reviews by Blum and Erel 2003; Bullen 2014; Shand et al. 2009). Sr shares chemical properties like charge and ionic radius with Ca (Sr = 1.13 Å vs. Ca = 0.99 Å; Faure and Powell 1972). Consequently, it appears as trace element in Ca-bearing minerals such as plagioclase, apatite, and carbonates. However, substitution is restricted by the fact that Sr ions favor eight-fold coordinated sites, whereas Ca ions are incorporated in six- and eight-fold coordinated lattice sites. Occasionally, Sr^{2+} ions are even able to replace K^+ in coupled substitutions ($K^+ + Si^{4+} \rightleftharpoons Sr^{2+} + Al^{3+}$).

Strontium has four naturally occurring stable isotopes ^{84}Sr (83.913426 u), ^{86}Sr (85.909265 u), ^{87}Sr (86.908881 u), and ^{88}Sr (87.905617 u) with natural relative abundances of 0.56 at.%, 9.86 at.%, 7.00 at.%, and 82.58 at.%, respectively (Audi and Wapstra 1993; De Biévre and Taylor 1993). ^{87}Sr is a so-called radiogenic isotope. It is being produced over geologic time by the radioactive decay of ^{87}Rb ($\lambda_{87} = 1.3972 \pm 0.0045 \times 10^{-11}$ yr^{-1}; Villa et al. 2015) to ^{87}Sr. Any mass-dependent isotope fractionation during chemical or biochemical reactions of the $^{87}Sr/^{86}Sr$ ratio is eliminated during analysis by normalizing to a fixed $^{88}Sr/^{86}Sr$ ratio of 8.375209 (Nier 1938).

Applications of the radiogenic Sr isotope ratio

Three main applications of the $^{87}Sr/^{86}Sr$ isotope ratio exist in geochemistry. First, the Rb-Sr system is used as one of the oldest and well-established isotope geochronometers (e.g. Bowen 1994; Hedge and Walthall 1963). Rb and Sr are structurally bond into the crystal lattice during mineral formation. With time the amount of ^{87}Sr increases by decay of ^{87}Rb. This increase is proportional to the Rb/Sr ratio, forming the basis of dating rocks using the isochron method (Capo et al. 1998). Hence older rocks, particularly those with high Rb/Sr ratios tend to have larger variations between different minerals and higher $^{87}Sr/^{86}Sr$ ratios than younger rocks (e.g. Bowen 1994; Faure and Powell 1972).

Second, the radiogenic $^{87}Sr/^{86}Sr$ isotope ratio is widely used in geological studies as a source tracer (e.g. Dasch 1969; Faure and Hurley 1963; Faure and Powell 1972, Fig. 1.2). The basic principles behind this are straightforward and are based on the differences in the Rb/Sr ratio between different substrates (i.e. minerals and rocks; Capo et al. 1998; Faure and Powell 1972). The variations in $^{87}Sr/^{86}Sr$ strictly result from the beta decay of ^{87}Rb to ^{87}Sr at a rate at which the $^{87}Sr/^{86}Sr$ ratio of a given reservoir changes is sufficiently slow that today these changes are not discernible, be that mineral, rock, soil, or atmospheric dust, and the ratio can be considered as constant and is only affected by mixing processes. Accordingly, radiogenic Sr isotope ratios have been used to quantify magma mixing and incorporation of country rocks (e.g. Civetta et al. 1991; Taylor 1980), magma mixing (e.g. Ginibre and Davidson 2014), and by e.g. Boy and Wilcke (2008), Chen et al. (2007), Grousset et al. (1992), Grousset and Biscaye (2005), Kumar et al. (2014), Scheuvens et al. (2013), and Zhao et al. (2018) to determine the key source areas of Saharan and Asian dust. In catchment-wide studies, the $^{87}Sr/^{86}Sr$ isotope ratio is used to explore mixing proportions of dissolved Sr, labile or soil exchangeable Sr, and plant utilized Sr from endmembers such as carbonate and silicate bedrock, as well as atmospheric dry and wet deposition (e.g. Åberg 1995; Aciego et al. 2017; Andrews et al. 2016; Bain and Bacon 1994; Bélanger and Holmden 2010; Bélanger et al. 2012; Blum et al. 2002; Chadwick et al. 1999; Graustein and Armstrong 1983; Miller et al. 1993; Pett-Ridge et al. 2009a;b; Reynolds et al. 2012).

Third, $^{87}Sr/^{86}Sr$ ratios are being used to constrain quantitative models of chemical weathering in rock (Clow et al. 1997) and soil (Åberg et al. 1989; Stewart et al. 1998). This application requires a substrate (e.g. rock) that is composed of minerals that differ in their Sr concentration, $^{87}Sr/^{86}Sr$ ratio, and dissolution kinetics. Hence, incongruent weathering of primary minerals and subsequent regolith formation result in differences in $^{87}Sr/^{86}Sr$ between bedrock and regolith (Blum and Erel 1997), and also between bedrock and the released dissolved Sr. Principles two and three are the foundation of the most recent application of radiogenic Sr isotopes in ecological studies. Although Sr is not a plant-essential nutrient itself, over the last 30 years, the use of $^{87}Sr/^{86}Sr$ isotope ratios has emerged as an important isotopic tool to determine the sources (e.g. atmospheric deposition or mineral weathering)

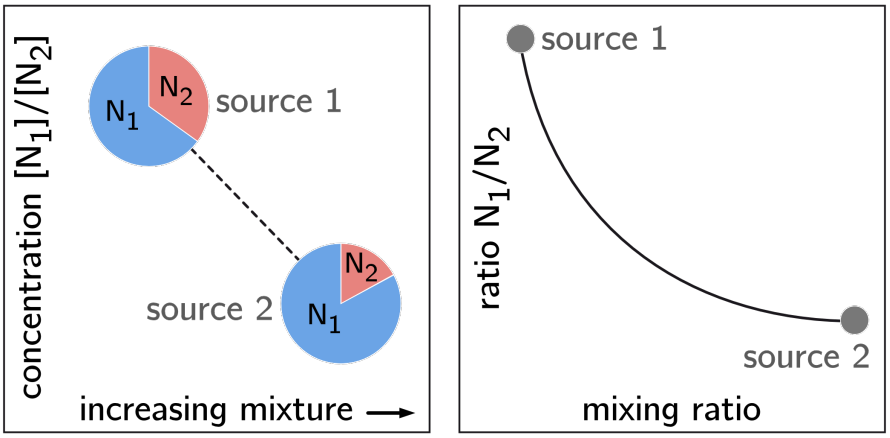

Figure 1.2: Sketch of the physical principles behind the use of isotope ratios N1/N2 as source tracer (a) and the dependence of isotope abundance on the mixing ratio (b). Modified from von Blanckenburg (2017)

of the plant-essential nutrient Ca from the soil pit to the catchment scale (e.g. Åberg et al. 1990; Bailey et al. 1996; Bélanger and Holmden 2010; Bullen and Bailey 2005; Capo et al. 1998; Graustein and Armstrong 1983; Graustein 1989; Meek et al. 2016; Pett-Ridge et al. 2009a). Like Ca, Sr is taken up through the Ca^{2+} channels of the root plasma membrane (White et al. 1998) into plants and has thus been used as a direct proxy for Ca movement from rock or dust to soil water into plants across different climatic, vegetation, and geologic settings (e.g. Åberg et al. 1990; Bailey et al. 1996; Chadwick et al. 1999; Dasch et al. 2006; Miller et al. 1993; Vitousek et al. 2010). Likewise, the two elements behave similarly during ion exchange on clay minerals and organic matter (Appelo and Postma 2004; Blum et al. 2008) and Sr is thus used to estimate the depth of Ca uptake by forest trees (e.g. Poszwa et al. 2002; McCulley et al. 2004).

In plants, however, these two geochemically similar elements are actively discriminated against each other. The active discrimination and the preferential transport of Ca over Sr within plants has been reported by numerous studies in e.g. beech and spruce (Poszwa et al. 2000), beech and oak (Drouet et al. 2007), and for the foliar and floral tissues in *R. ferrugineum* and *Vaccinium* (de Souza et al. 2010). One explanation for this increase is the preferential xylem transport from root to leaves of Ca over Sr. Sr can be re-mobilized from leaves, however, and this transport is via the phloem. A second explanation is thus Sr re-mobilization from leaves to other plant organs (review by Burger and Lichtscheidl 2019) combined with phloem-immobility of Ca (e.g. Clarkson 1984). Such Sr re-mobilization would result in the observed gradients in molar Ca/Sr despite similar behavior during transport in the xylem.

Applications of the stable Sr isotope ratio

In addition to the radioactive decay of Rb, the relative abundance of Sr isotopes is affected by mass-dependent isotope fractionation during physico-chemical and biological processes. Only recently have developments in modern Multicollector Inductively Coupled Plasma (MC-ICP-MS) and Double Spike Thermal Ionization Mass-Spectrometry (Fietzke and Eisenhauer 2006; Krabbenhöft et al. 2010; Neymark et al. 2014; Ohno et al. 2008) established the stable Sr isotope ratio (expressed as $\delta^{88/86}$Sr in permil, ‰) as a process tracer to monitor a broad range of geological and biological processes (e.g. de Souza et al. 2010; Halicz et al. 2008; Krabbenhöft et al. 2010; Neymark et al. 2018; Raddatz et al. 2013; Shalev et al. 2013). The strontium isotope system is unique in that its isotope composition records analytically resolvable information about a) the source of Sr (from its ^{87}Sr/^{86}Sr ratio), and b) the biogeochemical processes transferring Sr from one compartment to the other (from the associated mass-fractionation its ^{88}Sr/^{86}Sr ratio has experienced).

Any small differences in behavior of the isotopes during these processes are expressed relative to a well-characterized reference material. The $\delta^{88/86}$Sr value of a sample is calculated relative to the ^{88}Sr/^{86}Sr ratio of the NIST SRM 987 carbonate standard:

$$\delta^{88/86}\mathrm{Sr} = \left[\frac{\left(\frac{^{88}\mathrm{Sr}}{^{86}\mathrm{Sr}}\right)_{\mathrm{sample}}}{\left(\frac{^{88}\mathrm{Sr}}{^{86}\mathrm{Sr}}\right)_{\mathrm{SRM\text{-}987}}} - 1 \right] \tag{1.7}$$

These differences are commonly expressed in the ‰ (per mil) notation by multiplying the left-hand term in Equation 1.7 by 1000. $\delta^{88/86}$Sr values of most terrestrial rocks occupy a narrow range between 0.20‰ and 0.35‰ (e.g. Moynier et al. 2010) and only a few Ca-rich rock types (e.g. limestone, dolomite) yield negative values of $\delta^{88/86}$Sr up to –0.42‰ (review by Hajj et al. 2017). To date, the understanding and magnitude of stable Sr isotope fractionation during weathering, soil formation and ecological processes is very limited and restricted to a few studies. These have shown that little (Chao et al. 2015; Stevenson et al. 2016) to no isotope fractionation occurs during weathering of silicate rock (de Souza et al. 2010). However, a significant offset in $\delta^{88/86}$Sr values between initial substrate (i.e. rock and regolith) and waters draining rivers has been reported (Andrews et al. 2016; Neymark et al. 2014).

Various processes are known that can fractionate Sr isotopes, including (biogenic) carbonate precipitation (Fietzke and Eisenhauer 2006; Krabbenhöft et al. 2010; Raddatz et al. 2013; Stevenson et al. 2014; Widanagamage et al. 2015), clay formation (Halicz et al. 2008; Pearce et al. 2015a; Shalev et al. 2013; Wei et al. 2013), and plant uptake (de Souza et al. 2010). Sr isotope fractionation during Sr translocation in plants was described by de Souza et al. (2010) for Sr in a glaciated watershed. The authors report on preferential uptake of light ^{86}Sr from soil solution and the subsequent depletion of heavy ^{88}Sr along the plants' transpiration

stream. This isotope fractionation was accompanied by a systematic increase in the molar Ca/Sr ratio from the roots to the shoots. Intriguingly, this fractionation upon allocation from root to leaves is opposite to that described for the isotopes of the chemically similar element Ca (e.g. Page et al. 2008; Wiegand 2005). It is thus speculated that the sites at which Ca and Sr are being segregated within plants are also those that fractionate the isotopes of Sr and Ca.

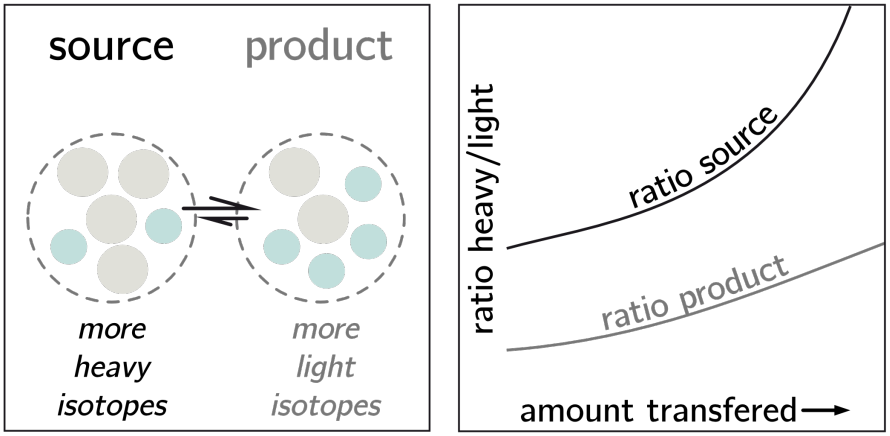

Figure 1.3: Sketch of the physical principles of stable isotope fractionation (left) and the dependency of the isotope ratio to the transferred amount (right). Modified from von Blanckenburg (2017).

Essentially, these isotope-segregating effects can be separated into equilibrium and kinetic effects. The former effects are reversible and temperature-dependent, relying on the dependency of bond strengths on atomic mass (Fig. 1.3a). A study by Widanagamage et al. (2014) suggests that, at least during precipitation from aqueous solutions the Sr isotopic fractionation is controlled by kinetic effects. These effects are based on fast, incomplete or unidirectional processes such as evaporation, diffusion, or non-equilibrium forward reactions during breaking of bonds or attachment of Sr to surfaces (Fig. 1.3b). The magnitude of Sr isotope fractionation between two compartments is expressed by the isotope fractionation factor:

$$\alpha_{a-b} = \frac{1000 + \delta^{88/86}Sr_A}{1000 + \delta^{88/86}Sr_B}. \tag{1.8}$$

Isotope mass balance models allow for the quantification of processes associated with isotope fractionation (e.g. Bouchez et al. 2013; Bullen and Chadwick 2016). The flux-based model of the weathering zone (i.e. 'the Bouchez model'; Bouchez et al. 2013) can be applied to the stable Sr isotope system. Importantly, these models require steady-state (i.e. incoming mass fluxes balance outgoing fluxes), and can e.g. be used to quantify the export of Sr as fractionated solid from the weathering zone:

$$\frac{\delta^{Sr}_{rock} - \delta^{Sr}_{diss}}{\Delta^{Sr}} = \frac{E^{Sr}_{org}}{S^{Sr}_{org} + S^{Sr}_{prim}}, \tag{1.9}$$

where the equation's right-hand term represents the fraction of Sr export (E^{Sr}_{org}) relative to its supply by weathering from rock (S^{Sr}_{rock}) at the weathering front and from remaining primary minerals in regolith (S^{Sr}_{prim}).

In this thesis I apply radiogenic and stable Sr isotope geochemistry to three of the compartments in the Critical Zone: (1) bulk bedrock and regolith, (2) the bio-available fraction in saprolite and soil (being representative for regolith fluid), and (3) in bulk plant samples. Bulk plant refers to whole plant Sr isotope ratios (estimated as described above for the plants' representative chemical composition), in contrast to these ratios in single plant organs (i.e. stem, twig, leaf), respectively. I applied radiogenic Sr isotopes in two ways. First, I determined the amount of atmospheric deposition into the study sites by employing a two-endmember mixing calculation using the $^{87}Sr/^{86}Sr$ of rock and sea spray. Second, I used the $^{87}Sr/^{86}Sr$ ratio as a conservative source tracer to identify the nutrient uptake depths of plants. To this end, the $^{87}Sr/^{86}Sr$ ratio in the bio-available fraction is compared with that ratio in living plant tissues. I applied stable Sr isotopes to quantify the various degrees of Sr export from ecosystems in arid, semi-arid, mediterranean, and humid-temperate climate. Further, I expanded the model of Sr isotope fractionation by and within plants introduced by de Souza et al. (2010) and highlight possible sites of Sr isotope fractionation within plants. Sr isotopes are measured on a multi collector inductively coupled plasma mass spectrometer (MC-ICP-MS) after sample digestion and subsequent purification by cation chromatography.

1.5 Introduction to the "EarthShape" study area

The research for this thesis was conducted within the framework of the "EarthShape: Earth Surface Shaping by Biota" priority program of the Deutsche Forschungsgemeinschaft (DFG-SPP 1803). In this research network, scientists from different disciplines (e.g. Ecology, Geochemistry, Geomorphology, Geophysics, Microbiology, Soil Sciences) question the paradigm that the Earth's surface is mainly shaped by climate through erosion and tectonic forces by the means of mountain building.

The integration of different Bio- and Geoscience communities is a challenging venture as both communities usually investigate completely different periods of time. These timescales range from hours (e.g. microbial proliferation) to decades (e.g. tree growth) in biology and from tens of thousands of years (e.g. natural climate fluctuations) over hundred thousands of years (e.g. soil formation by weathering) to many millions of years (e.g. plate tectonics and mountain building) in Geosciences (von Blanckenburg et al. 2019). The scientific focus ranges from surveys on how biota shapes the depositional environment of sediments at the continents' margin and large river basins, the investigation on how (micro-) biota act as a driver of weathering reactions, pedogenesis, and aggregate stability on the soil pit scale, to ecological studies on plant diversity and litter decay. Numerical models integrate the

different scientific fields and bridge between the different timescales involved, culminating in dynamic vegetation and landscape evolution models.

EarthShape research is conducted at four sites which are equally spaced along a 1300 km stretch in the Chilean Coastal Cordillera (Fig. 1.4 & 1.5). The sites form a precipitation sequence covering arid (Parque Nacional Pan de Azúcar, ~26°S), semi-arid (Reserva Natural Santa Gracia, ~30°S), mediterranean (Parque Nacional La Campana, ~33°S), and humid-temperate (Parque Nacional Nahuelbuta, ~38°S) climate regimes, where mean annual precipitation (MAP) increases from 10 mm yr^{-1} in the northernmost site to 1100 mm yr^{-1} in the very south (Ministerio de Obras Públicas 2017). This gradient captures a large ecological gradient ranging from barely vegetated desert soils with low gross primary productivity (GPP) to entirely covered forest ecosystems with high GPP (Jung et al. 2011; Werner et al. 2018) developed on similar (granitoid) bedrock (e.g. Berg and Breitkreuz 1983; Berg and Baumann 1985; Molina et al. 2015; Parada et al. 1999; 2002; 2007). The sites were not glaciated during the last glacial maximum (LGM; Hulton et al. 2002). Along this latitudinal transect,

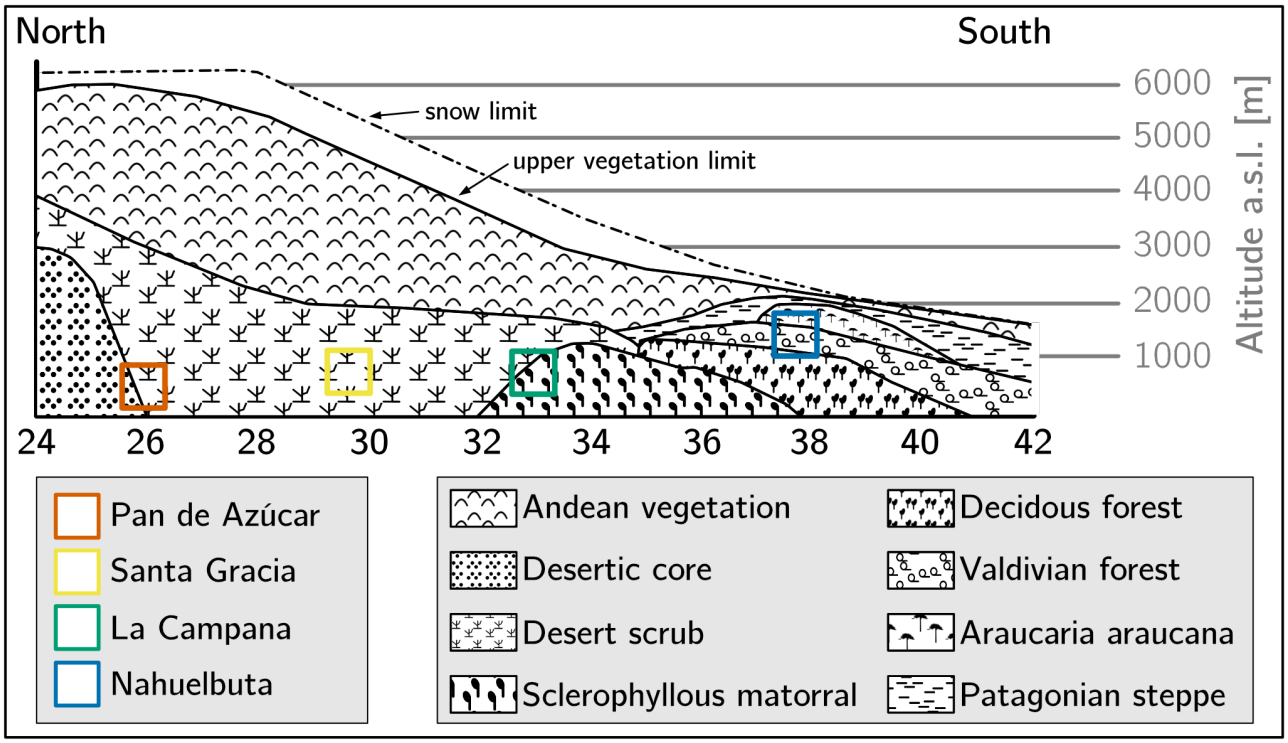

Figure 1.4: Vegetation formations in Chile from 24°S to 42°S according to Schmithüsen (1956) and Moreira-Munoz (2011) as well as the locations of the EarthShape study sites. The vegetation in Pan de Azúcar (red) is represented by mostly small shrubs, geophytes and annual plants Armesto et al. (2007). In the other sites, the vegetation belongs to the "Interior Mediterranean desert scrub of *Heliotropium stenophyllum* and *Flourensia thurifera*" formation (Santa Gracia, yellow), "Coastal Mediterranean sclerophyllous forest of *Lithraea caustica* and *Cryptocarya alba*" formation (La Campana, green), and "Coastal temperate forest of *Araucaria araucana*" formation (Nahuelbuta, blue; Luebert and Pliscoff 2006), respectively.

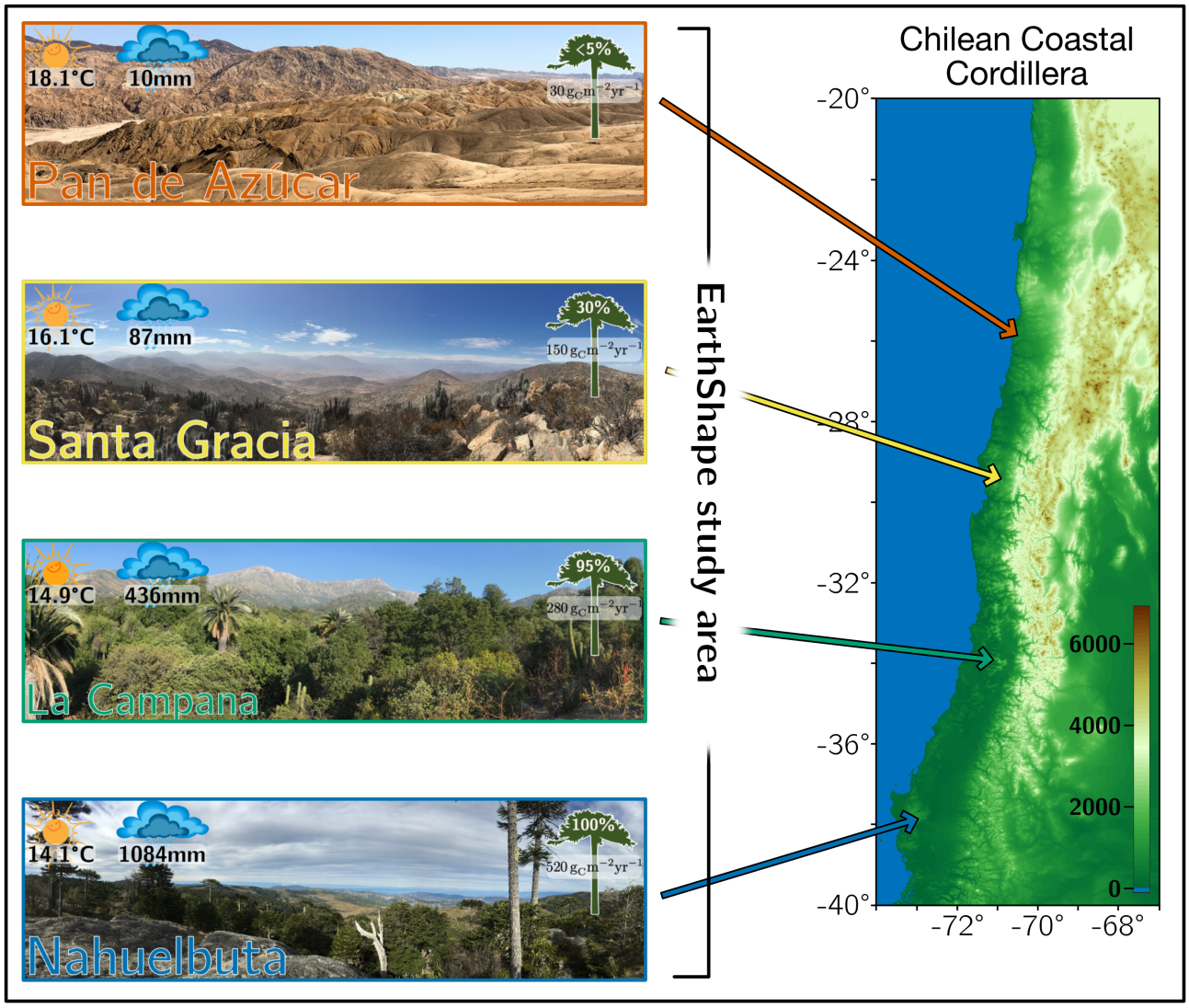

Figure 1.5: Overview over the EarthShape climate and vegetation gradient. Left: Characteristic images of the four sites (from north to south: Pan de Azúcar, Santa Gracia, La Campana, and Nahuelbuta) include information on net primary productivity (NPP), mean annual precipitation (MAP), mean annual air temperature (MAT), and vegetation cover (Bernhard et al. 2018; Ministerio de Obras Públicas 2017; Werner et al. 2018). Right: Position of the four sites in South America along the Chilean Coastal Cordillera.

tectonic uplift maintains topography with roughly uniform uplift rates of approximately 0.2 ± 0.1 mm yr^{-1} (Melnik 2016) south of 25°S.

In my thesis I follow the "climosequence" approach, where the effects of climate on combined ecological, pedogenic, and weathering processes are studied, whereas environmental differences among the study sites are kept as small as possible (e.g. Bullen and Chadwick 2016; Calmels et al. 2014; Egli et al. 2003). The large range in GPP and MAP along the EarthShape north-south transect allow for disentangling the effects of climate and ecology on weathering. The sites are thus particularly well-suited for deciphering the role of biota on weathering.

CHAPTER 2

Chemistry and microbiology of the Critical Zone along a steep climate and vegetation gradient in the Chilean Coastal Cordillera

Abstract

The Chilean Coastal Cordillera features a spectacular climate and vegetation gradient, ranging from arid and unvegetated areas in the north to humid and forested areas in the south. The EarthShape project ("Earth Surface Shaping by Biota") uses this natural gradient to investigate how climate and biological processes shape the Earth's surface. We explored the Critical Zone, the Earth's uppermost layer, in four key sites located in desert, semidesert, Mediterranean, and temperate climate zones of the Coastal Cordillera, with the focus on weathering of granitic rock. Here, we present first results from 16 approximately 2 m-deep regolith profiles to document: (1) architecture of weathering zone; (2) degree and rate of rock weathering, thus the release of mineral-derived nutrients to the terrestrial ecosystems; (3) denudation rates; and (4) microbial abundances of bacteria and archaea in the saprolite.

From north to south, denudation rates from cosmogenic nuclides are $\sim 10\,\mathrm{t\,km^{-2}\,yr^{-1}}$ at the arid Pan de Azúcar site, $\sim 20\,\mathrm{t\,km^{-2}\,yr^{-1}}$ at the semi-arid site of Santa Gracia, $\sim 60\,\mathrm{t\,km^{-2}\,yr^{-1}}$ at the Mediterranean climate site of La Campana, and $\sim 30\,\mathrm{t\,km^{-2}\,yr^{-1}}$ at the humid site of Nahuelbuta. A and B horizons increase in thickness and elemental depletion or enrichment increases from north ($\sim 26°$S) to south ($\sim 38°$S) in these horizons. Differences in the degree of chemical weathering, quantified by the chemical depletion fraction (CDF), are significant only between the arid and sparsely vegetated site and the other three sites. Differences in the CDF between the sites, and elemental depletion within the sites are sometimes smaller than the variations induced by the bedrock heterogeneity. Microbial abundances (bacteria and archaea) in saprolite substantially increase from the arid to the semi-arid sites.

With this study, we provide a comprehensive dataset characterizing the Critical Zone geochemistry in the Chilean Coastal Cordillera. This dataset confirms climatic controls on weathering and denudation rates and provides prerequisites to quantify the role of biota in future studies.

This chapter is published in:

Catena Vol. 170, pages 183-203

Ralf A. Oeser, Nicole Stroncik, Lisa-Marie Moskwa, Nadine Bernhard, Mirjam Schaller, Rafaella Canessa, Liesbeth van den Brink, Moritz Köster, Emanuel Brucker, Svenja Stock, Juan Pablo Fuentes, Roberto Godoy, Francisco Javier Matus, Rómulo Oses Pedraza, Pablo Osses McIntyre, Leandro Paulino, Oscar Seguel, Maaike Y. Bader, Jens Boy, Michaela A. Dippold, Todd A. Ehlers, Peter Kühn, Yakov Kuzyakov, Peter Leinweber, Thomas Scholten, Sandra Spielvogel, Marie Spohn, Kirstin Übernickel, Katja Tielbörger, Dirk Wagner, and Friedhelm von Blanckenburg (2018);
https://doi.org/10.1016/j.catena.2018.06.002

2.1 Introduction

The Earth's surface, where rock, the atmosphere, the hydrosphere, and the biosphere interact, is often referred to as the Critical Zone (Anderson et al. 2007). Soils, mantling 95% of the terrestrial Earth's surface, are the top layer of this zone. Soil is made "from below" by weathering, the breakdown of rocks and minerals (Riebe et al. 2016), and "from above" by the addition of organic matter and atmospheric inputs (Chorover et al. 2007). Weathering turns fresh rock into a loosely consolidated "regolith" (comprising both mobile soil at the top and weathered rock beneath it). The inorganic chemical process of weathering involves the dissolution of primary minerals and their partitioning into solutes and secondary minerals (e.g. amorphous and crystalline oxides, clays). These abiotic weathering products, as well as organic compounds, are exported from catchments via erosion and rivers (Gaillardet et al. 1999; Hilton 2017). The Critical Zone thus plays an important role in the cycling of mineral nutrients across the Earth's surface and the mechanisms of weathering are key.

Numerous studies have shown that soil physico-chemical parameters, such as soil organic matter, soil acidity, exchangeable ions, extractable oxides, and volumetric strain (ε) systematically change with temperature and precipitation (e.g. Bardelli et al. 2018; Bojko and Kabala 2016; Khomo et al. 2013; 2011; Khormali et al. 2012). Egli et al. (2003) have shown that the amount of smectite and the degree of weathering in Alpine soils increase with precipitation. Moreover, the degree of plagioclase weathering seems to increase exponentially with temperature and linearly with precipitation (Dere et al. 2013). Still, from studies that make use of climatic gradients no clear relationship between climate and denudation rates has yet emerged. Large variations in denudation rates in any given climate indicate that a potential climatic imprint might have been severely overprinted by factors such as uplift, physical and chemical bedrock characteristics, and biota (e.g. Dixon et al. 2009b; Egli et al. 2004; Ferrier et al. 2012; Riebe et al. 2004; Schaller et al. 2018b; Starke et al. 2017). In this context, Owen et al. (2011) postulated that a mean annual precipitation threshold exists below which bedrock denudation is precipitation-dependent and above which soil production from bedrock is controlled by complex feedback mechanisms between tectonics, temperature, and biota.

One of the key players in weathering processes is biota, which is receiving increasing scientific attention in this context (Amundson et al. 2015a; Brantley et al. 2011a; Egli et al. 2014; Hahm et al. 2014). A broad spectrum of biota (plants, animals, and microorganisms) interacts with the Earth's surface, although the direction and magnitude of the effects biota has on Earth-surface processes, and conversely the Earth surface effects on biota, are still not well understood (e.g. Wilcke et al. 2017). For example, little is known about microorganisms that live beneath soil, even though more than one third of the microbial biomass is concentrated in regolith depths deeper than 25 cm (Fierer et al. 2003; Schutz et al. 2010). Several studies demonstrated that even in the saprolite active bacterial cells

exist (Buss et al. 2005; Richter and Markewitz 1995). Biogenic weathering is a potentially important mechanism because microorganisms in the regolith are highly specialized to their environment (Fritze et al. 2000; Ghiorse and Wilson 1988; Zvyagintsev 1994). Fungi and their associated bacteria can directly weather minerals (Balogh-Brunstad et al. 2008a; Quirk et al. 2014; Smits et al. 2012). In this process they mobilize mineral-bound nutrients (e.g. P, Ca, Mg, K) that are essential elements to plants. When these nutrients are made available for plants, a biogeochemical cycle is induced that, for some elements, exceeds the weathering flux measured in rivers up to a factor of 40 and more (e.g. Uhlig et al. 2017; Wilcke et al. 2017). This biotically modulated silicate weathering is of major significance for global atmospheric CO_2 cycles in the Phanerozoic (Doughty et al. 2014; Pagani et al. 2009; Quirk et al. 2012) and for sustaining a continuous soil cover (Amundson et al. 2015b). Whether these biological mechanisms overwhelm the abiotic weathering mechanisms and whether they serve to provide a feedback balancing soil erosion and soil production have never been shown, owing to the lack of diagnostic observables that allow distinguishing between abiotic and biotic drivers.

To resolve the control of climate and biota on rock disintegration, we combined the fields of geochemistry, soil science, biogeochemistry, and geomorphology and applied these to different study sites along the Chilean Coastal Cordillera. We did this within the German-funded "EarthShape" (Earth surface shaping by biota) research priority program along four Critical Zone field sites along a latitudinal transect in the Chilean Coastal Cordillera. The Coastal Cordillera of Chile encompasses a prominent climate and vegetation gradient that provides a natural laboratory for investigating biotic and abiotic weathering processes. Soil formation processes in this region were previously explored by Owen et al. (2011). The authors found a 40-fold increase in soil production rate from 1 m My^{-1} in the hyper-arid to 40 m My^{-1} in the arid region. Vázquez et al. (2016) described a > 30 m thick weathering profile developed on granitic bedrock in the Coastal Cordillera in the Mediterranean climate of central Chile. The authors calculated denudation rates (derived from cosmogenic ^{10}Be) from 20 to 70 m My^{-1}, leading to mean residence times of 0.5 to 1.8 Ma for minerals in the saprolite.

The investigated areas of this study include (from north to south) the Pan de Azúcar National Park (~ 26°S), Santa Gracia Nature Reserve (~ 30°S), La Campana National Park (~ 33°S), and Nahuelbuta National Park (~ 38°S). Site selection for these areas was based on the minimal tectonic and lithologic differences, and their position along the climate (arid to humid) gradient. We thus followed the "climosequence" approach (e.g. Egli et al. 2003). In each of these four study sites, four regolith profiles were excavated on different slope positions.

In this paper, we (1) describe the architecture of the weathering zone; and quantify (2) the degree and rate of rock weathering, thus the release of mineral-derived nutrients to the

terrestrial ecosystems; (3) denudation rates from cosmogenic nuclides; and (4) microbial abundances of bacteria and archaea in the saprolite. We discuss these results on (1) a continental scale, on which the observed geochemical signatures are mainly caused by large scale variations in precipitation and vegetation cover, on (2) a hillslope scale, where influences on weathering and microbial abundances are caused by differing solar irradiation on N- and S-facing slopes, and on (3) a regolith profile scale. Within the scope of the "EarthShape" research program, we thus contribute towards addressing the question: how does the gradient in precipitation and vegetation cover influence weathering, microbial abundances, and mineral nutrient supply to ecosystems? In a companion paper (Bernhard et al. 2018) the site-specific characterization of the soil and its properties are described. With these two papers, we also provide the basic Critical Zone background data that will serve as basis for future studies employing other field and laboratory techniques to decipher the role of biota along this transect.

2.2 Study area

2.2.1 Geological and climatic conditions

Central Chile (~25 – 40°S) is built of three structural units (from West to East): The Coastal Cordillera, the Central Depression, and the Pre-Western Cordillera of the Andes. Of these, the Coastal Cordillera is the oldest and westernmost trench-parallel morpho-structural unit. The Coastal Cordillera is composed of the remnants of a Late Paleozoic to Mesozoic magmatic arc and Paleozoic metamorphic rocks (Charrier et al. 2007; Hervé et al. 2007; 1988; Pankhurst and Hervé 2007; Parada et al. 1988; Vázquez et al. 2016). The northern Coastal Cordillera (~21 – 27°S) is suggested to have experienced exhumation between ~118 – 152 Ma and 60 – 80 Ma prior to Andean mountain building (Juez-Larré et al. 2010). Following this (from ~40 Ma to present), deformation migrated to the east of the Coastal Cordillera and led to the onset of Andes mountain building and plateau formation (Barnes and Ehlers 2009). Less well known is the tectonic history of the Coastal Cordillera south of 27°S, although it is commonly assumed to be similar to the northern Cordillera. More recently, ongoing and minor amounts of Quaternary neotectonic activity have been documented in the northern Coastal Cordillera (Riquelme et al. 2003; Starke et al. 2017).

The EarthShape study area features a vegetation gradient controlled by climate, ranging over 1300 km (from 26°06′S to 37°48′S), spanning from arid, via Mediterranean, to humid-temperate climate conditions. Within this area four different sites were chosen, all located within 80 km of the Pacific coast and within plutonic rocks of the Chilean Coastal Cordillera (Fig. 2.1). The basement at those four sites is mainly composed of: (1) monzo- to syenogranitic intrusions (Pan de Azúcar, Triassic age; Parada et al. 2007), (2) pyroxene and hornblende-bearing diorites and monzodiorites (Santa Gracia granite, 98 – 89 Ma; Moscoso

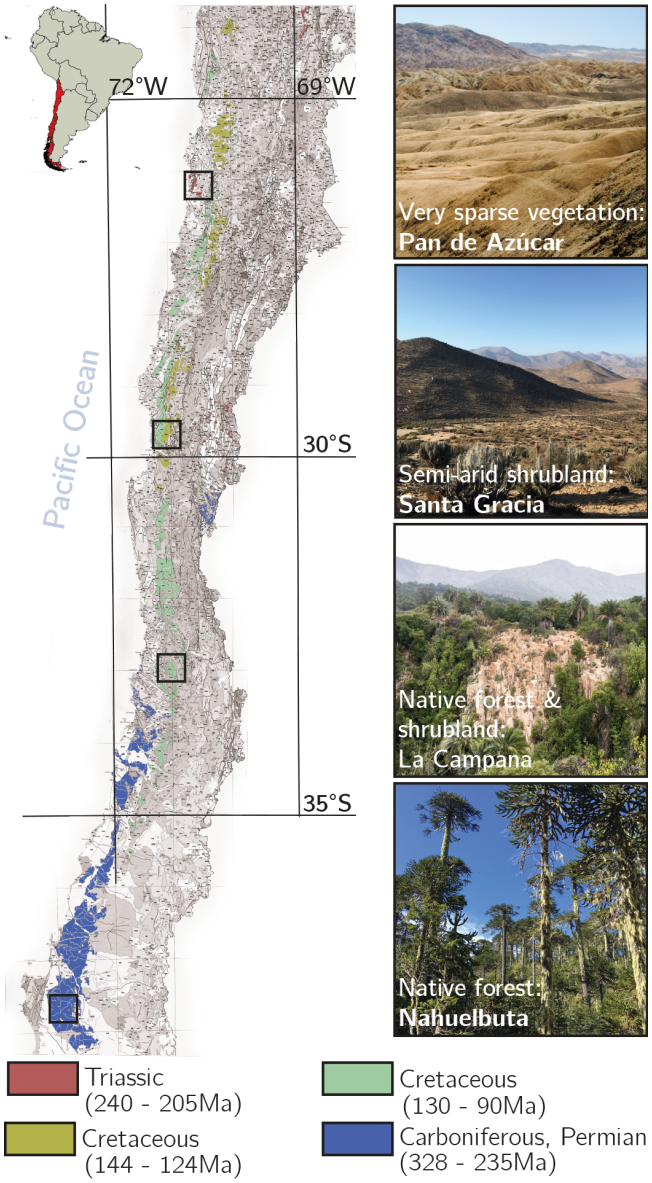

Figure 2.1: Intrusion age and spatial extension of the granitoid rocks in the four primary EarthShape study sites (open squares) along the Chilean Coastal Cordillera from north to south: Pan de Azúcar, Santa Gracia, La Campana, and Nahuelbuta. Map modified from SERNAGEOMIN (2003).

et al. 1982), and (3), (4) tonalites and granodiorites (Nahuelbuta complex, 294 Ma; Parada et al. 2007 and the Illapel Plutonic Complex in La Campana, 130 – 90 Ma; Parada et al. 1999).

The 30-year mean annual precipitation (MAP) at the study sites increases from north to south, from 10 mm yr^{-1} in Pan de Azúcar, 89 mm yr^{-1} in Santa Gracia, 436 mm yr^{-1} in La Campana, to 1084 mm yr^{-1} in Nahuelbuta, respectively Fig. 2.2a; Ministerio de Obras Públicas 2017). The mean annual air temperature (MAT) vary between 18.1°C in the northernmost site and 14.1°C in the southernmost site (Fig. 2.2b; Ministerio de Obras Públicas 2017). The northernmost site, Pan de Azúcar, is located at the southern border of the Atacama Desert. The aridity of the Atacama Desert has developed in the Miocene (Clarke 2006; Dunai et al.

2005), and the hyperaridity in the early Quaternary (Jungers et al. 2013). The sites were unglaciated during the last glacial maximum (Hulton et al. 2002) and are situated in national parks and nature reserves, where anthropogenic influence is minimized compared to the surrounding areas. However, occasional grazing by cows (La Campana; Rundel and Weisser 1975) and goats (Santa Gracia; Armesto et al. 2007; Bahre 1979) within the protected areas have been reported by local authorities.

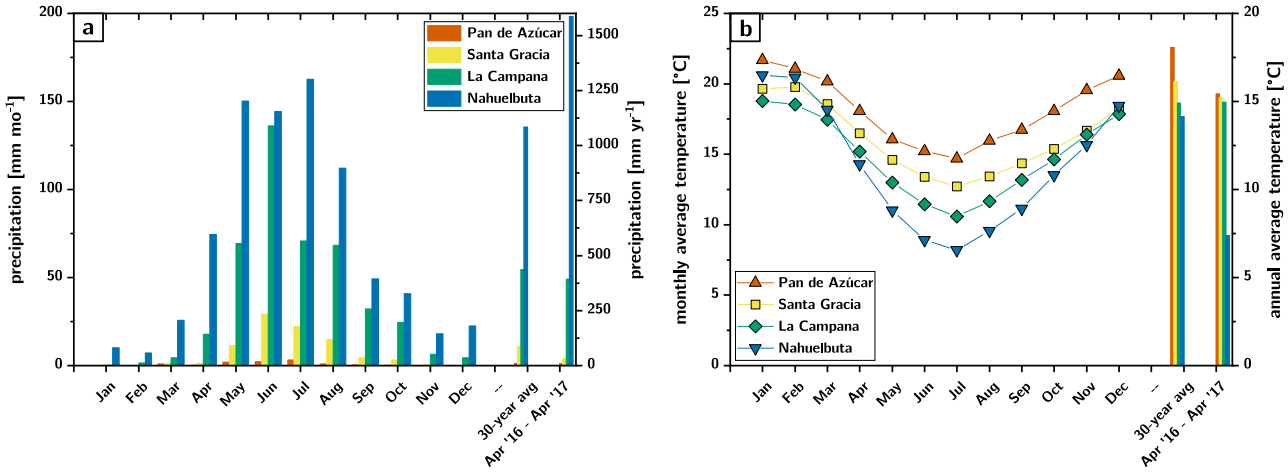

Figure 2.2: Compilation of precipitation (A) and temperature (B) data from climate stations in vicinity of the respective EarthShape study sites (Ministerio de Obras Públicas 2017). Bars on the very right-hand side of both panels show climate data from April ’16 to April ’17 at the EarthShape climate stations within the study sites (Ehlers et al. 2017).

2.2.2 Critical Zone description

In each study site, three south-facing (S-facing) profiles at top-, mid-, and toe-slope position and, as an initial cross-check for aspect, a single north-facing (N-facing) mid-slope regolith profile were investigated (Figs. 2.3 – 2.6; Table S2.1).

Here, we describe the soil as consisting of the O, A, and B horizon, underlain by a C horizon consisting of saprolite (bedrock that was weathered in situ). In this paper, we call the entire zone above unweathered bedrock “regolith” (Scott and Pain 2008), which thus comprises saprolite and soil. The vascular flora of each study site was classified after Marticorena and Quezada (1985) andLuebert and Pliscoff (2006).

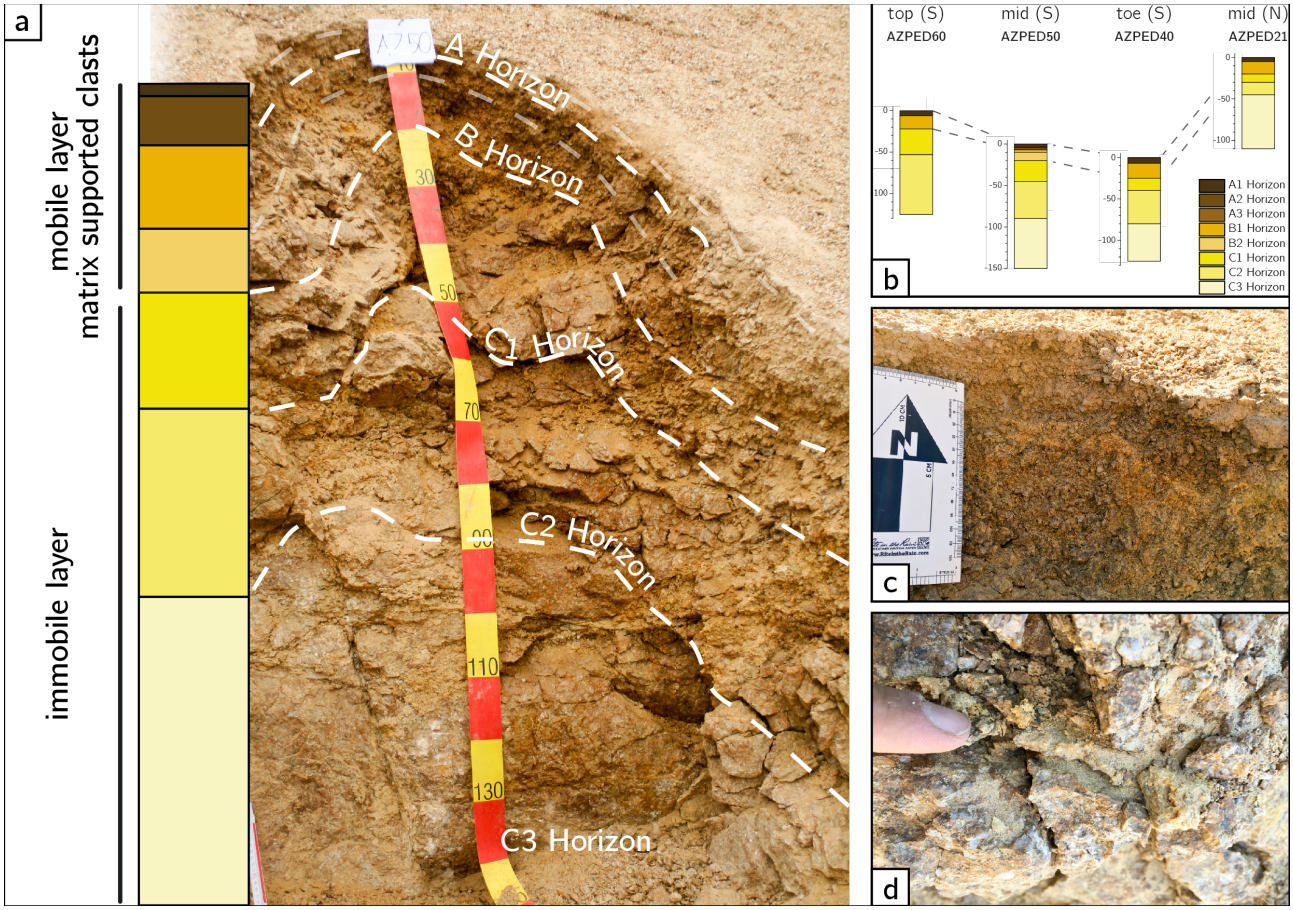

Figure 2.3: Photographs of the S-facing mid slope regolith profile (AZPED 50) in Parque Nacional Pan de Azúcar (AZ) including horizon boundaries (white dashed line), a schematic depth profile (a), a cross section through the S-facing catena and adjacent N-facing regolith profile (b). The regolith in AZ developed on a coarse-grained, feldspar-rich granite. Its cover lacks fine-grained particles which are removed by wind (c). Fractures are either filled with clay-sized particles of unknown composition or gypsum and carbonate (d).

Pan de Azúcar

The S-facing regolith profiles in Pan de Azúcar National Park (AZ) are located on a slope of 9 m length. The N-facing slope is located at a distance of 30 m from the S-facing slope. The elevations range from 328 to 343 m above sea level (asl) with hillslope angles between 25 and 40° (Fig. 2.3b; Table S2.1).

The profiles' surfaces are comprised of fine grained, quartz-rich granite gruss of a few cm in thickness with a grayish to yellow color (Fig. 2.3c). At the very top of this A horizon, where silt- and clay-sized particles are absent, angular fragments occur in size of up to 1 cm. Below the top layer, a B horizon of reddish-brown color is found. The size of fragments increases downwards. The transition to the saprolite of the C horizon occurs at 20 to 25 cm depth and does neither depend on slope position nor aspect.

The saprolite has a reddish-brown color and is characterized by coarse-grained material

(Fig. 2.3). The entire regolith is jointed, with joint width and joint spacing augmenting with depth. Joints are either filled with fine-grained material of unknown composition or with visible calcite and gypsum crystals (Fig. 2.3d). At the base of the regolith profiles, the width of the joints decreases; the joints pinch out to the bottom. Unweathered parent material was not observed. Dead root material has been found in the profiles only rarely.

The area belongs to the vegetation formation "Mediterranean coastal desert scrub of Euphorbia lactiflua and Eulychnia saint-pieana" (Luebert and Pliscoff 2006). The vegetation cover is very low (< 10%) and is represented only by small shrubs, geophytes and annual plants (Armesto et al. 1993), which are present in more abundance in small ravines. On the sampled S-facing slope, a few individuals of *Tetragonia maritima*, *Nolana mollis*, *Perityle* sp., and *Stipa plumosa* can be found. On the N-facing slope, single individuals of *N. mollis* and *Cristaria integerrima* are present. From these species, only *T. maritima*, *N. mollis*, and *C. integerrima* maintain their vegetative structures during dry years.

Santa Gracia

In the natural reserve of Santa Gracia SG the three S-facing regolith profiles are located on a 153-m long slope. The N-facing regolith profile is located at a distance of 160 m from the S-facing mid-slope profile. The elevations of these four profiles range from 628 to 718 m asl with the two mid-slope profiles at approximately 690 m asl. Slope angle is slightly lower than in Pan de Azúcar and varies between 15 and 25° at the mid-slope regolith profiles (Fig. 2.4b; Table S2.1).

The surface of the regolith profiles in Santa Gracia is composed of sub-angular, coarse sand-sized quartz and granodiorite fragments. This brownish A horizon is made of grussified granodioritic, silt to fine sand- sized particles, supporting fragments of up to 2 mm in diameter. Roots are abundant in this horizon and reach diameters of up to 1 cm (Fig. 2.4). This horizon is underlain by a brownish white-spotted transitional (B) horizon. Within this horizon, the proportion of fragments increases with their size, resulting in a fine-grained matrix that is supported by coarse fragments at the horizon's base. Fine roots pervade this horizon. The extent of the soil horizon (comprised of A and B horizon) increases from the top- to toe-slope regolith profiles of the S-facing slope from 30 to 55 cm (Table S2.1). The depth of the soil horizon in the regolith profile on the N-facing slope (SGPED70) is thinner (35 cm) and its brownish color less dominant.

The orange-brownish saprolite is dominated by greenish-black weathered biotite and hornblende and reddish feldspars, respectively. Fragments are up to 1 cm in size and are surrounded by fine-grained material and fine roots. Joint spacing in the weathered granodiorite is approximately 30 cm. Roots (average diameter of 1 mm) penetrate the fractures and weather the adjacent rock face (Fig. 2.4d). In contrast to the S-facing regolith profiles, the

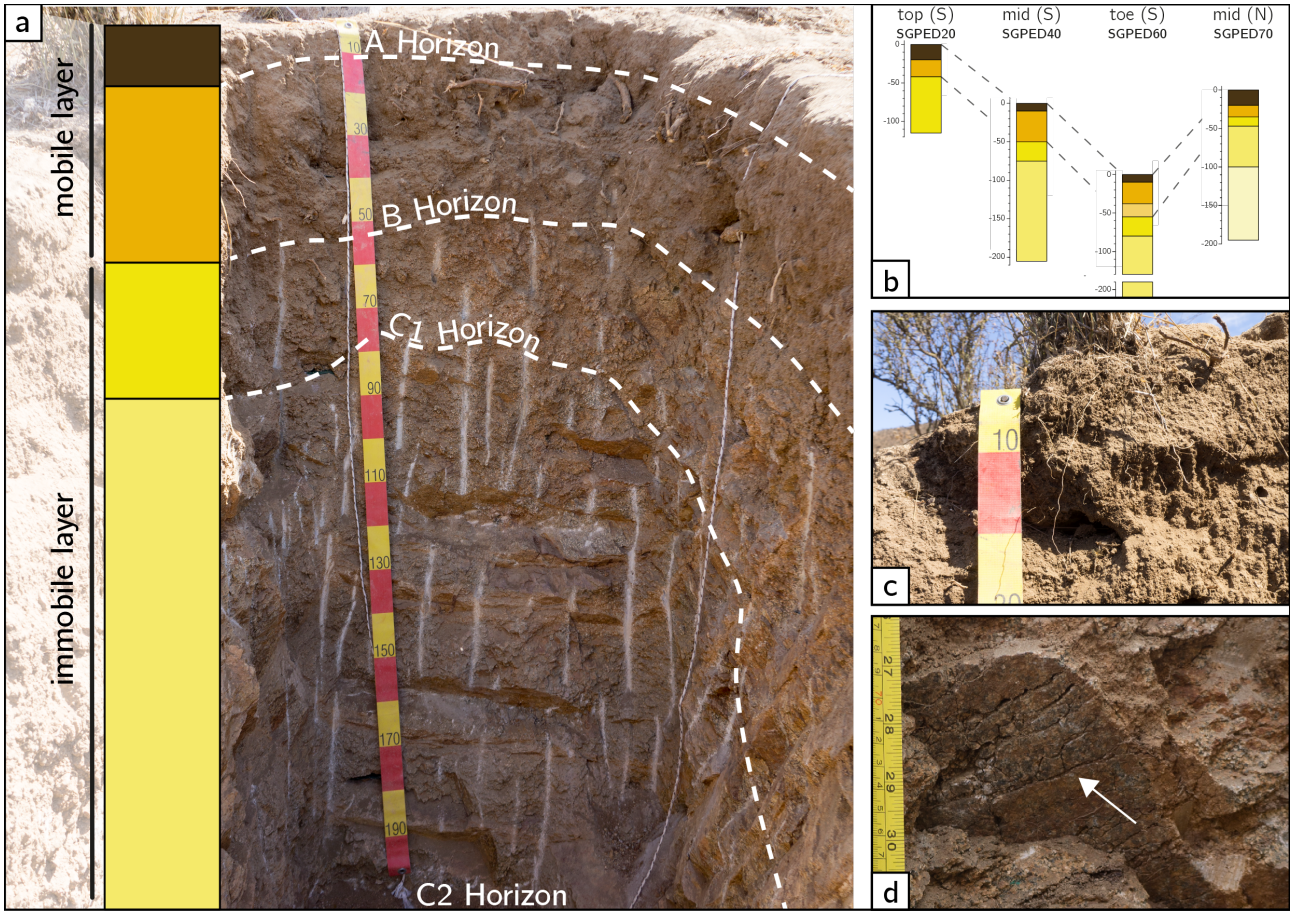

Figure 2.4: Photographs of the S-facing mid slope pit (SGPED 40) in Reserva Natural Santa Gracia (SG) including horizon boundaries (white dashed line), a profile sketch, and a cross section through the S-facing catena and adjacent N-facing pit. The catena developed on a medium grain size granitic substrate. The regoliths' upper layer is characterized by bioturbation and a high root density (a). At the pits' base, two major joint sets are preserved. Here, roots penetrate the fractures and weather the adjacent rock face (b).

weathered bedrock in the N-facing regolith profile exhibits a white and gray mottled pattern at depth, with only a few orange spots visible.

The vegetation belongs to the "Interior Mediterranean desert scrub of *Heliotropium stenophyllum* and *Flourensia thurifera*" formation (Luebert and Pliscoff 2006). The original vegetation has been highly disturbed and the current shrubby vegetation is influenced by livestock grazing (mostly goats; Bahre 1979). For these reasons, combined with the semi-arid climate, vegetation cover is low, especially in the herbaceous layer. The shrub layer is sparse (~30 – 40% cover) and is dominated by *Proustia cuneifolia* and *Senna cumingii* on the sampled S- facing slope, and by *Cordia decandra* and *Adesmia sp.* on the N-facing slope. On the latter slope, the cactus *Cumulopuntia sphaerica* is very abundant and the columnar cactus *Eulychnia acida* is present with individuals of > 2 m height (i.e. cardonal vegetation community; Bahre 1979). In the area, some individuals of the shrubs *Balbisia peduncularis*, *Baccharis paniculata*, and *Bulnesia chilensis* also occur.

La Campana

The regolith profiles in La Campana National Park (LC) are located on a S-facing slope of 152 m length where the S-facing and the N-facing mid-slope regolith profiles are separated by 173 m. The elevations of the four profiles range from 706 to 750 m asl with the two mid-slope profiles being at 730 and 734 m asl, respectively. The mean slope angle at the mid-slope profiles is around 18° (Fig. 2.5b; Table S2.1).

The regolith at this site is covered by an O horizon of a few centimeters thickness, composed of litter and tree-debris mixed with granitic gruss of sand size. The dark-brown A horizon on the S-facing catena has a thickness of up to 40 cm. In contrast, the N-facing regolith profile's A horizon is of grayish-brown color and measures only 12 cm. It is composed of fine-sand to silt-sized particles, hosting some granodioritic fragments of up to 3 mm in diameter and is highly permeated by roots of various sizes. The base of the soil horizon is characterized by a brown to orange-brown transitional (B) horizon. As the matrix is coarsening downwards, the number of fragments increases and the horizon shifts from a matrix- to a clast-supported one. The final transition from soil to saprolite occurs at a depth of 60 cm within 3 to 5 cm. At the N-facing slope, this transition occurs at a shallower depth.

The saprolite develops from (at least) two distinct granodiorite types: a coarse-grained and a fine-grained one (Fig. 2.5c). In both cases, the granodiorite fabric is still visible and the mineral composition (plagioclase ≫ quartz ≫ K-feldspar & biotite) is similar. Throughout the saprolite, fine roots are common and are most abundant within fractures.

The vegetation of La Campana belongs to the "Coastal Mediterranean sclerophyllous forest of *Lithraea caustica* and *Cryptocarya alba*" formation (Luebert and Pliscoff 2006) and includes examples of all the major biotic communities of sclerophyllous forest of central Chile (Gajardo 1994; Rundel and Weisser 1975). Vegetation cover is high, with almost 100% ground cover. The forest canopy is dominated by the evergreen sclerophyllous trees *L. caustica*, *C. alba*, *Quillaja saponaria*, and in lower abundance *Kageneckia oblonga*. The medium shrub layer is dense and dominated by *Colliguaja odorifera*, *Aristeguietia salvia* and *Retanilla trinervia*, and in less abundance *Podanthus mitiqui*. The herbaceous layer presents a high cover and diversity and is especially rich in annual species. The most abundant species are *Geranium robertianum*, *Stellaria media* and the fern *Adiantum chilense*. Along the S- facing catena, the trees *L. caustica* and *C. odorifera* are the most abundant and dominant species. In less abundance, *P. mitiqui* and *A. salvia* are found in the shrub layer, while the herbaceous layer is dominated by *Alstroemeria sp.*, *G. robertianum*, *S. media*, *Solenomelus pedunculatus*, and *A. chilense*. Near the N-facing slope profile, high vegetation is less abundant and less rich in species. The canopy is strongly dominated by *L. caustica*, accompanied by some individuals of *Jubaea chilensis*. The most abundant shrub is *R. trinervia*, followed by *A. salvia* and *C. odorifera*. *Poaceae spp.* and *Sonchus oleraceus*

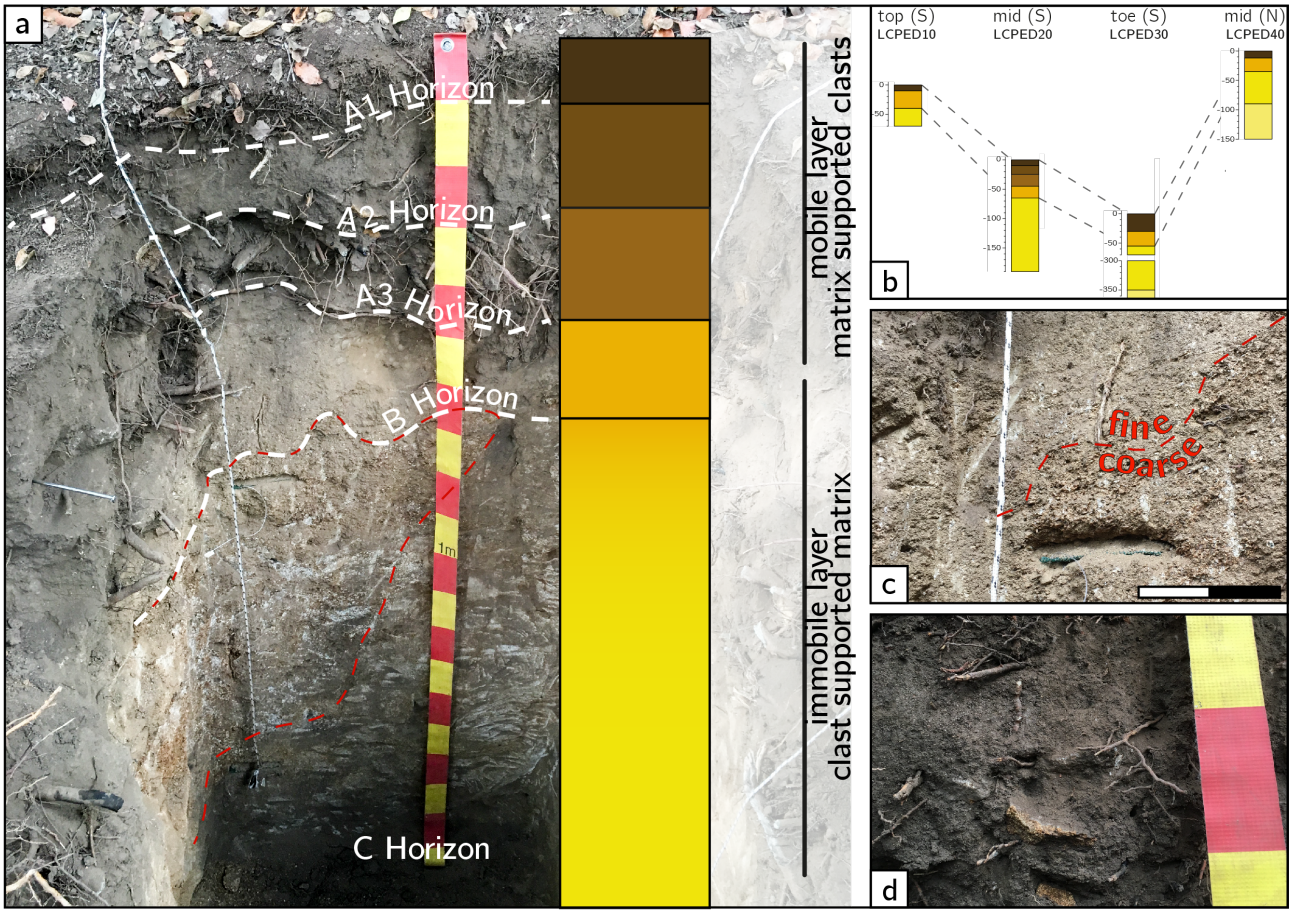

Figure 2.5: Photographs of the S-facing mid slope pit (LCPED 20) in Parque Nacional La Campana (LC) including horizon boundaries (white dashed line), a profile sketch, and a cross section through the S-facing catena and adjacent N-facing pit. Both coarse- and fine-grained granodiorite comprise the substrate of the regolith (boundary shown by the red dashed line) (a); scale bar size: 10 cm. Mid slope pits (S- and N-facing) are affected by mass movement downslope, leading to an accumulation of angular fragments in the soil columns (b). (For interpretation of the references to color in this figure legend, the reader is referred to the web version of this article.)

dominate the herbaceous layer, where climbing species like *Tropaeolum sp.* and *Dioscorea sp.* also occur.

Nahuelbuta

The regolith profiles in the Nahuelbuta National Park (NA) are located on a 136-m long S-facing slope where the S-facing and the N-facing mid-slope regolith profiles are separated by 145 m. The elevations of these four profiles range from 1219 to 1248 m asl, being the highest among the four study sites. Slope angles of around 14° at the mid-slope profiles are the smallest of the study area (Fig. 2.6b; Table S2.1).

The regolith at Nahuelbuta is covered by a 2 to 5 cm thick O hozizon, almost entirely composed of roots, leaves, and moss. The A horizon is characterized by a large number of roots (various sizes, up to 3 cm in diameter; Fig. 2.6) and a brown to black color. This horizon

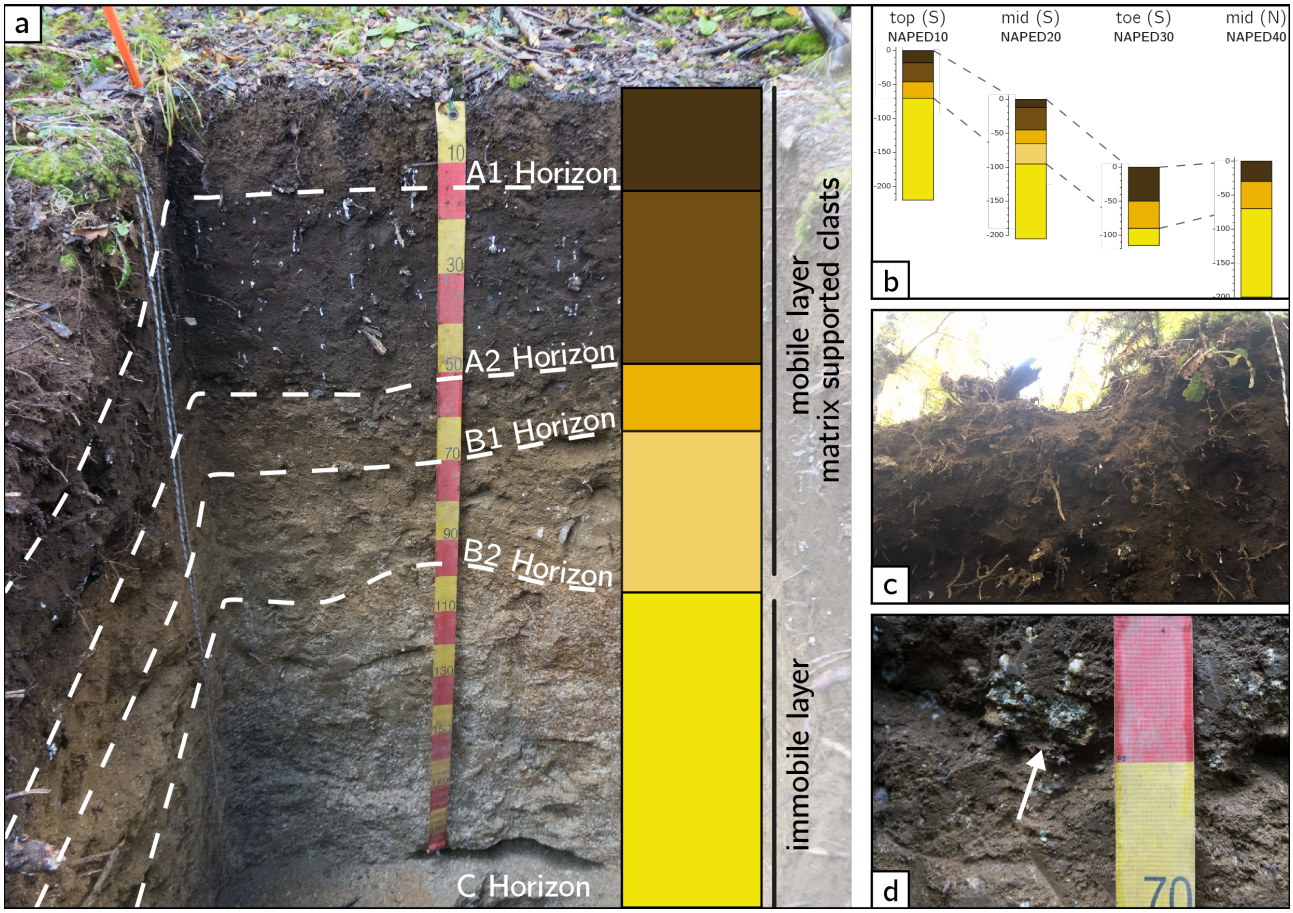

Figure 2.6: Photographs of the S-facing mid slope pit (NAPED 20) in Parque Nacional Nahuelbuta (NA) including horizon boundaries (white dashed line), a profile sketch, and a cross section through the S-facing catena and adjacent N-facing pit. Very high organic matter content, characterize the upper horizons of the four pits (a). Fragments are absent in the regoliths' A-Horizon; they occur in the B-Horizon in the form of weathered granodiorite (b). Rare fragments of mafic composition are also found.

is mainly composed of silt-sized particles, forming nodular soil aggregates, giving this layer a granular texture. In the upper part of the A horizon, up to 1 mm large quartz grains are embedded and at the base, larger granodioritic fragments occur. The transitional (B) horizon increases in thickness from the top to the toe slope regolith profile on the S-facing catena. Its matrix is made of fine-sand sized particles, hosting sub-angular granodioritic fragments. As depth increases, fragment abundance and size is increasing and the horizons' color is lighter. Unlike in the upper two S-facing regolith profiles, where the transition from soil to saprolite is gradual, the S-facing toe slope and the N-facing mid-slope profile are characterized by a thin soil-saprolite transition zone. At this transition, highly weathered mafic rock (NAPED30) and granodioritic core stones (NAPED40) appear, respectively.

The saprolite is coarse-grained and disaggregates readily. Its color varies from dark gray to whitish. The dark color is attributed to weathered bedrock of mafic composition and the whitish color to weathered rock with an increased plagioclase abundance. Some reddish

intercalations within the saprolite follow fluid pathways along formerly open fractures and pathways once occupied by roots.

The dominant vegetation belongs to the "Coastal temperate forest of Araucaria araucana" formation (Luebert and Pliscoff 2006). Here also, vegetation cover is 100%. The general area also supports tall evergreen mixed forest dominated by the broadleaved *Nothofagus dombeyi* and the iconic conifer *A. araucana*, but around the soil pits the forest is more open and dominated by the lower-stature deciduous trees *Nothofagus obliqua* and *Nothofagus antarctica*, together with the tall *A. araucana*. The dominant shrub species is *Gaultheria mucronata*, but other species like *Azara microphylla, Baccharis sp., Ribes magellanicum*, and *Berberis montana* are also present. At the herbaceous level, *Stipa sp.* and *Mutisia decurrens* are very abundant. However, herbaceous diversity is very high and is also represented by e.g. *Chusquea culeou, Bromus sp., Viola maculata*, and *Adenocaulon chilense*. Around the regolith profile on the N- facing slope, *N. obliqua* and *N. antarctica* are the most abundant species in the canopy and the understory is dominated by *G. mucronata* and *Stipa sp.*. Along the catena on the S-facing slope, the canopy is less dense and *A. araucana* is the most abundant species, followed by *N. antarctica*, while in the understory *C. culeou* is very common. Lichens of the genus *Usnea* abundantly cover most of the tree trunks and branches.

2.3 Material and analytical methods

2.3.1 Sampling

Regolith samples were collected from bottom to top (if applicable) in a continuous sequence of depth increments, amounting to a thickness of 5 cm (uppermost two samples), 10 cm (3rd sample from top), and 20 cm (4th sample from top and below), respectively. About 1 kg of material was taken per sample. In addition, saprolite samples (50 ml) were taken under sterile conditions for DNA-based analyses of microbial abundances. These latter samples were stored and transported under frozen conditions to Germany.

Underlying unweathered bedrock has not been reached in the regolith profiles of this study and the depth to bedrock remains unknown. However, a set of 20 bedrock samples (4 in Pan de Azúcar, 8 in Santa Gracia, 5 in La Campana and 3 in Nahuelbuta, respectively) was thus obtained from nearby outcrops.

All sample metadata are already available on a public server using unique sample identifiers in form of the new "International Geo Sample Number" (IGSN).

2.3.2 Bedrock and regolith geochemistry

Major and trace element concentration of bedrock and regolith samples were determined using the PANalytical AXIOS advanced X-Ray Fluorescence spectrometer at the GFZ German Research Centre for Geosciences, Section "Inorganic and Isotope Geochemistry". The device is equipped with a Rh anode X-ray tube, which was operated at an excitation voltage of 25 to 60 kV and currents between 60 and 160 mA. Measuring times for major elements varied between 10 and 20 s, for trace elements it was set to 40 s.

Prior to measurement, each sample was milled in an agate mortar and sieved through a 62 µm gauze sieve. Powdered samples were dried at 105°C for 24 h before glass bead preparation. Glass beads were made with 1 g of sample material, 6 g of dilithiumtetraborate, and up to 1 g of ammonium nitrate, brought to complete fusion in a heating system in six steps of up to 8-minute intervals. The intervals were adjusted depending on the concentration of organic compounds. The loss on ignition for each sample was determined by weighing the glass beads and the platinum crucibles used for glass bead preparation before and after fusion.

XRF data of regolith samples have been recalculated to a volatile free basis using:

$$[X]_{recalc} = \frac{[X_{measured}]}{SUM_{measured} - (LOI_{measured} - \overline{LOI}_{bedrock})} \tag{2.1}$$

where $[X]_{recalc}$ and $[X_{measured}]$ refers to the recalculated and measured concentration of an element, $SUM_{measured}$ to the sum of all elements analyzed, and $LOI_{measured}$ to the samples' loss on ignition, respectively. $\overline{LOI}_{bedrock}$ is the average LOI of associated bedrock samples.

Pedogenic oxides of Iron (Fe), Aluminum (Al), Manganese (Mn), and Silicon (Si) were determined at University Bern with the dithionitecitrate method as described by Mehra and Jackson (1958). Active oxides of the same elements were examined as ammonium-oxalate extractable compounds (Schwertmann 1964; modified after Tamm 1922). Oxides associated with soil organic matter (SOM) were extracted with a 0.1 M pyrophosphate reagent ($Na_2P_2O_7 \times 10H_2O$) at pH 10. Elements have been analyzed on an ICP-MS (7700x Agilent Technologies).

Mineral assemblages and approximate mineral abundances in representative bedrock samples were estimated at GFZ Potsdam using thin section microscopy and standard point counting techniques.

2.3.3 Cosmogenic ^{10}Be in Quartz

For determination of the in situ-produced ^{10}Be concentration in quartz, the saprolite samples were washed, dried, and sieved to a fraction of 0.25 to 2.0 mm at the University of Tübingen, Department of Geosciences, Germany. The 1.0 to 2.0 mm fraction was crushed to 0.25 to 1.0 mm. After magnetic separation and treatment with HCl, the sample material was leached with HF/HNO_3. The remaining non-quartz minerals were dissolved and meteoric ^{10}Be was removed from quartz grains by HF etching. A total of 15 to 35 g of cleaned quartz was spiked with ~0.3 mg ^{9}Be and dissolved with concentrated HF. Beryllium was separated from other elements with column chromatography and precipitation techniques after von Blanckenburg et al. (1996). After oxidation BeO was mixed with Nb powder for measurement of $^{10}Be/^{9}Be$ ratios at the accelerator mass spectrometer (AMS) facility in Cologne. Uncertainty on measured ratios is reported as 1 σ. Calculated sample concentrations were corrected for a combined mass spectrometry and chemistry blank of 3.4×10^4 atoms.

2.3.4 DNA extraction and quantification of 16S rRNA gene copies

Total genomic DNA was extracted at GFZ German Research Centre for Geosciences (GFZ Potsdam) from saprolite samples which were collected under sterile conditions. The PowerSoil® DNA Isolation Kit was used for soils from La Campana, Santa Gracia, and Nahuelbuta with a maximum sample amount of 0.25 g each. Samples from Pan de Azúcar were treated with the PowerMax® Soil DNA Isolation Kit (both from MoBio Laboratories, CA, USA). Before processing, saprolite samples from Pan de Azúcar and Santa Gracia were crushed by hand. Following this, DNA was extracted in triplicates following the manufacturer's protocol with one exception; DNA elution was done with PCR-grade water. Final concentrations were measured with a NanoPhotometer® (P360, Implen GmbH, Germany). Purity was controlled by the optical density values of OD_{260}/OD_{280} and OD_{260}/OD_{230}.

Gene copy numbers of universal bacteria and universal archaea were determined by quantitative polymerase chain reaction (qPCR). 16S rRNA genes were amplified by using the bacterial primer pair Eub341F (5'–CCT ACG GGA GGC AGC AG–3') and Eub534R (5'–ATT ACC GCG GCT GCT GG–3') (Muyzer et al. 1993), and the archaeal primer pair 340F (5'–CCC TAC GGG GYG CAS CAG–3') and 1000R (5'–GGC CAT GCA CYW CYT CTC–3') (Gantner et al. 2011). The qPCR assay was carried out in a total reaction volume of 20 µl using the KAPA SYBR® FAST qPCR Kit Master Mix (2X) Universal (Kapa Biosystems, Sigma-Aldrich, Germany) in accordance with the manufacturer's recommendations. Quantification was performed in the CFX96 Connect™ Real-Time System (Bio-Rad Laboratories, CA, USA) with the following cycling program for bacterial 16S rRNA genes (and archaeal 16S rRNA genes): initial denaturation at 95 °C for 3 min, followed by 40 (45) cycles of denaturation at 95 °C for 3 s, annealing at 60 °C (57 °C) for 20 s, elongation at 72 °C for 30 s. Fluorescence was measured at 80 °C. The melting curve was recorded by rising temperature from 65 to 95 °C. Due to preliminary experiments, DNA extracts were used in 1:10 for archaea and 1:100 dilutions for

bacteria to avoid putative inhibitions of co-extracted substrates. Every qPCR run included blanks, calibration standards in triplicates and saprolite samples in quadruplicates. The reaction efficiency ranged between 92.0 and 98.6%. Data analysis was carried out using the CFX Manager™ Software (Bio-Rad Laboratories, CA, USA).

2.3.5 Calculation of weathering indicators and denudation rates

To quantify the element fluxes as well as the weathering intensities that emerge when the bedrocks' elements are solubilized in percolating fluids and new elements are introduced from the atmosphere, various indices and coefficients have been developed. The common denominator of all these approaches is the identification of an element considered to be immobile during weathering. Furthermore, cosmogenic nuclide concentration can be converted into rates of mass removal. In the following, we outline these quantification approaches.

Chemical index of alteration (CIA), chemical depletion fraction (CDF), mass transfer coefficient (τ), and volumetric strain (ε)

To assess the relative degree of chemical weathering, we used the chemical index of alteration (CIA) (Eq. 2.2) developed by Nesbitt and Young (1982). In this approach, aluminum is assumed to be an immobile element and the degree of weathering is traced by comparing the aluminum content of a sample with this of the readily soluble cations calcium, sodium and potassium in silicate minerals.

$$\mathrm{CIA} = \frac{\mathrm{Al_2O_3}}{\mathrm{Al_2O_3} + \mathrm{CaO} + \mathrm{Na_2O} + \mathrm{K_2O}} \times 100 \tag{2.2}$$

The CIA in unweathered granitoid rock has values of 45 to 55. The degree of weathering has to be evaluated from the CIA in weathered material relative to its respective unweathered precursor. As weathering proceeds the CIA evolves to a maximum value of 100 (Nesbitt and Young 1982).

To calculate the relative mass loss caused by chemical weathering of the parent rock we used the chemical depletion fraction (CDF; Riebe et al. 2003):

$$\mathrm{CDF} = 1 - \frac{[\mathrm{X}_i]_{\mathrm{parent}}}{[\mathrm{X}_i]_{\mathrm{weathered}}}, \tag{2.3}$$

where $[\mathrm{X}_i]_{\mathrm{weathered}}$ and $[\mathrm{X}_i]_{\mathrm{parent}}$ represent the concentration of the immobile element X_i in weathered regolith and unweathered parent bedrock, respectively. If no element loss has occurred during the transition from parent rock to regolith, the CDF is zero. If weathering has proceeded to completion (i.e. only quartz, clay minerals, and secondary oxides remain), the CDF attains a maximum value of ca. 0.5 in granitic rock.

To estimate the relative loss of individual elements (X), we used the elemental mass transfer coefficient τ (tau; Anderson et al. 2002; Brimhall and Dietrich 1987). It is important to note

that the ratio of X in weathered material to X in unweathered parent rock depends on both the loss of X and the loss of other elements besides X. To take the loss of other elements into account, the calculation of τ involves concentrations of an immobile element X_i in parent material relative to weathered material:

$$\tau^{X} = \frac{[X]_{\text{weathered}}}{[X]_{\text{parent}}} \times \frac{[X_i]_{\text{parent}}}{[X_i]_{\text{weathered}}} - 1. \tag{2.4}$$

If $\tau = 0$ no loss of X has occurred compared relative to the parent material. $\tau < 0$ denotes relative elemental loss, $\tau > 0$ denotes gain, respectively.

The conversion of primary minerals into secondary phases and solutes is usually accompanied by a change in density ρ and volume V. A measure of this change and an estimate of deformation is the volumetric strain ε (Brimhall and Dietrich 1987):

$$\varepsilon = \frac{\rho_{\text{parent}}}{\rho_{\text{weathered}}} \times \frac{[X_i]_{\text{parent}}}{[X_i]_{\text{weathered}}} - 1. \tag{2.5}$$

Positive values of ε indicate dilation, negative ones collapse of a profile. Values near zero are evidence of isovolumetric weathering.

Denudation rates based on cosmogenic nuclides and immobile elements

At each primary study site, the total denudation rate D (in t km^{-2} yr^{-1}) was determined for the mid-slope regolith profile of the S-facing and N-facing catena (AZPED50 & 21, SGPED40 & 70, LCPED20 & 40, and NAPED20 & 40; Table S2.6). To ensure that the calculated D reflects that of the regolith profiles and is not influenced by mixing of the surface layer with material from above (e.g. Heimsath et al. 1997), mobile material from the soil layer was avoided. Thus, we determined the in situ-produced ^{10}Be concentrations in quartz from material sampled from the top of the physically immobile saprolite just below the mobile soil layer (see Schaller et al. 2018b). D measures the total mass loss within the adsorption depth of cosmic rays (ca. 1 m; e.g. Dixon et al. 2009b; Riebe and Granger 2013; Riebe et al. 2001), which entails chemical loss (weathering, W) and physical loss (erosion, E):

$$D = E + W \tag{2.6}$$

If mass loss by weathering occurs beneath the cosmic ray adsorption depth, as it is likely in the saprolite that is weathered at great depth in the Chilean Coastal Cordillera (Vázquez et al. 2016), then the ^{10}Be concentration does not account for this loss and D is a minimum estimate (Riebe and Granger 2013). Nucleonic, stopped muonic, and fast muonic production rates P at sea level and high latitude (SLHL) used for denudation rate calculation are 3.92 atoms g^{-1} yr^{-1} (Borchers et al. 2016), 0.012 atoms g^{-1} yr^{-1}, and 0.039 atoms g^{-1} yr^{-1},

respectively (Braucher et al. 2011). SLHL production rates were scaled to sample altitude and latitude with the online tool of Marrero et al. (2016) using the scaling procedure based on Lifton et al. (2014). Shielding factors for topography and slope are 1.0. No shielding by snow has been taken into account. However, in order to correct for the influence of increasing vegetation cover on the production rate, shielding by vegetation of 2.3% for acadian/boreal forest and 7.3% for rain forest have been applied in La Campana and Nahuelbuta, respectively Plug et al. (2007). Shielding factors due to sample overburden (depth and soil density) were calculated for nucleonic, stopped, and fast muonic production rates. The adsorption lengths used were 157, 1500, and 4320 g cm^{-2}, respectively (Braucher et al. 2011). Denudation rates D [t km^{-2} yr^{-1}] were calculated based on the blank-corrected nuclide concentrations [atoms g^{-1}], the ^{10}Be decay constant $\lambda = 4.99\times10^{-7}$ yr^{-1} (Chmeleff et al. 2010; Korschinek et al. 2010), and the respective production rates P [atoms g^{-1} yr^{-1}] at sample depths and adsorption lengths Λ [g cm^{-1}] for each production mechanism using Eq. 2.7:

$$D = \left(\frac{P}{[^{10}Be]} - \lambda \right) \times \Lambda \tag{2.7}$$

The weathering rate can be calculated from D by using the CDF, which is a measure of the fraction of the total denudation that is accounted for by chemical weathering or also the ratio of chemical weathering to total denudation W/D. W is given by:

$$W = D \times CDF \tag{2.8}$$

We determined W with the CDF averaged over all soil samples, thus calculating a maximum chemical loss over the entire regolith profile.

2.4 Results

2.4.1 Chemical and mineralogical bedrock composition and classification

Major and selected trace element concentrations and density of local bedrock for each of the study sites are listed in Table S2.2. The bedrock in Pan de Azúcar and La Campana is characterized by $SiO_2 > 71$ wt% and a high Na_2O and K_2O content (~7 wt%; Fig. 2.7a). Apart from Mg, Ca, and Ba, major and trace elements show uniform concentrations (i.e. standard deviations below 15%). In contrast, bedrock samples from Santa Gracia and Nahuelbuta show extensive compositional heterogeneities. In Santa Gracia and Nahuelbuta, the standard deviation of the major and trace element concentrations is 33 and 50%, respectively. At Santa Gracia, the SiO_2 concentration is by far the lowest (50 wt% $< SiO_2 <$ 64 wt%) whereas the MgO concentration is the highest (0.91 wt% $<$ MgO $<$ 5 wt%) of all analyzed bedrock samples. The major element bedrock composition at Nahuelbuta is similar to that of Santa Gracia with the exception of SiO_2 concentrations that are 65 – 70 wt%.

Modal mineral abundances based on CIPW norm calculation (Johannsen 1937) of average bedrock composition for each study site are given in Table S2.3. With the exception of Santa Gracia, bedrock composition includes quartz (≥ 35 vol%) and feldspar-rich (Pl ≥ 35 vol%; Kfs ≥ 17 vol%) granitoid rocks. According to the two classification schemes of igneous and volcanic rocks introduced by (Le Bas et al. 1986, Fig. 2.7a) and (Streckeisen and LeMaitre 1979, Fig. 2.7b), the bedrock samples from Pan de Azúcar, La Campana, and Nahuelbuta are granites, granodiorites, and tonalites, respectively. Santa Gracia bedrock yield CIPW-based mineral modes for plagioclase (An + Ab) of 67 vol%, pyroxenes (14 vol%), quartz (9 vol%), and K-feldspar (5 vol%) rock. Both schemes classify these rocks as gabbros and diorites – igneous rocks with a low quartz content.

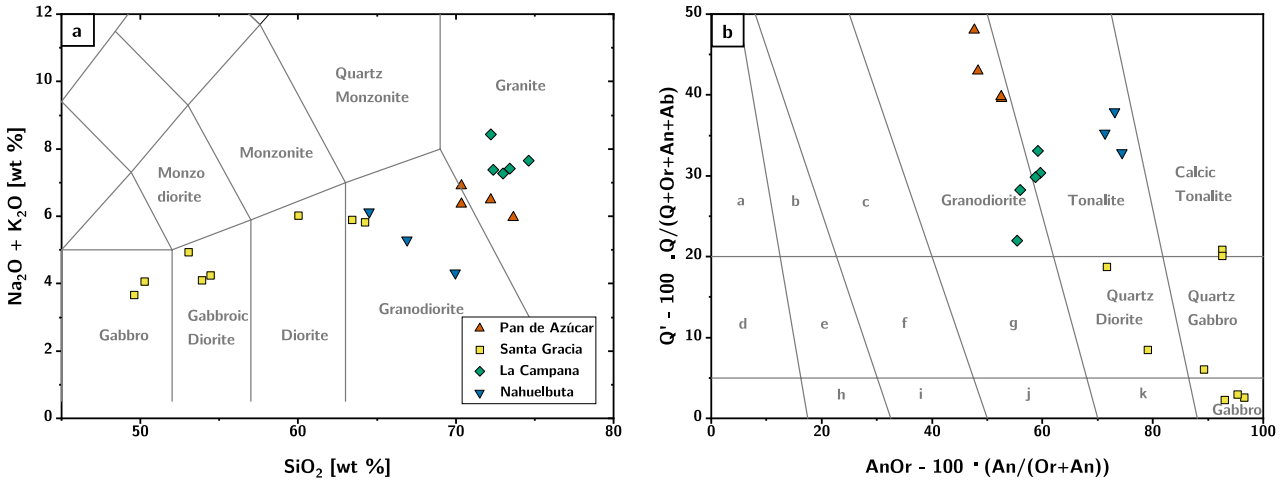

Figure 2.7: Classification diagrams for siliceous igneous and volcanic rocks. (a) Total alkali versus silica diagram introduced by Le Bas et al. (1986). (b) Q-AnOr diagram of Streckeisen and LeMaitre (1979), where the mineral modes were determined from XRF analyses by the CIPW norm calculation. Field association as follows: a - Alkali-feldspar granite; b - Syenogranite; c - Monzogranite; d - Alkali-feldspar Quartz Syenite; e - Quartz Syenite; f - Quartz Monzonite; g - Quartz Monzodiorite; h - Syenite; i - Monzonite; j - Monzogabbro; k – Diorite.

2.4.2 Regolith chemistry and weathering patterns

Major element concentrations of the four regolith profiles at each site are shown in Table S2.4 and Fig. 2.8. The principle differences in the overall compositions between the sites reflect the differences in bedrock composition. The compositional heterogeneity is small in Pan de Azúcar, Santa Gracia and La Campana within the saprolite. Only at Nahuelbuta the saprolite shows a high level of compositional heterogeneity between and within profiles, which is due to initial bedrock heterogeneity. Importantly, no gradients towards the base of the profiles are observed, implying that the weathering front has not been reached in any of these profiles. A and B horizon samples have a higher degree of heterogeneity, with some showing an increase in P and Ca concentrations.

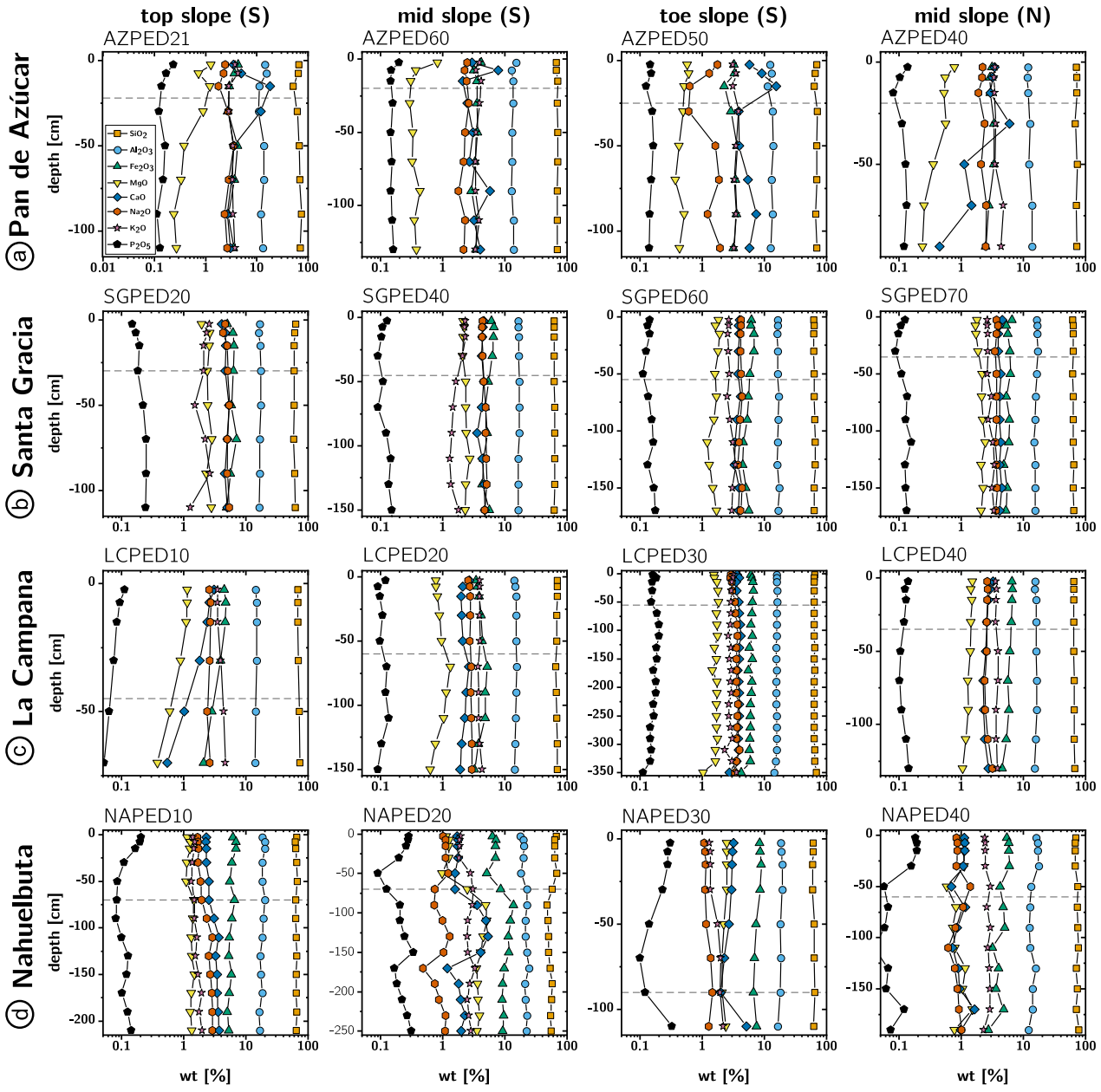

Figure 2.8: Depth-dependent major element composition (corrected for loss on ignition (LOI) following Eq. (2.1) of the four primary EarthShape study sites (regolith profile names indicated above). Differences between sites are attributed to large-scale bedrock variations and differences within the single catenae to small-scale lateral and vertical bedrock heterogeneities. Vertical variations within a profile (i.e. LCPED30, NAPED20, NAPED40) reflect a change in substrate. Dashed lines indicate the soil – saprolite boundary.

The compositional features translate into the following patterns of weathering intensity (CIA, Fig. 2.9). CIA of the EarthShape bedrock samples lie within the typical range of granitoid rocks (44-55; Nesbitt and Young 1982, Table S2.5). The CIA at Pan de Azúcar ranges from a bedrock average value of 55 ± 1 to a value as low as 32 in soil and saprolite (Table S2.5). This trend is opposite to that expected from weathering and is presumably due to atmospheric additions (see also Bernhard et al. 2018). The CIA at Santa Gracia ranges from a bedrock value of 43 ± 4 to 52 in regolith, which is due to the reaction of plagioclase to clay (Fig. 2.9a; Table S2.5). At La Campana the bedrock CIA value is 52 ± 1. The range of CIA of regolith samples between 50 and 58 is similar and indicates a low degree of weathering (Table S2.5). The bedrock CIA at Nahuelbuta is 54 ± 1, regolith samples show progressively increasing CIA values (Table S2.5) from 56 in saprolite to 75 in the A horizon. Thus, the degree of chemical weathering in the study area is generally relatively low, except for Nahuelbuta, and increases from Pan de Azúcar to Nahuelbuta.

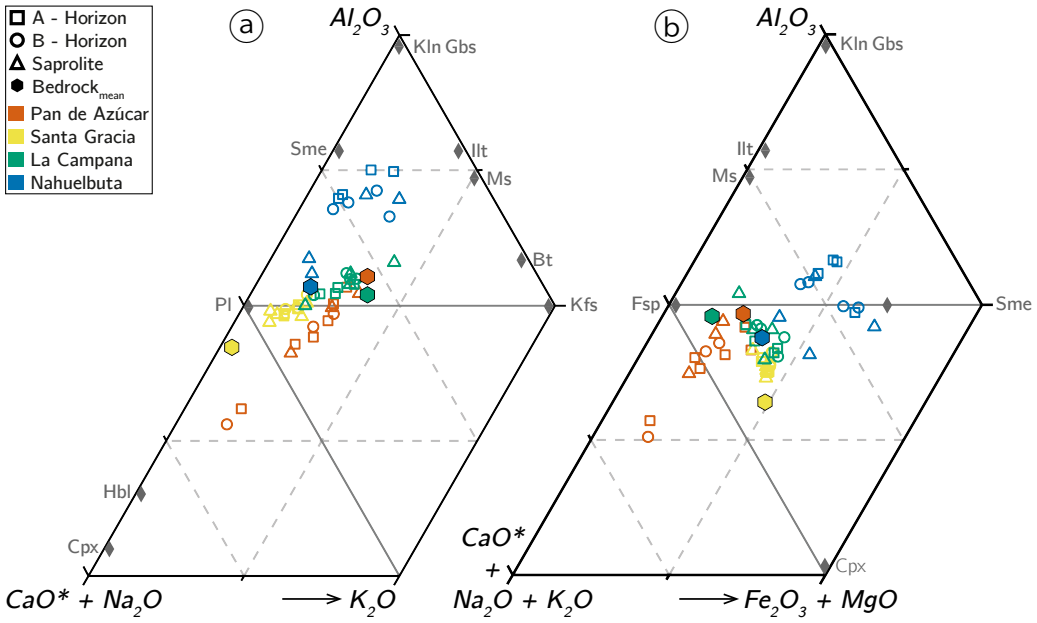

Figure 2.9: Weathering trends for regolith profiles in Pan de Azúcar (red), Santa Gracia (yellow), La Campana (green), and Nahuelbuta (blue) in the ternary space of A–CN–K (a) and A–CNK–FM (b) as introduced by Nesbitt and Young (1982) (molar proportions). Note that (a) corresponds to the CIA which is 100 at pure Al_2O_3, and 50 at connecting line between Pl and Kfs. The gray diamonds represent idealized mineral compositions: Bt - biotite; Cpx - clinopyroxene; Fsp - feldspar; Gbs - gibbsite; Hbl - hornblende; Ilt -illite; Kfs - K-feldspar; Kln - kaolinite; Ms. - muscovite; Pl - plagioclase; Sme – smectite.

Assessing Zr and Ti immobility in the study area

Zr, Ti, and Nb are commonly assumed to be least mobile during weathering (Chadwick et al. 1990; White et al. 1998) and are thus used in estimates of mass loss in the dissolved form during weathering (Eqs. 2.3 & 2.4). We first evaluated the suitability of these elements on a case to case basis, as their abundance can be biased from rock values by heterogeneity, loss, or external inputs. In Fig. 2.10 we perform this evaluation for Zr and Ti. A line (i.e. weathering enrichment line, including uncertainty envelopes representing bedrock heterogeneity) was constructed from the initial Ti/Zr ratios of bedrock samples. The line describes the expected relationship between these elements' concentration in regolith if they were entirely immobile during chemical weathering, and if a change in their concentration is solely due to weathering (i.e. no external input, no differential mobility), such that their concentrations increase in proportion to each other by loss of other elements (Hewawasam et al. 2013).

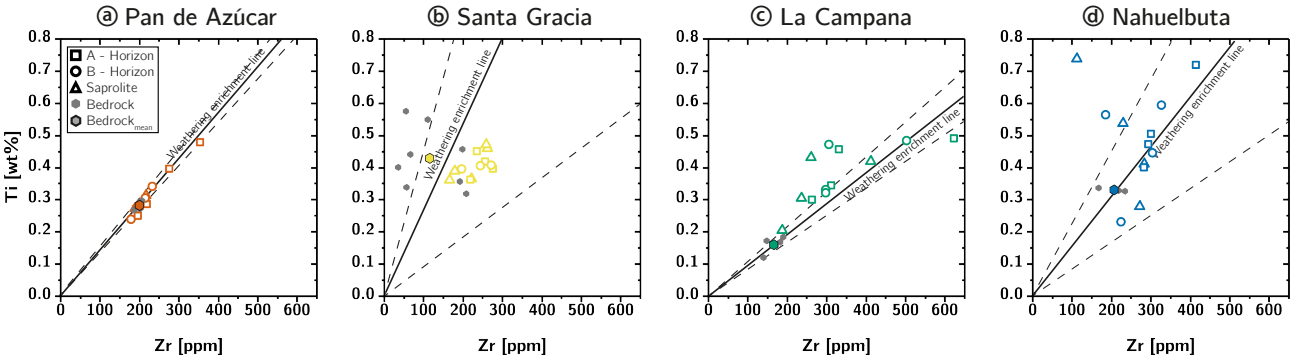

Figure 2.10: Ti and Zr concentration measured in soil, saprolite, and bedrock at the four primary EarthShape study sites. Solid lines (with error envelope, dashed) indicate the weathering enrichment line for bedrock composition, constructed from initial element ratios from bedrock samples and their uncertainty, as quantified by the Ti and Zr concentration of multiple bedrock samples.

Only Zr and Ti concentrations in regolith samples in Pan de Azúcar and La Campana roughly plot on the weathering enrichment line (Fig. 2.10a, c). In La Campana, exceptions are restricted to LCPED30 (Fig. 2.10c) and are most likely caused by compositional heterogeneities of the regoliths' parent material (Table S2.2). In Santa Gracia, regolith samples plot exclusively below the weathering enrichment line (Fig. 2.10b). Ti loss cannot be excluded, given the higher solubility of Ti-bearing minerals (i.e. biotite, titanite) when compared to zircon. In Nahuelbuta, most soil samples plot along the weathering enrichment line, but saprolite samples scatter widely (Fig. 2.10d). The high concentration of Ti in the saprolite and B horizon of samples from NAPED20 and NAPED40 can only be explained by heterogeneity in the substrate. Based on the possibility that Ti is mobile in some samples and the fact that Zr is used as a reference element in the majority of weathering and soil production studies worldwide (e.g. Green et al. 2006; Hewawasam et al. 2013; Riebe and Granger 2013; Riebe et al. 2001; Uhlig et al. 2017), we will use Zr as immobile reference element in our study.

Chemical depletion fraction (CDF)

Whereas the CIA presented above describes relative weathering trends, the CDF quantifies elemental loss. The CDF has been calculated using the study sites' average bedrock Zr concentration. The median CDF of the entire sampled regolith is between 0.2 and 0.5 for Nahuelbuta, La Campana, and Santa Gracia. At these sites, the CDF in the A and B horizon is also higher than that in the saprolite (Fig. 2.11).

This increase in the intensity of weathering between saprolite and soil is most pronounced in the S-facing mid-slope profile at Santa Gracia (weathering intensity increase by 28%) and in the top-slope pit at La Campana (weathering intensity increase by up to 35%; Table S2.5). Only in Pan de Azúcar the degree of weathering as quantified by the CDF is very low: at this site, the saprolite CDF is zero within uncertainty and only the thin A horizon shows some loss with a median CDF of 0.1. The B horizon shows enrichment ($CDF < 0$), which is due to atmospheric input and the formation of gypsum and calcite precipitates in this horizon. Differences in the degree of weathering between N- and S-facing regolith profiles are either not resolvable or, as in Nahuelbuta, caused by substrate heterogeneities within the profile. However, all CDF values are subject to high uncertainties, as shown by the standard deviation of the pooled samples at each site (Fig. 2.11). These uncertainties stem from the

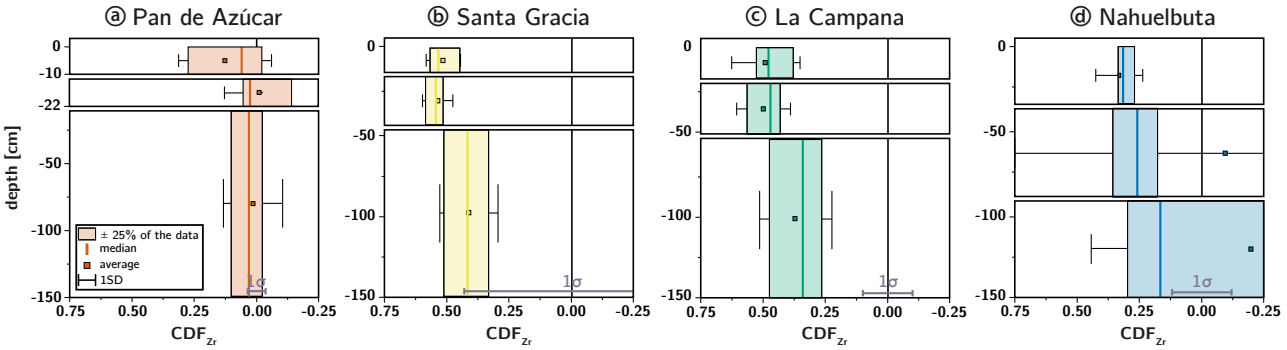

Figure 2.11: Chemical Depletion Fraction (CDF) for each study sites' averaged A horizon (top), B horizon (middle), and saprolite (bottom) samples. See legend in panel a for the explanation of the uncertainty bars. The accuracy of the absolute CDF values is limited by the variability in the respective sites' bedrock Zr concentration as indicated by the gray 1σ bar at the graphs' bottom. Note that the Y-axis scale is expanded by a factor of three for the A and B horizon in Pan de Azúcar.

chemical heterogeneity in the bedrock (Figs. 2.7 & 2.10; Table S2.2) and heterogeneities within the regolith profiles (Fig. 2.10; Table S2.4). This limits the attainable resolution in CDF to ± 0.04 at Pan de Azúcar, ± 0.6 at Santa Gracia, and ± 0.1 for Nahuelbuta and La Campana (Table S2.5). Due to the high uncertainty of the CDF in Santa Gracia, we cannot exclude that the degree of weathering is actually lower than estimated at this site. The large variation in the Zr concentration within the regolith profiles in Nahuelbuta, especially in NAPED20 (Table S2.4), account for the high variability in CDF values in this study site.

Elemental mass transfer coefficients (τ)

Elemental elemental mass transfer coefficients have been calculated using the Zr concentration of each regolith profile's lowermost sample as reference since the geochemical heterogeneity of bedrock (Table S2.2) does not allow the identification of a representative Zr concentration from rock samples. We thus evaluate vertical structure in elemental loss or gain relative to the base of the regolith profiles, rather than relative to bedrock. For Fig. 2.12, we averaged τ values for A, B and saprolite horizons within each site (Table S2.5) to resolve statistically significant patterns for each site.

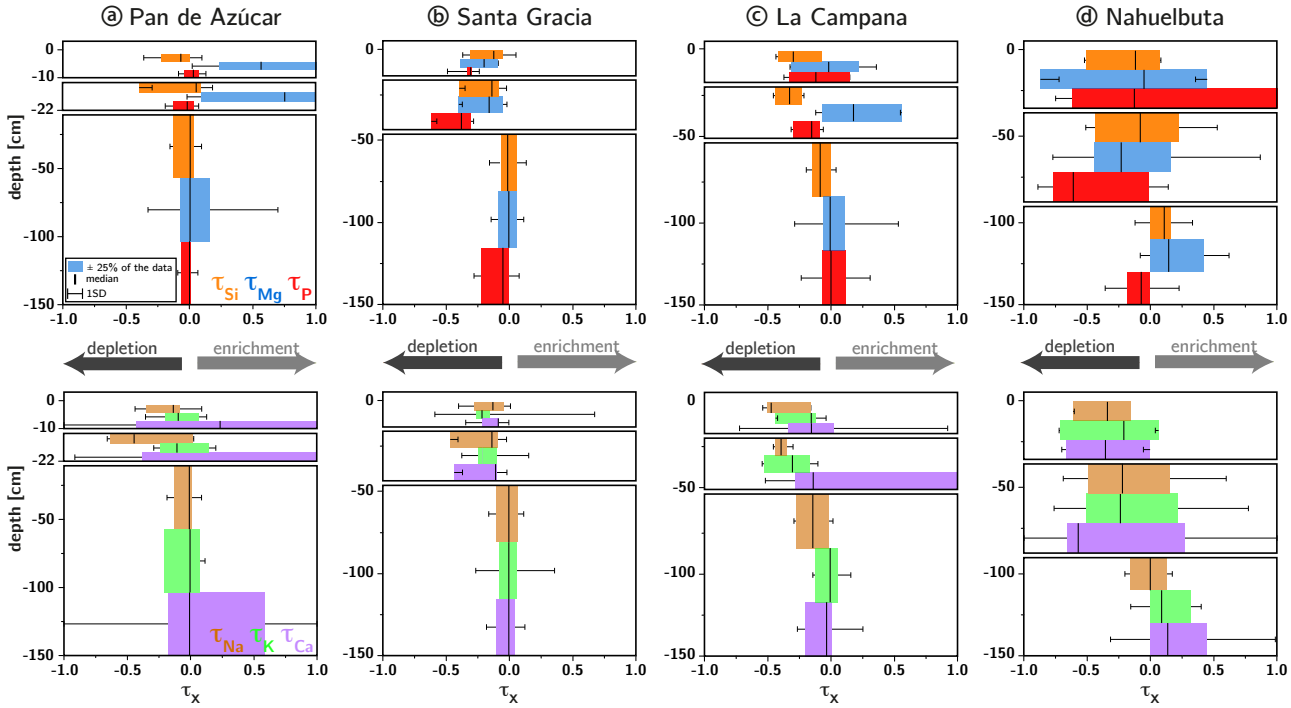

Figure 2.12: Elemental mass transfer coefficient (τ, the fractional element loss that was calculated here relative to the sample at the base of the regoliths profile) for each study sites' averaged A horizon (top box), B horizon (middle box), and saprolite (bottom box) samples. The upper graphs show τ values for Si, Mg, and P, whereas the lower graphs show τ values for Na, K, and Ca. Note that the shown τ values are only stacked for visualization reasons and represent τ values averaged over the study sites' specific horizons. Further, the Y-axis scale is expanded by a factor of three for the A and B horizon in Pan de Azúcar.

The regolith at Pan de Azúcar shows almost no losses, but an enrichment (i.e. $\tau > 0$) of Ca and Mg with decreasing depth. At Santa Gracia, averaged τ values for major elements and P in the saprolite indicate neither loss nor gain (i.e. $\tau = 0$; Fig. 2.12b). These elements are slightly depleted in A and B horizons. In La Campana, only Na and Si are lost in significant proportions from the saprolite (Fig. 2.12c; Table S2.5). These elements are progressively depleted with decreasing depth. P and K are depleted in the A and B horizon relative to the saprolite. Significant differences are apparent in the depletion of Ca, Mg, Fe, and Mn between

the N- and the S-facing mid slope profile (Table S2.5). In Nahuelbuta, τ values spread widely around their median values, which we attribute to the large chemical heterogeneity within the parent material (Fig. 2.12d; Table S2.4 and S2.5). In the A and B horizons, τ values indicate moderate (i.e. $\tau^{Ca,\,K,\,Mg}$ ~–0.25) to high depletion (i.e. $\tau^{P,\,Si}$ ~–0.60).

Volumetric strain (ε)

Volumetric strain has been calculated using each study sites' average bedrock density and Zr content (Table S2.2) along with the regolith samples' bulk density (Bernhard et al. 2018) and Zr content (Table S2.4). Largest volumetric expansion is seen in saprolite and soil samples from Nahuelbuta, ranging from 0.22 in saprolite to 1.54 in soil (Fig. 2.13; Table S2.5). The saprolite in the two sites further north (La Campana and Santa Gracia) experienced neither expansion nor collapse (Fig. 2.13; Table S2.5). For Pan de Azúcar, strain values in saprolite have not been calculated because no measurements of density were available. Whereas the soil horizons in La Campana and Santa Gracia are affected by minor dilation (ε ~0.25) and collapse (ε ~–0.25), respectively, the A- and B-horizons in Pan de Azúcar show a higher volume expansion (ε ~0.8; Fig. 2.13; Table S2.5).

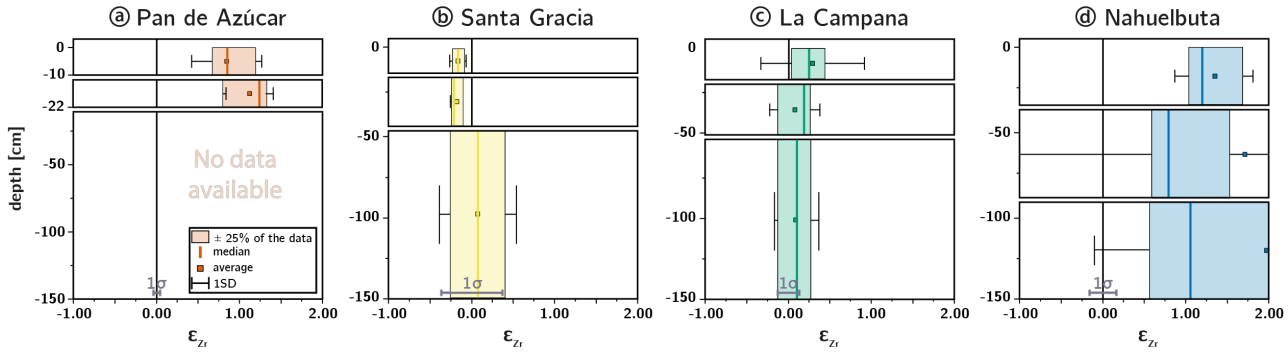

Figure 2.13: Volumetric strain (ε) for each study sites' averaged A horizon (top), B horizon (middle) and saprolite (bottom) samples. Positive values denote to expansion and negative values to collapse of the regolith profile. See legend in panel a for the explanation of the uncertainty bars. The accuracy of the absolute ε values is limited by the variability in the respective sites' bedrock Zr concentration as indicated by the gray 1σ bar at the graphs' bottom. Note that the Y-axis scale is expanded by a factor of three for the A and B horizon in Pan de Azúcar. In this study site, no ε is available for the saprolite, as bulk density has not been determined for these samples.

Pedogenic oxides

The oxalate-extractable Fe (Fe_o, ferrihydrite and poorly crystalized goethite) and dithionite-extractable Fe (Fe_d, well crystalized goethite, hematite, and lepidocrocite) were normalized to the total samples' Fe concentration determined from X-ray fluorescence (XRF) analyses (Table S2.4). The Fe_o/Fe_{tot} ratio in Pan de Azúcar, Santa Gracia, and La Campana ranges from 0.002 to 0.025 with slightly increasing proportions of extractable Fe towards the A horizon (Fig. 2.14a – c). Differences between oxalate- and dithionite-extractable Fe are most pronounced in Pan de Azúcar and La Campana. In Nahuelbuta, both the Fe_d/Fe_{tot} and Fe_o/Fe_{tot} ratios increase to values up to 0.24 in the A and B horizons. Pyrophosphate-extractable Fe (Fe_p, organic-bound colloidal Fe) range from 15 to 6870 ppm. The absolute Fe_p concentration substantially increase from La Campana to Nahuelbuta. The northern three study sites' average Fe_p is ~200 ppm.

From the oxalate-extractable Al (Al_o, amorphous Al-Si-OH) and dithionite-extractable Al (Al_d, clay) we have calculated oxalate-extractable (Al_o/Al_{tot}) and dithionite-extractable Al fractions (Al/Al_{tot}) that range between 0.1 and 0.2 (Fig. 2.14). Large differences between the two extracts were observed only in Nahuelbuta and to some extent in Santa Gracia (Fig. 2.14b and d). In Nahuelbuta, fractions of extractable Al increase towards the profiles' A and B horizons. Here, the differences between oxalate- and dithionite-extractable fractions become increasingly pronounced. Pyrophosphate-extractable Al (Al_p, organic-bound colloidal Al) ranges from 30 to 12500 ppm. Alike Fe_p, the highest absolute Al_p concentration is observed in Nahuelbuta.

Only small amounts of Si were extracted by oxalate (Si_o), dithionite (Si_d), and pyrophosphate (Si_p). Oxalate-extractable Si ranges from 65 to 1500 ppm, dithionite-extractable Si ranges from 65 to 3800 ppm, and pyrophosphate-extractable Si ranges from values below detection limit to 1615 ppm, respectively (Table S2.4). For all fractions, lowest values are observed in Pan de Azúcar (with the exception of Si_p in La Campana) and highest values are observed in Nahuelbuta. The oxalate- extractable Mn (Mn_o), dithionite-extractable Mn (Mn_d), and pyrophosphate-extractable Mn (Mn_p) range from 36 to 1400 ppm, from 22 to 1600 ppm, and from 1 to 420 ppm, respectively (Table S2.4).

Denudation, weathering, and erosion rates

In situ-produced ^{10}Be concentrations in quartz used for denudation rate calculations range between 8.9 ± 0.4 and $45.0 \pm 1.4 \times 10^4$ atoms g_{Qtz}^{-1} (Table S2.6). Denudation rates D calculated from these nuclide concentrations increase from Pan de Azúcar (S- facing: 11.0 ± 0.7 t km^{-2} yr^{-1}; N-facing: 8.2 ± 0.5 t km^{-2} yr^{-1}) to Santa Gracia (S-facing: 22.4 ± 1.5 t km^{-2} yr^{-1}; N-facing: 15.9 ± 0.9 t km^{-2} yr^{-1}) and La Campana (S-facing: 53.7 ± 3.4 t km^{-2} yr^{-1}; N-facing: 69.2 ± 4.6 t km^{-2} yr^{-1}). D at the southernmost loca-

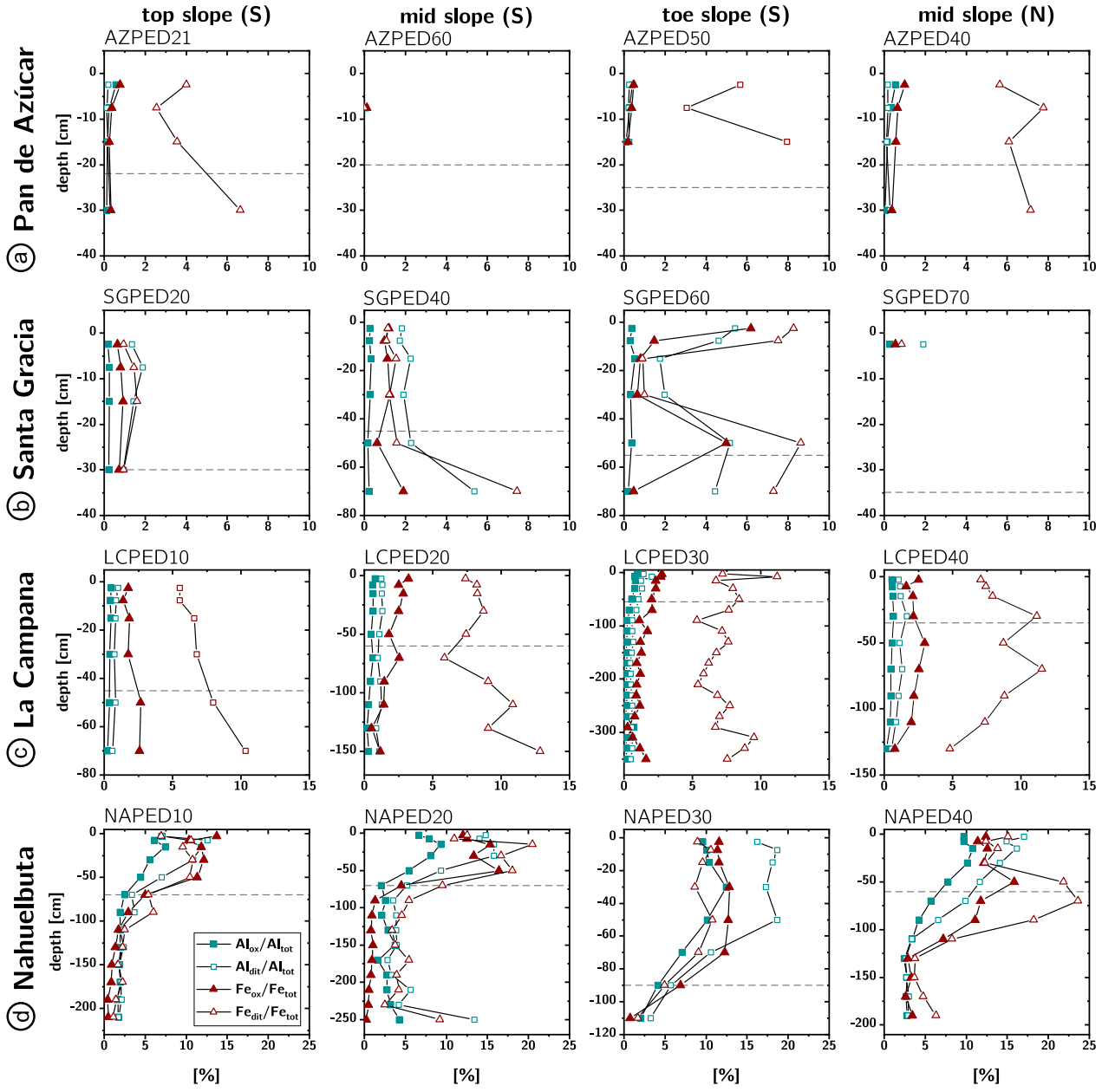

Figure 2.14: Ratios of Al and Fe concentrations of the pedogenic oxide fraction (oxalate extracted, closed symbols; dithionite extract, open symbols) relative to total sample concentration. Regolith profile names are indicated above and dashed lines indicate the soil–saprolite boundary.

tion, Nahuelbuta, is lower than that at La Campana (S-facing: 47.5 ± 3.0 t km^{-2} yr^{-1}; N-facing: 17.7 ± 1.1 t km^{-2} yr^{-1}; Table S2.6).

Based on denudation rates and the CDF derived from Zr concentrations in soil and bedrock samples, respectively, the chemical weathering rate and the physical erosion rate are calculated using Eqs. 2.6 and 2.8 (Table S2.6). The average chemical weathering rates increase from Pan de Azúcar (~0.9 t km^{-2} yr^{-1}; excluding the negative W value for AZPED21) to Santa Gracia (~9.5 t km^{-2} yr^{-1}) and La Campana (~32.8 t km^{-2} yr^{-1}). The physical erosion

rate is similar in Pan de Azúcar and Santa Gracia (~10.1 and ~9.6 t km^{-2} yr^{-1}), whereas the physical erosion rate is higher in La Campana (~28.7 t km^{-2} yr^{-1}) than at the locations further North. The heterogeneity in bedrock and regolith Zr concentrations prohibits the calculation of an accurate weathering rate at Nahuelbuta. Taking the total denudation rates at face value, the estimated chemical weathering rates in Nahuelbuta would be ~5.5 t km^{-2} yr^{-1} and the physical erosion rates would be ~27.1 t km^{-2} yr^{-1}. However, we have no confidence in the accuracy of these estimates.

Microbial abundance in saprolite

he extraction of total genomic DNA resulted in high variability (Fig. 2.15). Lowest DNA amounts were detected in saprolites from Pan de Azúcar with a minimum of 14.5 ± 2.5 µg $g^{-1}_{regolith}$, followed by Nahuelbuta ranging from 14.0 ± 1.0 to 26.0 ± 2.0 µg $g^{-1}_{regolith}$. In contrast, highest DNA yields and variations from 20.5 ± 0.5 to 44.1 ± 11.1 µg $g^{-1}_{regolith}$ were obtained in saprolites from Santa Gracia. DNA concentration in La Campana mainly varied around 27.0 µg $g^{-1}_{regolith}$ (Table S2.7).

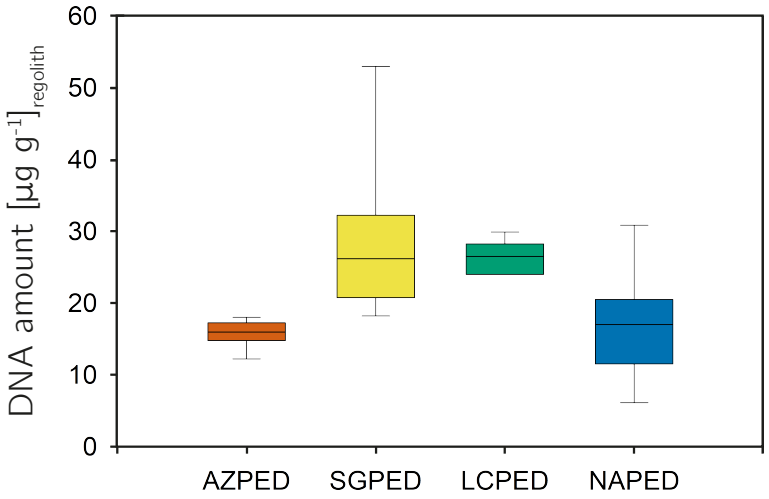

Figure 2.15: Concentration of extracted DNA, averaged over the entire sampled saprolite depth. Box plots represent the sum of values of all topographic positions combined in Nahuelbuta (NAPED), La Campana (LCPED), Santa Gracia (SGPED) and Pan de Azúcar (AZPED). Median lines are indicated within the boxes of which the size corresponds to ± 25% of the data, whereas the whiskers show ± 1 st dev of all data. DNA was extracted from saprolite samples in triplicates.

Quantification of 16S rRNA genes revealed consistently higher abundances of bacteria than archaea within the saprolite samples (Fig. 2.16). Pan de Azúcar was the only primary study site with no topography-specific variations. Bacterial cell numbers ranged constantly around 10^5 gene copy numbers per gram of regolith. Archaea were lower by up to two

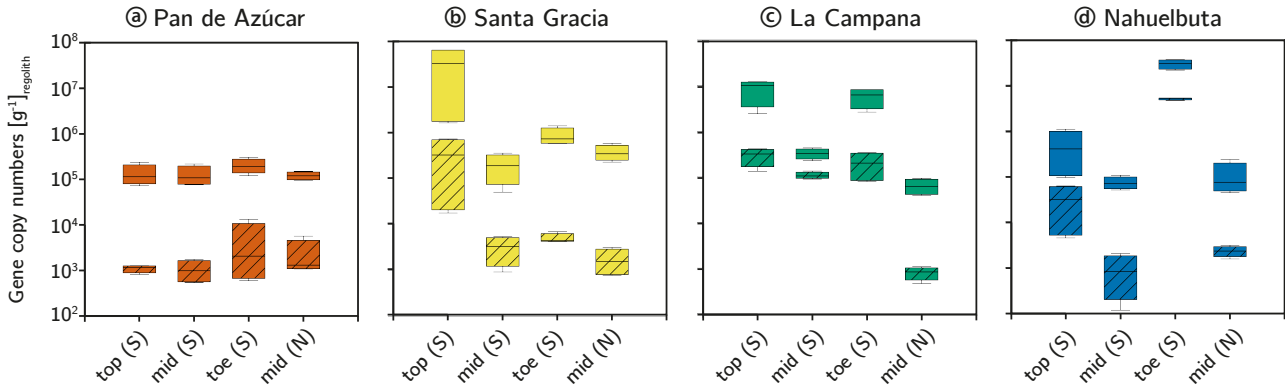

Figure 2.16: Abundance of bacterial (open) and archaeal (patterned boxes) 16S rRNA gene copy numbers per gram of regolith in the primary study sites, averaged over the entire sampled saprolite depth. Saprolite samples were collected along the hillslope catena at four different positions. Box plots represent the sum of all replicate samples, each measured in quadruplicate qPCR reactions. Median lines are indicated within the boxes of which the size corresponds to ± 25% of the data, whereas the whiskers show ± 1 st dev of all data. S = south facing, N = north facing.

orders of magnitude. Saprolites from Santa Gracia revealed the overall highest bacterial abundances in the top slope with 6.5×10^7 gene copies $g^{-1}_{regolith}$. The lowest bacterial cell numbers with 3.9×10^4 gene copies $g^{-1}_{regolith}$ were detected in the mid-slope (N) in La Campana. In Nahuelbuta, the highest and lowest archaeal abundances were obtained, ranging from 1.2×10^2 in the mid-slope (S) to 5.2×10^6 gene copies $g^{-1}_{regolith}$ in the toe-slope. However, relative microbial abundances did not significantly differ between the regions Nahuelbuta, La Campana, and Santa Gracia ($P > 0.09$). Only data from Pan de Azúcar turned out to be significantly different from all other study sites ($P < 0.05$). In general, bacteria outnumber archaea in all study sites. In the driest regions Santa Gracia and Pan de Azúcar, the highest archaea-to-bacteria ratios were detected (Table S2.7). The overall highest archaea-to-bacteria ratio (1:217) was obtained in the mid-slope (N) in Santa Gracia. The mid-slope (S) of La Campana showed the lowest archaea-to-bacteria ratio (1:3).

2.5 Discussion

Assuming that the EarthShape approach, namely that geological boundary conditions (i.e. bedrock, rock uplift rate) do not differ along the transect, the bio-climatic forcings can be evaluated. We initiate this evaluation by structuring the observed geochemical trends into three categories: (1) A continental latitudinal trend, where (chemical) weathering intensity increases from north to south as precipitation and vegetation cover increase; (2) a local trend, where regolith on the N- facing catenae is exposed to more incoming solar radiation and thus less moisture is available for weathering reactions and plant biomass com- pared to the S-facing slope, and (3) an in-situ trend, where weathering intensity decreases with increasing regolith depth. We discuss these trends for the four EarthShape study sites.

Further, we discuss the drivers of weathering and whether it is possible to discern abiotic from biotic processes.

2.5.1 The continental trend

Permanent slow erosion: denudation rates and saprolite residence times

Total denudation rates increase from Pan de Azúcar (8 – 11 t km^{-2} yr^{-1}) to Santa Gracia (16 – 22 t km^{-2} yr^{-1}) and reach a maximum in La Campana (54 – 69 t km^{-2} yr^{-1}). Although MAP (Fig. 2.2) and vegetation cover increase from north to south, the denudation rate in Nahuelbuta is lower (18 – 48 t km^{-2} yr^{-1}; Table S2.6) than in La Campana. If not caused by a differing influence of biota on denudation processes (Schaller et al. 2018b) between La Campana and Nahuelbuta, the difference in denudation rate between the two sites can be explained with (1) the hillslopes in La Campana that are the steepest of all study sites (Table S2.1); and (2) higher uplift rates in the region of La Campana compared to the other parts of the Chilean Coastal Cordillera (Carretier et al. 2013; 2018), both leading to higher denudation rates. The denudation rates of this study are in agreement with published data. Owen et al. (2011) reported average bedrock erosion rates of active slopes from locations near Pan de Azúcar and Santa Gracia of 2.7 ± 0.4 mm ky^{-1} and 26 ± 7 mm ky^{-1}, respectively. Based on a bedrock density of $\rho = 2.6$ g cm^{-3}, these rates equal a denudation rate of ~7 t km^{-2} yr^{-1} and ~70 t km^{-2} yr^{-1}, respectively. At a location 50 km south from La Campana, the total denudation rates range from 42 to 147 t km^{-2} yr^{-1} (Vázquez et al. 2016), which encompasses our value of 60 t km^{-2} yr^{-1}. All these rates are at the lower end of global cosmogenic nuclide-based soil denudation rates (Dixon et al. 2012). The relative uniformity and narrow range can be attributed to the uniform tectonic drivers in the whole study area (Blanco-Chao et al. 2014; Melnik 2016). Furthermore, the low denudation rates in the two northern sites are typical for those observed in arid areas (Carretier et al. 2015; Cockburn et al. 1999; Kober et al. 2007; Starke et al. 2017).

Residence times of material in the uppermost 60 cm of regolith (which is the cosmic ray mean attenuation pathway, used by convention to report residence times based on cosmogenic nuclides; von Blanckenburg 2005) and the denudation rate are around 200 kyr in Pan de Azúcar, 100 kyr in Santa Gracia, 30 kyr in La Campana, and 40 to 100 kyr in Nahuelbuta. Thus, over these averaging time scales, the material contained in a 60 cm depth interval of regolith is being replaced by supply of material from depth, its removal by erosion at the surface, and weathering in the weathering zone. The regolith is thus permanently turned over by slow erosion.

Degree of weathering

Prior to comparing the degree of weathering between the four study sites, differences in their bedrock composition and potential external inputs have to be evaluated. All study sites are underlain by granitoid rock. However, its composition differs between sites. Bedrock at Pan de Azúcar and La Campana is granodioritic, bedrock at Santa Gracia is more mafic, ranging to quartz gabbro, and Nahuelbuta is intermediate with tonalitic composition (Fig. 2.7).

External input in the form of volcanic ash potentially affects Nahuelbuta, given the sites' proximity to the Andean volcanic arc (Moreno and Clavero Riebes 2006; Naranjo S. and Moreno R. 2005; Parada et al. 2007; Petit-Breuilh and Lobato 1994). Volcanic input results in soils with andic properties. Andic soils are defined to exist if the bulk density is typically lower than 0.9 g cm^{-3}, $Al_o + 1/2\,Fe_o$ exceeds a value of 0.4 or 2% (Bäumler et al. 2005; Parfitt and Clayden 1991, and references therein), and a considerable amount of glass is found in the soil fraction < 2 mm (i.e. < 30%; Staff 1999). The formation of allophane and imogolite would emerge if these glasses weather and ultimately lead to Si_o/Al_o ratios between 0.5 and 1 (Wada 1989). In the soils of Nahuelbuta, bulk density is close to the threshold of 0.9 g cm^{-3} or below (Bernhard et al. 2018) and $Al_o + 1/2\,Fe_o$ ratios exceed 0.4% persistently. However, $Al_o + 1/2\,Fe_o > 2\%$ were never attained (Table S2.4) and no volcanic glass particles were found. Thus, the soils of Nahuelbuta reveal some features of andic soils. Still, neither the chemical composition of the investigated regolith samples nor the pedogenic oxides indicate the presence of volcanic ash: (1) No enrichment in Na, K, or Mg is observed in A or B horizons in any regolith profile. Mixing models between characteristic Mg and Na concentrations in andesitic volcanic ash and the Nahuelbuta saprolite indicate that volcanic ash additions, if occurring in soil, are insignificant and within the resolution of the sample, and are thus < 2% (Fig. 2.17); (2) Si_o/Al_o ratios are < 0.25; and (3) prevailing west winds (García 1994) would impede the deposition of thick volcanic ash layers in this area.

The input of sea spray into the soil profiles is well-documented only at Pan de Azúcar by (1) lower CIA values in regolith than in bedrock (Fig. 2.9), (2) positive τ_{Ca} and τ_{Mg} (Fig. 2.12), and (3) further supported by positive ε (Fig. 2.13) despite CDF being close to zero (Fig. 2.12) in the soil horizons.

In granitoid rock, the maximum degree of weathering (CDF) is typically 50%, as the remaining mass is insoluble quartz and clay minerals (Hewawasam et al. 2013). Such maximum CDF would correspond to a CIA of 1. In Pan de Azúcar, physical erosion exceeds chemical weathering by an order of magnitude (Table S2.6). Here, the processes disintegrating rock and developing regolith are mainly physical weathering (CDF ~0.1 over the entire profile; Fig. 2.11) and are mostly attributed to either insolation- or salt weathering, or a combination of both. This is also in agreement with the low abundance of microorganisms in the saprolite at this site. Upon insolation weathering, diurnal or annual heating and cooling cycles lead to a granular disintegration of biotite and to the grussification of feldspar and quartz.

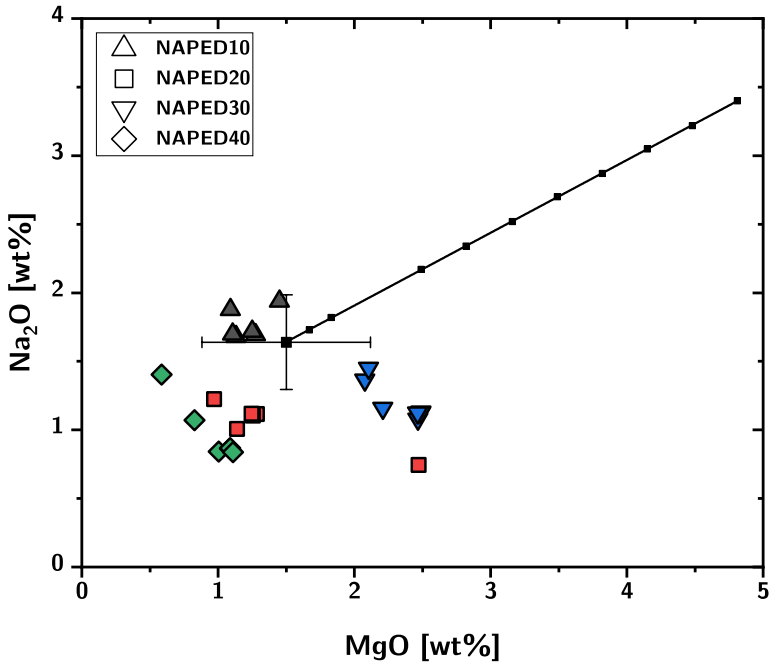

Figure 2.17: Mixing model between average Na and Mg concentrations of Nahuelbuta saprolites (Na_2O: 1.64 wt% and MgO: 1.50 wt%) and andesitic ash (Na_2O: 3.40 wt% and MgO: 4.81 wt%), respectively. The black line represents the mixing line between 0% volcanic ash input to the left and 100% volcanic ash input to the right. Symbols represent samples from the A and B horizons at Nahuelbuta. The model indicates that the contribution of ash at the Nahuelbuta site is, if existing at all, insignificant.

This process opens pathways along grain boundaries and ultimately increases the reactive surface of rock (e.g. Tchakerian and Pease 2015, and references therein). Sea spray in combination with coastal fog (i.e. camanchaca) provides considerable amounts of water (e.g. Larrain et al. 2002). Consequently, the formation of gypsum and anhydrite (Fig. 2.3) further fracture the rock (i.e. salt weathering) and percolating moisture and oxygen initiate biotite weathering. These processes release approximately 8 to 10% of the total Fe from primary minerals and form secondary phases (Fig. 2.14). In Santa Gracia, chemical weathering equals physical erosion (Table S2.6). The high degree of weathering (CDF ~0.4 – 0.5; Fig. 2.11) despite low precipitation can be attributed to the low abundance of quartz on the one and the high abundance of weatherable plagioclase and mafic minerals on the other hand (Fig. 2.9; Table S2.3). However, given the high uncertainty in the bedrocks' Zr content and arising CDF uncertainties, we cannot exclude that the fraction of chemical weathering on total denudation is lower in this study site. In La Campana, chemical weathering also equals physical erosion (Table S2.6). Such a degree of weathering (CDF ~0.3 – 0.6; Fig. 2.11) is expected in such a Mediterranean climate (e.g. Schoonejans et al. 2016). However, Al is also lost as indicated by negative τ values (Table S2.5). Thus, secondary mineral formation seems to be subordinate (Fig. 2.9). In Nahuelbuta, physical erosion outpaces chemical weathering

by a factor of 5 (Table S2.6). However, we are unable to assign reliable ratios of erosion to weathering due to the high heterogeneity in bedrock and regolith samples.

Concentrations of oxalate- and dithionite-extractable Fe and Al (relative to the samples' Fe and Al content; Fig. 2.14) are increasing with increasing precipitation. Together, the proportion of well-crystallized Fe oxides (e.g. goethite, lepidocrocite, hematite) in the extractable Fe decreases with increasing precipitation (Fe_o/Fe_d; Table S2.4). These observations are in accordance with (1) chemical pedogenic development that is higher in humid climates compared to arid climates and, hence, a higher production rate of pedogenic Fe oxides and hydroxides (Alexander 1985; Birkeland et al. 1989) and (2) a higher proportion of oxalate extractable oxides under more humid and, hence, higher soil moisture conditions (Schwertmann 1964; 1985).

Regolith density in saprolite is another indicator of the degree of weathering. Along the transect, saprolite density (Bernhard et al. 2018) is 1.5 – 1.7 g cm^{-3} in Santa Gracia, 1.4 – 1.8 g cm^{-3} in La Campana, and 0.9 – 1.3 g cm^{-3} in Nahuelbuta (Table S2.4). In Pan de Azúcar, no volumetric samples were taken from the hard saprolite. By comparison, typical density in saprolites measured in weathering studies over granitoid rock in a range of denudation and climate zones are 1.0 – 1.5 g cm^{-3} in deep, slow humid tropical weathering, 1.3 – 2.5 g cm^{-3} in tropical granite rejuvenated by constant erosion, and 2.0 – 2.6 g cm^{-3} in rapidly eroding temperate climate (Anderson et al. 2002; Braun et al. 2009; Brimhall et al. 1991; Buss et al. 2017; Hewawasam et al. 2013; Scholten 1997; White 2002). Within uncertainties, the volumetric strain ε is zero in saprolite samples from Santa Gracia and La Campana (Fig. 2.13b, c). In Nahuelbuta ε, in saprolite largely scatters around its median value of about 1 (Fig. 2.13d). However, this scatter arises from the high variation of Zr within the regolith profile and is not necessarily related to expansion upon the formation of secondary minerals. Consequently, the EarthShape transect is subject to strong isovolumetric weathering despite strong differences in mass loss.

2.5.2 The local trend: N-facing versus S-facing hillslopes

The A and B horizons are thicker (with the exception of Pan de Azúcar) on S-facing slopes (Table S2.1), which is expected on N-facing slopes in the southern hemisphere as they are more prone to solar radiation and therefore experience more xeric conditions (Dixon 2015). Still, neither in chemical property nor in the derived depletion indices (i.e. CDF & τ) we find significant differences between regolith profiles on N- and S-facing slopes. Additionally, pedogenic oxides neither differ significantly in (1) their total abundance, nor (2) their proportion of oxalate-extractable oxides, nor (3) their degree of chemical pedogenic development between regolith profiles on N- and S-facing slopes throughout all four study sites (Table S2.4).

In the two northern sites Pan de Azúcar and Santa Gracia, where solar inclination is high, the differences in micro-climate and hence changes in vegetation cover and type between

N- and S-facing slopes are minimal. Still, each combination of different (micro-) climate and biota might result in discernable weathering patterns. Thus, emerging differences in the weathering pattern in these sites might either not exist or might not be resolvable with the analyzes we applied. However, the absence of significant differences in La Campana and Nahuelbuta is particularly surprising given the substantial differences in the vegetation and species composition between the N- and S-facing slopes in these sites. If the exposure to sunlight indeed controls biomass growth, then the absence of N – S differences in the degree of weathering and other chemical pedogenic properties could indicate that either the differences in vegetation between slopes are not big enough to be reflected on regolith processes, or that the impact of biogenic weathering in these four study sites is low.

La Campana was the only site showing N – S differences in bacterial and archaeal gene copies in saprolite. Archaea- to bacteria ratios differed among slopes in all sites, but showing contrasting patterns in different sites. In the saprolite on S-facing slopes of the Pan de Azúcar and Nahuelbuta region, bacteria are outnumbering archaea by far. In La Campana and Santa Gracia, this trend is seen in the saprolite on the N- facing slopes.

2.5.3 The in-situ trend: vertical structure of the weathering zone

Along the gradient the degree of soil formation increased with precipitation and vegetation cover (Bernhard et al. 2018) as shown by increasing thickness of soil horizons and an increasing amount of oxalate- and dithionite-leachable Al and Fe (Fig. 2.14, Tables S2.1 & S2.4). However, neither do total denudation rates nor the degree of weathering regularly increase with precipitation and vegetation cover. We cannot establish whether this observation also holds for the depth of the weathering zone, because in none of the regolith profiles the weathering front has been encountered. As our profiles attain a depth of 2 m at the most, this observation is expected as global depth profiling in weathered granitoid rock resulted in a mean depth of 13 ± 5 m for the location of the weathering front (i.e. where rock is converted into saprolite; Bazilevskaya et al. 2013). In the Chilean Coastal Cordillera, this depth appears to be even higher, exceeding 30 m in some cases (Vázquez et al. 2016). Such great depth, if not due to an inherited weathering history, could also be explained with the overall low erosion rates that prevents a steady state between weathering front advance rate and erosion at the surface (Lebedeva et al. 2010).

Within the sampled regolith profiles, vertical gradients are virtually absent within the saprolite. This stability hints at a depletion gradient that is located at a much greater depth. However, gradients in elemental concentrations and depletion do appear within the soil horizons. Namely, P concentrations increase over those found in the saprolite in all sites, and strongly so in Nahuelbuta. This increase hints at nutrient uplift and recycling via leaf and root litter (Jobbágy and Jackson 2004). Vertical gradients in element depletion are not discernable due to the high initial bedrock heterogeneity.

That the depth profiles of pedogenic oxides show a relative decrease in pedogenic to total oxide ratios in Nahuelbuta and to a lesser extend in La Campana can be interpreted to be caused by gradients in regolith moisture. For the other two sites, there is no clear decrease of this ratio with depth, which can be explained by the lower infiltration into these profiles.

Total microbial abundances decrease with depth at all study sites, containing the highest abundances in surface soils as shown in (Bernhard et al. 2018). This pattern is in agreement with several other studies, which highlight the importance of soil depth and plant C input on microbial abundance and community structures (Agnelli et al. 2004; Eilers et al. 2012; Fierer et al. 2003; Will et al. 2010). Moreover, bacteria numerically dominate over archaea also in the saprolites in all sites.

2.5.4 Is the biogenic weathering engine discernable?

The coastal dry environments of northern Chile (from 20 to 32°S; Pan de Azúcar and Santa Gracia) are characterized by permanently low water availability and biotic activities that are controlled by rare episodic moisture inputs (Armesto et al. 2007; Rundel et al. 2007). Samples from these two sites show no significant element depletion in the soil compared to the saprolite (Figs. 2.11 & 2.12). In the samples from Nahuelbuta, which receive the largest amount of annual rainfall, elements such as Ca, Mg, K, and Na that do not form insoluble hydroxides and are readily leached, show the largest degree of depletion (Fig. 2.12). Thus, as a result of this increased leaching with increasing precipitation the pools of mineral-derived nutrients decrease along the precipitation gradient from north to south. Yet, at none of the sites the regolith is so depleted in mineral nutrients that the weathering zone would be "supply-limited". In the geochemical terminology, this means that nutritive elements are wholesale absent in regolith, which then depends on recycling and aeolian inputs Dixon et al. (2012); Porder et al. (2007); Uhlig et al. (2017). The main imprint of biogenic processes we found to be the enrichment of P and partly Mg that can be observed in samples from the A- compared to the B-horizons at La Campana and Nahuelbuta (Fig. 2.12c, d). This surface enrichment shows that nutrient uplift and vegetation recycling is at work at those sites (Jobbágy and Jackson 2004; Porder and Chadwick 2009).

All sites do contain distinct bio-signatures though. Properties found in the A and B horizons of soils that can, in theory, be interpreted to be influenced by biota, such as total organic carbon content and C/N ratios show pronounced trends along the transect (Bernhard et al. 2018). In the saprolite, bacterial gene copies (indicative for universal abundances) are highest at the non-arid sites. Previous studies already indicated that deeper soil layers contain microbial communities, specialized for low C and O_2 input (Fritze et al. 2000; Ghiorse and Wilson 1988; Zvyagintsev 1994). This strategy to exploit different ecological niches is also provided by the interaction with soil minerals (Ehrlich 1995). Several studies already demonstrated the crucial influence of minerals on the bacterial community structure (Carson et al. 2007;

2009; Certini et al. 2004). Thus, it is suggested that these microbes may provide a biological contribution to mineral-weathering processes.

2.6 Conclusions

We provided first interpretation of a comprehensive geochemical data set, addressing how climate and vegetation cover influence weathering, microbial abundance and potential activity, and mineral nutrient supply to different ecosystems in the Chilean Coastal Cordillera. We explored four sites along a climate gradient from arid to humid with S- and N-facing regolith profiles that experienced low and high insolation, respectively. We provided a complete description of (1) the regolith profiles and their vegetation cover; (2) the denudation rates that describe their permanent turnover by erosion and weathering; (3) a comprehensive geochemical characterization of regolith and bedrock as well as (4) microbial abundances in the saprolite.

We found that denudation rates generally increase with increasing precipitation and vegetation cover from north to south, being highest in the Mediterranean climate of La Campana, where hillslopes are also highest. Further south in Nahuelbuta where precipitation and the vegetation cover are highest, denudation rates are lower than in La Campana. However, hillslopes in Nahuelbuta are also lower than in La Campana. These low slopes can explain the difference in denudation rate if it is not due to the higher vegetation cover. Chemical depletion and microbial abundances in saprolite are low in Pan de Azúcar (arid and sparsely vegetated site) and are higher in the three southern (more humid and denser vegetated) sites that do not show pronounced differences between them. However, no clear trend of chemical depletion and microbial abundances with increasing precipitation and vegetation cover has been found.

We have shown that the thickness of the soil horizons is higher on S- facing slopes compared to the N-facing analogues. However, expected differences in the degree of chemical weathering between S- and N-facing slopes could not be detected. Thus, the N – S comparison did not yet allow to discern the effects of abiotic versus biotic weathering.

Even though indicators of weathering characteristics that allow to distinguish the abiotic (purely climate-related) from the biotic (climate- and bio-related) driver have not yet emerged, the EarthShape study sites are suited to evaluate biological effects on weathering, using advanced biological and geochemical techniques. Future studies should focus on the unique and puzzling features of the EarthShape Critical Zones such as (1) the low chemical weathering rates, which appear to be contradicted by the substantial depth of the weathering front; and (2) the interacting role of climate, vegetation, microbiota, and fauna in controlling the respective erosion and weathering rates. These findings will eventually be placed into the context of efforts to derive the abiotic and biotic driving forces that shape the Critical

Zone, both within future studies in the "EarthShape" project, and within global studies of the Critical Zone (Brantley et al. 2016; Chorover et al. 2007; Hilton 2017; Riebe et al. 2016).

Acknowledgements

Special thanks to CONAF for giving us the opportunity to work in the national parks of Pan de Azúcar, La Campana, and Nahuelbuta. We also thank CEAZA for facilitating access to the Reserva Natural Santa Gracia. We thank Anja Schleicher at GFZ Section 3.1 "Inorganic and Isotope Geochemistry" for support of XRF analyses. We are grateful for the comments of two anonymous reviewers that helped to improve this paper. This project is funded by the German Science Foundation DFG- SPP 1803 (EarthShape; www.earthshape.net).

2.7 Supplementary material

Data supplement to: Chemistry and Microbiology of the Critical Zone along a steep climate and vegetation gradient in the Chilean Coastal Cordillera

Abstract

The Chilean Coastal Cordillera features a spectacular climate and vegetation gradient, ranging from arid and unvegetated areas in the north to humid and forested areas in the south. The DFG Priority Program "EarthShape: (Earth Surface Shaping by Biota)" uses this natural gradient to investigate how climate and biological processes shape the Earth's surface. We explored the critical zone, the Earth's uppermost layer, in four key sites located in desert, semidesert, mediterranean, and temperate climate zones of the Coastal Cordillera, with the focus on weathering of granitic rock. Here, we present first results from four ~2 m-deep regolith profiles to document: (1) architecture of weathering zone; (2) degree and rate of rock weathering, thus the release of mineral-derived nutrients to the terrestrial ecosystems; (3) denudation rates; and (4) microbial abundances of bacteria and archaea in the saprolite.

From north to south, denudation rates from cosmogenic nuclides are ~10 t km^{-2} yr^{-1} at the arid Pan de Azúcar site, ~20 t km^{-2} yr^{-1} at the semi-arid site of Santa Gracia, ~60 t km^{-2} yr^{-1} at the mediterranean climate site of La Campana, and ~30 t km^{-2} yr^{-1} at the humid site of Nahuelbuta. A and B horizons increase in thickness and elemental depletion or enrichment increases from north (~26°S) to south (~38°S) in these horizons. Differences in the degree of chemical weathering, quantified by the chemical depletion fraction (CDF), are significant only between the arid and sparsely vegetated site and the other three sites. Differences in the CDF between the sites, and elemental depletion within the sites are sometimes smaller than the variations induced by the bedrock heterogeneity. Microbial abundances (bacteria and archaea) in saprolite substantially increase from the arid to the semi-arid sites.

With this study, we provide a comprehensive dataset characterizing the Critical Zone geochemistry in the Chilean Coastal Cordillera. This dataset confirms climatic controls on weathering and denudation rates and provides prerequisites to quantify the role of biota in future studies.

This dataset is published in:

GFZ Data Services

Oeser et al. (2018b);
https://doi.org/10.5880/GFZ.3.3.2018.001

Table S2.1: Catena properties of the four primary EarthShape study sites. Climate data obtained from nearby climate stations are given in brackets.

Soil Profile	Latitude	Longitude	Elevation [m asl]	Slope* [°]	Position	Aspect	Profile depth [m]	Soil horizon thickness [m]	Rooting depth‡ [m]
Pan de Azúcar (MAP: 10 mm yr^{-1}; MAT: 18.1 °C)†									
AZPED60	26.1101 S	70.5492 W	335	5	top	S	1.25	0.22	0
AZPED50	26.1102 S	70.5493 W	330	40	mid	S	1.4	0.2	0.45
AZPED40	26.1102 S	70.5493 W	328	33	toe	S	1.25	0.25	0
AZPED21	26.1093 S	70.5491 W	343	25	mid	N	1.1	0.2	0.3
Santa Gracia (MAP: 87 mm yr^{-1}; MAT: 16.1 °C)†									
SGPED20	29.7564 S	71.1672 W	718	2	top	S	1.15	0.3	0.65
SGPED40	29.7574 S	71.1664 W	682	25	mid	S	2.05	0.45	2.05
SGPED60	29.7583 S	71.1662 W	638	20	toe	S	2.1	0.55	1.8
SGPED70	29.7612 S	71.1656 W	690	15	mid	N	1.95	0.35	1.95
La Campana (MAP: 436 mm yr^{-1}; MAT: 14.9 °C)†									
LCPED10	32.9556 S	71.0629 W	750	7	top	S	0.7	0.45	0.7
LCPED20	32.9559 S	71.0635 W	730	23	mid	S	1.9	0.6	1.2
LCPED30	32.9562 S	71.0637 W	706	35	toe	S	3.6	0.55	3.6
LCPED40	32.9573 S	71.0643 W	734	12	mid	N	1.5	0.35	1.2
Nahuelbuta (MAP: 1084 mm yr^{-1}; MAT: 14.1 °C)†									
NAPED10	37.8073 S	73.0129 W	1248	5	top	S	2.2	0.7	2.2
NAPED20	37.8077 S	73.0135 W	1239	15	mid	S	2.05	0.7	2.05
NAPED30	37.8084 S	73.0135 W	1228	20	toe	S	1.15	0.9	1.15
NAPED40	37.8090 S	73.0138 W	1219	13	mid	N	2	0.6	1.8

* Bernhard et al. (2018)

† mean annual precipitation (MAP) and mean annual temperature (MAT) data from Ministerio de Obras Públicas (2017)

‡ as observed at the soil profiles

Table S2.2: Major and selected trace element concentration for bedrock samples.

	IGSN	ρ [g cm^{-3}]	SiO_2	TiO_2	Al_2O_3	Fe_2O_3	MnO	MgO	CaO	Na_2O	K_2O	P_2O_5	LOI	Sum	SO_3	Ba	Cr	Ga	Nb	Ni	Rb	Sc	Sr	V	Y	Zr
			[wt %]													[ppm]										
Pan de Azúcar																										
AZ.RO.010	GFRO100RK	2.73	70.35	0.49	13.81	3.23	0.03	0.94	0.95	3.05	3.85	0.16	2.79	99.65	0.01	751	25	17	11	8	162	5	119	35	27	202
AZ.RO.011	GFRO100RN	2.79	73.66	0.49	12.25	3.24	0.03	0.51	1.15	2.34	3.63	0.13	2.38	99.82	0.01	499	29	17	13	7	156	9	113	37	33	207
AZ.RO.012	GFRO100X1	2.75	72.20	0.45	13.04	3.12	0.03	0.39	1.43	2.58	3.91	0.14	2.52	99.82	0.01	566	33	16	11	10	154	12	101	37	35	202
AZ.RO.013	GFRO100RF	2.67	70.36	0.45	13.58	2.97	0.04	0.45	2.04	2.78	3.59	0.15	3.46	99.86	0.02	350	16	17	10	7	160	6	91	35	30	187
bedrock average		2.74	71.64	0.47	13.17	3.14	0.03	0.57	1.39	2.69	3.75	0.15	2.79	99.79	0.01	542	26	17	11	8	158	8	106	36	31	200
1 SD		0.04	1.39	0.02	0.60	0.11	0.00	0.22	0.41	0.26	0.14	0.01	0.42	0.08	0	144	6	0	1	1	3	3	11	1	3	8
Santa Gracia																										
SG.01.RO	GFRO100L7	2.66	50.25	0.74	18.80	8.58	0.12	5.10	10.29	3.68	0.38	0.11	1.76	99.81	0.01	152	20	17	4	15	9	43	554	216	19	66
SG.02.RO	GFRO100L8	2.81	53.06	0.916	16.56	9.71	0.13	4.42	8.64	3.59	1.34	0.15	1.21	99.73	0.01	359	14	18	7	5	33	36	435	331	22	110
SG.03.RO	GFRO100L9	2.72	54.43	0.96	18.30	2.24	0.03	4.53	14.04	4.06	0.19	0.21	0.79	99.79	0.01	151	12	19	2	5	3	40	652	236	21	55
SG.04.RO	GFRO100LA	2.51	64.23	0.53	16.59	3.08	0.08	2.10	6.12	5.25	0.57	0.38	0.90	99.82	0.01	225	9	17	8	5	18	17	515	103	26	209
SG.05.RO	GFRO100LB	2.57	63.43	0.60	17.36	4.16	0.07	0.91	6.29	5.30	0.60	0.18	0.93	99.83	0.01	91	16	17	9	0	23	22	287	109	60	192
SG.06.RO	GFRO100LC	2.65	53.89	0.56	17.42	5.64	0.16	4.97	12.40	3.51	0.59	0.11	0.51	99.76	0.01	263	47	18	4	18	10	45	585	189	22	57
SGTE002	GFTE10002	2.70	60.01	0.76	16.24	7.10	0.14	2.55	5.60	3.85	2.16	0.21	1.06	99.68	0.02	457	20	17	8	4	98	28	383	164	33	198
SGTE003	GFTE10003	2.79	49.60	0.67	19.38	8.75	0.14	4.95	10.81	3.44	0.23	0.16	1.51	99.64	0.03	158	23	17	0	9	4	39	575	340	14	36
bedrock average		2.68	56.11	0.72	17.58	6.16	0.11	3.69	9.27	4.09	0.76	0.19	1.08	99.76	0.01	232	20	18	5	8	25	34	498	211	27	115
1 SD		0.10	5.34	0.15	1.07	2.63	0.04	1.50	2.93	0.71	0.63	0.08	0.38	0.06	0	115	11	1	3	6	29	10	113	84	13	68
La Campana																										
LC.01.RO	GFRO10094	2.72	73.00	0.28	13.75	2.10	0.03	0.38	1.49	3.31	3.95	0.07	1.44	99.80	0.00	519	1	15	7	0	121	10	186	28	20	182
LC.02.RO	GFRO10098	2.39	73.40	0.27	13.61	2.06	0.03	0.31	1.45	3.24	4.17	0.07	1.27	99.87	0.00	568	5	13	7	2	124	10	183	17	23	171
LC.03.RO	GFRO10096	2.81	74.61	0.201	13.01	1.34	0.03	0.26	1.2	3.09	4.56	0.04	1.45	99.79	0.00	581	9	14	6	0	128	1	165	18	13	140
LC.04.RO	GFRO10095	3.12	72.36	0.31	13.56	2.28	0.05	0.43	1.81	3.51	3.86	0.07	1.57	99.81	0.00	536	14	14	6	2	129	12	207	27	21	190
LCTE002	GFTE10004	2.66	72.22	0.29	13.46	2.01	0.05	0.61	0.79	2.55	5.87	0.08	1.84	99.76	0.01	591	5	16	6	2	117	5	158	34	28	149
bedrock average		2.74	73.12	0.27	13.48	1.96	0.04	0.40	1.35	3.14	4.48	0.06	1.51	99.81	0.00	559	7	14	6	1	124	8	180	25	21	166
1 SD		0.24	0.86	0.04	0.25	0.32	0.01	0.12	0.34	0.32	0.73	0.01	0.19	0.03	0	27	4	1	0	1	4	4	17	6	5	19
Nahuelbuta																										
NA.01.RO	GFRO10009	2.69	66.90	0.55	16.14	4.67	0.07	1.18	3.98	3.24	2.05	0.15	0.84	99.77	0.01	411	11	22	6	3	121	17	215	64	16	219
NA.04.RO	GFRO1000C	2.54	69.98	0.54	14.45	4.28	0.06	1.41	3.21	2.51	1.81	0.06	1.45	99.75	0.01	451	28	18	8	14	102	15	226	84	7	235
NATE001	GFTE10005	2.65	64.51	0.56	16.51	5.02	0.08	1.54	3.55	3.21	2.92	0.23	1.63	99.76	0.01	375	18	20	12	4	132	19	242	79	16	168
bedrock average		2.63	67.13	0.55	15.70	4.66	0.07	1.38	3.58	2.99	2.26	0.14	1.31	99.76	0.01	412	19	20	9	7	118	17	228	76	13	207
1 SD		0.06	2.24	0.01	0.90	0.30	0.01	0.15	0.32	0.34	0.48	0.07	0.34	0.01	0.00	31	7	2	2	5	12	2	11	8	4	29

Table S2.3: Normative modal abundance of rock-forming minerals based on CIPW norm calculations of average bedrock com-position of each study area. Estimation of mineral abundances based on thin section microscopy: -: absence, x: presence (< 10 Vol%), xx: abundant (10 – 35 Vol%), xxx: very abundant (> 35 Vol%).

Study area	Qtz	An	Ab	Or	Px	Bt	Hbl	Other mineral phases [Vol%]
Pan de Azúcar								
	39.94	6.00	24.16	24.61	1.23	n.c.*	n.c.*	Crn (1.71), Hem (1.67), Ap (0.3), Zrn (0.03), Rt (0.29), Ilm (0.04)
	xxx	x	xxx	xxx	-	x	-	-
Santa Gracia						n.c.*	n.c.*	
	8.93	28.52	38.03	5.31	14.06	n.c.*	n.c.*	Hem (3.38), Ilm (0.14), Ap (0.4), Zrn (0.02), Ttn (1.21)
	xx	xxx	xxx	x	xx	-	x	-
La Campana						n.c.*	n.c.*	
	34.85	6.25	27.50	28.50	0.84	n.c.*	n.c.*	Crn (0.72), Rt (0.15), Ilm (0.05), Hem (1.01), Ap (0.12), Zrn (0.02)
	xx	xx		xx	-	x	-	-
Nahuelbuta						n.c.*	n.c.*	
	37.10	12.77	23.37	16.50	3.16	n.c.*	n.c.*	Crn (3.51), Rt (0.37), Ilm (0.08), Hem (2.79), Ap (0.29), Zrn (0.03)
	xx	xxx	xxx	xxx	-	x	-	-

*: hydrous minerals are not part of the CIPW norm calculation
Mineral abbreviations: Ab - albite; An - anorthite; Ap - apatite; Bt - biotite; Crn - corundum; Hbl - hornblende; Hem - hematite; Ilm - ilmenite; Or - orthoclase; Px - pyroxene; Rt - rutile; Ttn - titanite/ sphene; Zrn - zircon

Table S2.4: Major and selected trace element concentration for regolith samples of the four primary EarthShape study areas recalculated to a secondary volatile free basis following Eq. 2.1 and pedogenic oxides (oxalate, dithionite, and pyrophosphate soluble).

Soil profile Depth [cm]	IGSN	ρ^* [g cm^{-3}]	SiO_2	TiO_2	Al_2O_3	Fe_2O_3	MnO	MgO	CaO	Na_2O	K_2O	P_2O_5	Sum	SO_3	Ba	Cr	Ga	Nb	Ni	Rb	Sc	Sr	V	Y	Zr	Al_o	Al_d	Al_p	Si_o	Si_d	Si_p	Mn_o	Mn_d	Mn_p	Fe_o	Fe_d	Fe_p	$Al_o + 0.5 \times Fe_o$	$\frac{Si_o}{Al_o}$	$\frac{Fe_d - Fe_o}{Fe_{tot}}$	$\frac{Fe_o}{Fe_d}$
			[wt%]												[ppm]															[ppm]									[%]		[-]	
Pan de Azúcar *AZPED60*																																									
0 – 5	GFRO100TP	1.3	65.94	0.80	14.50	4.35	0.09	1.29	3.67	2.46	3.77	0.24	97.11	0.99	435	32	20	17	12	181	18	100	62	46	353	466	229	45	254	610	494	633	184	3	241	5684	25	0.06	0.54	17.9	0.04
5 – 10	GFRO100TQ	1.2	64.45	0.64	15.41	3.71	0.06	0.73	5.27	2.26	4.33	0.17	97.02	4.26	468	23	22	15	7	200	18	92	47	41	256	201	148	47	152	366	377	481	103	34	101	3700	873	0.03	0.76	13.9	0.03
10 – 20	GFRO100TR	n.d.	51.03	0.50	11.08	2.94	0.08	1.20	24.57	1.79	2.86	0.14	96.19	31.41	231	15	15	12	8	142	30	116	34	33	205	84	99	n.d.	107	354	391	230	64	n.d.	55	2006	n.d.	0.01	1.27	9.5	0.03
20 – 40	GFRO100TS	n.d.	61.13	0.45	11.01	2.70	0.08	0.90	14.56	2.80	2.86	0.12	96.62	15.51	242	13	13	12	6	148	19	92	35	30	195	81	103	37	108	292	338	426	92	1	61	2118	n.d.	0.01	1.32	10.9	0.03
40 – 60	GFRO100TT	n.d.	67.28	0.56	13.62	4.22	0.09	0.39	3.77	3.55	3.46	0.16	97.09	1.62	382	27	19	15	6	163	16	89	45	36	226	n.d.	n.d.	n.d.	n.d.	n.d.	n.d.	n.d.	n.d.	n.d.	n.d.	n.d.	n.d.	–	–	–	–
60 – 80	GFRO100TU	n.d.	69.07	0.51	13.86	3.64	0.07	0.34	3.31	2.87	3.34	0.15	97.15	0.45	386	25	19	12	6	163	7	84	42	35	206	n.d.	n.d.	n.d.	n.d.	n.d.	n.d.	n.d.	n.d.	n.d.	n.d.	n.d.	n.d.	–	–	–	–
80 – 100	GFRO100TW	n.d.	73.28	0.34	11.86	2.80	0.05	0.24	2.68	2.37	3.44	0.11	97.18	0.07	502	24	13	9	3	145	9	74	25	23	148	n.d.	n.d.	n.d.	n.d.	n.d.	n.d.	n.d.	n.d.	n.d.	n.d.	n.d.	n.d.	–	–	–	–
100 – 120	GFRO100TV	n.d.	70.21	0.41	13.01	3.51	0.07	0.27	3.14	2.68	3.74	0.13	97.17	0.25	577	19	15	10	6	158	7	90	34	28	170	n.d.	n.d.	n.d.	n.d.	n.d.	n.d.	n.d.	n.d.	n.d.	n.d.	n.d.	n.d.	–	–	–	–
AZPED50																																									
0 – 5	GFRO100TX	1.2	66.85	0.66	15.11	4.13	0.06	0.82	2.96	2.47	3.89	0.20	97.14	0.15	463	22	22	13	10	192	13	98	47	42	275	n.d.	n.d.	n.d.	n.d.	n.d.	n.d.	n.d.	n.d.	n.d.	n.d.	n.d.	n.d.	–	–	–	–
5 – 10	GFRO100TY	1.6	66.63	0.44	12.66	3.17	0.04	0.37	7.75	2.27	3.46	0.15	96.94	7.50	444	20	16	12	5	168	16	88	32	30	192	37	115	74	66	340	466	219	79	1	30	3936	n.d.	0.01	1.77	17.6	0.01
10 – 20	GFRO100TZ	n.d.	70.35	0.49	13.60	3.55	0.03	0.30	2.08	2.44	4.19	0.14	97.18	0.57	606	20	16	12	10	202	5	83	39	31	207	n.d.	n.d.	n.d.	n.d.	n.d.	n.d.	n.d.	n.d.	n.d.	n.d.	n.d.	n.d.	–	–	–	–
20 – 40	GFRO100U0	n.d.	70.06	0.53	13.49	3.56	0.04	0.30	2.50	2.62	3.91	0.16	97.16	1.09	542	35	17	13	7	178	12	94	40	35	225	n.d.	n.d.	n.d.	n.d.	n.d.	n.d.	n.d.	n.d.	n.d.	n.d.	n.d.	n.d.	–	–	–	–
40 – 60	GFRO100U1	n.d.	70.61	0.49	13.06	3.64	0.04	0.33	3.09	2.32	3.44	0.15	97.15	0.73	392	28	14	11	7	171	16	74	38	33	203	n.d.	n.d.	n.d.	n.d.	n.d.	n.d.	n.d.	n.d.	n.d.	n.d.	n.d.	n.d.	–	–	–	–
60 – 80	GFRO100U2	n.d.	71.50	0.56	13.02	3.33	0.03	0.33	2.68	2.19	3.38	0.15	97.16	0.59	392	27	17	12	9	166	12	78	42	35	227	n.d.	n.d.	n.d.	n.d.	n.d.	n.d.	n.d.	n.d.	n.d.	n.d.	n.d.	n.d.	–	–	–	–
80 – 100	GFRO100U3	n.d.	69.33	0.50	12.79	2.92	0.06	0.43	5.72	1.81	3.36	0.14	97.06	3.07	382	21	18	10	5	170	14	65	34	33	203	n.d.	n.d.	n.d.	n.d.	n.d.	n.d.	n.d.	n.d.	n.d.	n.d.	n.d.	n.d.	–	–	–	–
100 – 120	GFRO100U4	n.d.	69.34	0.52	13.88	3.52	0.04	0.35	3.20	2.31	3.84	0.15	97.14	0.95	555	25	17	11	8	178	12	86	38	33	219	n.d.	n.d.	n.d.	n.d.	n.d.	n.d.	n.d.	n.d.	n.d.	n.d.	n.d.	n.d.	–	–	–	–
120 – 140	GFRO100U5	n.d.	69.36	0.53	13.69	3.42	0.05	0.38	4.00	2.16	3.39	0.16	97.14	0.27	331	28	19	12	6	171	11	70	39	32	222	n.d.	n.d.	n.d.	n.d.	n.d.	n.d.	n.d.	n.d.	n.d.	n.d.	n.d.	n.d.	–	–	–	–
AZPED40																																									
0 – 5	GFRO100BJ	1.1	69.78	0.48	12.22	3.24	0.06	0.57	5.70	1.78	3.12	0.14	97.10	0.09	316	16	15	10	8	150	5	72	37	34	219	252	237	49	123	498	331	444	126	18	106	5463	32	0.03	0.49	23.6	0.02
5 – 10	GFRO100U6	1.4	65.35	0.48	13.03	3.32	0.07	0.60	9.12	1.30	3.53	0.15	96.95	4.45	279	17	17	11	5	173	13	66	43	32	206	205	169	40	118	360	268	525	119	4	92	3947	63	0.03	0.58	16.6	0.02
10 – 20	GFRO100U7	n.d.	63.10	0.42	11.14	2.27	0.03	0.51	15.33	0.63	3.15	0.12	96.70	12.51	130	17	14	12	4	157	18	65	39	32	175	64	153	43	71	290	189	176	43	1	33	2205	n.d.	0.01	1.11	13.7	0.02
20 – 40	GFRO100U8	n.d.	71.13	0.52	13.56	2.87	0.04	0.49	3.86	0.60	3.87	0.16	97.10	2.02	179	27	19	11	6	196	15	42	40	34	211	n.d.	n.d.	4	n.d.	n.d.	n.d.	n.d.	n.d.	n.d.	n.d.	n.d.	n.d.	–	–	–	–
40 – 60	GFRO100U9	n.d.	69.31	0.55	13.91	3.64	0.05	0.42	3.93	1.64	3.49	0.16	97.12	0.47	207	26	18	11	8	178	12	49	47	34	232	n.d.	n.d.	n.d.	n.d.	n.d.	n.d.	n.d.	n.d.	n.d.	n.d.	n.d.	n.d.	–	–	–	–
60 – 80	GFRO100UA	n.d.	69.00	0.51	12.93	3.43	0.04	0.37	5.46	1.88	3.33	0.15	97.11	0.06	324	29	17	12	7	164	7	66	41	30	216	n.d.	n.d.	n.d.	n.d.	n.d.	n.d.	n.d.	n.d.	n.d.	n.d.	n.d.	n.d.	–	–	–	–
80 – 100	GFRO100UB	n.d.	66.68	0.50	13.47	3.54	0.06	0.51	7.40	1.23	3.53	0.14	97.05	0.12	194	21	19	13	8	175	11	47	38	36	207	n.d.	n.d.	n.d.	n.d.	n.d.	n.d.	n.d.	n.d.	n.d.	n.d.	n.d.	n.d.	–	–	–	–
100 – 120	GFRO100UC	n.d.	69.31	0.47	12.59	3.18	0.05	0.43	5.77	1.95	3.23	0.14	97.10	0.03	224	23	16	10	9	157	15	48	42	33	202	n.d.	n.d.	n.d.	n.d.	n.d.	n.d.	n.d.	n.d.	n.d.	n.d.	n.d.	n.d.	–	–	–	–
AZPED21																																									
0 – 5	GFRO100UD	1.2	71.56	0.42	11.90	3.13	0.05	0.78	3.45	2.20	3.52	0.14	97.15	0.05	422	14	14	10	7	154	12	102	35	32	195	362	238	64	190	791	502	435	146	5	226	6591	45	0.05	0.52	29.0	0.03
5 – 10	GFRO100UE	1.4	72.93	0.38	11.54	2.91	0.04	0.55	3.17	2.17	3.36	0.10	97.15	0.51	407	12	16	11	5	152	11	82	31	32	168	206	119	30	184	384	401	493	80	3	133	3920	n.d.	0.03	0.90	18.6	0.03
10 – 20	GFRO100UF	1.3	72.88	0.42	11.91	2.92	0.02	0.53	2.97	1.92	3.45	0.08	97.11	3.10	389	16	17	8	5	159	7	83	34	30	188	101	122	41	135	478	362	123	33	n.d.	125	4998	n.d.	0.02	1.33	23.8	0.03
20 – 40	GFRO100UG	n.d.	67.68	0.51	12.77	3.38	0.04	0.56	6.02	2.38	3.57	0.11	97.02	4.30	378	22	15	13	6	170	16	101	40	37	217	41	90	36	80	337	240	180	32	1	89	3893	n.d.	0.01	1.98	16.1	0.02
40 – 60	GFRO100UH	n.d.	73.67	0.46	12.42	3.38	0.06	0.35	1.11	2.10	3.49	0.13	97.17	0.75	348	20	16	11	8	170	9	78	34	35	195	n.d.	n.d.	n.d.	n.d.	n.d.	n.d.	n.d.	n.d.	n.d.	n.d.	n.d.	n.d.	–	–	–	–
60 – 80	GFRO100UJ	n.d.	71.19	0.44	13.68	2.78	0.05	0.25	1.46	2.51	4.70	0.13	97.20	0.49	713	19	17	11	7	194	12	104	37	33	180	n.d.	n.d.	n.d.	n.d.	n.d.	n.d.	n.d.	n.d.	n.d.	n.d.	n.d.	n.d.	–	–	–	–
80 – 100	GFRO100UK	n.d.	72.66	0.44	13.87	2.47	0.05	0.24	0.45	2.50	4.43	0.12	97.23	0.09	629	21	17	10	4	187	5	102	39	33	198	n.d.	n.d.	n.d.	n.d.	n.d.	n.d.	n.d.	n.d.	n.d.	n.d.	n.d.	n.d.	–	–	–	–
Santa Gracia, *SGPED20*																																									
0 – 5	GFRO100UL	1.6	62.92	0.63	16.81	5.06	0.08	1.94	4.10	4.62	2.59	0.15	98.89	0.02	612	21	17	9	6	67	23	387	122	27	199	167	134	153	140	358	361	134	32	286	216	1114	158	0.03	0.84	2.5	0.19
5 – 10	GFRO100UM	1.5	61.52	0.80	16.20	6.14	0.11	2.62	4.64	4.35	2.35	0.17	98.89	0.02	558	31	16	10	11	64	33	368	153	33	243	221	173	202	147	354	286	186	45	201	353	2020	192	0.04	0.66	3.9	0.17
10 – 20	GFRO100UN	1.5	59.93	0.83	16.93	6.46	0.11	2.57	4.79	4.98	2.09	0.19	98.89	0.02	444	40	19	8	13	54	25	415	173	31	263	241	136	223	146	370	286	246	61	154	431	2320	238	0.05	0.61	4.2	0.19
20 – 40	GFRO100UP	1.6	59.98	0.76	17.39	6.31	0.10	2.37	4.65	5.08	2.08	0.18	98.90	0.01	461	31	16	7	10	47	23	457	162	26	262	202	91	165	123	314	331	248	55	97	350	1321	177	0.04	0.61	2.2	0.26
40 – 60	GFRO100UQ	n.d.	59.87	0.82	17.40	5.86	0.08	2.46	5.30	5.39	1.51	0.22	98.91	0.00	321	12	18	9	7	31	22	493	150	29	281	n.d.	n.d.	n.d.	n.d.	n.d.	n.d.	n.d.	n.d.	n.d.	n.d.	n.d.	n.d.	–	–	–	–
60 – 80	GFRO100UR	n.d.	58.93	0.84	16.73	7.02	0.10	2.83	5.03	4.98	2.20	0.25	98.91	0.00	541	22	17	12	9	50	32	436	172	36	275	n.d.	n.d.	n.d.	n.d.	n.d.	n.d.	n.d.	n.d.	n.d.	n.d.	n.d.	n.d.	–	–	–	–
80 – 100	GFRO100US	n.d.	61.05	0.74	16.70	5.60	0.08	2.30	4.55	5.01	2.64	0.25	98.91	0.00	749	7	17	11	6	53	20	443	140	31	244	n.d.	n.d.	n.d.	n.d.	n.d.	n.d.	n.d.	n.d.	n.d.	n.d.	n.d.	n.d.	–	–	–	–
100 – 120	GFRO100UT	n.d.	62.11	0.74	16.32	4.92	0.09	2.79	4.99	5.43	1.27	0.24	98.91	0.00	269	41	18	8	12	28	26	462	134	35	237	n.d.	n.d.	n.d.	n.d.	n.d.	n.d.	n.d.	n.d.	n.d.	n.d.	n.d.	n.d.	–	–	–	–
SGPED40																																									
0 – 5	GFRO100UU	1.5	62.01	0.68	16.44	6.13	0.10	2.15	4.59	4.39	2.28	0.13	98.90	0.02	588	10	16	9	4	63	19	361	146	28	246	237	159	273	78	350	304	211	42	191	534	1463	262	0.05	0.33	2.2	0.36
5 – 10	GFRO100UV	1.6	61.66	0.72	16.43	6.68	0.11	2.22	4.41	4.28	2.28	0.11	98.90	0.01	566	14	18	11	4	62	24	354	154	31	267	216	149	200	84	294	247	189	58	59	461	1497	203	0.04	0.39	2.2	0.31
10 – 20	GFRO100V3	1.6	61.88	0.70	16.58	6.55	0.11	2.11	4.30	4.30	2.29	0.10	98.90	0.01	594	13	17	11	3	61	23	358	152	30	250	298	189	271	99	349	283	262	48	69	534	2040	286	0.06	0.33	3.3	0.26
20 – 40	GFRO100UW	1.4	62.22	0.67	16.72	6.28	0.10	2.08	4.27	4.38	2.10	0.09	98.91	0.01	528	15	16	8	1	54	21	363	148	32	236	247	169	197	136	350	347	185	35	37	580	1626	202	0.05	0.55	2.4	0.36
40 – 60	GFRO100UX	1.4	62.39	0.55	17.13	5.45	0.09	2.36	4.60	4.60	1.64	0.11	98.90	0.00	447	12	19	7	4	33	17	385	139	28	153	162	210	161	71	485	300	60	22	14	244	1831	203	0.03	0.44	4.2	0.13
60 – 80	GFRO100UY	n.d.	63.22	0.59	17.13	4.80	0.07	2.36	4.23	4.94	1.47	0.09	98.90	0.00	395	12	17	6	4	30	15	385	133	22	153	206	487	28	n.d.	1299	n.d.	96	47	n.d.	659	7492	n.d.	0.05	–	20.4	0.09
80 – 100	GFRO100UZ	n.d.	63.72	0.64	16.92	5.18	0.06	2.38	3.57	4.89	1.41	0.12	98.90	0.01	299	12	18	7	5	35	19	350	142	28	170	n.d.	n.d.	n.d.	n.d.	n.d.	n.d.	n.d.	n.d.	n.d.	n.d.	n.d.	n.d.	–	–	–	–

Continued on the next page.

Table S2.4: ...continuation

Soil profile Depth [cm]	IGSN	ρ^* [g cm^{-3}]	SiO_2	TiO_2	Al_2O_3	Fe_2O_3	MnO	MgO	CaO	Na_2O	K_2O	P_2O_5	Sum	SO_3	Ba	Cr	Ga	Nb	Ni	Rb	Sc	Sr	V	Y	Zr	Al_o	Al_d	Al_p	Si_o	Si_d	Si_p	Mn_o	Mn_d	Mn_p	Fe_o	Fe_d	Fe_p	$Al_o + 0.5 \times Fe_o$	$\frac{Si_o}{Al_o}$	$\frac{Fe_d - Fe_o}{Fe_{tot}}$	$\frac{Fe_o}{Fe_d}$
			[wt%]												[ppm]																[ppm]							[%]		[-]	
100 – 120	GFRO100V0	n.d.	63.64	0.68	16.36	4.60	0.07	2.73	4.33	5.04	1.29	0.15	98.91	0.01	249	16	15	9	4	35	20	363	127	27	235	n.d.	n.d.	n.d.	n.d.	n.d.	n.d.	n.d.	n.d.	n.d.	n.d.	n.d.	n.d.	–	–	–	–
120 – 140	GFRO100V1	n.d.	63.88	0.56	16.39	4.33	0.08	2.36	4.67	5.16	1.35	0.13	98.91	0.00	350	13	16	6	3	30	19	385	128	24	161	n.d.	n.d.	n.d.	n.d.	n.d.	n.d.	n.d.	n.d.	n.d.	n.d.	n.d.	n.d.	–	–	–	–
140 – 160	GFRO100V2	n.d.	62.64	0.60	16.28	5.58	0.10	2.32	4.74	4.73	1.79	0.15	98.91	0.00	627	14	16	6	3	36	28	394	135	28	146	n.d.	n.d.	n.d.	n.d.	n.d.	n.d.	n.d.	n.d.	n.d.	n.d.	n.d.	n.d.	–	–	–	–
160 – 180	GFRO100CR	n.d.	63.06	0.59	16.41	5.09	0.09	2.12	4.70	5.02	1.67	0.16	98.91	0.00	526	11	15	8	4	34	21	399	120	24	145	n.d.	n.d.	n.d.	n.d.	n.d.	n.d.	n.d.	n.d.	n.d.	n.d.	n.d.	n.d.	–	–	–	–
SGPED60																																									
0 – 5	GFRO100V4	1.5	62.68	0.68	16.32	6.24	0.10	1.83	4.02	4.20	2.69	0.14	98.90	0.01	732	13	14	11	4	70	17	373	138	28	285	312	467	110	n.d.	864	n.d.	297	311	54	2730	10841	n.d.	0.17	–	18.6	0.25
5 – 10	GFRO100V5	1.5	63.16	0.64	16.39	6.02	0.09	1.65	3.86	4.26	2.70	0.13	98.90	0.01	736	10	16	10	5	71	25	369	128	26	266	268	401	89	n.d.	672	n.d.	307	288	32	629	9489	n.d.	0.06	–	21.0	0.07
10 – 20	GFRO100V6	1.5	62.32	0.74	16.14	6.83	0.10	1.92	3.95	4.18	2.57	0.14	98.89	0.01	678	12	16	10	5	69	21	351	149	30	287	225	139	267	126	273	305	218	44	63	194	1185	221	0.03	0.56	2.1	0.16
20 – 40	GFRO100V7	1.5	62.59	0.70	16.23	6.81	0.10	1.79	3.82	4.12	2.62	0.12	98.90	0.01	715	14	17	10	3	73	19	354	151	27	276	143	174	228	149	364	269	205	52	82	154	1442	213	0.02	1.04	2.7	0.11
40 – 60	GFRO100V8	1.4	63.44	0.62	16.53	5.86	0.08	1.61	3.75	4.20	2.73	0.11	98.91	0.01	759	14	17	10	2	66	21	359	127	25	251	340	451	90	n.d.	894	n.d.	266	223	13	2084	10581	n.d.	0.14	–	20.7	0.20
60 – 80	GFRO100V9	n.d.	62.74	0.60	17.03	5.57	0.07	1.70	4.14	4.39	2.54	0.14	98.91	0.00	716	5	17	10	4	64	16	394	120	29	226	181	399	50	n.d.	975	n.d.	143	108	3	175	8525	n.d.	0.03	–	21.5	0.02
80 – 100	GFRO100VA	n.d.	64.10	0.61	16.60	5.30	0.06	1.56	3.65	4.08	2.79	0.15	98.90	0.00	825	8	16	11	4	90	17	439	101	30	219	n.d.	n.d.	n.d.	n.d.	n.d.	n.d.	n.d.	n.d.	n.d.	n.d.	n.d.	n.d.	–	–	–	–
100 – 120	GFRO100VB	n.d.	65.74	0.55	16.23	4.59	0.05	1.20	3.34	3.91	3.12	0.16	98.91	0.01	890	4	16	9	3	79	14	377	92	28	197	n.d.	n.d.	n.d.	n.d.	n.d.	n.d.	n.d.	n.d.	n.d.	n.d.	n.d.	n.d.	–	–	–	–
120 – 140	GFRO100VC	n.d.	65.91	0.56	15.97	4.47	0.06	1.30	3.29	3.78	3.44	0.13	98.91	0.00	956	7	17	10	3	85	18	383	92	27	210	n.d.	n.d.	n.d.	n.d.	n.d.	n.d.	n.d.	n.d.	n.d.	n.d.	n.d.	n.d.	–	–	–	–
140 – 160	GFRO100VD	n.d.	62.96	0.61	17.27	5.00	0.06	1.48	3.95	4.36	3.06	0.17	98.91	0.01	952	6	17	10	3	72	19	418	104	29	229	n.d.	n.d.	n.d.	n.d.	n.d.	n.d.	n.d.	n.d.	n.d.	n.d.	n.d.	n.d.	–	–	–	–
160 – 180	GFRO100VE	n.d.	62.72	0.72	16.82	5.67	0.07	1.69	3.87	4.18	2.98	0.18	98.91	0.00	916	5	18	10	0	74	21	392	107	30	248	n.d.	n.d.	n.d.	n.d.	n.d.	n.d.	n.d.	n.d.	n.d.	n.d.	n.d.	n.d.	–	–	–	–
SGPED70																																									
0 – 5	GFRO100VF	1.5	62.49	0.62	16.33	6.58	0.09	1.80	4.53	3.70	2.64	0.12	98.90	0.02	668	12	16	9	3	74	24	385	161	25	258	240	163	124	120	417	683	190	34	201	260	1168	140	0.04	0.50	2.0	0.22
5 – 10	GFRO100VG	1.6	63.83	0.58	16.60	5.36	0.09	1.71	4.08	3.94	2.61	0.11	98.90	0.01	659	11	16	7	4	74	20	378	129	27	207	n.d.	n.d.	n.d.	n.d.	n.d.	n.d.	n.d.	n.d.	n.d.	n.d.	n.d.	n.d.	–	–	–	–
10 – 20	GFRO100VH	1.7	63.67	0.61	16.72	5.68	0.09	1.74	3.92	3.69	2.69	0.10	98.90	0.01	669	8	18	8	3	76	24	358	136	24	192	n.d.	n.d.	n.d.	n.d.	n.d.	n.d.	n.d.	n.d.	n.d.	n.d.	n.d.	n.d.	–	–	–	–
20 – 40	GFRO100VJ	1.7	63.02	0.66	16.93	6.13	0.10	1.86	3.90	3.53	2.69	0.09	98.90	0.01	601	15	15	7	5	69	21	344	149	24	195	n.d.	n.d.	n.d.	n.d.	n.d.	n.d.	n.d.	n.d.	n.d.	n.d.	n.d.	n.d.	–	–	–	–
40 – 60	GFRO100VK	n.d.	62.62	0.67	16.37	6.21	0.09	2.19	4.31	3.69	2.64	0.11	98.90	0.00	543	11	17	8	3	65	24	351	148	29	184	n.d.	n.d.	n.d.	n.d.	n.d.	n.d.	n.d.	n.d.	n.d.	n.d.	n.d.	n.d.	–	–	–	–
60 – 80	GFRO100VL	n.d.	63.85	0.62	15.88	5.31	0.09	2.14	4.15	3.69	3.06	0.13	98.91	0.00	642	8	16	7	5	78	21	353	128	28	181	n.d.	n.d.	n.d.	n.d.	n.d.	n.d.	n.d.	n.d.	n.d.	n.d.	n.d.	n.d.	–	–	–	–
80 – 100	GFRO100VM	n.d.	63.50	0.77	15.61	5.97	0.10	2.22	4.16	3.73	2.74	0.13	98.91	0.00	530	6	15	10	5	74	25	358	159	26	153	n.d.	n.d.	n.d.	n.d.	n.d.	n.d.	n.d.	n.d.	n.d.	n.d.	n.d.	n.d.	–	–	–	–
100 – 120	GFRO100VN	n.d.	63.63	0.69	15.02	5.80	0.10	2.41	4.29	3.56	3.24	0.16	98.91	0.00	631	8	15	9	3	82	19	334	148	29	194	n.d.	n.d.	n.d.	n.d.	n.d.	n.d.	n.d.	n.d.	n.d.	n.d.	n.d.	n.d.	–	–	–	–
120 – 140	GFRO100VP	n.d.	64.38	0.59	15.46	4.88	0.09	2.10	4.17	3.71	3.40	0.12	98.91	0.00	721	9	16	10	4	83	19	355	127	29	186	n.d.	n.d.	n.d.	n.d.	n.d.	n.d.	n.d.	n.d.	n.d.	n.d.	n.d.	n.d.	–	–	–	–
140 – 160	GFRO100VQ	n.d.	63.41	0.59	15.51	5.51	0.09	2.27	4.45	3.81	3.14	0.13	98.91	0.00	584	12	14	7	3	79	28	353	131	29	170	n.d.	n.d.	n.d.	n.d.	n.d.	n.d.	n.d.	n.d.	n.d.	n.d.	n.d.	n.d.	–	–	–	–
160 – 180	GFRO100VR	n.d.	64.38	0.61	15.33	5.19	0.09	2.08	4.13	3.64	3.35	0.13	98.91	0.00	724	6	14	6	4	87	21	350	125	28	184	n.d.	n.d.	n.d.	n.d.	n.d.	n.d.	n.d.	n.d.	n.d.	n.d.	n.d.	n.d.	–	–	–	–
La Campana, *LCPED10*																																									
0 – 5	GFRO10021	1.2	68.13	0.58	14.46	4.48	0.12	1.14	3.04	2.60	3.48	0.11	98.13	0.09	532	94	16	8	15	103	23	228	90	25	311	416	823	310	n.d.	705	0	381	406	179	604	5396	233	0.07	–	15.3	0.11
5 – 10	GFRO10022	1.3	68.00	0.58	14.89	4.72	0.10	1.13	2.60	2.71	3.47	0.09	98.30	0.03	493	100	15	6	14	108	15	210	98	25	316	371	721	255	n.d.	410	0	292	320	90	512	5792	203	0.06	–	16.0	0.09
10 – 20	GFRO10023	1.2	68.40	0.58	14.85	4.64	0.10	1.10	2.39	2.67	3.51	0.08	98.32	0.02	518	95	15	7	11	109	17	203	93	26	306	393	660	211	n.d.	374	0	327	338	42	645	6607	54	0.07	–	18.4	0.10
20 – 40	GFRO10024	1.4	69.72	0.50	14.85	3.92	0.08	0.89	1.78	2.62	3.91	0.07	98.33	0.01	589	62	16	7	10	116	16	180	74	23	265	346	602	200	n.d.	n.d.	0	271	281	17	527	5743	109	0.06	–	19.0	0.09
40 – 60	GFRO100VS	1.6	72.35	0.38	14.27	2.84	0.07	0.59	1.01	2.40	4.37	0.06	98.33	0.01	668	24	16	8	7	124	9	148	49	18	203	291	686	164	n.d.	462	0	269	288	14	580	5138	63	0.06	–	22.9	0.11
60 – 80	GFRO100VT	1.6	73.68	0.30	13.95	2.08	0.04	0.38	0.54	2.61	4.70	0.05	98.33	0.01	722	13	15	5	3	126	2	130	31	14	171	195	481	105	n.d.	524	0	209	224	11	415	4777	95	0.04	–	29.9	0.09
LCPED20																																									
0 – 5	GFRO10029	0.6	70.18	0.46	13.93	3.41	0.09	0.78	2.66	2.58	3.92	0.12	98.13	0.10	561	33	14	9	8	112	15	208	69	24	257	597	971	350	n.d.	1121	0	321	338	133	814	5608	131	0.10	–	20.1	0.15
5 – 10	GFRO1002A	1.0	69.99	0.49	14.49	3.63	0.08	0.78	2.09	2.74	3.90	0.09	98.28	0.03	567	35	16	7	10	120	9	188	63	23	275	470	1061	326	n.d.	730	0	253	321	73	650	6700	131	0.08	–	23.8	0.10
10 – 20	GFRO1002B	1.2	69.11	0.53	15.10	3.88	0.08	0.82	1.99	2.77	3.95	0.10	98.31	0.02	549	36	17	8	9	125	14	187	70	24	265	526	1103	260	n.d.	745	0	287	304	39	825	7269	125	0.09	–	23.8	0.11
20 – 40	GFRO1002C	1.3	68.79	0.53	15.09	4.13	0.08	0.89	2.02	2.77	3.91	0.11	98.31	0.02	532	24	17	8	8	121	16	182	79	25	253	544	1127	414	n.d.	835	0	254	286	28	777	8112	167	0.09	–	25.4	0.10
40 – 60	GFRO1002D	1.4	68.38	0.54	15.12	4.29	0.07	0.97	2.11	2.75	3.99	0.10	98.30	0.01	549	15	19	7	7	124	13	181	79	26	296	395	902	250	n.d.	777	0	204	177	10	577	7040	166	0.07	–	21.5	0.08
60 – 80	GFRO100VU	1.5	66.25	0.60	15.52	5.20	0.08	1.32	2.65	2.90	3.69	0.12	98.33	0.01	455	9	19	5	7	116	16	195	99	32	206	542	846	164	n.d.	690	0	154	122	9	1006	6750	66	0.10	–	15.8	0.15
80 – 100	GFRO100VV	1.5	67.44	0.56	15.19	4.85	0.07	1.14	2.39	2.82	3.76	0.12	98.34	0.00	472	12	18	7	7	121	13	190	94	30	210	384	971	144	n.d.	756	0	124	94	6	526	9609	na	0.06	–	26.8	0.05
100 – 120	GFRO100VW	1.5	67.94	0.55	14.85	4.80	0.07	1.03	2.28	2.89	3.79	0.13	98.33	0.01	494	7	16	7	3	116	11	186	94	27	246	257	1049	212	n.d.	704	0	154	162	13	516	11318	85	0.05	–	32.2	0.05
120 – 140	GFRO100VY	1.5	69.71	0.45	14.61	3.77	0.05	0.77	2.02	2.94	3.93	0.10	98.35	0.00	591	9	16	7	5	119	10	184	70	24	270	186	713	105	n.d.	677	0	131	104	4	149	7648	191	0.03	–	28.4	0.02
140 – 160	GFRO100VX	1.4	70.28	0.38	14.42	3.27	0.05	0.63	1.92	2.96	4.36	0.09	98.36	0.00	613	5	15	5	6	119	6	185	66	23	250	223	891	307	184	1151	0	127	163	16	278	9432	2161	0.04	0.83	40.0	0.03
LCPED30																																									
0 – 5	GFRO1002Q	1.2	63.96	0.76	15.84	6.11	0.15	1.54	3.65	2.88	3.16	0.16	98.21	0.05	514	38	19	9	13	100	18	252	118	26	321	844	1194	408	n.d.	1553	0	570	592	202	1256	9272	200	0.15	–	18.7	0.14
5 – 10	GFRO1002R	1.3	63.79	0.74	15.73	6.29	0.16	1.56	3.93	2.82	3.13	0.18	98.32	0.09	517	32	18	7	12	104	25	255	133	29	322	689	1688	405	n.d.	1852	0	542	1003	174	1262	14794	270	0.13	–	30.7	0.09
10 – 20	GFRO1002S	1.2	63.47	0.80	15.89	6.57	0.15	1.73	3.53	3.02	2.99	0.16	98.31	0.02	447	34	18	8	13	94	22	243	132	29	351	700	1047	206	n.d.	1289	0	505	678	76	1114	9262	77	0.13	–	17.7	0.12
20 – 40	GFRO1002T	1.1	63.13	0.80	16.01	6.66	0.14	1.80	3.59	3.09	2.97	0.16	98.33	0.02	459	34	17	10	12	97	25	251	143	31	324	693	1123	261	n.d.	1418	0	512	621	50	1165	11128	144	0.13	–	21.4	0.10
40 – 60	GFRO1002U	1.1	62.89	0.79	16.10	6.38	0.12	1.84	3.82	3.34	2.89	0.15	98.32	0.01	443	27	19	7	12	88	20	259	135	31	285	501	911	191	n.d.	1366	0	411	415	32	947	11287	42	0.10	–	23.2	0.08
60 – 80	GFRO100VZ	1.4	63.31	0.74	15.75	6.29	0.10	1.70	3.90	3.46	2.90	0.19	98.34	0.01	411	10	18	7	7	87	18	267	119	30	262	322	744	115	n.d.	1452	0	239	228	28	941	10126	n.d.	0.08	–	20.9	0.09
80 – 100	GFRO100W0	1.6	63.04	0.78	15.80	6.13	0.10	1.72	4.05	3.65	2.84	0.20	98.31	0.00	401	8	19	8	5	89	20	272	115	30	218	193	514	128	n.d.	1313	0	145	102	16	515	6878	36	0.05	–	14.8	0.07
100 – 120	GFRO100W1	1.7	63.04	0.78	15.63	6.41	0.10	1.77	4.12	3.68	2.62	0.20	98.35	0.00	374	5	18	6	1	92	24	275	118	30	251	212	498	101	n.d.	1322	0	145	107	6	842	9635	69	0.06	–	19.6	0.09

Continued on the next page.

Table S2.4: ...continuation

Soil profile Depth [cm]	IGSN	ρ^* [g cm^{-3}]	SiO_2	TiO_2	Al_2O_3	Fe_2O_3	MnO	MgO	CaO	Na_2O	K_2O	P_2O_5	Sum	SO_3	Ba	Cr	Ga	Nb	Ni	Rb	Sc	Sr	V	Y	Zr	Al_o	Al_d	Al_p	Si_o	Si_d	Si_p	Mn_o	Mn_d	Mn_p	Fe_o	Fe_d	Fe_p	$Al_o + 0.5 \times Fe_o$	$\frac{Si_o}{Al_o}$	$\frac{Fe_d - Fe_o}{Fe_{tot}}$	$\frac{Fe_o}{Fe_d}$
			[wt%]												[ppm]																[ppm]								[%]		[-]	
120 – 140	GFRO100W2	1.8	64.16	0.69	15.52	5.75	0.09	1.58	3.89	3.58	2.90	0.18	98.35	0.00	426	8	16	7	2	88	20	273	96	27	251	143	555	84	n.d.	1234	0	106	144	6	490	9195	221	0.04	–	21.6	0.05
140 – 160	GFRO100W3	1.8	63.55	0.79	15.44	6.38	0.09	1.70	3.94	3.54	2.73	0.19	98.35	0.00	388	3	18	7	4	97	18	270	113	26	227	172	457	67	n.d.	1063	0	140	92	5	595	9038	463	0.05	–	18.9	0.07
160 – 180	GFRO100W4	1.7	64.54	0.67	15.67	5.50	0.08	1.47	3.73	3.57	2.97	0.16	98.35	0.00	419	4	18	6	5	92	20	269	104	24	217	167	370	60	n.d.	847	0	115	67	5	385	7148	51	0.04	–	17.6	0.05
180 – 200	GFRO100W5	1.6	63.54	0.80	15.51	6.27	0.09	1.71	3.85	3.57	2.82	0.18	98.35	0.00	398	7	18	9	6	101	20	275	128	25	290	169	398	60	n.d.	1022	0	132	95	5	553	7648	n.d.	0.04	–	16.2	0.07
200 – 220	GFRO100W6	1.6	63.30	0.74	15.57	6.25	0.10	1.74	3.94	3.59	2.95	0.18	98.35	0.00	432	5	18	6	2	95	23	271	131	30	348	176	407	68	n.d.	1189	0	110	90	4	427	7099	14	0.04	–	15.3	0.06
220 – 240	GFRO100W7	1.6	63.70	0.70	15.58	6.01	0.10	1.71	3.95	3.75	2.70	0.16	98.36	0.00	408	6	19	9	4	85	21	271	126	33	251	129	470	40	n.d.	1253	0	101	94	na	399	8616	35	0.03	–	19.6	0.05
240 – 260	GFRO100WA	1.6	63.73	0.70	15.62	6.00	0.10	1.71	3.95	3.71	2.68	0.16	98.36	0.00	413	10	18	9	7	89	22	270	127	32	255	137	486	64	n.d.	1097	0	87	79	4	504	9734	n.d.	0.04	–	22.0	0.05
260 – 280	GFRO100W8	1.5	63.64	0.76	15.81	5.93	0.10	1.69	3.81	3.64	2.83	0.14	98.35	0.00	433	10	18	10	6	91	19	273	122	31	225	141	487	83	n.d.	1017	0	87	56	7	339	8707	55	0.03	–	20.2	0.04
280 – 300	GFRO100W9	1.6	63.59	0.75	15.69	5.90	0.10	1.75	3.80	3.56	3.06	0.14	98.36	0.00	503	12	18	7	4	91	22	265	123	35	291	602	462	82	n.d.	881	0	86	62	10	114	8295	n.d.	0.07	–	19.8	0.01
300 – 320	GFRO100WB	1.6	64.32	0.67	15.65	5.69	0.09	1.63	3.85	3.98	2.31	0.15	98.36	0.00	309	3	18	8	4	85	20	260	118	33	228	121	509	87	n.d.	1013	0	99	80	8	258	11376	n.d.	0.02	–	27.9	0.02
320 – 340	GFRO100WC	1.7	64.53	0.70	15.17	5.99	0.10	1.63	3.54	3.56	2.99	0.14	98.35	0.00	474	5	17	7	4	106	19	274	125	39	315	121	477	31	n.d.	1312	0	90	122	5	517	11130	182	0.04	–	25.3	0.05
340 – 360	GFRO100WD	1.7	68.33	0.51	14.46	4.22	0.06	1.03	2.72	3.35	3.55	0.11	98.36	0.00	596	4	16	6	3	103	20	238	80	22	264	134	378	140	207	1227	0	114	94	11	483	6681	52	0.04	1.54	21.0	0.07
LCPED40																																										
0 – 5	GFRO1002V	1.3	64.15	0.82	15.44	6.58	0.12	1.50	3.25	2.65	3.56	0.14	98.21	0.06	630	28	16	10	10	120	22	231	155	32	612	461	873	234	n.d.	1143	0	306	371	156	1200	9740	55	0.11	–	18.6	0.12
5 – 10	GFRO1002W	1.3	64.62	0.82	15.31	6.67	0.11	1.42	2.87	2.69	3.67	0.12	98.31	0.03	642	22	15	8	9	115	23	218	159	29	633	475	929	253	n.d.	870	0	300	333	88	751	10423	112	0.09	–	20.7	0.07
10 – 20	GFRO1002X	1.5	64.28	0.81	16.00	6.53	0.11	1.49	2.72	2.65	3.61	0.13	98.33	0.01	609	20	16	8	6	129	20	207	137	32	536	566	1024	206	n.d.	855	0	353	392	37	1001	10869	83	0.11	–	21.6	0.09
20 – 40	GFRO1002Y	1.5	64.55	0.80	16.13	6.46	0.11	1.44	2.57	2.56	3.59	0.12	98.33	0.01	630	20	18	8	6	124	13	202	139	34	466	583	1422	196	n.d.	1200	0	346	562	20	993	15107	101	0.11	–	31.3	0.07
40 – 60	GFRO1002Z	1.5	64.71	0.75	16.18	6.10	0.10	1.39	2.49	2.58	3.93	0.10	98.34	0.01	713	14	19	11	7	135	23	199	123	34	439	548	975	169	n.d.	1000	0	333	343	24	1328	11136	165	0.12	–	23.0	0.12
60 – 80	GFRO10030	1.6	65.62	0.71	16.34	5.62	0.10	1.26	2.26	2.40	3.90	0.10	98.33	0.01	704	11	18	8	7	135	17	196	105	32	385	414	1131	288	n.d.	1397	0	325	481	33	1005	13614	124	0.09	–	32.1	0.07
80 – 100	GFRO100WG	1.7	65.48	0.74	16.35	5.86	0.10	1.30	2.32	2.43	3.65	0.11	98.33	0.01	674	16	17	10	7	131	18	195	109	34	424	425	906	108	n.d.	1332	0	342	389	7	931	10800	n.d.	0.09	–	24.1	0.09
100 – 120	GFRO100WF	1.5	66.28	0.70	15.85	5.37	0.09	1.19	2.41	2.70	3.63	0.13	98.34	0.01	639	9	18	9	6	136	15	199	100	33	442	391	737	76	n.d.	1011	0	308	275	7	775	8280	n.d.	0.08	–	20.0	0.09
120 – 140	GFRO100WE	1.4	67.07	0.60	15.10	4.57	0.08	1.06	2.74	3.18	3.82	0.14	98.36	0.01	640	4	17	8	3	143	17	212	68	34	371	164	414	53	n.d.	984	0	152	147	10	261	4611	n.d.	0.03	–	13.6	0.06
***Nahuelbuta**, NAPED10*																																									
0 – 5	GFRO1000H	0.6	65.16	0.77	18.48	6.21	0.09	1.13	2.29	1.68	1.41	0.20	97.43	0.18	408	20	25	15	44	127	20	145	93	16	283	6863	7124	5139	202	1257	295	210	210	116	6279	9322	3056	1.00	0.03	7.0	0.67
5 – 10	GFRO1000J	0.6	62.55	0.86	20.14	7.01	0.12	1.28	2.26	1.69	1.52	0.20	97.62	0.15	454	24	27	14	10	147	20	143	100	16	296	6523	14071	6704	212	1936	414	286	494	158	5454	16363	3632	0.93	0.03	22.2	0.33
10 – 20	GFRO1000K	0.8	62.86	0.83	20.11	6.90	0.12	1.25	2.32	1.72	1.45	0.17	97.74	0.11	427	25	26	13	10	143	18	143	99	23	299	7969	13051	9801	403	1505	681	347	472	216	5995	14507	4504	1.10	0.05	17.6	0.41
20 – 40	GFRO1000L	0.9	66.25	0.71	18.35	5.94	0.09	1.11	2.30	1.70	1.38	0.11	97.94	0.06	429	18	23	12	7	126	21	142	84	19	295	5402	10998	5047	342	1244	365	259	424	80	4522	14068	2065	0.77	0.06	23.0	0.32
40 – 60	GFRO1000M	1.1	66.42	0.68	18.37	5.53	0.07	1.09	2.54	1.88	1.34	0.09	98.00	0.04	421	17	23	12	8	112	17	157	76	19	279	4354	7052	2030	358	834	93	221	284	13	4638	12585	691	0.67	0.08	20.5	0.37
60 – 80	GFRO1000N	1.1	62.99	0.82	20.04	6.59	0.08	1.45	2.54	1.94	1.48	0.08	98.01	0.03	467	17	26	16	8	130	24	158	84	22	328	2678	3769	1031	197	677	na	91	117	7	2332	7754	313	0.38	0.07	11.8	0.30
80 – 100	GFRO1000P	1.0	63.88	0.75	19.08	5.94	0.07	1.40	3.04	2.35	1.48	0.08	98.05	0.01	444	13	26	13	8	111	21	178	72	23	304	1976	3914	976	289	1048	na	58	94	5	1317	7873	463	0.26	0.15	15.8	0.17
100 – 120	GFRO1000Q	1.0	64.18	0.66	18.23	5.41	0.07	1.31	3.62	2.88	1.62	0.10	98.08	0.01	455	16	22	12	5	96	28	209	73	25	252	1845	1933	497	407	634	na	69	76	5	688	2965	59	0.22	0.22	6.0	0.23
120 – 140	GFRO1000R	1.0	66.34	0.66	16.87	5.36	0.07	1.35	3.25	2.52	1.54	0.13	98.09	0.01	413	11	21	13	4	111	34	186	75	23	244	1720	2202	625	441	705	62	77	83	7	538	2651	54	0.20	0.26	5.6	0.20
140 – 160	GFRO1000S	1.1	64.52	0.71	17.49	5.89	0.08	1.48	3.42	2.68	1.70	0.12	98.09	0.01	421	12	25	14	6	119	33	192	77	25	261	1712	1727	502	424	761	95	66	86	3	416	2114	42	0.19	0.25	4.1	0.20
160 – 180	GFRO1000T	1.1	64.09	0.69	18.19	5.41	0.06	1.33	3.46	2.81	1.94	0.10	98.09	0.01	491	12	25	12	8	116	23	202	74	17	294	1893	1945	944	478	669	81	63	72	4	339	2590	33	0.21	0.25	6.0	0.13
180 – 200	GFRO1000U	1.2	66.26	0.65	16.38	5.06	0.06	1.27	3.58	2.89	1.77	0.13	98.05	0.00	340	13	21	10	3	107	17	204	62	17	294	1391	1957	738	422	642	117	36	57	4	159	1601	41	0.15	0.30	4.1	0.10
200 – 220	GFRO1000V	n.d.	65.12	0.68	16.82	5.35	0.07	1.34	3.69	2.91	1.98	0.14	98.11	0.01	401	14	22	10	3	119	18	207	75	16	335	1554	1584	572	381	543	61	48	50	5	185	1283	23	0.16	0.25	2.9	0.14
NAPED20																																									
0 – 5	GFRO10019	0.7	66.51	0.78	17.67	6.34	0.17	1.14	1.68	1.01	1.92	0.28	97.51	0.15	562	24	23	13	9	119	17	118	94	21	270	6231	14100	8861	202	2134	1250	480	871	417	5118	16986	5233	0.88	0.03	26.7	0.30
5 – 10	GFRO10018	0.7	63.20	0.88	19.79	7.21	0.16	1.28	1.76	1.12	1.87	0.28	97.56	0.14	524	31	26	12	12	127	25	118	105	21	311	8262	15247	8147	309	2199	851	469	722	205	6323	17277	3561	1.14	0.04	21.7	0.37
10 – 20	GFRO1001A	0.7	63.23	0.87	20.00	7.15	0.16	1.26	1.73	1.11	1.88	0.25	97.64	0.13	527	30	26	13	11	123	16	117	108	20	306	9904	25666	12334	376	2831	1442	570	1131	316	7631	30689	6346	1.37	0.04	46.1	0.25
20 – 40	GFRO1001B	0.8	63.73	0.86	19.87	7.08	0.14	1.25	1.77	1.12	1.82	0.20	97.83	0.09	507	27	25	13	12	122	21	118	108	24	310	8478	19096	8284	471	2335	1288	398	792	159	6623	24787	3616	1.18	0.06	36.7	0.27
40 – 60	GFRO1001C	0.9	67.67	0.61	17.88	5.14	0.08	0.97	1.57	1.22	2.78	0.09	98.01	0.03	624	16	22	8	6	153	12	114	77	20	251	5160	9009	3791	430	831	515	297	411	40	5951	19450	1429	0.81	0.08	37.6	0.31
60 – 80	GFRO1001D	1.2	57.48	0.99	22.80	8.59	0.12	2.47	1.58	0.74	3.08	0.13	97.97	0.03	716	41	27	14	15	171	23	109	152	27	254	2515	5239	964	220	860	95	251	358	10	2818	17178	161	0.39	0.09	23.9	0.16
80 – 100	GFRO100WP	1.1	47.77	1.23	22.43	13.88	0.22	4.93	3.56	0.74	3.03	0.21	97.99	0.02	631	48	27	17	16	188	39	116	246	31	47	3024	4316	1425	496	1391	271	361	555	11	1316	16350	172	0.37	0.16	15.5	0.08
100 – 120	GFRO100WN	0.9	49.13	1.21	21.31	12.41	0.18	5.13	4.91	1.00	2.53	0.21	98.02	0.02	489	43	28	15	13	153	56	140	275	43	92	2370	4512	1199	418	1540	168	137	306	5	867	12312	113	0.28	0.18	13.2	0.07
120 – 140	GFRO100WM	0.9	49.94	1.11	21.43	11.48	0.20	4.50	5.36	1.29	2.47	0.24	98.01	0.01	484	38	24	8	15	140	43	186	301	37	181	3243	4494	1017	697	1470	na	118	221	2	693	8346	79	0.36	0.21	9.5	0.08
140 – 160	GFRO100WL	1.0	50.11	1.47	22.49	11.71	0.20	4.08	4.06	1.02	2.54	0.34	98.01	0.02	527	29	24	12	12	153	25	172	287	25	132	4494	4841	1214	1005	1555	85	154	265	3	946	9465	131	0.50	0.22	10.4	0.10
160 – 180	GFRO100WK	0.8	53.80	1.27	24.40	9.80	0.13	3.48	1.18	0.48	3.28	0.17	97.98	0.02	720	21	28	12	11	222	29	99	194	36	101	2138	3878	1094	269	1356	182	225	380	5	639	11799	91	0.25	0.13	16.3	0.05
180 – 200	GFRO100WQ	0.9	57.64	1.17	20.81	9.18	0.12	3.65	1.80	0.75	2.72	0.18	98.01	0.02	536	20	23	12	11	199	27	112	183	37	79	3028	3823	1267	550	1361	133	183	289	4	540	7832	78	0.33	0.18	11.4	0.07
200 – 220	GFRO100WR	n.d.	56.94	1.16	21.40	9.12	0.12	3.74	1.95	0.88	2.50	0.22	98.01	0.02	446	23	26	12	11	203	25	112	174	31	106	3129	6713	1322	601	2090	124	139	365	4	410	8419	207	0.33	0.19	12.6	0.05
220 – 240	GFRO100WJ	n.d.	54.21	1.25	22.63	9.58	0.12	3.94	2.27	1.11	2.62	0.27	98.01	0.02	455	34	28	13	12	212	25	135	183	31	97	3811	5151	1308	795	1650	103	130	221	3	389	5233	21	0.40	0.21	7.2	0.07
240 – 260	GFRO100WH	n.d.	55.32	1.22	22.24	9.29	0.12	3.60	1.97	1.10	2.84	0.31	98.01	0.01	541	26	26	9	12	206	21	149	170	30	115	2506	16229	6406	767	2295	1615	131	834	31	82	18484	512	0.25	0.31	28.3	0.00
NAPED30																																									
0 – 5	GFRO1001F	0.7	61.17	1.17	18.29	8.44	0.18	2.47	3.17	1.08	1.31	0.31	97.58	0.13	310	37	26	14	13	94	35	128	172	36	393	9270	16182	12502	474	2687	1435	350	558	285	6879	16300	6866	1.27	0.05	16.0	0.42
5 – 10	GFRO1001G	0.7	60.56	1.19	18.85	8.55	0.17	2.49	3.08	1.13	1.35	0.28	97.65	0.13	320	41	26	14	15	95	34	125	168	29	405	10055	19271	10456	562	3030	984	323	582	190	7105	18386	5095	1.36	0.06	18.9	0.39

Continued on the next page.

Table S2.4: ...continuation

Soil profile Depth [cm]	IGSN	ρ^* [g cm^{-3}]	SiO_2	TiO_2	Al_2O_3	Fe_2O_3	MnO	MgO	CaO	Na_2O	K_2O	P_2O_5	Sum	SO_3	Ba	Cr	Ga	Nb	Ni	Rb	Sc	Sr	V	Y	Zr	Al_o	Al_d	Al_p	Si_o	Si_d	Si_p	Mn_o	Mn_d	Mn_p	Fe_o	Fe_d	Fe_p	$Al_o + 0.5 \times Fe_o$	$\frac{Si_o}{Al_o}$	$\frac{Fe_d - Fe_o}{Fe_{tot}}$	$\frac{Fe_o}{Fe_d}$
			[wt%]												[ppm]																[ppm]								[%]		[-]	
10 – 20	GFRO1001H	0.7	59.58	1.23	19.58	8.83	0.17	2.49	3.01	1.13	1.34	0.28	97.66	0.12	324	41	26	14	14	96	34	122	182	31	441	10760	19529	8662	670	3078	957	330	520	150	7575	17638	3979	1.45	0.06	16.3	0.43
20 – 40	GFRO1001J	0.8	60.14	1.19	19.56	8.64	0.15	2.47	2.93	1.13	1.34	0.23	97.77	0.10	313	40	26	15	14	96	32	116	185	30	417	12879	18671	10262	1133	3301	1298	269	354	124	8270	16341	4518	1.70	0.09	13.4	0.51
40 – 60	GFRO1001K	0.8	63.42	1.00	18.03	7.41	0.10	2.21	2.67	1.16	1.78	0.14	97.92	0.06	471	38	24	13	11	104	27	116	145	28	321	9691	18577	8713	1166	3814	928	93	161	42	6794	17448	3417	1.31	0.12	20.6	0.39
60 – 80	GFRO100WU	1.1	63.83	0.91	18.42	6.95	0.10	2.08	2.27	1.36	1.97	0.10	97.99	0.04	402	36	22	13	11	119	25	113	135	31	304	6885	10684	4407	874	1754	502	79	109	18	6374	13732	1964	1.01	0.13	15.1	0.46
80 – 100	GFRO100WT	1.3	64.84	0.87	17.92	6.73	0.09	2.11	1.99	1.45	1.93	0.12	98.05	0.02	364	43	22	17	18	137	23	126	118	33	261	3921	5693	2041	553	1115	274	50	50	6	3513	7365	842	0.57	0.14	8.2	0.48
100 – 120	GFRO100WS	1.6	61.78	0.90	16.44	7.52	0.17	2.41	5.11	1.28	2.16	0.33	98.10	0.01	362	72	23	15	29	173	21	153	133	45	229	1740	2955	999	444	874	81	98	134	7	422	2760	173	0.20	0.26	4.4	0.15
NAPED40																																									
0 – 5	GFRO1001R	0.8	70.10	0.63	16.01	5.40	0.12	1.00	1.12	0.84	2.41	0.18	97.83	0.08	488	27	20	9	12	182	17	104	99	25	261	8213	14459	28	867	2344	n.d.	459	696	n.d.	4802	17130	n.d.	1.06	0.11	32.6	0.28
5 – 10	GFRO1001S	0.9	68.38	0.68	17.01	5.89	0.13	1.09	1.13	0.87	2.43	0.19	97.80	0.09	493	33	21	12	13	189	14	102	110	25	284	8747	13410	5059	926	2073	515	458	613	123	4858	15319	1244	1.12	0.11	25.4	0.32
10 – 20	GFRO1001T	0.9	68.31	0.68	17.07	5.88	0.13	1.09	1.14	0.87	2.45	0.19	97.79	0.10	501	28	22	11	11	189	13	102	105	27	282	9745	14627	6825	1206	2264	669	474	649	176	5249	17068	1951	1.24	0.12	28.8	0.31
20 – 40	GFRO1001U	1.0	67.86	0.70	17.59	5.99	0.12	1.11	1.08	0.84	2.42	0.16	97.87	0.08	478	29	20	11	11	184	16	99	109	33	301	9480	13104	6215	1542	2459	652	404	511	104	4958	15415	1541	1.20	0.16	24.9	0.32
40 – 60	GFRO1001V	1.2	74.56	0.33	13.19	4.20	0.12	0.58	0.69	1.40	2.93	0.06	98.07	0.03	320	17	17	14	4	201	16	56	72	36	166	5416	8142	2805	1180	1380	277	422	563	28	4985	19295	967	0.79	0.22	48.7	0.26
60 – 80	GFRO100X0	1.1	74.36	0.45	12.80	4.71	0.07	0.83	1.15	1.07	2.57	0.07	98.08	0.02	450	15	15	8	4	146	11	110	78	27	279	3878	6693	965	887	1079	310	410	602	12	4173	23373	442	0.60	0.23	58.3	0.18
80 – 100	GFRO10050	1.2	74.71	0.39	12.42	5.04	0.08	0.73	0.86	0.81	2.96	0.06	98.07	0.02	535	14	15	8	4	141	14	92	105	23	296	2816	4306	1025	829	926	131	328	478	6	4149	19312	323	0.49	0.29	43.0	0.21
100 – 120	GFRO100WZ	1.2	76.52	0.39	12.87	3.20	0.21	0.79	0.72	0.62	2.69	0.04	98.06	0.02	511	20	13	6	6	132	10	84	69	15	185	2296	2290	555	618	462	76	1371	1425	9	1713	5568	102	0.32	0.27	17.2	0.31
120 – 140	GFRO100WY	1.2	71.58	0.55	15.91	4.02	0.27	1.15	0.88	0.79	2.85	0.07	98.05	0.02	510	23	19	9	9	159	11	89	75	20	281	2032	2191	686	489	391	76	1174	1641	12	876	3191	69	0.25	0.24	8.2	0.27
140 – 160	GFRO100WX	1.3	73.95	0.51	14.02	3.67	0.11	1.06	0.94	0.87	2.89	0.06	98.07	0.01	518	20	18	10	9	156	10	94	70	20	313	2043	1996	495	617	344	na	561	697	5	968	2867	85	0.25	0.30	7.4	0.34
160 – 180	GFRO100WV	n.d.	71.43	0.58	14.03	4.85	0.13	1.51	1.62	0.92	2.90	0.12	98.08	0.01	457	16	18	8	5	164	14	108	93	33	252	2003	2249	495	573	515	145	868	742	10	938	4868	1129	0.25	0.29	11.6	0.19
180 – 200	GFRO100WW	n.d.	77.71	0.37	12.07	2.75	0.07	0.77	0.97	1.01	2.29	0.07	98.09	0.02	359	13	15	8	3	131	9	95	54	20	304	1742	1842	520	539	368	224	370	518	7	699	3657	50	0.21	0.31	15.4	0.19

* Bulk density data from Bernhard et al. (2018)

† Bulk chemical data determined at GFZ German Research Centre for Geosciences, Section "Inorganic and Isotope Geochemistry"

‡ Pedogenic oxides were determined at University Bern

n.d. ... not determined

Table S2.5: Weathering indices CDF and CIA, the mass transfer coefficients (τ) for major and trace elements and volumetric strain (ε). The given values represent median values for each horizon ± 1 standard deviation. CIA and CDF are calculated using Eq. 2.2 and Eq. 2.3, repsecitvely. τ-values are calculated uisng Eq. 2.4 and ε according Eq. 2.5. More information is given in the text.

Soil profile Depth [cm]	ρ [g cm^{-3}]	ε	CIA [-]	CDF	τ^{Si}	τ^{Ti}	τ^{Al}	τ^{Fe}	τ^{Mn}	τ^{Mg}	τ^{Ca}	τ^{Na}	τ^{K}	τ^{P}	τ^{Ba}	τ^{Cr}	τ^{Ga}	τ^{Nb}	τ^{Ni}	τ^{Rb}	τ^{Sc}	τ^{Sr}
					τ-values relative to the lowestmost pedon sample																	
***Pan de Azúcar**, AZPED60*																						
0 – 5[a]	1.35	0.15 ± -	50.45 ± -	0.43 ± -	-0.55 ± -	-0.06 ± -	-0.46 ± -	-0.40 ± -	-0.34 ± -	1.26 ± -	-0.45 ± -	-0.56 ± -	-0.51 ± -	-0.13 ± -	-0.64 ± -	-0.19 ± -	-0.36 ± -	-0.18 ± -	-0.04 ± -	-0.45 ± -	0.24 ± -	-0.46 ± -
5 – 10[b]	1.19	0.80 ± -	32.38 ± 20.30	0.12 ± 0.14	-0.39 ± 0.00	0.03 ± 0.02	-0.25 ± 0.06	-0.30 ± 0.00	-0.24 ± 0.26	1.70 ± 1.33	2.97 ± 3.80	-0.44 ± 0.00	-0.30 ± 0.09	-0.12 ± 0.01	-0.56 ± 0.15	-0.27 ± 0.11	-0.10 ± 0.10	0.00 ± 0.00	-0.06 ± 0.23	-0.21 ± 0.07	1.63 ± 1.31	-0.13 ± 0.28
10 – 120[c]	n.d.	- ± -	48.44 ± 10.75	-0.03 ± 0.18	-0.19 ± 0.20	0.00 ± 0.04	-0.12 ± 0.13	-0.10 ± 0.12	0.00 ± 0.13	0.02 ± 0.82	-0.02 ± 1.39	0.00 ± 0.06	-0.26 ± 0.18	-0.06 ± 0.07	-0.45 ± 0.30	0.07 ± 0.30	0.00 ± 0.11	0.03 ± 0.05	-0.17 ± 0.16	-0.15 ± 0.12	0.48 ± 0.61	-0.11 ± 0.11
AZPED50																						
0 – 5[a]	1.19	0.67 ± -	53.38 ± -	0.27 ± -	-0.22 ± -	0.00 ± -	-0.11 ± -	-0.02 ± -	0.02 ± -	0.74 ± -	-0.42 ± -	-0.08 ± -	-0.07 ± -	0.00 ± -	0.13 ± -	-0.37 ± -	-0.07 ± -	-0.13 ± -	0.35 ± -	-0.09 ± -	-0.05 ± -	0.13 ± -
5 – 10[b]	1.59	0.80 ± -	45.27 ± 11.17	0.00 ± 0.05	0.10 ± 0.02	-0.02 ± 0.01	0.07 ± 0.00	0.09 ± 0.03	-0.19 ± 0.13	0.00 ± 0.20	0.42 ± 1.19	0.21 ± 0.00	0.25 ± 0.10	0.02 ± 0.06	0.76 ± 0.29	-0.20 ± 0.04	-0.06 ± 0.05	0.11 ± 0.06	0.38 ± 0.58	0.20 ± 0.09	0.08 ± 0.84	0.36 ± 0.13
10 – 140[c]	n.d.	- ± -	50.68 ± 5.03	0.06 ± 0.12	0.01 ± 0.10	0.00 ± 0.02	0.01 ± 0.06	0.01 ± 0.07	-0.08 ± 0.19	-0.03 ± 0.28	-0.18 ± 0.53	0.04 ± 0.12	0.09 ± 0.12	0.00 ± 0.04	0.28 ± 0.32	-0.08 ± 0.17	-0.08 ± 0.07	0.00 ± 0.08	0.21 ± 0.28	0.04 ± 0.10	0.07 ± 0.34	0.14 ± 0.15
AZPED0																						
0 – 5[a]	1.14	1.19 ± -	42.82 ± -	0.09 ± -	-0.07 ± -	-0.06 ± -	-0.10 ± -	-0.06 ± -	0.20 ± -	0.24 ± -	-0.09 ± -	-0.16 ± -	-0.11 ± -	-0.04 ± -	0.30 ± -	-0.36 ± -	-0.14 ± -	-0.08 ± -	-0.18 ± -	-0.12 ± -	-0.69 ± -	0.38 ± -
5 – 10[b]	1.39	0.91 ± -	31.41 ± 7.92	-0.06 ± 0.12	-0.01 ± 0.09	0.02 ± 0.02	0.02 ± 0.00	-0.07 ± 0.14	0.13 ± 0.46	0.38 ± 0.00	1.35 ± 1.07	-0.49 ± 0.20	0.10 ± 0.04	0.04 ± 0.02	-0.05 ± 0.39	-0.21 ± 0.09	0.03 ± 0.02	0.23 ± 0.22	-0.47 ± 0.02	0.12 ± 0.05	0.12 ± 0.38	0.46 ± 0.15
10 – 120[c]	n.d.	- ± -	44.31 ± 5.32	0.05 ± 0.05	-0.06 ± 0.05	0.03 ± 0.02	0.00 ± 0.04	0.00 ± 0.08	-0.02 ± 0.22	0.00 ± 0.15	-0.12 ± 0.27	-0.27 ± 0.27	0.00 ± 0.08	0.01 ± 0.03	-0.15 ± 0.24	0.00 ± 0.12	0.00 ± 0.09	0.05 ± 0.12	-0.23 ± 0.14	0.00 ± 0.09	-0.28 ± 0.23	-0.04 ± 0.17
AZPED21																						
0 – 5[a]	1.30	1.34 ± -	47.07 ± -	-0.02 ± -	0.00 ± -	-0.04 ± -	-0.13 ± -	0.29 ± -	-0.04 ± -	2.30 ± -	10.43 ± -	-0.10 ± -	-0.19 ± -	0.17 ± -	-0.32 ± -	-0.31 ± -	-0.14 ± -	0.04 ± -	0.82 ± -	-0.16 ± -	1.50 ± -	0.02 ± -
5 – 10[b]	1.35	1.29 ± 0.06	48.59 ± 1.41	-0.13 ± 0.09	0.12 ± 0.09	0.01 ± 0.00	-0.05 ± 0.05	0.32 ± 0.10	-0.27 ± 0.42	1.53 ± 0.28	10.38 ± 0.95	-0.08 ± 0.15	-0.14 ± 0.05	-0.13 ± 0.23	-0.29 ± 0.08	-0.26 ± 0.07	0.09 ± 0.08	0.11 ± 0.32	0.45 ± 0.10	-0.07 ± 0.05	1.10 ± 0.80	-0.09 ± 0.06
10 – 100[c]	n.d.	- ± -	56.15 ± 8.48	-0.02 ± 0.08	0.02 ± 0.10	0.06 ± 0.04	-0.04 ± 0.11	0.25 ± 0.16	0.02 ± 0.27	0.33 ± 0.50	3.09 ± 5.05	-0.07 ± 0.12	-0.10 ± 0.20	0.04 ± 0.15	-0.22 ± 0.34	-0.01 ± 0.01	-0.01 ± 0.13	0.16 ± 0.10	0.71 ± 0.49	-0.04 ± 0.13	1.27 ± 0.87	-0.05 ± 0.14
***Santa Gracia**, SGPED20*																						
0 – 20[a]	1.52	-0.16 ± 0.10	47.75 ± 0.80	0.53 ± 0.07	-0.04 ± 0.17	0.02 ± 0.02	-0.03 ± 0.16	0.21 ± 0.02	0.13 ± 0.03	-0.17 ± 0.05	-0.08 ± 0.06	-0.18 ± 0.12	0.80 ± 0.48	-0.29 ± 0.02	1.02 ± 0.61	-0.28 ± 0.13	-0.04 ± 0.13	0.23 ± 0.23	-0.09 ± 0.20	1.22 ± 0.56	0.07 ± 0.19	-0.19 ± 0.12
20 – 40[b]	1.56	-0.25 ± -	48.28 ± -	0.56 ± -	-0.13 ± -	-0.07 ± -	-0.04 ± -	0.16 ± -	0.01 ± -	-0.23 ± -	-0.15 ± -	-0.15 ± -	0.48 ± -	-0.32 ± -	0.55 ± -	-0.31 ± -	-0.19 ± -	-0.21 ± -	-0.24 ± -	0.52 ± -	-0.20 ± -	-0.11 ± -
40 – 120[c]	n.d.	- ± -	46.84 ± 0.28	0.56 ± 0.04	-0.12 ± 0.10	-0.03 ± 0.03	-0.05 ± 0.06	0.05 ± 0.11	-0.07 ± 0.10	-0.16 ± 0.11	-0.11 ± 0.06	-0.13 ± 0.09	0.25 ± 0.49	-0.07 ± 0.11	0.37 ± 0.81	-0.65 ± 0.38	-0.12 ± 0.08	0.15 ± 0.20	-0.43 ± 0.24	0.27 ± 0.44	-0.13 ± 0.18	-0.08 ± 0.08
SGPED40																						
0 – 10[a]	1.52	-0.20 ± 0.07	48.45 ± 0.46	0.55 ± 0.03	-0.44 ± 0.04	-0.33 ± 0.01	-0.43 ± 0.03	-0.29 ± 0.00	-0.29 ± 0.00	-0.41 ± 0.02	-0.45 ± 0.05	-0.51 ± 0.04	-0.23 ± 0.05	-0.57 ± 0.08	-0.38 ± 0.05	-0.38 ± 0.11	-0.35 ± 0.02	-0.29 ± 0.06	-0.43 ± 0.03	0.04 ± 0.07	-0.42 ± 0.06	-0.49 ± 0.04
10 – 40[b]	1.5	-0.15 ± 0.08	49.36 ± 0.23	0.53 ± 0.02	-0.41 ± 0.03	-0.31 ± 0.01	-0.39 ± 0.03	-0.25 ± 0.01	-0.28 ± 0.02	-0.41 ± 0.02	-0.45 ± 0.02	-0.48 ± 0.03	-0.22 ± 0.02	-0.63 ± 0.02	-0.36 ± 0.03	-0.23 ± 0.11	-0.34 ± 0.00	-0.29 ± 0.13	-0.70 ± 0.20	0.00 ± 0.05	-0.37 ± 0.02	-0.46 ± 0.03
40 – 180[c]	1.43	0.41 ± -	48.73 ± 1.63	0.25 ± 0.11	-0.06 ± 0.13	-0.07 ± 0.10	-0.01 ± 0.14	-0.10 ± 0.18	-0.19 ± 0.21	0.01 ± 0.10	-0.10 ± 0.17	-0.07 ± 0.12	-0.17 ± 0.20	-0.33 ± 0.18	-0.29 ± 0.31	0.05 ± 0.12	0.04 ± 0.18	-0.25 ± 0.11	-0.04 ± 0.18	-0.11 ± 0.14	-0.22 ± 0.24	-0.08 ± 0.15
SGPED60																						
0 – 10[a]	1.5	-0.25 ± 0.06	49.47 ± 0.25	0.58 ± 0.02	-0.09 ± 0.05	-0.18 ± 0.01	-0.12 ± 0.05	-0.02 ± 0.02	0.26 ± 0.01	-0.07 ± 0.02	-0.07 ± 0.02	-0.09 ± 0.05	-0.18 ± 0.04	-0.30 ± 0.01	-0.28 ± 0.04	1.08 ± 0.29	-0.24 ± 0.11	-0.05 ± 0.02	- ± -	-0.15 ± 0.05	-0.09 ± 0.29	-0.15 ± 0.04
10 – 60[b]	1.46	-0.24 ± 0.06	49.96 ± 0.38	0.58 ± 0.03	-0.10 ± 0.07	-0.13 ± 0.02	-0.13 ± 0.07	0.04 ± 0.03	0.31 ± 0.08	-0.05 ± 0.02	-0.10 ± 0.04	-0.11 ± 0.07	-0.21 ± 0.08	-0.36 ± 0.04	-0.30 ± 0.09	1.53 ± 0.34	-0.15 ± 0.08	-0.10 ± 0.06	- ± -	-0.13 ± 0.04	-0.12 ± 0.09	-0.19 ± 0.07
60 – 180[c]	n.d.	- ± -	50.36 ± 0.55	0.48 ± 0.04	0.13 ± 0.12	-0.07 ± 0.04	0.12 ± 0.07	0.01 ± 0.06	0.02 ± 0.07	-0.02 ± 0.08	0.08 ± 0.07	0.12 ± 0.06	0.09 ± 0.18	0.00 ± 0.12	0.07 ± 0.15	0.20 ± 0.35	0.03 ± 0.06	0.12 ± 0.09	- ± -	0.19 ± 0.20	-0.05 ± 0.08	0.16 ± 0.09
SGPED70																						
0 – 20[a]	1.62	-0.08 ± 0.10	50.20 ± 1.07	0.44 ± 0.08	-0.12 ± 0.13	-0.15 ± 0.11	-0.04 ± 0.15	-0.08 ± 0.08	-0.15 ± 0.12	-0.27 ± 0.09	-0.12 ± 0.07	-0.04 ± 0.14	-0.31 ± 0.11	-0.29 ± 0.03	-0.19 ± 0.12	0.44 ± 0.18	0.03 ± 0.21	0.08 ± 0.13	-0.27 ± 0.18	-0.25 ± 0.12	-0.15 ± 0.16	-0.04 ± 0.11
20 – 40[b]	1.66	-0.05 ± -	52.06 ± -	0.41 ± -	-0.08 ± -	0.02 ± -	0.04 ± -	0.11 ± -	0.00 ± -	-0.16 ± -	-0.10 ± -	-0.09 ± -	-0.24 ± -	-0.37 ± -	-0.22 ± -	1.38 ± -	0.02 ± -	0.11 ± -	0.19 ± -	-0.26 ± -	-0.05 ± -	-0.07 ± -
40 – 180[c]	n.d.	- ± -	47.70 ± 1.04	0.37 ± 0.05	0.00 ± 0.08	0.05 ± 0.19	0.05 ± 0.09	0.06 ± 0.15	0.01 ± 0.11	0.05 ± 0.10	0.02 ± 0.09	0.01 ± 0.10	-0.02 ± 0.08	0.04 ± 0.11	-0.12 ± 0.09	0.36 ± 0.40	0.13 ± 0.11	0.35 ± 0.33	-0.01 ± 0.29	-0.06 ± 0.09	0.02 ± 0.24	0.01 ± 0.10
***La Campana**, LCPED10*																						
0 – 5[a]	1.15	0.27 ± -	52.09 ± -	0.47 ± -	-0.49 ± -	0.05 ± -	-0.43 ± -	0.18 ± -	0.71 ± -	0.66 ± -	2.35 ± -	-0.45 ± -	-0.59 ± -	0.18 ± -	-0.59 ± -	2.98 ± -	-0.41 ± -	-0.12 ± -	1.75 ± -	-0.55 ± -	5.32 ± -	-0.04 ± -
5 – 40[b]	1.29	0.22 ± 0.04	54.64 ± 1.13	0.46 ± 0.05	-0.48 ± 0.06	0.07 ± 0.02	-0.40 ± 0.06	0.22 ± 0.02	0.46 ± 0.06	0.62 ± 0.06	1.69 ± 0.25	-0.43 ± 0.05	-0.58 ± 0.07	-0.08 ± 0.04	-0.60 ± 0.08	3.08 ± 0.60	-0.44 ± 0.08	-0.22 ± 0.13	1.15 ± 0.25	-0.52 ± 0.07	3.75 ± 0.56	-0.13 ± 0.01
40 – 80[c]	1.57	0.57 ± 0.20	57.80 ± 0.17	0.11 ± 0.11	-0.09 ± 0.12	0.03 ± 0.04	-0.07 ± 0.10	0.07 ± 0.10	0.24 ± 0.34	0.16 ± 0.22	0.32 ± 0.40	-0.11 ± 0.16	-0.11 ± 0.15	0.01 ± 0.01	-0.11 ± 0.16	0.28 ± 0.39	-0.05 ± 0.07	0.17 ± 0.25	0.48 ± 0.68	-0.09 ± 0.12	1.40 ± 1.97	-0.02 ± 0.03
LCPED20																						
0 – 40[a]	1.04	0.51 ± 0.65	54.67 ± 1.71	0.36 ± 0.02	-0.05 ± 0.03	0.25 ± 0.10	-0.04 ± 0.05	0.07 ± 0.11	0.55 ± 0.13	0.22 ± 0.11	0.01 ± 0.17	-0.13 ± 0.04	-0.14 ± 0.03	0.13 ± 0.17	-0.15 ± 0.02	5.39 ± 0.91	0.02 ± 0.10	0.55 ± 0.20	0.37 ± 0.10	-0.05 ± 0.05	1.32 ± 0.56	-0.04 ± 0.07
40 – 60[b]	1.40	0.10 ± -	54.86 ± -	0.44 ± -	-0.18 ± -	0.20 ± -	-0.11 ± -	0.11 ± -	0.18 ± -	0.30 ± -	-0.07 ± -	-0.22 ± -	-0.23 ± -	-0.06 ± -	-0.24 ± -	1.53 ± -	0.07 ± -	0.18 ± -	-0.01 ± -	-0.12 ± -	0.83 ± -	-0.17 ± -
60 – 160[c]	1.49	0.26 ± 0.15	53.86 ± 0.55	0.33 ± 0.08	0.00 ± 0.10	0.47 ± 0.40	0.05 ± 0.16	0.49 ± 0.41	0.42 ± 0.43	0.66 ± 0.66	0.19 ± 0.31	0.00 ± 0.11	0.00 ± 0.09	0.47 ± 0.30	-0.10 ± 0.06	0.67 ± 0.72	0.08 ± 0.26	0.30 ± 0.25	0.00 ± 0.39	0.00 ± 0.13	0.86 ± 0.88	0.02 ± 0.15
LCPED30																						
0 – 20[a]	1.24	0.08 ± 0.10	52.38 ± 0.53	0.48 ± 0.03	-0.23 ± 0.04	0.18 ± 0.02	-0.11 ± 0.04	0.19 ± 0.03	0.98 ± 0.18	0.24 ± 0.01	0.10 ± 0.10	-0.31 ± 0.01	-0.28 ± 0.05	0.19 ± 0.15	-0.29 ± 0.08	5.56 ± 0.78	-0.08 ± 0.07	0.00 ± 0.15	2.28 ± 0.17	-0.20 ± 0.07	-0.17 ± 0.15	-0.13 ± 0.06
20 – 60[b]	1.12	0.34 ± 0.07	52.00 ± 0.82	0.45 ± 0.05	-0.20 ± 0.07	0.34 ± 0.11	-0.03 ± 0.09	0.34 ± 0.08	0.79 ± 0.05	0.53 ± 0.16	0.19 ± 0.16	-0.16 ± 0.12	-0.28 ± 0.05	0.21 ± 0.09	-0.34 ± 0.04	5.59 ± 0.48	-0.02 ± 0.17	0.22 ± 0.20	2.48 ± 0.32	-0.22 ± 0.02	-0.03 ± 0.07	-0.07 ± 0.11
60 – 320[c]	1.64	0.10 ± 0.16	49.93 ± 0.35	0.34 ± 0.09	-0.02 ± 0.13	0.43 ± 0.24	0.13 ± 0.16	0.50 ± 0.22	0.67 ± 0.25	0.71 ± 0.27	0.50 ± 0.25	0.14 ± 0.17	-0.20 ± 0.11	0.55 ± 0.34	-0.28 ± 0.12	0.58 ± 0.75	0.16 ± 0.18	0.23 ± 0.31	0.54 ± 0.67	-0.10 ± 0.11	0.05 ± 0.14	0.20 ± 0.16
LCPED40																						
0 – 10[a]	1.33	-0.45 ± 0.03	53.17 ± 0.45	0.73 ± 0.01	-0.43 ± 0.01	-0.18 ± 0.02	-0.39 ± 0.02	-0.14 ± 0.01	-0.10 ± 0.06	-0.18 ± 0.05	-0.32 ± 0.08	-0.50 ± 0.01	-0.44 ± 0.00	-0.44 ± 0.07	-0.41 ± 0.01	2.73 ± 0.81	-0.44 ± 0.04	-0.33 ± 0.10	0.90 ± 0.13	-0.51 ± 0.03	-0.22 ± 0.00	-0.37 ± 0.04
10 – 40[b]	1.52	-0.40 ± 0.05	55.89 ± 0.69	0.67 ± 0.03	-0.29 ± 0.07	0.01 ± 0.09	-0.21 ± 0.08	0.06 ± 0.10	0.09 ± 0.09	0.02 ± 0.08	-0.28 ± 0.04	-0.39 ± 0.05	-0.30 ± 0.07	-0.35 ± 0.03	-0.28 ± 0.09	2.79 ± 0.37	-0.24 ± 0.14	-0.24 ± 0.07	0.51 ± 0.15	-0.34 ± 0.05	-0.28 ± 0.15	-0.28 ± 0.06
40 – 140[c]	1.54	-0.30 ± 0.09	56.02 ± 2.39	0.61 ± 0.03	-0.15 ± 0.08	0.06 ± 0.07	-0.05 ± 0.07	0.12 ± 0.09	0.12 ± 0.12	0.07 ± 0.08	-0.22 ± 0.11	-0.29 ± 0.14	-0.13 ± 0.09	-0.31 ± 0.15	-0.06 ± 0.08	1.69 ± 1.00	-0.04 ± 0.06	0.00 ± 0.10	1.00 ± 0.50	-0.20 ± 0.09	-0.02 ± 0.15	-0.19 ± 0.09
***Nahuelbuta**, NAPED10*																						
0 – 40[a]	0.74	1.54 ± 0.61	70.34 ± 1.05	0.28 ± 0.02	0.13 ± 0.05	0.33 ± 0.10	0.31 ± 0.05	0.39 ± 0.10	0.79 ± 0.21	0.02 ± 0.06	-0.32 ± 0.02	-0.34 ± 0.01	-0.17 ± 0.03	0.44 ± 0.36	0.21 ± 0.04	0.83 ± 0.26	0.33 ± 0.08	0.52 ± 0.17	2.68 ± 6.96	0.31 ± 0.09	0.29 ± 0.10	-0.22 ± 0.03
40 – 80[b]	1.07	0.69 ± 0.15	67.87 ± 0.90	0.31 ± 0.08	0.11 ± 0.17	0.21 ± 0.02	0.26 ± 0.07	0.25 ± 0.01	0.23 ± 0.13	0.04 ± 0.09	-0.23 ± 0.09	-0.27 ± 0.07	-0.21 ± 0.03	-0.34 ± 0.09	0.22 ± 0.05	0.34 ± 0.16	0.24 ± 0.03	0.50 ± 0.15	2.12 ± 0.36	0.13 ± 0.01	0.25 ± 0.17	-0.16 ± 0.09
80 – 220[c]	1.08	0.22 ± 0.56	58.82 ± 5.65	0.26 ± 0.14	0.19 ± 0.19	0.20 ± 0.26	0.25 ± 0.20	0.23 ± 0.23	0.20 ± 0.34	0.21 ± 0.36	0.05 ± 0.44	-0.04 ± 0.22	-0.16 ± 0.18	0.02 ± 0.37	-0.15 ± 0.24	0.72 ± 1.74	0.04 ± 0.22	0.19 ± 0.31	0.55 ± 2.06	-0.07 ± 0.22	0.05 ± 1.05	0.00 ± 0.18
NAPED20																						
0 – 40[a]	0.72	1.42 ± 0.35	75.20 ± 0.66	0.30 ± 0.05	-0.55 ± 0.04	-0.73 ± 0.00	-0.67 ± 0.00	-0.71 ± 0.00	-0.51 ± 0.07	-0.87 ± 0.00	-0.65 ± 0.02	-0.62 ± 0.01	-0.75 ± 0.02	-0.68 ± 0.06	-0.64 ± 0.04	-0.59 ± 0.03	-0.64 ± 0.01	-0.50 ± 0.06	-0.63 ± 0.01	-0.77 ± 0.01	-0.64 ± 0.06	-0.71 ± 0.02
40 – 100[b]	1.04	1.53 ± 5.05	71.47 ± 4.20	-0.14 ± 2.08	0.05 ± 0.93	0.02 ± 1.26	0.10 ± 1.19	0.45 ± 1.93	0.74 ± 2.37	0.27 ± 1.82	-0.57 ± 2.34	-0.49 ± 0.72	-0.51 ± 1.24	-0.82 ± 0.84	-0.40 ± 1.33	-0.29 ± 2.30	-0.54 ± 1.19	-0.33 ± 2.24	-0.41 ± 1.72	-0.62 ± 1.08	-0.51 ± 2.44	-0.65 ± 0.91
100 – 260[c]	0.91	5.70 ± 1.83	70.95 ± 6.82	-0.87 ± 0.45	0.05 ± 0.28	0.08 ± 0.24	0.07 ± 0.24	0.19 ± 0.27	0.27 ± 0.29	0.20 ± 0.31	0.45 ± 0.75	-0.07 ± 0.23	0.05 ± 0.27	-0.17 ± 0.18	0.00 ± 0.31	-0.02 ± 0.41	0.15 ± 0.26	0.37 ± 0.45	0.03 ± 0.20	0.04 ± 0.32	0.36 ± 0.75	0.00 ± 0.16
NAPED30																						
0 – 60[a]	0.71	0.90 ± 0.24	69.67 ± 1.06	0.47 ± 0.07	-0.42 ± 0.09	-0.25 ± 0.03	-0.33 ± 0.06	-0.35 ± 0.03	-0.49 ± 0.07	-0.41 ± 0.04	-0.67 ± 0.03	-0.51 ± 0.07	-0.65 ± 0.11	-0.56 ± 0.09	-0.50 ± 0.20	-0.69 ± 0.03	-0.36 ± 0.06	-0.46 ± 0.06	-0.73 ± 0.02	-0.69 ± 0.06	-0.11 ± 0.05	-0.54 ± 0.05
60 – 100[b]	1.04	0.58 ± 0.03	69.33 ± 0.45	0.25 ± 0.08	-0.15 ± 0.10	-0.19 ± 0.06	-0.10 ± 0.08	-0.26 ± 0.06	-0.57 ± 0.02	-0.29 ± 0.08	-0.66 ± 0.00	-0.11 ± 0.13	-0.27 ± 0.07	-0.73 ± 0.06	-0.14 ± 0.03	-0.55 ± 0.10	-0.23 ± 0.07	-0.20 ± 0.23	-0.60 ± 0.18	-0.39 ± 0.12	-0.10 ± 0.05	-0.36 ± 0.11
100 – 120[c]	1.59	0.50 ± -	55.92 ± -	0.08 ± -	0.00 ± -	0.00 ± -	0.00 ± -	0.00 ± -	0.00 ± -	0.00 ± -	0.00 ± -	0.00 ± -	0.00 ± -	0.00 ± -	0.00 ± -	0.00 ± -	0.00 ± -	0.00 ± -	0.00 ± -	0.00 ± -	0.00 ± -	0.00 ± -
NAPED40																						
0 – 40[a]	0.89	1.12 ± 0.35	75.02 ± 0.73	0.25 ± 0.04	-0.05 ± 0.07	0.97 ± 0.03	0.51 ± 0.03	1.27 ± 0.05	1.01 ± 0.14	0.50 ± 0.03	0.08 ± 0.09	-0.08 ± 0.06	0.14 ± 0.07	1.81 ± 0.35	0.48 ± 0.10	1.32 ± 0.18	0.49 ± 0.09	0.40 ± 0.09	3.08 ± 0.42	0.55 ± 0.09	0.69 ± 0.30	0.14 ± 0.09
40 – 80[b]	1.17	1.23 ± 0.75	66.53 ± 0.20	0.05 ± 0.36	0.40 ± 0.51	0.50 ± 0.24	0.57 ± 0.60	1.33 ± 0.66	1.18 ± 1.44	0.27 ± 0.16	0.29 ± 0.00	0.86 ± 0.99	0.78 ± 0.79	0.21 ± 0.32	0.49 ± 0.19	0.84 ± 0.82	0.59 ± 0.71	1.16 ± 1.51	0.96 ± 0.71	1.01 ± 1.13	1.31 ± 1.38	0.17 ± 0.12
80 – 200[c]	1.22	0.56 ± 0.49	69.23 ± 2.75	0.23 ± 0.17	0.10 ± 0.26	0.46 ± 0.37	0.29 ± 0.28	0.63 ± 0.42	1.55 ± 1.75	0.49 ± 0.52	-0.01 ± 0.42	-0.08 ± 0.11	0.33 ± 0.31	-0.07 ± 0.45	0.53 ± 0.43	0.46 ± 0.52	0.25 ± 0.20	0.22 ± 0.11	1.48 ± 1.01	0.23 ± 0.25	0.48 ± 0.38	0.00 ± 0.22

* CDF_Z, and 1 SD for bedrock based on bedrock-Zr concentration ± 1 σ (Table S2.2)
† bulk density data from Bernhard et al. (2018)
‡ the CaO content of the samples have been corrected for calcium bound in apatite, such that CaO* (Eq. 2) denotes to the molar fraction of calcium in silicate minerals only: CaO* = CaO - ($P_2O_5 \times 10/3$
[a] extent of the A horizon
[b] extent of the B horizon
[c] extent of the saprolite

Table S2.6: Chemical weathering and physical erosion rates.

Study area Pedon	IGSN	Depth [cm]	$\rho_{cum.}$ [g cm^{-3}]	Production rates* P_{Nuc}	$P_{muon,S}$	$P_{muon,F}$	P_{tot} [10^4 atoms g^{-1}]	^{10}Be concentration† [atoms g^{-1} yr^{-1}]	Total denudation rate D [t km^{-2} yr^{-1}]	CDF‡ [-]	Chemical weathering rate W§ [t km^{-2} yr^{-1}]	Physical erosion rate E [t km^{-2} yr^{-1}]
Pan de Azucar												
AZPED50	GFTE10006	22.5 ± 10.0	1.54	3.102	0.011	0.035	3.148	38.6 ± 1.2	11.0 ± 0.7	0.09 ± 0.02	0.94 ± 0.20	10.06 ± 0.68
AZPED21	GFTE10007	37.5 ± 10.0	1.44	3.125	0.011	0.035	3.172	45.0 ± 1.4	8.2 ± 0.5	-0.12 ± -0.01	-0.97 ± 0.10	9.13 ± 0.49
Santa Gracia												
SGPED40	GFTE10008	62.5 ± 10.0	1.48	4.231	0.013	0.043	4.287	20.7 ± 0.8	22.4 ± 1.5	0.53 ± 0.34	11.91 ± 7.59	10.49 ± 7.73
SGPED70	GFTE10009	37.5 ± 10.0	1.58	4.259	0.013	0.043	4.315	35.2 ± 1.2	15.9 ± 0.9	0.45 ± 0.29	7.17 ± 4.66	8.71 ± 4.75
La Campana												
LCPED20	GFTE1000A	42.5 ± 10.0	1.13	4.352	0.013	0.044	4.409	12.0 ± 0.5	53.7 ± 3.4	0.37 ± 0.05	19.98 ± 3.11	33.77 ± 4.60
LCPED40	GFTE1000B	42.5 ± 10.0	1.47	4.374	0.013	0.044	4.431	8.9 ± 0.4	69.2 ± 4.6	0.66 ± 0.11	45.85 ± 8.00	23.36 ± 9.22
Nahuelbuta												
NAPED20	GFTE1000C	82.5 ± 20.0	0.89	6.626	0.017	0.055	6.698	17.3 ± 0.7	47.5 ± 3.0	0.16 ± 0.06	7.50 ± 3.10	39.98 ± 4.33
NAPED40	GFTE1000D	82.5 ± 20.0	1.04	6.424	0.016	0.054	6.494	38.3 ± 1.3	17.7 ± 1.1	0.20 ± 0.05	3.50 ± 0.88	14.22 ± 1.39

* Production rate at sampling location ceorrected for shielding by vegetation

† ^{10}Be concentration in saprolite samples as determined in Schaller et al. (2018b)

‡ calculated using the bedrocks' average Zr concentration and average Zr concentration in soil samples (i.e. A- and B-horizon)

§ Total weathering rates (from Eq. 8) using a CDF averaged over all soil samples, thus calculating a maximum chemical loss over the entire regolith profile

Table S2.7: Relative microbial abundances in the four study areas. Bacterial and archaeal abundances were measured by copy numbers of 16S rRNA genes per gram of soil. The given data represents mean values ± standard deviations.

Study area Soil profile	IGSN	Archaea to Bacteria ratio	∅ DNA amount [µm g^{-1}]$_{soil}$	∅ Bacterial gene copy numbers [g^{-1}]$_{regolith}$	∅ Archaeal gene copy numbers [g^{-1}]$_{regolith}$
Pan de Azúcar					
AZPED60	GFLMM00LQ	1:110	18.00 ± 0	1.34E+05 ± 6.17E+04	1.22E+03 ± 1.84E+02
AZPED50	GFLMM00MD	1:117	15.50 ± 0.5	1.27E+05 ± 5.67E+04	1.09E+03 ± 5.13E+02
AZPED40	GFLMM00LR	1:126	15.50 ± 1.5	2.02E+05 ± 6.56E+04	1.60E+03 ± 5.21E+03
AZPED21	GFLMM00ME	1:51	14.50 ± 2.5	1.21E+05 ± 2.22E+04	2.37E+03 ± 1.94E+03
Santa Gracia					
SGPED20	GFLMM00AV	1:93	44.10 ± 11.1	3.31E+07 ± 3.12E+07	3.55E+05 ± 3.33E+05
SGPED40	GFLMM00AU	1:62	21.00 ± 3	2.00E+05 ± 1.16E+05	3.24E+03 ± 1.80E+03
SGPED60	GFLMM00AT	1:175	28.00 ± 4	8.77E+05 ± 3.40E+05	5.02E+03 ± 1.11E+03
SGPED70	GFLMM00AS	1:217	20.50 ± 0.5	3.82E+05 ± 1.32E+05	1.75E+03 ± 9.79E+02
La Campana					
LCPED10	GFLMM00CP	1:26	26.00 ± 2	7.64E+06 ± 4.06E+06	2.95E+05 ± 1.06E+05
LCPED20	GFLMM00B1	1:3	27.00 ± 3	3.25E+05 ± 7.53E+04	1.08E+05 ± 1.66E+04
LCPED30	GFLMM00CC	1:28	25.50 ± 1.5	5.83E+06 ± 2.36E+06	2.05E+05 ± 1.18E+05
LCPED40	GFLMM00B8	1:81	27.50 ± 1.5	6.39E+04 ± 2.20E+04	7.93E+02 ± 2.19E+02
Nahuelbuta					
NAPED10	GFLMM00AZ	1:15	17.00 ± 1	4.88E+05 ± 4.03E+05	3.16E+04 ± 2.61E+04
NAPED20	GFLMM00AY	1:78	14.00 ± 1	7.26E+04 ± 2.03E+04	9.35E+02 ± 7.30E+02
NAPED30	GFLMM00AX	1:15	25.00 ± 7	2.90E+07 ± 6.22E+06	4.98E+06 ± 2.43E+05
NAPED40	GFLMM00AW	1:46	26.00 ± 2	1.05E+05 ± 7.45E+04	2.29E+03 ± 5.34E+02

* Microbial abundance has been determined at GFZ German Research Centre for Geosciences, Section "Geomicrobiology"

CHAPTER 3

Do degree and rate of silicate weathering depend on plant productivity?

Abstract

Plants and their associated below-ground microbiota possess the tools for rock weathering. Yet the quantitative evaluation of the impact of these biogenic weathering drivers relative to abiogenic parameters, such as the supply of primary minerals, of water, and of acids is an open question in Critical Zone research. Here we present a novel strategy to decipher the relative impact of these drivers. We quantified the degree and rate of weathering and compared these to nutrient uptake along the "EarthShape" transect in the Chilean Coastal Cordillera. These sites define a substantial north-south gradient in precipitation and primary productivity but overlie granitoid rock throughout. We present a substantial dataset of the chemistry of Critical Zone compartments (bedrock, regolith, soil, and vegetation) to quantify the relative loss of soluble elements (the "degree of weathering") and the inventory of bio-available elements. We use $^{87}Sr/^{86}Sr$ isotope ratios to identify the sources of mineral nutrients to plants. With rates from cosmogenic nuclides and biomass growth we determined fluxes ("weathering rates"), meaning the rate of loss of elements out of the ecosystems, averaged over weathering timescales (millennia), and quantified mineral nutrient recycling between the bulk weathering zone and the bulk vegetation cover. We found that neither the degree of weathering nor the weathering rates increase systematically with precipitation from north to south along the climate and vegetation gradient. Instead, the increase in biomass nutrient demand is accommodated by faster nutrient recycling. In the absence of an increase in weathering rate despite a five-fold increase in precipitation and net primary productivity (NPP), we hypothesize that plant growth might in fact dampen weathering rates. Because plants are thought to be key players in the global silicate weathering - carbon feedback, this hypothesis merits further evaluation.

This chapter is submitted to:

Biogeosciences by Ralf A. Oeser and Friedhelm von Blanckenburg

and has been accepted for publication on 02.09.2020 after peer review. The revision records and link to the final published paper can be found at https://doi.org/10.5194/bg-2020-69

3.1 Introduction

Ever since the emergence of land plants, their dependence on mineral-derived nutrients has impacted rock weathering, used here to mean the combined processes of primary mineral dissolution, secondary solid formation, and the loss of elements in aqueous solution. This impact results from three types of interaction. The first is mechanical processes, that weaken rock or change the depth of the weathering zone through roots and microbial symbionts (e.g. mycorrhizal fungi; Blum et al. 2002; Brantley et al. 2017; Hasenmueller et al. 2017; Minyard et al. 2012; Quirk et al. 2014; van Schöll et al. 2007). The second is a variety of biogeochemical processes that alter the susceptibility of minerals to weathering. These mechanisms include root respiration that releases protons and CO_2, lowering soil pH, the exudation of organic ligands through roots that increases the solubility of nutrients through complexation, and the uptake, uplift, and recycling of pore fluids and nutrients from solution (e.g. Berner et al. 2003; Brantley et al. 2012; Drever 1994; Kump et al. 2000; Lee and Boyce 2010; Jobbágy and Jackson 2001; Giehl and von Wiren 2014). The third interaction affects the water cycle which is impacted by rooting depth and seasonal water storage in saprolite and evapotranspiration (Kleidon et al. 2000; Ibarra et al. 2019). All of these interactions impact weathering, either directly by aiding plant acquisition of mineral nutrients from rock, or indirectly by modifying the water cycle (e.g. Brantley et al. 2011b; Porder 2019; Moulton et al. 2000). This means the presence and growth rate of land plants is commonly thought to have strongly impacted the evolution of Earth's atmosphere over geologic time by strengthening the negative feedback between silicate weathering rates and atmospheric CO_2 concentrations (Beerling and Berner 2005; Doughty et al. 2014; Lenton et al. 2012; Pagani et al. 2009; Porada et al. 2016).

While biota in general and plants in particular are undoubtedly key players in weathering and pedogenesis, a quantitative evaluation of their impact remains elusive. The reason is our inability to disentangle abiotic from biotic processes in field observations (Amundson et al. 2007). Almost all mass transfer in the weathering zone can have biotic and abiotic causes. An additional challenge is the difficulty in accounting for confounding effects. Environmental state variables shaping the Critical Zone (the zone of the Earth surface that extends from the top of unweathered bedrock to the top of the vegetation cover; the zone in which most biogeochemical reactions take place) can obscure or amplify the effects of biology, making the attribution of cause and effect challenging. Another reason for our inability to directly attribute weathering to plant growth arises from the ability of ecosystems to recycle nutrients through microbial mineralization from plant litter and organic matter, rather than acquiring fresh nutrient from rock (Chaudhuri et al. 2007; Lang et al. 2016; Lucas 2001; Spohn and Sierra 2018; Wilcke et al. 2002). Given the ability of ecosystems to buffer changes in nutrient fluxes (Spohn and Sierra 2018) the dependence of weathering on plant growth and biomass distribution can be expected to be a highly non-linear one.

A classical strategy in field studies that aim to decipher how ecosystem functioning and weathering shape the Critical Zone relies on exploring the interactions along natural environmental gradients. Studies along a Hawaiian chronosequence (soils of variable discrete initial formation age) have evaluated the role of soil age in weathering and the distribution and cycling of cations through plants. These studies revealed the dependency of nutrient cycling on the degree of weathering (e.g. Bullen and Chadwick 2016; Chadwick et al. 1999; Laliberte et al. 2013; Porder and Chadwick 2009; Vitousek 2004). Studies along a climosequence (gradients in climate whilst minimizing other environmental differences) have evaluated the effect of climate on ecological and pedogenic processes (Bullen and Chadwick 2016; Calmels et al. 2014; Dere et al. 2013; Egli et al. 2003; Ferrier et al. 2012). These studies generally show an increase in weathering rates with increasing mean annual air temperature (MAT) and mean annual precipitation (MAP), while vegetation plays a significant role in pedogenesis. Studies across different rock substrates have evaluated the availability of nutrients and the dissolution kinetics of minerals for ecosystem nutrient budgets (Hahm et al. 2014; Uhlig and von Blanckenburg 2019) and indicate a 'bottom-up' lithologic and mineralogical control on nutrient availability to ecosystems. Studies along gradients in erosion rates explored the supply of minerals to ecosystems and discovered an increase in nutrient supply through weathering with increasing erosion rates (Chadwick and Asner 2016; Eger et al. 2018; Porder et al. 2007; Schuessler et al. 2018). Studies that have tried to isolate just the role of vegetation cover show that the weathering fluxes in adjacent areas in which only vegetation differs showed higher fluxes with more vegetation (Moulton et al. 2000). All these studies differ widely in their methodology, time scale, spatial scale, conceptual framework and even discipline. We return to this topic below by comparing our conceptual perspective to other approaches.

In this study we explore weathering, nutrient uptake, and nutrient recycling along one of the Earth's impressive climate and vegetation gradient, located in the Chilean Coastal Cordillera (Oeser et al. 2018a). The study was conducted within the framework of the priority program of the Deutsche Forschungsgemeinschaft "EarthShape: Earth Surface Shaping by Biota" (DFG-SPP 1803). Along this gradient we quantify the degree of weathering (using chemical analyses of rock and regolith, Oeser et al. 2018a), rates of weathering (using cosmogenic ^{10}Be, Schaller et al. 2018b), and nutrient uptake (using net primary productivity, NPP and the chemical composition of the major plant species at each site). Sequential extraction protocols applied to bulk regolith were used to identify the stoichiometry of the main plant-available elements in the regolith. Radiogenic $^{87}Sr/^{86}Sr$ isotope ratios in bulk rock, regolith, the bio-available fraction in regolith, and plant biomass were used to identify the sources of mineral nutrients. We were thus able to identify gains and losses of nutritive elements in and out of these ecosystems and to quantify the efficiency of nutrient recycling. We applied the conceptual framework and parameterization of Uhlig and von Blanckenburg (2019) to place quantitative constraints on the "organic nutrient cycle" and the "geogenic nutrient

pathway" as detailed in the next section.

Specifically, we evaluated the following questions: (1) Do weathering rates increase along the north-south precipitation gradient because runoff, the main driver of weathering flux, increases? (2) Do the variations in NPP along the climate and vegetation gradient correlate with nutrient supply rates from weathering? We find that neither is the case. Rather than the expected increase in weathering rate, the recycling efficiency of nutrients increases instead along the north – south transect.

3.2 Conceptual perspectives

Two fundamentally different concepts describe the relationship between regolith formation and time, and their relationship to different geomorphic regimes (Lin 2010b; Smeck et al. 1983): the continuous evolution and the steady-state model. The continuous evolution model describes regolith or soil evolution with time from an initial point and describes chronosequences, where soils evolve on stable (non-eroding) surfaces. These soils have a distinct age and undergo several phases of soil development (e.g. Chadwick et al. 1999; Vitousek and Chadwick 2013). In contrast, the steady-state model assumes all regolith state variables are independent of an initial point. In this concept, regolith is constantly rejuvenated by production at depth and its removal through erosion from above (e.g. Heimsath et al. 1997). In other words, the regolith is continuously turned over and has no distinct age, but rather a residence time. This concept applies to all sloping landscapes on Earth, on which typical regolith residence times ($\leq 10^4$ yrs) are often less than or equal to the timescales over which tectonics and climate vary ($\geq 10^4$ yrs). This suggests that much of the Earth surface operates in a manner that is consistent with the steady-state model of soil formation (Dixon et al. 2009b; Ferrier et al. 2005; Riebe and Granger 2013). The state variables do not necessarily vary linearly with age (in the continuous evolution model) or residence time (in the steady-state model). Thus, in the continuous evolution model, pedogenic thresholds have been deduced based on certain soil properties (Dixon et al. 2016; Vitousek and Chadwick 2013). These have also been described to exist and strongly vary along the eroding surfaces in Chile explored in this study (Bernhard et al. 2018).

Although ecosystems respond over shorter time scales to environmental change, ranging from seasonal to decadal or longer climate cycles, their evolution can nevertheless be linked to the two regolith evolution models (Brantley and Lebedeva 2011). In the continuous evolution model, ecology and soil development are linked via progressive increases in soil stability and water retention capacity and a unidirectional decrease in mineral nutrient availability (Vitousek and Farrington 1997). In contrast, in the steady-state model, regolith replenishment by uplift and erosion sets the upward advection of mineral nutrients (Buendía et al. 2010; Porder et al. 2007; Vitousek et al. 2003; Uhlig and von Blanckenburg 2019) and availability of regolith moisture (Rempe and Dietrich 2018). Thus, the combination of regolith

residence time and mineral weathering rates determines whether an ecosystem is limited in a specific mineral nutrient which in turn is thought to set plant diversity and nutrient acquisition strategies. For example, ecosystems on strongly mineral nutrient-depleted soils seem to be characterized by high plant diversity (Laliberte et al. 2013; Lambers et al. 2008).

The methods employed to explore these processes span a range of time scales that are discipline specific. Plant ecology typically works on (sub-)annual timescales for ecosystem fertilization or manipulation experiments (Tielbörger et al. 2014; Tipping et al. 1999), while instrumental monitoring of water, gas, and nutrient fluxes between Critical Zone compartments in hydrology, soil ecology, and biogeochemistry can reach decadal timescales (Joos et al. 2010; Kelly and Goulden 2016; Lang et al. 2016; Sprenger et al. 2019; Sohrt et al. 2019; Wilcke et al. 2017). Geochemical estimates of rock weathering or evolution of plant-available nutrient inventories typically integrate over millennial timescales (Buendía et al. 2010; Porder et al. 2007; Riebe and Granger 2013; Uhlig and von Blanckenburg 2019; Vitousek et al. 2003).

To integrate these different time scales, some soil ecological models account for the coupled weathering – recycling – uptake systems by linking the short-term, biological cycle with the long-term, largely geological and hydrological-driven cycle (Porder and Chadwick 2009; Powers et al. 2015; Vitousek et al. 1998). Such models have recently been complemented by concepts and methods from geochemistry (Uhlig and von Blanckenburg 2019) that we pursue in this study. In this conceptual framework, the so-called "organic nutrient cycle" comprises a set of strategies for efficient nutrient re-utilization through microbial mineralization from plant litter and organic matter and entails rapid nutrient turnover. The "geogenic nutrient pathway" compensates the loss of nutrients by erosion and in solution through the slow but steady supply of nutrients from chemical weathering of rock (Buendía et al. 2010; Cleveland et al. 2013; Uhlig and von Blanckenburg 2019). This concept is particularly relevant where atmospheric wet and dry deposition (e.g. Boy and Wilcke 2008; Chadwick et al. 1999; Dosseto et al. 2012) do not suffice to balance the losses. These geogenic input fluxes are often minor compared to those in the organic nutrient cycle and may even be undetectable over the annual to decadal scales of ecosystem monitoring experiments. However, they sustain ecosystem nutrition over longer (decadal to millennial) time scales because they prevent nutrient deficiency that may otherwise develop (Hahm et al. 2014; Schuessler et al. 2018; Uhlig et al. 2017; Uhlig and von Blanckenburg 2019). Whether the geogenic nutrient pathway is sufficient to prevent development of nutrient limitation over the millennial scale depends on the rate of supply of fresh rock into the weathering zone, the bioavailability of the nutrients released, and whether plant roots and the associated mycorrhizal fungi can access them. Thus, any exploration of these links must constrain where nutrients are released in regolith relative to where plants obtain them. The aim of this study is to illustrate how these methods from geochemistry can be employed to assess the flux balances between the top of bedrock

and the top of the vegetation canopy as integrated over millennia, and how plant growth affects these in comparison to the geologic drivers like uplift and erosion or climatic drivers like precipitation and runoff.

3.3 Study area and previous results

The four study sites are part of the EarthShape study area which is located along the Chilean Coastal Cordillera. Three sites are located in national parks and one in a nature reserve, so human impact is minimized. The sites are located on the plutonic rocks of the Chilean Coastal Cordillera and are close to the Pacific coast (less than 80 km; Oeser et al. 2018a) and are detailed in two previous studies that introduced the field area, its pedogenic and weathering characteristics, and a substantial set of new soil- and geochemical data (Bernhard et al. 2018; Oeser et al. 2018a).

The sites define a vegetation gradient controlled by climate, ranging over 1300 km. From north to south, they cover arid (Pan de Azúcar National Park, ~26°S), semi-arid (Santa Gracia Nature Reserve, ~30°S), mediterranean (La Campana National Park, ~33°S), and humid-temperate (Nahuelbuta National Park, ~38°S) climate conditions. The mean annual precipitation (MAP) increases from 10 mm yr^{-1} in Pan de Azúcar, 89 mm yr^{-1} in Santa Gracia, 440 mm yr^{-1} in La Campana, to 1100 mm yr^{-1} in Nahuelbuta, respectively. The mean annual air temperature (MAT) ranges from 18.1°C in the northernmost site in Pan de Azúcar to 14.1°C in the southernmost site Nahuelbuta (Fig. 3.1, Table 3.1; Ministerio de Obras Públicas 2017).

Net primary productivity (NPP), derived from a dynamic vegetation model (LPJ-GUESS) that simulates vegetation cover and composition during the Holocene (Werner et al. 2018), ranges from 30 g_C m^{-2} yr^{-1} and 150 g_C m^{-2} yr^{-1} in the arid shrubland of Pan de Azúcar and Santa Gracia, respectively, to 280 g_C m^{-2} yr^{-1} in the sclerophyllous woodland of La Campana, and is highest (520 g_C m^{-2} yr^{-1}) in the humid-temperate forests of Nahuelbuta (Fig. 3.1, Table 3.1). The vegetation cover (< 5%) in Pan de Azúcar consists only of small shrubs, geophytes and annual plants (Armesto et al. 1993), which are mainly present in small ravines. The vegetation in Santa Gracia belongs to the "Interior Mediterranean desert scrub of *Heliotropium stenophyllum* and *Flourensia thurifera*" formation (Luebert and Pliscoff 2006). Plants are affected by livestock grazing (Bahre 1979), and vegetation cover is generally sparse. In La Campana the vegetation (almost 100% ground cover) is part of the "Coastal Mediterranean sclerophyllous forest of *Lithraea caustica* and *Cryptocarya alba*" formation (Luebert and Pliscoff 2006). The dominant vegetation in Nahuelbuta is associated with the "Coastal temperate forest of *Araucaria araucana*" formation (Luebert and Pliscoff 2006) and covers 100% of ground area.

Table 3.1: Characteristics of the four EarthShape study sites and soil profile names in Pan de Azúcar, Santa Gracia, La Campana, and Nahuelbuta.

		Pan de Azúcar		*Santa Gracia*		*La Campana*		*Nahuelbuta*		Reference
Regolith profile		*AZPED21*	*AZPED50*	*SGPED70*	*SGPED40*	*LCPED40*	*LCPED20*	*NAPED40*	*NAPED20*	
Latitude		26.1093 S	26.1102 S	29.7612 S	29.7574 S	32.9573 S	32.9559 S	37.8090 S	37.8077 S	†
Longitude		70.5491 W	70.5493 W	71.1656 W	71.1664 W	71.0643 W	71.0635 W	73.0138 W	73.0135 W	†
Altitude	[m asl]	343	330	690	682	734	730	1219	1239	*
Slope	[°]	25	40	15	25	12	23	13	15	‡
Aspect		N-facing	S-facing	N-facing	S-facing	N-facing	S-facing	N-facing	S-facing	†, ‡
Mean annual temperature (MAT)	[°C]	18.1		16.1		14.9		14.1		§
Mean annual precipitation (MAP)	[mm yr^{-1}]	10		87		436		1084		§
Lithology		granite		diorite		granodiorite		granodiorite		†
Mineralogy *	[Vol%]	Quartz xxx, Plagioclase x, K-feldspar xxx, Pyroxene -, Biotite x, Amphibole -		Quartz x, Plagioclase xx, K-feldspar xxx, Pyroxene xx, Biotite -, Amphibole x		Quartz xx, Plagioclase x, K-feldspar xxx, Pyroxene -, Biotite x, Amphibole -		Quartz xx, Plagioclase xx, K-feldspar xxx, Pyroxene x, Biotite x, Amphibole -		†
Soil type		Regosol	Regosol	Cambisol	Leptosol	Cambisol	Cambisol	umbric Podzol	orthodystric Umbrisol	‡
Soil thickness	[cm]	20	20	35	45	35	60	60	70	†
Soil pH**		8.1 ± 0.1	8.1 ± 0.1	6.0 ± 0.3	6.1 ± 0.3	5.2 ± 0.3	5.0 ± 0.3	4.7 ± 0.1	4.3 ± 0.2	‡
Cation exchange Capacity (CEC_{eff})**	[$\mu mol_C\ g^{-1}$]	-	-	108.5 ± 50.2	64.6 ± 23.4	86.4 ± 43.1	72.7 ± 62.1	21.0 ± 15.4	38.2 ± 24.7	‡
Catchment-wide denudation rate (D)	[t $km^{-2}\ yr^{-1}$]	7.7 ± 0.7		9.2 ± 0.8		200 ± 22		27.2 ± 2.4		‖
Soil denudation rate (D_{soil})	[t $km^{-2}\ yr^{-1}$]	8.2 ± 0.5	11.0 ± 0.7	15.9 ± 0.9	22.4 ± 1.5	69.2 ± 4.6	53.7 ± 3.4	17.7 ± 1.1	47.5 ± 3.0	†, #
Soil weathering rate (W)	[t $km^{-2}\ yr^{-1}$]	-1.0 ± 0.1***	0.9 ± 0.2	7.17 ± 4.7	11.9 ± 7.6	45.9 ± 8.0	20.0 ± 3.1	3.5 ± 0.9	7.5 ± 3.1	†, #
Soil erosion rate (E)	[t $km^{-2}\ yr^{-1}$]	9.1 ± 0.5	10.1 ± 0.7	8.7 ± 4.8	10.5 ± 7.7	23.24,± 9.2	33.8 ± 4.6	14.2 ± 1.4	40.0 ± 4.3	†, #
Chemical depletion fraction (CDF)	[-]	-0.1 ± -0.0***	0.1 ± 0.0	0.5 ± 0.3	0.5 ± 0.3	0.7 ± 0.1	0.4 ± 0.1	0.2 ± 0.1	0.2 ± 0.1	†, #
Vegetation cover	[%]	< 5		30 – 40		95		100		‡
Vegetation types		*Tetragonia maritima, Nolana mollis, Perityle sp., Stipa plumosa, Cristaria integerrima*		*Proustia cuneifolia, Senna cumingii, Cordia decandra, Adesmia sp., Cumulopuntia sphaerica Eulychnia acida*		*Lithraea caustica, Cryptocarya alba, Colliguaja odorifera, Aristeguietia salvia, Jubaea chilensis*		*Araucaria araucana, Chusquea culeou, Nothofagus antarctica*		*, ‡
Net primary production (NPP)	[$g_C\ m^{-2}\ yr^{-1}$]	30 ± 10		150 ± 40		280 ± 50		520 ± 130		¶

* Estimation of mineral abundances based on thin section microscopy: -: absence, x: presence (<10 Vol%), xx: abundant (10-35 Vol%), xxx: very abundant (>35 Vol%)

** Denoting to regolith-profile averages

*** N-facing slope in Pan de Azúcar yield negative CDF and hence weathering rates due to the input of seaspray

† Oeser et al. (2018a); ‡ Bernhard et al. (2018); § Ministerio de Obras Públicas (2017); ‖ van Dongen et al. (2019); # Schaller et al. (2018b), ¶ Werner et al. (2018)

The basement at those sites is mainly composed of granitoid intrusions of late Carboniferous to Cretaceous age. The compositional variation ranges from monzo- to syenogranites in Pan de Azúcar (199 Ma; Berg and Breitkreuz 1983; Berg and Baumann 1985; Parada et al. 2007), pyroxene and hornblende-bearing diorites and monzodiorites in Santa Gracia (98 – 89 Ma; Moscoso et al. 1982), as well as tonalites and granodiorites in Nahuelbuta (Nahuelbuta complex, 294 Ma; Parada et al. 2007), and in the Caleu Pluton in La Campana with an intrusion age of 130 Myr (Molina et al. 2015; Parada and Larrondo 1999; Parada et al. 2002).

For the soil pits studied here, denudation rates inferred from cosmogenic nuclides (*in situ* ^{10}Be), interpreted as soil production rates, are 8 – 11 t km^{-2} yr^{-1} in Pan de Azúcar, 16 – 22 t km^{-2} yr^{-1} in Santa Gracia, 54 – 69 t km^{-2} yr^{-1} in La Campana and 18 – 48 t km^{-2} yr^{-1} in Nahuelbuta (Schaller et al. 2018b). Catchment-wide denudation rates broadly agree with these soil-scale rates, except for in La Campana. Here, they are higher, attributed to debris flows in valley tops due to the higher channel steepness than elsewhere (e.g. mean slope 23° in La Campana, 9° in Nahuelbuta; van Dongen et al. 2019). The relative consistency of these rates along the climate gradient is ascribed to consistent tectonic forces acting along the whole gradient (e.g. Blanco-Chao et al. 2014; Melnik 2016), with the moderate increase in denudation rates at the two southern sites explainable with the combined effect of higher precipitation and increasing shielding by vegetation (Schaller et al. 2018b).

The architecture of the regolith profiles, their chemistry, mineralogy, and the physical properties of soils, saprolite, and the rocks beneath have been extensively described for four soil pits at each site by Bernhard et al. (2018), Dal Bo et al. (2019), Oeser et al. (2018a), and Schaller et al. (2018b). The regolith profiles in Pan de Azúcar are located between 330 and 340 m above sea level (asl) on steep (25 – 40°; Table 3.1) hill slopes. The soils on the north- and south-facing slopes were classified by Bernhard et al. (2018) as Regosols with only shallow A and B horizons of ~20 – 30 cm thickness, lacking any kind of organic and litter layer. In this area, the processes disintegrating rock and developing regolith are mainly physical weathering, specifically a combination of insolation- and salt weathering (Oeser et al. 2018a). The regolith profiles in Santa Gracia are situated at almost 700 m asl on gently sloping hills (15 – 25°; Table 3.1). The soils on the north- and on the south-facing slope are a Leptosol and a Cambisol, respectively (Bernhard et al. 2018). Distinct O-horizons and a litter layer are not apparent. The Ah horizons in both profiles reach depths of 10 cm and the transition from the mineral soil (Bw) into saprolite occurs at 25 – 30 cm depth. Oeser et al. (2018a) attribute this sites' high degree of elemental depletion (50% loss relative to bedrock as quantified by the CDF; Fig. A3.1; Table S3.2) despite low precipitation to the low abundance of quartz and the high abundance of readily weatherable plagioclase and mafic minerals. The regolith profiles in La Campana, located at 730 m asl and on gently sloping hills (12 – 23°), are classified as Cambisols. The O-horizon is ~5 cm thick and is followed by a Ah horizon,

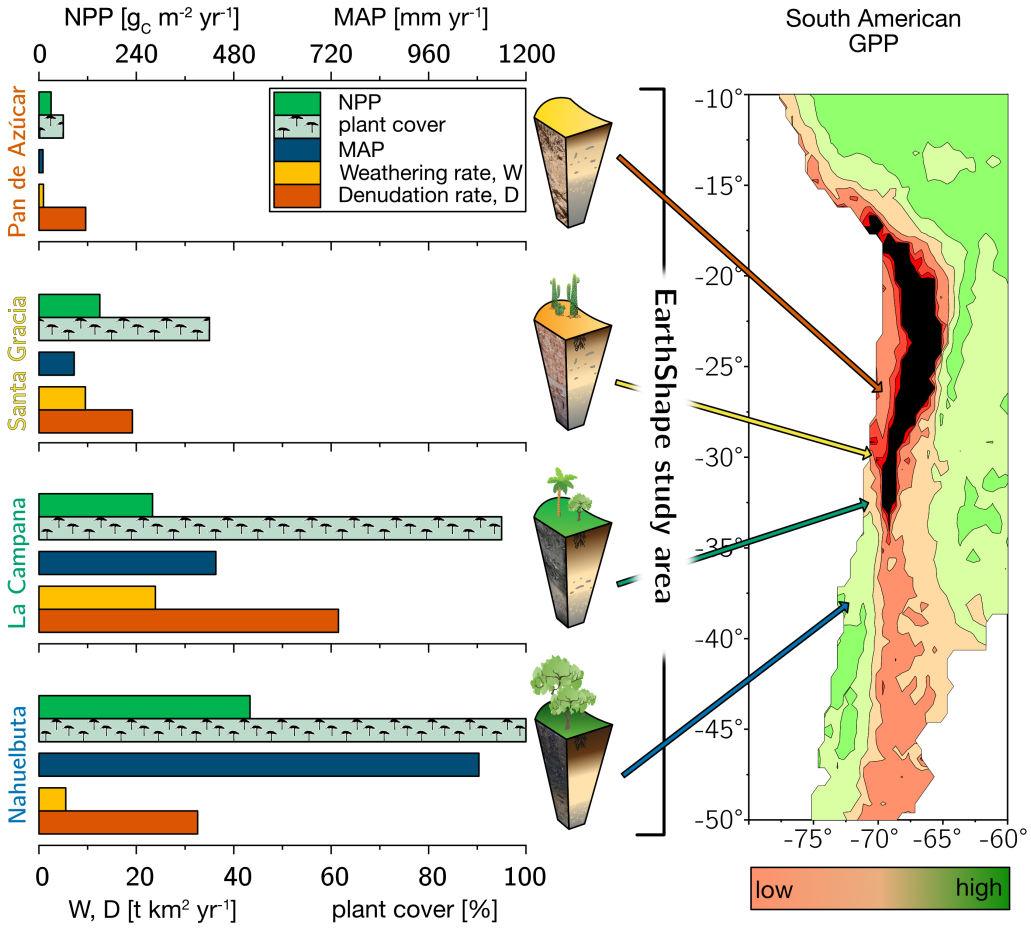

Figure 3.1: The climate and vegetation gradient of the four EarthShape study sites (from arid to humid-temperate: Pan de Azúcar, Santa Gracia, La Campana, and Nahuelbuta). Left: Net primary productivity (NPP), plant cover, annual precipitation (MAP). Denudation rate (D) and weathering rate (W) were determined with cosmogenic ^{10}Be. Right: Position of the four study sites in South America and their respective gross primary productivity (GPP) derived from the FLUXNET data base (Jung et al. 2011). Black color refers to very low GPP in the Atacama Desert. The uncertainties are not shown for clarity. They are provided in Table 3.1

extending up to 40 cm depth (Bernhard et al. 2018). Here, the mineral-soil layer turns into saprolite at approximately 110 cm in both profiles (Table 3.1). The elemental depletion of Ca relative to bedrock increases from ~45% at the profiles' bottom towards ~70% at their top and can be classified as depletion (north-facing) or depletion and enrichment profiles (south-facing, Fig. A3.1; Table S3.2; Brantley and Lebedeva 2011), respectively. The regolith profiles in Nahuelbuta are situated on gently sloping hills (~15°) at about 1200 m asl (Table 3.1). Bernhard et al. (2018) have classified the soils on the north- and south-facing slope as umbric Podsols and orthodystric Umbrisols, respectively. Here, the Ah horizons measure up to 50 cm (greater thickness on the south-facing slope) and are overlain by an organic horizon of 5.5 cm thickness. In the two regolith profiles, the soil-saprolite transition is at 100

and 120 cm depth, respectively. The coarse-grained saprolite disaggregates readily. These two profiles are characterized by highly heterogeneous weathering patterns caused by the incorporation of the metamorphic basement at various parts (e.g. Hervé 1977; Oeser et al. 2018a). Along the EarthShape north-south transect, many of the soil properties indicate crossing of several distinct pedogenic thresholds (Bernhard et al. 2018). We note that while the detailed geochemical work reported in this study is based on two profiles per site, the soil properties (Bernhard et al. 2018) and bulk geochemical data (Oeser et al. 2018a) of these profiles are corroborated by two additional replicates per site as reported in these previous studies. A comprehensive summary of the characteristics of the eight regolith profiles and major plant types is given in Table 3.1

3.4 Methods

3.4.1 Sampling

Regolith samples were collected in a continuous sequence of depth increments from bottom to top. Increments amount to a thickness of 5 cm for the uppermost two samples, 10 cm for the 3rd sample from top, and increase to 20 cm thickness for the 4th sample onwards. To account for the dependence on solar radiation, two regolith profiles on adjacent hillslopes (north- and south-facing) were sampled at each study site (see Appendix B for further information on sample replication).

The underlying unweathered bedrock was not reached in any of the regolith profiles and the depth to bedrock remains unknown. Thus, bedrock samples were collected from nearby outcrops. This sample set comprises the 20 bedrock samples already reported in Oeser et al. (2018a) and 15 additional bedrock samples (in total 12 in Pan de Azúcar, 8 in Santa Gracia, 10 in La Campana, and 5 in Nahuelbuta).

Vegetation samples from representative shrubs and trees (grasses have been excluded) of each study site were sampled in the austral summer to autumn 2016. The sample set comprises material from mature plants of the prevailing species: *Nolana mollis* (Pan de Azúcar), *Asterasia* sp., *Cordia decandra, Cumulopuntia sphaerica,* and *Proustia cuneifolia* (Santa Gracia), *Aristeguietia salvia, Colliguaja odorifera, Cryptocarya alba,* and *Lithraea caustica* (La Campana), *Araucaria araucana, Nothofagus antarctica,* and *Chusquea coleu* (Nahuelbuta). From each sampled plant (n = 20), multiple samples of leaves, twigs and stem were collected, pooled together, and homogenized prior to analysis. These samples were either taken using an increment borer (stem samples) or plant scissors (leaf and twig samples) equipped with a telescopic arm to reach the higher parts of trees. As is commonly the case in field studies, roots could not be sampled in a representative manner though we account for their influence on plant composition (see Appendix A). The litter layer in La Campana and Nahuelbuta was also sampled.

3.4.2 Analytical methods

Chemical composition of regolith and bedrock

The concentration of major and trace elements in bedrock and regolith samples were determined using a X-Ray Fluorescence spectrometer (PANalytical AXIOS Advanced) at the section for "Inorganic and Isotope Geochemistry", GFZ German Research Centre for Geosciences. A detailed description of the analytical protocols and sample preparation is given in Oeser et al. (2018a).

Chemical composition of vegetation

Major and trace element concentration of vegetation samples were determined using a Varian 720-ES axial ICP-OES at the Helmholtz Laboratory for the Geochemistry of the Earth Surface (HELGES), GFZ German Research Centre for Geosciences (von Blanckenburg et al. 2016) with relative uncertainties smaller than 10%. Prior to analysis, all samples were oven-dried at 120 °C for 12 hrs. Subsequently, leaves were crushed and homogenized. About 0.5 g of leaf and 1 g of woody samples were digested in PFA vials using a microwave (MLS start) and ultra-pure concentrated acid mixtures comprising H_2O_2 and HNO_3, HCl and HNO_3, and HF. In some plant samples Si-bearing precipitates formed upon evaporation after digestion. These sample cakes were redissolved in a mixture of concentrated HF and HNO_3 to ensure complete dissolution of Si prior to analysis. As some Si might have been lost by volatilization as SiF_4 in this process, we do not include these samples (indicated by a * in Table S3.5) for the compilation of the plant's Si budget. With each sample batch, the international reference material NIST SRM 1515 Apple leaves and a procedural blank were processed.

Extraction of the easily bio-available fraction and it's chemical analyses

The bio-available fraction of regolith samples was extracted using a sequential extraction procedure adapted from Arunachalam et al. (1996), He et al. (1995), and Tessier et al. (1979). The sequential extraction was performed in parallel on two regolith aliquots, and the supernatants were pooled together for analyses. About 2 g of dried and sieved (< 2 mm) sample material were immersed in 14 ml 18 MΩ Milli-Q H_2O (water-soluble fraction) and then in 1 M NH_4OAc (exchangeable extraction; maintaining a sample/ reactant ratio of ca. 1:7), and gently agitated. After each extraction, the mixture was centrifuged for 30 min at 4200 rpm and the supernatant was pipetted off. The remaining sample was then rinsed with 10 ml Milli-Q H_2O and centrifuged again (4200 rpm, 30 min) and the rinse solution was added to the supernatant. Subsequently, the supernatants were purified using a vacuum-driven filtration system (Millipore®; 0.2 µm acetate filter), evaporated to dryness, and redissolved with ultra-pure concentrated acid mixtures comprising H_2O_2, HNO_3, and HCl. With each sample batch, international reference materials (NIST SRM 2709a San Joaquin soil, CCRMP TILL-1) along with a procedural blank were processed.

The water-soluble fraction is comprised of elements contained in soil water in the form of free ions and ions which form complexes with soluble organic matter. It represents the most labile soil compartment and thus is most accessible to plants (e.g. He et al. 1995). This fraction was accessed by suspending the samples for 24 hrs in Milli-Q H_2O at room temperature. The exchangeable fraction comprises elements that form weak electrostatic bonds between the hydrated surfaces of phyllosilicates (i.e. clays and micas), oxyhydroxide minerals (e.g. boehmite, diaspore, goethite, lepidocrocite, ferrihydrite), and organic matter. This fraction was extracted by suspending the samples in a mechanical end over end shaker at room temperature in 1 M NH_4OAc for 2 hrs at 60 rpm. Note that none of the further extraction steps described in Tessier et al. (1979) have been applied to the regolith samples as they are believed to make a negligible contribution to the bio-available fraction.

The element concentrations of the water-soluble and exchangeable fraction were determined using a Varian 720-ES axial ICP-OES at HELGES, following the analytical procedures described in Schuessler et al. (2016) with relative uncertainties estimated at smaller than 10%.

Soil-P fractions were determined by Brucker and Spohn (2019). In this case, the bio-available fraction refers to the inorganic products of the modified Hedley sequential P fractionation method of Tiessen and Moir (1993), specifically the water-extractable P_i and labile P_i which was extracted by using 0.5 M $NaHCO_3$.

$^{87}Sr/^{86}Sr$ isotope ratios

The radiogenic Sr isotope ratio was determined on bulk bedrock and regolith, the bio-available fractions of saprolite and soil, and on the different plant organs at each study site.

After sample digestion (bulk samples) or sequential extraction (bio-available fraction), Sr was separated from matrix elements using 200 µl Sr-Spec resin. Matrix elements were removed by elution with 2.5 ml 3 M and 2 ml 7.5 M HNO_3. Subsequently, Sr was eluted with 4 ml of 18 M Ω Milli-Q H_2O. Any organic crown-ether which has been released from the Sr-spec resin was removed after evaporation and subsequent redissolution of the Sr fraction in 1 ml of a 1:1 mixture of concentrated H_2O_2 and HNO_3. This mixture was cooked in a tightly closed beaker at 150 °C for at least 12 hrs. Within each sample batch, a minimum of one standard reference material and a procedural blank were processed.

$^{87}Sr/^{86}Sr$ was measured in a 50-ng g^{-1} pure Sr solution in 0.3 M HNO_3 using a multi collector inductively coupled plasma mass spectrometer (MC-ICP-MS, Thermo Neptune) in medium mass resolution. The MC-ICP-MS was equipped with an APEX-Q (ESI) desolvater and a nebulizer with an uptake rate of 70 µl min^{-1} and a nickel sampler cone. Radiogenic Sr isotope ratios were determined over one block of 20 cycles with an integration time of 16 seconds each. The sequence of a sample run was comprised of 10 to 12 blocks, where each block comprised a blank, four samples, and five SRM 987 which were not processed

through chemistry. Blank correction of samples and reference material during the sequence was less than 0.4% of the sample signal. The intensities of the ion beams on the masses ^{82}Kr (L4), ^{83}Kr (L3), ^{84}Sr (L2), ^{85}Rb (L1), ^{86}Sr (central Cup), ^{87}Sr (H1) and ^{88}Sr (H2) were monitored using Faraday collectors equipped with $10^{11}\,\Omega$ and one $10^{12}\,\Omega$ (connected to L4 cup) resistors. Isobaric interference on the masses 84, 86, and 87 were corrected for with the Kr and Rb isotope ratios measured prior to the sequence run. To correct for any natural and instrumental isotope fractionation, the measured ^{87}Sr/^{86}Sr ratio was normalized to a ^{88}Sr/^{86}Sr ratio of 8.375209 (Nier 1938's value) by using an exponential law. Finally, the ^{87}Sr/^{86}Sr ratios were corrected for a session offset that account for the differences between the certified and measured ^{87}Sr/^{86}Sr ratio of the SRM 987 reference material, which in any case where smaller than ± 0.00006 (2SD).

3.4.3 Parameterizing geogenic and biogenic element fluxes in a terrestrial ecosystem

The parameterization of the "geogenic nutrient pathway" and the "organic nutrient cycle" (Fig. 3.2) to characterize element fluxes into, within, and from the Critical Zone and its ecosystem components, including the derivation of the corresponding equations has been thoroughly described in Uhlig and von Blanckenburg (2019). Here, we only briefly summarize the metrics, which are shown in Table 3.2. Calculations and parameters used for these metrics are presented in Appendix A, including the propagation of uncertainties. A statistical analysis (i.e. ANOVA, Pearson correlation coefficients) of the weathering parameters is presented in Appendix B.

3.5 Results

We structure the presentation of our results in the following sequence: (1) the element fluxes of the geogenic nutrient pathway; (2) the availability of elements in regolith to plants; and (3) the plant chemical composition along with the element fluxes that couple the geogenic nutrient pathway to the organic nutrient cycle. The fluxes are presented as study-site averages, with the full dataset available in an associated open access data publication (Oeser and von Blanckenburg 2020a), included as supplementary material in Section 3.9.

We focus the detailed presentation of these results on P and K, the two most important mineral nutrients to plants. Further data is provided for other plant-beneficial and plant-essential elements. Whether an element is considered as beneficial or essential to plants, however, is species-dependent (Marschner 1983). Following Marschner (1983) we refer to the elements Al, Na, and Si as plant-beneficial elements and include the micronutrient Fe in this group. We refer to the elements Ca, K, Mg, and Mn as plant-essential elements. In this presentation, we treat Sr as a plant-essential element due to its similar (bio-)chemical behavior to Ca (e.g. Blum et al. 2012; Faure and Mensing 2005; Faure and Powell 1972; Poszwa et al. 2002). All metrics are defined in Table 3.2.

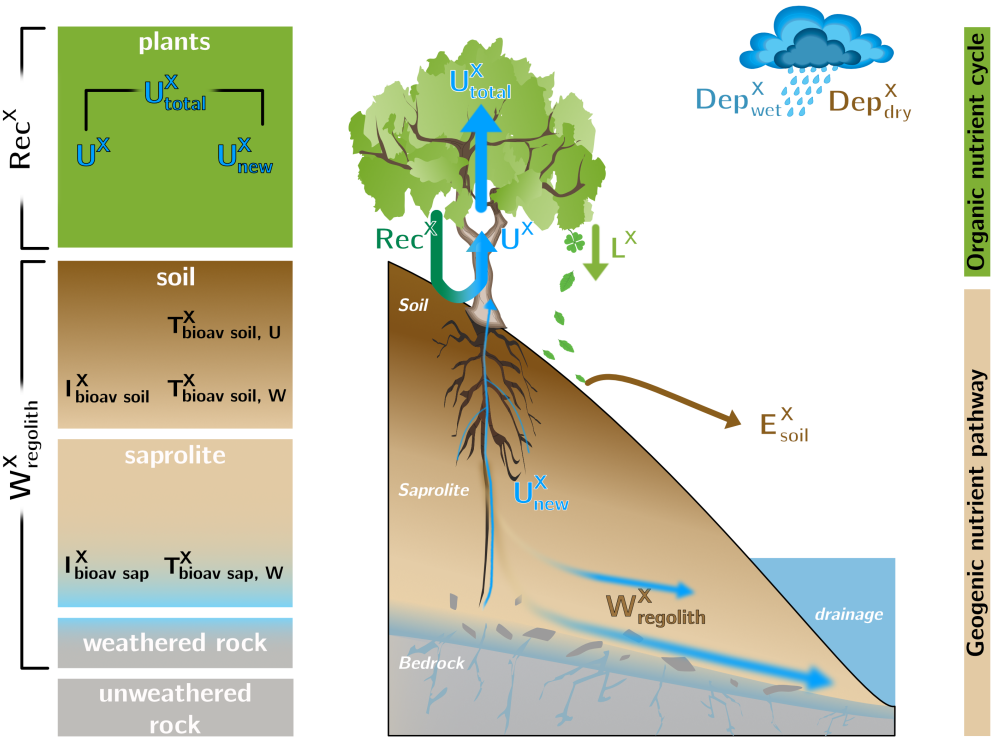

Figure 3.2: Conceptual framework of an ecosystem comprising the "geogenic nutrient pathway" and the "organic nutrient cycle" (modified after Uhlig and von Blanckenburg 2019). Whereas the former is mainly set by mineral nutrient release by weathering ($W^X_{regolith}$) and to a minor extent by atmospheric wet- (Dep^X_{wet}) and dry deposition (Dep^X_{dry}), the organic nutrient cycle is mainly affected by nutrient re-utilization (i.e. recycling) from organic matter (Rec^X). **Left:** The different compartments (i.e. rock, saprolite, soil, and plants) are shown as boxes. They include the metrics used to quantify their properties such as the inventory I^X_j and turnover time$T^X_{i,j}$ of element X in compartment *j*. **Right:** The compartments are linked by fluxes (arrows) with the thickness of them denoting to their relative proportions. E^X_{soil} denotes to erosion of soil.

3.5.1 Element fluxes contributing to the geogenic nutrient pathway

Degree of weathering and elemental gains and losses

The chemical depletion fraction (CDF; Table 3.2, Eq. 3.5 and Appendix A) and elemental mass transfer coefficient (τ; Table 3.2, Eq. 3.6 and Appendix A) disclose the total and the element-specific loss, respectively, of soluble elements relative to bedrock. Thus, both metrics quantify the degree of weathering. The average CDF of the shallowest mineral soil (combined analysis of north- and south-facing profiles) in Pan de Azúcar, Santa Gracia, La Campana, and Nahuelbuta amounts to 0.03, 0.54, 0.50, and 0.25, respectively (Fig. 3.3; Table S3.2). At all four sites, the elemental losses (Fig. A3.1; Table S3.2) can be attributed to a "kinetically limited weathering regime" (Brantley and Lebedeva 2011). This means that the erosion rate is at a sufficient level to continuously replenish the nutrient stock held in weatherable minerals that transit vertically through the weathering profile.

Systematic differences in chemical depletion (i.e. CDF and τ) are not discernible between north- and south-facing slopes. Anomalously high Zr concentrations throughout the entire north-facing profile at La Campana cause one exception to this rule. Moreover, we found that neither CDF nor τ differ significantly between Santa Gracia, La Campana, and Nahuelbuta, despite both increasing precipitation and increasing biomass growth.

A comprehensive presentation of these data can be found as Appendix in Fig. A3.1 and in the supplementary Table S3.2 (Oeser and von Blanckenburg 2020a).

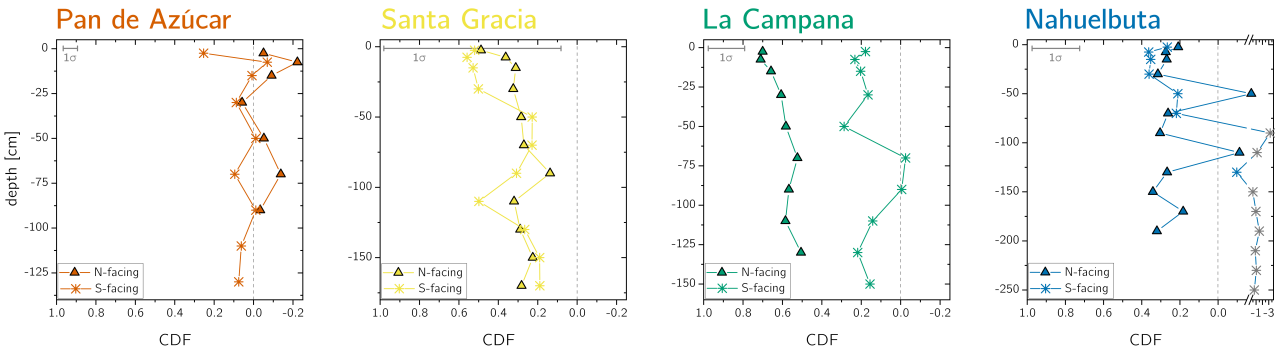

Figure 3.3: Chemical depletion fraction (CDF) for each study sites' north- and south- facing profile. The accuracy of the absolute CDF values is limited by the variability in the bedrock's Zr concentration in the respective study sites and are indicated as gray 1σ bar (Table S3.1). The gray symbols correspond mainly to saprolite samples in the south-facing regolith profile in Nahuelbuta and are excluded from further consideration. Note that in Nahuelbuta a different scaling compared to the other study sites applies after the axis break.

Elemental chemical weathering fluxes

The soil weathering rate W quantifies the bulk weathering flux from rock and regolith. This flux is lowest in Pan de Azúcar (0 – 0.9 t km^{-2} yr^{-1}) and highest in La Campana (53.7 – 69.2 t km^{-2} yr^{-1}). In Santa Gracia (7.2 – 11.9 t km^{-2} yr^{-1}) and Nahuelbuta (3.5 – 7.5 t km^{-2} yr^{-1}, Table 3.1; Oeser et al. 2018a; Schaller et al. 2018b), these fluxes are at a similarly intermediate level.

The elemental chemical weathering flux ($W^{X}_{regolith}$; Table 3.2, Eq. 3.3 and Appendix A) quantifies the elemental-specific release fluxes from rock and regolith by weathering. It thus assesses the maximum possible weathering supply of nutrients to plants by the "geogenic pathway", as some of this flux is potentially lost into groundwater before being accessible to roots. The weathering-release fluxes for phosphorus ($W^{P}_{regolith}$) amount to 1.3 ± 0.4, 12 ± 3, 19 ± 6, and 11 ± 4 mg m^{-2} yr^{-1} and of potassium ($W^{K}_{regolith}$) to 30 ± 30, 80 ± 50, 840 ± 220, and 100 ± 120 mg m^{-2} yr^{-1} (Fig. 3.4, Table 3.3) in Pan de Azúcar, Santa Gracia, La Campana, and Nahuelbuta, respectively. Similar trends are seen for the plant-beneficial elements Al, Na, and Si along with Fe and Sr. The rates of supply of P, K, and the plant-beneficial elements are thus similar at both Santa Gracia and Nahuelbuta despite the differences in MAP, NPP,

Table 3.2: Glossary of metrics for the parameterization of the geogenic nutrient pathway and organic nutrient cycle in terrestrial ecosystems after Uhlig and von Blanckenburg (2019).

Total mass fluxes (in e.g. t km^{-2} yr^{-1}		
(3.1)	$D = E + W$	denudation rate; the sum of chemical weathering and physical erosion
	E	physical erosion; physical removal of primary and secondary minerals along with biogenic material
(3.2)	$W = D \times CDF$	chemical weathering rate; net-chemical release flux from minerals as some fraction of which is being incorporated into secondary minerals and pedogenic (hydr-)oxides
	GPP	gross primary productivity; gross carbon input into biomass
	NPP	net primary productivity; net-carbon fixation by biomass
Elemental fluxes (in e.g. mg m^2 yr^{-1})		
(3.3)	$W^X_{regolith} = D \times [X]_{parent} \times \left(-\tau^X_{X_i}\right)$	Chemical weathering flux of element X; release flux of X from minerals minus the flux of incorporation of X into secondary minerals and oxides
(3.4)	$U^X_{total} = \frac{NPP \times [X]_{tree}}{[C]_{tree}}$	Total nutrient uptake flux of element X; uptake of X by trees at the ecosystem scale, where $[C]_{plant}$ denotes the carbon concentration in dry mass, typically 50 wt%
	Dep^X_{dry}	Atmospheric dry deposition of element X
	Dep^X_{wet}	Atmospheric wet deposition of element X as rainfall
Elemental mass fractions and flux ratios (dimensionless)		
(3.5)	$CDF = 1 - \frac{[X_i]_{parent}}{[X_i]_{weathered}}$	chemical depletion fraction; fractional mass loss by dissolution of elements from the regolith
(3.6)	$\tau^X = \frac{[X]_{weathered}}{[X]_{parent}} \times \frac{[X_i]_{parent}}{[X_i]_{weathered}} - 1$	elemental mass transfer coefficient; elemental loss or gain relative to unweathered bedrock
(3.7)	$Rec^X = \frac{U^X_{total}}{W^X_{regolith}}$	nutrient recycling factor; number of times, element X is re-utilized from plant litter after its initial release from rock weathering
Elemental inventories (in e.g. g m^{-2} or kg m^{-2})		
(3.8)	$I^X_j = \int_{z=a}^{z=b} [X_j] \times \rho \, dz$	Inventory of element X in compartment j
	$I^X_{bioav\ soil}$	Inventory of element X in compartment in the bio-available fraction in soil
	$I^X_{bioav\ sap}$	Inventory of element X in compartment in the bio-available fraction in saprolite
	I^X_{bulk}	Inventory of element X in compartment in bulk regolith
Elemental turnover times (in e.g. yr)		
(3.9)	$T^X_{i,j} = \frac{I^X_i}{j}$	Turnover time of element X in compartment i with respect to input or output flux j; the ratio of total stock of element X in i to input or output flux j
	$T^X_{bioav,\ U}$	Turnover time of element X in the forest floor with respect to uptake into trees; mean time a nutrient rest in the forest floor before re-utilization by forest trees
	$T^X_{bioav,\ W}$	Turnover time of element X in the bio-available fraction in regolith with respect to adsorption onto clay minerals; mean time over which the inventory of the bio-available fraction is replenished by chemical silicate weathering in the absence of other gains or losses

and vegetation cover. $W^{Ca}_{regolith}$ and $W^{Mg}_{regolith}$ do deviate from this general pattern: the highest Ca and Mg weathering-release fluxes occur in Santa Gracia followed by La Campana, Nahuelbuta, and Pan de Azúcar. These elevated fluxes in Santa Gracia are attributed to the initial bedrock mineralogy, with their high Ca and Mg concentration (Table S3.1).

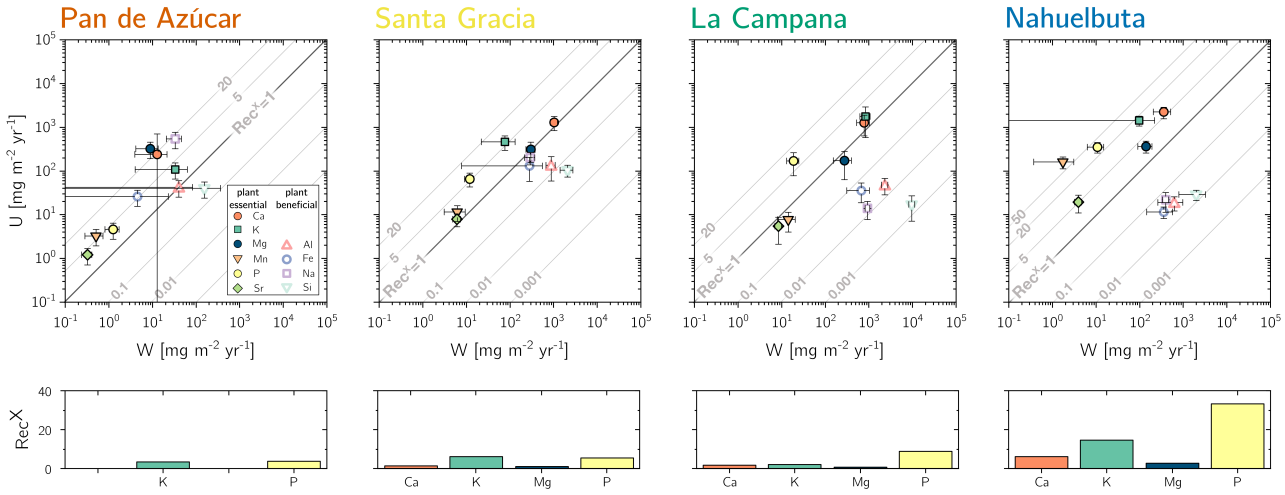

Figure 3.4: Chemical weathering flux ($W^X_{regolith}$) and plant nutrient-uptake fluxes (U^X_{total}) for Pan de Azúcar, Santa Gracia, La Campana, and Nahuelbuta (from left to right) for plant-essential and plant-beneficial elements. Grey contour lines emphasize the nutrient recycling factor (Rec^X), which is the ratio of U^X_{total} to$W^X_{regolith}$. Uncertainty bars show 1SD. Differences in nutrient recycling factors for the plant essential elements Ca, K, Mg, and P among the four study sites are highlighted in the lower panels. Note that here we use the Rec^X calculated for $W^X_{regolith}$ from silicate weathering only. In Table 3.7 and Fig. A3.4 we also show Rec^X including atmospheric inputs. Because Pan de Azúcar Ca and Mg inputs are exclusively atmospheric their Rec^X are overestimated and thus not plotted on the lower left panel.

3.5.2 Availability of mineral nutrients to plants

The maximum amount of nutrients present can be assessed by determining their inventory in bulk regolith (I^X_{bulk}; Table 3.2, Eq. 3.8 and Appendix A). For most elements I^X_{bulk} is by far greatest in Santa Gracia (apart from K and Si; Table 3.4). I^X_{bulk} at the other three study sites are mostly at a similar levels. Element concentrations in the bio-available fraction are orders of magnitude lower than in the bulk regolith (Fig. A3.2 & A3.3, Table S3.3). Bio-available P in saprolite ($I^P_{bio\text{-}av,\ sap}$) is virtually absent in Pan de Azúcar and amounts to 21, 39, and 23 g m^{-2} in Santa Gracia, La Campana, and Nahuelbuta, respectively (Table 3.4). $I^K_{bio\text{-}av,\ sap}$ equals 253 in the northernmost, and 23, 70, and 19 g m^{-2} at the sites progressively southwards. The inventory of the remaining mineral nutrients in saprolite generally decreases from north to south. Accordingly, the total inventory (i.e. the sum of all determined inventories) is highest in Pan de Azúcar (5100 g m^{-2}), intermediate in Santa Gracia (2100 g m^{-2}) and La Campana (1600 g m^{-2}), and lowest in Nahuelbuta (140 g m^{-2}; Table 3.4). Note that $I^X_{bio\text{-}av,\ sap}$ was calculated over the uppermost 1 m of saprolite, whereas in fact the zone of mineral nutrient extraction might extend deeper. Bio-availability in soil features a similar trend. The total inventory is highest in Pan de Azúcar (2100 g m^{-2}), on par in Santa Gracia (960 g m^{-2}) and La Campana (1000 g m^{-2}), and despite featuring the thickest soils, lowest in Nahuelbuta (200 g m^{-2}). P deviates from this general trend: $I^P_{bio\text{-}av,\ soil}$ amounts to 3.3 g m^{-2} in Pan de

Azúcar, 22 g m^{-2} in Santa Gracia, 28 g m^{-2} in La Campana, and 31 g m^{-2} in Nahuelbuta (Table 3.4). $I^{K}_{bio\text{-}av,\ soil}$ behaves differently, and amounts to 53, 38, 90, and 38 g m^{-2} in Pan de Azúcar, Santa Gracia, La Campana, and Nahuelbuta, respectively. Thus, K is almost equally available to plants in all four study sites.

3.5.3 Plant element composition and nutrient-uptake fluxes

Average elemental concentrations in bulk plants generally decrease from Pan de Azúcar towards Nahuelbuta. For example, the Al and Na concentrations in the plants of Pan de Azúcar reach 2700 and 34600 µg g^{-1}, respectively, compared with minima of 70 and 80 µg g^{-1} in Nahuelbuta. However, element specific deviations from this pattern exist (Table 3.5). The most prominent exceptions are those of P and K. Average P concentration increases from 290 µg g^{-1} in Pan de Azúcar to 1400 µg g^{-1} in Nahuelbuta. The average K concentration amounts to 6900, 6400, 12000, and 5400 µg g^{-1} along the north-south gradient. Thus, in Pan de Azúcar, Santa Gracia, and Nahuelbuta, average K concentrations are in a similar range, whereas in La Campana, K concentration in plants is almost 2× higher than in the

Table 3.3: Elemental weathering fluxes ($W^{X}_{regolith}$) and ecosystem uptake fluxes (U^{X}_{total}) in Pan de Azúcar, Santa Gracia, La Campana, and Nahuelbuta along with the respective study site's average denudation rate (D).

Study site	D	Al	Ca*	Fe	K	Mg	Mn	Na	P	Si	Sr
	[t km^{-2} yr^{-1}]	[mg m^{-2} yr^{-1}]									
Pan de Azúcar											
$W^{X}_{regolith}$	9.6	40	13	5	30	9	0.5	33	1.3	160	0.3
SD	0.6	43	9	18	30	5	0.2	13	0.4	210	0.1
U^{X}_{total}	-	40	200	30	110	300	3	500	5	40	1.2
SD	-	20	500	10	40	100	1	200	2	20	0.5
Santa Gracia											
$W^{X}_{regolith}$	19.2	870	1030	280	80	300	6	290	12	2100	6.1
SD	1.2	200	200	270	50	70	3	80	3	680	1.3
U^{X}_{total}	-	140	1300	130	500	300	12	200	70	100	8
SD	-	80	500	70	200	100	5	60	20	30	3
La Campana											
$W^{X}_{regolith}$	61.5	2330	770	670	840	280	14	930	19	9700	8.5
SD	4.0	370	250	350	220	120	6	110	6	1500	1.5
U^{X}_{total}	-	50	1300	40	2000	200	8	14	170	17	6
SD	-	20	600	20	1000	100	4	6	90	10	3
Nahuelbuta											
$W^{X}_{regolith}$	32.6	620	360	360	100	140	1	400	11	2000	4.0
SD	2.1	360	150	210	120	50	3	70	4	1200	0.7
U^{X}_{total}	-	19	2200	12	1400	400	160	22	350	30	19
SD	-	7	700	3	400	100	50	11	100	8	9

* $W^{Ca}_{regolith}$ only includes information from AZPED21 (N-facing slope regolith profile) as atmospheric deposition of Ca in the S-facing slope led to (theoretically) negative weathering fluxes.

Uncertainties on weathering fluxes are estimated by Monte-Carlo simulations, where the SD of the respective profile's denudation rate, the SD of the bedrocks' element concentration of interest, and 3% relative uncertainty on the element concentration in regolith samples have been used.

Uncertainties on nutrient uptake fluxes are estimated by Monte-Carlo simulations, where the SD of the respective study site's NPP and the SD of the chemical composition of the weighted above-ground living ecosystem have been used (Table 3.5)

other sites (Table 3.5). In Pan de Azúcar and Santa Gracia some elemental concentrations in plants are exceptionally high. This elevated mineral-nutrient storage is typical for plants growing in infertile habitats (Chapin III et al. 2011). Accumulation of such an internal nutrient pool allows for plant growth when conditions improve, e.g. during rare rain events (e.g. Chapin III 1980; Chapin III et al. 2011; Vitousek et al. 1998). For example, high amounts of Al and Na are incorporated into plants tissues, though they may hinder plant growth at high concentrations (e.g. Delhaize and Ryan 1995; Kronzucker and Britto 2011). However, Al-toxicity is prevented in these plants by accumulation of correspondingly high amounts of Si that compensates the effects of Al (Liang et al. 2007). The exceptional high Na concentration in *N. mollis* in Pan de Azúcar is typical of the metabolism of *N. mollis* which is known to be covered with salt glands on their leaves, aiding to retrieve water by directly condensing moisture from unsaturated air (Rundel et al. 1980; Mooney et al. 1980).

Table 3.4: Inventories of plant-essential and plant-beneficial elements in bulk regolith and the bio-available fraction in soil and saprolite. Apart from phosphorus, the accessibility of these elements was determined using a sequential extraction method described by Arunachalam et al. (1996); Tessier et al. (1979); He et al. (1995). P-accessibility in the bio-available fraction has been determined by Brucker and Spohn (2019) using a modified Hedley sequential P fractionation method. Supplementary Tables S3.3 & S3.4 include depth-dependent concentration of the bio-available fraction (pooled) and the Milli-Q and NH_4OAc extractions used for calculation of the inventories (Oeser and von Blanckenburg 2020a).

		extent* [m]	Al	Ca	Fe	K	Mg	Mn	Na	P	Si	Sr	Σ
Pan de Azúcar													
$I^X_{bioav;\,soil}$	[g m^{-2}]	0.2	0.3	1440	n.c.	53	92	0.1	493	3.3	19	1.5	2100
$I^X_{bioav;\,sap}$	[g m^{-2}]	1.0	1.7	3830	n.c.	253	243	0.6	681	0.0	75	3.5	5100
I^X_{bulk}	[kg m^{-2}]	1.0	140	21	44	65	8.6	0.5	39	1.3	636	0.2	950
Santa Gracia													
$I^X_{bioav;\,soil}$	[g m^{-2}]	0.4	10	616	7.2	38	221	1.4	18	22	19	4.6	7960
$I^X_{bioav;\,sap}$	[g m^{-2}]	1.0	20	1179	21	23	651	2.9	159	21	53	8.5	2100
I^X_{bulk}	[kg m^{-2}]	1.0	180	130	75	29	42	1.5	61	1.6	532	1.0	1100
La Campana													
$I^X_{bioav;\,soil}$	[g m^{-2}]	0.5	40	673	24	90	79	11	6.7	28	34	4.5	1000
$I^X_{bioav;\,sap}$	[g m^{-2}]	1.0	150	1026	23	70	191	12	31	39	142	8.0	1600
I^X_{bulk}	[kg m^{-2}]	1.0	120	26	49	46	10	0.9	31	0.7	456	0.3	740
Nahuelbuta													
$I^X_{bioav;\,soil}$	[g m^{-2}]	0.9	10	60	1.8	39	9.9	14	17	31	14	0.5	200
$I^X_{bioav;\,sap}$	[g m^{-2}]	1.0	1.5	52	<0.5	19	11	3.9	13	23	12	0.8	140
I^X_{bulk}	[kg m^{-2}]	1.0	90	15	47	22	13	1.0	10	0.7	309	0.1	510

$I^X_{bioav,\,soil}$ = inventory of element X in the soil bio-available fraction, extent amounts to maximum soil depth

$I^X_{bioav,\,sap}$ = inventory of element X in the saprolite bio-available fraction

I^X_{bulk} = inventory of element X in the regolith

* the extent of the saprolite and regolith inventory have been scaled to 1.0 m for purposes of comparisons between the four study sites and the lack of an absolute measure of the depth of saprolite.

n.c. = not calculated as the respective bio-available fraction (Table S3.3) was below the limit of calibration of ICP-OES measurements

The total nutrient-uptake flux (U^X_{total}; Table 3.2, Eq. 3.4 and Appendix A) of P and K increase from north to south, such that U^P_{total} amounts to 5 ± 2, 70 ± 20, 170 ± 90, and 350 ± 100 mg m^{-2} yr^{-1} and U^K_{total} to 110 ± 40, 500 ± 200, 2000 ± 1000, and 1400 ± 400 mg m^{-2} yr^{-1} in Pan de Azúcar, Santa Gracia, La Campana, and Nahuelbuta, respectively (Table 3.3). total nutrient-uptake flux (U^X_{total}) of the plant-essential elements Ca, K, Mg, Mn, P, and Sr exceed $W^X_{regolith}$ up to several times. U^X_{total} and $W^X_{regolith}$ are similar for Mg, Mn, and Sr in La Campana (Fig. 3.4; Table 3.3). U^X_{total} of the remaining plant-beneficial elements are, with the exception of from Fe and Na in Pan de Azúcar, always lower than their release by weathering.

Table 3.5: Chemical composition of the above-ground living plants. Plant organs have been weighted according to Niklas and Enquist (2002), using the plant organs' relative growth rate. Relative growth rates and relative abundance of the different plant species can be found in this table's footnotes. The unweighted chemical composition of each plant organ is listed in Table S3.5.

Study site	Al	Ca	Fe	K	Mg	Mn	Na	P	Si	Sr
					[μg g^{-1}]					
Pan de Azúcar[†]										
mean	2700	15200	1700	6900	20700	210	34600	290	2500	80
SD	300	1500	200	700	2100	20	3500	30	300	10
Santa Gracia[‡]										
mean	1900	17800	1800	6400	4200	160	2800	900	1400	110
SD	900	4400	900	1600	1700	50	500	220	300	20
SE (n=15)	700	2900	600	1100	1000	30	400	140	200	20
La Campana[§]										
mean	340	8900	250	12300	1200	50	100	1200	120	40
SD	120	4100	110	8000	700	20	40	600	70	20
SE (n=16)	70	2300	70	5300	400	20	20	400	40	10
Nahuelbuta[¶]										
mean	70	8500	40	5400	1400	610	80	1300	110	70
SD	20	1400	10	500	200	110	30	200	10	30
SE (n=10)	10	1000	10	300	200	80	20	100	10	20

Standard deviation and standard error relate to the variance within the data set of each ecosystem. Where natural replicates were not available (i.e. in Pan de Azúcar), 10% relative uncertainty has been assumed.

[†] Pan de Azúcar ecosystem composition: 100% *Nolona mollis*; 32% and 68% relative leaf and stem growth, respectively, accounting for 5% leaf and 95% stem standing biomass

[‡] Santa Gracia ecosystem composition: 25% each of *Asterasia sp.*, *Cordia decandra*, *Cumulopuntia sphaerica*, *Proustia cuneifolia*; 32% and 68% relative leaf and stem growth assumed for all species, respectively, accounting for 5% leaf and 95% stem standing biomass

[§] La Campana ecosystem composition: 5% each for *Aristeguieta salvia* and *Colliguaja odorifera* and 45% each for *Cryptocaria alba* and *Lithraea caustica*; 32% and 68% relative leaf and stem growth assumed for all species, respectively, accounting for 5% leaf and 95% stem standing biomass

[¶] Nahuelbuta ecosystem composition: 60% *Araucaria araucana*, 10% *Chusquea culeou*, and 30% *Nothofagus antarctica*; 48% and 52% relative leaf and stem growth assumed for *Araucaria araucana*, respectively, accounting for 16% leaf and 84% stem standing biomass, 32% and 68% relative leaf and stem growth assumed for *Chusquea culeou* and *Nothofagus antarctica*, respectively, accounting for 5% leaf and 95% stem standing biomass

3.5.4 $^{87}Sr/^{86}Sr$ isotope ratios

Radiogenic Sr isotope ratios on bulk bedrock and regolith samples disclose mineral-weathering reactions and the incorporation of external sources into the regolith profiles. Moreover, $^{87}Sr/\ ^{86}Sr$ in the bio-available fraction and plants reveal the plants' mineral nutrient sources.

In Pan de Azúcar, the $^{87}Sr/^{86}Sr$ ratio of average bedrock is 0.726 ± 0.002 (Fig. 3.5, Table 3.6). In regolith, $^{87}Sr/^{86}Sr$ differs significantly between the two profiles (0.728 ± 0.003 and 0.733 ± 0.003 on the north- and south-facing regolith profile, respectively) which can be attributed to varying degrees of atmospheric deposition ($^{87}Sr/^{86}Sr_{seaspray} = 0.7092$; Pearce et al. 2015a). The $^{87}Sr/^{86}Sr$ ratios in the bio-available fraction of saprolite and soil deviate by 0.02 from those of bulk bedrock and regolith but do not vary considerably between saprolite and soil, or between the north- and south-facing slopes. Bulk plant samples yield $^{87}Sr/^{86}Sr$ ratios of 0.710 and are thus indistinguishable from the $^{87}Sr/^{86}Sr$ in the bio-available fraction (0.710 ± 0.001; Fig. 3.5, Table 3.6).

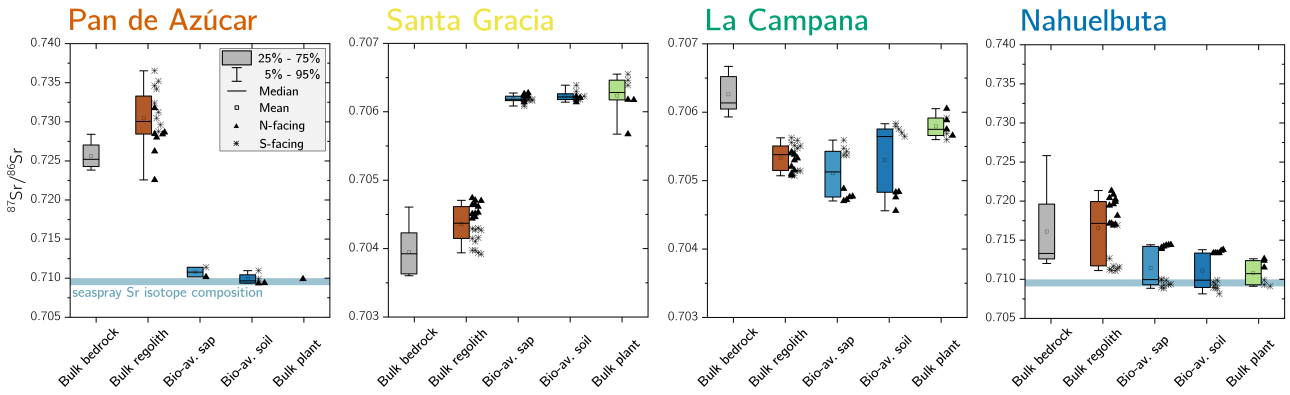

Figure 3.5: Average $^{87}Sr/^{86}Sr$ isotope composition of bedrock, bulk regolith, and the bio-available fraction in saprolite and soil, and plants. The $^{87}Sr/^{86}Sr$ isotope ratios of bulk plant (green) are weighted according to the single species' organs relative growth rate (see Table 3.5 for weighting parameters). Whiskers span 90% of the respective data set. On the boxes' right-hand site, the differences between north- and south-facing regolith profiles are depicted. Note that bulk regolith samples in Nahuelbuta with anomalously low Zr concentrations have been excluded from this analysis as they are suspected to comprise a different parent rock. Blue bar in Pan de Azúcar and Nahuelbuta denote seaspray Sr isotope composition. Y-axis covers broader range in Pan de Azúcar and Nahuelbuta than in Santa Gracia and La Campana.

In Santa Gracia, the $^{87}Sr/^{86}Sr$ ratios in both bedrock and the regolith profiles do not differ significantly ($^{87}Sr/^{86}Sr_{rock} = 0.7039 \pm 0.0004$, $^{87}Sr/^{86}Sr_{regolith} = 0.7043 \pm 0.0003$; Fig. 3.5, Table 3.6). The radiogenic Sr composition of the bio-available fractions in saprolite and soil are identical within uncertainty, and no differences in $^{87}Sr/\ ^{86}Sr$ between the north- and south-facing regolith profile are apparent. Plants yield an average $^{87}Sr/^{86}Sr$ ratio of

0.7062 ± 0.0001 and are thus indistinguishable from the bio-available fractions in saprolite and soil (Fig. 3.5, Table 3.6).

The bulk regolith $^{87}Sr/^{86}Sr$ ratio in La Campana ranges from 0.7051 in the north-facing to 0.7055 in the south-facing regolith profile. These ratios are lower than bedrock (0.7063 ± 0.0003; Fig. 3.5, Table 3.6) which can be attributed to the loss of a mineral with a high $^{87}Sr/^{86}Sr$ isotope ratio (e.g. biotite) beneath the sampled regolith profiles. The radiogenic Sr composition of the bio-available fraction in saprolite and soil amounts to 0.7051 and 0.7053, in the north- and south-facing slopes, respectively, and is within the range of bulk regolith. Here, the difference in the $^{87}Sr/^{86}Sr$ ratio between the north- and the south-facing regolith profile increases from bulk regolith to the bio-available fraction in saprolite and is highest in the soil bio-available fraction. The average $^{87}Sr/^{86}Sr$ ratio in plants is 0.7059 and can be as high as 0.7063 in *Cryptocaria alba* (Table S3.5) and is thus higher than the soil and saprolite bio-available fractions. All these ratios are lower than in bulk bedrock.

Table 3.6: Ecosystem average $^{87}Sr/^{86}$ ratio for bulk bedrock, bulk regolith, and the bio-available fraction in saprolite and soil. $^{87}Sr/^{86}$ in bulk ecosystem are weighted by the plant organs' relative growth rate and relative species abundance in the respective ecosystem (see Table 3.5). Radiogenic Sr composition for each single specimen are reported in Tables S3.2 (bulk regolith samples), S3.3 (bio-available fraction of saprolite and soil), and S3.5 (plant samples), respectively.

	bulk samples		bio-available fraction		bulk living ecosystem†	Seaspray
Study site	$^{87}Sr/^{86}Sr_{rock}$	$^{87}Sr/^{86}Sr_{regolith}$	$^{87}Sr/^{86}Sr_{sap}$	$^{87}Sr/^{86}Sr_{soil}$	$^{87}Sr/^{86}Sr_{plant}$	input‡
Pan de Azúcar	0.7257	0.7305	0.7108	0.7099	0.7099	93%
SD	0.0020	0.0036	0.0009	0.0008		
Santa Gracia	0.7039	0.7044	0.7062	0.7062	0.7062	43%
SD	0.0004	0.0003	0.0001	0.0001	0.0003	
La Campana	0.7063	0.7053	0.7051	0.7053	0.7059	
SD	0.0003	0.0002	0.0004	0.0005	0.0002	
Nahuelbuta	0.7161	0.7162	0.7115	0.7111	0.7111	
SD	0.0065	0.0036	0.0025	0.0023	0.0016	
Seaspray*				0.7092		

* Seaspray composition from Pearce et al. (2015b)

† Standard deviation and standard error corresponds to species-to-species differences in $^{87}Sr/^{86}Sr$

‡ Potential seaspray input into the bio-available fraction derived from a simple two-component mixing equation using bulk bedrock and seaspray as end-members. Substantial seaspray incorporation into the bio-available fraction in La Campana and Nahuelbuta is very unlikely (see text for discussion), therefore not shown.

In Nahuelbuta the radiogenic Sr isotope ratio in bedrock (0.716 ± 0.007) is in good agreement to those reported by Hervé et al. (1976) for the granitoid basement (0.717). However, the large spread among the bedrock samples implies petrological and geochemical heterogeneity of the Nahuelbuta mountain range (e.g. Hervé 1977). Thus, $^{87}Sr/^{86}Sr$ in regolith is also variable (Fig. 3.5, Table 3.6 & S3.2). The $^{87}Sr/^{86}Sr$ ratios in both bio-available fractions in Nahuelbuta are restricted to a relatively narrow range in both regolith profiles, equal to

0.711 ± 0.002 and are thus indistinguishable from the mean ratio in plants (Fig. 3.5, Table 3.6). Individual plants' radiogenic Sr signature are distinct from each other and reflect the slope's bio-available fraction they grow on.

3.6 Discussion

3.6.1 The source of mineral nutrients

Comparing the radiogenic Sr composition of the bio-available fractions in saprolite and soil with that of bulk plant serves as a proxy for the nutrient sources of plants. At all four sites, the $^{87}Sr/^{86}Sr$ ratio in plants is largely indistinguishable within uncertainty to the bio-available fraction they grow on (Table 3.6), and no differences in $^{87}Sr/^{86}Sr$ between leaves, to twig, or stem are apparent (Table S3.5). Neither the plant $^{87}Sr/^{86}Sr$ ratio nor the $^{87}Sr/^{86}Sr$ ratio of the bio-available fraction is identical to that of bedrock or of bulk regolith. We conclude that plants obtain their Sr from the bio-available fraction rather than directly from primary minerals or from the atmosphere through leaves. Only La Campana showed evidence for a deep nutrient source (i.e. somewhere between the bottom of the regolith profile and unweathered rock) in the elemental-depletion pattern (Fig. A3.1). Here, deep-rooting plants (e.g. *Lithraea caustica*; Canadell et al. 1996) bypass the bio-available fraction of saprolite and soil and take up Sr with a higher proportion of radiogenic ^{87}Sr which has been released through biotite weathering beneath the regolith profiles. We can also use the $^{87}Sr/^{86}Sr$ ratio to identify the ultimate source of bio-available Sr. In the southernmost mediterranean and humid-temperate sites of La Campana and Nahuelbuta, the bio-available Sr is supplied by release from rock and regolith through weathering, albeit from specific minerals rather than bulk rock. In arid Pan de Azúcar the Sr pool in the bio-available fraction is formed by deposition from atmospheric sources (up to 93% seaspray contribution; Table 3.6). In semi-arid Santa Gracia, we found a possible combination of both sources (up to 43% seaspray contribution; Table 3.6).

Expanding our analysis of the source of mineral nutrients to include other plant-essential (P, K, Ca, Mg, Mn) and plant-beneficial (Al, Fe, Na, Si) elements, we normalized both the mineral nutrient concentrations in plants (Table 3.5) and those in the bio-available fraction in saprolite and soil (Table S3.3) by the most-demanded mineral nutrient P (Fig. 3.6). This removes differences in concentrations induced by the very different matrices of regolith and plant. In this analysis, an element X that plots on the 1:1 line would have the same X:P ratio in plants and in the bio-available fraction. In turn, any deviation from that line would indicate positive or negative discrimination of an element contained in the regolith bio-available fraction by plants relative to P. We find a good correlation in the X:P ratios for all elements, and the ratios found in plants reflect those in the bio-available regolith fraction to within one order of magnitude. We interpret this correlation to confirm nutrient uptake mainly from the bio-available fraction. We also note that the X:P ratios increasingly approach the 1:1 line with

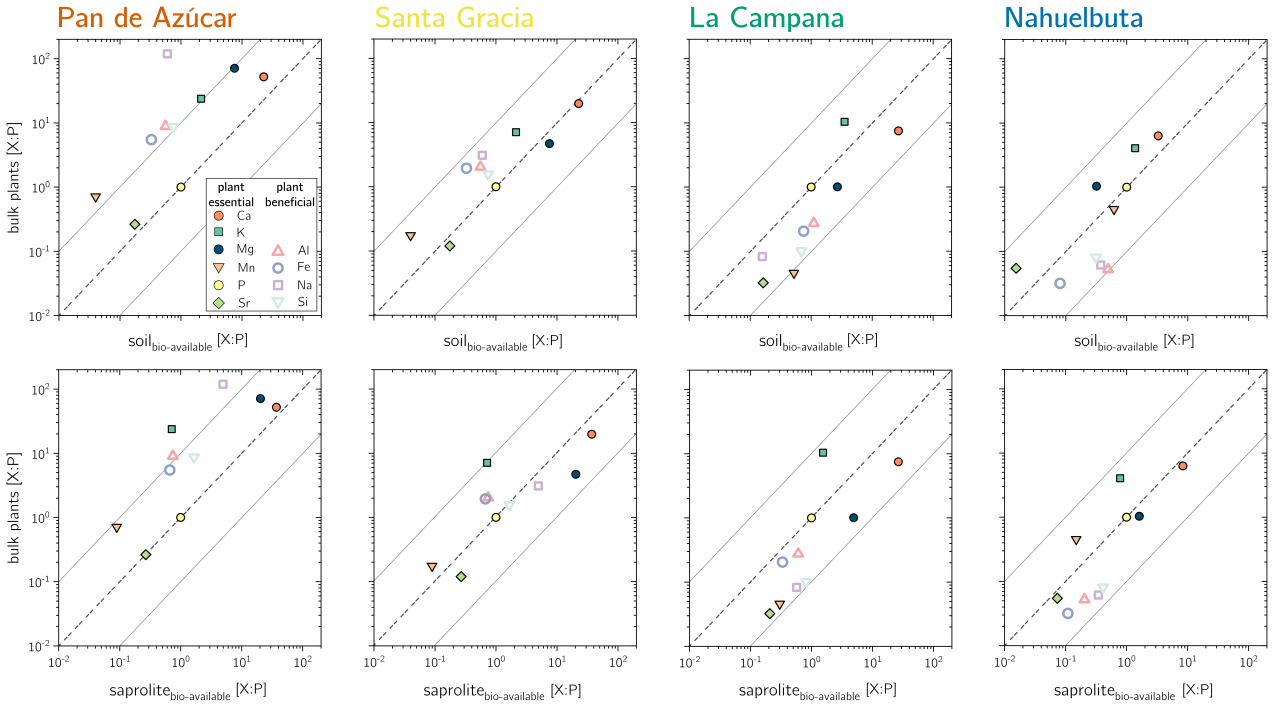

Figure 3.6: P-normalized element composition for bulk plants and the bio-available fraction in soil and saprolite. Solid gray lines reflect the 10-fold P and 0.1-fold P concentration, respectively. Note that with increasing recycling from Santa Gracia to Nahuelbuta, the bio-available fractions' X:P successively approaches X:P in vegetation.

increasing NPP from Pan de Azúcar to Nahuelbuta and the agreement is more pronounced in soil than in saprolite. We interpret these shifts to denote the increasing significance of recycling, a topic we return to in the next section.

3.6.2 An increase in nutrient recycling with NPP

In Section 3.5.1 we established that neither total weathering rate W, nor elemental weathering rates $W^X_{regolith}$, correlate with NPP. Only at La Campana weathering rates are elevated, as expected from the higher denudation rate. Santa Gracia and Nahuelbuta, have similar denudation rates and element release rates by weathering $W^X_{regolith}$, yet elemental uptake rates U^X_{total} of the plant-essential nutrients P, K, and Ca increase between a factor of two and five (Fig. 3.4). We examine these correlations in more detail in Section 3.6.5 Here we first focus on the question: How is nutrient demand satisfied at the more vegetated sites?

Recycling of mineral nutrients is the key mechanism enabling differences in NPP. We quantified recycling by the nutrient recycling factor Rec^X (Table 3.2, Eq. 3.7 and Appendix A; Table 3.7; note that in this discussion we use Rec^X calculated for $W^X_{regolith}$ from rock weathering, whereas in Table 3.7 and Fig. A3.4 we also show Rec^X including atmospheric inputs in Pan de Azúcar). The amplitude of recycling varies from nutrient to nutrient and site to site. In the arid Pan de Azúcar, nutrients are primarily recycled via photodegradation of shrubs (e.g. Gallo et al. 2006; Day et al. 2015). In the remaining sites Rec^X increases from Santa

Table 3.7: Nutrient recycling factors in Pan de Azúcar, Santa Gracia, La Campana, and Nahuelbuta. Rec^X for Ca, K, Mg, Na, and Sr in Pan de Azúcar has been corrected for atmospheric deposition of seaspray.

Study site	Rec^{Al}	Rec^{Ca}	Rec^{Fe}	Rec^{K}	Rec^{Mg}	Rec^{Mn}	Rec^{Na}	Rec^{P}	Rec^{Si}	Rec^{Sr}
Pan de Azúcar	1.1	1*	5.8	3*	30*	6	14*	4	0.26	3*
SD	0.4	2	0.6	1	23	6	15	4	0.08	5
Santa Gracia	0.1	1	0.4	6	1	1	1	5	0.04	1
SD	0.5	4	0.5	3	3	3	1	13	0.07	3
La Campana	0.0	2	0.1	2	1	1	0.0	9	0.00	1
SD	0.1	2	0.0	5	1	1	0.1	15	0.01	2
Nahuelbuta	0.0	6	0.0	15	3	190†	0.1	30	0.01	5
SD	0.0	4	0.0	3	2	70	0.2	20	0.01	10

* Recycling factors corrected for the influence of atmospheric seaspray deposition, resulting in a net increase in available mineral nutrients, hence lowering Rec^X. Ultimately the re-utilization of weathering-derived nutrients is decreased by 95, 22, 18, 12, and 10% for Ca, K, Mg, Na, and Sr, respectively (see supplementary information).

† values not being considered in the discussion as $W^{Mn}_{regolith}$ is potentially biased by high bedrock heterogeneities

Gracia to Nahuelbuta and is highest for the plant-essential elements Ca (increasing from 1 to 6), K (increasing from 6 to 15), and P (increasing from 5 to 30; Table 3.7). Thus, despite having the smallest nutrient inventory of bio-available nutrients (Table 3.4) but the highest NPP, Nahuelbuta can at least partially satisfy its nutrient requirements through efficient nutrient recycling. In contrast, in the (semi-) arid sites, where the bio-available pool is larger, plants forage nutrients by deep rooting from depth (McCulley et al. 2004).

The Rec^X metric reflects a mass balance between the total weathering zone and the total vegetation cover but does not yield insight to the mechanisms of recycling. The elemental stochiometric considerations presented above show that recycling is indeed fed from plant material accumulated in soil (Lang et al. 2017). With increasing recycling the nutrient pools in the soil bio-available fraction are increasingly dominated by the pool of recycled nutrients, thus shifting the X:P ratio in the bio-available fraction successively towards the X:P ratio in vegetation (Fig. 3.6). In other words, over the course of several recycling loops, the chemical composition of the bio-available fraction and biota eventually approaches a ratio close to the relative requirement of the ecosystem for the different nutrients (Vitousek et al. 1998).

3.6.3 Processes that set the size of the bio-available pool

In none of our sites is the bio-available nutrient pool entirely depleted (Table 3.4), but its elemental concentrations strongly shift along the gradient. The concentrations of the plant-essential mineral nutrients K, Ca, and Mg in saprolite are highest in the arid site, lower in the semi-arid and mediterranean site, and lowest in the humid-temperate site. The element concentration in the bio-available fraction translates into the size of the inventory, quantifying the pool size (note, however, that the true inventory can in fact be larger than the 1 m inventory that we have used for its calculation. This is suggested by the elevated

$^{87}Sr/^{86}Sr$ ratios in plants at La Campana suggesting extraction of a pool beneath the bio-available upper saprolite). The bio-available pool represents the link between the organic and the geogenic pathway. That is because weathering in the geogenic pathway supplies elements that plants take up and recycle in the organic pathway (Uhlig and von Blanckenburg 2019). We thus briefly review the potential processes that may set the pool size.

If a bio-available pool is in conceptual steady state, input fluxes and loss fluxes balance. Over millennial time scales or longer, we consider that such a balance must exist, as otherwise a pool might become depleted. In this case the inventory of the pool is set by the input fluxes of an element and a first-order rate constant that describes the relationship between the loss flux as a function of element inventory and thus the retention capacity. Essentially it is the inverse of the turnover time of an element. Biotic processes likely contribute towards setting this retention capacity directly or indirectly, a topic we return to below. Given that elemental weathering fluxes $W^{X}_{regolith}$ do not correlate with pool size we assume that retention capacity sets the pool size.

A first potential control over element retention capacity are pedogenic properties. The decrease of soil pH from 8 at the arid site to 4 at humid-temperate site (Bernhard et al. 2018) might cause the decrease in the bio-available divalent base cations Mg, Ca, and Sr. Conversely, the decrease in pH could be the result of the loss of these elements and thus their pH buffering capacity. Another possibility is the degree of complexing of elements to organic molecules. Such complexing might lead to either higher retention, or higher loss, depending on the element. Organic complexing is likely more pronounced in the mediterranean and humid-temperate sites where soil organic carbon concentrations are higher compared to the (semi-) arid sites (Bernhard et al. 2018). However, elements like Al and P, which are readily complexed, are available in higher concentration in the humid-temperate and mediterranean sites than in the other two sites. Differences in water flow is the third cause we discuss. Where fluid residence times are long, concentrations of solutes are more likely to be at equilibrium with secondary minerals (Maher and Chamberlain 2014) and the bio-available fraction, formed by precipitation and sorption from pore fluids, can build up. We consider this to be the case in the low-precipitation sites. At sites with high MAP regolith fluids may be diluted, and thus desorb elements from the bio-available pool. Such a dilution effect might be in effect at Nahuelbuta for elements like Mg and Ca. At Nahuelbuta these are also the elements with the lowest bio-available inventory. We thus consider water flow to be the main factor governing the size of the bio-available pool.

3.6.4 Concepts for biotas role in setting fluxes in the geogenic and the organic nutrient cycle

Even if negligible on ecological timescales, ecosystems experience losses of nutrients through erosion (e.g. Heartsill Scalley et al. 2012) and as solutes (e.g. Chaudhuri et al. 2007). To prevent bio-available nutrients becoming depleted over longer timescales, the pool must be replenished (Uhlig and von Blanckenburg 2019). Biological mechanisms comprise two means to regulate this delicate balance between nutrient replenishment by weathering and plant uptake. The first is by adjusting the recycling of nutrients, as shown in Section 3.6.2. At Nahuelbuta, where the bio-available pool is smallest, nutrient recycling rates are the highest. If the bio-available pool is small, plants may invest energy into re-using P and other elements from leaf litter, rather than foraging P at depth which is associated with higher energy expenditure (Andrino et al. 2019). This is a component of the organic nutrient cycle. The biochemical mechanisms of nutrient-recycling are beyond the scope of this paper, but are thought to be related to leaf litter quality (Hattenschwiler et al. 2011), soil fungal and bacterial communities (Fabian et al. 2017; Lambers et al. 2008), and plant diversity (Lambers et al. 2011; Oelmann et al. 2011; van der Heijden et al. 1998).

Table 3.8: Turnover times for the soil and saprolite bio-available fraction with respect to the release by weathering and turnover times for bio-available fraction in soil with respect to uptake into the ecosystem.

	Al	Ca	Fe	K	Mg	Mn	Na	P	Si	Sr
						[yr]				
Pan de Azúcar										
$T^X_{bioav.\ soil,\ U}$	10	6000	n.d.	490	280	40	910	710	480	1200
$T^X_{bioav.\ soil,\ W}$	10	n.d.	n.d.	1600	10300	280	14800	2600	120	4700
$T^X_{bioav.\ sap,\ W}$	40	n.d.	n.d.	7600	27400	1240	20400	n.d.	490	10900
Santa Gracia										
$T^X_{bioav.\ soil,\ U}$	90	480	50	80	710	120	90	330	180	590
$T^X_{bioav.\ soil,\ W}$	10	600	30	510	730	230	60	1850	10	760
$T^X_{bioav.\ sap,\ W}$	30	1100	100	300	2200	500	500	1800	30	1400
La Campana										
$T^X_{bioav.\ soil,\ U}$	780	530	660	50	460	1420	480	160	1970	820
$T^X_{bioav.\ soil,\ W}$	20	870	40	110	290	770	10	1470	0	530
$T^X_{bioav.\ sap,\ W}$	20	1300	30	100	700	800	30	2000	10	1000
Nahuelbuta										
$T^X_{bioav.\ soil,\ U}$	760	30	160	30	30	90	790	90	490	20
$T^X_{bioav.\ soil,\ W}$	20	170	10	400	70	17440	40	2900	10	120
$T^X_{bioav.\ sap,\ W}$	0	100	0	200	100	5000	30	2100	10	200

$T^X_{bioav\ soil,\ U}$ = turnover time of element X in the soil bio-available fraction with respect to uptake into the ecosystem

$T^X_{bioav\ soil,\ W}$ = turnover time of element X in the soil bio-available fraction with respect to supply from dissolution of primary minerals and secondary precipitates

$T^X_{bioav\ sap,\ W}$ = turnover time of element X in the saprolite bio-available fraction with respect to supply from dissolution of primary minerals and secondary precipitates

n.d. = not determined; not determined turnover times because the respective inventory (Table 3.4) could not be determined

The second means for biota to influence the bio-available pool is via the geogenic pathway. Nutrient replenishment may take place either by exogenous inputs (e.g. Boy and Wilcke 2008; Porder et al. 2007; Vitousek 2004; Vitousek et al. 2010), or by weathering of primary minerals at depth (Uhlig et al. 2017; Uhlig and von Blanckenburg 2019). In arid Pan de Azúcar, where weathering-release fluxes are low, these pools are being replenished by the deposition of atmospheric sources (up to 93%; Table 3.6). In the other study sites the bio-available pools are replenished by weathering of rock and regolith. The timescales $T^{X}_{bio\text{-}av,W}$ (Table 3.2, Eq. 3.9 and Appendix A) of replenishment from weathering are long, and typically orders of magnitude longer than their turnover times with respect to plant uptake $T^{X}_{bio\text{-}av,U}$. For example, the inventory of K in the bio-available soil pool at Nahuelbuta is turned over every 30 years between soil and plants, but it takes 400 years to be replenished in its entirety by weathering (Table 3.8). Previous models in ecosystem science (e.g. Bormann et al. 1969; Vitousek and Reiners 1975; Vitousek et al. 1998) suggest that increasing nutrient demand will eventually lead to tightly coupled recycling loops such that nutrient losses will be minimized, and plant nutrition is sustained. Our data is also consistent with a relationship between demand (i.e. NPP) and recycling efficiency.

If recycling indeed exerts the dominant role in the supply of mineral nutrients, then we need to revisit the significance of biogenic weathering towards the nutrition of plants. The direct and indirect impacts of plants and their associated microbiota on weathering is well-documented and can be categorized into four suites of processes:

(A) Direct primary mineral dissolution by ectomycorrhizal fungi. Ectomycorrhizal fungi can directly extract nutrients such as P, K, Ca, Mg, and Fe from minerals distant from the root, even under dry conditions, and thereby actively increase mineral dissolution kinetics. Laboratory dissolution experiments (Balogh-Brunstad et al. 2008b; Gerrits et al. 2020; Kalinowski et al. 2000), plant growth mesocosms (Bonneville et al. 2011; Smits et al. 2012), and deployment of minerals within the soil of natural ecosystems (Balogh-Brunstad et al. 2008a) all show either evidence for mineral dissolution by mycorrhiza, or quantify an increase in mineral dissolution over abiotic controls. Whether these short-term experiments can be extrapolated to the millennial time scales of the geogenic nutrient pathway is not obvious (review by Finlay et al. 2020). Over these time scales, mineral dissolution is often slowed by the development of nanoscale layers at the interface (Gerrits et al. 2020) or coatings by secondary precipitates (Oelkers et al. 2015). Slowing of mineral dissolution with time, known from weathering zone studies, has also been attributed to coating by secondary precipitates (White and Brantley 2003), or to chemical saturation of pore fluids (Maher 2010).

(B) Roots deepening regolith thickness. Tree roots can physically penetrate and biogeochemically alter the immobile regolith underlying mobile soil (Brantley et al. 2017). They can take water up from depth, recycle water to depth for storage, or provide pathways in which water bypasses rather than infiltrating the shallow regolith (Fan et al. 2017). Deep roots aid nutrient transfer from the subsoil to shallow levels (Jobbágy and Jackson 2004).

(C) Canopy and roots converting precipitation into evapotranspiration (Drever and Zobrist 1992). In sites with higher vegetation cover, water vapor is recycled and does not immediately enter runoff. By providing canopy, trees both modulate infiltration while turning water back into transpiration (Ibarra et al. 2019). For example Ibarra et al. (2019) have shown that total runoff can decrease by up to 23% as vegetation cover increases from barely vegetated to highly vegetated sites. Water recycling hence decreases total runoff and potentially reduces weathering-release fluxes in the highly vegetated sites.

(D) Increasing mineral solubility by release of soil CO_2 and organic complexing agents. Through the respiratory release of soil CO_2 and excretion of organic complexing agents, plants, hyphae, and their associated microbiota can increase the solubility limits of primary and secondary minerals by a factor of up to < 10 (Perez-Fodich and Derry 2019; Winnick and Maher 2018) . If dissolution is not kinetically limited, we would indeed expect higher solute concentrations with higher soil CO_2, and hence higher dissolution rates of primary minerals (Winnick and Maher 2018).

Studies of biogenic weathering in natural Critical Zone systems struggle to disentangle expressions of these biogenic drivers of weathering rates from various competing drivers of weathering. Although the sites were selected to minimize potential confounding effects, this study also faces this challenge. We turn to a statistical approach in isolating any potential biogenic weathering signal.

3.6.5 Is weathering modulated by biota? A statistical analysis

To single out the possible biogenic weathering driver from the confounding factors at the EarthShape sites we used correlational statistics between indicators of weathering and metrics for its potential drivers along the EarthShape gradient. We determined Pearson correlation coefficients to determine how the degree of weathering (CDF, τ^X) and the flux of weathering (W, $W^X_{regolith}$) depend on denudation rate denudation rate (D), water availability (approximated by mean annual precipitation, MAP), and biomass growth as quantified by net primary productivity (NPP). See Appendix B for a detailed description on statistical analysis and Table A3.1, A3.2, and A3.3 for the results. We used these statistics to evaluate three starting hypotheses that reflect the basic confounding factors: (1) Where denudation rate D is high bulk weathering fluxes are high, since minerals with fast dissolution kinetics, such as plagioclase and P-bearing apatite, are supply limited (Dixon et al. 2012; Porder et al. 2007). Where D is high, regolith residence times are low such that τ^X for elements not mostly contained in rapidly dissolving minerals are not depleted. (2) At sites at which MAP

and hence runoff is high, weathering fluxes are high. This is because weathering rate is proportional to runoff for the chemostatic elements that comprise the bulk of the weathering flux, amongst them Si that contributes roughly half of the flux (e.g. Godsey et al. 2019; Maher and Chamberlain 2014). As a result, CDF and τ^X will also be high. τ^X of soluble elements (e.g. Na) will be higher at higher runoff than τ^X of elements that strongly partition into secondary phases. (3) If NPP is high the degree (CDF, τ^X) and rate of weathering (W, $W^X_{regolith}$) will be high (e.g. Berner et al. 2003; Brantley et al. 2011b; Buss et al. 2005; Kelly et al. 1998; Porder 2019; Schwartzman 2015), for the reasons predicted in Section 3.6.4.

In support of hypothesis (1) we find that total and elemental weathering rates correlate well with D (the average of the correlation coefficients is $r(10) \sim .88$, $p < .01$; Table A3.1) and only a weak correlation relates denudation rate with the degree of weathering and elemental depletion. Thus, denudation rate is the predominant driver of weathering rate. However, D itself is also correlated with MAP and NPP. To evaluate whether D is nevertheless the main driver we exclude the La Campana site of unusually high D. The correlations between W, $W^X_{regolith}$, and D are still significant (the average of the correlation coefficients is $r(7) \sim .72$, $p < .05$; Table A3.2) confirming that D is the main driver of weathering rate. Concerning hypothesis (2), neither the degree nor rates of weathering correlate with MAP. Only the soluble element Na becomes more depleted (τ^{Na}: $r(7) = .73$, $p < .05$; Table A3.2) at higher MAP. Thus, a competing effect seem to counteract the expected increase in weathering rate with precipitation. As NPP is an output of the LPJ-GUESS model for which MAP is the basis, it is no surprise that both parameters are strongly correlated ($r(7-10) \sim 1.00$, $p < .01$; Table A3.1 & A3.2). We would thus expect the same strong relationship between the degree and rates of weathering and NPP as with MAP. This is indeed the case. However, weathering release rates $W^X_{regolith}$ for elements like Na, P, and Si correlate slightly more strongly with NPP (the average of the correlation coefficients is $r(7) \sim .62$, $p < .05$; Table A3.2) than with MAP (the average of the correlation coefficients is $r(7) \sim .51$, $p > .05$; Table A3.2). This is the only indication that biomass growth exerts any control over weathering at all. In summary, neither MAP nor NPP seem to have a major impact on the degree and rates of weathering, and D is the main driver of total and elemental weathering rate at the EarthShape sites.

In this analysis we have not evaluated the potential confounding effects of differences in bedrock mineral composition. Because of the lack of an unequivocal metric allowing a statistical evaluation of the resulting differences in rock weatherability we focus on a comparison between the two study sites in semi-arid (Santa Gracia) and humid-temperate climate (Nahuelbuta). At these two sites, denudation rates ($15-48\,t\,km^{-2}\,yr^{-1}$) and soil residence times (22 – 28 kyr; Schaller et al. 2018b) are similar. Although both granitoid, bedrock between the two sites differs. Santa Gracia is underlain by diorite, a mafic rock, while Nahuelbuta is underlain by granodiorite (Oeser et al. 2018a). Thus, the suite of primary minerals in Santa Gracia is more prone to weathering than in Nahuelbuta. Specifically,

this means a higher amount of plagioclase and amphibole, and less unreactive quartz, at Santa Gracia. These differences in predominantly Ca- and Mg-bearing minerals are reflected in higher Ca and Mg inventories in bulk regolith in Santa Gracia (Table 3.4), that also translate into higher Ca and Mg weathering fluxes (Table 3.3). Total soil weathering rates ($5-10\,t\,km^{-2}\,yr^{-1}$; Table 3.1), and differences in weathering properties are not statistically significant (Table A3.3). The weathering-release fluxes (Fig. 3.4, Table 3.3) for K, Na, P, and Si are similar despite massive differences in vegetation cover, NPP, and even MAP (Table 3.1 & A3.3). These similarities, and the higher weathering fluxes of Ca and Mg at Santa Gracia can be explained with the confounding effects of higher rock weatherability at Santa Gracia and the higher precipitation at Nahuelbuta. A comparison of concentration-discharge relationships between catchments underlain by mafic (basaltic) and granitoid rock (Ibarra et al. 2016) shows higher solute concentrations for all major elements in the basaltic catchments at a given runoff, and the preservation of chemostatic solute concentrations to higher runoff than in granitoid catchments. As a result, weathering fluxes in mafic catchments at low runoff are similar to fluxes from granitoid rock subjected to high runoff, as we observe at Santa Gracia and Nahuelbuta. Regardless, an increase in either weathering rate or degree of weathering at Nahuelbuta resulting from the 3.5 times higher NPP at Nahuelbuta is not discernible.

3.6.6 Do negative feedbacks decouple biomass growth from weathering rate and degree?

Why do neither the degree nor the rate of weathering increase with NPP or MAP, nor does higher biomass growth overwhelm differences in rock mineralogy? Nutrient recycling may be the mechanism that decouples weathering from NPP, as shown in Section 3.6.2. Even so, the higher runoff results in a greater loss of nutrients from the bio-available pool and thus requires higher weathering rate to balance the loss. We thus speculate that the increased vegetation cover might even counteract a potential increase in weathering that would be caused by the increase in MAP, essentially damping the geogenic pathway. We return to the four suites of processes as outlined in Section 3.6.4 on the direct and indirect impacts of plants and their associated microbiota on weathering and discuss their potential operation at the EarthShape sites.

(A) Direct primary mineral dissolution by ectomycorrhizal fungi. As yet we have no direct observations on nutrient foraging by fungi and other microbes in regolith from the EarthShape sites as obtained on other mountain sites in Chile (Godoy and Mayr 1989). Proxies for total microbial biomass in saprolite do not increase along the gradient: total gene copy numbers have similar ranges from Santa Gracia to Nahuelbuta, and DNA amounts even decrease slightly (Oeser et al. 2018a). Common strategies of microbial symbionts with tree roots suggest that energy investment into nutrient recycling from leaf litter is more advantageous than dissolving primary minerals (Andrino et al. 2019). Thus, we would expect

that mycorrhiza predominantly aid recycling in Nahuelbuta. In Santa Gracia, however, the absence of a litter layer may prompt the subsurface fungal network to invest in primary mineral dissolution, adding microbial weathering to total weathering at that that site.

(B) Roots deepening regolith thickness. A detailed survey of rooting depth along the gradient has not been completed, but deep roots were not observed in Santa Gracia whereas in Nahuelbuta and La Campana, individual roots reach several meters into the saprolite. A and B horizons in Santa Gracia are shallow (20 – 40 cm), whereas they are deep in Nahuelbuta (80 – 100 cm; Bernhard et al. 2018; Oeser et al. 2018a). We do not know the depth of the weathering front which appears to be at least a dozen of meters depth or more at both sites. Thus, deep rooting can benefit plant growth by increasing the size of the bio-available pool.

(C) Canopy and roots converting precipitation into evapotranspiration. Along the EarthShape transect the potential 23% reduction in runoff predicted by Ibarra et al. (2019) is minor considering the 100-fold increase in precipitation over the entire gradient. A larger effect may occur if roots provide preferential flow paths such that infiltrating water bypasses the regolith matrix available for weathering (Brantley et al. 2017). However, given the deep weathering fronts - likely beneath rooting depth - we consider this effect to be minor, or even acting to increase deep weathering. Thus, we consider the hydrological impact of plants on weathering to be minor along the gradient.

(D) Increasing solubility by release of soil CO_2 and organic complexing agents. Although with increasing NPP soil respiration of CO_2 should lead to increased primary mineral dissolution, plants potentially impose a negative feedback onto this dependence by influencing the silicon cycle. Because silicon is the most abundant element in felsic rock and regolith (besides oxygen), it exerts a major control on the total weathering fluxes. The Si concentration in the bio-available pool is key in setting the saturation with respect to the various dissolving and precipitating minerals in regolith. Plants can impact this pool in both directions. Some plant species accumulate Si by active transporter-mediated uptake or through passive uptake within the transpiration stream, whole others exclude Si and avoid accumulation (Ma and Yamaji 2008; Schaller et al. 2018a). Enhanced Si uptake from soil solution by Si accumulating plants would result in Si undersaturation of solutions with respect to secondary minerals and would thus result in an increase in weathering rates. However, this increase may be damped. That is because these plants would also convert silicon into biosilica (e.g. phytoliths). If returned to soil in plant debris this biosilica becomes a key factor in the stability of secondary minerals (e.g. kaolinite; Lucas 2001). However, neither factor seems to be the case: In the EarthShape sites, the average Si concentration in the above-ground living ecosystems ranges from 110 µg g^{-1} in Nahuelbuta to 2500 µg g^{-1} in Pan de Azúcar (Table 3.5). Thus, the Si weathering flux $W^{Si}_{regolith}$ exceeds the Si uptake flux U^{Si}_{total} throughout (Table 3.3) and uptake from soil solution by plants equates to only 5%, 0.2%, and 2% of the Si release flux in Santa Gracia, La Campana, and Nahuelbuta, respectively. Only in Pan de Azúcar, relative uptake of Si is higher (25%).The ecosystems at

our sites can thus be regarded to be below the threshold considered for Si accumulators (Schaller et al. 2018a). We can therefore exclude plant Si uptake and recycling of Si as a factor that increases weathering rates substantially. Rather, if plants in these ecosystems are discriminating against Si uptake whilst taking up water, the residual pore waters will get oversaturated with respect to secondary minerals. In this regard a key observation is provided by the analysis of pedogenic oxides (i.e. dithionite-extractable Al, Si extracted by oxalate, dithionite, and pyrophosphate; Oeser et al. 2018a) and cation exchange capacity (Bernhard et al. 2018). These analyses suggest high amounts of amorphous precipitates and secondary minerals in the regolith of Nahuelbuta. We thus argue that Si is effectively captured in these barely soluble secondary minerals after initial dissolution from rock and regolith. In turn, $W^{Si}_{regolith}$ in Nahuelbuta is subdued despite elevated solubility of primary minerals due to increased CO_2 respiration by roots.

Ecosystems thus exert substantial control over weathering by both directly and indirectly modulating processes. These processes can either enhance or reduce weathering fluxes and result, in combination with effective recycling loops of plant-litter material, in well-balanced nutrient cycles. From our field data, we did not find evidence for coupling of silicate weathering fluxes with the nutrient demands of biota to an extent that exceeds other controlling factors of weathering. Our data suggests that the combination of recycling and negative feedbacks on weathering by secondary mineral formation within the regolith decrease weathering rates in areas of high vegetation cover and net primary productivity from what they would be in the absence of high biomass density.

3.7 Conclusions

While the EarthShape study sites define a north-south gradient in precipitation and biomass production, no such gradient is apparent for weathering rates and weathering intensity between the study sites situated in semi-arid, mediterranean, and humid-temperate climate.

At all four sites we locate the primary mineral nutrient source to plants in the bio-available fraction. This pool of mineral nutrients is initially fed by geogenic sources, which comprise the weathering of primary minerals. It is further fed from organic sources, which comprise the weathering of primary minerals and organic sources, which involves recycling of nutrients from leaf litter. The size of the bio-available nutrient pool decreases from north to south and while pedogenic properties (e.g. pH) likely contribute to set its size, we attribute its decrease mainly to an increase in the below-ground water flow. To fulfill their nutrient demand at increasing NPP but decreasing pool size, ecosystems increase nutrient recycling rather than enhancing biogenic weathering. We consequently find that the organic nutrient cycle intensifies, whereas the geogenic nutrient pathway is steady despite increasing MAP and NPP.

In fact, the presence of plants might even counteract a potential weathering increase along the gradient by inducing secondary mineral formation rather than nutrient-acquisition through weathering. Due to nutrient buffering by recycling and a potential biological dampening of weathering, any additional contribution to weathering by NPP is unresolvable in our data and is certainly smaller than abiotic controls like denudation, rainfall, or bedrock mineralogy. The global silicate-weathering cycle may thus not be as sensitive to plant growth as commonly thought and cannot be simulated in a straightforward manner in weathering models. This non-linear behavior is of relevance for models of the global weathering and the linked carbon cycle, of which accelerated weathering by land plants since the Ordovician is a common component.

3.8 Appendices

Appendix A: Calculation of fluxes and inventories in terrestrial ecosystems

Weathering indices (CDF & τ)

Zr, Ti, and Nb are commonly used to estimate mass losses to the dissolved form during weathering (Eqs. 3.5 & 3.6) as they are presumed to be the least mobile elements during weathering (Chadwick et al. 1990; White et al. 1998). The suitability of these elements for the EarthShape study sites has been evaluated and thoroughly discussed on a site to site basis in Oeser et al. (2018a). Based on possible Ti-mobility in some samples and the fact that Zr is used as a reference element in the majority of weathering and soil production studies worldwide (e.g. Fisher et al. 2017; Green et al. 2006; Hewawasam et al. 2013; Riebe and Granger 2013; Riebe et al. 2001; Schuessler et al. 2018; Uhlig et al. 2017), Zr was taken as immobile reference element in this study.

The calculations of these weathering indices rely on a good approximation of the chemical composition of the initial bedrock from which regolith formed. To this end, any regolith sample with a Zr concentration that was lower than the mean of unweathered bedrock by more than one standard deviation (1SD) was excluded from further consideration. Because a lower Zr concentration cannot be due to weathering, such regolith samples likely originate from chemically distinct bedrock or small-scale bedrock heterogeneities (e.g. a pegmatitic vein). Saprolite samples were also excluded from our data set if Cr and Ti concentrations were twice those of unweathered bedrock (+ 1SD). Elevated concentrations of these elements imply the presence of mafic precursor rock such as commonly present in bedrocks' mafic enclaves. All such excluded samples are marked in gray color in Figs. 3.3 & A3.1, and mainly affect only the lower section of the south-facing Nahuelbuta profile.

The concentration of K throughout the entire regolith profiles in Santa Gracia is three-fold higher than K contained in local bedrock samples (Oeser et al. 2018a). We thus assume that

the K concentration in the bedrock samples of Santa Gracia as determined by Oeser et al. (2018a) underestimates the actual occurring K concentration of local bedrock. Thus, τ^{K} has been calculated using published values for K and Zr concentration from a study nearby (Miralles González 2013).

Weathering fluxes

To estimate elemental release fluxes from regolith (Eq. 3.3) for each study site, the most negative τ-values from the shallowest mineral-soil sample of each regolith profile were used (red-circled symbols in Fig. A3.1). This practice is common in eroding regolith, where the loss indicators τ and CDF represent the integrated mass loss over the time and depth interval that a given sample moved from bedrock reference level to its present position (Brantley and Lebedeva 2011; Ferrier et al. 2010; Hewawasam et al. 2013; Uhlig and von Blanckenburg 2019). The elemental chemical weathering flux ($W^{X}_{regolith}$) at each study site has been averaged. Because not all of this flux might not be within reach of plant roots (e.g. if a fraction is lost into deep groundwater), this is an upper estimate of the nutrient supply from rock into vegetation results. $W^{X}_{regolith}$ is reported in Table 3.3.

Ecosystem nutrient uptake fluxes

Total ecosystem nutrient uptake fluxes (U^{X}_{total}) have been evaluated using Eq. 3.4 and are reported in Table 3.3. Because we compare these to the weathering fluxes that integrate over several millennia, we estimate uptake fluxes that are representative for the Holocene. Net primary productivity (NPP), has been derived from a dynamic vegetation model (LPJ-GUESS) simulating vegetation cover and composition during the Holocene (Werner et al. 2018) and is reported in Table 3.1. Biomass production was estimated from NPP(C) by assuming that dry biomass consists of 50 wt% carbon. To obtain the element-specific uptake rate U^{X}_{total}, NPP is multiplied with the bulk concentration of X in the plants $[X]_{Plant}$.

The sampling and analyses of roots was not done in this study, because of the difficulties in obtaining entire roots or representative root segments from a specific tree or shrub including fine roots. For elemental analysis this difficulty is compounded by the need to remove any remaining soil particles or attached precipitates that might bias measured concentrations. To nevertheless estimate bulk plant elemental composition, we applied the dimensionless organ growth quotients GL/GS (leaf growth relative to stem growth) and GL/GR (leaf growth relative to root growth) in accordance with Niklas and Enquist (2002). This estimation invokes several assumptions: (1) Roots biomass growth contributes little to total plant growth, namely 9% in angiosperms and 17% in gymnosperms (Niklas and Enquist 2002). We thus treat roots and stem/ twig as one plant compartment. In total, the pooled growth of root, stem, and twig amounts to 68% and 52% of relative growth in angiosperms and gymnosperms, respectively. (2) Differences in biomass allocation are relevant only between angiosperms and gymnosperms and not between single plant species of a given class. (3) The pattern of

relative growth and standing biomass allocation holds true across a minimum of eight orders of magnitude of species size (Niklas and Enquist 2002). We thus adapted the organ growth quotients from the work of Niklas and Enquist (2002), such that we only differentiate between the growth rate of leaves and stem, respectively, and the adapt these quotients between angiosperms and gymnosperms. The bulk elemental ecosystem composition (Table 3.5) has been determined by weighting the averaged elemental composition for each sampled plant for their relative abundance in the respective ecosystem.

Inventories

The inventories for the bio-available fraction (I^X_{bioav}) and in bulk regolith (I^X_{bulk}) have been calculated using Eq. 3.8 and are reported in Table 3.4. I^X_{bioav} was determined for both the bio-available fraction in soil (comprised of the A and B horizon; $I^X_{bioav,\,soil}$) and saprolite of 1 m thickness ($I^X_{bioav,\,sap}$). For the calculation of all inventories we used the soils' bulk density determined by Bernhard et al. (2018). I^X_{bulk} is comprised of elements contained in fine-earth material and in fragmented rocks and coarse material (e.g. core stones). We derive the relative amount of coarse material of each depth increment from Bernhard et al. (2018) and allocate them the bedrocks' chemical composition (Table S3.1). If information on either bulk density or the relative amount of coarse material was unavailable, the respective horizons' average has been used for the calculation of $I^X_{i,j}$. In none of the eight regolith profiles is the depth to unweathered bedrock known. Thus, for comparison purposes, we calculated the inventories of the bio-available fraction in saprolite ($I^X_{bioav,\,sap}$) and in bulk regolith (I^X_{bulk}) to the depth of the respective regolith profile and normalized this value to the arbitrary value of 1 m.

Nutrient recycling factor

We call the ratio of nutrient uptake to nutrient supply by weathering the "nutrient recycling factor" Rec^X which was calculated using Eq. 3.7 and is reported in Table 3.7. Importantly, as defined, this factor ratios fluxes between entire regolith and total uptake into the entire vegetation cover (the same rationale as used by Cleveland et al. 2013, for the inverse; the "new" fraction of P). Rec^X thus might represent a minimum estimate as some fraction of $W^X_{regolith}$ will bypass nutrient uptake by plants if it is drained directly via groundwater into streams. Rec^X represents an underestimate for some elements that are returned to soil by stem-flow or throughfall. According to e.g. Wilcke et al. (2017), these fluxes are generally highest for K compared to other plant-essential elements. Rec^X might also be an overestimate, if a substantial fraction of nutrient is eroded by leaf litter and other plant debris after uptake, rendering it unavailable for recycling. In Pan de Azúcar, where atmospheric deposition (Dep^X_{dry} and Dep^X_{wet}) is known to be an important component of ecosystem element budgets (e.g. increasing τ-values towards the profiles top in absence of bio-lifting of elements and field observation; Oeser et al. 2018a) we need to consider

these inputs in addition to the weathering release fluxes ($W^X_{regolith}$). Thus, to account for all potential sources of elements available for plant uptake, the nutrient recycling factor in Pan de Azúcar is given as:

$$Rec^X = \frac{U^X_{total}}{W^X_{regolith} + Dep^X_{wet} + Dep^X_{dry}}.$$

Atmospheric deposition fluxes have been estimated by determining the absolute difference between the lowest τ-value in the shallowest mineral-soil sample and the highest τ-value in the soil profile above it. Further, we assume that elemental gains (i.e. increasing τ-values) in the regolith profiles are attributed solely to atmospheric deposition. We test these estimates for atmospheric depositional fluxes by placing the elemental gains in proportion to the initially determined weathering release fluxes ($W^X_{regolith}$, Eq. 3.3; Table 3.3).

Uncertainty estimation of nutrient fluxes

The analytical uncertainty of measured samples and certified international reference materials are reported in Section 3.4.2 and in Oeser and von Blanckenburg (2020a).

The uncertainties on the nutrient fluxes of $W^X_{regolith}$ and U^X_{total} were estimated by Monte Carlo simulations in which 20 000 random data sets were sampled within the standard deviation of all input parameters using a Box-Muller transformation (Box and Muller 1958). The simulation of each regolith profiles' $W^X_{regolith}$ incorporates the SD of the average soil denudation rate D (Table 3.1), the SD of the concentration of the element of interest in bedrock (Table S3.1), and 3% relative uncertainty on the element concentration in regolith samples. In the case of U^X_{total} the SD of the respective study sites' NPP and the SD of the chemical composition of the weighted plants (Table 3.5) were used. The resultant uncertainties on both fluxes are reported in Table 3.3.

Appendix B: Data presentation and Statistical analyses

Replication

We present our results on nutrient fluxes, inventories, and turnover times as study-site averages for synthesis reasons only. Indeed, at each study site four replicate regolith profiles have been analyzed in previous studies. Within a given site, these profiles show no significant differences in chemistry and pedogenic properties (Bernhard et al. 2018; Oeser et al. 2018a). In this study we focused on two regolith profiles situated on opposing slopes (north- and south facing midslope profiles) to account for the variations in substrate and/ or the effects of insolation and microclimate on weathering and nutrient uptake by plants. However, these profiles are natural replicates.

Statistical analysis

An analysis of variance (ANOVA) was performed to evaluate how denudation rate (D), the chemical depletion fraction (CDF), soil weathering rate (W), and the elemental weathering rates for Ca, K, Na, P, and Si ($W^{X}_{regolith}$) vary among sites. Variance homogeneity was tested using Levene's Test before applying ANOVAs and pair-wise differences were assessed using Tukey's HSD test. In these, p values ≤ 0.05 were considered as significant. The correlations between D, MAP, NPP, and the degree (CDF, τ^{X}) and rate (W, $W^{X}_{regolith}$) of weathering were evaluated using Pearson's correlation coefficients. To test for the significance of D on these weathering parameters, Pearson's correlation coefficients were evaluated twice: with (Table A3.1) and without La Campana (Table A3.2). This test is possible because of the high denudation rate of this site which originates from the steepest relief of all sites (Oeser et al. 2018a; Schaller et al. 2018b; van Dongen et al. 2019). The sample set includes study site average values from all tested parameters and those of the single regolith profiles. Statistical analyses were conducted using the statistics packages included in the software OriginPro (Version 2020).

Table A3.1: Correlation matrix with Pearson's correlation coefficients and significance (bold values; **: $p < 0.01$, *: $p < 0.05$) for net primary productivity (NPP), denudation rate (D), mean annual precipitation (MAP), and indices of total and elemental degree and rate of weathering. Correlation coefficients involve the entire EarthShape study area.

	D	MAP	NPP	CDF	W	$W^{Ca}_{regolith}$	$W^{K}_{regolith}$	$W^{Na}_{regolith}$	$W^{P}_{regolith}$	$W^{Si}_{regolith}$	τ^{Ca}	τ^{K}	τ^{Na}	τ^{P}	τ^{Si}
D		0.4	**0.48***	0.56	**0.88****	0.44	**0.83****	**0.95****	**0.87****	**0.88****	0.35	**0.72****	**0.60***	0.24	**0.59***
MAP			**0.98****	-0.16	0.06	-0.09	0.08	0.31	0.3	0.13	0.29	0.11	**0.66***	0.21	-0.06
NPP				0.01	0.16	0.09	0.15	0.4	0.43	0.21	0.45	0.19	**0.76****	0.36	0.1

CDF = chemical depletion fraction; W = soil weathering rate; $W^{X}_{regolith}$ = elemental chemical weathering flux; τ^{X} = elemental mass transfer coefficient

Note that because CDF and τ^{X} are per definition different in sign (i.e. a CDF of +1 denote entire depletion, whereas a τ^{X} of -1 denote entire depletion), τ^{X} was multiplied by -1 for presentation purposes.

Equal variances could be assumed throughout and all weathering patterns differed among sites on the total population (Table A3.3). However, post-hoc comparisons indicated that sites did not always differ, and that differences between sites varied for the different weathering parameters (Table A3.3). Particularly, few statistically significant differences exist between the semi-arid Santa Gracia and humid-temperate Nahuelbuta. In these two sites the weathering release fluxes for K ($W^{K}_{regolith}$), Na ($W^{Na}_{regolith}$), P ($W^{P}_{regolith}$), and Si ($W^{Si}_{regolith}$) do not differ significantly (Table A3.3) despite massive differences in D, MAP, and NPP (Table 3.1).

Table A3.2: Correlation matrix with Pearson's correlation coefficients and significance (bold values; **: $p < 0.01$, *: $p < 0.05$) for net primary productivity (NPP), denudation rate (D), mean annual precipitation (MAP), and indices of total and elemental degree and rate of weathering. Correlation coefficients involve the study sites Pan de Azúcar, Santa Gracia, and Nahuelbuta. La Campana has been excluded because it features the steepest relief of all sites which causes elevated denudation rates.

	D	MAP	NPP	CDF	W	$W^{Ca}_{regolith}$	$W^{K}_{regolith}$	$W^{Na}_{regolith}$	$W^{P}_{regolith}$	$W^{Si}_{regolith}$	τ^{Ca}	τ^{K}	τ^{Na}	τ^{P}	τ^{Si}
D		**0.74***	**0.78***	0.05	**0.51***	0.29	**0.59***	**0.94****	**0.76***	**0.80***	0.4	0.14	0.66	0.29	0.19
MAP			**0.99****	-0.24	0.09	-0.11	0.47	**0.67***	0.43	0.44	0.29	0.18	**0.73***	0.22	-0.11
NPP				-0.07	0.25	0.05	0.53	**0.76***	**0.56***	**0.56***	0.45	0.27	**0.83****	0.37	0.06

CDF = chemical depletion fraction; W = soil weathering rate; $W^{X}_{regolith}$ = elemental chemical weathering flux; τ^{X} = elemental mass transfer coefficient

Note that because CDF and τ^{X} are per definition different in sign (i.e. a CDF of +1 denote entire depletion, whereas a τ^{X} of -1 denote entire depletion), τ^{X} was multiplied by -1 for presentation purposes.

Table A3.3: evaluating variations in denudation rate (D), the chemical depletion fraction (CDF), soil weathering rate (W), and the elemental weathering rates for Ca, K, Na, P, and Si ($W^{Ca}_{regolith}$, $W^{K}_{regolith}$, $W^{Na}_{regolith}$, $W^{P}_{regolith}$, $W^{Si}_{regolith}$) among sites. The Tukey HSD test for site comparison is shown below. Sig = 1 indicates significant differences between the sites. The comparison between Santa Gracia and Nahuelbuta is highlighted in bold because of their importance in the discussion.

		D		CDF		W		$W^{Ca}_{regolith}$		$W^{K}_{regolith}$		$W^{Na}_{regolith}$		$W^{P}_{regolith}$		$W^{Si}_{regolith}$	
		F ratio	p>F	F ratio	p>F	F ratio	p>F	F ratio	p>F	F ratio	p>F	F ratio	p>F	F ratio	p>F	F ratio	p>F
Homogeneity of variance		1.96	0.20	2.90	0.10	3.08	0.09	1.52	0.28	3.51	0.07	2.37	0.15	1.38	0.32	1.38	0.32
Overal ANOVA		20.75	0.00	24.22	0.00	13.74	0.00	23.59	0.00	6.67	0.01	10.88	0.00	10.57	0.00	10.57	0.00
Site 1	**Site 2**	**p value**	**Sig**	**p value**	**Sig**	**p value**	**Sig**	**p value**	**Sig**	**p value**	**Sig**	**p value**	**Sig**	**p value**	**Sig**	**p value**	**Sig**
Santa Gracia	Pan de Azúcar	0.55	0	0.00	1	0.44	0	0.00	1	1.00	0	0.43	0	0.04	1	0.04	1
La Campana	Pan de Azúcar	0.00	1	0.00	1	0.00	1	0.00	1	0.02	1	0.00	1	0.00	1	0.00	1
La Campana	Santa Gracia	0.00	1	0.98	0	0.01	1	0.28	0	0.03	1	0.02	1	0.20	0	0.20	0
Nahuelbuta	Pan de Azúcar	0.04	1	0.50	0	0.83	0	0.11	0	0.99	0	0.19	0	0.07	0	0.07	0
Nahuelbuta	**Santa Gracia**	**0.29**	**0**	**0.00**	**1**	**0.88**	**0**	**0.00**	**1**	**1.00**	**0**	**0.91**	**0**	**0.98**	**0**	**0.98**	**0**
Nahuelbuta	La Campana	0.01	1	0.00	1	0.00	1	0.05	0	0.03	1	0.04	1	0.12	0	0.12	0

F ratio = ratio of two mean square values.

P value ≥ .05 = Populations have significant different mean values

Sig = significance; 0: not significant, 1: significant

Appendix C: Supporting figures

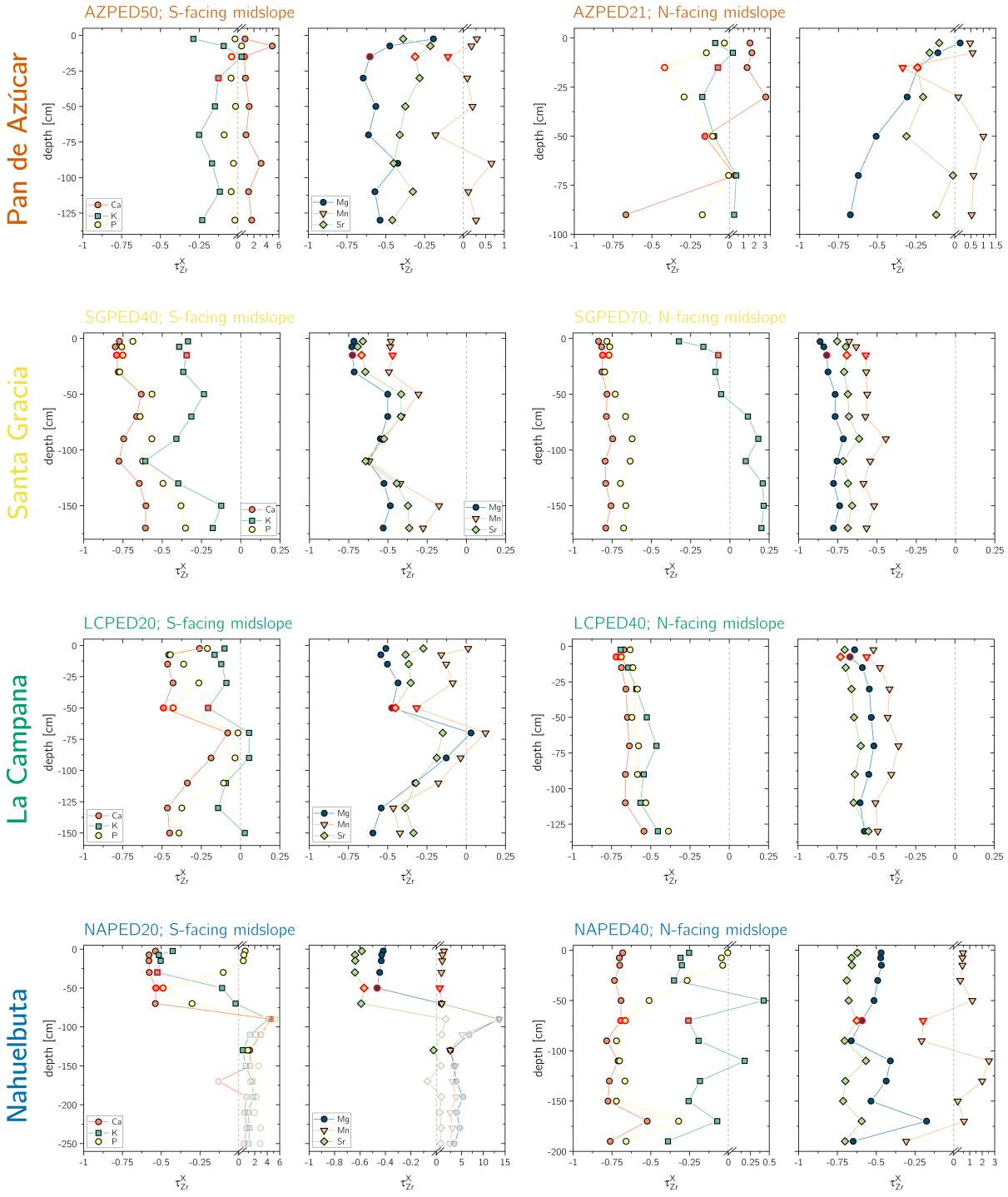

Figure A3.1: Depth distribution of the elemental loss and gain fractions (i.e. elemental mass transfer coefficient, τ). The vertical dashed line indicates $\tau^X = 0$ and represents unweathered parent bedrock. τ-values corresponding to the shallowest mineral soil samples are highlighted with a red rim. Gray symbols in Nahuelbuta are discarded due to the samples' anomalous low Zr concentration. Note that these τ-values deviate from those reported in Oeser et al. (2018a), such that in this work they have been calculated relative to the bedrocks' initial chemical composition.

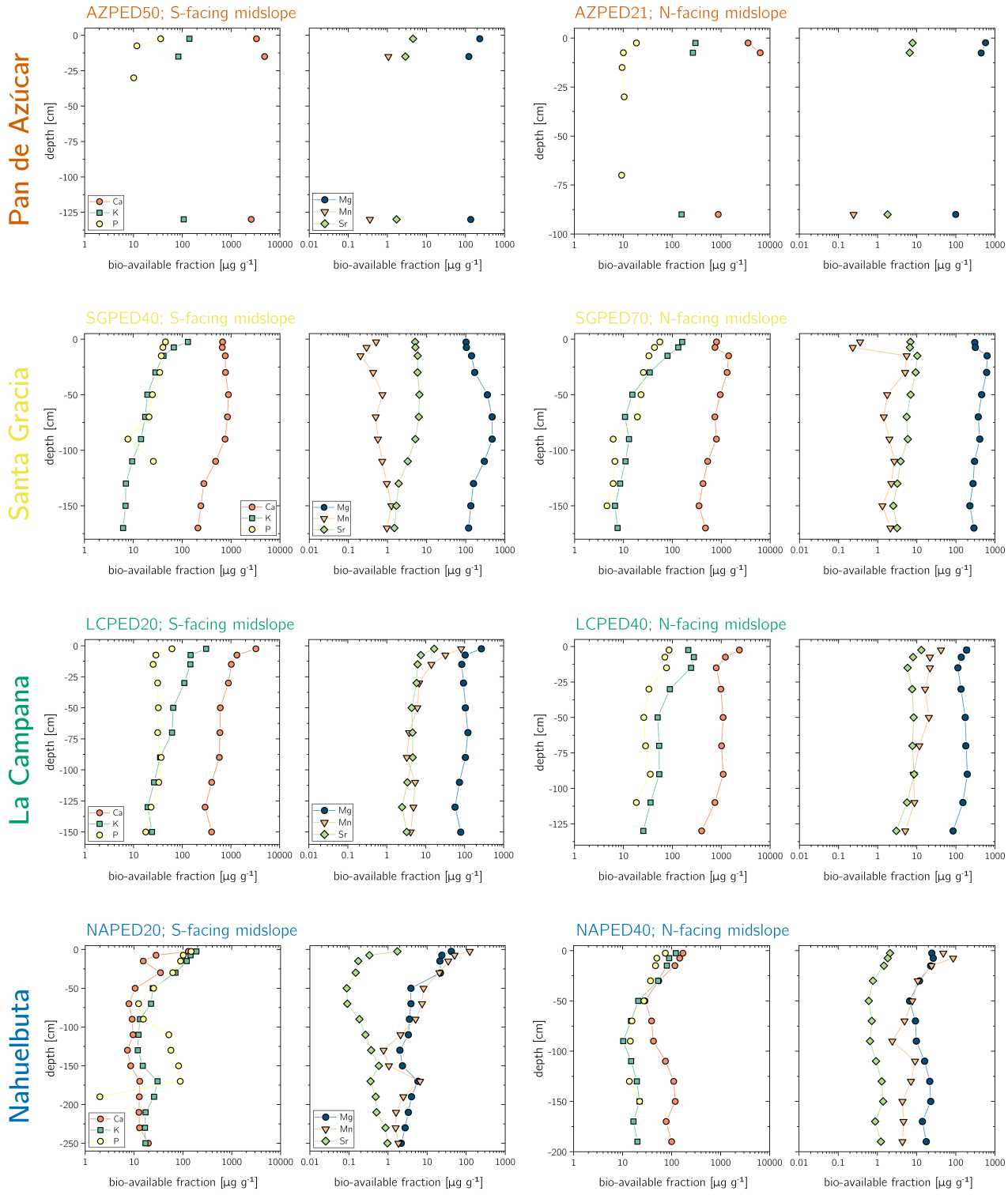

Figure A3.2: Depth distribution of the concentration of sequentially extracted bio-available fraction of plant-essential elements including Sr, comprised of the water soluble (18 MΩ Milli-Q H_2O) and the exchangeable (1 M NH_4OAc) fraction. P-accessibility in the bio-available fraction has been determined by Brucker and Spohn (2019) using a modified Hedley sequential P fractionation method. Note that in Pan de Azúcar the acquisition of the bio-available fraction was only possible on three samples per site. Data gaps do occur if both extractions of one sample were below limit of detection.

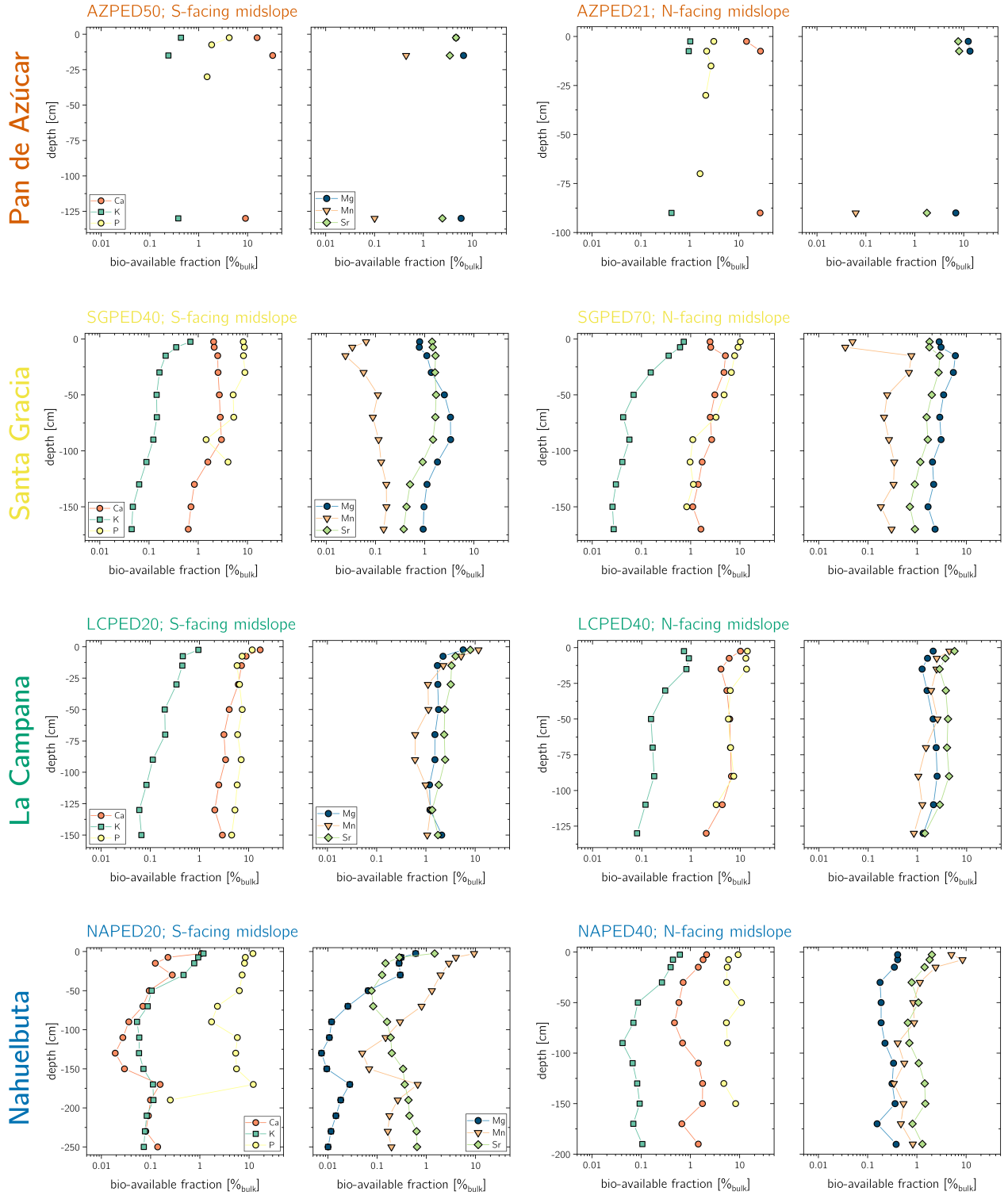

Figure A3.3: Depth distribution of the sequentially extracted bio-available fraction of plant-essential elements relative to their respective amount contained in bulk regolith including Sr, comprised of the water soluble (18 MΩ Milli-Q H_2O) and the exchangeable (1 M NH_4OAc) fraction. P-accessibility in the bio-available fraction has been determined by Brucker and Spohn (2019) using a modified Hedley sequential P fractionation method. Note that in Pan de Azúcar the acquisition of the bio-available fraction was only possible on three samples per site. Data gaps do occur if both extractions of one sample were below limit of detection.

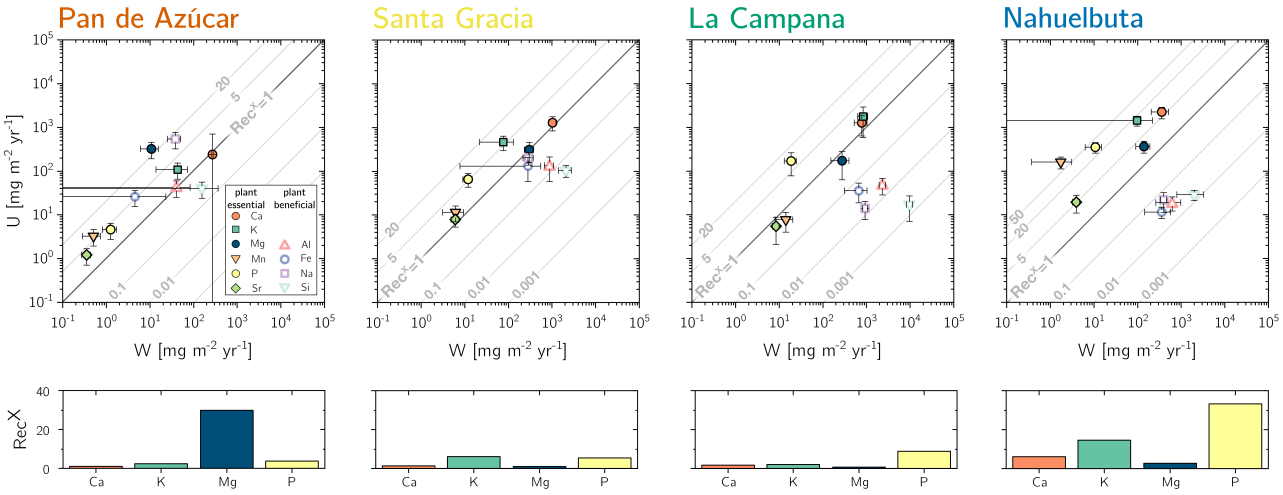

Figure A3.4: Chemical weathering flux ($W^X_{regolith}$) and ecosystem nutrient-uptake fluxes (U^X_{total}) for Pan de Azúcar, Santa Gracia, La Campana, and Nahuelbuta (from left to right) for plant-essential (closed symbols) and plant-beneficial elements (open symbols). Weathering-release fluxes for Ca, K, Mg, Na, and Sr in Pan de Azúcar have been complemented by atmospheric depositional fluxes such that the total amount of available nutrients increase by 95, 22, 18, 12, and 10%, respectively. Gray contour lines emphasize the nutrient recycling factor (Rec^X), which is the ratio of U^X_{total} to $W^X_{regolith}$. Uncertainty bars show 1SD. Differences in nutrient recycling factors for the plant essential elements Ca, K, Mg, and P among the four study sites are highlighted in the lower panels.

Sample availability

All sample metadata are already available on a public server using unique sample identifiers in form of the new "International Geo Sample Number" (IGSN).

Author contributions

R.A. Oeser conducted field sampling, analyzed samples, interpreted data, and wrote text. F. von Blanckenburg designed study, selected the study sites, interpreted data, and wrote text.

Competing financial interests

The authors declare no competing financial interests.

Acknowledgements

We acknowledge CONAF in Chile for providing us with the opportunity to work in the national parks of Pan de Azúcar, La Campana, and Nahuelbuta. We also thank CEAZA for facilitating access to the Reserva Natural Santa Gracia. We are grateful to J. Boy (Soil Sciences, Leibniz Universität Hannover, Germany) for discussions, and D. Uhlig (Institute of Bio- and Geosciences, Forschungszentrum Jülich, Germany), Michaela Dippold (Department of Crop Sciences, Georg-August University Goettingen, Germany), Matthew Winnick (Department of Geosciences, University of Massachusetts, USA), and Patrick Frings (Section "Earth Surface

Geochemistry", GFZ German Research Centre for Geosciences, Germany) for vivid discussions and informal reviews of the text. We thank the three anonymous referees and Marjin van de Broeck and his MSc students for their detailed critique of our work which led us to revise the manuscript with the aim of attempting to avoiding the pitfalls emerging when working across disciplines. R.A. Oeser and F. von Blanckenburg are grateful for funding by the German National Science Foundation Priority Program DFG-SPP 1803 (EarthShape; www.earthshape.net). We thank Leandro Paulino (Departamento de Suelos y Recursos Naturales, Universitad de Concepción, Chile) and Kirstin Übernickel for managing the priority program and Todd Ehlers (both Institute for Geosciences, Universität Tübingen, Germany) for its co-coordination.

3.9 Supplementary material

Dataset for evaluation element fluxes released by weathering and taken up by plants along the EarthShape climate and vegetation gradient

Abstract

With this data, we expand the data set characterizing the Critical Zone geochemistry along the Chilean Coastal Cordillera provided by Oeser et al. (2018a). This data set completes the results of bulk geochemical analysis of bedrock and regolith with those of bulk analysis of major plants and those of the bio-available fraction in saprolite and soil (determined using a modified sequential extraction method on bulk regolith samples after Arunachalam et al. 1996; He et al. 1995; Tessier et al. 1979). For all those compartments of the Earth's Critical Zone, we further present $^{87}Sr/^{86}Sr$ isotope ratios. A detailed graphical presentation and discussion of this data as well as method description is given in Oeser and von Blanckenburg (2020b), Decoupling primary productivity from silicate weathering – how ecosystems regulate nutrient uptake along a climate and vegetation gradient.

Using this data, we were thus, able to determine weathering rates and nutrient uptake along the "EarthShape" climate and vegetation gradient in the Chilean Coastal Cordillera and to identify the sources of mineral nutrients to plants. Ultimately, we were able to budget inventories, gains and losses of nutritive elements in and out of these ecosystems and to quantify nutrient recycling. We found that the weathering rate does not increase from north to south along the climate gradient. Instead, the increase in biomass growth rate is accommodated by faster nutrient recycling. The absence of an increase in weathering rate in spite of a five-fold increase in precipitation led us to hypothesize that the presence of plants even negatively impacts weathering through reducing the water flow, inducing secondary-mineral formation, and fostering a microbial community specializing on nutrient-recycling rather than nutrient-acquisition through weathering.

This dataset is published in:

GFZ Data Services

Oeser and von Blanckenburg (2020a);
https://doi.org/10.5880/GFZ.3.3.2020.003

Table S3.1: Average bedrock composition in Pan de Azúcar, Santa Gracia, and Nahuelbuta derived from Oeser et al. (2018a) complemented by additional bedrock samples from the respective study sites.

Study site	Al_2O_3	CaO	Fe_2O_3	K_2O^*	MgO	MnO	Na_2O	P_2O_5	SiO_2	TiO_2	Sr	Zr
	[wt%]										[µg g^{-1}]	
Pan de Azúcar												
GFRO100RK	13.8	0.9	3.2	3.9	0.9	0.03	3.0	0.16	70.3	0.5	119	202
GFRO100RN	12.2	1.1	3.2	3.6	0.5	0.03	2.3	0.13	73.7	0.5	113	207
GFRO100X1	13.0	1.4	3.1	3.9	0.4	0.03	2.6	0.14	72.2	0.5	101	202
GFRO100RF	13.6	2.0	3.0	3.6	0.5	0.04	2.8	0.15	70.4	0.5	91	187
GFRO100RG	14.0	2.0	1.9	2.0	0.6	0.05	4.4	0.05	73.9	0.2	195	86
GFRO100LU	14.6	1.2	1.9	6.9	0.3	0.02	2.5	0.12	69.8	0.3	154	121
GFRO100RM	14.3	1.7	3.8	4.1	1.0	0.04	3.1	0.18	68.4	0.6	151	234
GFRO100RH	14.0	2.2	4.6	3.5	1.3	0.05	3.2	0.18	66.9	0.7	140	276
GFRO100LT	12.3	0.9	3.4	3.3	1.0	0.03	2.7	0.14	73.3	0.5	121	220
GFRO100RL	13.0	1.2	3.2	4.3	0.9	0.03	2.6	0.15	71.7	0.5	128	206
GFRO100RJ	13.4	1.4	2.9	4.1	0.6	0.03	3.0	0.13	71.4	0.4	93	161
GFRO100LS	13.3	0.9	3.9	4.2	0.8	0.04	2.6	0.18	70.9	0.6	112	223
mean	**13.4**	**1.4**	**3.3**	**4.1**	**0.8**	**0.03**	**2.8**	**0.15**	**70.8**	**0.5**	**120**	**205**
SD	*0.7*	*0.4*	*0.6*	*0.9*	*0.3*	*0.01*	*0.3*	*0.02*	*1.9*	*0.1*	*21*	*38*
SE (n=12)	*0.2*	*0.1*	*0.2*	*0.3*	*0.1*	*0.00*	*0.1*	*0.01*	*0.6*	*0.0*	*6*	*11*
Santa Gracia												
GFRO100L7	18.8	10.3	8.6	0.4	5.1	0.12	3.7	0.11	50.3	0.7	554	66
GFRO100L8	16.6	8.6	9.7	1.3	4.4	0.13	3.6	0.15	53.1	0.9	435	110
GFRO100LA	18.3	14.0	2.2	0.2	4.5	0.03	4.1	0.21	54.4	1.0	652	55
GFRO100LB	16.6	6.1	3.1	0.6	2.1	0.08	5.2	0.38	64.2	0.5	515	209
GFRO100LC	17.4	6.3	4.2	0.6	0.9	0.07	5.3	0.18	63.4	0.6	287	192
GFRO100X2	17.4	12.4	5.6	0.6	5.0	0.16	3.5	0.11	53.9	0.6	585	57
GFRO100RU	16.2	5.6	7.1	2.2	2.5	0.14	3.8	0.21	60.0	0.8	383	198
GFRO100L9	18.5	14.2	2.3	0.2	4.6	0.03	4.1	0.22	55.0	1.0	659	56
mean	**17.5**	**9.7**	**5.3**	**0.8**	**3.6**	**0.10**	**4.2**	**0.20**	**56.8**	**0.8**	**509**	**118**
SD	*1.0*	*3.6*	*2.9*	*0.7*	*1.6*	*0.05*	*0.7*	*0.09*	*5.1*	*0.2*	*132*	*70*
SE (n=8)	*0.3*	*1.3*	*1.0*	*0.2*	*0.6*	*0.02*	*0.3*	*0.03*	*1.8*	*0.1*	*47*	*25*
La Campana												
GFRO10094	13.8	1.5	2.1	3.9	0.4	0.03	3.3	0.07	73.0	0.3	186	182
GFRO10098	13.6	1.4	2.1	4.2	0.3	0.03	3.2	0.07	73.4	0.3	183	171
GFRO10096	13.0	1.2	1.3	4.6	0.3	0.03	3.1	0.04	74.6	0.2	165	140
GFRO10095	13.6	1.8	2.3	3.9	0.4	0.05	3.5	0.07	72.4	0.3	207	190
GFRO1019T	13.5	0.8	2.0	5.9	0.6	0.05	2.5	0.08	72.2	0.3	158	149
GFRO10097	16.6	5.3	7.0	2.5	2.9	0.11	3.8	0.20	58.4	0.8	316	180
GFRO100RP	15.7	4.6	6.3	2.7	2.2	0.11	3.6	0.17	62.1	0.7	294	331
GFRO1019S	16.1	4.5	6.3	2.6	2.1	0.11	3.7	0.20	61.8	0.7	295	185
GFRO100DH	16.3	4.3	6.4	2.5	2.0	0.11	3.5	0.20	61.4	0.8	287	246
GFRO1019U	15.5	4.1	5.7	3.1	1.9	0.10	3.7	0.15	63.9	0.6	259	337
mean	**14.8**	**3.0**	**4.2**	**3.6**	**1.3**	**0.07**	**3.4**	**0.13**	**67.3**	**0.5**	**235**	**211**
SD	*1.4*	*1.7*	*2.3*	*1.1*	*1.0*	*0.04*	*0.4*	*0.06*	*6.3*	*0.3*	*61*	*71*
SE (n=10)	*0.4*	*0.6*	*0.7*	*0.3*	*0.3*	*0.01*	*0.1*	*0.02*	*2.0*	*0.1*	*19*	*22*
Nahuelbuta												
GFRO10009	16.1	4.0	4.7	2.1	1.2	0.07	3.2	0.15	66.9	0.5	215	219
GFRO10006	19.9	0.5	9.0	3.6	2.2	0.07	0.7	0.16	59.3	1.1	142	260
GFRO1000C	14.4	3.2	4.3	1.8	1.4	0.06	2.5	0.06	70.0	0.5	226	235
GFRO1017N	16.5	3.6	5.0	2.9	1.5	0.08	3.2	0.23	64.5	0.6	242	168
GFRO10004	14.8	2.1	2.8	1.9	0.8	0.04	3.1	0.10	71.5	0.4	217	109
mean	**16.4**	**2.7**	**5.1**	**2.5**	**1.4**	**0.06**	**2.6**	**0.14**	**66.5**	**0.6**	**208**	**198**
SD	*2.2*	*1.4*	*2.3*	*0.8*	*0.5*	*0.02*	*1.1*	*0.06*	*4.8*	*0.3*	*39*	*60*
SE (n=5)	*1.0*	*0.6*	*1.0*	*0.3*	*0.2*	*0.01*	*0.5*	*0.03*	*2.2*	*0.1*	*17*	*27*

* K concentration in Santa Gracia from Melnik (2016). See text for further discussion

Table S3.2: Weathering indizes CDF and τ along with radiogenic $^{87}Sr/^{86}Sr$ ratios of the 2×4 regolith profiles. Bold τ-values represent the depth increment which has been used for the calculation of $W^{X}_{regolith}$. τ-profiles of the 2×4 regolith profiles are visualized in Fig. A3.1.

Soil profile depth [cm]	IGSN	Sample type*	τ^{Al}	τ^{Ca}	τ^{Fe}	τ^{K}	τ^{Mg}	τ^{Mn}	τ^{Na}	τ^{P}	τ^{Si}	τ^{Sr}	CDF	$^{87}Sr/^{86}Sr$	2SE
								[-]							[-]
Pan de Azúcar	*AZPED21*	**Regosol**													
0 - 5	GFRO100UD	Aycz	−0.07	1.60	0.00	−0.09	0.08	0.48	−0.16	−0.03	0.06	−0.10	−0.05	0.72257	$4.1 \cdot 10^{-6}$
5 - 10	GFRO100UE	Bycz	0.05	1.78	0.08	0.01	−0.11	0.58	−0.04	−0.15	0.26	−0.16	−0.22	0.72846	$5.2 \cdot 10^{-6}$
10 - 20	GFRO100UF	Bycz	**−0.03**	1.33	**−0.03**	**−0.07**	**−0.24**	**−0.34**	**−0.24**	**−0.42**	0.13	**−0.24**	−0.09	0.72801	$1.03 \cdot 10^{-5}$
20 - 40	GFRO100UG	BCycz	−0.10	3.07	−0.03	−0.17	−0.31	0.01	−0.18	−0.29	**−0.10**	−0.20	0.06	0.72623	$4.3 \cdot 10^{-6}$
40 - 60	GFRO100UH	C	−0.02	**−0.16**	0.08	−0.10	−0.51	1.00	−0.20	−0.11	0.10	−0.31	−0.05	0.73177	$6.2 \cdot 10^{-6}$
60 - 80	GFRO100UJ	C	0.16	0.19	−0.04	0.32	−0.62	0.61	0.04	−0.01	0.15	−0.01	−0.14	0.72841	$1.15 \cdot 10^{-5}$
80 - 100	GFRO100UK	C	0.07	−0.67	−0.22	0.13	−0.67	0.54	−0.06	−0.17	0.06	−0.12	−0.03	0.72866	$1 \cdot 10^{-6}$
AZPED50		**Regosol**													
0 - 5	GFRO100TX	Aycz	−0.16	0.58	−0.06	−0.29	−0.19	0.27	−0.33	−0.02	−0.30	−0.39	0.25	0.72877	$1.69 \cdot 10^{-5}$
5 - 10	GFRO100TY	Bycz	0.01	4.94	0.03	−0.09	−0.47	0.13	−0.12	0.05	0.01	−0.21	−0.07	0.72961	$4.9 \cdot 10^{-6}$
10 - 20	GFRO100TZ	Bycz	0.00	**0.47**	0.07	0.02	**−0.60**	**−0.10**	**−0.12**	**−0.04**	**−0.01**	**−0.31**	0.01	0.73463	$1.38 \cdot 10^{-5}$
20 - 40	GFRO100U0	BCycz	**−0.08**	0.64	**−0.01**	**−0.13**	−0.65	0.02	−0.13	−0.04	−0.10	−0.28	0.09	0.73047	$8.2 \cdot 10^{-6}$
40 - 60	GFRO100U1	BCycz	−0.02	1.24	0.12	−0.15	−0.56	0.15	−0.15	−0.02	0.01	−0.37	−0.01	0.73418	$1.21 \cdot 10^{-5}$
60 - 80	GFRO100U2	C	−0.12	0.74	−0.09	−0.25	−0.61	−0.18	−0.28	−0.09	−0.09	−0.41	0.10	0.73240	$2.12 \cdot 10^{-5}$
80 - 100	GFRO100U3	C	−0.04	3.15	−0.11	−0.17	−0.42	0.66	−0.34	−0.03	−0.01	−0.45	−0.01	0.73652	$6 \cdot 10^{-6}$
100 - 120	GFRO100U4	C	−0.03	1.15	0.00	−0.12	−0.57	0.04	−0.21	−0.04	−0.08	−0.33	0.06	0.73123	$2.9 \cdot 10^{-6}$
120 - 140	GFRO100U5	C	−0.06	1.65	−0.04	−0.23	−0.54	0.25	−0.27	−0.02	−0.09	−0.46	0.08	0.73521	$3.31 \cdot 10^{-5}$
Santa Gracia, *SGPED70*		**Cambisol**													
0 - 5	GFRO100VF	Ah	−0.68	−0.84	−0.54	−0.32	−0.86	−0.68	−0.68	−0.78	−0.61	−0.75	0.66	0.70451	$4 \cdot 10^{-6}$
5 - 10	GFRO100VG	Ah	−0.59	−0.82	−0.54	−0.17	−0.84	−0.63	−0.58	−0.77	−0.50	−0.70	0.58	0.70444	$5.8 \cdot 10^{-6}$
10 - 20	GFRO100VH	Bwi	**−0.56**	**−0.81**	**−0.47**	**−0.07**	**−0.82**	**−0.57**	**−0.57**	**−0.77**	**−0.47**	**−0.69**	0.54	0.70451	$7 \cdot 10^{-7}$
20 - 40	GFRO100VJ	C	−0.56	−0.81	−0.44	−0.09	−0.81	−0.57	−0.60	−0.80	−0.48	−0.71	0.55	0.70453	$3.8 \cdot 10^{-6}$
40 - 60	GFRO100VK	C	−0.55	−0.78	−0.39	−0.06	−0.77	−0.56	−0.55	−0.73	−0.45	−0.69	0.52	0.70446	$1.06 \cdot 10^{-5}$
60 - 80	GFRO100VL	C	−0.56	−0.79	−0.47	0.11	−0.77	−0.57	−0.55	−0.66	−0.43	−0.68	0.51	0.70464	$4 \cdot 10^{-6}$
80 - 100	GFRO100VM	C	−0.48	−0.75	−0.30	0.18	−0.72	−0.44	−0.46	−0.62	−0.33	−0.61	0.43	0.70464	$5.4 \cdot 10^{-6}$
100 - 120	GFRO100VN	C	−0.61	−0.79	−0.46	0.10	−0.76	−0.54	−0.59	−0.64	−0.47	−0.72	0.55	0.70474	$5.5 \cdot 10^{-6}$
120 - 140	GFRO100VP	C	−0.58	−0.79	−0.53	0.21	−0.78	−0.59	−0.55	−0.70	−0.44	−0.68	0.53	0.70471	$1.26 \cdot 10^{-5}$
140 - 160	GFRO100VQ	C	−0.54	−0.76	−0.42	0.22	−0.74	−0.52	−0.50	−0.66	−0.40	−0.66	0.48	0.70461	$5.7 \cdot 10^{-6}$
160 - 180	GFRO100VR	C	−0.58	−0.79	−0.49	0.20	−0.78	−0.57	−0.56	−0.68	−0.44	−0.69	0.52	0.70470	$4.1 \cdot 10^{-6}$
SGPED40		**Cambisol**													
0 - 5	GFRO100UU	Ah	−0.55	−0.77	−0.45	−0.34	−0.72	−0.48	−0.50	−0.69	−0.48	−0.66	0.52	0.70429	$8.2 \cdot 10^{-6}$

Continued on the next page.

Table S3.2: ...continuation

Soil profile depth [cm]	IGSN	Sample type*	τ^{Al}	τ^{Ca}	τ^{Fe}	τ^{K}	τ^{Mg}	τ^{Mn} [-]	τ^{Na}	τ^{P}	τ^{Si}	τ^{Sr}	CDF	$^{87}Sr/^{86}Sr$ [-]	2SE
5 - 10	GFRO100UV	Ah	−0.58	−0.80	−0.45	−0.39	−0.73	−0.49	−0.55	−0.76	−0.52	−0.69	0.56	0.70427	$1.69 \cdot 10^{-5}$
10 - 20	GFRO100V3	Bw	**−0.55**	**−0.79**	**−0.42**	**−0.34**	**−0.73**	**−0.47**	**−0.51**	**−0.75**	**−0.49**	**−0.67**	0.53	0.70431	$1.65 \cdot 10^{-5}$
20 - 40	GFRO100UW	BCw	−0.52	−0.78	−0.41	−0.37	−0.72	−0.49	−0.48	−0.77	−0.45	−0.64	0.50	0.70427	$1.32 \cdot 10^{-5}$
40 - 60	GFRO100UX	BCw	−0.24	−0.63	−0.21	−0.23	−0.50	−0.30	−0.15	−0.57	−0.15	−0.42	0.23	0.70415	$3.07 \cdot 10^{-5}$
60 - 80	GFRO100UY	C	−0.24	−0.66	−0.31	−0.31	−0.50	−0.41	−0.09	−0.64	−0.14	−0.42	0.23	0.70398	$1.18 \cdot 10^{-5}$
80 - 100	GFRO100UZ	C	−0.33	−0.75	−0.33	−0.41	−0.55	−0.54	−0.19	−0.57	−0.22	−0.52	0.31	0.70411	$1.06 \cdot 10^{-5}$
100 - 120	GFRO100V0	C	−0.53	−0.78	−0.57	−0.61	−0.62	−0.62	−0.39	−0.63	−0.44	−0.64	0.50	0.70416	$6.8 \cdot 10^{-6}$
120 - 140	GFRO100V1	C	−0.31	−0.65	−0.41	−0.40	−0.53	−0.42	−0.09	−0.50	−0.17	−0.44	0.27	0.70397	$4.9 \cdot 10^{-6}$
140 - 160	GFRO100V2	C	−0.25	−0.60	−0.16	−0.12	−0.48	−0.17	−0.08	−0.38	−0.11	−0.37	0.19	0.70394	$8.7 \cdot 10^{-6}$
160 - 180	GFRO100CR	C	−0.24	−0.61	−0.23	−0.18	−0.53	−0.28	−0.02	−0.35	−0.10	−0.36	0.19	0.70392	$6 \cdot 10^{-6}$
***La Campana**, LCPED40*		**Cambisol**													
0 - 5	GFRO1002V	Ah	−0.68	−0.67	−0.50	−0.69	−0.64	−0.52	−0.77	−0.63	−0.72	−0.70	0.70	0.70510	$2.14 \cdot 10^{-5}$
5 - 10	GFRO1002W	Bw1	**−0.70**	**−0.72**	**−0.51**	**−0.69**	**−0.67**	**−0.56**	**−0.78**	**−0.69**	**−0.72**	**−0.73**	0.71	0.70508	$1.54 \cdot 10^{-5}$
10 - 20	GFRO1002X	Bw1	−0.62	−0.69	−0.44	−0.64	−0.59	−0.48	−0.74	−0.61	−0.68	−0.70	0.66	0.70515	$2.47 \cdot 10^{-5}$
20 - 40	GFRO1002Y	Bw2	−0.57	−0.66	−0.36	−0.59	−0.55	−0.42	−0.71	−0.58	−0.63	−0.66	0.61	0.70521	$2.27 \cdot 10^{-5}$
40 - 60	GFRO1002Z	BCw	−0.54	−0.65	−0.36	−0.53	−0.53	−0.43	−0.69	−0.62	−0.60	−0.64	0.58	0.70530	$4.85 \cdot 10^{-5}$
60 - 80	GFRO10030	BCw	−0.47	−0.64	−0.33	−0.46	−0.52	−0.36	−0.67	−0.58	−0.54	−0.60	0.52	0.70542	$1.76 \cdot 10^{-5}$
80 - 100	GFRO100WG	BCw	−0.52	−0.66	−0.36	−0.54	−0.55	−0.40	−0.70	−0.58	−0.58	−0.64	0.57	0.70540	$2.86 \cdot 10^{-5}$
100 - 120	GFRO100WF	C	−0.55	−0.66	−0.44	−0.57	−0.60	−0.51	−0.68	−0.53	−0.60	−0.65	0.58	0.70538	$3.98 \cdot 10^{-5}$
120 - 140	GFRO100WE	C	−0.49	−0.54	−0.43	−0.45	−0.58	−0.49	−0.55	−0.39	−0.51	−0.55	0.51	0.70533	$1.41 \cdot 10^{-5}$
LCPED20		**Cambisol**													
0 - 5	GFRO10029	Ah1	−0.22	−0.26	−0.33	−0.10	−0.51	0.01	−0.38	−0.21	−0.14	−0.27	0.18	0.70556	$4.73 \cdot 10^{-5}$
5 - 10	GFRO1002A	Ah1	−0.25	−0.46	−0.33	−0.17	−0.54	−0.16	−0.38	−0.45	−0.20	−0.39	0.23	0.70551	$4.84 \cdot 10^{-5}$
10 - 20	GFRO1002B	Ah2	−0.18	−0.46	−0.26	−0.12	−0.50	−0.13	−0.35	−0.36	−0.18	−0.37	0.20	0.70563	$8.1 \cdot 10^{-6}$
20 - 40	GFRO1002C	Ah3	−0.15	−0.43	−0.17	−0.09	−0.43	−0.09	−0.32	−0.27	−0.15	−0.35	0.17	0.70559	$4.1 \cdot 10^{-6}$
40 - 60	GFRO1002D	Bw	**−0.27**	**−0.49**	**−0.26**	**−0.21**	**−0.47**	**−0.32**	**−0.42**	**−0.43**	**−0.28**	**−0.45**	0.29	0.70551	$6.18 \cdot 10^{-5}$
60 - 80	GFRO100VU	BCw	0.08	−0.08	0.28	0.05	0.03	0.12	−0.13	−0.02	0.01	−0.15	−0.02	0.70507	$5.1 \cdot 10^{-6}$
80 - 100	GFRO100VV	BCw	0.03	−0.19	0.17	0.05	−0.13	−0.04	−0.17	−0.03	0.01	−0.19	−0.01	0.70515	$5.6 \cdot 10^{-6}$
100 - 120	GFRO100VW	BCw	−0.14	−0.34	−0.01	−0.09	−0.33	−0.18	−0.27	−0.11	−0.13	−0.32	0.14	0.70514	$3.29 \cdot 10^{-5}$
120 - 140	GFRO100VY	C	−0.23	−0.47	−0.29	−0.14	−0.54	−0.46	−0.33	−0.37	−0.19	−0.39	0.22	0.70543	$1.09 \cdot 10^{-5}$
140 - 160	GFRO100VX	C	−0.17	−0.45	−0.33	0.03	−0.59	−0.42	−0.27	−0.39	−0.12	−0.34	0.16	0.70548	$4.64 \cdot 10^{-5}$
***Nahuelbuta**, NAPED40*		**umbric Podzol**													
0 - 5	GFRO1001R	Ah1	−0.26	−0.68	−0.20	−0.25	−0.47	0.47	−0.75	0.00	−0.20	−0.62	0.24	0.71713	$6.6 \cdot 10^{-6}$

Continued on the next page.

Table S3.2: ...continuation

Soil profile depth [cm]	IGSN	Sample type*	τ^{Al}	τ^{Ca}	τ^{Fe}	τ^{K}	τ^{Mg}	τ^{Mn} [-]	τ^{Na}	τ^{P}	τ^{Si}	τ^{Sr}	CDF	$^{87}Sr/^{86}Sr$ [-]	2SE
5 - 10	GFRO1001S	Ah1	−0.27	−0.70	−0.20	−0.31	−0.47	0.43	−0.76	−0.04	−0.28	−0.66	0.30	0.71715	$1.27 \cdot 10^{-5}$
10 - 20	GFRO1001T	Ah1	−0.27	−0.70	−0.20	−0.30	−0.47	0.43	−0.76	−0.04	−0.28	−0.66	0.30	0.71689	$6.9 \cdot 10^{-6}$
20 - 40	GFRO1001U	Ah2	−0.29	−0.73	−0.23	−0.35	−0.49	0.25	−0.78	−0.27	−0.33	−0.69	0.34	0.71702	$5 \cdot 10^{-6}$
40 - 60	GFRO1001V	Bw	−0.04	−0.69	−0.03	0.43	−0.51	1.22	−0.34	−0.51	0.34	−0.68	−0.19	0.72041	$6 \cdot 10^{-6}$
60 - 80	GFRO100X0	BCs1	**−0.44**	**−0.69**	**−0.35**	**−0.26**	**−0.59**	**−0.20**	**−0.70**	**−0.66**	**−0.21**	**−0.63**	0.29	0.71944	$5.4 \cdot 10^{-6}$
80 - 100	GFRO10050	BCs2	−0.49	−0.78	−0.34	−0.19	−0.66	−0.21	−0.79	−0.72	−0.25	−0.70	0.33	0.71962	$5.4 \cdot 10^{-6}$
100 - 120	GFRO100WZ	C1	−0.16	−0.71	−0.33	0.17	−0.41	2.54	−0.74	−0.70	0.23	−0.57	−0.07	0.72133	$7.1 \cdot 10^{-6}$
120 - 140	GFRO100WY	C1	−0.32	−0.77	−0.45	−0.18	−0.44	2.01	−0.78	−0.67	−0.24	−0.70	0.30	0.72084	$1.71 \cdot 10^{-5}$
140 - 160	GFRO100WX	C1	−0.46	−0.78	−0.55	−0.26	−0.53	0.05	−0.78	−0.72	−0.30	−0.71	0.37	0.71992	$3.6 \cdot 10^{-6}$
160 - 180	GFRO100WV	C2	−0.33	−0.52	−0.26	−0.07	−0.18	0.55	−0.72	−0.32	−0.16	−0.59	0.21	0.71814	$1.24 \cdot 10^{-5}$
180 - 200	GFRO100WW	C2	−0.52	−0.76	−0.65	−0.39	−0.65	−0.31	−0.74	−0.66	−0.24	−0.70	0.35	0.72022	$6.2 \cdot 10^{-6}$
NAPED20		**orthodystric Umbrisol**													
0 - 5	GFRO10019	Ah1	−0.21	−0.54	−0.10	−0.43	−0.42	0.96	−0.71	0.48	−0.27	−0.59	0.27	0.71127	$1.62 \cdot 10^{-5}$
5 - 10	GFRO10018	Ah1	−0.23	−0.58	−0.11	−0.52	−0.43	0.61	−0.72	0.27	−0.39	−0.64	0.36	0.71114	$2.12 \cdot 10^{-5}$
10 - 20	GFRO1001A	Ah2	−0.21	−0.58	−0.10	−0.50	−0.43	0.57	−0.72	0.18	−0.38	−0.64	0.35	0.71169	$2.88 \cdot 10^{-5}$
20 - 40	GFRO1001B	Ah3	−0.22	−0.58	−0.12	−0.53	−0.45	0.37	−0.72	−0.10	−0.39	−0.64	0.36	0.71109	$1.36 \cdot 10^{-5}$
40 - 60	GFRO1001C	Bw1	**−0.14**	**−0.53**	**−0.21**	**−0.11**	**−0.47**	**0.00**	**−0.62**	**−0.49**	**−0.20**	**−0.57**	0.21	0.71137	$1.21 \cdot 10^{-5}$
60 - 80	GFRO1001D	Bw2	0.09	−0.54	0.30	−0.02	0.35	0.46	−0.77	−0.30	−0.32	−0.59	0.22	0.71690	$1.01 \cdot 10^{-5}$
80 - 100	GFRO100WP	BCw	4.80	4.64	10.41	4.21	13.54	13.78	0.22	5.24	2.04	1.36	−3.23	0.71886	$1.57 \cdot 10^{-5}$
100 - 120	GFRO100WN	C1	1.82	2.98	4.22	1.23	6.74	5.16	−0.15	2.17	0.60	0.45	−1.16	0.71532	$6.1 \cdot 10^{-6}$
120 - 140	GFRO100WM	C2	0.44	1.21	1.45	0.11	2.44	2.40	−0.45	0.91	−0.17	−0.02	−0.10	0.71270	$3.3 \cdot 10^{-6}$
140 - 160	GFRO100WL	C2	1.07	1.28	2.42	0.56	3.27	3.63	−0.40	2.61	0.13	0.24	−0.50	0.71368	$8.9 \cdot 10^{-6}$
160 - 180	GFRO100WK	C2	1.94	−0.13	2.75	1.63	3.78	2.92	−0.63	1.33	0.59	−0.07	−0.97	0.72056	$7.2 \cdot 10^{-6}$
180 - 200	GFRO100WQ	C3	2.18	0.69	3.46	1.77	5.36	3.75	−0.27	2.25	1.17	0.34	−1.50	0.71637	$4.3 \cdot 10^{-6}$
200 - 220	GFRO100WR	C3	1.46	0.38	2.33	0.91	3.89	2.41	−0.36	1.96	0.61	0.01	−0.88	0.71280	$7.5 \cdot 10^{-6}$
220 - 240	GFRO100WJ	C3	1.82	0.74	2.79	1.18	4.59	2.90	−0.11	2.92	0.66	0.32	−1.04	0.71158	$2.03 \cdot 10^{-5}$
240 - 260	GFRO100WH	C3	1.34	0.28	2.11	0.99	3.32	2.30	−0.26	2.86	0.43	0.23	−0.72	0.71419	$9.8 \cdot 10^{-6}$
International reference materials for concentration data quality control (element concentration in µg g^{-1}) and radiogenic $^{87}Sr/^{86}Sr$ isotope ratios			Al	Ca	Fe	K	Mg	Mn	Na	P		Sr			
BCR-2	mean (n=6/18)		64730	43735	88252	13060	19185	1403	21514	1655		304		0.70501	$1.2 \cdot 10^{-5}$
BCR-2	SD		4658	4144	7603	1219	1922	137	1933	127		31			
BCR-2	RSD		7%	9%	9%	9%	10%	10%	9%	8%		10%			
Certified values			70284	51030	95472	14777	21470	1471	22849	1353		340		0.70502†	$1.3 \cdot 10^{-5}$

Continued on the next page.

Table S3.2: ...continuation

Soil profile depth [cm]	IGSN	Sample type*	τ^{Al}	τ^{Ca}	τ^{Fe}	τ^{K}	τ^{Mg}	τ^{Mn} [-]	τ^{Na}	τ^{P}	τ^{Si}	τ^{Sr}	CDF	$^{87}Sr/^{86}Sr$ [-]	2SE
Relative difference			8%	14%	8%	12%	11%	5%	6%	-22%		11%			
BHVO-2	mean (n=7/72)		66869	72988	80012	3973	38883	1215	15296	1159		359		0.70349	$5 \cdot 10^{-6}$
BHVO-2	SD		2878	5782	3396	227	744	51	876	104		11			
BHVO-2	RSD		4%	8%	4%	6%	2%	4%	6%	9%		3%			
Certified values			70814	81833	85540	4234	43604	1317	15876	960		394		0.70344‡	$8.3 \cdot 10^{-6}$
Relative difference			6%	11%	6%	6%	11%	8%	4%	-21%		9%			
JG-2	mean (n=7/18)		63489	4661	6349	35904	209	121	25212	19		14		0.75889	$9 \cdot 10^{-6}$
JG-2	SD		2596	174	198	1448	7	6	1285	1		3			
JG-2	RSD		4%	4%	3%	4%	3%	5%	5%	3%		22%			
Certified values			65997	5003	6784	39101	223	124	26262	9		18		0.75805$	$4.0 \cdot 10^{-6}$
Relative difference			4%	7%	6%	8%	6%	3%	4%	-115%		21%			
NIST2709a	mean (n=7/72)		69913	17482	31860	18876	13466	501	11652	769		221		0.70814	$1.2 \cdot 10^{-5}$
NIST2709a	SD		3245	604	1234	602	238	12	565	35		8			
NIST2709a	RSD		5%	3%	4%	3%	2%	2%	5%	5%		4%			
Certified values			73566	19297	33573	20754	14474	542	11870	698		239		0.70815‖	$5.0 \cdot 10^{-5}$
Relative difference			5%	9%	5%	9%	7%	8%	2%	-10%		7%			
SRM-987	mean (n=/1910)													0.71028	$2 \cdot 10^{-6}$
Certified values														0.71025	$1.5 \cdot 10^{-5}$
Sr-ICP	mean (n=/240)													0.70752	$7 \cdot 10^{-6}$

* Pedogenic soil-horizon classification from Bernhard et al. (2018).

† Balcaen et al. (2005)

‡ Weis et al. (2006)

$ Ma et al. (2013)

‖ Uhlig and von Blanckenburg (2019)

Table S3.3: Concentration of the bio-available fraction, comprised of the water-soluble and the exchangeable fraction, in Pan de Azúcar, Santa Gracia, La Campana, and Nahuelbuta for the S- and N-facing regolith profiles, respectively. P-accessibility in the bio-available fraction has been determined by Brucker and Spohn (2019) using a modified Hedley sequential P fractionation method and comprises the water-extractable P and the labile P. The $^{87}Sr/^{86}Sr$ ratios of the bio-available fraction were determined on pooled samples from both, the milli-Q H_2O and the NH_4OAc leach.

Soil profile depth	IGSN	sample type*	Al	Ca	Fe	K	Mg	Mn	Na	P	Si	Sr	$^{87}Sr/^{86}Sr$	2SE
			[µg g^{-1}]											[-]
Pan de Azúcar	AZPED21	**Regosol**												
0 - 5	GFRO100UD	Aycz	0.5	3558	<0.1	299	578	<0.04	3301	18.6	65.6	7.88	0.70935	$7.21 \cdot 10^{-6}$
5 - 10	GFRO100UE	Bycz	0.5	6323	<0.1	265	447	<0.04	3114	10.1	86.9	6.61	0.70939	$6.8 \cdot 10^{-6}$
10 - 20	GFRO100UF	Bycz	n.d.	n.d.	n.d.	n.d.	n.d.	n.d.	n.d.	9.5	n.d.	n.d.	n.d.	n.d.
20 - 40	GFRO100UG	BCycz	n.d.	n.d.	n.d.	n.d.	n.d.	n.d.	n.d.	10.4	n.d.	n.d.	n.d.	n.d.
40 - 60	GFRO100UH	C	n.d.	n.d.	n.d.	n.d.	n.d.	n.d.	n.d.	0.0	n.d.	n.d.	n.d.	n.d.
60 - 80	GFRO100UJ	C	n.d.	n.d.	n.d.	n.d.	n.d.	n.d.	n.d.	9.3	n.d.	n.d.	n.d.	n.d.
80 - 100	GFRO100UK	C	0.6	878	<0.1	155	100	0.24	833	n.d.	22.8	1.80	0.71016	$2.87 \cdot 10^{-6}$
AZPED50		Regosol												
0 - 5	GFRO100TX	Aycz	0.5	3308	<0.1	139	232	<0.04	604	36.2	48.6	4.56	0.70991	$1.716 \cdot 10^{-5}$
5 - 10	GFRO100TY	Bycz	n.d.	n.d.	n.d.	n.d.	n.d.	n.d.	n.d.	11.8	n.d.	n.d.	n.d.	n.d.
10 - 20	GFRO100TZ	Bycz	1.4	4838	<0.1	83	122	1.06	393	0.00	53.5	2.89	0.71096	$1.184 \cdot 10^{-5}$
20 - 40	GFRO100U0	BCycz	n.d.	n.d.	n.d.	n.d.	n.d.	n.d.	n.d.	10.1	n.d.	n.d.	n.d.	n.d.
40 - 60	GFRO100U1	BCycz	n.d.	n.d.	n.d.	n.d.	n.d.	n.d.	n.d.	n.d.	n.d.	n.d.	n.d.	n.d.
60 - 80	GFRO100U2	C	n.d.	n.d.	n.d.	n.d.	n.d.	n.d.	n.d.	n.d.	n.d.	n.d.	n.d.	n.d.
80 - 100	GFRO100U3	C	n.d.	n.d.	n.d.	n.d.	n.d.	n.d.	n.d.	n.d.	n.d.	n.d.	n.d.	n.d.
100 - 120	GFRO100U4	C	n.d.	n.d.	n.d.	n.d.	n.d.	n.d.	n.d.	n.d.	n.d.	n.d.	n.d.	n.d.
120 - 140	GFRO100U5	C	1.0	2585	<0.1	107	136	0.36	574	n.d.	47.1	1.72	0.71139	$7.38 \cdot 10^{-6}$
Santa Gracia, SGPED70		**Leptosol**												
0 - 5	GFRO100VF	Ah	14.38	799	9.48	159	303	0.36	14.6	55.2	30.3	6.85	0.70623	$8.19 \cdot 10^{-6}$
5 - 10	GFRO100VG	Ah	14.12	744	8.93	131	314	0.23	12.6	42.9	29.7	6.67	0.70621	$1.226 \cdot 10^{-5}$
10 - 20	GFRO100VH	Bwi	14.26	1412	9.14	79.5	626	5.50	33.6	33.1	44.2	10.3	0.70614	$8.18 \cdot 10^{-6}$
20 - 40	GFRO100VJ	C	10.46	1316	6.97	34.3	609	5.05	35.2	25.6	37.7	9.35	0.70618	$1.09 \cdot 10^{-5}$
40 - 60	GFRO100VK	C	8.94	951	6.80	15.1	454	1.75	28.9	22.8	29.7	6.94	0.70623	$1.285 \cdot 10^{-5}$
60 - 80	GFRO100VL	C	8.22	739	7.24	10.7	372	1.44	26.7	19.2	26.2	5.49	0.70626	$7.69 \cdot 10^{-6}$
80 - 100	GFRO100VM	C	7.95	793	6.81	12.9	407	2.00	29.8	6.2	29.7	5.88	0.70625	$2.43 \cdot 10^{-6}$
100 - 120	GFRO100VN	C	6.6	525	6.71	11.0	298	2.66	26.7	6.7	27.6	3.86	0.70627	$7.98 \cdot 10^{-6}$
120 - 140	GFRO100VP	C	7.7	422	8.26	8.53	274	2.24	31.8	6.2	24.7	3.18	0.70623	$5.33 \cdot 10^{-6}$
140 - 160	GFRO100VQ	C	6.1	350	7.35	6.71	226	1.32	32.4	4.6	22.7	2.51	0.70617	$6.02 \cdot 10^{-6}$

Continued on the next page.

Table S3.3: ...continuation

Soil profile depth	IGSN	sample type*	Al	Ca	Fe	K	Mg	Mn	Na	P	Si	Sr	$^{87}Sr/^{86}Sr$	2SE
							[µg g^{-1}]							[-]
160 - 180	GFRO100VR	C	7.6	473	10.42	7.55	289	2.11	52.1	n.d.	25.7	3.14	0.70614	$5.52 \cdot 10^{-6}$
SGPED40		Cambisol												
0 - 5	GFRO100UU	Ah	39.3	670	22.1	131	102	0.51	18.1	45.5	25.2	5.08	0.70639	$8.47 \cdot 10^{-6}$
5 - 10	GFRO100UV	Ah	31.6	661	17.2	67.4	104	0.29	16.6	40.3	22.0	5.17	0.70630	$5.21 \cdot 10^{-6}$
10 - 20	GFRO100V3	Bw	29.2	760	16.3	41.3	141	0.20	22.9	37.2	23.2	5.92	0.70623	$6.14 \cdot 10^{-6}$
20 - 40	GFRO100UW	BCw	21.9	768	12.7	28.3	172	0.43	34.5	34.8	22.6	5.87	0.70618	$1.441 \cdot 10^{-5}$
40 - 60	GFRO100UX	BCw	20.8	879	12.2	19.4	357	0.75	52.8	24.6	26.5	6.54	0.70617	$9.99 \cdot 10^{-6}$
60 - 80	GFRO100UY	C	17.3	844	10.7	17.5	475	0.50	75.8	20.9	30.3	6.31	0.70619	$7.61 \cdot 10^{-6}$
80 - 100	GFRO100UZ	C	18.1	752	13.1	14.3	481	0.57	153	7.7	23.6	5.14	0.70618	$2.85 \cdot 10^{-6}$
100 - 120	GFRO100V0	C	12.1	483	12.3	9.47	299	0.73	164	25.6	23.2	3.30	0.70618	$7.63 \cdot 10^{-6}$
120 - 140	GFRO100V1	C	12.4	278	13.3	7.06	158	0.97	121	n.d.	22.4	1.93	0.70616	$7.42 \cdot 10^{-6}$
140 - 160	GFRO100V2	C	13.4	240	14.0	6.94	135	1.26	124	n.d.	22.6	1.69	0.70611	$9.32 \cdot 10^{-6}$
160 - 180	GFRO100CR	C	12.0	210	13.5	6.17	119	0.97	138	n.d.	20.2	1.49	0.70608	$8.23 \cdot 10^{-6}$
***La Campana**, LCPED40*		**Cambisol**												
0 - 5	GFRO1002V	Ah	57.3	2349	44.2	212.4	188	41.5	7.16	85.9	46.0	13.0	0.70483	$6.77 \cdot 10^{-6}$
5 - 10	GFRO1002W	Bw1	74.9	1219	56.6	276	137	21.7	10.1	70.2	45.4	8.02	0.70484	$2.92 \cdot 10^{-6}$
10 - 20	GFRO1002X	Bw1	146	790	106	242	112	21.7	12.3	76.1	47.2	5.83	0.70456	$2.8245 \cdot 10^{-4}$
20 - 40	GFRO1002Y	Bw2	41.0	981	26.5	89	135	16.4	13.2	33.2	33.6	7.58	0.70476	$9.92 \cdot 10^{-6}$
40 - 60	GFRO1002Z	BCw	19.8	1089	10.5	50.2	173	20.4	16.4	26.2	23.8	8.31	0.70470	$4.57 \cdot 10^{-6}$
60 - 80	GFRO10030	BCw	17.9	1018	8.57	53.9	183	11.6	20.0	28.3	23.8	7.78	0.70472	$1.07 \cdot 10^{-5}$
80 - 100	GFRO100WG	BCw	23.0	1096	12.1	54.1	196	8.33	23.4	35.5	29.5	8.55	0.70476	$1.166 \cdot 10^{-5}$
100 - 120	GFRO100WF	C	15.7	742	8.24	35.8	151	8.69	21.3	18.3	27.7	5.64	0.70477	$1.225 \cdot 10^{-5}$
120 - 140	GFRO100WE	C	10.5	398	9.59	25.5	84.7	5.06	14.5	0.0	22.3	3.00	0.70488	$7.94 \cdot 10^{-6}$
LCPED20		Cambisol												
0 - 5	GFRO10029	Ah1	12.4	3252	9.66	309	268	81.3	5.90	61.5	52.9	16.54	0.70583	$9.36 \cdot 10^{-6}$
5 - 10	GFRO1002A	Ah1	40.5	1323	23.6	149	105	32.2	5.03	28.9	27.0	7.52	0.70580	$6.69 \cdot 10^{-6}$
10 - 20	GFRO1002B	Ah2	39.5	1016	22.3	147	84.4	14.0	5.33	25.3	21.3	6.20	0.70575	$1.035 \cdot 10^{-5}$
20 - 40	GFRO1002C	Ah3	34.6	886	19.1	111	93.2	6.81	5.19	31.3	21.2	5.80	0.70570	$8.72 \cdot 10^{-6}$
40 - 60	GFRO1002D	Bw	30.2	605	16.9	65.3	106	6.09	5.96	32.3	16.6	4.37	0.70565	$9.61 \cdot 10^{-6}$
60 - 80	GFRO100VU	BCw	20.0	595	10.6	61.6	121	3.75	6.56	31.3	17.7	4.58	0.70559	$5.5 \cdot 10^{-6}$
80 - 100	GFRO100VV	BCw	16.7	578	9.00	35.1	104	3.27	10.6	36.8	15.5	4.66	0.70547	$8.59 \cdot 10^{-6}$
100 - 120	GFRO100VW	BCw	12.3	402	7.30	26.4	73.5	5.36	9.66	33.1	14.7	3.39	0.70543	$1.063 \cdot 10^{-5}$
120 - 140	GFRO100VY	C	9.06	295	5.08	19.5	56.8	4.84	8.59	22.9	13.5	2.47	0.70537	$9.86 \cdot 10^{-6}$

Continued on the next page.

Table S3.3: ...continuation

Soil profile depth	IGSN	sample type*	Al	Ca	Fe	K	Mg	Mn	Na	P	Si	Sr	$^{87}Sr/^{86}Sr$	2SE
			[µg g^{-1}]										[-]	
140 - 160	GFRO100VX	C	6.34	400	3.09	23.9	80.4	4.11	11.3	17.7	16.5	3.25	0.70537	$8.8 \cdot 10^{-6}$
***Nahuelbuta**, NAPED40*		**umbric Podzol**												
0 - 5	GFRO1001R	Ah1	28.6	170	8.54	122	24.6	48.0	13.0	74.5	17.0	2.09	0.71335	$9.61 \cdot 10^{-6}$
5 - 10	GFRO1001S	Ah1	26.8	146	6.23	89.2	26.7	86.0	19.5	50.0	16.0	1.84	0.71336	$8.2 \cdot 10^{-6}$
10 - 20	GFRO1001T	Ah1	19.9	117	1.62	80.0	22.8	24.1	30.3	46.9	15.5	1.46	0.71335	$7.38 \cdot 10^{-6}$
20 - 40	GFRO1001U	Ah2	23.4	54.6	5.56	52.9	12.0	10.8	22.7	37.1	15.2	0.77	0.71336	$5.6 \cdot 10^{-6}$
40 - 60	GFRO1001V	Bw	2.40	28.6	0.12	20.8	6.59	7.78	20.3	27.3	15.1	0.60	0.71366	$5.08 \cdot 10^{-6}$
60 - 80	GFRO100X0	BCs1	0.76	39.1	0.01	14.9	9.35	4.93	18.3	15.5	14.1	0.72	0.71378	$4.66 \cdot 10^{-6}$
80 - 100	GFRO10050	BCs2	0.27	42.6	0.01	10.3	9.87	2.40	3.88	14.4	8.30	0.65	0.71389	$6.5 \cdot 10^{-6}$
100 - 120	GFRO100WZ	C1	0.31	74.6	0.00	14.9	16.0	9.13	12.2	0.00	13.7	0.92	0.71406	$3.64 \cdot 10^{-6}$
120 - 140	GFRO100WY	C1	0.41	111	0.00	19.6	21.7	7.20	16.5	13.8	10.5	1.29	0.71421	$4.38 \cdot 10^{-6}$
140 - 160	GFRO100WX	C1	0.52	118	0.00	22.2	22.9	4.37	15.4	22.3	14.3	1.40	0.71434	$5.27 \cdot 10^{-6}$
160 - 180	GFRO100WV	C2	0.21	77.3	0.00	16.7	14.1	4.64	14.1	n.d.	10.4	0.88	0.71440	$2.57 \cdot 10^{-6}$
180 - 200	GFRO100WW	C2	0.18	100	0.00	20.1	17.6	4.37	14.5	n.d.	9.0	1.23	0.71442	$8.13 \cdot 10^{-6}$
NAPED20		**orthodystric Umbrisol**												
0 - 5	GFRO10019	Ah1	70.0	129	13.5	189	41.7	124	20.9	147	21.1	1.73	0.70895	$1.01 \cdot 10^{-6}$
5 - 10	GFRO10018	Ah1	64.0	28.3	11.4	144	23.9	50.3	16.3	102	19.3	0.33	0.70891	$3.03 \cdot 10^{-6}$
10 - 20	GFRO1001A	Ah2	54.3	15.4	8.94	120	21.2	34.7	14.2	89.8	17.2	0.17	0.70885	$5.47 \cdot 10^{-6}$
20 - 40	GFRO1001B	Ah3	40.2	34.8	1.36	70.4	22.2	20.7	60.0	62.1	17.5	0.15	0.70814	$7.79 \cdot 10^{-6}$
40 - 60	GFRO1001C	Bw1	8.41	10.5	0.05	24.1	3.87	8.15	7.93	25.1	20.3	0.09	0.70964	$3.13 \cdot 10^{-6}$
60 - 80	GFRO1001D	Bw2	9.27	7.84	0.02	22.3	3.81	7.45	7.64	12.4	16.6	0.09	0.70935	$3.52 \cdot 10^{-6}$
80 - 100	GFRO100WP	BCw	3.90	9.13	0.01	13.3	3.53	5.07	9.08	15.5	14.1	0.19	0.70990	$6.87 \cdot 10^{-6}$
100 - 120	GFRO100WN	C1	2.22	9.53	0.01	12.3	3.32	2.10	10.9	51.6	16.5	0.26	0.70989	$4.3 \cdot 10^{-6}$
120 - 140	GFRO100WM	C2	1.05	7.32	0.00	11.9	2.01	0.77	11.5	56.8	22.7	0.37	0.71004	$1.116 \cdot 10^{-5}$
140 - 160	GFRO100WL	C2	1.38	8.53	0.02	15.1	2.33	1.06	14.5	81.8	20.1	0.58	0.70922	$5.03 \cdot 10^{-6}$
160 - 180	GFRO100WK	C2	5.78	13.1	0.00	30.2	5.83	6.61	13.5	88.1	7.91	0.36	0.70990	$2.688 \cdot 10^{-5}$
180 - 200	GFRO100WQ	C3	2.68	12.8	0.00	25.7	4.01	2.48	10.6	1.99	11.5	0.49	0.70932	$7.41 \cdot 10^{-6}$
200 - 220	GFRO100WR	C3	1.67	12.6	0.00	17.2	3.29	1.61	6.12	n.d.	3.5	0.51	0.70940	$3.95 \cdot 10^{-6}$
220 - 240	GFRO100WJ	C3	2.46	12.9	0.00	16.7	2.74	1.57	9.62	n.d.	5.17	0.86	0.70897	$5.24 \cdot 10^{-6}$
240 - 260	GFRO100WH	C3	2.97	19.6	0.00	17.2	2.19	1.86	17.0	n.d.	10.61	0.96	0.70885	$6.48 \cdot 10^{-6}$
bio-available fraction of international reference materials														
TILL #1			32.3	1204	42.69	80.5	169	95.11	62.3	6.2	100.9	3.03	0.70429	$7.52 \cdot 10^{-6}$

Continued on the next page.

Table S3.3: ...continuation

Soil profile depth	IGSN	sample type*	Al	Ca	Fe	K	Mg	Mn	Na	P	Si	Sr	$^{87}Sr/^{86}Sr$	2SE
							[µg g^{-1}]						[-]	
TILL #2			29.1	1033	42.70	76.0	170	77.68	55.4	6.2	52.0	2.47	0.71016	$9.14 \cdot 10^{-6}$
TILL #3			83.1	1042	111.61	84.4	180	104.99	61.0	5.7	60.7	2.83	0.71020	$8.39 \cdot 10^{-6}$
TILL #4			24.4	1013	32.18	76.5	175	139.92	58.1	4.2	49.3	2.75	0.71016	$1.63 \cdot 10^{-5}$
TILL #6			44.5	1243	29.73	219.8	216	258.01	125.7	13.4	94.9	4.70	0.71017	$9.4 \cdot 10^{-6}$
TILL #7			29.4	1032	42.44	73.2	171	79.55	56.0	5.7	75.6	2.94	0.71017	$1.06 \cdot 10^{-5}$
TILL-1	**mean**		40.5	1094	50.23	101.7	180	125.87	69.8	6.9	72.2	3.12		
TILL-1	SD		22.0	101	30.62	58.0	18	68.60	27.6	3.3	22.0	0.80		
TILL-1	RSD		54%	9%	61%	57%	10%	54%	39%	47%	30%	26%		
NIST #1			107.2	12711	80.20	755.8	939	23.29	301.0	49.5	386.9	60.67	0.70765	$6.1 \cdot 10^{-6}$
NIST #2			68.6	10972	48.46	713.3	965	26.07	268.5	50.0	320.7	59.01	0.70765	$9.72 \cdot 10^{-6}$
NIST #3			37.4	9248	25.79	818.6	951	25.42	296.6	43.0	417.6	59.70	0.70768	$2.4 \cdot 10^{-6}$
NIST #4			48.0	11308	33.71	726.0	933	21.79	287.5	56.5	305.4	60.89	0.70768	$1.19 \cdot 10^{-5}$
NIST #6			86.9	9530	115.33	463.2	868	29.61	203.4	50.9	356.8	45.72	0.70765	$9.4 \cdot 10^{-7}$
NIST #7			119.6	10829	77.52	742.0	1033	31.28	276.2	88.1	506.5	62.35	0.70765	$3.18 \cdot 10^{-6}$
NIST2709a	**mean**		78.0	10767	63.50	703.2	948	26.25	272.2	56.4	382.3	58.06		
MIST2709a	SD		32.5	1261	33.76	123.1	53	3.60	35.8	16.1	73.6	6.15		
NIST2709a	RSD		42%	12%	53%	18%	6%	14%	13%	29%	19%	11%		

* Pedogenic soil-horizon classification from Bernhard et al. (2018).

n.d. not determined

Table S3.4: Concentration of the water-soluble and exchangeable fraction comprising the bio-available fraction in in Pan de Azúcar, Santa Gracia, La Campana, and Nahuelbuta for the S- and N-facing regolith profiles, respectively. P-accessibility in the bio-available fraction has been determined by Brucker and Spohn (2019) using a modified Hedley sequential P fractionation method and comprises the water-extractable P and the labile P.

			water-soluble fraction										exchangeable fraction									
Soil profile depth	IGSN	sample type*	Al	Ca	Fe	K	Mg	Mn	Na	P	Si	Sr	Al	Ca	Fe	K	Mg	Mn	Na	P	Si	Sr
			[µg g^{-1}]										[µg g^{-1}]									
Pan de Azúcar	AZPED21	**Regosol**																				
0 - 5	GFRO100UD	Aycz	0.20	705	<0.1	164	300	<0.04	3200	2.53	10.5	3.08	0.20	705	<0.1	164	300	<0.04	3200	2.53	10.5	3.08
5 - 10	GFRO100UE	Bycz	0.26	3268	<0.1	175	307	<0.04	3051	0.00	36.2	3.89	0.26	3268	<0.1	175	307	<0.04	3051	0.00	36.2	3.89
10 - 20	GFRO100UF	Bycz	n.d.	n.d.	n.d.	n.d.	n.d.	n.d.	n.d.	0.00	n.d.	n.d.	n.d.	n.d.	n.d.	n.d.	n.d.	n.d.	n.d.	0.00	n.d.	n.d.
20 - 40	GFRO100UG	BCycz	n.d.	n.d.	n.d.	n.d.	n.d.	n.d.	n.d.	0.00	n.d.	n.d.	n.d.	n.d.	n.d.	n.d.	n.d.	n.d.	n.d.	0.00	n.d.	n.d.
40 - 60	GFRO100UH	C	n.d.	n.d.	n.d.	n.d.	n.d.	n.d.	n.d.	0.00	n.d.	n.d.	n.d.	n.d.	n.d.	n.d.	n.d.	n.d.	n.d.	0.00	n.d.	n.d.
60 - 80	GFRO100UJ	C	n.d.	n.d.	n.d.	n.d.	n.d.	n.d.	n.d.	0.00	n.d.	n.d.	n.d.	n.d.	n.d.	n.d.	n.d.	n.d.	n.d.	0.00	n.d.	n.d.
80 - 100	GFRO100UK	C	0.42	375	<0.1	91.2	52.6	<0.04	797	n.d.	7.79	0.52	0.42	375	<0.1	91.2	52.6	<0.04	797	n.d.	7.79	0.52
AZPED50		Regosol																				
0 - 5	GFRO100TX	Aycz	0.25	560	<0.1	60.6	107	<0.04	565	2.92	10.2	1.43	0.25	560	<0.1	60.6	107	<0.04	565	2.92	10.2	1.43
5 - 10	GFRO100TY	Bycz	n.d.	n.d.	n.d.	n.d.	n.d.	n.d.	n.d.	0.00	n.d.	n.d.	n.d.	n.d.	n.d.	n.d.	n.d.	n.d.	n.d.	0.00	n.d.	n.d.
10 - 20	GFRO100TZ	Bycz	1.02	2867	<0.1	50.0	90.0	<0.04	378	0.00	29.7	1.97	1.02	2867	<0.1	50.0	90.0	<0.04	378	0.00	29.7	1.97
20 - 40	GFRO100U0	BCycz	n.d.	n.d.	n.d.	n.d.	n.d.	n.d.	n.d.	0.00	n.d.	n.d.	n.d.	n.d.	n.d.	n.d.	n.d.	n.d.	n.d.	0.00	n.d.	n.d.
40 - 60	GFRO100U1	BCycz	n.d.	n.d.	n.d.	n.d.	n.d.	n.d.	n.d.	n.d.	n.d.	n.d.	n.d.	n.d.	n.d.	n.d.	n.d.	n.d.	n.d.	n.d.	n.d.	n.d.
60 - 80	GFRO100U2	C	n.d.	n.d.	n.d.	n.d.	n.d.	n.d.	n.d.	n.d.	n.d.	n.d.	n.d.	n.d.	n.d.	n.d.	n.d.	n.d.	n.d.	n.d.	n.d.	n.d.
80 - 100	GFRO100U3	C	n.d.	n.d.	n.d.	n.d.	n.d.	n.d.	n.d.	n.d.	n.d.	n.d.	n.d.	n.d.	n.d.	n.d.	n.d.	n.d.	n.d.	n.d.	n.d.	n.d.
100 - 120	GFRO100U4	C	n.d.	n.d.	n.d.	n.d.	n.d.	n.d.	n.d.	n.d.	n.d.	n.d.	n.d.	n.d.	n.d.	n.d.	n.d.	n.d.	n.d.	n.d.	n.d.	n.d.
120 - 140	GFRO100U5	C	0.69	45.5	<0.1	67.3	90.9	<0.04	556	n.d.	15.4	0.95	0.69	45.5	<0.1	67.3	90.9	<0.04	556	n.d.	15.4	0.95
Santa Gracia, SGPED70		**Leptosol**																				
0 - 5	GFRO100VF	Ah	14.3	32.2	9.48	41.2	18.0	0.14	11.0	25.7	16.9	0.25	14.3	32.2	9.48	41.2	18.0	0.14	11.0	25.7	16.9	0.25
5 - 10	GFRO100VG	Ah	14.0	13.4	8.93	26.4	9.07	0.09	8.73	17.6	17.5	0.10	14.0	13.4	8.93	26.4	9.07	0.09	8.73	17.6	17.5	0.10
10 - 20	GFRO100VH	Bwi	14.1	12.5	9.14	8.47	8.78	0.05	20.7	14.3	22.4	0.09	14.1	12.5	9.14	8.47	8.78	0.05	20.7	14.3	22.4	0.09
20 - 40	GFRO100VJ	C	10.4	17.5	6.97	4.00	11.8	0.09	23.3	11.5	16.0	0.12	10.4	17.5	6.97	4.00	11.8	0.09	23.3	11.5	16.0	0.12
40 - 60	GFRO100VK	C	8.85	6.63	6.80	1.64	5.00	<0.04	17.7	9.97	13.2	<0.05	8.85	6.63	6.80	1.64	5.00	<0.04	17.7	9.97	13.2	<0.05
60 - 80	GFRO100VL	C	8.13	2.57	7.24	1.08	2.82	<0.04	14.1	19.2	12.4	<0.05	8.13	2.57	7.24	1.08	2.82	<0.04	14.1	19.2	12.4	<0.05
80 - 100	GFRO100VM	C	7.85	3.63	6.81	1.45	3.83	0.05	17.2	6.15	15.0	<0.05	7.85	3.63	6.81	1.45	3.83	0.05	17.2	6.15	15.0	<0.05
100 - 120	GFRO100VN	C	6.50	1.33	6.71	1.09	2.17	0.07	13.5	6.65	17.1	<0.05	6.50	1.33	6.71	1.09	2.17	0.07	13.5	6.65	17.1	<0.05
120 - 140	GFRO100VP	C	7.61	0.76	8.26	0.67	1.95	0.05	13.9	6.15	13.9	<0.05	7.61	0.76	8.26	0.67	1.95	0.05	13.9	6.15	13.9	<0.05
140 - 160	GFRO100VQ	C	6.08	0.78	7.35	0.43	1.75	0.04	11.9	4.59	11.7	<0.05	6.08	0.78	7.35	0.43	1.75	0.04	11.9	4.59	11.7	<0.05
160 - 180	GFRO100VR	C	7.57	0.79	10.4	0.48	2.26	0.08	15.7	n.d.	14.0	<0.05	7.57	0.79	10.4	0.48	2.26	0.08	15.7	n.d.	14.0	<0.05

Continued on the next page.

Table S3.4: ...continuation

			water-soluble fraction										exchangeable fraction									
Soil profile depth	IGSN	sample type*	Al	Ca	Fe	K	Mg	Mn	Na	P	Si	Sr	Al	Ca	Fe	K	Mg	Mn	Na	P	Si	Sr
			[µg g^{-1}]										[µg g^{-1}]									
SGPED40		Cambisol																				
0 - 5	GFRO100UU	Ah	39.1	50.4	22.1	41.8	15.1	0.51	13.8	18.2	13.3	0.35	39.1	50.4	22.1	41.8	15.1	0.51	13.8	18.2	13.3	0.35
5 - 10	GFRO100UV	Ah	31.4	24.4	17.2	13.2	7.94	0.29	11.3	19.0	9.95	0.16	31.4	24.4	17.2	13.2	7.94	0.29	11.3	19.0	9.95	0.16
10 - 20	GFRO100V3	Bw	29.0	18.8	16.3	6.60	7.35	0.20	15.8	17.8	9.97	<0.05	29.0	18.8	16.3	6.60	7.35	0.20	15.8	17.8	9.97	<0.05
20 - 40	GFRO100UW	BCw	21.7	9.16	12.7	3.52	4.58	0.17	21.7	16.9	8.45	<0.05	21.7	9.16	12.7	3.52	4.58	0.17	21.7	16.9	8.45	<0.05
40 - 60	GFRO100UX	BCw	20.7	5.15	12.2	2.38	3.66	<0.04	27.7	12.6	9.38	<0.05	20.7	5.15	12.2	2.38	3.66	<0.04	27.7	12.6	9.38	<0.05
60 - 80	GFRO100UY	C	17.1	3.21	10.7	1.42	2.44	<0.04	31.9	7.87	12.4	<0.05	17.1	3.21	10.7	1.42	2.44	<0.04	31.9	7.87	12.4	<0.05
80 - 100	GFRO100UZ	C	17.8	0.89	13.1	0.78	1.31	<0.04	31.3	7.71	7.84	<0.05	17.8	0.89	13.1	0.78	1.31	<0.04	31.3	7.71	7.84	<0.05
100 - 120	GFRO100V0	C	11.8	0.59	12.3	0.45	1.04	<0.04	22.9	10.7	6.94	<0.05	11.8	0.59	12.3	0.45	1.04	<0.04	22.9	10.7	6.94	<0.05
120 - 140	GFRO100V1	C	12.3	0.49	13.3	0.45	1.07	0.14	20.2	n.d.	7.40	<0.05	12.3	0.49	13.3	0.45	1.07	0.14	20.2	n.d.	7.40	<0.05
140 - 160	GFRO100V2	C	13.3	0.50	14.0	0.50	1.10	0.25	21.2	n.d.	10.3	<0.05	13.3	0.50	14.0	0.50	1.10	0.25	21.2	n.d.	10.3	<0.05
160 - 180	GFRO100CR	C	11.9	0.53	13.5	0.44	1.01	0.20	20.7	n.d.	9.28	<0.05	11.9	0.53	13.5	0.44	1.01	0.20	20.7	n.d.	9.28	<0.05
***La Campana**, LCPED40*		**Cambisol**																				
0 - 5	GFRO1002V	Ah	56.9	32.3	43.7	49.0	9.58	1.21	3.43	42.2	23.2	0.19	56.9	32.3	43.7	49.0	9.58	1.21	3.43	42.2	23.2	0.19
5 - 10	GFRO1002W	Bw1	74.6	119	56.5	112	25.7	1.48	6.14	36.3	33.2	0.68	74.6	119	56.5	112	25.7	1.48	6.14	36.3	33.2	0.68
10 - 20	GFRO1002X	Bw1	146	18.9	106	60.6	11.3	3.99	7.60	29.5	37.7	0.12	146	18.9	106	60.6	11.3	3.99	7.60	29.5	37.7	0.12
20 - 40	GFRO1002Y	Bw2	41.0	11.0	26.5	12.5	4.30	0.88	6.58	11.7	23.7	0.07	41.0	11.0	26.5	12.5	4.30	0.88	6.58	11.7	23.7	0.07
40 - 60	GFRO1002Z	BCw	19.8	14.6	10.5	5.08	4.58	0.81	7.47	9.76	12.9	0.10	19.8	14.6	10.5	5.08	4.58	0.81	7.47	9.76	12.9	0.10
60 - 80	GFRO10030	BCw	17.9	8.57	8.57	5.10	3.27	0.42	9.67	5.33	12.3	0.05	17.9	8.57	8.57	5.10	3.27	0.42	9.67	5.33	12.3	0.05
80 - 100	GFRO100WG	BCw	23.0	5.06	12.1	4.75	2.45	0.26	9.89	15.6	13.3	<0.05	23.0	5.06	12.1	4.75	2.45	0.26	9.89	15.6	13.3	<0.05
100 - 120	GFRO100WF	C	15.7	6.24	8.24	4.45	2.75	0.24	10.9	6.45	13.1	<0.05	15.7	6.24	8.24	4.45	2.75	0.24	10.9	6.45	13.1	<0.05
120 - 140	GFRO100WE	C	10.5	5.25	9.59	5.05	2.86	0.24	8.30	n.d.	9.92	<0.05	10.5	5.25	9.59	5.05	2.86	0.24	8.30	n.d.	9.92	<0.05
LCPED20		Cambisol																				
0 - 5	GFRO10029	Ah1	11.4	155	6.45	109	22.6	0.07	3.71	23.8	14.4	0.69	11.4	155	6.45	109	22.6	0.07	3.71	23.8	14.4	0.69
5 - 10	GFRO1002A	Ah1	39.9	56.9	23.3	43.4	10.2	0.45	3.17	8.74	13.0	0.28	39.9	56.9	23.3	43.4	10.2	0.45	3.17	8.74	13.0	0.28
10 - 20	GFRO1002B	Ah2	39.2	37.2	22.2	34.0	7.14	0.34	3.33	6.01	11.0	0.19	39.2	37.2	22.2	34.0	7.14	0.34	3.33	6.01	11.0	0.19
20 - 40	GFRO1002C	Ah3	34.3	24.9	19.0	20.3	5.76	0.23	2.91	4.14	12.1	0.13	34.3	24.9	19.0	20.3	5.76	0.23	2.91	4.14	12.1	0.13
40 - 60	GFRO1002D	Bw	30.0	14.0	16.9	10.8	4.70	0.33	3.62	11.5	9.86	0.08	30.0	14.0	16.9	10.8	4.70	0.33	3.62	11.5	9.86	0.08
60 - 80	GFRO100VU	BCw	19.9	7.75	10.6	8.91	2.74	0.15	3.75	10.4	9.82	<0.05	19.9	7.75	10.6	8.91	2.74	0.15	3.75	10.4	9.82	<0.05
80 - 100	GFRO100VV	BCw	16.6	5.30	9.00	4.11	1.88	0.10	6.28	9.31	7.82	<0.05	16.6	5.30	9.00	4.11	1.88	0.10	6.28	9.31	7.82	<0.05
100 - 120	GFRO100VW	BCw	12.3	4.23	7.30	3.40	1.40	0.18	5.99	11.4	8.25	<0.05	12.3	4.23	7.30	3.40	1.40	0.18	5.99	11.4	8.25	<0.05
120 - 140	GFRO100VY	C	9.01	2.93	5.08	2.96	1.08	0.12	5.44	3.06	7.40	<0.05	9.01	2.93	5.08	2.96	1.08	0.12	5.44	3.06	7.40	<0.05

Continued on the next page.

Table S3.4: ...continuation

Soil profile depth	IGSN	sample type*	water-soluble fraction [µg g^{-1}]										exchangeable fraction [µg g^{-1}]									
			Al	Ca	Fe	K	Mg	Mn	Na	P	Si	Sr	Al	Ca	Fe	K	Mg	Mn	Na	P	Si	Sr
140 - 160	GFRO100VX	C	6.29	2.52	3.09	2.77	1.03	0.08	6.85	0.00	6.23	<0.05	6.29	2.52	3.09	2.77	1.03	0.08	6.85	0.00	6.23	<0.05
***Nahuelbuta**, NAPED40*		**umbric Podzol**																				
0 - 5	GFRO1001R	Ah1	15.7	7.56	8.13	21.3	3.16	0.34	8.21	1.92	9.86	0.07	15.7	7.56	8.13	21.3	3.16	0.34	8.21	1.92	9.86	0.07
5 - 10	GFRO1001S	Ah1	11.3	7.47	5.65	14.0	3.70	0.72	12.8	1.81	8.09	0.07	11.3	7.47	5.65	14.0	3.70	0.72	12.8	1.81	8.09	0.07
10 - 20	GFRO1001T	Ah1	2.68	27.1	0.90	20.2	10.5	9.15	24.2	1.47	9.39	0.28	2.68	27.1	0.90	20.2	10.5	9.15	24.2	1.47	9.39	0.28
20 - 40	GFRO1001U	Ah2	11.6	3.43	5.28	4.91	1.95	1.44	14.5	1.55	8.74	<0.05	11.6	3.43	5.28	4.91	1.95	1.44	14.5	1.55	8.74	<0.05
40 - 60	GFRO1001V	Bw	0.22	1.57	<0.1	1.15	0.58	0.94	12.8	1.47	7.16	<0.05	0.22	1.57	<0.1	1.15	0.58	0.94	12.8	1.47	7.16	<0.05
60 - 80	GFRO100X0	BCs1	<0.18	1.48	<0.1	0.98	0.48	0.43	11.9	0.76	5.80	<0.05	<0.18	1.48	<0.1	0.98	0.48	0.43	11.9	0.76	5.80	<0.05
80 - 100	GFRO10050	BCs2	<0.18	<0.2	<0.1	<0.1	<0.1	<0.04	<0.3	1.57	<0.2	<0.05	<0.18	<0.2	<0.1	<0.1	<0.1	<0.04	<0.3	1.57	<0.2	<0.05
100 - 120	GFRO100WZ	C1	<0.18	2.83	<0.1	1.22	0.80	0.78	8.14	0.00	6.49	<0.05	<0.18	2.83	<0.1	1.22	0.80	0.78	8.14	0.00	6.49	<0.05
120 - 140	GFRO100WY	C1	<0.18	2.75	<0.1	0.92	0.36	0.17	9.32	1.31	5.16	<0.05	<0.18	2.75	<0.1	0.92	0.36	0.17	9.32	1.31	5.16	<0.05
140 - 160	GFRO100WX	C1	<0.18	0.75	<0.1	0.74	0.20	0.06	7.41	0.00	8.47	<0.05	<0.18	0.75	<0.1	0.74	0.20	0.06	7.41	0.00	8.47	<0.05
160 - 180	GFRO100WV	C2	<0.18	2.66	<0.1	0.90	0.34	0.14	8.48	n.d.	5.14	<0.05	<0.18	2.66	<0.1	0.90	0.34	0.14	8.48	n.d.	5.14	<0.05
180 - 200	GFRO100WW	C2	<0.18	0.62	<0.1	0.69	0.15	0.05	6.93	n.d.	3.11	<0.05	<0.18	0.62	<0.1	0.69	0.15	0.05	6.93	n.d.	3.11	<0.05
NAPED20		**orthodystric Umbrisol**																				
0 - 5	GFRO10019	Ah1	38.0	15.4	8.57	63.9	9.36	19.5	15.7	2.81	16.2	0.18	38.0	15.4	8.57	63.9	9.36	19.5	15.7	2.81	16.2	0.18
5 - 10	GFRO10018	Ah1	28.6	4.67	7.82	46.2	7.75	12.5	12.5	3.74	15.2	<0.05	28.6	4.67	7.82	46.2	7.75	12.5	12.5	3.74	15.2	<0.05
10 - 20	GFRO1001A	Ah2	20.8	2.93	5.92	34.9	7.76	10.5	10.7	1.73	14.5	<0.05	20.8	2.93	5.92	34.9	7.76	10.5	10.7	1.73	14.5	<0.05
20 - 40	GFRO1001B	Ah3	21.5	26.4	0.24	25.4	16.4	12.6	49.2	0.00	15.2	0.09	21.5	26.4	0.24	25.4	16.4	12.6	49.2	0.00	15.2	0.09
40 - 60	GFRO1001C	Bw1	0.19	2.71	<0.1	3.04	1.09	3.17	5.49	1.18	16.8	<0.05	0.19	2.71	<0.1	3.04	1.09	3.17	5.49	1.18	16.8	<0.05
60 - 80	GFRO1001D	Bw2	0.15	1.53	<0.1	2.31	0.85	2.40	5.22	0.00	13.1	<0.05	0.15	1.53	<0.1	2.31	0.85	2.40	5.22	0.00	13.1	<0.05
80 - 100	GFRO100WP	BCw	<0.18	0.50	<0.1	0.46	<0.1	0.19	3.18	0.00	11.0	<0.05	<0.18	0.50	<0.1	0.46	<0.1	0.19	3.18	0.00	11.0	<0.05
100 - 120	GFRO100WN	C1	<0.18	0.80	<0.1	0.63	0.16	0.14	4.66	1.50	13.8	<0.05	<0.18	0.80	<0.1	0.63	0.16	0.14	4.66	1.50	13.8	<0.05
120 - 140	GFRO100WM	C2	<0.18	0.71	<0.1	0.49	<0.1	<0.04	4.34	2.73	18.6	<0.05	<0.18	0.71	<0.1	0.49	<0.1	<0.04	4.34	2.73	18.6	<0.05
140 - 160	GFRO100WL	C2	<0.18	0.83	<0.1	0.69	0.17	<0.04	6.11	2.50	17.4	<0.05	<0.18	0.83	<0.1	0.69	0.17	<0.04	6.11	2.50	17.4	<0.05
160 - 180	GFRO100WK	C2	<0.18	<0.2	<0.1	0.56	<0.1	<0.04	3.70	1.45	4.57	<0.05	<0.18	<0.2	<0.1	0.56	<0.1	<0.04	3.70	1.45	4.57	<0.05
180 - 200	GFRO100WQ	C3	<0.18	0.41	<0.1	0.94	<0.1	<0.04	3.26	1.99	8.32	<0.05	<0.18	0.41	<0.1	0.94	<0.1	<0.04	3.26	1.99	8.32	<0.05
200 - 220	GFRO100WR	C3	<0.18	<0.2	<0.1	<0.1	<0.1	<0.04	<0.3	n.d.	1.02	<0.05	<0.18	<0.2	<0.1	<0.1	<0.1	<0.04	<0.3	n.d.	1.02	<0.05
220 - 240	GFRO100WJ	C3	<0.18	<0.2	<0.1	<0.1	<0.1	<0.04	0.29	n.d.	<0.2	<0.05	<0.18	<0.2	<0.1	<0.1	<0.1	<0.04	0.29	n.d.	<0.2	<0.05
240 - 260	GFRO100WH	C3	<0.18	0.23	<0.1	0.50	<0.1	0.11	3.65	n.d.	4.18	<0.05	<0.18	0.23	<0.1	0.50	<0.1	0.11	3.65	n.d.	4.18	<0.05

Continued on the next page.

Table S3.4: ...continuation

Soil profile depth	IGSN	sample type*	water-soluble fraction Al	Ca	Fe	K	Mg	Mn	Na	P	Si	Sr	exchangeable fraction Al	Ca	Fe	K	Mg	Mn	Na	P	Si	Sr
			[µg g^{-1}]										[µg g^{-1}]									
			water-soluble fraction of international reference materials										exchangeable fraction of international reference materials									
TILL-1 #1			30.7	137	42.7	27.0	43.9	10.0	52.8	3.52	83.0	0.31	1.57	1067	<0.1	53.5	125	85.1	9.50	2.66	18.0	2.72
TILL-1 #2			27.4	151	42.0	23.9	48.6	11.6	46.5	3.93	35.0	<0.05	1.78	882	0.74	52.0	122	66.1	8.83	2.28	16.9	2.47
TILL-1 #3			80.8	128	110	26.0	47.9	12.6	48.0	5.71	41.9	0.25	2.32	914	1.12	58.4	132	92.4	13.0	<0.2	18.8	2.57
TILL-1 #4			22.3	132	30.7	25.2	44.2	8.72	48.0	2.16	24.5	0.27	2.06	881	1.47	51.2	131	131	10.2	2.05	24.8	2.48
TILL-1 #6			41.8	329	28.2	169	82.4	<0.04	113	13.4	69.4	2.25	2.61	914	1.52	50.9	134	258	12.6	<0.2	25.4	2.46
TILL-1 #7			26.9	159	41.2	26.2	51.4	12.0	47.9	3.44	57.8	0.35	2.53	873	1.23	47.0	120	67.6	8.12	2.23	17.8	2.59
TILL-1	mean		38.3	172	49.2	49.6	53.1	11.0	59.4	5.36	51.9	0.69	2.15	922	1.21	52.2	127	117	10.4	2.31	20.3	2.55
TILL-1	SD		21.8	77	30.6	58.5	14.7	1.60	26.4	4.10	22.1	0.87	0.42	73.4	0.32	3.73	5.93	73.1	2.00	0.26	3.80	0.10
TILL-1	RSD		57%	45%	62%	118%	28%	14%	44%	77%	43%	127%	19%	8%	26%	7%	5%	63%	19%	11%	19%	4%
NIST2709a #1			106	534	80.2	309	155	0.92	261	27.6	237	4.08	1.16	12177	<0.1	447	784	22.4	39.8	21.9	150	56.6
NIST2709a #2			68.6	612	48.5	321	157	<0.04	230	28.8	105	4.49	0.00	10360	<0.1	392	808	26.1	38.4	21.2	215	54.5
NIST2709a #3			36.0	483	25.8	284	123	0.35	233	20.4	194	3.52	1.42	8765	<0.1	535	828	25.1	63.2	22.7	224	56.2
NIST2709a #4			46.7	541	33.7	293	136	0.41	239	23.7	67.9	3.95	1.32	10767	<0.1	433	797	21.4	48.5	32.8	237	56.9
NIST2709a #6			84.4	416	115	85.0	139	3.2	150	10.6	145	<0.05	2.46	9115	<0.1	378	729	26.4	53.3	40.3	212	45.7
NIST2709a #7			120	1007	77.5	405	228	0.86	235	33.2	262	7.57	<0.05	9822	<0.1	337	805	30.4	41.3	54.9	244	54.8
NIST2709a	mean		76.9	598	63.5	283	156	1.15	225	24.1	168	4.72	1.27	10168		420	792	25.3	47.4	32.3	214	54.1
NIST2709a	SD		32.8	211	33.8	106	37.4	1.19	38.3	7.92	75.8	1.63	0.87	1235		68.4	33.9	3.22	9.60	13.4	33.5	4.23
NIST2709a	RSD		43%	35%	53%	38%	24%	103%	17%	33%	45%	35%	69%	12%		16%	4%	13%	20%	42%	16%	8%

* Pedogenic soil-horizon classification from Bernhard et al. (2018).

n.d. not determined

Table S3.5: Chemical composition of the study sites' single plant organs along with their respective $^{87}Sr/^{86}Sr$ ratio. Weighted average ecosystem composition as well as radiogenic Sr isotopic composition for each site is given in Table 3.5 and Table 3.6, respectively.

Study site		slope	IGSN	Al	Ca	Fe	K	Mg	Mn	Na	P	Si	Sr	$^{87}Sr/^{86}Sr$	2SE
Plant species	organ							[µg g^{-1}]						[-]	
Pan de Azúcar															
Nolona mollis	leaf	N	GFRO10119	4855	24937	3386	8001	29558	434	33468	495	3348	83	0.71047	$1.3 \cdot 10^{-5}$
Nolona mollis	branch	N	GFRO10118	1712	10573	840	6430	16517	101	35102	196	2172	74	0.70964	$3 \cdot 10^{-6}$
Santa Gracia															
Asterasia sp.	leaf	S	GFRO10138	3963	10091	3599	11855	4308	251	8389	2407	88	43	0.70670	$1.2 \cdot 10^{-5}$
Asterasia sp.	stem	S	GFRO10137	1900	9600	2217	2158	2084	93	3745	577	81	59	0.70648	$4 \cdot 10^{-6}$
Cordia decandra	leaf	N	GFRO100ZV	331	34625	1156	4860	7598	103	1514	462	n.d.	219	0.70617	$4 \cdot 10^{-6}$
Cordia decandra	twig	N	GFRO1013D	729	16128	759	5286	3412	27	1217	1311	n.d.	107	0.70618	$8 \cdot 10^{-6}$
Cordia decandra	leaf	N	GFRO1008V	1546	63895	1413	10028	13463	131	2207	1386	12390	328	0.70616	$1.1 \cdot 10^{-5}$
Cordia decandra	twig	N	GFRO1017L	513	15793	460	8613	2533	27	1132	1108	801	91	0.70618	$4 \cdot 10^{-6}$
Cumulopuntia sphaerica	leaf	N	GFRO1011C	7969	5614	6184	2761	1626	219	2782	117	71	44	0.70497	$1.6 \cdot 10^{-5}$
Cumulopuntia sphaerica	stem	N	GFRO1011B	432	34432	359	13908	17172	311	216	1687	298	197	0.70601	$3 \cdot 10^{-6}$
Cumulopuntia sphaerica	root	N	GFRO1011A	2059	26709	1708	7112	6741	573	513	612	1179	252	0.70600	$5 \cdot 10^{-6}$
Cumulopuntia sphaerica	leaf	S	GFRO1017K	717	3503	751	1207	844	139	637	123	237	19	0.70686	$3 \cdot 10^{-6}$
Cumulopuntia sphaerica	stem	S	GFRO1017J	1240	35676	1074	7859	11977	228	426	715	343	190	0.70629	$1.9 \cdot 10^{-5}$
Cumulopuntia sphaerica	root	S	GFRO1017H	1691	15689	1050	14022	2955	646	628	633	1372	140	0.70626	$3.1 \cdot 10^{-5}$
Proustia cuneifolia	blossoms	S	GFRO1017D	1399	4388	1514	13806	1407	56	3069	2455	347	23	0.70642	$7 \cdot 10^{-6}$
Proustia cuneifolia	leaf	S	GFRO1017E	2965	21634	2654	4234	3451	150	7507	491	1040	108	0.70631	$5 \cdot 10^{-6}$
Proustia cuneifolia	twig	S	GFRO1017F	2299	7783	2973	5339	1319	54	2460	804	343	51	0.70640	$4 \cdot 10^{-6}$
La Campana															
forest floor	litter	S	GFRO10152	3073	14163	1640	4648	1752	117	717	447	118	60	0.70574	$8 \cdot 10^{-6}$
forest floor	litter	N	GFRO10174	832	22836	670	3888	3413	266	510	669	317	100	0.70487	$5 \cdot 10^{-6}$
Aristeguieta salvia	stem	N	GFRO1008H	19	4896	45	2278	406	6	13	200	48	30	0.70575	$2.2 \cdot 10^{-5}$
Colliguaja odorifera	leaf	S	GFRO10172	480	12714	430	20917	4005	80	112	3119	202	51	0.70561	$7 \cdot 10^{-6}$
Colliguaja odorifera	twig	S	GFRO10173	119	12747	96	7725	1239	76	66	615	147	70	0.70559	$1.1 \cdot 10^{-5}$
Colliguaja odorifera	stem	S	GFRO1011E	89	10620	65	7674	1472	41	59	1088	90	62	0.70560	$2 \cdot 10^{-6}$
Colliguaja odorifera	stem	N	GFRO1011D	25	11213	47	5146	720	81	12	435	104	61	0.70566	$1.1 \cdot 10^{-5}$
Cryptocaria alba	leaf	S	GFRO1013C	406	4720	275	12384	942	69	105	1108	n.d.	22	0.70570	$4 \cdot 10^{-6}$
Cryptocaria alba	twig	S	GFRO1008N	314	12526	203	6373	409	103	89	991	103	75	0.70568	$1.1 \cdot 10^{-5}$
Cryptocaria alba	leaf	N	GFRO10178	931	4876	774	23280	1788	57	174	2260	158	14	0.70593	$8 \cdot 10^{-6}$
Cryptocaria alba	twig	N	GFRO10179	431	10054	349	30067	1780	54	137	2281	159	34	0.70611	$3 \cdot 10^{-6}$

Continued on the next page.

Table S3.5: ...continuation

Study site		slope	IGSN	Al	Ca	Fe	K	Mg	Mn	Na	P	Si	Sr	$^{87}Sr/^{86}Sr$	2SE
Plant species	organ							[µg g^{-1}]						[-]	
Lithraea caustica	leaf	S	GFRO1013B	410	9325	270	6886	2270	53	148	814	n.d.	27	0.70582	$7 \cdot 10^{-6}$
Lithraea caustica	twig	S	GFRO1008P	365	5620	239	8373	1950	38	103	1119	n.d.	18	0.70580	$6 \cdot 10^{-6}$
Lithraea caustica	stem	S	GFRO10139	67	2665	65	2578	220	5	26	209	28	16	0.70612	$8 \cdot 10^{-6}$
Lithraea caustica	leaf	N	GFRO10176	441	3982	346	14742	1691	26	95	1574	125	10	0.70595	$6 \cdot 10^{-6}$
Lithraea caustica	twig	N	GFRO10177	338	23427	228	11070	1417	67	130	950	265	92	0.70595	$1.7 \cdot 10^{-5}$
Lithraea caustica	stem	N	GFRO10175	27	8970	49	5995	278	59	16	282	98	38	0.70576	$8 \cdot 10^{-6}$
Nahuelbuta															
forest floor	litter	S	GFRO10153	611	14432	309	1054	1797	877	83	513	119	116	0.71065	$3.8 \cdot 10^{-5}$
Araucaria araucana	leaf	S	GFRO1010B	36	9941	22	6568	1104	594	30	1102	n.d.	56	0.70877	$3 \cdot 10^{-6}$
Araucaria araucana	twig	S	GFRO10163	60	9330	34	5941	1732	638	184	2073	110	127	0.71098	$4 \cdot 10^{-6}$
Araucaria araucana	leaf	N	GFRO10164	42	10700	26	8050	891	749	45	1192	133	116	0.71046	$5 \cdot 10^{-6}$
Araucaria araucana	twig	N	GFRO10169	44	9357	25	5920	2494	620	75	1695	103	87	0.71251	$3 \cdot 10^{-6}$
Chusquea culeou	leaf	S	GFRO10168	93	4378	76	8075	864	715	83	880	n.d.	34	0.70912	$7 \cdot 10^{-6}$
Chusquea culeou	twig	S	GFRO10167	103	375	69	4903	339	558	127	587	n.d.	5	0.70911	$4 \cdot 10^{-6}$
Chusquea culeou	leaf	N	GFRO10109	147	4013	96	8671	368	383	69	961	n.d.	19	0.71239	$1.1 \cdot 10^{-5}$
Nothofagus antarctica	leaf	S	GFRO10166	94	8547	60	4549	1752	1161	115	2036	122	33	0.70929	$4 \cdot 10^{-6}$
Nothofagus antarctica	twig	S	GFRO10165	82	12290	61	2154	1248	494	66	1012	148	74	0.70930	$7 \cdot 10^{-6}$
Nothofagus antarctica	leaf	N	GFRO1010A	181	4813	79	3858	1675	600	83	1519	n.a	25	0.71262	$8 \cdot 10^{-6}$
Nothofagus antarctica	twig	N	GFRO1016A	123	5406	76	2525	1124	329	44	851	109	41	0.71263	$5 \cdot 10^{-6}$

CHAPTER 4

Element release and cycling in the Critical Zone along a climate and vegetation gradient from Sr radiogenic and stable isotope ratios

Abstract

Weathering and ecosystem nutrition are intimately linked through the supply of fresh mineral nutrients from regolith and bedrock (the "geogenic nutrient pathway"). However, this link is muted if re-utilization of nutrients from plant litter during litter mineralization is strong (the "organic nutrient cycle"). Here, we report on applications of Sr isotopes in combination with mass balance calculations to quantify how the balance between these two nutrient cycles shifts along the "EarthShape" climate and primary production gradient in the coastal mountains of Chile. We measured radiogenic and stable Sr isotopes, and determined molar Ca/Sr ratios in the different compartments of the Critical Zone (bedrock, bulk regolith, the bio-available fraction, and vegetation) to detect the Sr sources and quantify its fluxes. We found that Sr release through weathering is isotopically congruent and that the isotope ratio of the released Sr does not shift during secondary mineral formation or Sr transfer into the exchangeable pool. However, the $^{88}Sr/^{86}Sr$ ratio of bio-available Sr is higher than that of rock and regolith. This cause of this offset is found in plants: while $^{88}Sr/^{86}Sr$ in plant organs at the four study sites systematically increases from roots towards their leaves, plants preferentially take up Sr with low $^{88}Sr/^{86}Sr$. By estimating whole-plant Sr isotope compositions, we found that this shift occurs after preferential uptake of isotopically light Sr into plants and its subsequent loss from the ecosystem in organic solid material. This export provides further evidence for organic solids proving a significant export path of elements released during weathering. Thus, export potentially impairs the ability for direct Sr acquisition from solid plant debris and thus reduces the recycling factor of Sr and possibly

of other mineral nutrients.

This chapter is submitted to:

Chemical Geology by Ralf A. Oeser and Friedhelm von Blanckenburg

and has been accepted for publication on 31.08.2020 after peer review. A revised version of that manuscript is already in press and can be accessed at https://doi.org/10.1016/j.chemgeo.2020.119861 (CC BY 4.0)

4.1 Introduction

To sustain the continuous supply of mineral nutrients to ecosystems, losses of nutritive elements by erosion or as solutes in flowing water need to be balanced by fresh input. This balance is established over some 10^3 yrs through the conversion of pristine bedrock into regolith. This nutrient-replacing mechanism has been termed the "geogenic nutrient pathway": the slow but steady release of nutrients through chemical weathering of rock to counterbalance losses (Buendía et al. 2010; Cleveland et al. 2013; Uhlig and von Blanckenburg 2019). Over shorter timescales, nutrient supply within ecosystems is sustained through a tightly coupled biogeochemical cycle termed the "organic nutrient cycle". This cycle comprises a set of strategies for efficient nutrient uptake and re-utilization through microbial mineralization from plant litter and organic matter (Uhlig and von Blanckenburg 2019; Vitousek et al. 1998). However, this cycle is leaky. In particular in sloping landscapes ecosystems permanently lose a fraction of these internally cycled nutrients by plant-litter erosion (Heartsill Scalley et al. 2012; Scatena and Lugo 1995) and after decomposition by subsequent export in solution (Baskaran et al. 2017; Chaudhuri et al. 2007; Moore et al. 2005; Silver and Miya 2001). The geogenic pathway replaces these losses. These two pathways describe the fundamental workings of the "Critical Zone" – the zone where rock meets life.

The stable and radiogenic isotopes of the nutritive elements are a tool to shed light onto the processes releasing nutrients from rock and their subsequent journey from regolith into plants (Bouchez et al. 2013; Bullen and Chadwick 2016; Schmitt et al. 2012). Radiogenic $^{87}Sr/^{86}Sr$ isotope ratios are widely used in Earth sciences and their application as source tracer in geological studies dates back to Dasch (1969), Faure and Hurley (1963), and Faure and Powell (1972). Although Sr itself is not a plant-essential nutrient, over the last 30 years $^{87}Sr/^{86}Sr$ isotope ratios have emerged as an important geochemical tool to constrain the sources (e.g. atmospheric deposition or mineral weathering) of essential nutrients to ecosystems like Ca from the soil profile to catchment scale (e.g. Capo et al. 1998; Graustein 1989; Graustein and Armstrong 1983; Pett-Ridge et al. 2009a). Depending in their magmatic source and age, granitoid rocks are composed of minerals that are distinct in their Sr concentration and their $^{87}Sr/^{86}Sr$ ratio. Differences in parent rock mineralogy and age thus translate into differing $^{87}Sr/^{86}Sr$ ratios. The $^{87}Sr/^{86}Sr$ ratio is thus used to quantify the conversion of rock into soil and the subsequent transfer and cycling of mineral nutrients in terrestrial ecosystems (e.g. Åberg 1995; Bullen and Bailey 2005; Meek et al. 2016; Pett-Ridge et al. 2009b; Schuessler et al. 2018; Stewart et al. 1998; Uhlig and von Blanckenburg 2019). These applications rely on the emergence of distinct isotopic source fingerprints by the radiogenic inheritance of ^{87}Sr from ^{87}Rb decay over geologic time. In this application, any mass-dependent fractionation of $^{87}Sr/^{86}Sr$ is removed during data reduction after $^{87}Sr/^{86}Sr$ ratios measurement by mass spectrometry (Faure and Mensing 2005).

The strontium isotope system is unique in that its isotope composition records analytically resolvable information about the source of Sr (from its $^{87}Sr/^{86}Sr$ ratio), and the biogeochemical processes transferring Sr from one compartment to the other. During such a reaction the $^{88}Sr/^{86}Sr$ ratio shifts by mass-dependent isotope fractionation. Whereas it has been possible to resolve differences in $^{87}Sr/^{86}Sr$ ratios for decades, only recently have developments in modern Multicollector Inductively Coupled Plasma (MC-ICP-MS) and Double Spike Thermal Ionization Mass-Spectrometry (Fietzke and Eisenhauer 2006; Krabbenhöft et al. 2010; Neymark et al. 2014; Ohno et al. 2008) established the stable Sr isotope ratio (expressed as $\delta^{88/86}Sr$ in permil, ‰) as a process tracer. $\delta^{88/86}Sr$ values of most terrestrial rocks occupy a narrow range between 0.20‰ and 0.35‰ (e.g. Amsellem et al. 2018; Charlier et al. 2012; Moynier et al. 2010) and only a few Ca-rich rocks (e.g. limestone, dolomite) yield negative values of $\delta^{88/86}Sr$ up to –0.42‰ (review by Hajj et al. 2017). Our understanding of stable Sr isotope fractionation during weathering, soil formation and ecological processes is very limited and restricted to a few studies. These have shown that little (Chao et al. 2015; Stevenson et al. 2016) to no (de Souza et al. 2010) isotope fractionation occurs during weathering of silicate rock. However, a significant offset in $\delta^{88/86}Sr$ values between initial substrate (i.e. rock and regolith) and continental waters has been reported (Andrews et al. 2016; Neymark et al. 2014). Various processes are known to potentially fractionate Sr isotopes, including (biogenic) carbonate precipitation (Fietzke and Eisenhauer 2006; Krabbenhöft et al. 2010; Raddatz et al. 2013; Stevenson et al. 2014; Widanagamage et al. 2015) and potentially clay formation (Halicz et al. 2008; Shalev et al. 2013). Organisms in particular fractionate Sr stable isotopes when taken up into cells (e.g. Fruchter et al. 2016; Raddatz et al. 2013; Rüggeberg et al. 2008).

The uptake and subsequent internal translocation of elements by plants has been shown to be a particularly prominent driver of isotope fractionation in numerous isotope systems (e.g. Ca: Page et al. 2008; Wiegand 2005; Fe: Guelke and von Blanckenburg 2007; Mg: Black et al. 2008; Si: Opfergelt et al. 2008; Zn: Weiss et al. 2005). Sr isotope fractionation during Sr translocation in plants was also described by de de Souza et al. (2010) for Sr in a glaciated watershed. The authors report on preferential uptake of light ^{86}Sr from soil solution and the subsequent depletion of heavy ^{88}Sr along the transpiration stream of plants. This isotope fractionation was accompanied by a systematic increase in the molar Ca/Sr ratio from the roots to the leaves. Intriguingly, this isotope fractionation upon allocation from root to leaves is opposite to that described for the isotopes of the chemically similar element Ca (e.g. Page et al. 2008; Wiegand 2005). It is thus speculated that the sites at which Ca and Sr are being segregated within plants are also those that fractionate the isotopes of Sr and Ca. The active discrimination between the elements Ca and Sr and the preferential transport of Ca over Sr within plants has been reported by numerous studies in e.g. beech and spruce (Poszwa et al. 2000), beech and oak (Drouet et al. 2007), and for the foliar and floral tissues in *R. ferrugineum* and *Vaccinium* (de Souza et al. 2010). Hence, de Souza et al. (2010) proposed

that Sr isotope fractionation within plants takes place because the light isotopes of Sr are preferentially moved to the higher plant organs during partial Sr transport associated with kinetic isotope fractionation.

This study aims to contribute to an increased knowledge in Sr release and cycling through the different compartments of the Critical Zone. We applied an isotope mass balance model (Bouchez et al. 2013) to quantify the export fluxes in four study sites located in arid, semi-arid, mediterranean, humid-temperate climate zones, respectively. The sites are situated along the "EarthShape" (Oeser et al. 2018a) climate and vegetation gradient in the Chilean Coastal Cordillera. Whereas lithology is all granitoid, and tectonic uplift as well as erosion rates are within a restricted range (Schaller et al. 2018b), precipitation forms a gradient and increases by a factor of 100 from north to south (Ministerio de Obras Públicas 2017). We determined radiogenic ($^{87}Sr/^{86}Sr$) and stable ($\delta^{88/86}Sr$) Sr isotope ratios in bulk bedrock and regolith, the bio-available fraction in saprolite and soil (representing the fraction of elements which is easily available for plants' nutrition; e.g. Uhlig and von Blanckenburg 2019), and in different plant compartments. In all these compartments we further measured Ca/Sr ratios. Using radiogenic Sr isotopes, stable Sr isotope mass balance, and elemental concentrations we identified and quantified the Ca and Sr sources, fluxes, and their cycling between the different Critical Zone compartments. By using a novel approach to estimate whole-plant Sr isotope composition we determined a representative Sr fractionation factor upon uptake by plants for each study site. The main aims of this study were to (1) determine the source of Sr as a proxy for mineral nutrients; (2) establish budgets for the relative release of Sr from rock and uptake by plants; (3) identify how Sr is lost once taken up by plants; and (4) evaluate how the "geogenic" and the "organic" nutrient pathway interact (i.e. via recycling) in settings that differ in precipitation and primary production.

4.2 Study area and previous results

The four study sites Pan de Azúcar, Santa Gracia, La Campana, and Nahuelbuta are equally distributed between ~26°S and ~38°S along the Chilean Coastal Cordillera. They form a climate sequence covering arid, semi-arid, mediterranean, and humid-temperate conditions. The mean annual precipitation (MAP) varies between 10 mm yr^{-1} in the northernmost site to 1100 mm yr^{-1} in the very south. In contrast, mean annual air temperature (MAT) shows minor differences: from 18.1°C in Pan de Azúcar to 14.1°C in Nahuelbuta (Ministerio de Obras Públicas 2017).

The studied weathering profiles at all four sites are located in natural parks and nature reserves and developed on granitoid rocks of Cretaceous to Permian intrusion age (Berg and Breitkreuz 1983; Berg and Baumann 1985; Moscoso et al. 1982; Molina et al. 2015; Parada and Larrondo 1999; Parada et al. 2002; 2007). The sites were not glaciated during the last glacial maximum (LGM; Hulton et al. 2002) and have not received inputs in the form

of volcanic material (Oeser et al. 2018a). From north to south, the EarthShape gradient captures a large ecological gradient ranging from barely vegetated (< 5% cover) desert soils and low net primary productivity (NPP) in Pan de Azúcar (30 g_C m^{-2} yr^{-1}) to entirely covered forest ecosystems with high NPP in Nahuelbuta (520 g_C m^{-2} yr^{-1}; Bernhard et al. 2018; Oeser et al. 2018a; Werner et al. 2018).

Along this latitudinal transect tectonic uplift maintains topography with uniform uplift rates of approximately 0.2 ± 0.1 mm yr^{-1} (Melnik 2016) south of 25°S. A trend in denudation rates D is reported by Schaller et al. (2018b). D increases from 8 – 11 t km^{-2} yr^{-1} in Pan de Azúcar to 16 – 24 t km^{-2} yr^{-1} in Santa Gracia and are highest in the mediterranean climate of La Campana (54 – 69 t km^{-2} yr^{-1}). In Nahuelbuta, denudation rate (D) is intermediate (18 – 48 t km^{-2} yr^{-1}). All these rates are thus towards the lower end of global cosmogenic nuclide-derived soil production rates (Dixon et al. 2012). Weathering rates are low in Pan de Azúcar (0 – 1 t km^{-2} yr^{-1}), are higher in Santa Gracia (7 – 12 t km^{-2} yr^{-1}), peak in La Campana (20 – 46 t km^{-2} yr^{-1}), and amount to 4 – 8 t km^{-2} yr^{-1} in Nahuelbuta (Oeser et al. 2018a). That both W and D largely correlate suggests weathering is set by denudation rate, with both being highest in La Campana due to the steep slopes and relief there. However, the degree of weathering as quantified by the chemical depletion fraction (CDF) does not depend on topography, and amounts to 0.0 – 0.1, 0.5, 0.4 – 0.7, and 0.2 in Pan de Azúcar, Santa Gracia, La Campana, and Nahuelbuta, respectively (Oeser et al. 2018a).

The architecture of the regolith profiles, their chemistry and mineralogy, as well as the physical properties of soils, saprolite, and the rocks beneath them have been extensively described by Bernhard et al. (2018); Dal Bo et al. (2019); Oeser et al. (2018a) and Schaller et al. (2018b).

We focus our study on two representative profiles at each site, one on a N-facing and one on a S-facing slope. The regolith profiles in Pan de Azúcar are located between 330 and 340 m asl on steep (25 – 40 °) hill slopes. The soils on the N- and on the S-facing slope were classified as Regosols (Bernhard et al., 2018) with shallow A and B horizons. In Pan de Azúcar, the processes disintegrating rock and developing regolith are mainly attributed to physical weathering (Oeser et al. 2018a). The vegetation consists only of small shrubs, geophytes, and annual plants (Armesto et al. 1993), which are mainly present in small ravines. In Santa Gracia the N- and S-facing regolith profiles are situated on mild sloping hills (15 – 25 °) at approximately 700 m asl. The soils are classified as Leptosol and Cambisol, respectively (Bernhard et al. 2018). Distinct O horizons do not exist, and the Ah horizons are shallow and measure up to 10 cm thickness. The subsequent transition from the mineral soil (Bw) into saprolite is found at 25 – 30 cm depth. This site's high degree of chemical weathering (as quantified by CDF) and elemental depletion (i.e. τ) is attributed to the low abundance of quartz and high amounts of readily weatherable plagioclase and mafic minerals (e.g. hornblende, pyroxene; Oeser et al. 2018a). The vegetation cover is generally sparse and

belongs to the "Interior Mediterranean desert scrub of *Heliotropium stenophyllum* and *Flourensia thurifera*" formation (Luebert and Pliscoff 2006). In La Campana the regolith profiles, located at 730 m asl and on mild sloping hills (12 – 23 °), are classified as Cambisols (Bernhard et al. 2018). The O horizon is approximately 5 cm thick and is followed by an Ah horizon which extents up to 40 cm depth. In both profiles, the mineral-soil layer turns into saprolite at approximately 110 cm depth (Bernhard et al. 2018). Luebert and Pliscoff (2006) describes the vegetation to be part of the "Coastal Mediterranean sclerophyllous forest of *Lithraea caustica* and *Cryptocarya alba*" formation. In Nahuelbuta the regolith profiles are situated at about 1200 m asl and an umbric Podsol and orthodystric Umbrisol developed on the gently sloping (~15 °) N- and S-facing hills, respectively (Bernhard et al. 2018). Ah horizons measure up to 50 cm thickness and are overlain by a 5.5-cm thick organic horizon. The transition from soil into the coarse-grained and readily disaggregating saprolite is found at 100 and 120 cm depth, respectively. These regolith profiles are highly heterogeneous which is caused by the incorporation of the metamorphic basement at various parts of the profile (e.g. Oeser et al. 2018a; Hervé 1977). The dominant vegetation in Nahuelbuta is associated with the "Coastal temperate forest of Araucaria araucana" formation (Luebert and Pliscoff 2006).

A comprehensive summary of the eight regolith profiles' characteristics and the prevailing major plant types are given in Table 3.1.

4.3 Methods

4.3.1 Sampling

At each study site four replicate regolith profiles have been analyzed in previous studies (Bernhard et al. 2018; Oeser et al. 2018a), in which no significant differences in chemistry and pedogenesis where detected within a given site. In this study we focused on sampling two regolith profiles situated on opposing slopes (N- and S-facing midslope profiles) to account for the variations in substrate and a differing plant community on weathering, nutrient uptake and recycling by plants. However, these profiles are natural replicates.

Regolith samples were taken along a continuous sequence of depth increments amounting to a thickness of 5 cm for the uppermost two samples, 10 cm for the third sample from top, and 20 cm for the 4th sample onward. Underlying unweathered bedrock was not reached in the regolith profiles of this study and the depth to bedrock remains unknown. Instead, in total 35 representative bedrock samples from all sites were thus obtained from nearby outcrops.

Vegetation samples from representative shrubs and trees of each study site were sampled in the austral summer to autumn 2016. The sample set comprises stem, twig, and leaf samples from mature specimens of the prevailing species. In addition, the litter layer in La Campana and Nahuelbuta was sampled.

Water samples were not taken, for the simple reason that in the arid and the semi-arid site no water was present at their surface. The La Campana and Nahuelbuta areas are drained by small perennial streams. However, these drain multiple rock types and were thus not deemed representative for the soil profiles sampled. The remoteness of the sample sites further excluded the installation and permanent sampling of soil lysimeters. Instead we approach regolith solution chemical and isotope composition by extractions of the exchangeable fraction in regolith, as explained in the next section.

4.3.2 Analytical methods

Chemical composition of regolith and bedrock

The chemical composition of bedrock and regolith samples was determined using the PANalytical AXIOS advanced X-Ray Fluorescence spectrometer at the GFZ German Research Centre for Geosciences, Section "Inorganic and Isotope Geochemistry". A detailed description of sample preparation and analytical protocols is provided by Oeser et al. (2018a).

Chemical composition of vegetation

The chemical composition of vegetation samples were determined using a Varian 720-ES axial ICP-OES at the Helmholtz Laboratory for the Geochemistry of the Earth Surface (HELGES), GFZ German Research Centre for Geosciences (von Blanckenburg et al. 2016) with relative uncertainties smaller than 10%. Prior to analysis, samples were dried, crushed, and homogenized. Samples were then acid-dissolved in PFA vials using a microwave (MLS start) and ultra-pure concentrated acid mixtures (H_2O_2, HNO_3, and HCl). A detailed description of sample preparation and analytical protocols is provided by Oeser and von Blanckenburg (2020b).

Extraction of the easily bio-available fraction and it's chemical analyses

The easily bio-available fraction was extracted from bulk regolith samples using a sequential extraction procedure adapted from Arunachalam et al. (1996), Tessier et al. (1979), and He et al. (1995).

To extract the so-called "water-soluble" fraction, dried and sieved (< 2 mm) sample material were immersed in 18 MΩ Milli-Q H_2O for 24 h. Subsequently, the exchangeable fraction was extracted by immersing the remaining sample for 2 h in 1 M NH_4OAc. A sample to reactant ratio of 1:7 was maintained throughout. None of the further extraction steps described in Tessier et al. (1979) were applied to the regolith samples in this study as it is believed to have only minor contribution to the bio-available fraction (rewiew by Filgueiras et al. 2002). After each extraction step, the suspension was centrifuged, the supernatant pipetted off, the remaining sample rinsed with Milli-Q H_2O, centrifuged again, and the supernatants pooled together. Finally, the supernatants were filtered through vacuum driven filtration (Millipore®) using a 0.2 µm acetate filter and redissolved with ultra-pure concentrated acid mixtures.

The element concentration of both fractions was determined using a Varian 720-ES axial ICP-OES at the HELGES with relative uncertainties estimated to be better than 10%. For a detailed description on analytical procedures and sample preparation, the reader is referred to Schuessler et al. (2016) and Oeser and von Blanckenburg (2020b), respectively.

Radiogenic $^{87}Sr/^{86}Sr$ and stable $\delta^{88/86}Sr$ isotope ratios

Upon sample digestion or sequential extraction, Sr was separated from matrix elements using self-made columns (inverted disposable pipettes), loaded with 200 µl of Sr-Spec resin (particle size 50 – 100 µm; Eichrom Technologies LCC, USA). Matrix elements were removed by elution with 2.5 ml 3 M and 2 ml 7.5 M HNO_3, respectively. Finally, Sr was eluted with 4 ml Milli-Q H_2O. To remove any organic molecules released from the Sr-Spec resin, the Sr fraction was evaporated and redissolved in 1 ml of a 1:1 mixture of concentrated H_2O_2 and HNO_3. This sample-acid mixture was cooked for at least 12 hrs in a tightly closed beaker at 150 °C. With each sample batch, at least one international reference material (see below) and a procedural blank was processed.

The purity and yield of the Sr fraction was monitored by Quadrupole ICP-MS analyses at the HELGES. Strontium isotope composition was measured in a 50-ng g^{-1} pure Sr solution in 0.3 M HNO_3 on a multi collector inductively coupled plasma mass spectrometer (MC-ICP-MS, ThermoFischer Neptune) in medium mass resolution, using an APEX-Q (ESI) desolvator and a teflon nebulizer with 70 µl min^{-1} uptake rate. The intensities of the ion beams on the masses ^{82}Kr (L4), ^{83}Kr (L3), ^{84}Sr (L2), ^{85}Rb (L1), ^{86}Sr (central cup), ^{87}Sr (H1) and ^{88}Sr (H2) were measured using Faraday collectors equipped with $10^{11}\ \Omega$ and one $10^{12}\ \Omega$ (connected to L4 cup) resistors. Isobaric interference on masses 84 (^{84}Kr contribution on ^{84}Sr), 86 (^{86}Kr contribution on ^{86}Sr), and 87 (^{87}Rb contribution on ^{87}Sr) were corrected for, using the background Kr and Rb isotope ratios measured prior to the sequence run and the measured SRM 984 (rubidium chloride) ^{83}Kr and ^{85}Rb signals. A natural isotopic composition of Kr and Rb was assumed, and these elements were assumed to have been affected by the same instrumental mass fractionation as Sr. The operating conditions were optimized for maximum Sr signal and stability such that the ^{88}Sr intensity in 50 ng g^{-1} Sr was typically 4 to 6 V. Both the $^{87}Sr/^{86}Sr$ ratios and $\delta^{88/86}Sr$ were determined simultaneously during the sample run (1 block of 20 cycles, 16 s integration time). Including wash-out time, this equates to a measurement time of ~8 min per sample. The sequence of a sample run consisted of 10 to 12 blocks, where each block comprised a blank, four samples, and five SRM 987 (strontium carbonate; as bracketing standard for the determination of $\delta^{88/86}Sr$; not processed through chemistry). Blank correction of samples and reference material during the sequence was less than 0.4% of sample signal. $^{87}Sr/^{86}Sr$ ratios are reported after correction for session offset and any occurring natural and instrumental mass-dependent fractionation, by normalizing to an $^{88}Sr/^{86}Sr$ ratio of 8.375209 (Nier's value, 1938) using an exponential mass fractionation law.

$^{88}Sr/^{86}Sr$ is reported normalized to the Sr isotope ratio of the sample relative to the SRM 987 standard isotope reference material using the delta notation defined as

$$\delta^{88/86}\mathrm{Sr} = \left[\frac{\left(\frac{^{88}\mathrm{Sr}}{^{86}\mathrm{Sr}}\right)_{\mathrm{sample}}}{\left(\frac{^{88}\mathrm{Sr}}{^{86}\mathrm{Sr}}\right)_{\mathrm{SRM\text{-}987}}} - 1 \right], \tag{4.1}$$

and is reported in permil (‰). $\delta^{88/86}$Sr were corrected for instrumental mass bias and drift by using a standard-sample-bracketing procedure. Based on repeated measurements of reference materials, the long-term uncertainty is estimated to be ± 0.03 ‰ ($2SE_t$) from repeated measurements of $\delta^{88/86}$Sr the reference materials BCR-2 and BHVO-2 (Columbia river and Hawaiian basalt, respectively), JG-2 (Naegi granite), SRM 1515 (apple leaves), SRM 2709a (San Joaquin soil), and Till-1 (till), respectively (Table 4.1 and 4.2). This uncertainty is similar to the 95% confidence interval $2SE_t$ of individual samples which is calculated as standard deviation/ sqrt(n) of n mass-spectrometric replicate analyses multiplied by the t as correction factor from Student's t-distribution at 95% probability.

4.4 Results

4.4.1 Element concentrations

We report previously published Ca and Sr concentration of bulk bedrock and regolith, the bio-available fraction, and those of plant organs (stem, twig, leaf) along with the soil profiles' chemical depletion fraction (CDF) and fractional elemental loss (τ; Brimhall and Dietrich 1987) in Table 4.1 and 4.2 (Oeser et al. 2018a; Oeser and von Blanckenburg 2020b). The vertical distribution of these elements in the regolith profiles is shown as molar Ca/Sr ratios and in terms of elemental mass transfer coefficient (τ)-values denoting elemental gain or loss relative to bulk bedrock in Figs. 4.1 – 4.4.

Ca and Sr concentrations in bulk regolith samples are in general homogeneously distributed with depth, and do not differ significantly between the single regolith profiles of a given site. Bio-available Ca and Sr concentrations show similar distributions with depth and are only enriched in the soil horizons of La Campana and Nahuelbuta. In Pan de Azúcar and Santa Gracia, the depth-concentration distribution in the bio-available fraction is closely linked to that of bulk samples (Oeser and von Blanckenburg 2020b).

The molar Ca/Sr ratio in bulk regolith samples is invariant with depth (except the profiles subject to atmospheric deposition of Ca and Sr: Pan de Azúcar N- and S-facing profile, Fig. 4.1; or subject substantial substrate heterogeneities: S-facing profile in Nahuelbuta, Fig. 4.4b) and typically range from 0.17 – 0.03 mol mmol^{-1} and 0.18 – 0.01 mol mmol^{-1} in Nahuelbuta and Santa Gracia, respectively, to 0.19 – 0.02 mol mmol^{-1} in La Campana. In the bio-available fraction, this ratio is with one exception (S-facing profile in Nahuelbuta) higher than in bulk regolith samples. The molar Ca/Sr ratio in the bio-available fraction is either

uniformly distributed with depth (Pan de Azúcar, Santa Gracia), or increases from saprolite to soil (La Campana, Nahuelbuta). Molar Ca/Sr ratios in root and stem samples are in most samples identical within error to those of the bio-available fraction they grow on. In plants this ratio increases from stem to twig and is highest in leaf samples.

4.4.2 Sr isotope ratios

We report new $\delta^{88/86}$Sr results on bulk bedrock and regolith, the bio-available fraction, and vegetation samples. We complement this data set with a radiogenic Sr data set previously published (Oeser and von Blanckenburg 2020b) from the same Critical Zone compartments. A summary of these data is presented in the Tables 4.1, 4.2, and 4.3. Sr depth profiles of the different regolith profiles are shown in Figs. 4.1 – 4.4.

$^{87}Sr/^{86}Sr$ ratios

Radiogenic Sr isotope ratios on bulk bedrock and regolith samples discloses the source rock, incongruent weathering reactions of minerals that differ in their ^{87}Sr/ ^{86}Sr ratio, and the incorporation of external (atmospheric) sources into the regolith profiles. The comparison between ^{87}Sr/ ^{86}Sr in the bio-available fraction and that in plants yields information on the plants' nutrient source and nutrient uptake depth.

The bedrocks' radiogenic Sr isotope composition in the study sites of Pan de Azúcar, Santa Gracia, and La Campana, varies very little at each site, with values of 0.7260 ± 0.0020, 0.7039 ± 0.0004, and 0.7063 ± 0.0003, respectively. In Nahuelbuta, this ratio (0.716 ± 0.007) is in good agreement to those reported by Hervé et al. (1976) for the granitoid basement in Nahuelbuta (0.717). However, the large spread among the bedrock samples is remarkable and arises from the high petrological and chemical variability of the Nahuelbuta mountain range (e.g. Hervé 1977).

At most sites, bulk regolith ^{87}Sr/^{86}Sr are identical within uncertainty to those of the study sites' bedrock. Regolith ratios differ from bedrock in the S-facing regolith profile in Pan de Azúcar (Table 4.1). In all profiles, the ^{87}Sr/^{86}Sr ratios do not show systematic variation with depth (Figs. 4.1 – 4.4). However, these ratios are distinct between the two profiles at a given site. These differences are attributed to either small-scale heterogeneities in the initial substrate (Oeser and von Blanckenburg 2020b), or in the case of Pan de Azúcar, to varying degrees of atmospheric deposition (Oeser and von Blanckenburg 2020b). Variations in bulk regolith ^{87}Sr/^{86}Sr can be correlated with patterns of elemental gain or depletion (i.e. τ^{Sr}) in the regolith profiles of La Campana (Fig. 4.3). There, regolith ratios that differ from bedrock can be attributed to specific weathering reactions such as the preferential dissolution of biotite high in ^{87}Sr/^{86}Sr beneath the regolith profiles (Oeser and von Blanckenburg 2020b).

Table 4.1: Pedogenic classification and chemical characterization of the regolith profiles in the EarthShape study area. The published data is complemented here by radiogenic strontium ($^{87}Sr/^{86}Sr$ ‡), stable strontium ($\delta^{88/86}Sr$), and molar Ca/Sr ratios in bulk regolith and the bio-available fraction.

								bulk regolith							bio-available fraction						
			weathering indices †			concentration †								concentration ‡							
Soil profile		sample	τ^{Ca}	τ^{Sr}	CDF	Ca	Sr	Ca/Sr	$^{87}Sr/^{86}Sr$	$2SE_t$	$\delta^{88/86}Sr$	$2SE_t$	n	Ca	Sr	Ca/Sr	$^{87}Sr/^{86}Sr$	$2SE_t$	$\delta^{88/86}Sr$	$2SE_t$	n
depth	IGSN	type*	[-]			[µg g^{-1}]		[mol mmol^{-1}]			[‰]			[µg g^{-1}]		[mol mmol^{-1}]			[‰]		
Pan de Azúcar	AZPED21	**Regosol**																			
0 - 5	GFRO100UD	Aycz	1.60	−0.10	−0.05	24724	102	0.53	0.722566	$1.3 \cdot 10^{-5}$	0.22	0.06	3	3558	8	0.99	0.709352	$1.8 \cdot 10^{-5}$	0.24	0.02	6
5 - 10	GFRO100UE	Bycz	1.78	−0.16	−0.22	22694	82	0.61	0.728455	$1.7 \cdot 10^{-5}$	0.28	0.07	3	6323	7	2.09	0.709392	$1.7 \cdot 10^{-5}$	0.33	0.02	6
10 - 20	GFRO100UF	Bycz	1.33	−0.24	−0.09	21320	83	0.56	0.728005	$3.3 \cdot 10^{-5}$	0.25	0.02	3	n.d.	n.d.	n.d.	n.d.	n.d.	n.d.	n.d.	0
20 - 40	GFRO100UG	BCycz	3.07	−0.20	0.06	43129	101	0.94	0.726234	$1.4 \cdot 10^{-5}$	0.31	0.08	3	n.d.	n.d.	n.d.	n.d.	n.d.	n.d.	n.d.	0
40 - 60	GFRO100UH	C	−0.16	−0.31	−0.05	7990	78	0.22	0.731768	$2.0 \cdot 10^{-5}$	0.26	0.07	3	n.d.	n.d.	n.d.	n.d.	n.d.	n.d.	n.d.	0
60 - 80	GFRO100UJ	C	0.19	−0.01	−0.14	10441	104	0.22	0.728410	$3.7 \cdot 10^{-5}$	0.16	0.04	3	n.d.	n.d.	n.d.	n.d.	n.d.	n.d.	n.d.	0
80 - 100	GFRO100UK	C	−0.67	−0.12	−0.03	3210	102	0.07	0.728664	$3.1 \cdot 10^{-6}$	0.17	0.02	3	878	2	1.07	0.710159	$7.4 \cdot 10^{-6}$	0.15	0.04	5
AZPED50		**Regosol**																			
0 - 5	GFRO100TX	Aycz	0.58	−0.39	0.25	21169	98	0.47	0.728773	$5.4 \cdot 10^{-5}$	0.19	0.03	3	3308	5	1.59	0.709911	$4.2 \cdot 10^{-5}$	0.25	0.03	6
5 - 10	GFRO100TY	Bycz	4.94	−0.21	−0.07	55396	88	1.38	0.729611	$1.4 \cdot 10^{-5}$	0.27	0.03	4	n.d.	n.d.	n.d.	n.d.	n.d.	n.d.	n.d.	0
10 - 20	GFRO100TZ	Bycz	0.47	−0.31	0.01	14830	83	0.39	0.734629	$3.8 \cdot 10^{-5}$	0.20	0.03	4	4838	3	3.67	0.710962	$2.9 \cdot 10^{-5}$	0.47	0.01	6
20 - 40	GFRO100U0	BCycz	0.64	−0.28	0.09	17889	94	0.42	0.730475	$1.9 \cdot 10^{-5}$	0.23	0.04	7	n.d.	n.d.	n.d.	n.d.	n.d.	n.d.	n.d.	0
40 - 60	GFRO100U1	BCycz	1.24	−0.37	−0.01	22063	74	0.65	0.734182	$3.4 \cdot 10^{-5}$	0.21	0.02	4	n.d.	n.d.	n.d.	n.d.	n.d.	n.d.	n.d.	0
60 - 80	GFRO100U2	C	0.74	−0.41	0.10	19140	78	0.54	0.732401	$5.9 \cdot 10^{-5}$	0.21	0.02	4	n.d.	n.d.	n.d.	n.d.	n.d.	n.d.	n.d.	0
80 - 100	GFRO100U3	C	3.15	−0.45	−0.01	40917	65	1.38	0.736524	$1.7 \cdot 10^{-5}$	0.28	0.01	4	n.d.	n.d.	n.d.	n.d.	n.d.	n.d.	n.d.	0
100 - 120	GFRO100U4	C	1.15	−0.33	0.06	22856	86	0.58	0.731231	$9.3 \cdot 10^{-6}$	0.23	0.03	3	n.d.	n.d.	n.d.	n.d.	n.d.	n.d.	n.d.	0
120 - 140	GFRO100U5	C	1.65	−0.46	0.08	28588	70	0.89	0.735206	$9.2 \cdot 10^{-5}$	0.23	0.03	4	2585	2	3.29	0.711395	$1.8 \cdot 10^{-5}$	0.47	0.01	6
Santa Gracia, SGPED70		**Leptosol**																			
0 - 5	GFRO100VF	Ah	−0.84	−0.75	0.66	32351	385	0.18	0.704508	$1.3 \cdot 10^{-5}$	0.30	0.04	3	799	7	0.26	0.706227	$2.1 \cdot 10^{-5}$	0.56	0.03	5
5 - 10	GFRO100VG	Ah	−0.82	−0.70	0.58	29162	378	0.17	0.704441	$1.9 \cdot 10^{-5}$	0.29	0.04	3	744	7	0.24	0.706206	$3.2 \cdot 10^{-5}$	0.58	0.02	5
10 - 20	GFRO100VH	Bwi	−0.81	−0.69	0.54	27982	358	0.17	0.704514	$2.4 \cdot 10^{-6}$	0.29	0.04	3	1412	10	0.30	0.706141	$2.1 \cdot 10^{-5}$	0.33	0.02	5
20 - 40	GFRO100VJ	C	−0.81	−0.71	0.55	27854	344	0.18	0.704528	$1.2 \cdot 10^{-5}$	0.28	0.06	3	1316	9	0.31	0.706179	$2.8 \cdot 10^{-5}$	0.20	0.01	5
40 - 60	GFRO100VK	C	−0.78	−0.69	0.52	30786	351	0.19	0.704462	$3.4 \cdot 10^{-5}$	0.29	0.05	3	951	7	0.30	0.706228	$3.3 \cdot 10^{-5}$	0.18	0.02	5
60 - 80	GFRO100VL	C	−0.79	−0.68	0.51	29664	353	0.18	0.704638	$1.3 \cdot 10^{-5}$	0.30	0.02	3	739	5	0.29	0.706262	$2.0 \cdot 10^{-5}$	0.20	0.02	5
80 - 100	GFRO100VM	C	−0.75	−0.61	0.43	29722	358	0.18	0.704641	$1.7 \cdot 10^{-5}$	0.30	0.03	3	793	6	0.30	0.706251	$6.2 \cdot 10^{-6}$	0.20	0.03	5
100 - 120	GFRO100VN	C	−0.79	−0.72	0.55	30693	334	0.20	0.704741	$1.7 \cdot 10^{-5}$	0.29	0.03	3	525	4	0.30	0.706274	$2.1 \cdot 10^{-5}$	0.21	0.00	5
120 - 140	GFRO100VP	C	−0.79	−0.69	0.53	29837	355	0.18	0.704706	$4.0 \cdot 10^{-5}$	0.27	0.03	3	422	3	0.29	0.706226	$1.3 \cdot 10^{-5}$	0.25	0.02	7
140 - 160	GFRO100VQ	C	−0.76	−0.66	0.48	31804	353	0.20	0.704614	$1.8 \cdot 10^{-5}$	0.25	0.03	3	350	3	0.31	0.706175	$1.5 \cdot 10^{-5}$	0.23	0.01	5
160 - 180	GFRO100VR	C	−0.79	−0.69	0.52	29519	350	0.18	0.704699	$1.3 \cdot 10^{-5}$	0.27	0.05	3	473	3	0.33	0.706141	$1.4 \cdot 10^{-5}$	0.18	0.03	5
SGPED40		**Cambisol**																			
0 - 5	GFRO100UU	Ah	−0.77	−0.66	0.52	32788	361	0.20	0.704289	$1.8 \cdot 10^{-5}$	0.32	0.04	8	670	5	0.29	0.706389	$2.2 \cdot 10^{-5}$	0.22	0.01	5
5 - 10	GFRO100UV	Ah	−0.80	−0.69	0.56	31512	354	0.19	0.704274	$4.0 \cdot 10^{-5}$	0.27	0.00	7	661	5	0.28	0.706300	$1.3 \cdot 10^{-5}$	0.32	0.04	5
10 - 20	GFRO100V3	Bw	−0.79	−0.67	0.53	30700	358	0.19	0.704300	$3.6 \cdot 10^{-5}$	0.40	0.06	5	760	6	0.28	0.706229	$1.6 \cdot 10^{-5}$	0.35	0.01	5
20 - 40	GFRO100UW	BCw	−0.78	−0.64	0.50	30535	363	0.18	0.704271	$3.7 \cdot 10^{-5}$	0.34	0.09	4	768	6	0.29	0.706178	$3.7 \cdot 10^{-5}$	0.29	0.03	5
40 - 60	GFRO100UX	BCw	−0.63	−0.42	0.23	32877	385	0.19	0.704149	$8.5 \cdot 10^{-5}$	0.35	0.11	4	879	7	0.29	0.706174	$2.6 \cdot 10^{-5}$	0.33	0.04	5
60 - 80	GFRO100UY	C	−0.66	−0.42	0.23	30230	385	0.17	0.703977	$3.3 \cdot 10^{-5}$	0.32	0.03	4	844	6	0.29	0.706186	$2.0 \cdot 10^{-5}$	0.42	0.03	5
80 - 100	GFRO100UZ	C	−0.75	−0.52	0.31	25491	350	0.16	0.704105	$3.0 \cdot 10^{-5}$	0.34	0.03	4	752	5	0.32	0.706182	$7.3 \cdot 10^{-6}$	0.47	0.05	5
100 - 120	GFRO100V0	C	−0.78	−0.64	0.50	30934	363	0.19	0.704159	$1.9 \cdot 10^{-5}$	0.32	0.03	4	483	3	0.32	0.706183	$2.0 \cdot 10^{-5}$	0.40	0.03	5
120 - 140	GFRO100V1	C	−0.65	−0.44	0.27	33349	385	0.19	0.703974	$1.4 \cdot 10^{-5}$	0.34	0.02	4	278	2	0.31	0.706164	$1.9 \cdot 10^{-5}$	0.36	0.01	5

Continued on the next page.

Table 4.1: ...continuation

Soil profile depth	IGSN	sample type*	weathering indices † τ^{Ca}	τ^{Sr} [-]	CDF	bulk regolith concentration † Ca [µg g^{-1}]	Sr	Ca/Sr [mol mmol^{-1}]	$^{87}Sr/^{86}Sr$	$2SE_t$	$\delta^{88/86}Sr$ [‰]	$2SE_t$	n	bio-available fraction concentration ‡ Ca [µg g^{-1}]	Sr	Ca/Sr [mol mmol^{-1}]	$^{87}Sr/^{86}Sr$	$2SE_t$	$\delta^{88/86}Sr$ [‰]	$2SE_t$	n
140 - 160	GFRO100V2	C	−0.60	−0.37	0.19	33854	394	0.19	0.703938	$2.4\cdot10^{-5}$	0.31	0.03	4	240	2	0.31	0.706113	$2.4\cdot10^{-5}$	0.35	0.02	5
160 - 180	GFRO100CR	C	−0.61	−0.36	0.19	33606	399	0.18	0.703920	$1.7\cdot10^{-5}$	0.31	0.02	4	210	1	0.31	0.706084	$2.1\cdot10^{-5}$	0.34	0.03	5
La Campana, LCPED40		**Cambisol**																			
0 - 5	GFRO1002V	Ah	−0.67	−0.70	0.70	23249	231	0.22	0.705103	$5.1\cdot10^{-5}$	0.25	0.05	7	2349	13	0.39	0.704830	$1.9\cdot10^{-5}$	0.32	0.02	4
5 - 10	GFRO1002W	Bw1	−0.72	−0.73	0.71	20500	218	0.21	0.705076	$3.7\cdot10^{-5}$	0.26	0.05	7	1219	8	0.33	0.704838	$8.1\cdot10^{-6}$	0.34	0.04	4
10 - 20	GFRO1002X	Bw1	−0.69	−0.70	0.66	19431	207	0.21	0.705151	$6.9\cdot10^{-5}$	0.33	0.04	4	790	6	0.30	0.704560	$7.3\cdot10^{-4}$	0.34	0.04	5
20 - 40	GFRO1002Y	Bw2	−0.66	−0.66	0.61	18386	202	0.20	0.705205	$5.4\cdot10^{-5}$	0.23	0.01	7	981	8	0.28	0.704758	$2.8\cdot10^{-5}$	0.38	0.04	4
40 - 60	GFRO1002Z	BCw	−0.65	−0.64	0.58	17811	199	0.20	0.705299	$1.1\cdot10^{-4}$	0.23	0.03	7	1089	8	0.29	0.704704	$1.2\cdot10^{-5}$	0.39	0.04	5
60 - 80	GFRO10030	BCw	−0.64	−0.60	0.52	16176	196	0.18	0.705416	$4.2\cdot10^{-5}$	0.27	0.03	7	1018	8	0.29	0.704720	$2.7\cdot10^{-5}$	0.39	0.04	5
80 - 100	GFRO100WG	BCw	−0.66	−0.64	0.57	16577	195	0.19	0.705400	$6.8\cdot10^{-5}$	0.23	0.02	7	1096	9	0.28	0.704761	$3.0\cdot10^{-5}$	0.41	0.06	5
100 - 120	GFRO100WF	C	−0.66	−0.65	0.58	17243	199	0.19	0.705380	$9.4\cdot10^{-5}$	0.30	0.06	7	742	6	0.29	0.704769	$3.0\cdot10^{-5}$	0.44	0.02	6
120 - 140	GFRO100WE	C	−0.54	−0.55	0.51	19581	212	0.20	0.705327	$3.9\cdot10^{-5}$	0.30	0.06	4	398	3	0.29	0.704882	$1.9\cdot10^{-5}$	0.41	0.04	6
LCPED20		Cambisol																			
0 - 5	GFRO10029	Ah1	−0.26	−0.27	0.18	19011	208	0.20	0.705557	$1.1\cdot10^{-4}$	0.25	0.04	8	3252	17	0.43	0.705832	$2.4\cdot10^{-5}$	0.29	0.02	5
5 - 10	GFRO1002A	Ah1	−0.46	−0.39	0.23	14937	188	0.17	0.705514	$1.1\cdot10^{-4}$	0.23	0.03	8	1323	8	0.38	0.705795	$1.6\cdot10^{-5}$	0.27	0.02	6
10 - 20	GFRO1002B	Ah2	−0.46	−0.37	0.20	14223	187	0.17	0.705626	$1.9\cdot10^{-5}$	0.20	0.02	8	1016	6	0.36	0.705755	$2.5\cdot10^{-5}$	0.27	0.03	6
20 - 40	GFRO1002C	Ah3	−0.43	−0.35	0.17	14437	182	0.17	0.705591	$9.3\cdot10^{-6}$	0.21	0.02	9	886	6	0.33	0.705700	$2.1\cdot10^{-5}$	0.31	0.02	6
40 - 60	GFRO1002D	Bw	−0.49	−0.45	0.29	15080	181	0.18	0.705507	$1.4\cdot10^{-4}$	0.24	0.02	8	605	4	0.30	0.705645	$2.4\cdot10^{-5}$	0.33	0.02	6
60 - 80	GFRO100VU	BCw	−0.08	−0.15	−0.02	18940	195	0.21	0.705072	$1.2\cdot10^{-5}$	0.26	0.02	8	595	5	0.28	0.705593	$1.3\cdot10^{-5}$	0.38	0.01	6
80 - 100	GFRO100VV	BCw	−0.19	−0.19	−0.01	17081	190	0.20	0.705148	$1.3\cdot10^{-5}$	0.28	0.03	8	578	5	0.27	0.705474	$2.1\cdot10^{-5}$	0.39	0.02	6
100 - 120	GFRO100VW	BCw	−0.34	−0.32	0.14	16295	186	0.19	0.705141	$7.6\cdot10^{-5}$	0.29	0.02	8	402	3	0.26	0.705429	$2.6\cdot10^{-5}$	0.42	0.01	6
120 - 140	GFRO100VY	C	−0.47	−0.39	0.22	14437	184	0.17	0.705427	$2.5\cdot10^{-5}$	0.33	0.01	8	295	2	0.26	0.705374	$2.4\cdot10^{-5}$	0.44	0.01	6
140 - 160	GFRO100VX	C	−0.45	−0.34	0.16	13722	185	0.16	0.705475	$1.1\cdot10^{-4}$	0.33	0.05	7	400	3	0.27	0.705373	$2.2\cdot10^{-5}$	0.49	0.01	6
Nahuelbuta, NAPED40		**umbric Podzol**																			
0 - 5	GFRO1001R	Ah1	−0.68	−0.62	0.24	7999	104	0.17	0.717127	$2.1\cdot10^{-5}$	0.13	0.05	3	170	2	0.18	0.713352	$2.4\cdot10^{-5}$	0.22	0.03	6
5 - 10	GFRO1001S	Ah1	−0.70	−0.66	0.30	8105	102	0.17	0.717146	$4.1\cdot10^{-5}$	0.15	0.03	3	146	2	0.17	0.713361	$2.0\cdot10^{-5}$	0.24	0.03	6
10 - 20	GFRO1001T	Ah1	−0.70	−0.66	0.30	8117	102	0.17	0.716891	$2.2\cdot10^{-5}$	0.19	0.05	3	117	1	0.17	0.713352	$1.8\cdot10^{-5}$	0.25	0.02	6
20 - 40	GFRO1001U	Ah2	−0.73	−0.69	0.34	7692	99	0.17	0.717018	$1.6\cdot10^{-5}$	0.16	0.03	3	55	1	0.15	0.713364	$1.4\cdot10^{-5}$	0.21	0.03	6
40 - 60	GFRO1001V	Bw	−0.69	−0.68	−0.19	4909	56	0.19	0.720405	$1.9\cdot10^{-5}$	0.13	0.02	3	29	1	0.10	0.713663	$1.3\cdot10^{-5}$	0.20	0.00	5
60 - 80	GFRO100X0	BCs1	−0.69	−0.63	0.29	8237	110	0.16	0.719441	$1.7\cdot10^{-5}$	0.20	0.03	3	39	1	0.12	0.713783	$1.1\cdot10^{-5}$	0.23	0.03	6
80 - 100	GFRO10050	BCs2	−0.78	−0.70	0.33	6154	92	0.15	0.719617	$1.7\cdot10^{-5}$	0.18	0.06	3	43	1	0.14	0.713891	$1.6\cdot10^{-5}$	0.22	0.03	6
100 - 120	GFRO100WZ	C1	−0.71	−0.57	−0.07	5155	84	0.13	0.721327	$2.3\cdot10^{-5}$	0.11	0.02	3	75	1	0.18	0.714057	$8.9\cdot10^{-6}$	0.28	0.02	6
120 - 140	GFRO100WY	C1	−0.77	−0.70	0.30	6287	89	0.15	0.720840	$5.4\cdot10^{-5}$	0.01	0.11	3	111	1	0.19	0.714206	$1.1\cdot10^{-5}$	0.29	0.01	6
140 - 160	GFRO100WX	C1	−0.78	−0.71	0.37	6753	94	0.16	0.719923	$1.2\cdot10^{-5}$	0.14	0.04	3	118	1	0.19	0.714336	$1.3\cdot10^{-5}$	0.25	0.03	6
160 - 180	GFRO100WV	C2	−0.52	−0.59	0.21	11566	108	0.23	0.718143	$4.0\cdot10^{-5}$	0.13	0.01	3	77	1	0.19	0.714397	$6.3\cdot10^{-6}$	0.27	0.02	6
180 - 200	GFRO100WW	C2	−0.76	−0.70	0.35	6966	95	0.16	0.720216	$2.0\cdot10^{-5}$	0.10	0.03	3	100	1	0.18	0.714420	$2.0\cdot10^{-5}$	0.24	0.04	6
NAPED20		**orthodystric Umbrisol**																			
0 - 5	GFRO10019	Ah1	−0.54	−0.59	0.27	12022	118	0.22	0.711267	$4.5\cdot10^{-5}$	0.37	0.05	4	129	2	0.16	0.708952	$4.7\cdot10^{-5}$	0.21	0.06	5
5 - 10	GFRO10018	Ah1	−0.58	−0.64	0.36	12612	118	0.23	0.711144	$5.9\cdot10^{-5}$	0.37	0.06	4	28	0	0.19	0.708911	$6.1\cdot10^{-5}$	0.20	0.01	5
10 - 20	GFRO1001A	Ah2	−0.58	−0.64	0.35	12386	117	0.23	0.711692	$8.0\cdot10^{-5}$	0.32	0.07	4	15	0	0.20	0.708852	$1.3\cdot10^{-5}$	0.21	0.05	6
20 - 40	GFRO1001B	Ah3	−0.58	−0.64	0.36	12618	118	0.23	0.711095	$3.8\cdot10^{-5}$	0.34	0.07	4	35	0	0.51	0.708139	$1.9\cdot10^{-5}$	0.21	0.05	6
40 - 60	GFRO1001C	Bw1	−0.53	−0.57	0.21	11238	114	0.22	0.711374	$3.4\cdot10^{-5}$	0.36	0.04	4	11	0	0.26	0.709643	$6.5\cdot10^{-6}$	0.40	0.07	4
60 - 80	GFRO1001D	Bw2	−0.54	−0.59	0.22	11263	109	0.23	0.716905	$2.8\cdot10^{-5}$	0.35	0.06	4	8	0	0.19	0.709349	$8.6\cdot10^{-6}$	0.16	0.02	6
80 - 100	GFRO100WP	BCw	4.64	1.36	−3.23	25432	116	0.48	0.718857	$4.4\cdot10^{-5}$	0.37	0.06	4	9	0	0.11	0.709888	$2.5\cdot10^{-5}$	0.14	0.03	4

Continued on the next page.

Table 4.1: ...continuation

Soil profile depth	IGSN	sample type*	weathering indices † τ^{Ca}	τ^{Sr} [-]	CDF	concentration † Ca [µg g^{-1}]	Sr	bulk regolith Ca/Sr [mol mmol^{-1}]	$^{87}Sr/^{86}Sr$	2SE$_t$	$\delta^{88/86}Sr$ [‰]	2SE$_t$	n	concentration ‡ Ca [µg g^{-1}]	Sr	bio-available fraction Ca/Sr [mol mmol^{-1}]	$^{87}Sr/^{86}Sr$	2SE$_t$	$\delta^{88/86}Sr$ [‰]	2SE$_t$	n
100 - 120	GFRO100WN	C1	2.98	0.45	−1.16	35086	140	0.55	0.715317	$1.4\cdot10^{-5}$	0.31	0.02	8	10	0	0.08	0.709877	$3.1\cdot10^{-5}$	0.09	0.08	4
120 - 140	GFRO100WM	C2	1.21	−0.02	−0.10	38331	186	0.45	0.712697	$7.6\cdot10^{-6}$	0.38	0.02	8	7	0	0.04	0.710036	$2.7\cdot10^{-5}$	0.48	0.06	6
140 - 160	GFRO100WL	C2	1.28	0.24	−0.50	28981	172	0.37	0.713677	$2.0\cdot10^{-5}$	0.38	0.02	8	9	1	0.03	0.709221	$1.6\cdot10^{-5}$	−0.08	0.00	3
160 - 180	GFRO100WK	C2	−0.13	−0.07	−0.97	8418	99	0.19	0.720560	$2.0\cdot10^{-5}$	0.37	0.02	4	13	0	0.08	0.709896	$6.9\cdot10^{-5}$	−0.22	0.04	5
180 - 200	GFRO100WQ	C3	0.69	0.34	−1.50	12846	112	0.25	0.716367	$1.2\cdot10^{-5}$	0.41	0.01	4	13	0	0.06	0.709305	$4.3\cdot10^{-5}$	−0.21	0.03	3
200 - 220	GFRO100WR	C3	0.38	0.01	−0.88	13951	112	0.27	0.712798	$2.1\cdot10^{-5}$	0.43	0.04	4	13	1	0.05	0.709391	$1.3\cdot10^{-5}$	0.01	0.03	9
220 - 240	GFRO100WJ	C3	0.74	0.32	−1.04	16254	135	0.26	0.711577	$5.6\cdot10^{-5}$	0.42	0.02	4	13	1	0.03	0.708969	$1.3\cdot10^{-5}$	−0.12	0.02	6
240 - 260	GFRO100WH	C3	0.28	0.23	−0.72	14106	149	0.21	0.714187	$2.7\cdot10^{-5}$	0.46	0.05	4	20	1	0.04	0.708851	$1.7\cdot10^{-5}$	−0.22	0.01	5
Bedrock samples																					
Pan de Azúcar	GFRO100RK					6790	119	0.12	0.723831	$2.8\cdot10^{-5}$	0.16	0.05	3								
	GFRO100RN					8219	113	0.16	0.724739	$2.0\cdot10^{-5}$	0.11	0.02	3								
	GFRO100X1					10220	101	0.22	0.725667	$3.0\cdot10^{-5}$	0.14	0.04	3								
	GFRO100RF					14580	91	0.35	0.728398	$4.6\cdot10^{-6}$	0.16	0.00	3								
	GFRO100RG					14366	195	0.16													
	GFRO100LU					8719	154	0.12													
	GFRO100RM					12150	151	0.18													
	GFRO100RH					15795	140	0.25													
	GFRO100LT					6146	121	0.11													
	GFRO100RL					8648	128	0.15													
	GFRO100RJ					10363	93	0.24													
	GFRO100LS					6218	112	0.12													
	mean					10184	120	0.18	0.725659		0.14										
	1SD					3359	21	0.07	0.001974		0.02										
Santa Gracia	GFRO100L7					73543	554	0.29	0.703630	$9.5\cdot10^{-6}$	0.29	0.04	3								
	GFRO100L8					61750	435	0.31	0.703925	$7.2\cdot10^{-6}$	0.28	0.04	3								
	GFRO100LA					100344	652	0.34	0.703934	$1.8\cdot10^{-5}$	0.35	0.03	3								
	GFRO100LB					43740	515	0.19	0.704230	$2.5\cdot10^{-6}$	0.33	0.07	3								
	GFRO100LC					44955	287	0.34	0.703707	$2.1\cdot10^{-5}$	0.26	0.05	3								
	GFRO100X2					88623	585	0.33	0.704607	$1.7\cdot10^{-5}$	0.26	0.11	3								
	GFRO100RU					40023	383	0.23	0.703603	$1.2\cdot10^{-5}$	0.26	0.08	3								
	GFRO100L9					101361	659	0.34													
	mean					69292	509	0.30	0.703948		0.29										
	1SD					25476	132	0.06	0.000363		0.03										
La Campana	GFRO10094					10649	186	0.13	0.706047	$1.7\cdot10^{-5}$	0.26	0.03	3								
	GFRO10098					10363	183	0.12	0.706136	$3.5\cdot10^{-5}$	0.29	0.09	3								
	GFRO10096					8576	165	0.11	0.706671	$2.3\cdot10^{-5}$	0.17	0.01	3								
	GFRO10095					12936	207	0.14	0.705931	$4.9\cdot10^{-6}$	0.29	0.03	6								
	GFTE10004					5646	158	0.08	0.706521	$3.8\cdot10^{-5}$	0.25	0.00	3								
	GFRO10097					38022	316	0.26													
	GFRO100RP					32662	294	0.24													
	GFRO1019S					32162	295	0.24													
	GFRO100DH					30947	287	0.24													

Continued on the next page.

Table 4.1: ...continuation

Soil profile depth	IGSN	sample type*	weathering indices † τ^{Ca}	τ^{Sr}	CDF	bulk regolith concentration † Ca [µg g^{-1}]	Sr	Ca/Sr [mol mmol^{-1}]	$^{87}Sr/^{86}Sr$	2SE$_t$	$\delta^{88/86}Sr$ [‰]	2SE$_t$	n	bio-available fraction concentration ‡ Ca [µg g^{-1}]	Sr	Ca/Sr [mol mmol^{-1}]	$^{87}Sr/^{86}Sr$	2SE$_t$	$\delta^{88/86}Sr$ [‰]	2SE$_t$	n
	GFRO1019U					29446	259	0.25													
	mean					21141	235	0.18	0.706261		0.25										
	1SD					12453	61	0.07	0.000319		0.05										
Nahuelbuta	GFRO10009					28445	215	0.29	0.713426	$1.4\cdot10^{-5}$	0.34	0.07	3								
	GFRO10006					3716	142	0.06	0.725813	$1.2\cdot10^{-5}$	0.21	0.05	3								
	GFRO1000C					22942	226	0.22	0.712020	$1.4\cdot10^{-5}$	0.27	0.02	6								
	GFRO1017N					25372	242	0.23	0.713192	$6.0\cdot10^{-6}$	0.20	0.05	3								
	GFRO10004					14794	217	0.15													
	mean					19054	208	0.19	0.716113		0.25										
	1SD					9958	39	0.09	0.006496		0.07										
International reference materials for concentration data quality control (element concentration in µg g^{-1}, radiogenic $^{87}Sr/^{86}Sr$, and Ca/Sr ratio in mol mmol^{-1})																					
BCR-2	mean	(n=6/18)§				43735	304	0.32	0.705012	$1.2\cdot10^{-5}$	0.31	0.04									
BCR-2	RSD					9%	10%														
BHVO-2	mean	(n=7/72)§				72988	359	0.45	0.703469	$1.1\cdot10^{-5}$	0.27	0.02									
BHVO-2	RSD					8%	3%														
JG-2	mean	(n=7/18)§				4661	14	0.75	0.758886	$8.9\cdot10^{-3}$	−0.12	0.08									
JG-2	RSD					4%	22%														
NIST2709a	mean	(n=7/72)§				17482	221	0.17	0.708147	$1.1\cdot10^{-5}$	0.23	0.01									
NIST2709a	RSD					3%	4%														
TILL-1	mean	(n=6/15)§												1094	3	0.79	0.709192	$1.0\cdot10^{-3}$	0.12	0.04	
TILL-1	RSD													9%	26%						
NIST2709a	mean	(n=6/17)§												10767	58	0.41	0.707660	$1.0\cdot10^{-5}$	0.25	0.02	
NIST2709a	RSD													12%	11%						
SRM-987	mean	(n=/1910)§							0.710280	$3.6\cdot10^{-6}$											
Sr-ICP	mean	(n=/240)§							0.707516	$3.5\cdot10^{-6}$	0.09	0.01									

* Pedogenic soil-horizon classification from Bernhard et al. (2018); † Oeser et al. (2018a); ‡ Oeser and von Blanckenburg (2020b); § chemical and mass spectrometrical replicates, respectively

2SE$_t$ are the 95% confidence intervals calculated as $t \times SD/\sqrt{n}$; SD = standard deviation of n mass spectrometrical replicate analysis, t = correction factor from Student's t-distribution at 95% probability.

n.d. not determined

The $^{87}Sr/^{86}Sr$ ratios in the sites' respective bio-available fractions are uniformly distributed with depth and are not correlated with the corresponding regolith $^{87}Sr/^{86}Sr$ profile. In the arid and semi-arid sites of Pan de Azúcar and Santa Gracia, radiogenic Sr isotope ratios in the bio-available fraction do not differ between the N- and S-facing slope. In mediterranean and humid-temperate sites of La Campana and Nahuelbuta, these ratios are distinct for each profile.

Plant samples' $^{87}Sr/^{86}Sr$ ratios are in most cases indistinguishable from that of the corresponding bio- available fraction (Figs. 4.1 – 4.4; Table 4.1 & 4.2). Exceptions are the spikes of *C. sphaerica* in Santa Gracia (Fig. 4.2) and the plants on both slopes in La Campana (Fig. 4.3). The deviations between the plant samples' $^{87}Sr/^{86}Sr$ ratio and that in the bio-available fraction in La Campana can be attributed to a nutrient uptake depth that is beneath the regolith profile (N-facing profile), and species-dependent uptake depths from different parts of the regolith profile (S-facing profile; Oeser and von Blanckenburg 2020b), respectively.

$\delta^{88/86}$*Sr values*

The similarity between rock and bulk regolith seen in $^{87}Sr/^{86}Sr$ ratios is also reflected in their $\delta^{88/86}$Sr values. Bedrock $\delta^{88/86}$Sr in Pan de Azúcar is 0.14 ± 0.02‰(n = 4) and in Santa Gracia 0.29 ± 0.03‰(n = 7). In La Campana and Nahuelbuta $\delta^{88/86}$Sr amounts to 0.25 ± 0.05‰(n = 5) and 0.25 ± 0.07‰(n = 4), respectively. With the exception of Pan de Azúcar, these values are thus within the range of bulk silicate Earth (0.30 ± 0.02‰; Amsellem et al. 2018).

Regolith $\delta^{88/86}$Sr do not vary outside uncertainty from bedrock $\delta^{88/86}$Sr values (Table 4.3). However, $\delta^{88/86}$Sr show a significant trend with depth in the N-facing profile in Pan de Azúcar and Nahuelbuta, and the S-facing profile in La Campana. In these, variations in $\delta^{88/86}$Sr are concomitant with increasing τ^{Ca} and τ^{Sr}, reflecting either changes in initial substrate (La Campana and Nahuelbuta) or incorporation of externally derived Sr (Pan de Azúcar). Atmospherically-derived Sr will have $\delta^{88/86}$Sr values of 0.23‰or 0.39‰if derived from marine carbonates or sea salts, respectively (Fietzke and Eisenhauer 2006; Halicz et al. 2008; Krabbenhöft et al. 2010; Pearce et al. 2015a).

$\delta^{88/86}$Sr in bio-available fractions differs substantially from that of bulk regolith and is, bar two exceptions (Santa Gracia N-facing and Nahuelbuta S-facing profile; Fig. 4.2a & 4.4b), isotopically heavier than bulk regolith. $\delta^{88/86}$Sr values in the bio-available fraction are subject to a substantial variation with depth. In the La Campana N- and S-facing and in Nahuelbuta N-facing profiles, the bio-available fraction mimics the depth-distribution pattern of the corresponding regolith samples (Fig. 4.3a, b & 4.4a). Only in Santa Gracia N-facing and Nahuelbuta S-facing profile $\delta^{88/86}$Sr in bio-available fractions exceeds $\delta^{88/86}$Sr of bedrock (Fig. 4.2a & 4.4b).

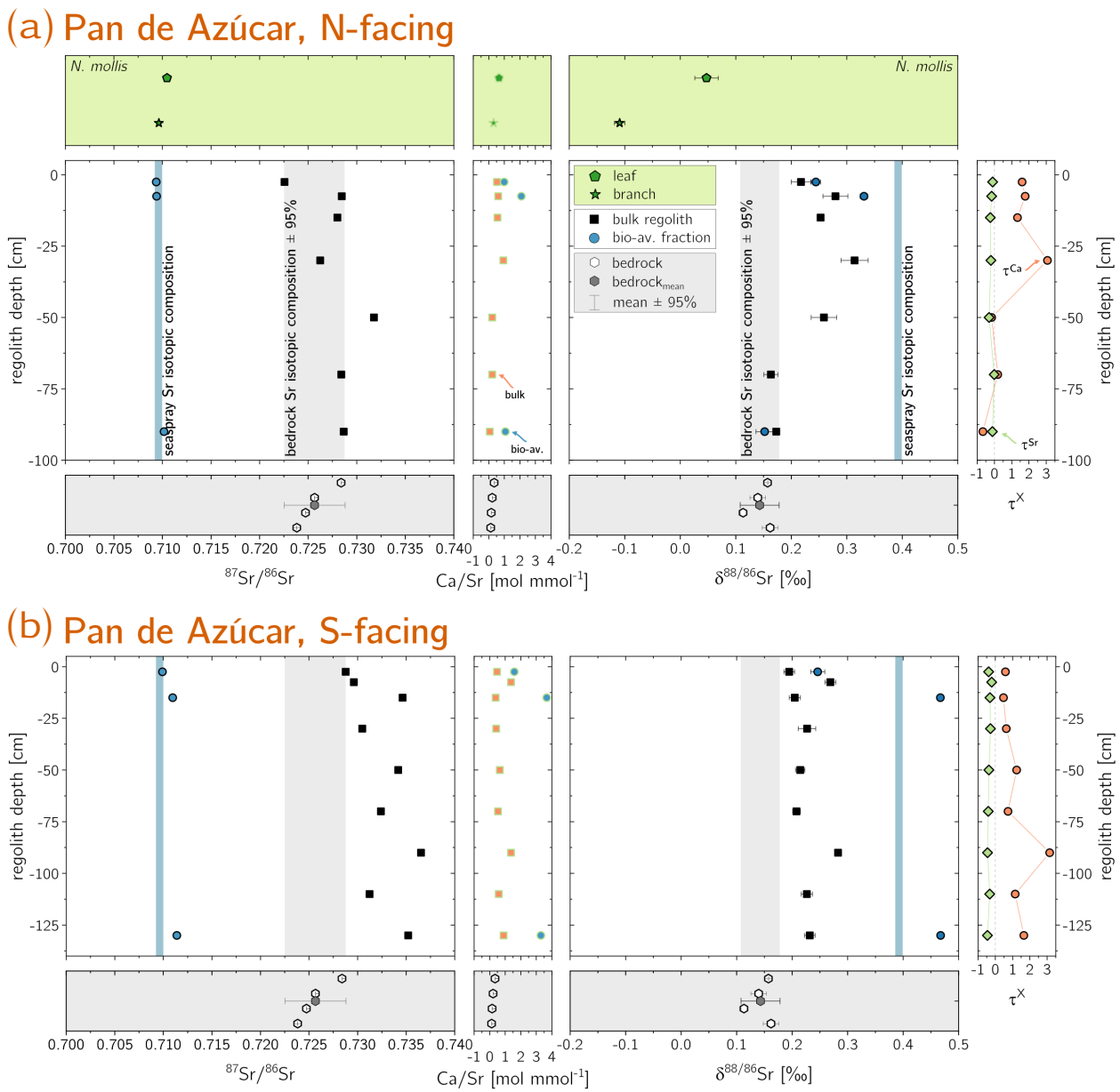

Figure 4.1: Radiogenic $^{87}Sr/^{86}Sr$ (left) and stable $\delta^{88/86}Sr$ (right) isotope composition with molar Ca/Sr ratios in the center panel in the N- (a) and S-facing (b) regolith profile in Pan de Azúcar. Shown are the isotope composition of bulk regolith and the bio-available fraction vs. depth as well as those of the single plant compartments. τ-values (very right) denote the fraction of Ca and Sr loss and gain relative to bedrock, respectively. Error bars on radiogenic and stable Sr denote 2SE uncertainty – in the case of radiogenic Sr they are smaller than the datapoint.

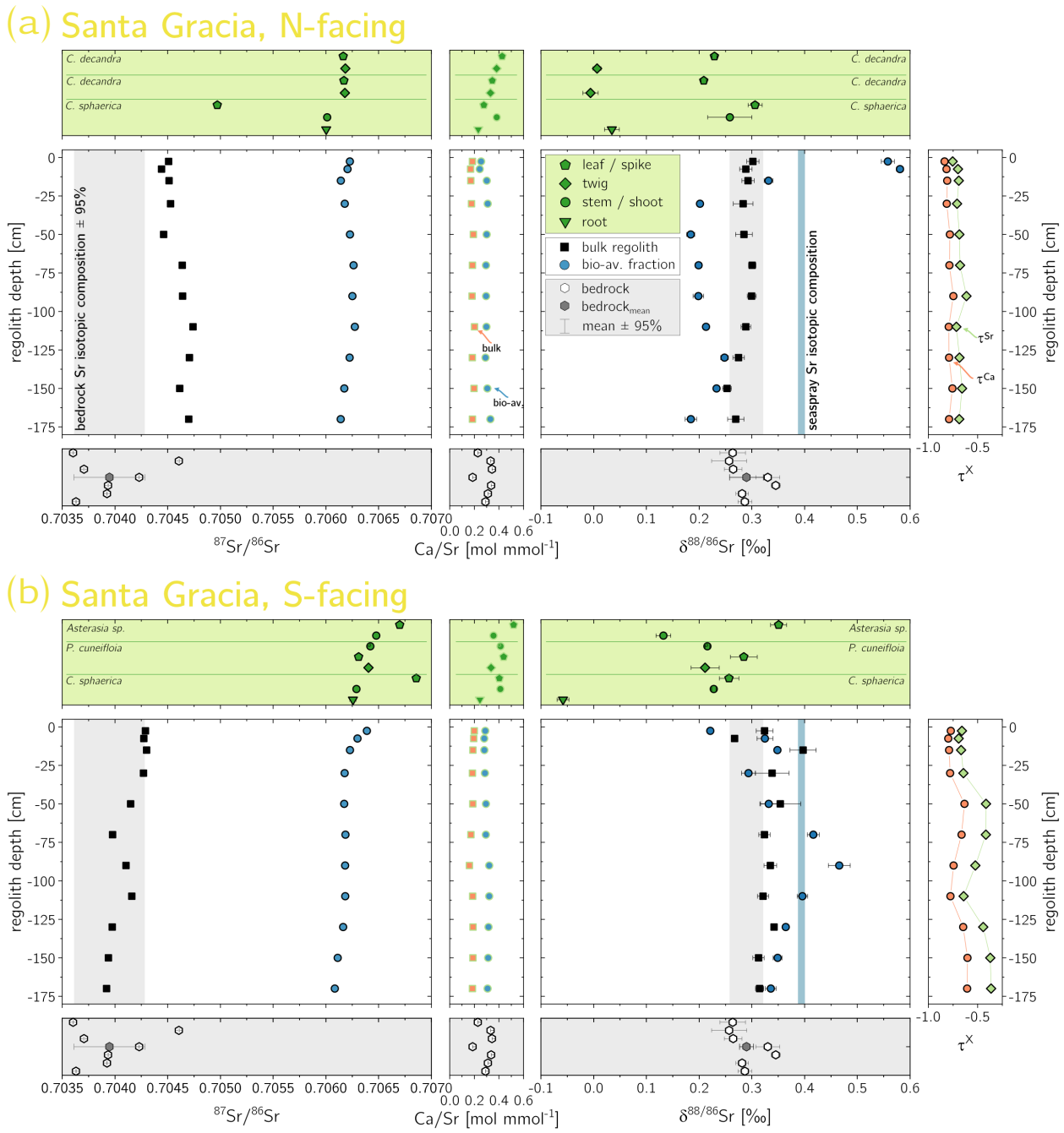

Figure 4.2: Radiogenic $^{87}Sr/^{86}Sr$ (left) and stable $\delta^{88/86}Sr$ (right) isotope composition with molar Ca/Sr ratios in the center panel in the N- (a) and S-facing (b) regolith profile in Santa Gracia. Shown are the isotope composition of bulk regolith and the bio-available fraction vs. depth as well as those of the single plant compartments. τ-values (very right) denote the fraction of Ca and Sr loss and gain relative to bedrock, respectively. Error bars on radiogenic and stable Sr denote 2SE uncertainty – in the case of radiogenic Sr they are smaller than the datapoint.

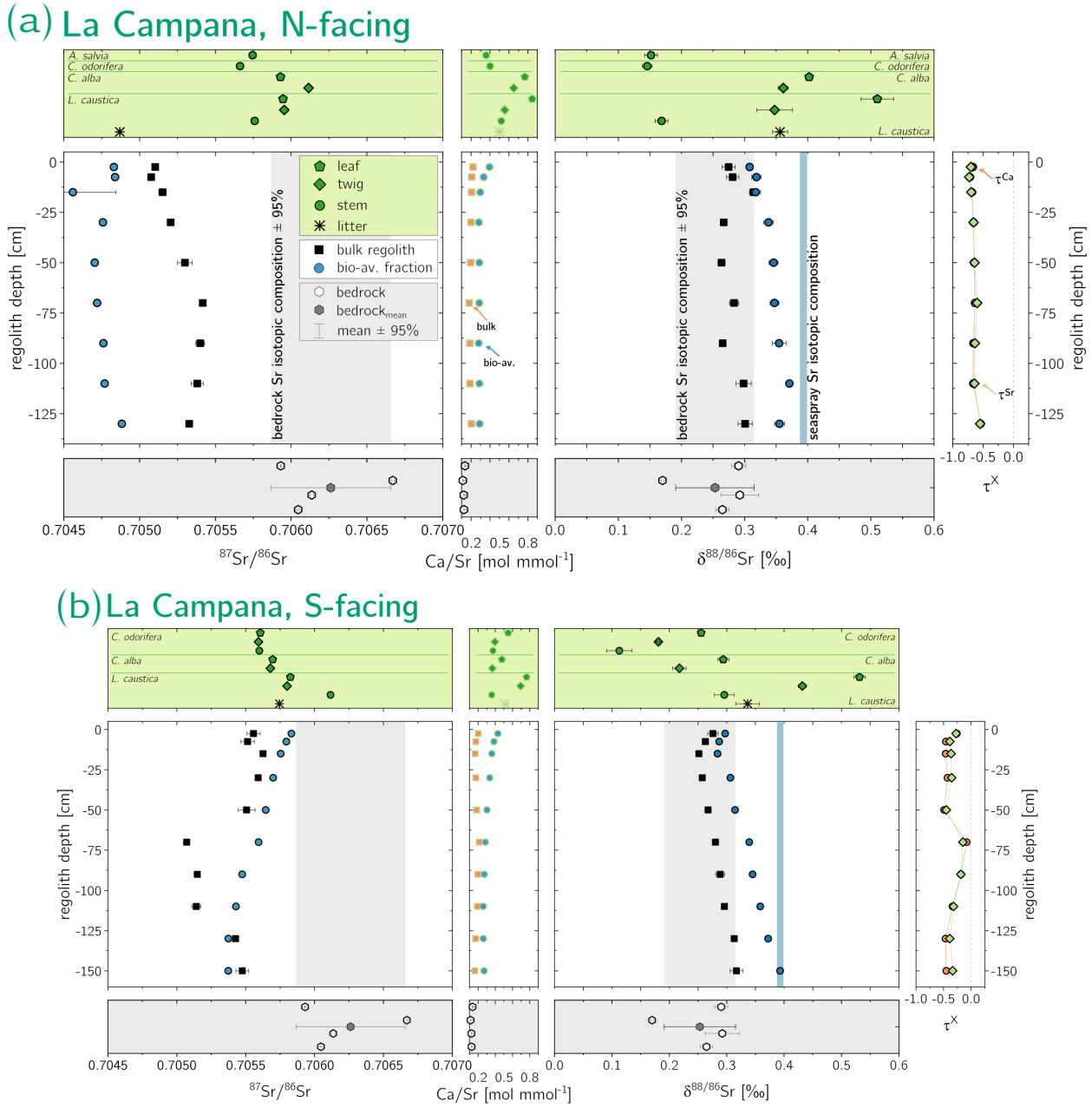

Figure 4.3: Radiogenic $^{87}Sr/^{86}Sr$ (left) and stable $\delta^{88/86}Sr$ (right) isotope composition with molar Ca/Sr ratios in the center panel in the N- (a) and S-facing (b) regolith profile in La Campana. Shown are the isotope composition of bulk regolith and the bio-available fraction vs. depth as well as those of the single plant compartments. τ-values (very right) denote the fraction of Ca and Sr loss and gain relative to bedrock, respectively. Error bars on radiogenic and stable Sr denote 2SE uncertainty – in the case of radiogenic Sr they are smaller than the datapoint.

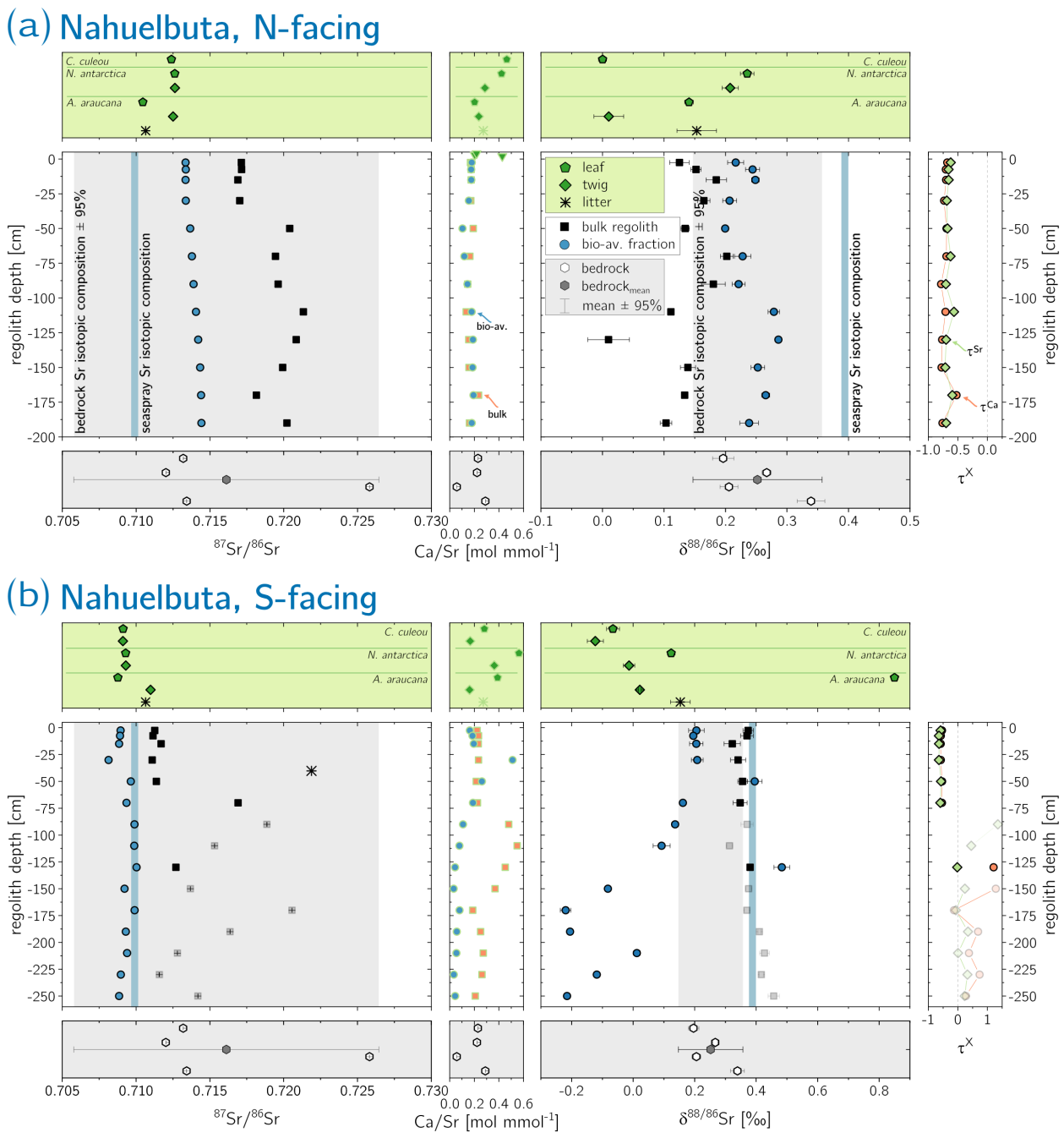

Figure 4.4: Radiogenic $^{87}Sr/^{86}Sr$ (left) and stable $\delta^{88/86}Sr$ (right) isotope composition with molar Ca/Sr ratios in the center panel in the N- (a) and S-facing (b) regolith profile in Nahuelbuta. Shown are the isotope composition of bulk regolith and the bio-available fraction vs. depth as well as those of the single plant compartments. τ-values (very right) denote the fraction of Ca and Sr loss and gain relative to bedrock, respectively. Error bars on radiogenic and stable Sr denote 2SE uncertainty – in the case of radiogenic Sr they are smaller than the datapoint. Gray symbols refer to excluded samples because they putatively stem from different bedrock (Oeser and von Blanckenburg 2020b).

Table 4.2: Chemical composition of single plant organs, their radiogenic $^{87}Sr/^{86}Sr$, stable $\delta^{88/86}Sr$ isotope ratio, and molar Ca/Sr ratio. For organs that do not list an IGSN, their $\delta^{88/86}Sr_{veg}$ has been estimated (see discussion) to derive an estimate for bulk plant Sr isotope composition (bold value in brackets). Δ^{Sr}_{upt} is the fractionation factor during Sr uptake by plants.

Study site *Plant species*	organ	slope	IGSN	Ca [µg g^{-1}]	Sr	Ca/Sr [mol $mmol^{-1}$]	$^{87}Sr/^{86}Sr$	$2SE_t$	$\delta^{88/86}Sr_{veg}$ [‰]	$2SE_t$	n	Δ^{Sr}_{upt} † [‰]
Pan de Azúcar												
Nolona mollis	leaf	N	GFRO10119	24937	83	0.66	0.710470	$4.1 \cdot 10^{-5}$	0.05	0.07	3	
	branch	N	GFRO10118	10573	74	0.31	0.709640	$9.2 \cdot 10^{-6}$	−0.11	0.03	3	
	root	N							−0.27			
	bulk plant	N							-0.06 (**-0.11**)			-0.30 (**-0.35**)
Santa Gracia												
Cordia decandra	leaf	N	GFRO100ZV	34625	219	0.35	0.706170	$1.2 \cdot 10^{-5}$	0.21	0.01	4	
	twig	N	GFRO1013D	16128	107	0.33	0.706180	$2.1 \cdot 10^{-5}$	−0.01	0.04	4	
	stem	N							−0.22			
	root	N							−0.44			
	bulk plant	N							0.06 (**-0.08**)			-0.21 (**-0.07**)
Cordia decandra	leaf	N	GFRO1008V	63895	328	0.43	0.706160	$3.4 \cdot 10^{-5}$	0.23	0.01	3	
	twig	N	GFRO1017L	15793	91	0.38	0.706180	$1.2 \cdot 10^{-5}$	0.01	0.02	3	
	stem	N							−0.22			
	root	N							−0.44			
	bulk plant	N							0.08 (**-0.07**)			-0.22 (**-0.08**)
Cumulopuntia sphaerica	leaf	N	GFRO1011C	5614	44	0.28	0.704970	$3.6 \cdot 10^{-5}$	0.31	0.03	7	
	stem	N	GFRO1011B	34432	197	0.38	0.706010	$7.8 \cdot 10^{-6}$	0.26	0.10	3	
	root	N	GFRO1011A	26709	252	0.23	0.706000	$1.1 \cdot 10^{-5}$	0.03	0.03	7	
	bulk plant	N							0.20			-0.09
Asterasia sp.	leaf	S	GFRO10138	10091	43	0.52	0.706700	$3.7 \cdot 10^{-5}$	0.35	0.05	3	
	twig	S							0.24			
	stem	S	GFRO10137	9600	59	0.36	0.706480	$1.3 \cdot 10^{-5}$	0.13	0.04	3	
	root	S							0.02			
	bulk plant	S							0.20 (**0.20**)			-0.15 (**-0.15**)
Cumulopuntia sphaerica	leaf	S	GFRO1017K	3503	19	0.40	0.706860	$1.4 \cdot 10^{-5}$	0.26	0.08	2	
	stem	S	GFRO1017J	35676	190	0.41	0.706290	$6.0 \cdot 10^{-5}$	0.23	0.01	3	
	root	S	GFRO1017H	15689	140	0.25	0.706260	$9.7 \cdot 10^{-5}$	−0.06	0.04	3	
	bulk plant	S							0.14			-0.21
Proustia cuneifolia	blossoms	S	GFRO1017D	4388	23	0.41	0.706420	$2.8 \cdot 10^{-5}$	0.22	0.02	2	

Continued on the next page.

Table 4.2: ...continuation

Study site *Plant species*	organ	slope	IGSN	Ca [µg g^{-1}]	Sr	Ca/Sr [mol $mmol^{-1}$]	$^{87}Sr/^{86}Sr$	$2SE_t$	$\delta^{88/86}Sr_{veg}$ [‰]	$2SE_t$	n	Δ^{Sr}_{upt} † [‰]
	leaf	S	GFRO1017E	21634	108	0.44	0.706310	$1.6 \cdot 10^{-5}$	0.28	0.08	3	
	twig	S	GFRO1017F	7783	51	0.34	0.706400	$1.4 \cdot 10^{-5}$	0.21	0.08	3	
	stem	S							0.15			
	root	S							0.08			
	bulk plant	S							0.22 (**0.19**)			-0.13 (**-0.16**)
La Campana												
forest floor	litter	N	GFRO10174	22836	100	0.50	0.704870	$1.2 \cdot 10^{-5}$	0.36	0.03	5	
Aristeguieta salvia	leaf	N							0.35			
	twig	N							0.24			
	stem	N	GFRO1008H	4896	30	0.36	0.705750	$6.0 \cdot 10^{-5}$	0.14	0.03	4	
	root	N							0.03			
	bulk plant	N							0.14 (**0.20**)			-0.24 (**-0.17**)
Colliguaja odorifera	leaf	N							0.36			
	twig	N							0.25			
	stem	N	GFRO1011D	11213	61	0.40	0.705660	$4.8 \cdot 10^{-5}$	0.15	0.03	2	
	root	N							0.04			
	bulk plant	N							0.15 (**0.21**)			-0.23 (**-0.17**)
Cryptocaria alba	leaf	N	GFRO10178	4876	14	0.77	0.705930	$3.6 \cdot 10^{-5}$	0.40	0.03	2	
	twig	N	GFRO10179	10054	34	0.65	0.706110	$4.7 \cdot 10^{-5}$	0.36	0.01	2	
	stem	N							0.32			
	root	N							0.28			
	bulk plant	N							0.37 (**0.35**)			-0.00 (**-0.03**)
Lithraea caustica	leaf	N	GFRO10176	3982	10	0.85	0.705950	$2.0 \cdot 10^{-5}$	0.51	0.08	3	
	twig	N	GFRO10177	23427	92	0.56	0.705950	$5.4 \cdot 10^{-5}$	0.35	0.09	3	
	stem	N	GFRO10175	8970	38	0.52	0.705760	$2.5 \cdot 10^{-5}$	0.17	0.03	3	
	root	N							0.00			
	bulk plant	N							0.34 (**0.28**)			-0.4 (**-0.10**)
forest floor	litter	S	GFRO10152	14163	60	0.51	0.705740	$2.5 \cdot 10^{-5}$	0.34	0.07	3	
Colliguaja odorifera	leaf	S	GFRO10172	12714	51	0.55	0.705610	$1.8 \cdot 10^{-5}$	0.26	0.01	5	
	twig	S	GFRO10173	12747	70	0.40	0.705590	$8.6 \cdot 10^{-6}$	0.18	0.02	5	
	stem	S	GFRO1011E	10620	62	0.37	0.705600	$9.0 \cdot 10^{-6}$	0.11	0.09	2	
	root	S							0.04			

Continued on the next page.

Table 4.2: ...continuation

Study site *Plant species*	organ	slope	IGSN	Ca [µg g^{-1}]	Sr	Ca/Sr [mol mmol^{-1}]	$^{87}Sr/^{86}Sr$	$2SE_t$	$\delta^{88/86}Sr_{veg}$ [‰]	$2SE_t$	n	Δ^{Sr}_{upt} † [‰]
	bulk plant	S							0.18 (**0.16**)			-0.25 (**-0.27**)
Cryptocaria alba	leaf	S	GFRO1013C	4720	22	0.48	0.705700	$1.2 \cdot 10^{-5}$	0.29	0.03	4	
	twig	S	GFRO1008N	12526	75	0.37	0.705680	$3.6 \cdot 10^{-5}$	0.22	0.04	3	
	stem	S							0.14			
	root	S							0.06			
	bulk plant	S							0.24 (**0.19**)			-0.19 (**-0.24**)
Lithraea caustica	leaf	S	GFRO1013B	9325	27	0.76	0.705820	$1.9 \cdot 10^{-5}$	0.53	0.03	4	
	twig	S	GFRO1008P	5620	18	0.69	0.705800	$1.6 \cdot 10^{-5}$	0.43	0.02	4	
	stem	S	GFRO10139	2665	16	0.36	0.706120	$2.1 \cdot 10^{-5}$	0.30	0.04	5	
	root	S							0.18			
	bulk plant	S							0.42 (**0.38**)			-0.1 (**-0.5**)
Nahuelbuta												
Araucaria araucana	leaf	N	GFRO10164	10700	116	0.24	0.710460	$1.6 \cdot 10^{-5}$	0.14	0.08	3	
	twig	N	GFRO10169	9357	87	0.20	0.712510	$6.9 \cdot 10^{-6}$	0.01	0.02	6	
	stem	N							−0.12			
	root	N							−0.25			
	bulk plant	N							0.07 (**-0.04**)			-0.17 (**-0.28**)
Chusquea culeou	leaf	N	GFRO10109	4013	19	0.46	0.712390	$3.1 \cdot 10^{-5}$	0.00	0.02	4	
	twig	N							−0.06			
	root	N							−0.12			
	bulk plant	N							0.00 (**-0.06**)			-0.24(**-0.30**)
Nothofagus antarctica	leaf	N	GFRO1010A	4813	25	0.42	0.712620	$2.2 \cdot 10^{-5}$	0.24	0.03	4	
	twig	N	GFRO1016A	5406	41	0.29	0.712630	$1.4 \cdot 10^{-5}$	0.21	0.04	3	
	stem	N							0.18			
	root	N							0.15			
	bulk plant	N							0.22 (**0.20**)			-0.02 (**-0.04**)
forest floor	litter	S	GFRO10153	14432	116	0.27	0.710650	$9.7 \cdot 10^{-5}$	0.15	0.08	5	
Araucaria araucana	leaf	S	GFRO1010B	9941	56	0.39	0.708770	$9.1 \cdot 10^{-6}$	0.85	0.03	4	
	twig	S	GFRO10163	9330	127	0.16	0.710980	$8.8 \cdot 10^{-6}$	0.02	0.01	6	
	stem	S							−0.81			
	root	S							−1.63			
	bulk plant	S							0.42 (**-0.01**)			0.34 (**-0.10**)

Continued on the next page.

Table 4.2: ...continuation

Study site *Plant species*	organ	slope	IGSN	Ca [µg g^{-1}]	Sr	Ca/Sr [mol mmol^{-1}]	$^{87}Sr/^{86}Sr$	$2SE_t$	$\delta^{88/86}Sr_{veg}$ [‰]	$2SE_t$	n	Δ^{Sr}_{upt} † [‰]
Chusquea culeou	leaf	S	GFRO10168	4378	34	0.28	0.709120	$2.1 \cdot 10^{-5}$	−0.07	0.07	3	
	twig	S	GFRO10167	375	5	0.17	0.709110	$1.6 \cdot 10^{-5}$	−0.12	0.11	2	
	root	S							−0.18			
	bulk plant	S							-0.11 (**-0.12**)			-0.19 (**-0.21**)
Nothofagus antarctica	leaf	S	GFRO10166	8547	33	0.56	0.709290	$1.1 \cdot 10^{-5}$	0.12	0.03	5	
	twig	S	GFRO10165	12290	74	0.36	0.709300	$1.7 \cdot 10^{-5}$	−0.01	0.05	5	
	stem	S							−0.15			
	root	S							−0.29			
	bulk plant	S							0.03 (**-0.06**)			-0.05 (**-0.15**)
International reference materials for concentration data quality control												
SRM 1515 mean	(n=6/24)‡			17023	24		0.713950	$7.7 \cdot 10^{-6}$	0.23	0.01		
SRM 1515 RSD				15%	4%							

† Δ^{Sr}_{upt} was calculated according Eq. 4.2; bold values in brackets denote Δ^{Sr}_{upt} derived using $\delta^{88/86}Sr^{*}_{veg}$ (i.e. bulk plants' Sr isotope composition including estimated plant organs)

‡ chemical and mass spectrometrical replicates, respectively

$2SE_t$ are the 95% confidence intervals calculated as $t \times SD/\sqrt{n}$ SD = standard deviation of n mass spectrometrical replicate analysis, t = correction factor from Student's t-distribution at 95% probability.

In plants, $\delta^{88/86}$Sr increases systematically from stem (and roots if sampled) towards leaves (Fig. 4.1a – 4.4 & 4.5). This increase is associated with an increase in the molar Ca/Sr ratio throughout and differs in magnitude from species to species and even within species. The differences between the individual organs within a plant can be as small as 0.04 ± 0.02‰ in *C. alba* and as large as 0.83 ± 0.01‰ in *A. araucana* (Table 4.2).

4.5 Discussion

4.5.1 Strontium isotopes in the weathering zone

We use mass balance-based indicators of weathering as a benchmark to interpret the Sr isotope ratios. The degree of weathering is quantified by the chemical depletion fraction (CDF) and the elemental (X) loss fraction (τ^X), which disclose the total and the element-specific loss of soluble elements, respectively, relative to bedrock. In Pan de Azúcar, the degree of chemical weathering is low. In Santa Gracia, La Campana, and Nahuelbuta, CDF and τ-values indicate a substantial loss of nutritive elements, in particular of Ca and Sr, through weathering. However, the regolith profiles are not entirely depleted in weatherable primary minerals. The primary mineral stock that transits vertically through the weathering profile by erosion is at high (Pan de Azúcar) to moderate (Santa Gracia, La Campana, and Nahuelbuta) levels (Oeser et al. 2018a; Oeser and von Blanckenburg 2020b). The four EarthShape study sites are thus characterized as "kinetically limited" weathering systems, and the question is whether Sr isotopes reflect this regime of partial dissolution.

The molar Ca/Sr ratio in regolith is used as proxy to detect bedrock heterogeneities and incongruent dissolution of minerals which differ in their Ca/Sr ratio (e.g. Bailey et al. 1996; Blum et al. 2002; Jacobson et al. 2002). For example, the preferential dissolution of carbonates over silicates would lead to a substantial decrease in regolith bulk Ca/Sr ratios. At the EarthShape sites, bedrock consists of silicate rock without carbonates. Ca/Sr ratios in the EarthShape regolith profiles are uniformly distributed with depth, and are largely identical to bedrock Ca/Sr. This uniformity suggests homogenous source rock Ca/Sr ratios beneath each profile. Furthermore, uniform and bedrock-like regolith Ca/Sr ratios suggest the absence of preferential dissolution of a mineral with Ca/Sr that differs strongly from that of bedrock. Only the profiles in Pan de Azúcar (Fig. 4.1) and the S-facing profile in Nahuelbuta (Fig. 4.4b) show vertical heterogeneity. In Pan de Azúcar, these variations are due to the incorporation of atmospheric derived Ca and Sr into the regolith profiles (Oeser and von Blanckenburg 2020b). In the S-facing profile of Nahuelbuta, variations in Ca/Sr result from the presence of metamorphic rock inclusions in the granite (Oeser et al. 2018a). They become particularly apparent in the lower parts of the regolith profile.

The ^{87}Sr/^{86}Sr in the regolith profiles are typical of the bedrock at all EarthShape sites, which is granitoid rock (Oeser and von Blanckenburg 2020b). However, small-scale parent rock heterogeneity may also translate into differences in the ^{87}Sr/^{86}Sr ratio within a single

regolith profile (e.g. Nahuelbuta; Oeser et al. 2018a; Oeser and von Blanckenburg 2020b). Primary minerals are further distinct in their dissolution kinetics. Hence, the incongruent dissolution of primary minerals results in differences in $^{87}Sr/^{86}Sr$ between bedrock and regolith (Blum and Erel 1997), and also between bedrock and the released dissolved Sr. Ca/Sr ratios do not indicate such incongruent dissolution in most profiles, even though τ^{Sr} and τ^{Ca} indicate between 50 and 100% loss of Sr and Ca. In regolith $^{87}Sr/^{86}Sr$ ratios are identical within uncertainties to that of bedrock. Only in the regolith profiles of La Campana, is a significant loss of biotite beneath the bottom of the regolith profiles recorded in a shift towards less radiogenic Sr values in the regolith; a mechanism that is also supported by negative τ^{K} and τ^{Sr} (Oeser and von Blanckenburg 2020b).

Like Ca/Sr and $^{87}Sr/^{86}Sr$, the $\delta^{88/86}Sr$ value of bulk regolith can be modified from that of the bedrock by preferential dissolution of one mineral over another, as observed for e.g. Mg on the bulk rock scale (Ryu et al. 2011). To date relatively few mineral-specific $\delta^{88/86}Sr$ values have been published. Andrews and Jacobson (2018) have shown that apatite (+0.61‰) and K-feldspar (+0.46‰) record higher $\delta^{88/86}Sr$ than plagioclase (+0.35‰). In the EarthShape sites however, neither negative τ^{K} nor τ^{Ca} (indicative of K-feldspar and plagioclase weathering, respectively) correlate with significant shifts in regolith $\delta^{88/86}Sr$ value. We thus assume that the primary rock-forming minerals do not differ significantly in their $\delta^{88/86}Sr$ value. This assumption has profound implications for the isotopic composition of the bio-available fraction, which obtains its Sr mainly from weathering; namely, that deviations in the $\delta^{88/86}Sr$ value of the bio-available fraction with respect to bedrock cannot be attributed to isotopically incongruent release of Sr by preferential mineral dissolution. A further potential source for isotopically-distinct stable Sr in the fluid or the bio-available fraction is incipient weathering. In this scenario, fast initial dissolution would release isotopically light Sr from the mineral's surface layer into the fluid, forming a "light" bio-available fraction and a "heavy" residual regolith, as reported for other isotope systems (Brantley et al. 2004; Pokharel et al. 2019; Wimpenny et al. 2010). In the EarthShape sites this possibility can likely be excluded, however, as the rocks weather at quasi steady-state, thereby obliterating any fingerprint of early fast mineral dissolution. We thus argue that mineral dissolution is most likely isotopically congruent. Indeed, this would be supported by good agreement between bedrock and bulk regolith $\delta^{88/86}Sr$ at Santa Gracia and La Campana, although atmospheric deposition and metamorphic rock inclusions at Pan de Azúcar and Nahuelbuta respectively mean this pattern is not universally observable. Notably, however, bio-available fraction $\delta^{88/86}Sr$ at all eight profiles differs from bedrock and bulk regolith, indicating other processes that must have occurred after Sr release from weathering.

One mechanism to explain $\delta^{88/86}Sr$ values in the bio-available fraction differing from bedrock source $\delta^{88/86}Sr$ is isotope fractionation during adsorption. We can discount this possibility, however, as other studies have shown that both the Ca/Sr and the $\delta^{88/86}Sr$ stable isotope

ratios agree between fluid and exchangeable fraction (e.g. Bélanger et al. 2012; Bullen and Chadwick 2016). Sr isotope ratios in the bio-available fraction can thus be used as proxy for dissolved Sr in regolith pore fluid if these fluids could not be sampled. This is the case for the EarthShape sites. Another potential cause for the differences in $\delta^{88/86}$Sr is isotope fractionation during the formation of secondary minerals like pedogenic carbonates and clay minerals. The abundance of secondary minerals in the EarthShape sites is low (except Nahuelbuta; Oeser et al. 2018a) and pedogenic carbonates were only found at Pan de Azúcar (Bernhard et al. 2018). Precipitation of these carbonates is resolvable in molar Ca/Sr and $\delta^{88/86}$Sr of bulk samples and the bio-available fraction. Whereas the changes in molar Ca/Sr depend on the mineral which forms (i.e. each mineral is thought to have distinct partition coefficients for Ca and Sr), formation of carbonates and associated Sr isotope fractionation depends on precipitation rate (Böhm et al. 2012). At very low precipitation rates (which likely prevail; see review by Zamanian et al. 2016) and ambient temperature, this fractionation however, is negligible. Finally, incorporation of externally sourced Sr derived from dust, rain, and/or seaspray is another potential mechanism to explain the modified Sr isotopic composition of the bio-available fraction. Whether atmospheric deposition is resolvable in the bio-available fraction depends on the relative Sr fluxes of atmospheric- and weathering-derived Sr and the difference in their ^{87}Sr/^{86}Sr. Among the four EarthShape sites, atmospheric deposition of Sr derived from seaspray (^{87}Sr/^{86}Sr$_{seaspray}$ = 0.70918; Pearce et al. 2015a) is most significant in Pan de Azúcar (up to ~90%) and Santa Gracia (up to ~40%), but negligible in La Campana and Nahuelbuta (Oeser and von Blanckenburg 2020b). Deposition of Sr with a marine Sr isotope signature ($\delta^{88/86}$Sr$_{seaspray}$ = 0.39‰; Pearce et al. 2015a) would shift $\delta^{88/86}$Sr in the bio-available fraction towards isotopically heavier values than those of EarthShape bedrock and regolith. This is the case for the S-facing profile at the semi-arid site Santa Gracia for both profiles at the arid site Pan de Azúcar. However, neither ^{87}Sr/^{86}Sr nor Ca/Sr in the bio-available fraction at these sites correlate with $\delta^{88/86}$Sr (Fig. 4.1 & 4.2), as one would expect if the primary control on Sr isotopes is delivery from a non-bedrock source. The absence of such a correlation thus suggests modification of $\delta^{88/86}$Sr in the bio-available fraction even after atmospheric deposition of Sr.

In summary, then, none of the potential fractionating processes discussed above are likely to induce Sr isotope fractionation between rock and regolith, Sr contained in soil water, or the bio-available fraction in the EarthShape sites. We thus hypothesize that $\delta^{88/86}$Sr in the bio-available fraction is shifted by the uptake of isotopically fractionated Sr by plants.

Table 4.3: Ecosystem average Sr isotopic composition for bulk bedrock, bulk regolith, and the bio-available fraction in saprolite and soil. Average Ca/Sr is shown for the bio-available fraction and bulk plants. $\delta^{88/86}$Sr and Ca/Sr ratios in bulk plants are weighted by the plant organs' relative growth rate and relative species abundance. Data on each single specimen are reported in Tables 4.1 (bulk regolith and bio-available fraction of saprolite and soil) and 4.2 (plant and litter samples), respectively.

Study site	bedrock	regolith	bio-available fraction		bulk plants				
	$\delta^{88/86}Sr_{rock}$	$\delta^{88/86}Sr_{parent}$ [‰]	$\delta^{88/86}Sr_{bio\text{-}av}$	Ca/Sr [mol mmol^{-1}]	$\delta^{88/86}Sr^{*}_{veg}$ [‰]	$\delta^{88/86}Sr_{veg}$	Ca/Sr [mol mmol^{-1}]	Δ^{Sr}_{upt} [‰]	e^{Sr}_{org}
Pan de Azúcar									
mean	0.14	0.23	0.32						
uncertainty	0.02	0.04	0.13						
N-facing mean		0.24	0.24†	1.38	−0.11	−0.06	0.42	−0.33	0.01
uncertainty		0.06	0.03	0.62				0.04	0.20
S-facing mean		0.23	0.41†	2.85					–
uncertainty		0.03	0.03	1.11					–
Santa Gracia									
mean	0.29	0.31	0.32						
uncertainty	0.03	0.03	0.12						
N-facing mean		0.29	0.24†	0.18	0.01	0.11	0.34	−0.18	–
uncertainty		0.01	0.03	0.01				0.07	–
S-facing mean		0.33	0.36†	0.18	0.18	0.19	0.37	−0.18	0.19
uncertainty		0.03	0.03	0.01				0.01	0.24
La Campana									
mean	0.25	0.26	0.37						
uncertainty	0.05	0.04	0.06						
N-facing mean		0.27	0.39†	0.30	0.30	0.34	0.63	−0.07	0.91§
uncertainty		0.04	0.03	0.04				0.02	0.42§
S-facing mean		0.26 (0.30)†,‡	0.36 (0.44)†,‡	0.32	0.27	0.31	0.50	−0.14	1.00
uncertainty		0.05	0.03	0.06				0.03	0.53
Nahuelbuta									
mean	0.25	0.27	0.15						
uncertainty	0.07	0.13	0.18						
N-facing mean		0.15	0.25†	0.16	0.03	0.11	0.28	−0.18	0.57
uncertainty		0.03	0.03	0.03				0.05	0.26
S-facing mean		0.37	-0.02†	0.14	−0.04	0.25	0.31	0.02	–
uncertainty		0.04	0.03	0.13				0.20	–

Δ^{Sr}_{upt} was calculated according Eq. 4.2 and denote the average of Δ^{Sr}_{upt} derived using $\delta^{88/86}Sr_{veg}$ and $\delta^{88/86}Sr^{*}_{veg}$. Uncertainties show minimum and maximum estimates based on $\delta^{88/86}Sr_{veg}$ and $\delta^{88/86}Sr^{*}_{veg}$, respectively. Uncertainties of $\delta^{88/86}Sr_{rock}$, $\delta^{88/86}Sr_{regolith}$, and Ca/Sr in the bio-available fraction denote ± 1SD of the respective sample set (Table 4.1). Uncertainties of $\delta^{88/86}Sr_{bio\text{-}av}$ are conservative estimates based on repeated measurements of international standard reference materials. Total uncertainties on e^{Sr}_{org} were estimated by performing Monte Carlo simulations in which 3000 random data sets were sampled within the here listed uncertainty of all input parameters using a Box-Mueller transformation (Box and Muller 1958).

† $\delta^{88/86}$Sr weighted in relation to its concentration in the bio-available fraction (Table 4.1) and averaged over the entire nutrient-uptake depth; ‡ values in brackets denote to $\delta^{88/86}$Sr used for calculation of the Sr fractionation factor during plant uptake and is calculated using $\delta^{88/86}Sr_{parent}$ and $\delta^{88/86}Sr_{bio\text{-}av}$ from the different plants' uptake depth: *C. alba* 20 – 160 cm; *C. odorifera* 20 – 80 cm; *L. caustica* 140 – 160 cm; § e^{Sr}_{org} calculated using Δ^{Sr}_{upt} from the S-facing regolith profile (0.14 ± 0.03). See text for further information.

4.5.2 Strontium isotope and Ca/Sr fractionation by plants during uptake and translocation

Most of the plant tissues analyzed (root, twig, stem, leaf) yield a lower $\delta^{88/86}$Sr than those of rock, regolith, and the bio-available fraction they uptake from (Fig. 4.5). Thus, the Sr isotope fractionation factor during uptake (α^{Sr}_{upt}) appears to be smaller than unity. Conversely, we find that in all plants sampled (n = 20), $\delta^{88/86}$Sr systematically increases towards the plants' leaves. We discuss these opposing trends.

We first explore the fractionating processes taking place during Sr translocation. In all sampled plants (n = 20), we find that $\delta^{88/86}$Sr systematically increases towards the plants' leaves, a trend identical to that observed for Ca stable isotopes (Page et al. 2008; Wiegand 2005). Intriguingly, this trend in Sr isotope fractionation during intra-plant translocation is opposite to that described by de Souza et al. (2010) for the species *R. ferrugineum* and *Vaccinium* in their study of the Damma Glacier forefield. To detect the loci and processes of isotope fractionation, de Souza et al. (2010) made use of changes in the molar Ca/Sr ratios between plant organs, which has been demonstrated to occur in numerous studies (e.g. Drouet et al. 2007; Poszwa et al. 2000). This trend in increasing Ca/Sr can also be seen in this study, which covers 13 different plant species across four different climate zones (Figs. 4.1 – 4.4). One explanation for this increase is the preferential xylem transport of Ca over Sr from root to leaves. A second explanation is Sr remobilization from leaves to other plant organs via the phloem (review by Burger and Lichtscheidl 2019) combined with phloem-immobility of Ca (e.g. Clarkson 1984). Such Sr remobilization would result in the observed gradients in molar Ca/Sr even without preferential transport in the xylem. These hypotheses can be used to explain stable Sr isotope fractionation during Sr translocation. Two similar loci of Sr isotope fractionation within plants can be hypothesized: (1) During allocation from one plant organ to another in the xylem (transpiration stream). Here, possible processes of Sr isotope fractionation involve those that actively discriminate between Ca and Sr (e.g. Dasch et al. 2006; de Souza et al. 2010; Stevenson et al. 2014) and range from ion exchange with pectates to metabolic removal during oxalate crystal formation and through "lateral leakage" in neighboring tissues (Hanger 1979). It may be that these processes involve kinetic isotope fractionation (de Souza et al. 2010). (2) During phloem transport. This "backward transport" of Sr from leaves to other plant organs is poorly understood and highly species-dependent (review by Burger and Lichtscheidl 2019). One possible mechanism of Sr isotope fractionation, however, is the formation of insoluble phosphate salts in the phloem (Lake and Bock 1997). However, whether these salts would preferentially retain light or heavy Sr isotopes is not reported.

We now explore isotope fractionation during uptake. The fact that all our plant material is isotopically lighter than its corresponding source material strongly suggests that plants preferentially uptake light Sr isotopes- most likely during uptake from soil solution by roots. This

uptake involves diffusion and enzymatic pumping (e.g. Epstein and Leggett 1954; Marschner 1993; White et al. 1998) and might be accompanied by kinetic isotope fractionation, favoring light Sr isotopes (de Souza et al. 2010). Determining the fractionation factor α^{Sr}_{upt} associated with this uptake process requires knowledge of the isotope composition of a total plant, and from field data this cannot be determined easily. First, $\delta^{88/86}$Sr is not uniform within the plants we measured. Second, due to limited access or the large volume of plants (e.g. trees) it is not feasible to measure $\delta^{88/86}$Sr in a complete plant including all plant organs. Third, fractionation of Sr may vary with time, being dependent on the growth season and other physiological or pedogenic variables (e.g. growth competition, nutrient limitation, soil pH). To compute whole-plant stable Sr isotope composition we thus used the knowledge developed above for Sr translocation to estimate $\delta^{88/86}$Sr of plant compartments that were not analyzed.

We initially estimated a plant $\delta^{88/86}$Sr following to the same procedures described in Oeser and von Blanckenburg (2020b) for bulk plants' chemical composition. Accordingly, the plants' leaf $\delta^{88/86}$Sr is weighted relative to the $\delta^{88/86}$Sr of woody parts (equally weighted twig, stem, root), such that 32% and 48% of the Sr is attributed to leaf growth in angiosperms and gymnosperms, respectively. We thus derived $\delta^{88/86}Sr_{veg}$ from analyzed plant organs only. To interpolate the $\delta^{88/86}$Sr value of non-analyzed plant organs we first assumed that upon the pathway of Sr from root to stem, stem to twig, and twig to leaves, the light ^{86}Sr is preferentially retained. The extent of this retention was inferred from the average isotopic difference measured between two adjacent plant organs (e.g. between twig and leaves; $\Delta^{88/86}_{twig\text{-}leaf}$Sr). Thus, for all organs the $\delta^{88/86}$Sr value of root, stem, twig, and leaf of any plant specimen is either measured or assigned (Table 4.2). These estimates will be referred to as $\delta^{88/86}Sr^{*}_{veg}$ (Table 4.3). The differences between $\delta^{88/86}Sr_{veg}$ (bulk plant composition inferred from analyzed plant organs only) and $\delta^{88/86}Sr^{*}_{veg}$ are generally small (0.01 – 0.09‰) except for one plant in Nahuelbuta.

Determining fractionation factors for Sr uptake by plants

Using ^{87}Sr/^{86}Sr ratios and element distribution patterns in the bio-available fraction and plants, Oeser and von Blanckenburg (2020b) traced the plants' nutrient source to the bio-available fraction. If the uptake of Sr from this source involves a stable isotope fractionation, we can use the fractionation factor and the difference between $\delta^{88/86}$Sr of the source (bedrock) and the residue (bio-available Sr) to derive a mass balance for this uptake (Bouchez et al. 2013). Knowledge of the isotope fractionation factor α^{Sr}_{upt} is therefore a prerequisite, but this value is not known. In the steady state weathering reactor, it can be estimated from the measured plant composition, however.

The calculation of this fractionation factor requires knowledge of (1) the stable Sr isotope composition of plants ($\delta^{88/86}Sr_{veg}$); (2) the stable Sr isotope composition of the source compartment (i.e. the bio-available fraction; $\delta^{88/86}Sr_{bio\text{-}av}$), and (3) whether the isotopic

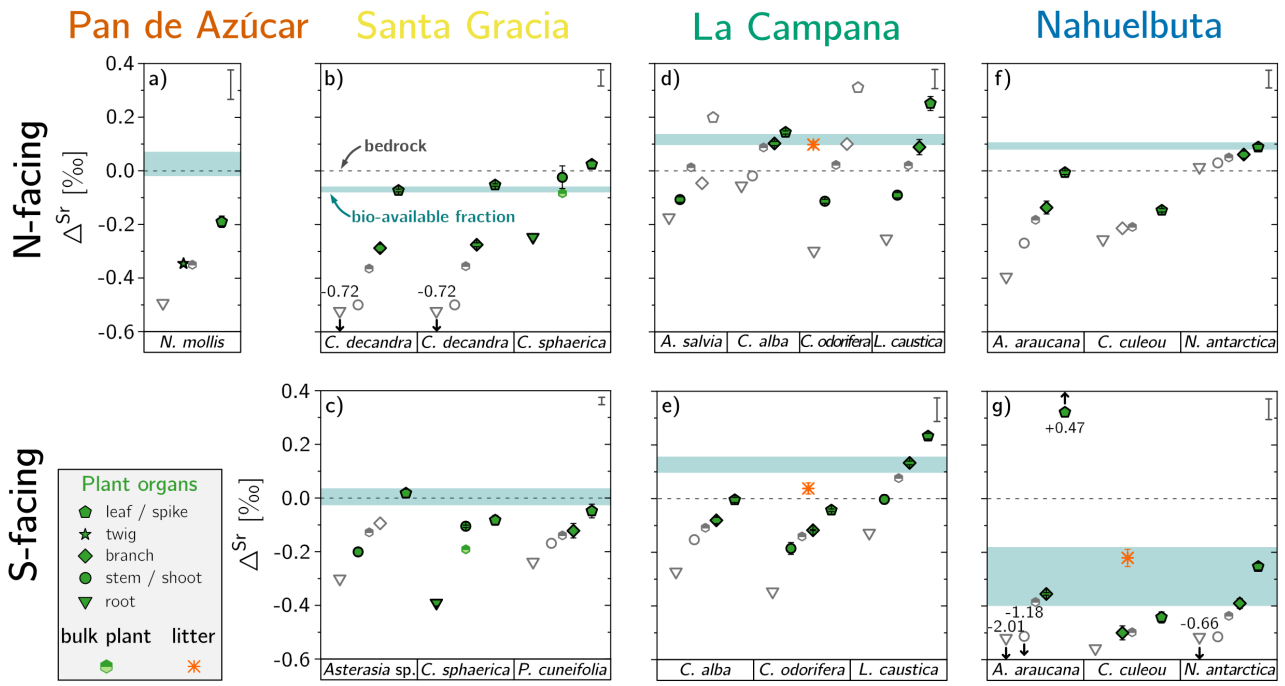

Figure 4.5: Sr isotope fractionation during uptake by plants shown as the ‰-difference between plants and the assumed Sr source. The isotopic deviation of the bio-available fraction ($\delta^{88/86}Sr_{bio\text{-}av}$) from $\delta^{88/86}Sr_{parent}$ is shown as cyan rectangle. Green and open symbols refer to measured and estimated plant organs, respectively (Table 4.2). Error bars show 2SD of $\delta^{88/86}Sr_{parent}$ (upper left) and $\delta^{88/86}Sr_{veg}$ (mostly within symbols), respectively. Note that the Sr source is the bio-available fraction in regolith. However, its initial$\delta^{88/86}$Sr is equal to $\delta^{88/86}Sr_{parent}$ as no Sr isotope fractionation is recorded during weathering and soil formation.

exchange occurs in an "open" (modeled as "Rayleigh fractionation") or a "closed system" (modeled with continous exchange as reaction advances; see e.g. Johnson et al. 2004). A weathering zone in which fluxes are at steady state can be treated as a continuous flow-through reactor (or "batch reactor"), where like in the closed system source and product compartments interact with each other (Bouchez et al. 2013). Even though the system is not closed in the sense of a closed chemical reactor, the mass balance is identical to the closed system because incoming mass fluxes balance outgoing fluxes. These prerequisites are met in the EarthShape study sites (e.g. Oeser et al. 2018a; Schaller et al. 2018b; van Dongen et al. 2019). Because all sites are permanently eroding, removal of mass through weathering and erosion equals its supply, and over some timescale a constant regolith thickness is maintained. Identifying the boundary conditions (1)–(3) of the system allows us to apply the isotope mass balance model as described in Bouchez et al. (2013). In such a closed system or batch reactor, the Sr isotope fractionation during plant uptake can be calculated by

$$\Delta^{Sr}_{upt} = \delta^{88/86}Sr_{bio\text{-}av} - \delta^{88/86}Sr_{veg}\,. \tag{4.2}$$

To derive a representative range in Sr isotope fractionation during plant uptake, we calculate Δ^{Sr}_{upt} for both $\delta^{88/86}Sr_{veg}$ (derived from analyzed plant organs only) and $\delta^{88/86}Sr^{*}_{veg}$ (including estimates of non-determined plant organs). Note that the latter involves assumptions on Sr isotope fractionation during the translocation from one plant organ to another. However, this estimate most likely represents a more accurate plant isotopic composition, and in any case the differences between $\delta^{88/86}Sr_{veg}$ and $\delta^{88/86}Sr^{*}_{veg}$ are small (0.01 – 0.09‰). For this calculation $\delta^{88/86}Sr_{bio\text{-}av}$, weighted by its concentration at a given depth interval, was integrated over the entire nutrient uptake depth of plants which is, unless otherwise stated in Table 4.3, the entire regolith profile. In doing so we assume that plants can take up Sr from the entire profile, an assumption compatible but not strictly validated by the uniform $^{87}Sr/^{86}Sr$ in the bio-available fraction which is identical to that of plants. From $\delta^{88/86}Sr_{veg}$ and $\delta^{88/86}Sr^{*}_{veg}$ values we derive minimum and maximum estimates on Sr isotope fractionation during uptake by plants. We report Δ^{Sr}_{upt} for single plant species in Table 4.2. Accordingly, Δ^{Sr}_{upt} ranges from –0.35 to +0.34‰. We list average Δ^{Sr}_{upt} for each of the sites in Table 4.3 (in which case Δ^{Sr}_{upt} ranges from -0.07 ± 0.02‰ to -0.33 ± 0.04‰).

4.5.3 A lost Sr flux

$\delta^{88/86}Sr_{bio\text{-}av}$, assumed to reflect the isotope composition of dissolved Sr, differs from $\delta^{88/86}Sr_{parent}$ (Fig. 4.1 – 4.4). Such a difference would only appear if a fractionated Sr pool is removed and does not re-appear in the dissolved Sr pool. Such fractionated Sr pool could for example arise if a significant amount of fractionated Sr is captured in fine colloids (100 – 450 nm; e.g. Gottselig et al. 2020; Zirkler et al. 2012) and is exported from regolith (Ma et al. 2015) without entering the bio-available pool. However, as the presence of Sr in the colloid fraction is usually minimal (e.g. Trostle et al. 2016) this explanation seems unlikely. Thus, we explore whether plant uptake (U^{Sr}) accounts for the isotopic difference between the Sr source pool and the bio-available fraction. Mass balance dictates that complete reutilization of Sr from plant litter (Rec^{Sr}) is an "isotope ratio-neutral" effect (Bouchez et al. 2013), since the flux at which Sr is taken up from soil solution equals its return flux into soil via litter fall. This holds true regardless of biomass production rate (gross primary productivity, GPP) and whether plants fractionate Sr isotopes or not. Therefore, as according to Bouchez et al. (2013), recycling cannot be complete if $\delta^{88/86}Sr_{bio\text{-}av}$ differs from $\delta^{88/86}Sr_{parent}$, hence some Sr must be eroded as solids from the studied profiles.

To illustrate how these isotope differences can be converted into an estimate of solid export flux we applied the flux-based model of the weathering zone (Bouchez et al. 2013) as shown in Fig. 4.6. Terminology and corresponding fluxes are explained briefly: Sr is released from rock or regolith ($\delta^{88/86}Sr_{parent}$) through congruent weathering (i.e. $\delta^{88/86}Sr_{parent} \equiv \delta^{88/86}Sr_{diss}$). Sr from the 'dissolved' pool is either available as free soil water or adsorbed as the bio-available fraction onto reactive surfaces. As previously discussed, we assume that secondary mineral formation and adsorption onto clay minerals does not involve Sr isotope fractionation (i.e.

$\delta^{88/86}Sr_{diss} \equiv \delta^{88/86}Sr_{bio\text{-}av}$), and thus the Sr source pool available to plants should inherit the isotopic composition of parent material. The Sr loss fraction e^{Sr}_{org} (Eq. 4.3) is based on Equation 9 in Bouchez et al. (2013) and is the ratio between export of isotopically fractionated solids, and the total flux of Sr in solution derived from weathering of primary minerals. This export fraction is estimated using:

$$e^{Sr}_{org} = \frac{\delta^{88/86}Sr_{parent} - \delta^{88/86}Sr_{bio\text{-}av}}{\Delta^{Sr}_{upt}}, \tag{4.3}$$

which is essentially the "closed system" equation applied to fluxes at steady state. If the export fluxes as solid material e^{Sr}_{org} are low, most of the Sr liberated from primary minerals is exported in the dissolved form. Mass balance dictates that in this case $\delta^{88/86}Sr_{bio\text{-}av}$ is close to that of parent material ($\delta^{88/86}Sr_{parent}$). If most of the Sr released from primary minerals is taken up by plants followed by export as fractionated solids, e^{Sr}_{org} is close to one, and $\delta^{88/86}Sr_{bio\text{-}av}$ will be shifted from the source rock composition by $-\Delta^{Sr}_{upt}$. All variables and uncertainties used to calculate e^{Sr}_{org} according Eq. 4.3 are given in Table 4.3: $\delta^{88/86}Sr_{parent}$ and $\delta^{88/86}Sr_{bio\text{-}av}$ were derived from bulk regolith samples and sequential extractions, respectively. As for the calculation of Δ^{Sr}_{upt} (Eq. 4.2) explained above, $\delta^{88/86}Sr_{bio\text{-}av}$ were integrated over the entire nutrient-uptake depth which is, unless otherwise stated in Table 4.3, the entire depth of the regolith profile. In doing so we treat bio-available Sr as a single pool that also includes atmospheric Sr deposition. Uncertainties on e^{Sr}_{org} were estimated from propagation of uncertainties of all input parameters (see Table 4.3 for further details). In Fig. 4.7 we plot the dependence of $\delta^{88/86}Sr$ in the bio-available fraction ($\delta^{88/86}Sr_{bio\text{-}av}$) on e^{Sr}_{org} in blue. The Y-intercept was set at the mean $\delta^{88/86}Sr_{parent}$ from each site. The slope of the blue line was calculated from $e^{Sr}_{org} \times \Delta^{Sr}_{upt}$. The shaded area shows the range in e^{Sr}_{org} arising from a minimum and a maximum estimate in Δ^{Sr}_{upt}

In Pan de Azúcar, e^{Sr}_{org} from the N-facing slope is only ~1% of the Sr derived from weathering. In the S-facing profile in Santa Gracia e^{Sr}_{org} amounts to ~20% relative of the Sr released by mineral dissolution. In the S-facing regolith profile in La Campana we estimate that from this hillslope up to ~100% of the Sr released by weathering is exported. In the N-facing regolith profile in Nahuelbuta ~60% of the Sr formerly released from weathering has been exported. We do not wish to overemphasize these estimates of e^{Sr}_{org}, given that the sometimes minute differences between $\delta^{88/86}Sr_{parent}$ and $\delta^{88/86}Sr_{bio\text{-}av}$ result in high uncertainties for e^{Sr}_{org}. Further, in some of the profiles the mass balance could not be closed. For example, in the N-facing regolith profile in Santa Gracia and the S-facing slope in Nahuelbuta the complementary bio-available fraction is isotopically lighter than $\delta^{88/86}Sr_{parent}$ (Table 4.3), even though plants preferentially take up the light ^{86}Sr from solution (Fig. 4.5b). We have no explanation for this phenomenon. Thus, we regard these calculations to be a demonstration of the potential of isotope-based mass balances in the Critical Zone rather producing values

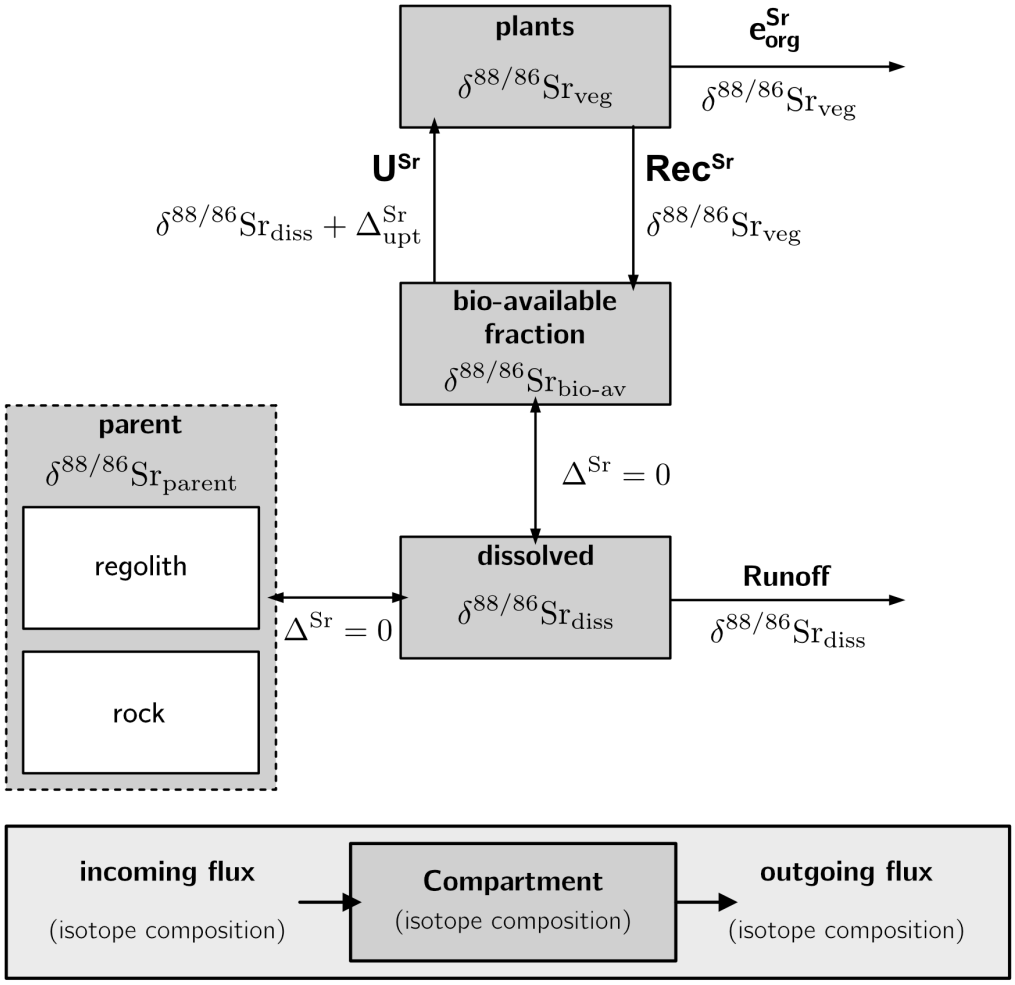

Figure 4.6: Box model of the weathering zone after Bouchez et al. (2013) as applied to the stable Sr isotope system. Sr is released into the dissolved form ($\delta^{88/86}\mathrm{Sr}_{\mathrm{diss}}$) from rock and regolith ($\delta^{88/86}\mathrm{Sr}_{\mathrm{parent}}$) through congruent weathering (i.e. no isotope fractionation). Plants preferentially take up light Sr from $\delta^{88/86}\mathrm{Sr}_{\mathrm{diss}}$. At ecologic quasi-steady state, $\delta^{88/86}\mathrm{Sr}_{\mathrm{diss}}$ should experience no isotope shift resulting from uptake- and return-fluxes (through plant litter recycling) are equal.

that can be used at face value. Bearing these major caveats in mind, the results nevertheless appear to vary systematically along the EarthShape transect with bulk erosion rate (Fig. 4.8), providing tentative evidence that export of solid plant matter is indeed driven by erosion. In any case this conclusion is almost inescapable because $\delta^{88/86}\mathrm{Sr}_{\mathrm{bio\text{-}av}}$ differs from $\delta^{88/86}\mathrm{Sr}_{\mathrm{parent}}$, and such a difference would only appear if a bio-utilized Sr pool is removed as organic solids.

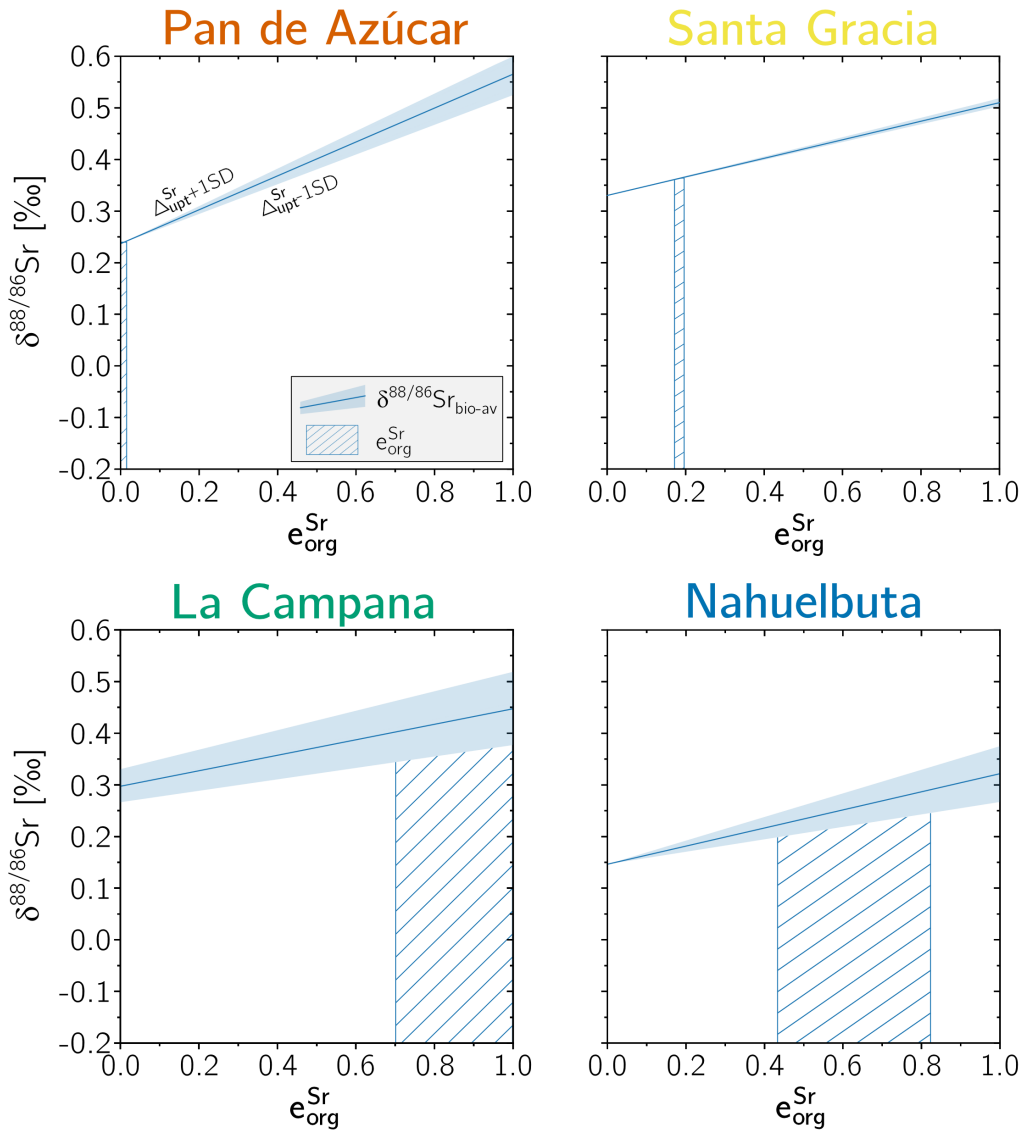

Figure 4.7: $\delta^{88/86}$Sr predicted by Eq. 4.3)in the bio-available Sr (blue solid line) as a function of e^{Sr}_{org}. The blue shaded area shows the range of the "lost" Sr export fraction as inferred from the bio-avialble Sr fraction. The 1 standard deviation (light blue) from its mean is delineated by the two estimations on the isotope fractionation during plant uptake ($\Delta^{Sr}_{upt} \pm 1$SD, Table 4.3), which in turn is a function of the plants' isotope composition ($\delta^{88/86}Sr_{veg}$ and $\delta^{88/86}Sr^{*}_{veg}$, respectively). Note that at $e^{Sr}_{org} = 0$ the $\delta^{88/86}$Sr of the bio-available fraction is equal to the respective parent composition ($\delta^{88/86}Sr_{parent} \equiv \delta^{88/86}Sr_{bio\text{-}av}$). No solution was possible for N-facing profile in Santa Gracia and the S-facing profiles in Pan de Azúcar and Nahuelbuta.

What is the lost Sr fraction? Various mechanisms may account for the net removal of a bio-utilized element from the dissolved pool. They range from anthropogenic disturbances over leaf litter and tree log erosion (Uhlig et al. 2017). Key to evaluating the likelihood of each mechanism is knowledge of the size of the bio-available Sr pool and the timescale $\delta^{88/86}$Sr over which the bio-available Sr pool resides in the weathering zone. This timescale is determined by the turnover time ($T^{X}_{i,j}$). In hydrology and geochemistry, this term is synony-

mous to the residence time. The size of these reservoirs is determined by their inventory (I_j^X), such that:

$$I_j^X = \int_{z=a}^{z=b} [X_j] \times \rho \, dz, \tag{4.4}$$

where $[X_j]$ denotes the average concentration of the element of interest (Table 4.1), ρ dz is the regolith's bulk density (from Bernhard et al. 2018) in the depth increment dz, which is integrated from depth a to b. The turnover time of a specific element in the bio-available pool in regolith with respect to the supply from weathering of bedrock ($W^X_{regolith}$; see Appendix for further details on element fluxes in the Critical Zone) is given by:

$$T^X_{bio\text{-}av,\,W} = \frac{I^X_{bio\text{-}av,\,soil}}{W^X_{regolith}}. \tag{4.5}$$

$T^X_{bio\text{-}av,\,W}$ provides a minimum time estimate as some fraction of $W^X_{regolith}$ could be directly drained via groundwater into streams instead of arriving in the bio-available pool (Uhlig and von Blanckenburg 2019). Similarly, we define

$$T^X_{bio\text{-}av,\,U} = \frac{I^X_{bio\text{-}av,\,soil}}{U^{Sr}} \tag{4.6}$$

as the time a particle spends in the bio-available inventory of regolith with respect to its uptake by plants, and U^X is the uptake flux of element X into plants. We list these inventories and the turnover times in Table 4.4.

Being able to infer the sensitivity to perturbations from these turnover times we can evaluate the likely processes of Sr loss. First, we evaluate anthropogenic perturbations. Because the four sites are located within national parks and natural reserves, we assume that anthropogenic perturbation of these ecosystems is minimal. However, they might still have been subject to deforestation in the not-so-distant past, or grazing today (Bahre 1979). Consequently, substantial amounts of organic matter (i.e. complete tree trunks and shrubs enriched in isotopically light ^{86}Sr) may have been exported and ecosystems would have shifted from their quasi-steady state into a transient state characterized by growth that exceeds mortality (e.g. Sommer et al. 2013). Such net growth would transfer a pool of mineral nutrients into new biomass with U^X (Eq. A4.1), where the uptake flux would exceed uptake at climax conditions. An apparent increase in e^{Sr}_{org} would be detectable if this uptake induced a shift in $\delta^{88/86}Sr_{bio\text{-}av}$. However, we see that for Ca and Sr $T^X_{bio\text{-}av,\,U}$ is similar to $T^{Sr}_{bio\text{-}av,\,W}$, i.e. a few centuries (Table 4.4), which is a timescale much longer than that of early ecosystem succession. Only at Nahuelbuta does uptake of Sr and Ca into plants outpace its supply by weathering. However, even in the succession stage some of this deficit would be buffered by litter recycling (Oeser and von Blanckenburg 2020b). Further, $T^{Sr}_{bio\text{-}av,\,W}$ and $T^{Sr}_{bio\text{-}av,\,U}$ represent minimum estimates since the saprolite in all four sites likely constitutes a

much larger inventory than that calculated here for the depth of soil only (Oeser and von Blanckenburg 2020b). In the case of the four EarthShape study sites, we thus regard it as unlikely that deforestation would have substantially altered the stable Sr isotope composition in the bio-available fraction, because $\delta^{88/86}Sr_{bio\text{-}av}$ is buffered against shifts by the large bio-available pool. Hence anthropogenic disturbances cannot explain the observed isotopic difference between $\delta^{88/86}Sr_{parent}$ and $\delta^{88/86}Sr_{bio\text{-}av}$.

Table 4.4: The study sites' denudation rate (D; min – max), erosion rate (E; min – max) and net primary productivity (NPP; ± 1SD). Availability of Ca and Sr is listed as inventories in the bio-available fraction ($I^X_{bio\text{-}av,\,soil}$) and the turnover times with respect to uptake by plants and their supply by weathering ($T^X_{bio\text{-}av,\,U}$, $T^X_{bio\text{-}av,\,W}$).

		Pan de Azúcar		*Santa Gracia*		*La Campana*		*Nahuelbuta*	
D †	[t km^{-2} yr^{-1}]	8.2 – 11.0		15.9 – 22.4		53.7 – 69.2		17.7 – 47.5	
E †	[t km^{-2} yr^{-1}]	9.1 – 10.1		8.7 – 10.5		23.4 – 33.8		14.2 – 40.0	
NPP ‡	[g_C m^{-2} yr^{-1}]	30 ± 10		150 ± 40		280 ± 50		520 ± 130	
		Ca	Sr	Ca	Sr	Ca	Sr	Ca	Sr
$I^X_{bio\text{-}av,\,soil}$ §	[g m^{-2}]	1440	1.5	616	4.6	673	4.5	60	0.5
$T^X_{bio\text{-}av,\,U}$ §	[yr]	6040	1250	480	590	530	820	30	20
$T^X_{bio\text{-}av,\,W}$ §	[yr]	n.a. *	4670	600	760	870	530	170	120

* determination of $T^X_{bio\text{-}av,\,W}$ not available as $W^X_{regolith}$ yield negative values

† (Oeser et al. 2018a)

‡ (Werner et al. 2018)

§ (Oeser and von Blanckenburg 2020b)

To be recorded in $\delta^{88/86}Sr_{bio\text{-}av}$ this loss must operate over timescales that exceed those of $T^{Sr}_{bio\text{-}av,\,W}$ and $T^{Sr}_{bio\text{-}av,\,U}$. We attribute this loss to the erosion of leaf litter and woody debris from sloping hills. Although erosion of woody debris is not as obvious as erosion of leaf litter, wood can be removed nevertheless by stochastic events like wildfires, wind throw, and tree turnover after tree death (Heartsill Scalley et al. 2012; Roering et al. 2010; Wohl et al. 2012). A high loss of elements contained in isotopically fractionated organic matter can be expected for fast-eroding, mineral-nutrient rich ecosystems (Andrews et al. 2016; Uhlig and von Blanckenburg 2019)

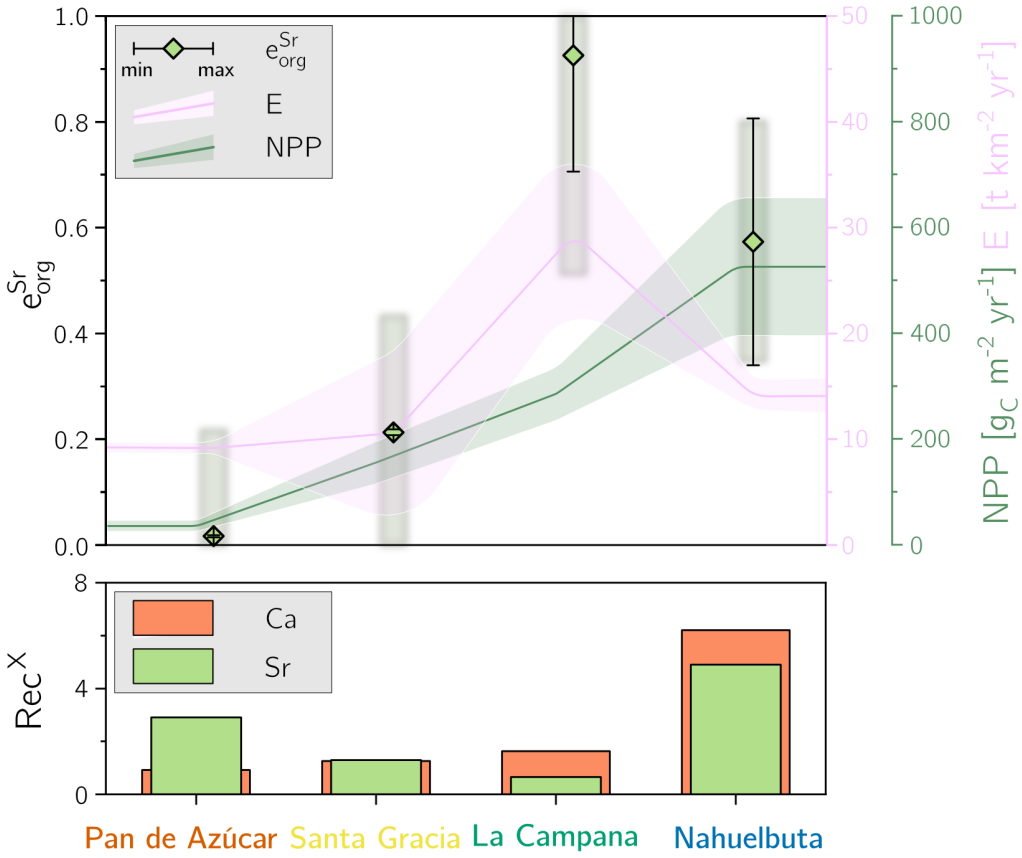

Figure 4.8: e^{Sr}_{org} (green diamonds), erosion rate (pink envelope) and net primary productivity (NPP, green envelope). Envelopes and error bars show study site minimum and maximum values. Grey boxes show total uncertainty (± 1SD) on e^{Sr}_{org} estimated by Monte Carlo simulations. Erosion of Sr in the form of fractionated organic matter scales with erosion rate but does not correlate with NPP. The recycling factor for Ca and Sr is shown in the lower panel. Note that estimates on nutrient recycling factor (Rec^X) in Pan de Azúcar include the atmospheric deposition of Ca and Sr.

What are the implications of e^{Sr}_{org} on Sr recycling rates? The weathering rate elemental chemical weathering flux ($W^X_{regolith}$) determines whether sufficient nutrient X is available in solution to fulfill ecosystem mineral nutrient demands. This demand is in turn driven by primary productivity. The ratio of these two variables, termed Rec^X for a given element X (as defined originally by Uhlig et al. 2017; Uhlig and von Blanckenburg 2019, see Appendix for details on parameterization) defines the difference between acquiring and recycling ecosystems. At steady state, meaning a constant biomass stock, the uptake rate of element X (U^X) is equal to the litterfall of element X (L^X; which can be seen to include other return fluxes like stemflow and throughfall). The recycling factor Rec^X thus is

$$Rec^X = \frac{U^X}{W^X_{regolith}} = \frac{L^X}{W^X_{regolith}}. \tag{4.7}$$

Along the EarthShape transect nutrient uptake increases with increasing biomass production. However, because mineral nutrient release by weathering does not increase proportionally, the nutrient recycling factor must increase accordingly from Pan de Azúcar to Nahuelbuta (Fig. 4.8, Table A4.1; Oeser and von Blanckenburg 2020b). A high recycling factor means that elements (either plant-essential or -beneficial; Marschner 1983) are re-utilized multiple times from leaf litter after litter solubilization (Wilcke et al. 2017) or are directly taken up by plants and their associated mycorrhizal fungi from litter (van der Heijden et al. 2014). However, a high e^{Sr}_{org}, if truly due to erosion of organic particles, would diminish the litter pool available for recycling. In that case a corrected recycling factor needs to be employed which is

$$Rec^{X}_{corr} = \frac{U^{X} - E^{X}_{org}}{W^{X}_{regolith}} = Rec^{X} - e^{X}_{org}. \quad (4.8)$$

Any fraction of U^{Sr} apportioned to e^{Sr}_{org} will thus result in lower recycling rates, and only stable isotopes allow one to quantify the effect of e^{Sr}_{org} on Rec^{Sr}. For the EarthShape gradient, Rec^{X}_{corr} barely differs from Rec^{Sr} in Pan de Azúcar and Santa Gracia where e^{Sr}_{org} is low, but shifts from 1 to almost zero recycling in La Campana, and is roughly halves recycling from 5 to 2 – 3 in Nahuelbuta (Table A4.1). In other words, this export potentially impairs the ability for direct Sr acquisition and that of other mineral nutrients from leaf litter.

4.6 Conclusion

A first important finding of this study are the locations and direction of stable Sr isotope fractionation in plants. In plants, $\delta^{88/86}$Sr systematically increases from the species roots towards their leaves. This systematic trend is opposite to that described in the literature (de Souza et al. 2010). By applying molar Ca/Sr ratios we identified three possible locations of Sr isotope fractionation by and within plants: (1) During allocation from one plant organ to another in the transpiration stream (xylem). (2) During transport in the assimilation stream (phloem). (3) During uptake of Sr from soil solution by roots.

A second important finding is on the controls over $\delta^{88/86}$Sr in the weathering zone, including its plant cover, and how these isotopes can be used to estimate elemental mass balance in the Critical Zone. Three main controls set the stable Sr isotope composition of the bio-available fraction ($\delta^{88/86}Sr_{bio\text{-}av}$) in our EarthShape study sites:

(1) The Sr source releasing Sr into solution through weathering. Except in Pan de Azúcar, Sr is mainly sourced from rock and regolith through congruent weathering. In Pan de Azúcar, weathering release fluxes are very low, and Sr is in part sourced through atmospheric deposition.

(2) The fractionation factor during Sr uptake from soil solution into plants (α^{Sr}_{upt}). α^{Sr}_{upt} is exclusively smaller than 1. Consequently Δ^{Sr}_{upt} yield negative values only (-0.33 ± 0.04, -0.18 ± 0.01, -0.14 ± 0.03, and -0.18 ± 0.05 in Pan de Azúcar, Santa Gracia, La Campana, and Nahuelbuta, respectively), hence plants deplete the soil solution in the light ^{86}Sr.

(3) Isotope mass balance. The Sr isotope composition in the bio-available fraction in the EarthShape sites discloses the separation between isotopically light Sr accumulated in plants and isotopically heavy Sr in soil water, which forms the complementary Sr pool after uptake by plants. A steady-state isotope mass balance suggests that the EarthShape study sites are subject to loss of Sr in isotopically fractionated organic solids (e^{Sr}_{org}). These losses generally increase from north to south and are almost negligible in Pan de Azúcar, low in Santa Gracia and peak in La Campana. In Nahuelbuta, e^{Sr}_{org} is intermediate.

The large bio-available Sr inventory buffers short-term deviations of isotope ratios from ecological quasi-steady state by anthropogenic ecosystem disturbances like deforestation and subsequent biomass growth. These can thus be discounted to account for the differences between $\delta^{88/86}Sr_{parent}$ and $\delta^{88/86}Sr_{bio\text{-}av}$. Instead, the Sr losses occur through fractionated organic solids (i.e. leaf litter and woody debris). The main driver of this solid Sr export is the erosion rate (E) which is in turn mainly set by relief and surface runoff. In strongly recycling ecosystems (i.e. Nahuelbuta), a significant fraction of e^{Sr}_{org} impairs the ability for direct Sr acquisition from leaf litter and thus reduces the mineral nutrient recycling factor.

4.7 Appendices

Plant Ca and Sr nutrient uptake and recycling fluxes

The plants' total nutrient-uptake fluxes (U^{X}_{total}) were estimated using the NPP derived from a dynamic vegetation model which simulates vegetation cover and composition during the Holocene (Werner et al. 2018). To obtain nutrient-specific U^{X}_{total}, NPP is multiplied by the mean concentration of element X in bulk living ecosystem. This elemental bulk ecosystem composition $[X]_{tree}$ has been estimated by applying the dimensionless organ growth quotients GL/GS (leaf growth relative to stem growth) and GL/GR (leaf growth relative to root growth) in accordance with Niklas and Enquist (2002). Ultimately, the elemental bulk ecosystem composition was determined by weighting the averaged elemental composition for each sampled plant for their relative abundance in the respective ecosystem as reported by Oeser and von Blanckenburg (2020b). Further, the C-based NPP was multiplied by the plants carbon

concentration of typically 50% (Martin et al. 2018) to obtain the total biomass NPP. Thus, U^X was calculated using:

$$U^X = \frac{NPP \times [X]_{veg}}{[C]_{veg}}. \quad \text{(A4.1)}$$

Nutrient uptake fluxes are lowest in the arid Pan de Azúcar and highest in the humid-temperate Nahuelbuta (Table 4.3). U^{Sr} amounts to 1.2 ± 0.5, 8 ± 2.6, 6 ± 3.3, and 19 ± 8.5 mg m^{-2} yr^{-1} in Pan de Azúcar, Santa Gracia, La Campana, and Nahuelbuta. Alike, U^{Ca} increase from north to south and amounts to 200 ± 500, 1300 ± 500, 1300 ± 600, and 2200 ± 700 mg m^{-2} yr^{-1}.

To estimate how often an element can be recycled, i.e. re-utilized after its initial release by chemical weathering from rock, we compare the uptake flux into the ecosystem (U^X_{total}) relative to its release by weathering ($W^X_{regolith}$), yielding the nutrient recycling factor (Uhlig et al. 2017):

$$Rec^X = \frac{U^X}{W^X_{regolith}}. \quad \text{(A4.2)}$$

Rec^X presents a minimum estimate as some fraction of $W^X_{regolith}$ can be partitioned into deep fluid inaccessible to plants, or a maximum estimate as some fraction of U^X is resorbed within-plant. It can also be reduced if e^{Sr}_{org} is high (see main text). We obtain recycling factors Rec^X for Sr and Ca which increase from the arid north towards the humid-temperate south, such that Rec^{Sr} increases from 3 ± 5 to 5 ± 12 and Rec^{Ca} from 1 ± 2 to 6 ± 4, respectively along the EarthShape transect. This means that Sr and Ca are cycled one to six times through the different ecosystems' biomass after it has been made available through weathering of rock, and before it is lost by drainage or erosion. Despite the two elements' hugely differing weathering-release fluxes within the four study sites, the pattern of nutrient recycling of Sr and Ca remains consistent among the four sites and do not differ in its magnitude between the two elements (Table A4.1).

Ca and Sr weathering release fluxes were determined by

$$W^X_{regolith} = D \times [X]_{parent} \times \left(-\tau^X_{X_i}\right), \quad \text{(A4.3)}$$

where $[X]_{parent}$ is the element concentration in bedrock and τ is a measure of elemental loss or gain relative to bedrock (Brimhall and Dietrich 1987):

$$\tau^X = \frac{[X]_{weathered}}{[X]_{parent}} \times \frac{[X_i]_{parent}}{[X_i]_{weathered}} - 1. \quad \text{(A4.4)}$$

Throughout, Zr was used as the immobile element for the calculation due to its demonstrated immobility in these study sites (Oeser et al. 2018a). At each study site, the most negative τ-values from the shallowest mineral-soil sample of each regolith profile were used, resulting in an integrated net-elemental release over each entire regolith profile. Ultimately, $W^X_{regolith}$

at each study site has been combined, culminating in an upper estimate of the nutrient fluxes from rock into the ecosystems' vegetation. Elemental chemical weathering fluxes for Ca and Sr (Oeser and von Blanckenburg 2020b) are reported in Table A4.1.

Weathering-release fluxes are generally lowest in Pan de Azúcar and highest in La Campana. $W^{Sr}_{regolith}$ amounts to 0.3 ± 0.1, 6.1 ± 1.3, 8.5 ± 1.5, and 4.0 ± 0.7 mg m^{-2} yr^{-1} in Pan de Azúcar, Santa Gracia, La Campana, and Nahuelbuta, respectively. This is a trend similar to that of Ca, where $W^{Ca}_{regolith}$ are lowest in Pan de Azúcar (13 ± 9 mg m^{-2} yr^{-1}) and due to mineralogical constraints (Oeser and von Blanckenburg 2020b) highest in Santa Gracia (1030 ± 200 mg m^{-2} yr^{-1}). In La Campana and Nahuelbuta, the weathering release flux for Ca amounts to 770 ± 250, and 360 ± 150 mg m^{-2} yr^{-1}, respectively. Oeser and von Blanckenburg (2020b) highlight several environmental controls on these fluxes and argue that the increasing presence of plants along the EarthShape transect might regulate weathering release fluxes down despite increasing NPP and MAP.

Table A4.1: Elemental weathering ($W^{X}_{regolith}$), total nutrient uptake fluxes (U^{X}_{total}), and nutrient recycling factors (Rec^{X}) for Ca and Sr. Rec^{Sr}_{corr} Eq. 4.8 shows the effect of e^{Sr}_{org} on Rec^{Sr}.

		Pan de Azúcar		*Santa Gracia*		*La Campana*		*Nahuelbuta*	
		Ca	Sr	Ca	Sr	Ca	Sr	Ca	Sr
$W^{X}_{regolith}$	[mg m^{-2} yr^{-1}]	13 * ± 9	0.3 ± 0.1	1030 ± 200	6.1 ± 1.3	770 ± 250	8.5 ± 1.5	360 ± 150	4.0 ± 0.7
U^{X}_{total}	[mg m^{-2} yr^{-1}]	200 ± 500	1.2 ± 0.5	1300 ± 500	8 ± 2.6	1300 ± 600	6 ± 3.3	2200 ± 700	19 ± 8.5
Rec^{X}		1 † ± 2	3 † ± 5	1 ± 4	1 ± 3	2 ± 2	1 ± 2	6 ± 4	5 ± 12
Rec^{Sr}_{corr}			3		1		0		2

* $W^{Ca}_{regolith}$ only includes information from AZPED21 (N-facing slope regolith profile) as atmospheric deposition of Ca in the S-facing slope led to apparent negative weathering fluxes.

† Rec^{X} include the atmospheric deposition of Ca and Sr; calculated for silicate weathering only, Rec^{Ca} and Rec^{Sr} amount to 19 and 4, respectively (Oeser and von Blanckenburg 2020b)

Uncertainties on weathering fluxes are estimated by Monte-Carlo simulations, where the SD of the respective profile's denudation rate, the SD of the bedrocks' element concentration of interest, and 3% relative uncertainty on the element concentration in regolith samples have been used.

Uncertainties on nutrient uptake fluxes are estimated by Monte-Carlo simulations, where the SD of the respective study site's NPP (Werner et al. 2018) and the SD of the chemical composition of the weighted above-ground living ecosystem have been used.

Sample availability

All sample metadata are already available on a public server using unique sample identifiers in form of the "International Geo Sample Number" (IGSN).

Acknowledgments

We thank CONAF in Chile for providing us with the opportunity to work in the national parks of Pan de Azúcar, La Campana, and Nahuelbuta. We also thank CEAZA for facilitating access to the Reserva Natural Santa Gracia. We are grateful to Michael Henehan (GFZ Potsdam) for discussions and informal reviews of an earlier text version. R.A. Oeser and F. von Blanckenburg are grateful for funding by the German National Science Foundation Priority Program DFG-SPP 1803 (EarthShape; www.earthshape.net). We acknowledge Leandro Paulino (Departamento de Suelos y Recursos Naturales, Universitad de Concepción, Chile) and Kirstin Übernickel for managing the priority program and Todd Ehlers (both Institute for Geosciences, Universität Tübingen, Germany) for its co-coordination.

References

Åberg G (1995), The use of natural strontium isotopes as tracers in environmental studies, *Water, Air, & Soil Pollution*, 79(1-4), 309–322. doi:10.1007/bf01100444.

Åberg G, Jacks G, Hamilton PJ (1989), Weathering rates and 87Sr/86Sr ratios: an isotopic approach, *Journal of Hydrology*, 109, 65–78.

Åberg G, Jacks G, Wickman T, Hamilton PJ (1990), Strontium isotopes in trees as an indicator for calcium availability, *Catena*, 17(1), 1–11. doi:10.1016/0341-8162(90)90011-2.

Aciego SM, Riebe CS, Hart SC, Blakowski MA, Carey CJ, Aarons SM, Dove NC, Botthoff JK, Sims KW, Aronson EL (2017), Dust outpaces bedrock in nutrient supply to montane forest ecosystems, *Nat Commun*, 8, 14800. doi:10.1038/ncomms14800.

Adams TS, McCormack ML, Eissenstat DM (2013), Foraging strategies in trees of different root morphology: the role of root lifespan, *Tree Physiology*, 33(9), 940–8, URL `https://www.ncbi.nlm.nih.gov/pubmed/24128849`. URL `https://www.ncbi.nlm.nih.gov/pubmed/24128849`, doi:10.1093/treephys/tpt067.

Agnelli A, Ascher J, Corti G, Ceccherini MT, Nannipieri P, Pietramellara G (2004), Distribution of microbial communities in a forest soil profile investigated by microbial biomass, soil respiration and DGGE of total and extracellular DNA, *Soil Biology and Biochemistry*, 36(5), 859–868. doi:10.1016/j.soilbio.2004.02.004.

Alexander EB (1985), Estimating relative ages from iron-oxide/total-iron ratios of soils in the Western Po Valley, Italy - a discussion, *Geoderma*, 35, 257–259.

Amsellem E, Moynier F, Day JMD, Moreira M, Puchtel IS, Teng FZ (2018), The stable strontium isotopic composition of ocean island basalts, mid-ocean ridge basalts, and komatiites, *Chemical Geology*, 483, 595–602. doi:10.1016/j.chemgeo.2018.03.030.

Amundson R, Berhe AA, Hopmans JW, Olson C, Sztein AE, Sparks DL (2015a), Soil science. Soil and human security in the 21st century, *Science*, 348(6235), 1261071. doi:10.1126/science.1261071.

Amundson R, Heimsath A, Owen J, Yoo K, Dietrich WE (2015b), Hillslope soils and vegetation, *Geomorphology*, 234, 122–132. doi:10.1016/j.geomorph.2014.12.031.

Amundson R, Richter DD, Humphreys GS, Jobbágy EG, Gaillardet J (2007), Coupling between Biota and Earth Materials in the Critical Zone, *Elements*, 3(5), 327–332. doi:10.2113/gselements.3.5.327.

Anderson SP, von Blanckenburg F, White AF (2007), Physical and Chemical Controls on the Critical Zone, *Elements*, 3(5), 315–319. doi:10.2113/gselements.3.5.315.

Anderson SP, Dietrich WE, Brimhall Jr GH (2002), Weathering profiles, mass-balance analysis, and rates of solute loss: Linkages between weathering and erosion in a small, steep catchment, *GSA Bulletin*, 114(9), 1143–1158.

Andrews MG, Jacobson AD (2018), Controls on the solute geochemistry of subglacial discharge from the Russell Glacier, Greenland Ice Sheet determined by radiogenic and stable Sr isotope ratios, *Geochimica et Cosmochimica Acta*, 239, 312–329. doi:10.1016/j.gca.2018.08.004.

Andrews MG, Jacobson AD, Lehn GO, Horton TW, Craw D (2016), Radiogenic and stable Sr isotope ratios (87Sr/86Sr, δ88/86Sr) as tracers of riverine cation sources and biogeochemical cycling in the Milford Sound region of Fiordland, New Zealand, *Geochimica et Cosmochimica Acta*, 173, 284–303. doi:10.1016/j.gca.2015.10.005.

Andrino A, Boy J, Mikutta R, Sauheitl L, Guggenberger G (2019), Carbon Investment Required for the Mobilization of Inorganic and Organic Phosphorus Bound to Goethite by an Arbuscular Mycorrhiza (Solanum lycopersicum x Rhizophagus irregularis), *Frontiers in Environmental Science*, 7, 26. doi:10.3389/fenvs.2019.00026.

Appelo CAJ, Postma D (2004), *Geochemistry, groundwater and pollution*, CRC press.

Arens S, Kleidon A (2011), Eco-hydrological versus supply-limited weathering regimes and the potential for biotic enhancement of weathering at the global scale, *Applied Geochemistry*, 26, S274–S278. doi:10.1016/j.apgeochem.2011.03.079.

Armesto JJ, Arroyo MT, Hinojosa LF (2007), The Mediterranean environment of central Chile, in: T Veblen, K Young, A Orme (eds.), *The physical geography of South America*, chapter 11, 184–199, Oxford Univ. Press, New York.

Armesto JJ, Vidiella PE, Gutiérrez JR (1993), Plant communities of the fog-free coastal desert of Chile: plant strategies in a fluctuating environment., *Revista Chilena de Historia Natural*, 66, 271–282.

Arunachalam J, Emons H, Krasnodebska B, Mohl C (1996), Sequential extraction studies on homogenized forest soil samples, *The Science of the Total Environment*, 181, 147–159.

Audi G, Wapstra AH (1993), The 1993 atomic mass evaluation. (I) Atomic mass table., *Nuclear Physics A*, 565, 1–65. doi:10.1016/0375-9474(93)90024-R.

Bacon JR, Farmer JG, Dunn SM, Graham MC, Vinogradoff SI (2006), Sequential extraction combined with isotope analysis as a tool for the investigation of lead mobilisation in soils: application to organic-rich soils in an upland catchment in Scotland, *Environmental Pollution*, 141(3), 469–81, URL https://www.ncbi.nlm.nih.gov/pubmed/16246474. URL https://www.ncbi.nlm.nih.gov/pubmed/16246474, doi:10.1016/j.envpol.2005.08.067.

Bahre CJ (1979), *Destruction of the natural vegetation of north-central Chile*, volume 23, Univ of California Press.

Bailey SW, Hornbeck JW, Driscoll CT, Gaudette HE (1996), Calcium Inputs and Transport in A Base-Poor Forest Ecosystem as Interpreted by Sr Isotopes, *Water Resources Research*, 32(3), 707–719. doi:10.1029/95wr03642.

Bain DC, Bacon JR (1994), Strontium isotopes as indicators of mineral weathering in catchments, *Catena*, 22(3), 201–214.

Balcaen L, Schrijver ID, Moens L, Vanhaecke F (2005), Determination of the 87Sr/86Sr isotope ratio in USGS silicate reference materials by multi-collector ICP–mass spectrometry, *International Journal of Mass Spectrometry*, 242(2-3), 251–255. doi:10.1016/j.ijms.2004.10.025.

Balogh-Brunstad Z, Keller CK, Gill RA, Bormann BT, Li CY (2008a), The effect of bacteria and fungi on chemical weathering and chemical denudation fluxes in pine growth experiments., *Biogeochemistry*, 88(2), 153–167.

Balogh-Brunstad Z, Kent Keller C, Thomas Dickinson J, Stevens F, Li CY, Bormann BT (2008b), Biotite weathering and nutrient uptake by ectomycorrhizal fungus, Suillus tomentosus, in liquid-culture experiments, *Geochimica et Cosmochimica Acta*, 72(11), 2601–2618. doi:10.1016/j.gca.2008.04.003.

Bardelli T, Ascher-Jenull J, Burkia Stocker E, Fornasier F, Fravolini G, Egli M, Pietramellara G, Insam H, Gómez-Brandón M (2018), *Impact of slope exposure on chemical and microbiological properties of Norway spruce deadwood and underlying soil during early stages of decomposition in the Italian Alps*, volume 167, Catena. doi:10.1016/j.catena.2018.04.031.

Barnes JB, Ehlers TA (2009), End member models for Andean Plateau uplift, *Earth-Science Reviews*, 91(1), 105–132.

Baskaran P, Hyvonen R, Berglund SL, Clemmensen KE, Agren GI, Lindahl BD, Manzoni S (2017), Modelling the influence of ectomycorrhizal decomposition on plant nutrition and

soil carbon sequestration in boreal forest ecosystems, *New Phytol*, 213(3), 1452–1465. doi:10.1111/nph.14213.

Bäumler R, Caspari T, Totsche KU, Dorji T, Norbu C, Baillie IC (2005), Andic properties in soils developed from nonvolcanic materials in Central Bhutan, *Journal of Plant Nutrition and Soil Science*, 168(5), 703–713. doi:10.1002/jpln.200521793.

Bazilevskaya E, Lebedeva M, Pavich M, Rother G, Parkinson D, Cole D, Brantley SL (2013), Where fast weathering creates thin regolith and slow weathering creates thick regolith., *Earth Surface Processes and Landforms*, 38(8), 847–858.

Beerling DJ, Berner RA (2005), Feedbacks and the coevolution of plants and atmospheric CO2, *Proc Natl Acad Sci U S A*, 102(5), 1302–5. doi:10.1073/pnas.0408724102.

Bélanger N, Holmden C (2010), Influence of landscape on the apportionment of Ca nutrition in a Boreal Shield forest of Saskatchewan (Canada) using87Sr/86Sr as a tracer, *Canadian Journal of Soil Science*, 90(2), 267–288. doi:10.4141/cjss09079.

Bélanger N, Holmden C, Courchesne F, Côté B, Hendershot WH (2012), Constraining soil mineral weathering 87Sr/86Sr for calcium apportionment studies of a deciduous forest growing on soils developed from granitoid igneous rocks, *Geoderma*, 185-186, 84–96. doi:10.1016/j.geoderma.2012.03.024.

Berg K, Baumann A (1985), Plutonic and metasedimentary rocks from the Coastal Range of northern Chile: Rb-Sr and U-Pb isotopic systematics, *Earth and Planetary Science Letters*, 75, 101–115.

Berg K, Breitkreuz C (1983), *Mesozoische Plutone in der nordchilenischen Küstenkordillere*, Schweizerbart Science Publishers, Stuttgart, Germany.

Berner EK, Berner RA, Moulton KL (2003), *Plants and Mineral Weathering: Present and Past*, 169–188, Elsevier. doi:10.1016/b0-08-043751-6/05175-6.

Bernhard N, Moskwa LM, Schmidt K, Oeser RA, Aburto F, Bader MY, Baumann K, von Blanckenburg F, Boy J, van den Brink L, Brucker E, Canessa R, Dippold MA, Ehlers TA, Fuentes JP, Godoy R, Köster M, Kuzyakov Y, Leinweber P, Neidhard H, Matus F, Mueller CW, Oelmann Y, Oses R, Osses P, Paulino L, Schaller M, Schmid M, Spielvogel S, Spohn M, Stock S, Stroncik N, Tielbörger K, Übernickel K, Scholten T, Seguel O, Wagner D, Kühn P (2018), Pedogenic and microbial interrelations to regional climate and local topography: new insights from a climate gradient (arid to humid) along the Coastal Cordillera of Chile, *Catena*, 170.

Birkeland PW, Burke RM, Benedict JB (1989), Pedogenic Gradients for Iron and Aluminum Accumulation and Phosphorus Depletion in Arctic and Alpine Soils as a Function of Time and Climate, *Quarternary Research*, 32, 193–204. doi:10.1016/0033-5894(89)90075-6.

Black JR, Epstein E, Rains WD, Yin Qz, Casey WH (2008), Magnesium-Isotope Fractionation During Plant Growth, *Environmental Science & Technology*, 42(21), 7831–7836. doi:10.1021/es8012722.

von Blanckenburg F (2005), The control mechanisms of erosion and weathering at basin scale from cosmogenic nuclides in river sediment, *Earth and Planetary Science Letters*, 237(3-4), 462–479. doi:10.1016/j.epsl.2005.06.030.

von Blanckenburg F (2017), Isotope: Uhren und Fingerabdrücke für das System Erde, *System Erde*, 7, 6–11. doi:10.2312/GFZ.syserde.07.01.1.

von Blanckenburg F, Dümcke W, Übernickel K (2019), The Skin of the Earth - Where Life Meets Rocks, *GFZ Data Service*, URL `https://www.youtube.com/watch?v=4dIU8v9ulRo`. URL `https://www.youtube.com/watch?v=4dIU8v9ulRo`, doi:10.2312/GFZ.3.3.2019.002.

von Blanckenburg F, O'Nions RK, Belshaw NS, Gibb A, Hein JR (1996), Global distribution of beryllium isotopes in deep ocean water as derived from Fe-Mn crusts, *Earth and Planetary Science Letters*, 141(1-4), 213–226. doi:10.1016/0012-821x(96)00059-3.

von Blanckenburg F, Willenbring JK (2014), Cosmogenic Nuclides: Dates and Rates of Earth-Surface Change, *Elements*, 10(5), 341–346. doi:10.2113/gselements.10.5.341.

von Blanckenburg F, Wittmann H, Schuessler JA (2016), HELGES: Helmholtz Laboratory for the Geochemistry of the Earth Surface, *Journal of large-scale research facilities JLSRF*, 2. doi:10.17815/jlsrf-2-141.

Blanco-Chao R, Pedoja K, Witt C, Martinod J, Husson L, Regard V, Audin L, Nexer M, Delcaillau B, Saillard M, Melnick D, Dumont JF, Santana E, Navarrete E, Martillo C, Pappalardo M, Ayala L, Araya JF, Feal-Perez A, Correa D, Arozarena-Llopis I (2014), The rock coast of South and Central America, in: *Rock Coast Geomorphology: A Global Synthesis.*, volume 40, 155–191, The Geological Society, London. doi:10.1144/m40.10.

Blum JD, Dasch AA, Hamburg SP, Yanai RD, Arthur MA (2008), Use of foliar Ca/Sr discrimination and 87Sr/86Sr ratios to determine soil Ca sources to sugar maple foliage in a northern hardwood forest, *Biogeochemistry*, 87(3), 287–296. doi:10.1007/s10533-008-9184-9.

Blum JD, Erel Y (1997), Rb/Sr isotope systematics of a granitic soil chronosequence: The importance of biotite weathering, *Geochimica et Cosmochimica Acta*, 61(15), 3193–3204. doi:10.1016/s0016-7037(97)00148-8.

Blum JD, Erel Y (2003), *Radiogenic Isotopes in Weathering and Hydrology*, 365–392, Elsevier. doi:10.1016/b0-08-043751-6/05082-9.

Blum JD, Hamburg SP, Yanai RD, Arthur MA (2012), Determination of foliar Ca/Sr discrimination factors for six tree species and implications for Ca sources in northern hardwood forests, *Plant and Soil*, 356(1-2), 303–314. doi:10.1007/s11104-011-1122-2.

Blum JD, Klaue A, Nezat CA, Driscoll CT, Johnson CE, Siccama TG, Eagar C, Fahey TJ, Likens GE (2002), Mycorrhizal weathering of apatite as an important calcium source in base-poor forest ecosystems, *Nature*, 417(6890), 729–31. doi:10.1038/nature00793.

Böhm F, Eisenhauer A, Tang J, Dietzel M, Krabbenhöft A, Kisakürek B, Horn C (2012), Strontium isotope fractionation of planktic foraminifera and inorganic calcite, *Geochimica et Cosmochimica Acta*, 93, 300–314. doi:10.1016/j.gca.2012.04.038.

Bojko O, Kabala C (2016), Transformation of physicochemical soil properties along a mountain slope due to land management and climate changes —A case study from the Karkonosze Mountains, SW Poland, *Catena*, 140, 43–54. doi:10.1016/j.catena.2016.01.015.

Bonneville S, Morgan DJ, Schmalenberger A, Bray A, Brown A, Banwart SA, Benning LG (2011), Tree-mycorrhiza symbiosis accelerate mineral weathering: Evidences from nanometer-scale elemental fluxes at the hypha–mineral interface, *Geochimica et Cosmochimica Acta*, 75(22), 6988–7005. doi:10.1016/j.gca.2011.08.041.

Bonneville S, Smits MM, Brown A, Harrington J, Leake JR, Brydson R, Benning LG (2009), Plant-driven fungal weathering: Early stages of mineral alteration at the nanometer scale, *Geology*, 37(7), 615–618. doi:10.1130/g25699a.1.

Borchers B, Marrero S, Balco G, Caffee M, Goehring B, Lifton N, Nishiizumi K, Phillips F, Schaefer J, Stone J (2016), Geological calibration of spallation production rates in the CRONUS-Earth project, *Quaternary Geochronology*, 31, 188–198. doi:10.1016/j.quageo.2015.01.009.

Bormann F, Likens G, Eaton J (1969), Biotic regulation of particulate and solution losses from a forest ecosystem, *BioScience*, 19, 600–610. doi:10.2307/1294934.

Bouchez J, von Blanckenburg F, Schuessler JA (2013), Modeling novel stable isotope ratios in the weathering zone, *American Journal of Science*, 313(4), 267–308. doi:10.2475/04.2013.01.

Bowen RNC (1994), *Isotopes in the Earth Sciences*, Chapman & Hall. doi:10.1007/978-94-009-2611-0.

Box GEP, Muller ME (1958), A note on the generation of random normal deviates, *Ann. Math. Statist.*, 29, 610–611. doi:10.1214/aoms/1177706645.

Boy J, Godoy R, Guevara G (2014), Transporte aerosoles, biometeorización y cambio global., in: C Donoso, M Gonzalez, A Lara (eds.), *Ecología Forestal: Bases para el Manejo Sustentable y Conservación de los Bosques Nativos de Chile.*, chapter 8, 281–295, Ediciones Universidad Austral de Chile.

Boy J, Wilcke W (2008), Tropical Andean forest derives calcium and magnesium from Saharan dust, *Global Biogeochemical Cycles*, 22(1), n/a–n/a. doi:10.1029/2007gb002960.

Boyce CK, Lee JE (2017), Plant Evolution and Climate Over Geological Timescales, *Annual Review of Earth and Planetary Sciences*, 45(1), 61–87. doi:10.1146/annurev-earth-063016-015629.

Brantley SL, Buss H, Lebedeva M, Fletcher RC, Ma L (2011a), Investigating the complex interface where bedrock transforms to regolith, *Applied Geochemistry*, 26, S12–S15. doi:10.1016/j.apgeochem.2011.03.017.

Brantley SL, DiBiase RA, Russo TA, Shi Y, Lin H, Davis KJ, Kaye M, Hill L, Kaye J, Eissenstat DM, Hoagland B, Dere AL, Neal AL, Brubaker KM, Arthur DK (2016), Designing a suite of measurements to understand the critical zone, *Earth Surface Dynamics*, 4(1), 211–235. doi:10.5194/esurf-4-211-2016.

Brantley SL, Eissenstat DM, Marshall JA, Godsey SE, Balogh-Brunstad Z, Karwan DL, Papuga SA, Roering J, Dawson TE, Evaristo J, Chadwick O, McDonnell JJ, Weathers KC (2017), Reviews and syntheses: on the roles trees play in building and plumbing the critical zone, *Biogeosciences*, 14(22), 5115–5142. doi:10.5194/bg-14-5115-2017.

Brantley SL, Goldhaber MB, Ragnarsdottir KV (2007), Crossing Disciplines and Scales to Understand the Critical Zone, *Elements*, 3(5), 307–314. doi:10.2113/gselements.3.5.307.

Brantley SL, Lebedeva M (2011), Learning to Read the Chemistry of Regolith to Understand the Critical Zone, *Annual Review of Earth and Planetary Sciences*, 39(1), 387–416. doi:10.1146/annurev-earth-040809-152321.

Brantley SL, Lebedeva M, Heimshath EH (2012), *A Geobiological View of Weathering and Erosion*, book section 12, Blackwell Publishing.

Brantley SL, Liermann LJ, Guynn RL, Anbar A, Icopini GA, Barling J (2004), Fe isotopic fractionation during mineral dissolution with and without bacteria, *Geochimica et Cosmochimica Acta*, 68(15), 3189–3204. doi:10.1016/j.gca.2004.01.023.

Brantley SL, Megonigal JP, Scatena FN, Balogh-Brunstad Z, Barnes RT, Bruns MA, Van Cappellen P, Dontsova K, Hartnett HE, Hartshorn AS, Heimsath A, Herndon E, Jin L, Keller CK, Leake JR, McDowell WH, Meinzer FC, Mozdzer TJ, Petsch S, Pett-Ridge J, Pregitzer KS, Raymond PA, Riebe CS, Shumaker K, Sutton-Grier A, Walter R, Yoo K (2011b),

Twelve testable hypotheses on the geobiology of weathering, *Geobiology*, 9(2), 140–65. doi:10.1111/j.1472-4669.2010.00264.x.

Brantley SL, White T, White A, Sparks D, Richter D, Pregitzer K, Derry L, Chorover J, Chadwick O, April R, Anderson S, Amundson R (2006), Frontiers in Exploration of the Critical Zone: Report of a workshop sponsored by the National Science Foundation (NSF), Report, Newark, DE.

Braucher R, Merchel S, Borgomano J, Bourlès DL (2011), Production of cosmogenic radionuclides at great depth: A multi element approach, *Earth and Planetary Science Letters*, 309(1-2), 1–9. doi:10.1016/j.epsl.2011.06.036.

Braun JJ, Descloitres M, Riotte J, Fleury S, Barbiéro L, Boeglin JL, Violette A, Lacarce E, Ruiz L, Sekhar M, Mohan Kumar MS, Subramanian S, Dupré B (2009), Regolith mass balance inferred from combined mineralogical, geochemical and geophysical studies: Mule Hole gneissic watershed, South India, *Geochimica et Cosmochimica Acta*, 73(4), 935–961. doi:10.1016/j.gca.2008.11.013.

van Breemen N (1998), *Plant-Induced Soil Changes: Processes and Feedbacks*, Kluwer Academic Publishers.

van Breemen N, Finlay R, Lundström U, Jongmans AG, Giesler R, Olsson M (2000), Mycorrhizal weathering: A true case of mineral plant nutrition?, *Biogeochemistry*, 49(1), 53–67. doi:10.1023/a:1006256231670.

Brimhall GH, Christopher J L, Ford C, Bratt J, Taylor G, Warin O (1991), Quantitative geochemical approach to pedogenesis: importance of parent material reduction, volumetric expansion, and eolian influx in lateritization, *Geoderma*, 51(1-4), 51–91. doi:10.1016/0016-7061(91)90066-3.

Brimhall GH, Dietrich WE (1987), Constitutive mass balance relations between chemical composition, volume, density, porosity, and strain in metasomatic hydrochemical systems: Results on weathering and pedogenesis, *Geochimica et Cosmochimica Acta*, 51(3), 567–587. doi:10.1016/0016-7037(87)90070-6.

Brucker E, Spohn M (2019), Formation of soil phosphorus fractions along a climate and vegetation gradient in the Coastal Cordillera of Chile, *Catena*, 180, 203–211. doi:10.1016/j.catena.2019.04.022.

Buendía C, Kleidon A, Porporato A (2010), The role of tectonic uplift, climate, and vegetation in the long-term terrestrial phosphorous cycle, *Biogeosciences*, 7(6), 2025–2038. doi:10.5194/bg-7-2025-2010.

Bullen T, Chadwick O (2016), Ca, Sr and Ba stable isotopes reveal the fate of soil nutrients along a tropical climosequence in Hawaii, *Chemical Geology*, 422, 25–45. doi:10.1016/j.chemgeo.2015.12.008.

Bullen TD (2014), *Metal Stable Isotopes in Weathering and Hydrology*, 329–359, Elsevier, 2nd edition. doi:10.1016/b978-0-08-095975-7.00511-8.

Bullen TD, Bailey SW (2005), Identifying calcium sources at an acid deposition-impacted spruce forest: a strontium isotope, alkaline earth element multi-tracer approach, *Biogeochemistry*, 74(1), 63–99. doi:10.1007/s10533-004-2619-z.

Burger A, Lichtscheidl I (2019), Strontium in the environment: Review about reactions of plants towards stable and radioactive strontium isotopes, *Science of The Total Environment*, 653, 1458–1512. doi:10.1016/j.scitotenv.2018.10.312.

Buss HL, Bruns MA, Schultz DJ, Moore J, Mathur CF, Brantley SL (2005), The coupling of biological iron cycling and mineral weathering during saprolite formation, Luquillo Mountains, Puerto Rico, *Geobiology*, 3, 247–260.

Buss HL, Chapela Lara M, Moore OW, Kurtz AC, Schulz MS, White AF (2017), Lithological influences on contemporary and long-term regolith weathering at the Luquillo Critical Zone Observatory, *Geochimica et Cosmochimica Acta*, 196, 224–251. doi:10.1016/j.gca.2016.09.038.

Calmels D, Gaillardet J, François L (2014), Sensitivity of carbonate weathering to soil CO 2 production by biological activity along a temperate climate transect, *Chemical Geology*, 390, 74–86. doi:10.1016/j.chemgeo.2014.10.010.

Calvaruso C, Turpault MP, Frey-Klett P (2006), Root-associated bacteria contribute to mineral weathering and to mineral nutrition in trees: a budgeting analysis, *Appl Environ Microbiol*, 72(2), 1258–66, URL `https://www.ncbi.nlm.nih.gov/pubmed/16461674`. URL `https://www.ncbi.nlm.nih.gov/pubmed/16461674`, doi:10.1128/AEM.72.2.1258-1266.2006.

Canadell J, Jackson R, Ehleringer J, Mooney H, Sala O, Schulze ED (1996), Maximum rooting depth of vegetation types at the global scale, *Oecologia*, 108(4), 583–595.

Capo RC, Stewart BW, Chadwick OA (1998), Strontium isotopes as tracers of ecosystem processes: theory and methods, *Geoderma*, 82(1-3), 197–225. doi:10.1016/s0016-7061(97)00102-x.

Carretier S, Regard V, Vassallo R, Aguilar G, Martinod J, Riquelme R, Christophoul F, Charrier R, Gayer E, Farías M, Audin L, Lagane C (2015), Differences in 10Be concentrations between river sand, gravel and pebbles along the western side of the central Andes, *Quaternary Geochronology*, 27, 33–51. doi:10.1016/j.quageo.2014.12.002.

Carretier S, Regard V, Vassallo R, Aguilar G, Martinod J, Riquelme R, Pepin E, Charrier R, Hérail G, Farías M, Guyot JL, Vargas G, Lagane C (2013), Slope and climate variability control of erosion in the Andes of central Chile, *Geology*, 41(2), 195–198. doi:10.1130/g33735.1.

Carretier S, Tolorza V, Regard V, Aguilar G, Bermúdez MA, Martinod J, Guyot JL, Hérail G, Riquelme R (2018), Review of erosion dynamics along the major N-S climatic gradient in Chile and perspectives, *Geomorphology*, 300, 45–68. doi:10.1016/j.geomorph.2017.10.016.

Carson JK, Campbell L, Rooney D, Clipson N, Gleeson DB (2009), Minerals in soil select distinct bacterial communities in their microhabitats, *FEMS Microbiology Ecology*, 67(3), 381–8. doi:10.1111/j.1574-6941.2008.00645.x.

Carson JK, Rooney D, Gleeson DB, Clipson N (2007), Altering the mineral composition of soil causes a shift in microbial community structure, *FEMS Microbiology Ecology*, 61(3), 414–23. doi:10.1111/j.1574-6941.2007.00361.x.

Certini G, Campbell CD, Edwards AC (2004), Rock fragments in soil support a different microbial community from the fine earth, *Soil Biology and Biochemistry*, 36(7), 1119–1128. doi:10.1016/j.soilbio.2004.02.022.

Chadwick KD, Asner GP (2016), Tropical soil nutrient distributions determined by biotic and hillslope processes, *Biogeochemistry*, 127(2-3), 273–289. doi:10.1007/s10533-015-0179-z.

Chadwick OA, Brimhall GH, Hendricks DM (1990), From a black to a gray box —a mass balance interpretation of pedogenesis, *Geomorphology*, 3(3-4), 369–390. doi:10.1016/0169-555x(90)90012-f.

Chadwick OA, Derry LA, Vitousek PM, Huebert BJ, Hedin LO (1999), Changing sources of nutrients during four million years of ecosystem development, *Nature*, 397, 491–497.

Chao HC, You CF, Liu HC, Chung CH (2015), Evidence for stable Sr isotope fractionation by silicate weathering in a small sedimentary watershed in southwestern Taiwan, *Geochimica et Cosmochimica Acta*, 165, 324–341. doi:10.1016/j.gca.2015.06.006.

Chapin III FS (1980), The mineral nutrition of wild plants, *Annual review of ecology and systematics*, 11(1), 233–260.

Chapin III FS, Matson PA, Vitousek PM (2011), *Principles of Terrestrial Ecosystem Ecology*, Springer Science & Business Media, 2nd edition. doi:10.1007/978-1-4419-9504-9.

Charlier BLA, Nowell GM, Parkinson IJ, Kelley SP, Pearson DG, Burton KW (2012), High temperature strontium stable isotope behaviour in the early solar system and planetary bodies, *Earth and Planetary Science Letters*, 329-330, 31–40. doi:10.1016/j.epsl.2012.02.008.

Charrier R, Pinto L, Rodríguez MP (2007), *Tectonostratigraphic evolution of the Andean Orogen in Chile*, 21–114, The Geological Society of London.

Chaudhuri S, Clauer N, Semhi K (2007), Plant decay as a major control of river dissolved potassium: A first estimate, *Chemical Geology*, 243(1-2), 178–190. doi:10.1016/j.chemgeo.2007.05.023.

Chen J, Li G, Yang J, Rao W, Lu H, Balsam W, Sun Y, Ji J (2007), Nd and Sr isotopic characteristics of Chinese deserts: Implications for the provenances of Asian dust, *Geochimica et Cosmochimica Acta*, 71(15), 3904–3914. doi:10.1016/j.gca.2007.04.033.

Chmeleff J, von Blanckenburg F, Kossert K, Jakob D (2010), Determination of the 10Be half-life by multicollector ICP-MS and liquid scintillation counting, *Nuclear Instruments and Methods in Physics Research Section B: Beam Interactions with Materials and Atoms*, 268(2), 192–199. doi:10.1016/j.nimb.2009.09.012.

Chorover J, Kretzschmar R, Garcia-Pichel F, Sparks DL (2007), Soil Biogeochemical Processes within the Critical Zone, *Elements*, 3(5), 321–326. doi:10.2113/gselements.3.5.321.

Civetta L, Galati R, Santacroce R (1991), Magma mixing and convective compositional layering within the Vesuvius magma chamber, *Bulletin of Volcanology*, 53(4), 287–300. doi:10.1007/bf00414525.

Clarke JDA (2006), Antiquity of aridity in the Chilean Atacama Desert, *Geomorphology*, 73(1-2), 101–114. doi:10.1016/j.geomorph.2005.06.008.

Clarkson DT (1984), Calcium transport between tissues and its distribution in the plant, *Plant, Cell and Environment*, 7(6), 449–456. doi:10.1111/j.1365-3040.1984.tb01435.x.

Cleveland CC, Houlton BZ, Smith WK, Marklein AR, Reed SC, Parton W, Del Grosso SJ, Running SW (2013), Patterns of new versus recycled primary production in the terrestrial biosphere, *Proc Natl Acad Sci U S A*, 110(31), 12733–7. doi:10.1073/pnas.1302768110.

Clow DW, Mast MA, Bullen TD, Turk JT (1997), Strontium 87/strontium 86 as a tracer of mineral weathering reactions and calcium sources in an Alpine/Subalpine Watershed, Loch Vale, Colorado, *Water Resources Research*, 33(6), 1335–1351. doi:10.1029/97wr00856.

Cockburn hAP, Seid MA, Summerfield MA (1999), Quantifying denudation rates on inselbergs in the central Namib Desert using in situ–produced cosmogenic 10Be and 26Al, *Geology*, 27(5), 399–402.

Dal Bo I, Klotzsche A, Schaller M, Ehlers TA, Kaufmann MS, Fuentes Espoz JP, Vereecken H, van der Kruk J (2019), Geophysical imaging of regolith in landscapes along a climate and vegetation gradient in the Chilean coastal cordillera, *Catena*, 180, 146–159. doi:10.1016/j.catena.2019.04.023.

Dasch AA, Blum JD, Eagar C, Fahey TJ, Driscoll CT, Siccama TG (2006), The relative uptake of Ca and Sr into tree foliage using a whole-watershed calcium addition, *Biogeochemistry*, 80(1), 21–41. doi:10.1007/s10533-005-6008-z.

Dasch EJ (1969), Strontium isotopes in weathering profiles, deep-sea sediments, and sedimentary rocks, *Geochimica et Cosmochimica Acta*. doi:10.1016/0016-7037(69)90153-7.

Day TA, Guénon R, Ruhland CT (2015), Photodegradation of plant litter in the Sonoran Desert varies by litter type and age, *Soil Biology and Biochemistry*, 89, 109–122. doi:10.1016/j.soilbio.2015.06.029.

De Biévre P, Taylor P (1993), Table of the isotopic compositions of the elements., *International Journal of Mass Spectrometry and Ion Processes*, 123, 149–166. doi:10.1016/0168-1176(93)87009-H.

Delhaize E, Ryan PR (1995), Aluminum Toxicity and Tolerance in Plants, *Plant Physiology*, 107(2), 315–321.

Dere AL, White TS, April RH, Reynolds B, Miller TE, Knapp EP, McKay LD, Brantley SL (2013), Climate dependence of feldspar weathering in shale soils along a latitudinal gradient, *Geochimica et Cosmochimica Acta*, 122, 101–126. doi:10.1016/j.gca.2013.08.001.

Dixon JC (2015), Soil Morphology in the Critical Zone: The Role of Climate, Geology, and Vegetation in Soil Formation in the Critical Zone, in: *Principles and Dynamics of the Critical Zone, Developments in Earth Surface Processes*, volume 19, chapter 5, 147–172, Elsevier. doi:10.1016/b978-0-444-63369-9.00005-7.

Dixon JL, von Blanckenburg F (2012), Soils as pacemakers and limiters of global silicate weathering, *Comptes Rendus Geoscience*, 344(11-12), 597–609. doi:10.1016/j.crte.2012.10.012.

Dixon JL, Chadwick OA, Vitousek PM (2016), Climate-driven thresholds for chemical weathering in postglacial soils of New Zealand, *Journal of Geophysical Research: Earth Surface*, 121(9), 1619–1634. doi:10.1002/2016jf003864.

Dixon JL, Hartshorn AS, Heimsath AM, DiBiase RA, Whipple KX (2012), Chemical weathering response to tectonic forcing: A soils perspective from the San Gabriel Mountains, California, *Earth and Planetary Science Letters*, 323-324, 40–49. doi:10.1016/j.epsl.2012.01.010.

Dixon JL, Heimsath AM, Amundson R (2009a), The critical role of climate and saprolite weathering in landscape evolution, *Earth Surface Processes and Landforms*, 34(11), 1507–1521. doi:10.1002/esp.1836.

Dixon JL, Heimsath AM, Kaste J, Amundson R (2009b), Climate-driven processes of hillslope weathering, *Geology*, 37(11), 975–978. doi:10.1130/g30045a.1.

van Dongen R, Scherler D, Wittmann H, von Blanckenburg F (2019), Cosmogenic 10Be in river sediment: where grain size matters and why, *Earth Surface Dynamics*, 7(2), 393–410. doi:10.5194/esurf-7-393-2019.

Dosseto A, Buss HL, Suresh PO (2012), Rapid regolith formation over volcanic bedrock and implications for landscape evolution, *Earth and Planetary Science Letters*, 337-338, 47–55. doi:10.1016/j.epsl.2012.05.008.

Doughty CE, Taylor LL, Girardin CAJ, Malhi Y, Beerling DJ (2014), Montane forest root growth and soil organic layer depth as potential factors stabilizing Cenozoic global change, *Geophysical Research Letters*, 41(3), 983–990. doi:10.1002/2013gl058737.

Drever JI (1994), The effect of land plants on weathering rates of silicate minerals, *Geochimica et Cosmochimica Acta*, 58(10), 2325–2332. doi:10.1016/0016-7037(94)90013-2.

Drever JI, Zobrist J (1992), Chemical weathering of silicate rocks as a function of elevation in the southern Swiss Alps, *Geochimica et Cosmochimica Acta*, 56(8), 3209–3216. doi:10.1016/0016-7037(92)90298-w.

Drouet T, Herbauts J, Demaiffe D (2007), *Change of the Origin of Calcium in Forest Ecosystems in the Twentieth Century Highlighted by Natural Sr Isotopes*, 333–343, Terrestrial Ecology, Elsevier. doi:10.1016/s1936-7961(07)01021-4.

Dunai TJ, González López GA, Juez-Larré J (2005), Oligocene–Miocene age of aridity in the Atacama Desert revealed by exposure dating of erosion-sensitive landforms., *Geology*, 33(4), 321.

Eger A, Yoo K, Almond PC, Boitt G, Larsen IJ, Condron LM, Wang X, Mudd SM (2018), Does soil erosion rejuvenate the soil phosphorus inventory?, *Geoderma*, 332, 45–59. doi:10.1016/j.geoderma.2018.06.021.

Egli M, Dahms D, Norton K (2014), Soil formation rates on silicate parent material in alpine environments: Different approaches-different results?, *Geoderma*, 213, 320–333. doi:10.1016/j.geoderma.2013.08.016.

Egli M, Mirabella A, Mancabelli A, Sartori G (2004), Weathering of Soils in Alpine Areas as Influenced by Climate and Parent Material, *Clays and Clay Minerals*, 52(3), 287–303. doi:10.1346/ccmn.2004.0520304.

Egli M, Mirabella A, Sartori G, Fitze P (2003), Weathering rates as a function of climate: results from a climosequence of the Val Genova (Trentino, Italian Alps)., *Geoderma*, 111(1), 99–121.

Ehlers TA, von Blanckenburg F, Übernickel K. EarthShape weather data collection [online] (2017). URL https://esdynamics.geo.uni-tuebingen.de/earthshape/index.php?id=68 [cited 2017-06-19].

Ehrlich HL (1995), How microbes influence mineral growth and dissolution, *Chemical Geology*, 132, 5–9.

Eilers KG, Debenport S, Anderson S, Fierer N (2012), Digging deeper to find unique microbial communities: The strong effect of depth on the structure of bacterial and archaeal communities in soil, *Soil Biology and Biochemistry*, 50, 58–65. doi:10.1016/j.soilbio.2012.03.011.

Eissenstat DM, Kucharski JM, Zadworny M, Adams TS, Koide RT (2015), Linking root traits to nutrient foraging in arbuscular mycorrhizal trees in a temperate forest, *New Phytol*, 208(1), 114–24, URL https://www.ncbi.nlm.nih.gov/pubmed/25970701. URL https://www.ncbi.nlm.nih.gov/pubmed/25970701, doi:10.1111/nph.13451.

Epstein E, Leggett JE (1954), The Absorption of Alkaline Earth Cations by Barley Roots: Kinetics and Mechanism, *American Journal of Botany*, 41(10). doi:10.1002/j.1537-2197.1954.tb14413.x.

Fabian J, Zlatanovic S, Mutz M, Premke K (2017), Fungal-bacterial dynamics and their contribution to terrigenous carbon turnover in relation to organic matter quality, *ISME J*, 11(2), 415–425, URL https://www.ncbi.nlm.nih.gov/pubmed/27983721. URL https://www.ncbi.nlm.nih.gov/pubmed/27983721, doi:10.1038/ismej.2016.131.

Fan Y, Miguez-Macho G, Jobbagy EG, Jackson RB, Otero-Casal C (2017), Hydrologic regulation of plant rooting depth, *Proc Natl Acad Sci U S A*, 114(40), 10572–10577, URL https://www.ncbi.nlm.nih.gov/pubmed/28923923. URL https://www.ncbi.nlm.nih.gov/pubmed/28923923, doi:10.1073/pnas.1712381114.

Faure G, Hurley PM (1963), The Isotopic Composition of Strontium in Oceanic and Continental Basalts: Application to the Origin of Igneous Rocks, *Journal of Petrology*, 4(1), 31–50. doi:10.1093/petrology/4.1.31.

Faure G, Mensing TM (2005), *Isotopes: principles and applications*, Wiley-Blackwell.

Faure G, Powell JL (1972), *Strontium Isotope Geology*, Isotopes in Geology, Springer.

Ferrier KL, Kirchner JW, Finkel RC (2005), Erosion rates over millennial and decadal timescales at Caspar Creek and Redwood Creek, Northern California Coast Ranges, *Earth Surface Processes and Landforms*, 30(8), 1025–1038. doi:10.1002/esp.1260.

Ferrier KL, Kirchner JW, Finkel RC (2012), Weak influences of climate and mineral supply rates on chemical erosion rates: Measurements along two altitudinal transects

in the Idaho Batholith, *Journal of Geophysical Research: Earth Surface*, 117(F2). doi:10.1029/2011jf002231.

Ferrier KL, Kirchner JW, Riebe CS, Finkel RC (2010), Mineral-specific chemical weathering rates over millennial timescales: Measurements at Rio Icacos, Puerto Rico, *Chemical Geology*, 277(1-2), 101–114. doi:10.1016/j.chemgeo.2010.07.013.

Fierer N, Schimel JP, Holden PA (2003), Variations in microbial community composition through two soil depth profiles, *Soil Biology and Biochemistry*, 35(1), 167–176. doi:10.1016/s0038-0717(02)00251-1.

Fietzke J, Eisenhauer A (2006), Determination of temperature-dependent stable strontium isotope (88Sr/86Sr) fractionation via bracketing standard MC-ICP-MS, *Geochemistry, Geophysics, Geosystems*, 7(8). doi:10.1029/2006GC001243.

Filgueiras AV, Lavilla I, Bendicho C (2002), Chemical sequential extraction for metal partitioning in environmental solid samples, *J Environ Monit*, 4(6), 823–57, URL https://www.ncbi.nlm.nih.gov/pubmed/12509036. URL https://www.ncbi.nlm.nih.gov/pubmed/12509036, doi:10.1039/b207574c.

Finlay RD, Mahmood S, Rosenstock N, Bolou-Bi EB, Köhler SJ, Fahad Z, Rosling A, Wallander H, Belyazid S, Bishop K, Lian B (2020), Reviews and syntheses: Biological weathering and its consequences at different spatial levels - from nanoscale to global scale, *Biogeosciences*, 17(6), 1507–1533. doi:10.5194/bg-17-1507-2020.

Fisher BA, Rendahl AK, Aufdenkampe AK, Yoo K (2017), Quantifying weathering on variable rocks, an extension of geochemical mass balance: Critical zone and landscape evolution, *Earth Surface Processes and Landforms*, 42(14), 2457–2468. doi:10.1002/esp.4212.

Frey B, Rieder SR, Brunner I, Plotze M, Koetzsch S, Lapanje A, Brandl H, Furrer G (2010), Weathering-associated bacteria from the Damma glacier forefield: physiological capabilities and impact on granite dissolution, *Appl Environ Microbiol*, 76(14), 4788–96, URL https://www.ncbi.nlm.nih.gov/pubmed/20525872. URL https://www.ncbi.nlm.nih.gov/pubmed/20525872, doi:10.1128/AEM.00657-10.

Fritze H, Pietikäinen J, Pennanen T (2000), Distribution of microbial biomass and phospholipid fatty acids in Podzol profiles under coniferous forest, *European Journal of Soil Science*, 51(4), 565–573. doi:10.1111/j.1365-2389.2000.00346.x.

Fruchter N, Eisenhauer A, Dietzel M, Fietzke J, Böhm F, Montagna P, Stein M, Lazar B, Rodolfo-Metalpa R, Erez J (2016), 88Sr/86Sr fractionation in inorganic aragonite and in corals, *Geochimica et Cosmochimica Acta*, 178, 268–280. doi:10.1016/j.gca.2016.01.039.

Gaillardet J, Dupré B, Louvat P, Allègre C (1999), Global silicate weathering and CO2 consumption rates deduced from the chemistry of large rivers., *Chemical Geology*, 159, 3–30.

Gajardo R (1994), La vegetación natural de Chile: clasificación y distribución geográfica.

Gallo ME, Sinsabaugh RL, Cabaniss SE (2006), The role of ultraviolet radiation in litter decomposition in arid ecosystems, *Applied Soil Ecology*, 34(1), 82–91. doi:10.1016/j.apsoil.2005.12.006.

Gantner S, Andersson AF, Alonso-Sáez L, Bertilsson S (2011), Novel primers for 16S rRNA-based archaeal community analyses in environmental samples., *Journal of Microbiological Methods*, 84, 12–18. doi:10.1016/j.mimet.2010.10.001.

García NO (1994), South American Climatology, *Quarternary International*, 21, 7–27.

Gerrits R, Pokharel R, Breitenbach R, Radnik J, Feldmann I, Schuessler JA, von Blanckenburg F, Gorbushina AA, Schott J (2020), How the rock-inhabiting fungus K. petricola A95 enhances olivine dissolution through attachment, *Geochimica et Cosmochimica Acta*, 282, 76–97. doi:10.1016/j.gca.2020.05.010.

Ghiorse WC, Wilson JT (1988), Microbial Ecology of the Terrestrial Subsurface, *Advances in Applied Microbiology*, 33, 107–172. doi:10.1016/S0065-2164(08)70206-5.

Giehl RF, von Wiren N (2014), Root nutrient foraging, *Plant Physiol*, 166(2), 509–17, URL https://www.ncbi.nlm.nih.gov/pubmed/25082891. URL https://www.ncbi.nlm.nih.gov/pubmed/25082891, doi:10.1104/pp.114.245225.

Ginibre C, Davidson JP (2014), Sr Isotope Zoning in Plagioclase from Parinacota Volcano (Northern Chile): Quantifying Magma Mixing and Crustal Contamination, *Journal of Petrology*, 55(6), 1203–1238. doi:10.1093/petrology/egu023.

Godoy R, Mayr R (1989), Caracterización morfológica de micorrizas vesículo-arbusculares en coníferas endémicas del sur de Chile., *Bosque*, 10(2), 89–98.

Godsey SE, Hartmann J, Kirchner JW (2019), Catchment chemostasis revisited: Water quality responds differently to variations in weather and climate, *Hydrological Processes*, 33(24), 3056–3069. doi:10.1002/hyp.13554.

Gottselig N, Sohrt J, Uhlig D, Nischwitz V, Weiler M, Amelung W (2020), Groundwater controls on colloidal transport in forest stream waters, *Sci Total Environ*, 717, 134638, URL https://www.ncbi.nlm.nih.gov/pubmed/31837854. URL https://www.ncbi.nlm.nih.gov/pubmed/31837854, doi:10.1016/j.scitotenv.2019.134638.

Granger D, Riebe C (2014), *Cosmogenic nuclides in weathering and erosion*, 1–43, Elsevier.

Graustein WC (1989), *87Sr/86Sr Ratios Measure the Sources and Flow of Strontium in Terrestrial Ecosystems*, volume 68, 491–512, Springer. doi:10.1007/978-1-4612-3498-2_28.

Graustein WC, Armstrong RL (1983), The Use of Strontium-87/Strontium-86 Ratios to Measure Atmospheric Transport into Forested Watersheds, *Science*, 219, 289–292.

Green E, Dietrich W, Banfield J (2006), Quantification of chemical weathering rates across an actively eroding hillslope, *Earth and Planetary Science Letters*, 242(1-2), 155–169. doi:10.1016/j.epsl.2005.11.039.

Grousset FE, Biscaye PE (2005), Tracing dust sources and transport patterns using Sr, Nd and Pb isotopes, *Chemical Geology*, 222(3-4), 149–167. doi:10.1016/j.chemgeo.2005.05.006.

Grousset FE, Rognon P, Coudé-Gaussen G, Pédemay P (1992), Origins of peri-Saharan dust deposits traced by their Nd and Sr isotopic composition, *Palaeogeography, Palaeoclimatology, Palaeoecology*, 93(3-4), 203–212. doi:10.1016/0031-0182(92)90097-o.

Guelke M, von Blanckenburg F (2007), Fractionation of stable iron isotopes in higher plants, *Environ Sci Technol*, 41(6), 1896–901, URL `https://www.ncbi.nlm.nih.gov/pubmed/17410781`. URL `https://www.ncbi.nlm.nih.gov/pubmed/17410781`, doi:10.1021/es062288j.

Hahm WJ, Riebe CS, Lukens CE, Araki S (2014), Bedrock composition regulates mountain ecosystems and landscape evolution, *Proceedings of the National Academy of Sciences*, 111(9), 3338–43. doi:10.1073/pnas.1315667111.

Hajj F, Poszwa A, Bouchez J, Guérold F (2017), Radiogenic and "stable"strontium isotopes in provenance studies: A review and first results on archaeological wood from shipwrecks, *Journal of Archaeological Science*, 86, 24–49. doi:10.1016/j.jas.2017.09.005.

Halicz L, Segal I, Fruchter N, Stein M, Lazar B (2008), Strontium stable isotopes fractionate in the soil environments?, *Earth and Planetary Science Letters*, 272(1-2), 406–411. doi:10.1016/j.epsl.2008.05.005.

Hall GEM, Vaive JE, Button P (1997), Detection of past underground nuclear events by geochemical signatures in soils, *Journal of Geochemical Exploration*, 59(3), 145–162. doi:10.1016/s0375-6742(97)00019-8.

Hanger BC (1979), The movement of calcium in plants, *Communications in Soil Science and Plant Analysis*, 10(1-2), 171–193. doi:10.1080/00103627909366887.

Hasenmueller EA, Gu X, Weitzman JN, Adams TS, Stinchcomb GE, Eissenstat DM, Drohan PJ, Brantley SL, Kaye JP (2017), Weathering of rock to regolith: The activity of deep roots in bedrock fractures, *Geoderma*, 300, 11–31. doi:10.1016/j.geoderma.2017.03.020.

Hattenschwiler S, Coq S, Barantal S, Handa IT (2011), Leaf traits and decomposition in tropical rainforests: revisiting some commonly held views and towards a new hypothesis, *New Phytol*, 189(4), 950–65, URL https://www.ncbi.nlm.nih.gov/pubmed/21374832. URL https://www.ncbi.nlm.nih.gov/pubmed/21374832, doi:10.1111/j.1469-8137.2010.03483.x.

He XT, Logan TJ, Traina SJ (1995), Physical and chemical characteristics of selected US municipal solid waste composts., *Journal of Environmental Quality*, 24, 543–552. doi:10.2134/jeq1995.00472425002400030022x.

Heartsill Scalley T, Scatena FN, Moya S, Lugo AE (2012), Long-term dynamics of organic matter and elements exported as coarse particulates from two Caribbean montane watersheds, *Journal of Tropical Ecology*, 28(2), 127–139. doi:10.1017/s0266467411000733.

Hedge CE, Walthall FG (1963), Radiogenic Strontium-87 as an Index of Geologic Processes, *Science*, 140(3572), 1214–7. doi:10.1126/science.140.3572.1214-a.

van der Heijden G, Legout A, Pollier B, Ranger J, Dambrine E (2014), The dynamics of calcium and magnesium inputs by throughfall in a forest ecosystem on base poor soil are very slow and conservative: evidence from an isotopic tracing experiment (26Mg and 44Ca), *Biogeochemistry*, 118(1-3), 413–442. doi:10.1007/s10533-013-9941-2.

van der Heijden MGA, Klironomos JN, Ursic M, Moutoglis P, Streitwolf-Engel R, Boller T, Wiemken A, Sanders IR (1998), Mycorrhizal fungal diversity determines plant biodiversity, ecosystem variability and productivity, *Nature*, 396(6706), 69–72. doi:10.1038/23932.

Heimsath AM, Dietrich WE, Nishiizumi K, Finkel RC (1997), The soil production function and landscape equilibrium, *Nature*, 388, 358–361. doi:10.1038/41056.

Hervé F (1977), *Petrology of the crystalline basement of the Nahuelbuta Mountains, south-central Chile*, Comparative studies on the Geology of the Circum-Pacific orogenic belt in Japan and Chile, Japan Society for the Promotion of Science.

Hervé F, Faundez V, Calderon M, Massonne HJ, Willner AP (2007), Metamorphic and plutonic basement complexes, in: T Moreno, W Gibbons (eds.), *The Geology of Chile*, chapter 2, The Geological Society, London.

Hervé F, Munizaga F, Mantovani M, Hervé M (1976), Edades Rb/Sr neopaleozoicas del basamento cristallino de la Cordillera de Nahuelbuta, *Primer Congresso Geologico Chileno*.

Hervé F, Munizaga F, Parada MA, Brook M, Pankhurst RJ, Snelling NJ, Drake R (1988), Granitoids of the Coast Range of central Chile: Geochronology and geologic setting, *Journal of South American Earth Sciences*, 1(2), 185–194.

Hewawasam T, von Blanckenburg F, Bouchez J, Dixon JL, Schuessler JA, Maekeler R (2013), Slow advance of the weathering front during deep, supply-limited saprolite formation in the tropical Highlands of Sri Lanka, *Geochimica et Cosmochimica Acta*, 118, 202–230. doi:10.1016/j.gca.2013.05.006.

Hilton RG (2017), Climate regulates the erosional carbon export from the terrestrial biosphere, *Geomorphology*, 277, 118–132. doi:10.1016/j.geomorph.2016.03.028.

Hulton NRJ, Purves RS, McCulloch RD, Sugden DE, Bentley MJ (2002), The Last Glacial Maximum and deglaciation in southern South America, *Quaternary Science Reviews*, 21(1-3), 233–241. doi:10.1016/s0277-3791(01)00103-2.

Ibarra DE, Caves JK, Moon S, Thomas DL, Hartmann J, Chamberlain CP, Maher K (2016), Differential weathering of basaltic and granitic catchments from concentration–discharge relationships, *Geochimica et Cosmochimica Acta*, 190, 265–293. doi:10.1016/j.gca.2016.07.006.

Ibarra DE, Rugenstein JKC, Bachan A, Baresch A, Lau KV, Thomas DL, Lee JE, Boyce CK, Chamberlain CP (2019), Modeling the consequences of land plant evolution on silicate weathering, *American Journal of Science*, 319(1), 1–43. doi:10.2475/01.2019.01.

Jacobson AD, Blum JD, Chamberlain CP, Poage MA, Sloan VF (2002), Ca/Sr and Sr isotope systematics of a Himalayan glacial chronosequence: carbonate versus silicate weathering rates as a function of landscape surface age, *Geochimica et Cosmochimica Acta*, 66(1), 13–27. doi:10.1016/s0016-7037(01)00755-4.

Jasechko S, Sharp ZD, Gibson JJ, Birks SJ, Yi Y, Fawcett PJ (2013), Terrestrial water fluxes dominated by transpiration, *Nature*, 496(7445), 347–50, URL `https://www.ncbi.nlm.nih.gov/pubmed/23552893`. URL `https://www.ncbi.nlm.nih.gov/pubmed/23552893`, doi:10.1038/nature11983.

Jobbágy EG, Jackson RB (2001), The distribution of soil nutrients with depth: global patterns and the imprint of plants, *Biogeochemistry*, 53, 51–77.

Jobbágy EG, Jackson RB (2004), The uplift of soil nutrients by plants: Biogeochemical consequences across scales., *Ecology*, 85(9), 2380–2389.

Johannsen A (1937), *A Descriptive Petrography of the Igneous Rocks*, volume 3 - The Intermediate Rocks, Taylor & Francis.

Johnson CM, Beard BL, Albarede F (2004), Overview and General Concepts, *Reviews in Mineralogy and Geochemistry*, 55(1), 1–24. doi:10.2138/gsrmg.55.1.1.

Jongmans AG, van Breemen N, Lundström U, van Hees PAW, Finlay RD, Srinivasan M, Unestam T, Giesler R, Melkerud PA, Olsson M (1997), Rock-eating fungi, *Nature*, 389(6652), 682–683. doi:10.1038/39493.

Joos O, Hagedorn F, Heim A, Gilgen AK, Schmidt MWI, Siegwolf RTW, Buchmann N (2010), Summer drought reduces total and litter-derived soil CO2 effluxes in temperate grassland – clues from a 13C litter addition experiment, *Biogeosciences*, 7(3), 1031–1041. doi:10.5194/bg-7-1031-2010.

Juez-Larré J, Kukowski N, Dunai TJ, Hartley AJ, Andriessen PAM (2010), Thermal and exhumation history of the Coastal Cordillera arc of northern Chile revealed by thermochronological dating, *Tectonophysics*, 495(1-2), 48–66. doi:10.1016/j.tecto.2010.06.018.

Jung M, Reichstein M, Margolis HA, Cescatti A, Richardson AD, Arain MA, Arneth A, Bernhofer C, Bonal D, Chen J, Gianelle D, Gobron N, Kiely G, Kutsch W, Lasslop G, Law BE, Lindroth A, Merbold L, Montagnani L, Moors EJ, Papale D, Sottocornola M, Vaccari F, Williams C (2011), Global patterns of land-atmosphere fluxes of carbon dioxide, latent heat, and sensible heat derived from eddy covariance, satellite, and meteorological observations, *Journal of Geophysical Research*, 116. doi:10.1029/2010jg001566.

Jungers MC, Heimsath AM, Amundson R, Balco G, Shuster D, Chong G (2013), Active erosion–deposition cycles in the hyperarid Atacama Desert of Northern Chile, *Earth and Planetary Science Letters*, 371-372, 125–133. doi:10.1016/j.epsl.2013.04.005.

Kalinowski BE, Liermann LJ, Givens S, Brantley SL (2000), Rates of bacteria-promoted solubilization of Fe from minerals: a review of problems and approaches, *Chemical Geology*, 169(3-4), 357–370. doi:10.1016/s0009-2541(00)00214-x.

Kelly AE, Goulden ML (2016), A montane Mediterranean climate supports year-round photosynthesis and high forest biomass, *Tree Physiol*, 36(4), 459–68, URL `https://www.ncbi.nlm.nih.gov/pubmed/26764269`. URL `https://www.ncbi.nlm.nih.gov/pubmed/26764269`, doi:10.1093/treephys/tpv131.

Kelly EF, Chadwick OA, Hilinski TE (1998), The effect of plants on mineral weathering, *Biogeochemistry*, 42(1/2), 21–53. doi:10.1023/a:1005919306687.

Khomo L, Bern CR, Hartshorn AS, Rogers KH, Chadwick OA (2013), Chemical transfers along slowly eroding catenas developed on granitic cratons in southern Africa, *Geoderma*, 202-203, 192–202. doi:10.1016/j.geoderma.2013.03.023.

Khomo L, Hartshorn AS, Rogers KH, Chadwick OA (2011), Impact of rainfall and topography on the distribution of clays and major cations in granitic catenas of southern Africa, *Catena*, 87(1), 119–128. doi:10.1016/j.catena.2011.05.017.

Khormali F, Ghergherechi S, Kehl M, Ayoubi S (2012), Soil formation in loess-derived soils along a subhumid to humid climate gradient, Northeastern Iran, *Geoderma*, 179-180, 113–122. doi:10.1016/j.geoderma.2012.02.002.

Kleidon A, Fraedrich K, Heimann M (2000), A Green Planet Versus a Desert World: Estimating the Maximum Effect of Vegetation on the Land Surface Climate, *Climatic Change*, 44(4), 471–493. doi:10.1023/a:1005559518889.

Kober F, Ivy-Ochs S, Schlunegger F, Baur H, Kubik PW, Wieler R (2007), Denudation rates and a topography-driven rainfall threshold in northern Chile: Multiple cosmogenic nuclide data and sediment yield budgets, *Geomorphology*, 83(1-2), 97–120. doi:10.1016/j.geomorph.2006.06.029.

Korschinek G, Bergmaier A, Faestermann T, Gerstmann UC, Knie K, Rugel G, Wallner A, Dillmann I, Dollinger G, von Gostomski CL, Kossert K, Maiti M, Poutivtsev M, Remmert A (2010), A new value for the half-life of 10Be by Heavy-Ion Elastic Recoil Detection and liquid scintillation counting, *Nuclear Instruments and Methods in Physics Research Section B: Beam Interactions with Materials and Atoms*, 268(2), 187–191. doi:10.1016/j.nimb.2009.09.020.

Krabbenhöft A, Eisenhauer A, Böhm F, Vollstaedt H, Fietzke J, Liebetrau V, Augustin N, Peucker-Ehrenbrink B, Müller MN, Horn C, Hansen BT, Nolte N, Wallmann K (2010), Constraining the marine strontium budget with natural strontium isotope fractionations (87Sr/86Sr*,$\delta^{88/86}$Sr) of carbonates, hydrothermal solutions and river waters, *Geochimica et Cosmochimica Acta*, 74(14), 4097–4109. doi:10.1016/j.gca.2010.04.009.

Krishnamurti GSR, Huang PM, Van Rees KCJ, Kozak LM, Rostad HPW (1995), Speciation of particulate-bound Cadmium of soils and its bioavailability, *The Analyst*, 120(3). doi:10.1039/an9952000659.

Kronzucker HJ, Britto DT (2011), Sodium transport in plants: a critical review, *New Phytol*, 189(1), 54–81, URL `https://www.ncbi.nlm.nih.gov/pubmed/21118256`. URL `https://www.ncbi.nlm.nih.gov/pubmed/21118256`, doi:10.1111/j.1469-8137.2010.03540.x.

Kumar A, Abouchami W, Galer SJG, Garrison VH, Williams E, Andreae MO (2014), A radiogenic isotope tracer study of transatlantic dust transport from Africa to the Caribbean, *Atmospheric Environment*, 82, 130–143. doi:10.1016/j.atmosenv.2013.10.021.

Kump LR, Brantley SL, Arthur MA (2000), Chemical Weathering, Atmospheric CO2, and Climate, *Annual Review of Earth and Planetary Sciences*, 28(1), 611–667. doi:10.1146/annurev.earth.28.1.611.

Lake JV, Bock GR (1997), Health impacts of large releases of radionuclides, in: *CIBA. Symposium*, 664.0288 L3.

Laliberte E, Grace JB, Huston MA, Lambers H, Teste FP, Turner BL, Wardle DA (2013), How does pedogenesis drive plant diversity?, *Trends Ecol Evol*, *28*(6), 331–40. doi:10.1016/j.tree.2013.02.008.

Lambers H, Brundrett MC, Raven JA, Hopper SD (2011), Plant mineral nutrition in ancient landscapes: high plant species diversity on infertile soils is linked to functional diversity for nutritional strategies, *Plant and Soil*, 348(1-2), 7–27. doi:10.1007/s11104-011-0977-6.

Lambers H, Nascimento DL, Oliveira RS, Shi J (2019), Do cluster roots of red alder play a role in nutrient acquisition from bedrock?, *Proc Natl Acad Sci U S A*, 116(24), 11575–11576, URL https://www.ncbi.nlm.nih.gov/pubmed/31164427. URL https://www.ncbi.nlm.nih.gov/pubmed/31164427, doi:10.1073/pnas.1905336116.

Lambers H, Raven JA, Shaver GR, Smith SE (2008), Plant nutrient-acquisition strategies change with soil age, *Trends Ecol Evol*, *23*(2), 95–103, URL https://www.ncbi.nlm.nih.gov/pubmed/18191280. URL https://www.ncbi.nlm.nih.gov/pubmed/18191280, doi:10.1016/j.tree.2007.10.008.

Landeweert R, Hoffland E, Finlay RD, Kuyper TW, van Breemen N (2001), Linking plants to rocks ectomycorrhizal fungi mobilize nutrients from minerals, *Trends in Ecology & Evolution*, 16(5), 248–254.

Lang F, Bauhus J, Frossard E, George E, Kaiser K, Kaupenjohann M, Krüger J, Matzner E, Polle A, Prietzel J, Rennenberg H, Wellbrock N (2016), Phosphorus in forest ecosystems: New insights from an ecosystem nutrition perspective, *Journal of Plant Nutrition and Soil Science*, 179(2), 129–135. doi:10.1002/jpln.201500541.

Lang F, Krüger J, Amelung W, Willbold S, Frossard E, Bünemann EK, Bauhus J, Nitschke R, Kandeler E, Marhan S, Schulz S, Bergkemper F, Schloter M, Luster J, Guggisberg F, Kaiser K, Mikutta R, Guggenberger G, Polle A, Pena R, Prietzel J, Rodionov A, Talkner U, Meesenburg H, von Wilpert K, Hölscher A, Dietrich HP, Chmara I (2017), Soil phosphorus supply controls P nutrition strategies of beech forest ecosystems in Central Europe, *Biogeochemistry*, 136(1), 5–29. doi:10.1007/s10533-017-0375-0.

Larrain H, Velásquez F, Cereceda P, Espejo R, Pinto R, Osses P, Schemenauer RS (2002), Fog measurements at the site "Falda Verde" north of Chañaral compared with other fog stations of Chile, *Atmospheric Research*, 64, 273–284. doi:10.1016/S0169-8095(02)00098-4.

Le Bas MJ, Le Maitre RW, Streckeisen AL, Zanettin B (1986), A Chemical Classification of Volcanic Rocks Based on the Total Alkali - Silica Diagram, *Journal of Petrology*, *27*(3), 745–750.

Lebedeva MI, Fletcher RC, Brantley SL (2010), A mathematical model for steady-state regolith production at constant erosion rate., *Earth Surface Processes and Landforms*, 35(5), 508–524.

Lee JE, Boyce K (2010), Impact of the hydraulic capacity of plants on water and carbon fluxes in tropical South America, *Journal of Geophysical Research*, 115(D23). doi:10.1029/2010jd014568.

Lenton TM, Crouch M, Johnson M, Pires N, Dolan L (2012), First plants cooled the Ordovician, *Nature Geoscience*, 5(2), 86–89. doi:10.1038/ngeo1390.

Liang Y, Sun W, Zhu YG, Christie P (2007), Mechanisms of silicon-mediated alleviation of abiotic stresses in higher plants: a review, *Environ Pollut*, 147(2), 422–8. doi:10.1016/j.envpol.2006.06.008.

Lifton NA, Sato T, Dunai TJ (2014), Scaling in situ cosmogenic nuclide production rates using analytical approximations to atmospheric cosmic-ray fluxes., *Earth and Planetary Science Letters*, 386, 149–160. doi:doi.org/10.1016/j.epsl.2013.10.052.

Lin H (2010a), Earth's Critical Zone and hydropedology: concepts, characteristics, and advances, *Hydrol. Earth Syst. Sci.*, 14(1), 25–45, URL https://www.hydrol-earth-syst-sci.net/14/25/2010/. URL https://www.hydrol-earth-syst-sci.net/14/25/2010/, doi:10.5194/hess-14-25-2010.

Lin H (2010b), Linking principles of soil formation and flow regimes, *Journal of Hydrology*, 393(1-2), 3–19. doi:10.1016/j.jhydrol.2010.02.013.

Lucas Y (2001), The Role of Plants in Controlling Rates and Products of Weathering: Importance of Biological Pumping, *Annual Review of Earth and Planetary Sciences*, 29(1), 135–163. doi:10.1146/annurev.earth.29.1.135.

Luebert F, Pliscoff P (2006), *Sinópsis bioclimática y vegetacional de Chile.*, Editorial Universitaria, Santiago de Chile.

Ma J, Wei G, Liu Y, Ren Z, Xu Y, Yang Y (2013), Precise measurement of stable ($\delta^{88/86}$Sr) and radiogenic (87Sr/86Sr) strontium isotope ratios in geological standard reference materials using MC-ICP-MS, *Chinese Science Bulletin*, 58(25), 3111–3118. doi:10.1007/s11434-013-5803-5.

Ma JF, Yamaji N (2008), Functions and transport of silicon in plants, *Cell Mol Life Sci*, 65(19), 3049–57, URL https://www.ncbi.nlm.nih.gov/pubmed/18560761. URL https://www.ncbi.nlm.nih.gov/pubmed/18560761, doi:10.1007/s00018-008-7580-x.

Ma L, Teng FZ, Jin L, Ke S, Yang W, Gu HO, Brantley SL (2015), Magnesium isotope fractionation during shale weathering in the Shale Hills Critical Zone Observatory: Accumulation of light Mg isotopes in soils by clay mineral transformation, *Chemical Geology*, 397, 37–50. doi:10.1016/j.chemgeo.2015.01.010.

Maher K (2010), The dependence of chemical weathering rates on fluid residence time, *Earth and Planetary Science Letters*, 294(1-2), 101–110. doi:10.1016/j.epsl.2010.03.010.

Maher K, Chamberlain CP (2014), Hydrologic regulation of chemical weathering and the geologic carbon cycle, *Science*, 343(6178), 1502–4. doi:10.1126/science.1250770.

Marrero SM, Phillips FM, Borchers B, Lifton N, Aumer R, Balco G (2016), Cosmogenic nuclide systematics and the CRONUScalc program, *Quaternary Geochronology*, 31, 160–187. doi:10.1016/j.quageo.2015.09.005.

Marschner H (1983), General introduction to the mineral nutrition of plants, *Inorganic plant nutrition*, 5–60.

Marschner H (1993), *Marschner's mineral nutrition of higher plants*, Elsevier, 2nd edition.

Marticorena C, Quezada M (1985), Catálogo de la flora vascular de Chile, *Gayana Botánica*, 42, 5–157.

Martin AR, Doraisami M, Thomas SC (2018), Global patterns in wood carbon concentration across the world's trees and forests, *Nature Geoscience*, 11(12), 915–920. doi:10.1038/s41561-018-0246-x.

McCulley RL, Jobbágy EG, Pockman WT, Jackson RB (2004), Nutrient uptake as a contributing explanation for deep rooting in arid and semi-arid ecosystems, *Oecologia*, 141(4), 620–8. doi:10.1007/s00442-004-1687-z.

Meek K, Derry L, Sparks J, Cathles L (2016), 87Sr/86Sr, Ca/Sr, and Ge/Si ratios as tracers of solute sources and biogeochemical cycling at a temperate forested shale catchment, central Pennsylvania, USA, *Chemical Geology*, 445, 84–102. doi:10.1016/j.chemgeo.2016.04.026.

Mehra OP, Jackson ML (1958), Iron oxide removal from soils and clays by a dithionite-citrate system buffered with sodium bicarbonate., in: *National conference on clays and clays minerals*, volume 7, 317–327.

Melnik D (2016), Rise of the central Andean coast by Earthquakes straddling the Moho., *Nature Geoscience*, 9, 401–407. doi:10.1038/ngeo2683.

Miller EK, Blum JD, Friedland AJ (1993), Determination of soil exchangeable-cation loss and weathering rates using Sr isotopes, *Nature*, 362(6419), 438–441. doi:10.1038/362438a0.

Minyard ML, Bruns MA, Liermann LJ, Buss HL, Brantley SL (2012), Bacterial Associations with Weathering Minerals at the Regolith-Bedrock Interface, Luquillo Experimental Forest, Puerto Rico, *Geomicrobiology Journal*, 29(9), 792–803. doi:10.1080/01490451.2011.619640.

Miralles González C (2013), Evaluación de los factores que controllan la geoquímica de sedimentos fluviales de la cuenca del Río Elqui, Región de Coquimbo, Chile.

Molina PG, Parada MA, Gutiérrez FJ, Ma C, Li J, Yuanyuan L, Reich M, Aravena Á (2015), Protracted late magmatic stage of the Caleu pluton (central Chile) as a consequence of heat redistribution by diking: Insights from zircon data and thermal modeling, *Lithos*, 227, 255–268. doi:10.1016/j.lithos.2015.04.008.

Mooney H, Gulmon S, Ehleringer JR, Rundel P (1980), Atmospheric Water Uptake by an Atacama Desert Shrub, *Science*, 209, 693–694.

Moore TR, Trofymow JA, Siltanen M, Prescott C, Group CW (2005), Patterns of decomposition and carbon, nitrogen, and phosphorus dynamics of litter in upland forest and peatland sites in central Canada, *Canadian Journal of Forest Research*, 35(1), 133–142. doi:10.1139/x04-149.

Moreira-Munoz A (2011), *Plant Geography of Chile*, Springer. doi:10.1007/978-90-481-8748-5.

Moreno H, Clavero Riebes J (2006), Geología del Volcán Villarrica - Regiones de La Araucanía y de Los Lagos., Map.

Moscoso R, Nasi C, Salinas P (1982), Hoja Vallenar y parte norte de La Serena: regiones de Atacama y Coquimbo: carta geológica de Chile 1: 250.000.

Moulton KL, West J, Berner RA (2000), Solute flux and mineral mass balance approaches to the quantification of plant effects on silicate weathering, *American Journal of Science*, 300(7), 539–570. doi:10.2475/ajs.300.7.539.

Moynier F, Agranier A, Hezel DC, Bouvier A (2010), Sr stable isotope composition of Earth, the Moon, Mars, Vesta and meteorites, *Earth and Planetary Science Letters*, 300(3-4), 359–366. doi:10.1016/j.epsl.2010.10.017.

Muyzer G, De Waal EC, Uitterlinden AG (1993), Profiling of complex microbial populations by denaturing gradient gel electrophoresis analysis of polymerase chain reaction-amplified genes coding for 16S rRNA, *Applied and Environmental Microbiology*, 59(3), 695–700.

Naranjo S J, Moreno R H (2005), Geología del Volcán Llaima, Región de La Araucanía, Escala: 1:50.000, Map, URL `http://repositoriodigitalonemi.cl/web/handle/2012/541`. URL `http://repositoriodigitalonemi.cl/web/handle/2012/541`.

Nesbitt HW, Young GM (1982), Early Proterozoic climates and plate motions inferred from major element chemistry of lutites, *Nature*, 299, 715–717.

Neymark LA, Premo WR, Emsbo P (2018), Combined radiogenic (87Sr/86Sr, 234U/238U) and stable (δ^{88}Sr) isotope systematics as tracers of anthropogenic groundwater contamination within the Williston BasinUSA, *Applied Geochemistry*, 96, 11–23. doi:10.1016/j.apgeochem.2018.06.006.

Neymark LA, Premo WR, Mel'nikov NN, Emsbo P (2014), Precise determination of δ^{88}Sr in rocks, minerals, and waters by double-spike TIMS: a powerful tool in the study of geological, hydrological and biological processes, *J. Anal. At. Spectrom.*, 29(1), 65–75. doi:10.1039/c3ja50310k.

Nier AO (1938), The Isotopic Constitution of Strontium, Barium, Bismuth, Thallium and Mercury, *Physical Review*, 54(4), 275–278. doi:10.1103/PhysRev.54.275.

Niklas KJ, Enquist BJ (2002), Canonical rules for plant organ biomass partitioning and annual allocation., *American Journal of Botany*, 89(5), 812–819.

Norton KP, von Blanckenburg F, DiBiase R, Schlunegger F, Kubik PW (2011), Cosmogenic 10Be-derived denudation rates of the Eastern and Southern European Alps, *International Journal of Earth Sciences*, 100(5), 1163–1179. doi:10.1007/s00531-010-0626-y.

Ministerio de Obras Públicas M. Información Oficial Hidrometeorológica y de Calidad de Aguas en Línea [online] (2017). URL `http://snia.dga.cl/BNAConsultas/reportes` [cited 2017-06-12].

Oelkers EH, Benning LG, Lutz S, Mavromatis V, Pearce CR, Plümper O (2015), The efficient long-term inhibition of forsterite dissolution by common soil bacteria and fungi at Earth surface conditions, *Geochimica et Cosmochimica Acta*, 168, 222–235. doi:10.1016/j.gca.2015.06.004.

Oelmann Y, Richter AK, Roscher C, Rosenkranz S, Temperton VM, Weisser WW, Wilcke W (2011), Does plant diversity influence phosphorus cycling in experimental grasslands?, *Geoderma*, 167-168, 178–187. doi:10.1016/j.geoderma.2011.09.012.

Oeser RA, von Blanckenburg F (2020a), Dataset for evaluation element fluxes released by weathering and taken up by plants along the EarthShape climate and vegetation gradient, Report, GFZ Data Services. doi:10.5880/GFZ.3.3.2020.003.

Oeser RA, von Blanckenburg F (2020b), Do degree and rate of silicate weathering depend on plant productivity?, accepted for review.

Oeser RA, Stroncik N, Moskwa LM, Bernhard N, Schaller M, Canessa R, van den Brink L, Köster M, Brucker E, Stock S, Fuentes JP, Godoy R, Matus FJ, Oses Pedraza R, Osses McIntyre P, Paulino L, Seguel O, Bader MY, Boy J, Dippold MA, Ehlers TA, Kühn P, Kuzyakov Y, Leinweber P, Scholten T, Spielvogel S, Spohn M, Übernickel K, Tielbörger K, Wagner D, von Blanckenburg F (2018a), Chemistry and Microbiology of the Critical Zone along a steep climate and vegetation gradient in the Chilean Coastal Cordillera., *Catena*, 170, 183–203. doi:10.1016/j.catena.2018.06.002.

Oeser RA, Stroncik N, Moskwa LM, Bernhard N, Schaller M, Canessa R, van den Brink L, Köster M, Brucker E, Stock S, Fuentes JP, Godoy R, Matus FJ, Oses Pedraza R, Osses McIntyre P, Paulino L, Seguel O, Bader MY, Boy J, Dippold MA, Ehlers TA, Kühn P, Kuzyakov Y, Leinweber P, Scholten T, Spielvogel S, Spohn M, Übernickel K, Tielbörger K, Wagner D, von Blanckenburg F (2018b), Data supplement to: Chemistry and Microbiology of the Critical Zone along a steep climate and vegetation gradient in the Chilean Coastal Cordillera. GFZ Data Services., GFZ Data Services. doi:10.5880/GFZ.3.3.2018.001.

Ohno T, Komiya T, Ueno Y, Hirata T, Maruyama S (2008), Determination of 88Sr/86Sr mass-dependent isotopic fractionation and radiogenic isotope variation of 87Sr/86Sr in the Neoproterozoic Doushantuo Formation, *Gondwana Research*, 14(1-2), 126–133. doi:10.1016/j.gr.2007.10.007.

Opfergelt S, Delvaux B, André L, Cardinal D (2008), Plant silicon isotopic signature might reflect soil weathering degree, *Biogeochemistry*, 91(2-3), 163–175. doi:10.1007/s10533-008-9278-4.

OriginPro (Version 2020), *OriginPro*, OriginLab Corporation, Northampton, MA, USA.

Owen JJ, Amundson R, Dietrich WE, Nishiizumi K, Sutter B, Chong G (2011), The sensitivity of hillslope bedrock erosion to precipitation, *Earth Surface Processes and Landforms*, 36(1), 117–135. doi:10.1002/esp.2083.

Pagani M, Caldeira K, Berner R, Beerling DJ (2009), The role of terrestrial plants in limiting atmospheric CO(2) decline over the past 24 million years, *Nature*, 460(7251), 85–8. doi:10.1038/nature08133.

Page BD, Bullen TD, Mitchell MJ (2008), Influences of calcium availability and tree species on Ca isotope fractionation in soil and vegetation, *Biogeochemistry*, 88(1), 1–13. doi:10.1007/s10533-008-9188-5.

Pankhurst RJ, Hervé F (2007), Introduction and overview, in: T Moreno, W Gibbons (eds.), *The Geology of Chile*, The Geological Society of London.

Parada M, Larrondo P (1999), Thermochronology of the Lower Cretaceous Caleu Pluton in the coastal range of central Chile: tectonostratigraphic implications, in: *Abstracts, 4th International Symposium of Andean Geodynamics, Göttingen*, 563–566.

Parada MA, Larrondo P, Guiresse C, Roperch P (2002), Magmatic Gradients in the Cretaceous Caleu Pluton (Central Chile): Injections of Pulses from a Stratified Magma Reservoir, *Gondwana Research*, 5(2), 307–324. doi:10.1016/s1342-937x(05)70725-5.

Parada MA, López-Escobar L, Oliveros V, Fuentes F, Morata D, Calderón M, Aguirre L, Féraud G, Espinoza F, Moreno H, Figueroa O, Muñoz Bravo J, Vásquez RT, Stern CR (2007), *Andean magmatism*, 115–146, The Geological Society of London. doi:10.1144/GOCH.4.

Parada MA, Nyström JO, Levi B (1999), Multiple sources for the Coastal Batholith of central Chile (31–34°S): geochemical and Sr–Nd isotopic evidence and tectonic implications, *Lithos*, 46(3), 505–521. doi:10.1016/s0024-4937(98)00080-2.

Parada MA, Rivano S, Sepulveda P, Herve M, Herve F, Puig A, Munizaga F, Brook M, Pankhurst R, Snelling N (1988), Mesozoic and cenozoic plutonic development in the Andes of central Chile (30°30′–32°30′S), *Journal of South American Earth Sciences*, 1(3), 249–260. doi:10.1016/0895-9811(88)90003-x.

Parfitt RL, Clayden B (1991), Andisols - the development of a new order in Soil Taxonomy, *Geoderma*, 49, 181–198.

Pawlik Ł (2013), The role of trees in the geomorphic system of forested hillslopes — A review, *Earth-Science Reviews*, 126, 250–265. doi:10.1016/j.earscirev.2013.08.007.

Pawlik Ł, Phillips JD, Šamonil P (2016), Roots, rock, and regolith: Biomechanical and biochemical weathering by trees and its impact on hillslopes—A critical literature review, *Earth-Science Reviews*, 159, 142–159. doi:10.1016/j.earscirev.2016.06.002.

Pearce CR, Parkinson IJ, Gaillardet J, Charlier BLA, Mokadem F, Burton KW (2015a), Reassessing the stable (δ88/86Sr) and radiogenic (87Sr/86Sr) strontium isotopic composition of marine inputs, *Geochimica et Cosmochimica Acta*, 157, 125–146. doi:10.1016/j.gca.2015.02.029.

Pearce CR, Parkinson IJ, Gaillardet J, Chetelat B, Burton KW (2015b), Characterising the stable (δ88/86 Sr) and radiogenic (87Sr/86Sr) isotopic composition of strontium in rainwater, *Chemical Geology*, 409, 54–60. doi:10.1016/j.chemgeo.2015.05.010.

Perez-Fodich A, Derry LA (2019), Organic acids and high soil CO2 drive intense chemical weathering of Hawaiian basalts: Insights from reactive transport models, *Geochimica et Cosmochimica Acta*, 249, 173–198. doi:10.1016/j.gca.2019.01.027.

Petit-Breuilh ME, Lobato J (1994), Análisis comparativo de la cronología eruptiva histórica de los volcanes Llaima y Villarrica (38°-39°L.S.)., in: *7"Congresso Geológico Chileno*, 366–370.

Pett-Ridge JC, Derry LA, Barrows JK (2009a), Ca/Sr and 87Sr/86Sr ratios as tracers of Ca and Sr cycling in the Rio Icacos watershed, Luquillo Mountains, Puerto Rico, *Chemical Geology*, 267(1-2), 32–45. doi:10.1016/j.chemgeo.2008.11.022.

Pett-Ridge JC, Derry LA, Kurtz AC (2009b), Sr isotopes as a tracer of weathering processes and dust inputs in a tropical granitoid watershed, Luquillo Mountains, Puerto Rico, *Geochimica et Cosmochimica Acta*, 73(1), 25–43. doi:10.1016/j.gca.2008.09.032.

Plug LJ, Gosse JC, McIntosh JJ, Bigley R (2007), Attenuation of cosmic ray flux in temperate forest, *Journal of Geophysical Research-Earth Surface*, 112(F2), 1–9. doi:10.1029/2006jf000668.

Pokharel R, Gerrits R, Schuessler JA, von Blanckenburg F (2019), Mechanisms of olivine dissolution by rock-inhabiting fungi explored using magnesium stable isotopes, *Chemical Geology*, 525, 18–27. doi:10.1016/j.chemgeo.2019.07.001.

Poorter H, Niklas KJ, Reich PB, Oleksyn J, Poot P, Mommer L (2012), Biomass allocation to leaves, stems and roots: meta-analyses of interspecific variation and environmental control, *New Phytol*, 193(1), 30–50, URL `https://www.ncbi.nlm.nih.gov/pubmed/22085245`. URL `https://www.ncbi.nlm.nih.gov/pubmed/22085245`, doi:10.1111/j.1469-8137.2011.03952.x.

Porada P, Lenton TM, Pohl A, Weber B, Mander L, Donnadieu Y, Beer C, Poschl U, Kleidon A (2016), High potential for weathering and climate effects of non-vascular vegetation in the Late Ordovician, *Nat Commun*, 7, 12113. doi:10.1038/ncomms12113.

Porder S (2019), How Plants Enhance Weathering and How Weathering is Important to Plants, *Elements*, 15(4), 241–246. doi:10.2138/gselements.15.4.241.

Porder S, Chadwick OA (2009), Climate and soil-age constraints on nutrient uplift and retention by plants, *Ecology*, 90(3), 623–636. doi:10.1890/07-1739.1.

Porder S, Vitousek PM, Chadwick OA, Chamberlain CP, Hilley GE (2007), Uplift, Erosion, and Phosphorus Limitation in Terrestrial Ecosystems, *Ecosystems*, 10(1), 159–171. doi:10.1007/s10021-006-9011-x.

Poszwa A, Dambrine E, Ferry B, Pollier B, Loubet M (2002), Do deep tree roots provide nutrients to the tropical rainforest, *Biogeochemistry*, 60, 97–118.

Poszwa A, Dambrine E, Pollier B (2000), A comparison between Ca and Sr cycling in forest ecosystems, *Plant and Soil*, 225(1/2), 299–310. doi:10.1023/A:1026570812307.

Powers JS, Becklund KK, Gei MG, Iyengar SB, Meyer R, O'Connell CS, Schilling EM, Smith CM, Waring BG, Werden LK (2015), Nutrient addition effects on tropical dry forests: a mini-review from microbial to ecosystem scales, *Frontiers in Earth Science*, 3. doi:10.3389/feart.2015.00034.

Quirk J, Andrews MY, Leake JR, Banwart SA, Beerling DJ (2014), Ectomycorrhizal fungi and past high CO2 atmospheres enhance mineral weathering through increased below-ground carbon-energy fluxes., *Biology Letters*, 10(7).

Quirk J, Beerling DJ, Banwart SA, Kakonyi G, Romero-Gonzalez ME, Leake JR (2012), Evolution of trees and mycorrhizal fungi intensifies silicate mineral weathering, *Biology Letters*, 8(6), 1006–11, URL `https://www.ncbi.nlm.nih.gov/pubmed/22859556`. URL `https://www.ncbi.nlm.nih.gov/pubmed/22859556`, doi:10.1098/rsbl.2012.0503.

Raddatz J, Liebetrau V, Rüggeberg A, Hathorne E, Krabbenhöft A, Eisenhauer A, Böhm F, Vollstaedt H, Fietzke J, López Correa M, Freiwald A, Dullo WC (2013), Stable Sr-isotope, Sr/Ca, Mg/Ca, Li/Ca and Mg/Li ratios in the scleractinian cold-water coral Lophelia pertusa, *Chemical Geology*, 352, 143–152. doi:10.1016/j.chemgeo.2013.06.013.

Rauret G, López-Sánchez JF, Sahuquillo A, Rubio R, Davidson CM, Ure AM, Quevauviller P (1999), Improvement of the BCR three step sequential extraction procedure prior to the certification of new sediment and soil reference materials, *J. Environ. Monit.*, 1, 57–61.

Rempe DM, Dietrich WE (2018), Direct observations of rock moisture, a hidden component of the hydrologic cycle, *Proceedings of the National Academy of Sciences*. doi:10.1073/pnas.1800141115.

Reynolds AC, Quade J, Betancourt JL (2012), Strontium isotopes and nutrient sourcing in a semi-arid woodland, *Geoderma*, 189-190, 574–584. doi:10.1016/j.geoderma.2012.06.029.

Richter DD, Markewitz D (1995), How deep is soil?, *BioScience*, 45(9), 600–609.

Riebe CS, Granger DE (2013), Quantifying effects of deep and near-surface chemical erosion on cosmogenic nuclides in soils, saprolite, and sediment, *Earth Surface Processes and Landforms*, 38(5), 523–533. doi:10.1002/esp.3339.

Riebe CS, Hahm WJ, Brantley SL (2016), Controls on deep critical zone architecture: a historical review and four testable hypotheses, *Earth Surface Processes and Landforms*. doi:10.1002/esp.4052.

Riebe CS, Kirchner JW, Finkel RC (2003), Long-term rates of chemical weathering and physical erosion from cosmogenic nuclides and geochemical mass balance, *Geochimica et Cosmochimica Acta*, 67(22), 4411–4427. doi:10.1016/s0016-7037(03)00382-x.

Riebe CS, Kirchner JW, Finkel RC (2004), Erosional and climatic effects on long-term chemical weathering rates in granitic landscapes spanning diverse climate regimes, *Earth and Planetary Science Letters*, 224, 547–562.

Riebe CS, Kirchner JW, Granger DE, Finkel RC (2001), Strong tectonic and weak climatic control of long-term chemical weathering rates, *Geology*, 29(6), 511–514. doi:10.1130/0091-7613.

Riquelme R, Martinod J, Hérail G, Darrozes J, Charrier R (2003), A geomorphological approach to determining the Neogene to Recent tectonic deformation in the Coastal Cordillera of northern Chile (Atacama)., *Tectonophysics*, 361(3-4), 255–275.

Roering JJ, Marshall J, Booth AM, Mort M, Jin Q (2010), Evidence for biotic controls on topography and soil production, *Earth and Planetary Science Letters*, 298(1-2), 183–190. doi:10.1016/j.epsl.2010.07.040.

Rüggeberg A, Fietzke J, Liebetrau V, Eisenhauer A, Dullo WC, Freiwald A (2008), Stable strontium isotopes (δ88/86Sr) in cold-water corals – A new proxy for reconstruction of intermediate ocean water temperatures, *Earth and Planetary Science Letters*, 269(3-4), 570–575. doi:10.1016/j.epsl.2008.03.002.

Rundel PW, Ehleringer J, Mooney HA, Gulmon SL (1980), Patterns of drought response in leaf-succulent shrubs of the coastal Atacama Desert in Northern Chile, *Oecologia*, 46(2), 196–200, URL `https://www.ncbi.nlm.nih.gov/pubmed/28309673`. URL `https://www.ncbi.nlm.nih.gov/pubmed/28309673`, doi:10.1007/BF00540126.

Rundel PW, Villagra P, Dillon M, Roig-Junent S (2007), Arid and semi-arid ecosystems, in: T Veblen, K Young, A Orme (eds.), *The physical geography of South America*, 158–183, Oxford Univ. Press, New York.

Rundel PW, Weisser PJ (1975), La Campana, a new national park in central Chile, *Biological Conservation*, 8(1), 35–46. doi:10.1016/0006-3207(75)90077-4.

Ryu JS, Jacobson AD, Holmden C, Lundstrom C, Zhang Z (2011), The major ion, $\delta^{44/40}$Ca, $\delta^{44/42}$Ca, and $\delta^{26/24}$Mg geochemistry of granite weathering at pH=1 and T=25°C: power-law processes and the relative reactivity of minerals, *Geochimica et Cosmochimica Acta*, 75(20), 6004–6026. doi:10.1016/j.gca.2011.07.025.

Scatena FN, Lugo AE (1995), Geomorphology, disturbance, and the soil and vegetation of two subtropical wet steepland watersheds of Puerto Rico, *Geomorphology*, 13(1-4), 199–213. doi:10.1016/0169-555x(95)00021-v.

Schaller J, Turner BL, Weissflog A, Pino D, Bielnicka AW, Engelbrecht BMJ (2018a), Silicon in tropical forests: large variation across soils and leaves suggests ecological significance, *Biogeochemistry*, 140(2), 161–174. doi:10.1007/s10533-018-0483-5.

Schaller M, Ehlers TA, Lang KAH, Schmid M, Fuentes-Espoz JP (2018b), Addressing the contribution of climate and vegetation cover on hillslope denudation, Chilean Coastal Cordillera (26°–38°S), *Earth and Planetary Science Letters*, 489, 111–122. doi:10.1016/j.epsl.2018.02.026.

Scheuvens D, Schütz L, Kandler K, Ebert M, Weinbruch S (2013), Bulk composition of northern African dust and its source sediments — A compilation, *Earth-Science Reviews*, 116, 170–194. doi:10.1016/j.earscirev.2012.08.005.

Schmithüsen J (1956), Die räumliche Ordnung der chilenischen Vegetation, *Bonn Geogr Abh*, 17, 1–86.

Schmitt AD, Vigier N, Lemarchand D, Millot R, Stille P, Chabaux F (2012), Processes controlling the stable isotope compositions of Li, B, Mg and Ca in plants, soils and waters: A review, *Comptes Rendus Geoscience*, 344(11-12), 704–722. doi:10.1016/j.crte.2012.10.002.

van Scholl L, Hoffland E, van Breemen N (2006a), Organic anion exudation by ectomycorrhizal fungi and Pinus sylvestris in response to nutrient deficiencies, *New Phytologist*, 170(1), 153–63, URL https://www.ncbi.nlm.nih.gov/pubmed/16539612. URL https://www.ncbi.nlm.nih.gov/pubmed/16539612, doi:10.1111/j.1469-8137.2006.01649.x.

van Schöll L, Kuyper TW, Smits MM, Landeweert R, Hoffland E, Breemen Nv (2007), Rock-eating mycorrhizas: their role in plant nutrition and biogeochemical cycles, *Plant and Soil*, 303(1-2), 35–47. doi:10.1007/s11104-007-9513-0.

van Scholl L, Smits MM, Hoffland E (2006b), Ectomycorrhizal weathering of the soil minerals muscovite and hornblende, *New Phytologist*, 171(4), 805–13, URL https://www.ncbi.nlm.nih.gov/pubmed/16918551. URL https://www.ncbi.nlm.nih.gov/pubmed/16918551, doi:10.1111/j.1469-8137.2006.01790.x.

Scholten T (1997), Hydrology and erodibility of the soils and saprolite cover of the Swaziland Middleveld, *Soil Technology*, 247–262.

Schoonejans J, Vanacker V, Opfergelt S, Ameijeiras-Mariño Y, Christl M (2016), Kinetically limited weathering at low denudation rates in semiarid climatic conditions, *Journal of Geophysical Research: Earth Surface*, 121(2), 336–350. doi:10.1002/2015jf003626.

Schuessler JA, von Blanckenburg F, Bouchez J, Uhlig D, Hewawasam T (2018), Nutrient cycling in a tropical montane rainforest under a supply-limited weathering regime traced

by elemental mass balances and Mg stable isotopes, *Chemical Geology*, 497, 74–87. doi:10.1016/j.chemgeo.2018.08.024.

Schuessler JA, Kämpf H, Koch U, Alawi M (2016), Earthquake impact on iron isotope signatures recorded in mineral spring water, *Journal of Geophysical Research: Solid Earth*, 121, 1–21. doi:10.1002/2016JB013408.

Schutz K, Kandeler E, Nagel P, Scheu S, Ruess L (2010), Functional microbial community response to nutrient pulses by artificial groundwater recharge practice in surface soils and subsoils, *FEMS Microbiology Ecology*, 72(3), 445–55, URL https://www.ncbi.nlm.nih.gov/pubmed/20557572. URL https://www.ncbi.nlm.nih.gov/pubmed/20557572, doi:10.1111/j.1574-6941.2010.00855.x.

Schwartzman D. The Geobiology of Weathering: a 13th Hypothesis [online] (2015). URL https://arxiv.org/pdf/1509.04234.pdf.

Schwertmann U (1964), Differenzierung der Eisenoxide des Bodens durch Extraktion mit Ammoniumoxalat-Lösung., *Journal of Plant Nutrition and Soil Science*, 105(3), 194–202.

Schwertmann U (1985), *The Effect of Pedogenic Environments on Iron Oxide Minerals.*, volume 1, 171–200, Springer, New York.

Scott KM, Pain CF (2008), *Regolith Science*, Springer, URL https://books.google.de/books?id=xBF0AQAAIAAJ. URL https://books.google.de/books?id=xBF0AQAAIAAJ.

SERNAGEOMIN (2003), Mapa Geológico de Chile: versión digital., Map.

Shalev N, Lazar B, Halicz L, Stein M, Gavrieli I, Sandler A, Segal I (2013), Strontium Isotope Fractionation in Soils and Pedogenic Processes, *Procedia Earth and Planetary Science*, 7, 790–793. doi:10.1016/j.proeps.2013.03.074.

Shand P, Darbyshire DPF, Love AJ, Edmunds WM (2009), Sr isotopes in natural waters: Applications to source characterisation and water–rock interaction in contrasting landscapes, *Applied Geochemistry*, 24(4), 574–586. doi:10.1016/j.apgeochem.2008.12.011.

Silver WL, Miya RK (2001), Global patterns in root decomposition: comparisons of climate and litter quality effects, *Oecologia*, 129(3), 407–419, URL https://www.ncbi.nlm.nih.gov/pubmed/28547196. URL https://www.ncbi.nlm.nih.gov/pubmed/28547196, doi:10.1007/s004420100740.

Smeck NE, Runge E, Mackintosh E (1983), *Dynamics and genetic modeling of soil systems.*, 51 – 81, Elsevier.

Smits MM, Bonneville S, Benning LG, Banwart SA, Leake JR (2012), Plant-driven weathering of apatite - the role of an ectomycorrhizal fungus., *Geobiology*, 10(5), 445–456.

Sohrt J, Uhlig D, Kaiser K, von Blanckenburg F, Siemens J, Seeger S, Frick DA, Krüger J, Lang F, Weiler M (2019), Phosphorus Fluxes in a Temperate Forested Watershed: Canopy Leaching, Runoff Sources, and In-Stream Transformation, *Frontiers in Forests and Global Change*, 2. doi:10.3389/ffgc.2019.00085.

Sommer M, Jochheim H, Höhn A, Breuer J, Zagorski Z, Busse J, Barkusky D, Meier K, Puppe D, Wanner M, Kaczorek D (2013), Si cycling in a forest biogeosystem & the importance of transient state biogenic Si pools, *Biogeosciences*, 10(7), 4991–5007. doi:10.5194/bg-10-4991-2013.

de Souza GF, Reynolds BC, Kiczka M, Bourdon B (2010), Evidence for mass-dependent isotopic fractionation of strontium in a glaciated granitic watershed, *Geochimica et Cosmochimica Acta*, 74(9), 2596–2614, URL <GotoISI>://WOS:000276493900005. URL <GotoISI>://WOS:000276493900005, doi:10.1016/j.gca.2010.02.012.

Spohn M, Sierra CA (2018), How long do elements cycle in terrestrial ecosystems?, *Biogeochemistry*, 139(1), 69–83. doi:10.1007/s10533-018-0452-z.

Sprenger M, Stumpp C, Weiler M, Aeschbach W, Allen ST, Benettin P, Dubbert M, Hartmann A, Hrachowitz M, Kirchner JW, McDonnell JJ, Orlowski N, Penna D, Pfahl S, Rinderer M, Rodriguez N, Schmidt M, Werner C (2019), The Demographics of Water: A Review of Water Ages in the Critical Zone, *Reviews of Geophysics*, 57(3), 800–834. doi:10.1029/2018rg000633.

Staff SS (1999), *Soil Taxonomy. A basic system of soil classification for making and interpreting soil surveys.*, volume Handbook 210, USDA Natural Resources Conservation Service, Washington, 870 pp.

Starke E, Ehlers TA, Schaller M (2017), Tectonic and Climatic Controls on the Spatial Distribution of Denudation Rates in Northern Chile (18°S to 23 °S) Determined From Cosmogenic Nuclides., *Journal of Geophysical Research: Earth Surface*, 122. doi:10.1002/2016JF004153.

Sterner RW, Elser JJ (2003), *Ecological Stoichiometry: The Biology of Elements from Molecules to the Biosphere*, Princeton University Press.

Stevenson EI, Aciego SM, Chutcharavan P, Parkinson IJ, Burton KW, Blakowski MA, Arendt CA (2016), Insights into combined radiogenic and stable strontium isotopes as tracers for weathering processes in subglacial environments, *Chemical Geology*, 429, 33–43. doi:10.1016/j.chemgeo.2016.03.008.

Stevenson EI, Hermoso M, Rickaby REM, Tyler JJ, Minoletti F, Parkinson IJ, Mokadem F, Burton KW (2014), Controls on stable strontium isotope fractionation in coccolithophores with

implications for the marine Sr cycle, *Geochimica et Cosmochimica Acta*, 128, 225–235. doi:10.1016/j.gca.2013.11.043.

Stewart BW, Capo RC, Chadwick OA (1998), Quantitative strontium isotope models for weathering, pedogenesis and biogeochemical cycling, *Geoderma*, 82(1-3), 173–195. doi:10.1016/s0016-7061(97)00101-8.

Stone M, Droppo IG (1996), Distribution of lead, copper and zinc in size-fractionated river bed sediment in two agricultural catchments of southern Ontario, Canada, *Environmental Pollution*, 93(3), 353–362. doi:10.1016/s0269-7491(96)00038-3.

Streckeisen AL, LeMaitre RW (1979), Chemical approximation to modal QAPF classification of the igneous rocks., *Neues Jahrbuch für Mineralogie*, 136, 169–206.

Tamm O (1922), Method for the estimation of the inorganic components of the gel-complex in soils., *Medd Statens Skogsförsöksanst.*, 19, 385–404.

Taylor HP (1980), The effects of assimilation of country rocks by magmas on 18O/16O and 87Sr/86Sr systematics in igneous rocks, *Earth and Planetary Science Letters*, 47(2), 243–254. doi:10.1016/0012-821x(80)90040-0.

Taylor SR, McLennan SM (1995), The geochemical evolution of the continental crust., *Reviews of Geophysics*, 33, 241–265. doi:10.1029/95RG00262.

Tchakerian V, Pease P (2015), *The Critical Zone in Desert Environments*, 449–472, Developments in Earth Surface Processes, Elsevier. doi:10.1016/b978-0-444-63369-9.00014-8.

Tessier A, Campbell PGC, Bisson M (1979), Sequential Extraction Procedure for the Speciation of Particulate Trace Metals, *Analytical Chemistry*, 51(7), 844–851.

Tielbörger K, Bilton MC, Metz J, Kigel J, Holzapfel C, Lebrija-Trejos E, Konsens I, Parag HA, Sternberg M (2014), Middle-Eastern plant communities tolerate 9 years of drought in a multi-site climate manipulation experiment, *Nature Communications*, 5(1). doi:10.1038/ncomms6102.

Tiessen H, Moir J (1993), *Characterization of available P by sequential extraction*, volume 7, chapter 25, 5–229, Lewis Publishers Boca Raton, FL, USA.

Tipping E, Woof C, Rigg E, Harrison A, Ineson P, Taylor K, Benham D, Poskitt J, Rowland A, Bol R (1999), Climatic influences on the leaching of dissolved organic matter from upland UK moorland soils, investigated by a field manipulation experiment, *Environment International*, 25(1), 83–95. doi:10.1016/s0160-4120(98)00098-1.

Trostle KD, Ray Runyon J, Pohlmann MA, Redfield SE, Pelletier J, McIntosh J, Chorover J (2016), Colloids and organic matter complexation control trace metal concentration-discharge relationships in Marshall Gulch stream waters, *Water Resources Research*, 52(10), 7931–7944. doi:10.1002/2016wr019072.

Turner BL, Brenes-Arguedas T, Condit R (2018), Pervasive phosphorus limitation of tree species but not communities in tropical forests, *Nature*, 555(7696), 367–370, URL https://www.ncbi.nlm.nih.gov/pubmed/29513656. URL https://www.ncbi.nlm.nih.gov/pubmed/29513656, doi:10.1038/nature25789.

Uhlig D, von Blanckenburg F (2019), How slow rock weathering balances nutrient loss during fast forest floor turnover in montane, temperate forest ecosystems., *Frontiers in Earth Science*.

Uhlig D, Schuessler JA, Bouchez JL, Dixon JL, von Blanckenburg F (2017), Quantifying nutrient uptake as driver of rock weathering in forest ecosystems by magnesium stable isotopes, *Biogeosciences Discussions*, 1–28. doi:10.5194/bg-2016-521.

Uroz S, Calvaruso C, Turpault MP, Frey-Klett P (2009), Mineral weathering by bacteria: ecology, actors and mechanisms, *Trends Microbiol*, 17(8), 378–87, URL https://www.ncbi.nlm.nih.gov/pubmed/19660952. URL https://www.ncbi.nlm.nih.gov/pubmed/19660952, doi:10.1016/j.tim.2009.05.004.

Uroz S, Oger P, Lepleux C, Collignon C, Frey-Klett P, Turpault MP (2011), Bacterial weathering and its contribution to nutrient cycling in temperate forest ecosystems, *Res Microbiol*, 162(9), 820–31, URL https://www.ncbi.nlm.nih.gov/pubmed/21315149. URL https://www.ncbi.nlm.nih.gov/pubmed/21315149, doi:10.1016/j.resmic.2011.01.013.

Vázquez M, Ramírez S, Morata D, Reich M, Braun JJ, Carretier S (2016), Regolith production and chemical weathering of granitic rocks in central Chile, *Chemical Geology*, 446, 87–98. doi:10.1016/j.chemgeo.2016.09.023.

Villa IM, De Bièvre P, Holden NE, Renne PR (2015), IUPAC-IUGS recommendation on the half life of 87 Rb, *Geochimica et Cosmochimica Acta*, 164, 382–385. doi:10.1016/j.gca.2015.05.025.

Vitousek P, Chadwick O, Matson P, Allison S, Derry L, Kettley L, Luers A, Mecking E, Monastra V, Porder S (2003), Erosion and the Rejuvenation of Weathering-derived Nutrient Supply in an Old Tropical Landscape, *Ecosystems*, 6(8), 762–772. doi:10.1007/s10021-003-0199-8.

Vitousek PM (2004), *Nutrient Cycling and Limitation: Hawai'i as a Model System*, PRINCETON ENVIRONMENT AL INSTITUTE SERIES, Princeton University Press.

Vitousek PM, Chadwick OA (2013), Pedogenic Thresholds and Soil Process Domains in Basalt-Derived Soils, *Ecosystems*, 16(8), 1379–1395. doi:10.1007/s10021-013-9690-z.

Vitousek PM, Farrington H (1997), Nutrient limitation and soil development: Experimental test of a biogeochemical theory, *Biogeochemistry*, 37(1), 63–75. doi:10.1023/a:1005757218475.

Vitousek PM, Hedin LO, Matson PA, Fownes JH, Neff J (1998), *Within-System Element Cycles, Input-Output Budgets, and Nutrient Limitation*, book section Chapter 18, 432–451, Springer, New York. doi:10.1007/978-1-4612-1724-4_18.

Vitousek PM, Porder S, Houlton BZ, Chadwick OA (2010), Terrestrial phosphorus limitation: mechanisms, implications, and nitrogen–phosphorus interactions, *Ecological Applications*, 20(1), 5–15. doi:10.1890/08-0127.1.

Vitousek PM, Reiners WA (1975), Ecosystem Succession and Nutrient Retention: A Hypothesis, *BioScience*, 25(6), 376–381. doi:10.2307/1297148.

Wada K (1989), *Allophane and Imogolite*, 1051–1087, Soil Science Society of America Book Series, Soil Science Society of America Inc.(SSSA), 2 edition.

Wei G, Ma J, Liu Y, Xie L, Lu W, Deng W, Ren Z, Zeng T, Yang Y (2013), Seasonal changes in the radiogenic and stable strontium isotopic composition of Xijiang River water: Implications for chemical weathering, *Chemical Geology*, 343, 67–75. doi:10.1016/j.chemgeo.2013.02.004.

Weis D, Kieffer B, Maerschalk C, Barling J, de Jong J, Williams GA, Hanano D, Pretorius W, Mattielli N, Scoates JS, Goolaerts A, Friedman RM, Mahoney JB (2006), High-precision isotopic characterization of USGS reference materials by TIMS and MC-ICP-MS, *Geochemistry, Geophysics, Geosystems*, 7(8), n/a–n/a. doi:10.1029/2006gc001283.

Weiss DJ, Mason TF, Zhao FJ, Kirk GJ, Coles BJ, Horstwood MS (2005), Isotopic discrimination of zinc in higher plants, *New Phytol*, 165(3), 703–10, URL `https://www.ncbi.nlm.nih.gov/pubmed/15720681`. URL `https://www.ncbi.nlm.nih.gov/pubmed/15720681`, doi:10.1111/j.1469-8137.2004.01307.x.

Werner C, Schmid M, Ehlers TA, Fuentes-Espoz JP, Steinkamp J, Forrest M, Liakka J, Maldonado A, Hickler T (2018), Effect of changing vegetation and precipitation on denudation – Part 1: Predicted vegetation composition and cover over the last 21 thousand years along the Coastal Cordillera of Chile, *Earth Surface Dynamics*, 6(4), 829–858. doi:10.5194/esurf-6-829-2018.

West A, Galy A, Bickle M (2005), Tectonic and climatic controls on silicate weathering, *Earth and Planetary Science Letters*, 235(1-2), 211–228. doi:10.1016/j.epsl.2005.03.020.

White AF (2002), Determining mineral weathering rates based on solid and solute weathering gradients and velocities: application to biotite weathering in saprolites, *Chemical Geology*, 190(1-4), 69–89. doi:10.1016/s0009-2541(02)00111-0.

White AF, Blum AE, Schulz MS, Vivit DV, Stonestrom DA, Larsen M, Murphy SF, Eberl D (1998), Chemical Weathering in a Tropical Watershed, Luquillo Mountains, Puerto Rico: I. Long-Term Versus Short-Term Weathering Fluxes, *Geochimica et Cosmochimica Acta*, 62(2), 209–226. doi:10.1016/s0016-7037(97)00335-9.

White AF, Brantley SL (2003), The effect of time on the weathering of silicate minerals: why do weathering rates differ in the laboratory and field?, *Chemical Geology*, 202(3-4), 479–506. doi:10.1016/j.chemgeo.2003.03.001.

Widanagamage IH, Griffith EM, Singer DM, Scher HD, Buckley WP, Senko JM (2015), Controls on stable Sr-isotope fractionation in continental barite, *Chemical Geology*, 411, 215–227. doi:10.1016/j.chemgeo.2015.07.011.

Widanagamage IH, Schauble EA, Scher HD, Griffith EM (2014), Stable strontium isotope fractionation in synthetic barite, *Geochimica et Cosmochimica Acta*, 147, 58–75. doi:10.1016/j.gca.2014.10.004.

Wiegand BA (2005), Ca cycling and isotopic fluxes in forested ecosystems in Hawaii, *Geophysical Research Letters*, 32(11). doi:10.1029/2005gl022746.

Wilcke W, Velescu A, Leimer S, Bigalke M, Boy J, Valarezo C (2017), Biological versus geochemical control and environmental change drivers of the base metal budgets of a tropical montane forest in Ecuador during 15 years, *Biogeochemistry*, 136(2), 167–189. doi:10.1007/s10533-017-0386-x.

Wilcke W, Yasin S, Abramowski U, Valarezo C, Zech W (2002), Nutrient storage and turnover in organic layers under tropical montane rain forest in Ecuador, *European Journal of Soil Science*, 53, 15–27.

Will C, Thurmer A, Wollherr A, Nacke H, Herold N, Schrumpf M, Gutknecht J, Wubet T, Buscot F, Daniel R (2010), Horizon-specific bacterial community composition of German grassland soils, as revealed by pyrosequencing-based analysis of 16S rRNA genes, *Appl Environ Microbiol*, 76(20), 6751–9, URL `https://www.ncbi.nlm.nih.gov/pubmed/20729324`. URL `https://www.ncbi.nlm.nih.gov/pubmed/20729324`, doi:10.1128/AEM.01063-10.

Wimpenny J, Gíslason SR, James RH, Gannoun A, Pogge Von Strandmann PAE, Burton KW (2010), The behaviour of Li and Mg isotopes during primary phase dissolution and secondary mineral formation in basalt, *Geochimica et Cosmochimica Acta*, 74(18), 5259–5279. doi:10.1016/j.gca.2010.06.028.

Winnick MJ, Maher K (2018), Relationships between CO_2, thermodynamic limits on silicate weathering, and the strength of the silicate weathering feedback, *Earth and Planetary Science Letters*, 485, 111 – 120. doi:10.1016/j.epsl.2018.01.005.

Wittmann H, von Blanckenburg F, Guyot JL, Laraque A, Bernal C, Kubik PW (2011), Sediment production and transport from in situ-produced cosmogenic 10Be and river loads in the Napo River basin, an upper Amazon tributary of Ecuador and Peru, *Journal of South American Earth Sciences*, 31(1), 45–53. doi:10.1016/j.jsames.2010.09.004.

Wittmann H, Oelze M, Gaillardet J, Garzanti E, von Blanckenburg F (2020), A global rate of denudation from cosmogenic nuclides in the Earth's largest rivers, *Earth-Science Reviews*. doi:10.1016/j.earscirev.2020.103147.

Wohl E, Dwire K, Sutfin N, Polvi L, Bazan R (2012), Mechanisms of carbon storage in mountainous headwater rivers, *Nat Commun*, 3, 1263, URL `https://www.ncbi.nlm.nih.gov/pubmed/23232393`. URL `https://www.ncbi.nlm.nih.gov/pubmed/23232393`, doi:10.1038/ncomms2274.

Zamanian K, Pustovoytov K, Kuzyakov Y (2016), Pedogenic carbonates: Forms and formation processes, *Earth-Science Reviews*, 157, 1–17. doi:10.1016/j.earscirev.2016.03.003.

Zhao W, Balsam W, Williams E, Long X, Ji J (2018), Sr–Nd–Hf isotopic fingerprinting of transatlantic dust derived from North Africa, *Earth and Planetary Science Letters*, 486, 23–31. doi:10.1016/j.epsl.2018.01.004.

Zirkler D, Lang F, Kaupenjohann M (2012), "Lost in filtration"—The separation of soil colloids from larger particles, *Colloids and Surfaces A: Physicochemical and Engineering Aspects*, 399, 35–40. doi:10.1016/j.colsurfa.2012.02.021.

Zvyagintsev D (1994), *Vertical Distribution of microbial communities in soils.*, 29–37, Wiley, West Sussex, UK.